Chapter 7

A steradian of the southern sky at 151.5 MHz

Never let go of hope,
One day you will see that it all has finally come together,
What you have always wished for has finally come to be,
You will look back and laugh at what has passed,
and you will ask yourself,
"How did I get through all of that?"
Just never let go of hope,
Just never quit dreaming,
and never let love depart from your life.
- Jancarl Campi

7.1 Introduction

The outline of the MRT survey, its motivation, techniques developed and used for data processing have been discussed in the earlier chapters. In this chapter, we present the final images in the form of a set of overlapping contour maps in the (RA, $\sin(za)$) coordinates (J2000). The overall quality of the images would be discussed including their quantitative analysis. This is followed by an accompanying source list providing the positions and the flux densities of nearly 2,800 discrete radio sources.

In the first part of this chapter, we discuss various steps involved in the flux density calibration of the images. The images covering different sidereal hours (both dirty as well as deconvolved) are in arbitrary units and are not on the same flux density scale. We describe the method employed to bring them to a common scale and discuss the internal consistency of the measured flux densities and positions of unresolved sources. We then discuss the estimation of the primary beam of the helix. We then describe the procedure used to recover the amplitude information of the signal lost in a 2-bit 3-level correlator with an AGC. This is followed by a discussion on our choice of MRC2354-350 as our primary flux calibrator.

After flux calibration, we present the deconvolved images with a resolution of $4'\times4.'6\sec(\delta+20.^\circ14)$ in the form of overlapping contour maps covering more than one steradian of the sky ($18^h \leq$RA$\leq 24^h30^m$, -75°$\leq \delta \leq$-10°). In an Appendix A to this chapter, the flux calibrated dirty images with a resolution of $4'\times4.'6\sec(\delta+20.^\circ14)$ covering about half a steradian of the sky ($15^h06^m \leq$RA$\leq 18^h$, -75°$\leq \delta \leq$-10°) which includes a large part of the southern Galactic plane are also presented as contour maps. The southern Galactic plane remains unexplored at meter wavelengths with the achieved brightness sensitivity ($\approx 2.1\times10^{-21}$ W m^{-2} Hz^{-1} Sr^{-1}; 1σ at 151.5 MHz) and resolution. The images have been made using good data selected after scanning through ≈7,500 hours of observations from all the three cycles (Sec. 2.1.2). Visibility measurements were obtained by correlating all the 32 EW groups (EW arm 2048 m) of the $\top$ with the NS groups, using the NS baselines from 2 m all the way up to 881 m (every 1 m) with different delay settings (up to four). The imaging was carried out on a sidereal hour basis. In each sidereal hour four sets of images were synthesized to cover the full declination range without appreciable decorrelation (<18%). An overall discussion of the deconvolved images including their noise characteristics and surface brightness sensitivity is given.

The second part of the chapter deals with the construction of a source catalogue from the deconvolved images. Details of the algorithm developed for catalogue construction, various factors affecting it, like rms noise, artifacts in images etc. are discussed. The cat-

alogue format and the source list are presented in the Appendix B. Preliminary analysis of the catalogue including accuracy of positions and flux densities is discussed. The images and the catalogue presented contain a lot of astronomical information and is beyond the scope of this dissertation to discuss it to a reasonable depth primarily due to lack of time. However as a representative of interesting sources in the images, we briefly discuss a few steep spectrum sources, giant radio sources, double sources, cluster radio relics/fossil galaxies and report the structure of a few resolved supernova remnants.

7.2 MRT images and their analysis

7.2.1 Flux calibration

The flux calibration of the MRT images is carried out in four major steps. In the first step the images covering different sidereal hours are scaled to a common level. In the next step the primary beam of the helix is estimated. The third step involves recovery of the amplitude information of the signal lost in a 2-bit 3-level correlator with an AGC. The last step involves the choice of the primary flux calibrator for the images. We discuss each of these aspects related to flux calibration in the following sections.

7.2.1.1 Scaling images to a common level

As discussed earlier the visibilities for each sidereal hour undergo various steps of data processing separately. For each sidereal hour, in order to obtain the dirty images, the images of each allocation are combined with relative weights which are estimated using well known unresolved strong sources (present in the sidereal hour range under consideration). The images covering different sidereal hours (both dirty as well as deconvolved) are in arbitrary units and are not on a common reference. In order to have a uniform flux density calibration scheme, it is necessary to bring all the images to a common level.

As mentioned earlier, the images for any one sidereal hour range also include guard zones[1] which cover a region extending to about 39 minutes in RA on each side of the sidereal hour range of interest. So any two adjacent sidereal hour images have an overlap of about 01:18 hrs in RA. The flux densities in the two images in the region of overlap, differ from each other, only by a multiplicative constant which is given by the ratio of the peak amplitudes of common sources in the two images. This is used to bring two adjacent sidereal hour images to a common level.

In order to estimate the required multiplicative factor, first all the unresolved sources which have their peak amplitude strengths more than 10σ (σ refers to the rms noise in the

[1]Actually the guard zones on each side in RA extend to about 54 min, but only 39 min are considered to minimize the effect of sources near the ends which may not have been deconvolved properly.

image) were detected in the deconvolved images for all the sidereal hours (including guard zones). Nonlinear fitting with a two dimensional elliptical Gaussian was carried out to estimate the fitted peak amplitudes and positions of these sources. Similarly for the images which were not deconvolved[2] (covering the sidereal hour range 15:21-17:39 hrs and 16:21-18:39 hrs shown by the superscript ^{d} in the Table 7.1), the fitted peak amplitudes were obtained by fitting a 2-D *sinc* function[3] (the expected response of a T-array) of the expected beam width. Only bright sources were considered so as to have an accurate estimate of the peak amplitudes. We then estimated average of the ratios of peak deflections of common sources for all the adjacent pairs of images in RA. The primary beam response of the helix being same does not modify this ratio.

Two sources are defined as common[4], if the angular distance between their fitted peak positions is less than 1′and there is only one source within this search radius. The angular distance (d) between two sources with positions (α_1,δ_1) and (α_2,δ_2), is estimated using the expression[5] for spherical geometry (Volmer et. al., 2005),

$$d = \arccos\left[\cos\left(\alpha_1 - \alpha_2\right)\,\cos(\delta_1)\,\cos(\delta_2) + \sin(\delta_1)\,\sin(\delta_2)\right] \tag{7.1}$$

Fig. 7.1 shows the histograms of distribution of the ratios of the peak amplitudes of common sources (mean ratio normalized to unity) for various pairs of adjacent sidereal hour images. Table 7.1 shows the mean values of the peak flux density ratios of common sources in the overlapped regions of the various pairs of adjacent sidereal hour images, along with the rms spread and the number of common sources used to estimate the ratio. The rms spread in the ratio of the peak amplitudes of the common sources is due to a variety of reasons. In case of MRT assuming the FWHM of the elliptical Gaussian as 4′×4′and the noise is uncorrelated, the % accuracy in the estimation of the peak amplitude for a $10\,\sigma$ source is ≈5.6% and the corresponding uncertainity in the ratio of the peak amplitude would be ≈7.8%. Since there are sources which have strengths much higher than 10σ the actual uncertainity obtained, would be less. In addition to this, the images covering different sidereal hours are deconvolved down to a 5σ level, where σ refers to the rms noise in

[2]The delay beam corresponding to the dirty images for two sidereal hours is slightly different and would introduce amplitude errors. For deconvolved images there is no effect of bandwidth decorrelation as the peak flux densities have been appropriately restored during deconvolution.

[3]formed by the product of two 1-D *sinc* functions of appropriate beam widths along RA and declination.

[4]For the full resolution images taking the FWHM of the elliptical Gaussian beam as 4′×4′and considering rms noise is uncorrelated, the positional uncertainty for a $10\,\sigma$ source is ≈0.″15 (using expressions as given in Condon (1997)). Thus difference in the positions will have uncertainty of ≈0.″21. To accommodate all genuine common sources and taking into account any small systematics in position (Sec. 7.3.1) a upper limit of 1′ was considered. Since the source densities are very low (<1 deg^{-2}), the chances of associating two different sources within 1′ of each other as common is negligible.

[5]all variables are expressed in radians in the equatorial coordinate system.

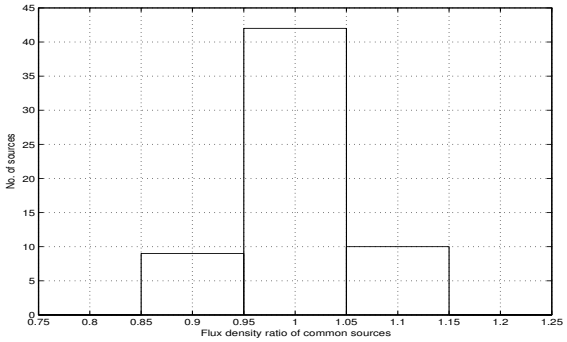

(a) Image I - 16:21-18:39 hrs, Image II - 15:21-17:39 hrs

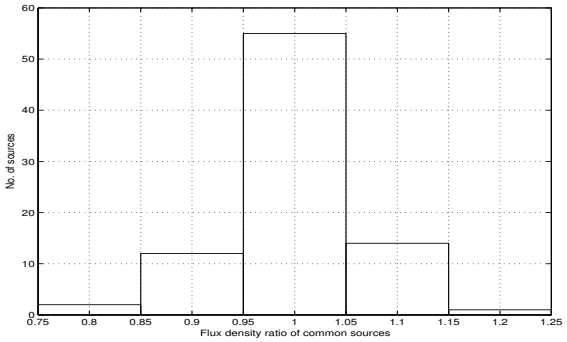

(b) Image I - 17:21-19:39 hrs, Image II - 16:21-18:39 hrs

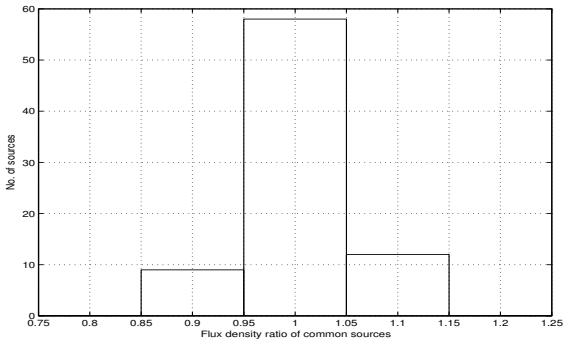

(c) Image I - 18:21-20:39 hrs, Image II - 17:21-19:39 hrs

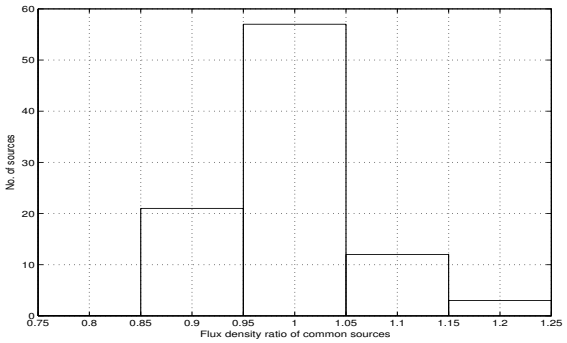

(d) Image I - 19:21-21:39 hrs, Image II - 18:21-20:39 hrs

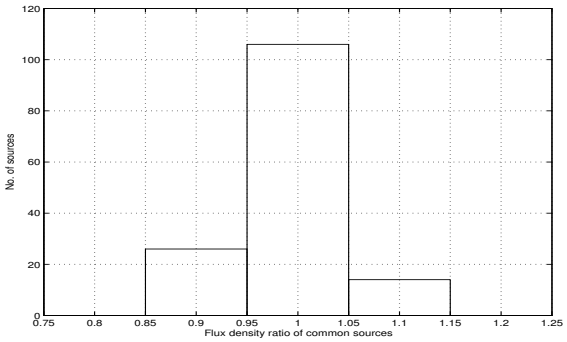

(e) Image I - 20:21-22:39 hrs, Image II - 19:21-21:39 hrs

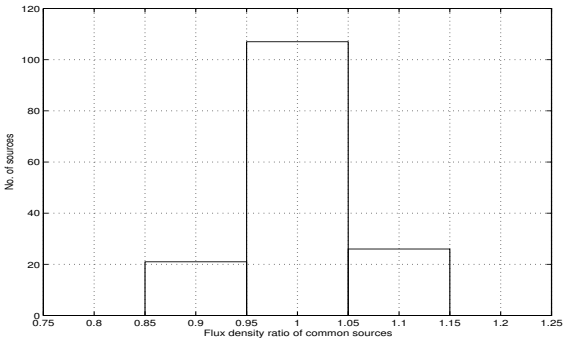

(f) Image I - 21:21-23:39 hrs, Image II - 20:21-22:39 hrs

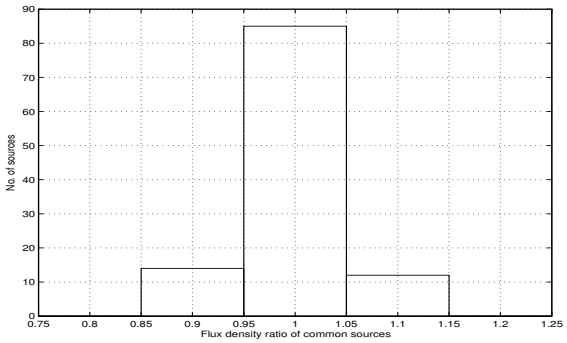

(g) Image I - 22:21-24:39 hrs, Image II - 21:21-23:39 hrs

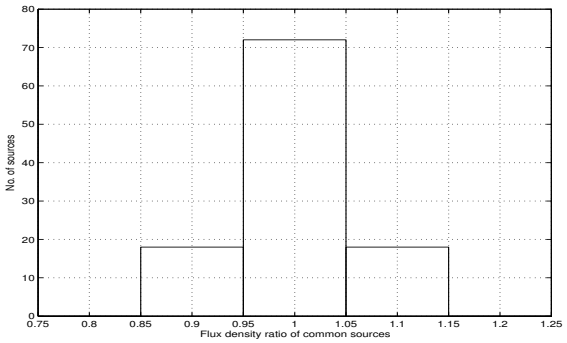

(h) Image I - 23:21-01:39 hrs, Image II - 22:21-24:39 hrs

Fig. 7.1: Histograms of ratio of the peak flux densities (mean ratio normalized to unity) of the common sources (strength>10σ) in the overlapping regions of the images corresponding to adjacent sidereal hour images. The RA coverage of both the adjacent images is also shown for each plot. The rms spread of the ratio from the mean value is symmetrical on both the sides and is typically within 5% for most of the sources.

the sidereal range of interest (and not in the guard zones). Since the noise in the images in two adjacent sidereal hours is different, the overlapped regions have not been deconvolved to the same flux density level. Also strong sources just outside the range of guard zones in RA and declination may affect the flux densities of the sources near the ends due to insufficeant deconvolution. In addition the overlapped regions corresponding to different sidereal hours have been synthesized using independent visibilities only on 30-40% of the baselines, due to which the rms on the ratio of the peak amplitudes obtained would be less than the expected value for images obtained using completely different dataset. The spread in the ratio of peak amplitudes of common sources in the two images is also a rough indicator of the repeatability of the data.

We note from the Table 7.1 and Fig. 7.1 that the average rms on the ratio of the peak amplitudes of common sources in overlapped regions of two adjacent hours is $\approx$5 to 6%. These numbers are within expected values.

Image-I RA range (hh:mm)	Image-II RA range (hh:mm)	Number of common sources	flux density comparison: mean ratio of peak amplitudes $\left(\frac{\text{Image-I}}{\text{Image-II}}\right)$	rms spread: value	rms spread: (%)	σ_{mean}	scaling factor (f)	σ_{f}	error (%)	Position: angular dist. in ($'$) mean	Position: angular dist. in ($'$) rms
15:21-17:39[d]	16:21-18:39[d]	61	1.77371	0.08355	4.71	0.010697	0.663807	0.008996	1.355275	0.25	0.24
16:21-18:39[d]	17:21-19:39[d]	84	1.05214	0.07477	7.10	0.008158	1.174362	0.014240	1.212598	0.22	0.20
17:21-19:39	18:21-20:39	79	3.42576	0.16649	4.86	0.018852	1.239711	0.011467	0.924984	0.17	0.10
18:21-20:39	19:21-21:39	93	0.30150	0.01980	6.56	0.002053	4.267950	0.032333	0.757579	0.18	0.12
19:21-21:39	20:21-22:39	146	0.77801	0.03240	4.16	0.002663	1.285928	0.004600	0.357760	0.18	0.11
20:21-22:39	21:21-23:39	154	2.65688	0.12382	4.66	0.010043	2.656882	0.010043	0.378028	0.24	0.14
21:21-23:39	22:21-24:39	111	0.59966	0.02576	4.29	0.002434	1.593233	0.008838	0.554736	0.13	0.10
22:21-24:39	23:21-01:39	108	0.55748	0.02831	5.07	0.002737	0.888210	0.006580	0.740859	0.16	0.11
23:21-01:39	00:21-02:39	86	0.97210	0.04651	4.78	0.004987	0.863430	0.007780	0.901148	0.25	0.19

Table 7.1: Comparison of ratio of peak flux densities and positions of common sources in the overlapping regions in the MRT images of adjacent sidereal hours. Col. 1 and 2 show the RA coverage of the two images considered, Col. 3 shows the number of common sources with peak amplitude >10σ, Col. 4 shows the mean of the ratio of peak amplitudes of the common sources, Col. 5 and 6 show the rms spread in the peak amplitude ratio and its value as % of the mean, Col. 7 shows the uncertainity in the estimation of the mean of the ratio of peak amplitudes, Col. 8 shows the scaling factor to bring the Image-I to the reference image (20:21-22:39 hrs), Col. 9 and 10 show the uncertianity in the estimation of scaling factor itself and the uncertainity inroduced due to scaling in %. Col. 11 shows the mean angular distance in the positions of the common sources and Col. 12 shows the rms in the difference between the angular distances. [d] denotes the images which were not deconvolved. The rms variation of the ratio of the peak amplitudes of common sources for any two adjacent images is typically between 5 to 6%.

Any two adjacent images can be brought to a common level by using the mean of the ratios of the peak amplitudes of the common sources as given in Table. 7.1. Subsequently we use the method of differences to scale all the images to a common reference. The process of scaling two images to a common level also introduces errors due to uncertainty in determination of the mean of the ratios of the peak amplitudes of the common sources. This error due to scaling propagates with the increase in the number of sidereal hour gaps between the two images being scaled to a common level. In order to minimize this error the image covering the sidereal hour range 21-22 hrs (20:21 hrs to 21:39 hrs if the guard zones are also considered) was considered as the reference image as it is approximately in the center of the RA range of the deconvolved images presented in this thesis. This image also happens to have the minimum rms noise. The scaling factors (f) required for each sidereal hour image to bring them to the common level of this reference image is given in Table 7.1. The uncertainty in the estimation of mean ($\sigma_{\rm mean}$), is inversely proportional to the square root of the number of common sources used to estimate the ratio and is given in Table 7.1 for various pairs of adjacent sidereal hour images. Since the scaling factor to bring an image to the reference image is simply given by the product of all the mean ratios of peak flux densities in the adjacent images between the sidereal hours under consideration, the net uncertainty($\sigma_{\rm f}$) in the scaling factor assuming the cross terms to be negligible is given by,

$$\frac{\sigma_f^2}{f^2} = \frac{\sigma_{f_1}^2}{f_1^2} + \frac{\sigma_{f_2}^2}{f_2^2} + ... \tag{7.2}$$

where $(f_1, \sigma_{f_1}), (f_2, \sigma_{f_2}), ...$ are the mean ratios of the peak flux densities of the common sources and its uncertainty in the successive pairs of adjacent sidereal hour images using the above expression. The estimated value of errors in scaling any image to the common reference image is given in Table 7.1. From the table we note that the maximum error in scaling the deconvolved images is ≈0.9% while for the images which were not deconvolved the maximum error is 1.35% (as they are the farthest from the reference image).

In a similar way, an interesting analysis can be carried out to estimate the positional uncertainty of the common sources in the overlapping regions by measuring the positional differences in the adjacent sidereal hour images. The angular distance between the positions of the two sources were estimated using Eqn. 7.1 and are given in Table. 7.1 for various pairs of adjacent sidereal hour images. The mean value of the positional difference is about 0.′18 with a maximum value of 0.′25. The rms spread of the absolute difference in positions is also generally about 0.′12 with a maximum value of 0.′24. The histograms of the of the difference in positions of common sources in adjacent sidereal hour images

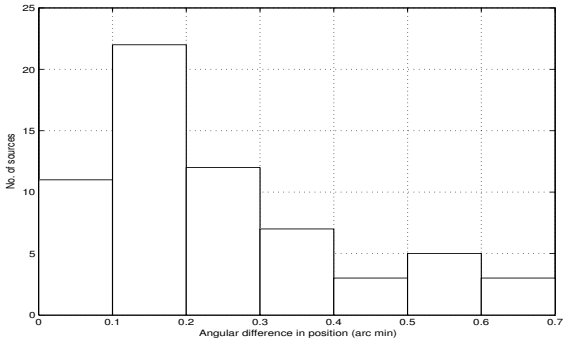

(a) Image I - 16:21-18:39 hrs, Image II - 15:21-17:39 hrs

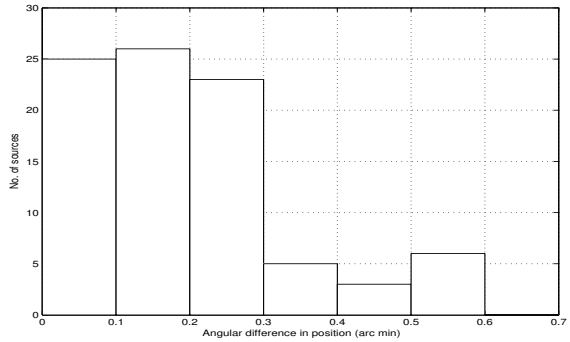

(b) Image I - 17:21-19:39 hrs, Image II - 16:21-18:39 hrs

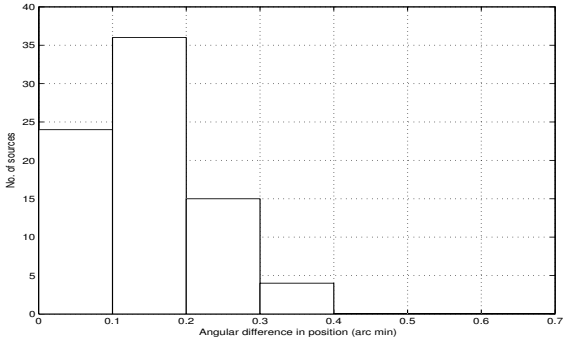

(c) Image I - 18:21-20:39 hrs, Image II - 17:21-19:39 hrs

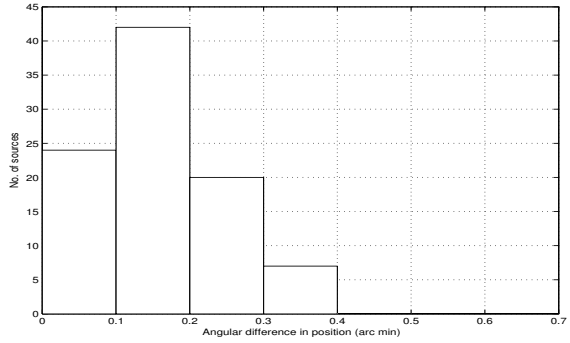

(d) Image I - 19:21-21:39 hrs, Image II - 18:21-20:39 hrs

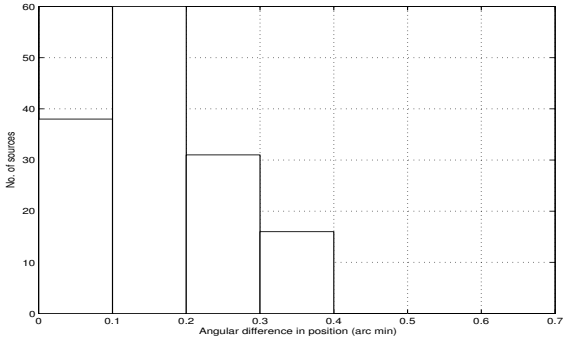

(e) Image I - 20:21-22:39 hrs, Image II - 19:21-21:39 hrs

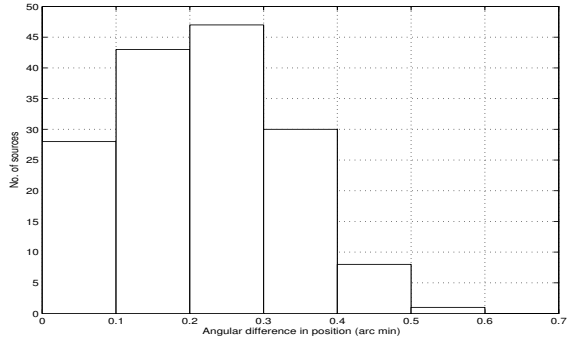

(f) Image I - 21:21-23:39 hrs, Image II - 20:21-22:39 hrs

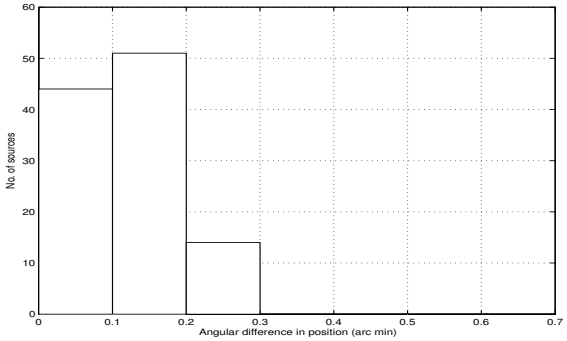

(g) Image I - 22:21-24:39 hrs, Image II - 21:21-23:39 hrs

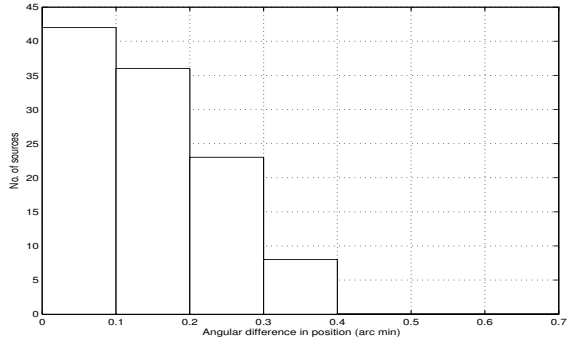

(h) Image I - 23:21-01:39 hrs, Image II - 22:21-24:39 hrs

Fig. 7.2: Histograms of angular distance between the common sources (strength>10σ) in the overlapping regions of the images corresponding to adjacent sidereal hours. The RA coverage is also shown for each plot. The angular distance is typically within 0.′18 and the rms spread in the angular distance from the mean is 0.′12 for most of the sources.

are given in Fig. 7.2. The uncertainty in the position of the sources with strength of 10σ is expected to be about $0'.21$ and thus the difference in positions is on the expected lines.

Using the scaling factors (f) given in Table 7.1, images corresponding to all the sidereal hour ranges were scaled to the common level of the reference image. We now discuss the next step in the flux calibration, estimation of the primary beam of the helix.

7.2.1.2 Estimation of the Primary beam of the Helix

The relative flux densities measured in the MRT images after scaling them to a common level are affected by two factors, the primary beam response of the helix along declination and the variation of the brightness temperature of the sky as a function of RA as seen by an EW×NS interferometer due to the usage of AGC in the path of the digitiser (see Sec. 7.2.1.3). Since the imaging is carried out on the meridian, these two factors affect the flux densities in orthogonal directions along RA and along declination respectively. At any given declination there is no effect of primary beam shape of helix along RA while at any given RA there is no effect of variation of sky background along declination. Due to this, it is possible to estimate each of these two effects independently even if the images are not corrected for the other one. However it is to be noted that in case there is a large variation in one of them which is not taken into account (in the region of the sky considered to estimate the other), it would increase the uncertainty with which the other effect can be estimated.

To estimate the primary beam shape of the helix along declination we use the ratio of peak amplitudes[6] of common sources at 151.5 MHz in the MRT images and the MRC catalogue at 408 MHz. This ratio is expected to follow the primary beam response of the helix with an inherent noise due to spectral index distribution of the sample of sources. In order to minimize the effect of variation of sky background along RA, we estimated the primary beam shape of the helix using the images covering region of the sky from RA 20:21 hrs to 24:39 hrs (i.e. 00:39 hrs) and the entire declination range of MRT. The expected variation due to changing sky in this RA range is less than 10% (see Fig. 1.4(b)). The subimages considered for the present analysis cover the RA range 20:21-22:30 hrs and 22:30-24:39 hrs respectively.

Using the algorithm for catalogue construction (Sec.7.3.1) described in the second part of this chapter, all unresolved sources with peak flux densities exceeding 5σ were detected in both the subimages (after images have been scaled to a common level). It is important to ensure that while using the ratio of peak amplitudes of common sources in the MRT images and the MRC catalog, we do not introduce any bias. For example if we consider all the

[6]We recall that the amplitudes in the MRT images which have been scaled to a uniform level are still in arbitrary units and not on the true flux density scale.

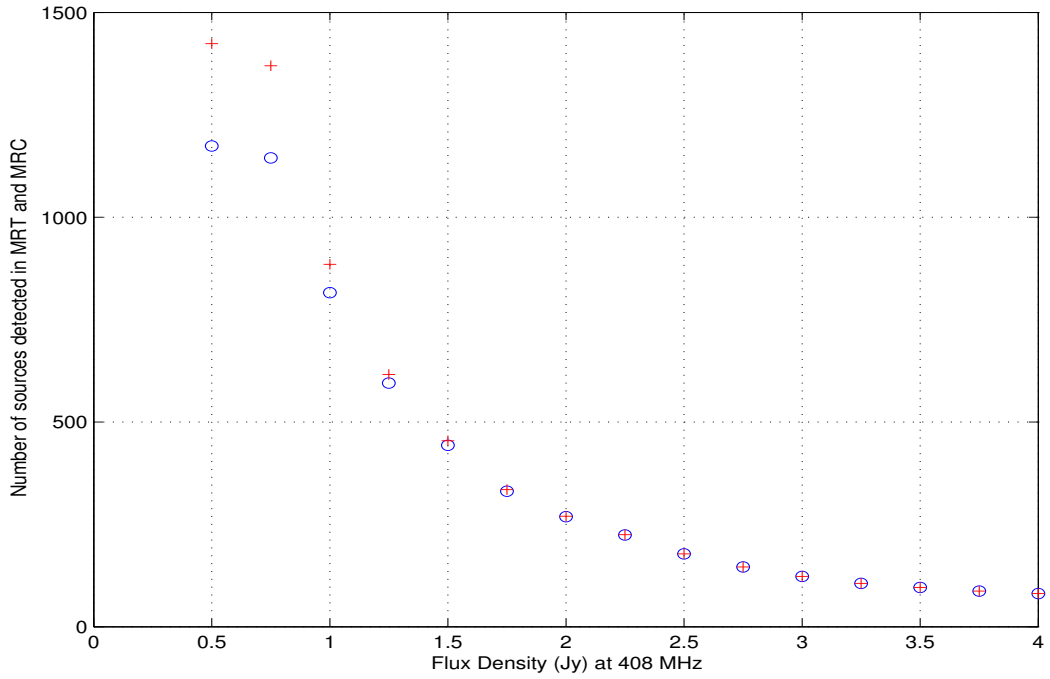

(a)

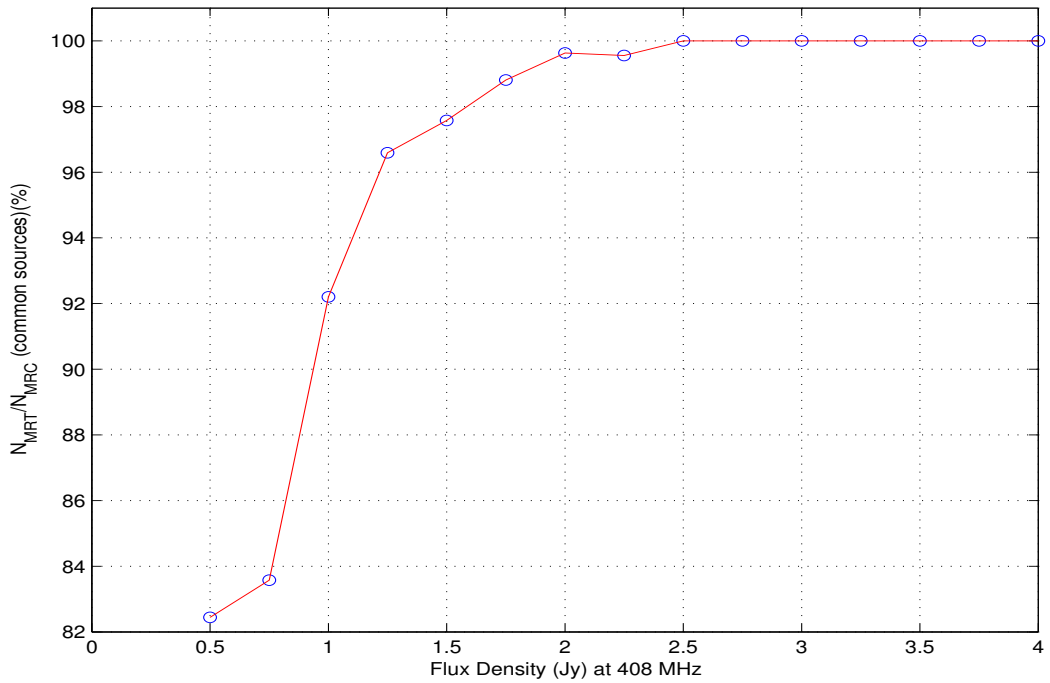

(b)

Fig. 7.3: The upper plot shows the total number of sources in the MRC catalogue (+) with strengths more than a given flux density at 408 MHz and the number of sources among them also detected in the MRT images (o). The lower plot shows it in the form of % of MRC sources which have been also detected in the MRT images. Among MRC sources with flux densities exceeding 1.25 Jy at 408 MHz, 96.5% are detected in the MRT images.

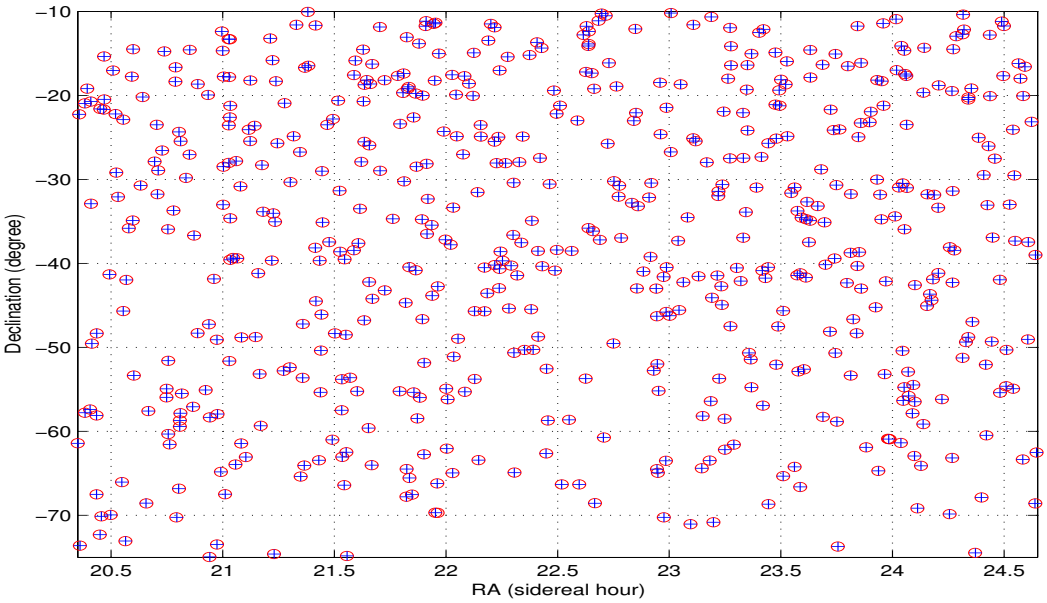

Fig. 7.4: Distribution of 560 common source positions in the MRT images and MRC having a flux density more than 1.25 Jy at 408 MHz in the region used for comparison to estimate the primary beam of the helix.

common sources between MRC and MRT, we would be having larger number of sources towards the declinations in which the response of the helix primary beam is maximum. In addition, sources with steeper spectral index would be favored and this effect would be more predominant towards declinations away from the peak response. This would apparently make the observed values of the ratio higher towards declinations away from the direction of maximum response, resulting in an apparently broader helix beam.

The number of sources in the MRC catalogue above a given flux density at 408 MHz, and the corresponding number of sources among them[7] also detected in the MRT images are shown as a function of flux density at 408 MHz in Fig. 7.3(a). This is also represented as the % of MRC sources above a given flux density at 408 MHz which were also detected in the MRT images in Fig. 7.3(b).

In order to avoid any bias due to the spectral index distribution, it is important to consider the common sources which form a flux density limited complete sample. The MRC catalogue is 99.9% complete above a flux density limit of 1.0 Jy at 408 MHz. From Fig. 7.3 we note that the % of MRC sources above flux densities of 1.0 Jy and 1.25 Jy at 408 MHz detected in the MRT images is 92% and 96.5% respectively. The increase in the % of MRC

[7]The sources were labeled as common if they lie within 4′ of each other (See Eqn. 7.1). In case of more than one source present in the MRT image within 4′ of an MRC source, such sources were not considered for the present analysis. A large angular distance was allowed to accommodate systematics in positions if any. Since the MRC catalogue has source density of about 0.5 source deg^{-2}, the chances of considering two unrelated sources as common is extremely low.

sources detected in the MRT images increases gradually above a flux density limit of 1.25 Jy at 408 MHz. In order to minimize the population bias due to the width of spectral distribution and at the same time to have a large enough sample to accurately estimate the primary beam shape of the helix, we considered a lower flux density limit of 1.25 Jy at 408 MHz. Sources labeled as extended and complex were excluded.

This yielded a source list of 560 sources for estimating the primary beam. It is to be noted that the solid angle covered by a region of the sky for a given RA range decreases for equal declination intervals when we consider regions towards poles. Due to this the number of common sources available would be still higher towards declinations closer to the equator. Anyway this would not affect the primary beam shape estimation if there are enough sources in each declination zone.

First for each subimage covering the RA range 20:21 hrs to 22:30 hrs and 22:30 hrs to 24:39 hrs and later for the entire region covering the RA range 20:21-24:39 hrs, the ratio of the peak amplitudes at 151.5 MHz and at 408 MHz were estimated and plotted as a function of declination as shown in Fig. 7.5. This is expected to follow the primary beam shape of the helix along declination. Here we assume that the mean ratio of flux density of sources at 151.5 MHz and 408 MHz for a large number of sources (of extragalactic origin) forming a complete sample in any part of the sky is constant. Our estimation is not affected by the exact value of this mean ratio.

It is worth recalling that an approximate normalized far field power pattern of the helix P(θ), in the direction of angle θ from the axis of the helix, for an axial mode helix is given by (Kraus, 1988b),

$$P(\theta) = V^2(\theta) = \left[\frac{\sin(n\psi/2)}{\sin(\psi/2)} \sin\left(\frac{\pi}{2n}\right) \cos(\theta)\right]^2 \tag{7.3}$$

where $V(\theta)$ is the voltage pattern, n is the number of turns and $\psi = 2\pi[S_\lambda(1 - \cos\theta) + (1/2n)]$, where S_λ is the spacing between the turns in units of wavelength. We can also represent the power pattern of the helix as a function of declination (P(δ)), by a polynomial of the form,

$$P(\delta) = a_0 + a_1(\delta - \delta_0) + a_2(\delta - \delta_0)^2 + a_3(\delta - \delta_0)^3 + a_4(\delta - \delta_0)^4 + ... \tag{7.4}$$

where $a_0, a_1, a_2, a_3, a_4, ...$ are constants and δ_0 is the declination where the primary beam response of the helix is maximum. We fitted curves of different orders (Eqn. 7.4) to the ratios of the peak flux densities for the above three cases separately. We noticed that the coefficients for all the odd order terms were very small and insignificant. This is on the expected lines as the primary beam shape of the helix is expected to be symmetrical around

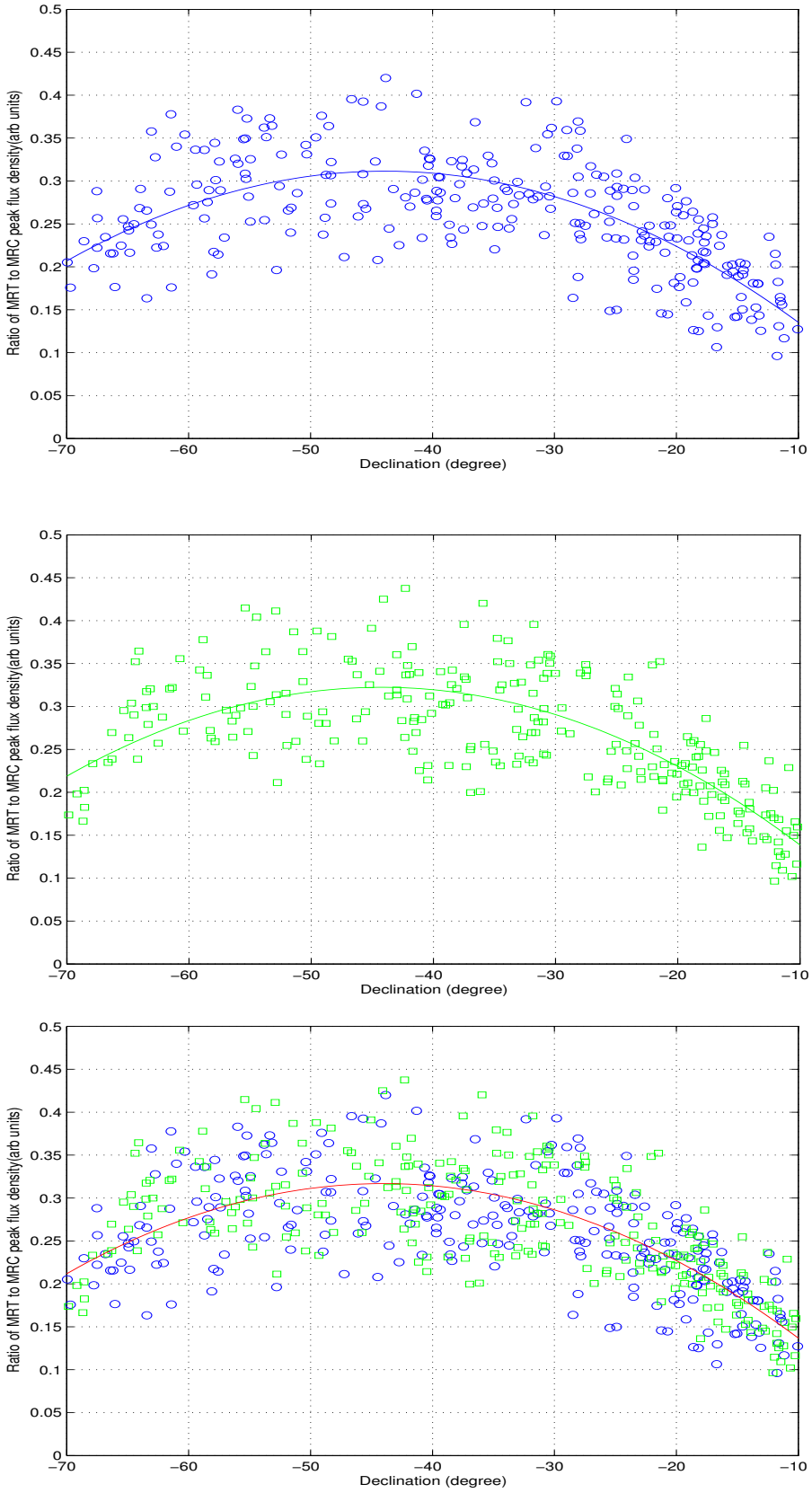

Fig. 7.5: The plots show the ratio of the fitted peak amplitude (arbitrary units) of common sources in the MRT images to their peak flux densities at 408 MHz in the MRC catalogue. The three plots correspond to the images covering the sidereal hour range 20:21-22:30 hrs (upper), 22:30-24:39 hrs (middle) and 22:30-24:39 hrs (lower) respectively. The derived primary beam shape of the helix by fitting the curve of the form as in Eqn. 7.5 are also shown (solid lines).

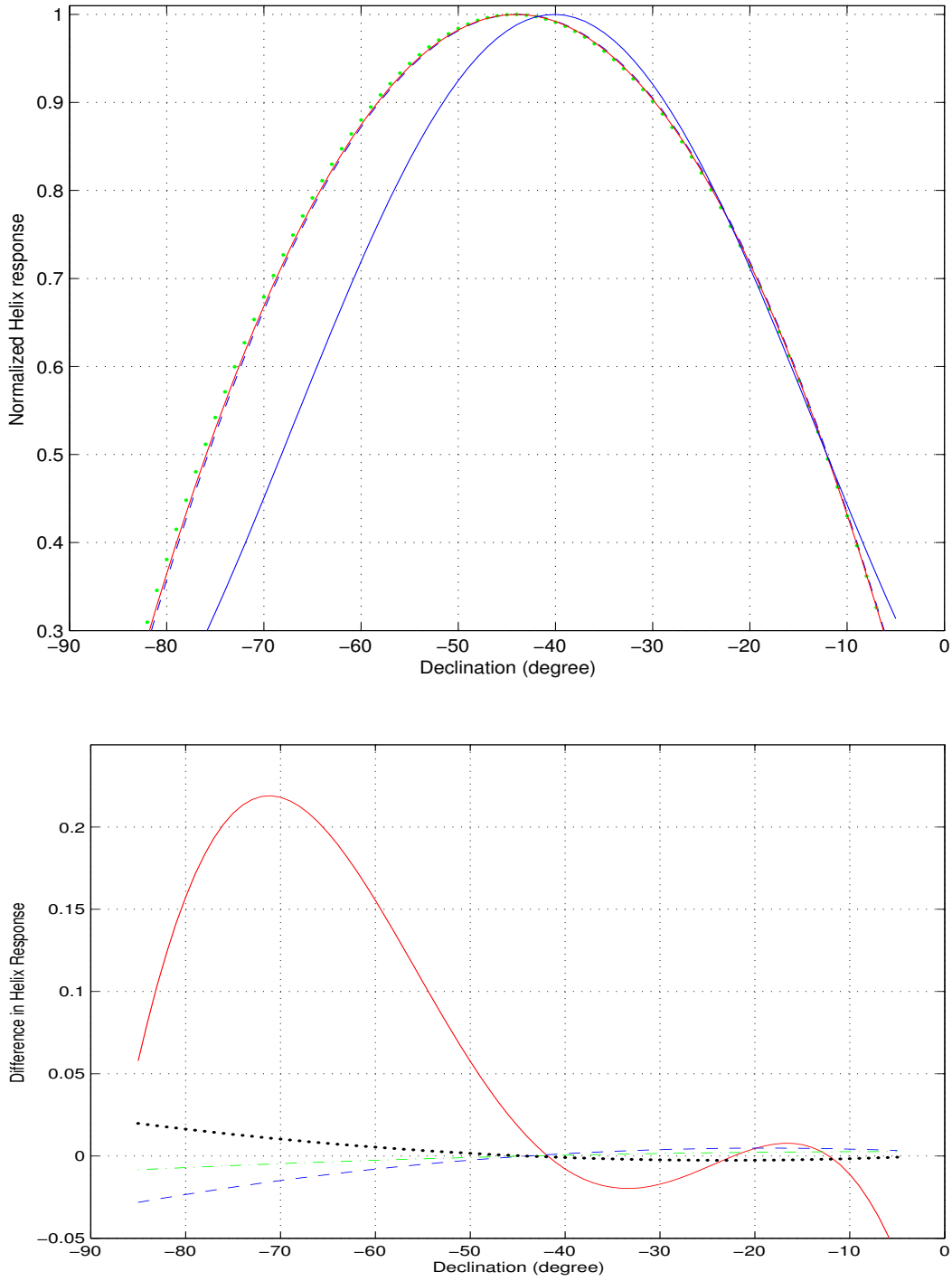

Fig. 7.6: The upper plot shows the comparison between the primary beam shapes of the helix estimated from the images covering sidereal hour ranges 20:21-22:30 hrs (dashed blue), 22:30-24:39 hrs (dotted green), and 20:21-24:39 hrs (solid red). The expected primary beam response of the helix is also shown (solid blue). The lower plot shows the difference between the estimated primary beam response using images covering 20:21-22:30 hrs and 22:30-24:39 hrs(blue dashed), 20:21-22:30 hrs and 20:21-24:39 hrs(green dashed dotted), 22:30-24:39 hrs and 20:21-24:39 hrs(black dotted), 20:21-24:39 hrs and the expected primary beam response (red line). The helix beam estimated using images covering different sidereal hour ranges are consistent with each other within 3%. The estimated primary beam response is different from the expected beam shape. It peaks at declination ≈-44° instead of expected -40.14 and its HPBW is ≈64°, nearly 8° wider than the theoritical response.

S.No.	Image range (RA)	No. of sources	a_0	σ_{a_0}	a_2	σ_{a_2}	δ_0	σ_{δ_0}
1	20:21-22:30 hrs	289	1.0	1.37%	-1.6171	6.00%	-0.765878	1.18%
2	22:30-24:39 hrs	271	1.0	1.31%	-1.5924	5.97%	-0.772671	1.31%
3*	20:21-24:39 hrs	560	1.0	0.95%	-1.6116	4.21%	-0.768265	0.87%

Table 7.2: The fitted parameters for the estimated primary beam of the helix response as given in Eqn. 7.5. The parameters obtained using the combined data set (image marked as *) being the most accurate have been used for applying the helix primary beam correction.

the direction in which it peaks and thus expected to contain only even order terms. This can also be noticed if we expand the theoretical beam shape given in Eqn. 7.3 in powers of θ. In view of this all the odd order terms were excluded. We also noticed that the coefficients of the fourth and higher order terms were insignificant and retaining them did not contribute to any significant improvement in the fit. Based on these observations in our analysis, the following expression was found to be sufficient to represent the primary beam of the helix in the declination range of interest to MRT.

$$P(\delta) = a_0 + a_2(\delta - \delta_0)^2 \tag{7.5}$$

The above expression was used for fitting the data set of ratios of the flux densities in both the subimages individually and later on both the data sets combined together. The ratio of flux densities and the fitted curves obtained for all the three cases are shown in Fig. 7.5. The normalized fitted parameters for the helix primary beam for all the three cases are given in Table 7.2. Fig. 7.6(a) shows the estimated and the expected beam shapes (Eqn. 7.3). Fig. 7.6(b) shows the difference between the estimated responses in the three cases. It also shows the difference between the expected and the estimated response using the combined data set. The helix beam estimated using images covering different sidereal hour ranges are consistent with each other within 3%. However, the estimated and the expected primary beam shapes are quite different and the maximum difference is about 20% (at declinations near -70°). The estimated primary beam shape does not peak as expected at declination δ=-40.°14 but peaks at $\delta\approx$-44°, about 4° towards south. In addition the estimated primary beam shape is broader with a FWHM ≈64°as compared to ≈56°of the expected beam. The fitted beam obtained using the combined data set of both the subimages is the most accurate and has been used to apply the primary beam correction of the helix (a_0=1.0, a_2=-1.6116, δ_0=-0.768265) in this dissertation instead of the expected beam.

Now we discuss the next step in flux calibration which involves estimation of the unnormalized correlation coefficient in order to incorporate the correction required for vari-

ation of background temperature of the sky in the images.

7.2.1.3 Calculation of the unnormalized correlation coefficient

In the 2-bit, 3-level correlator at MRT, the AGCs maintain a constant signal level to the samplers, even though the brightness distribution of the sky changes. Therefore we do not get the amplitude information of the signal from the sky. This results in a similar correlation for a weak source in a weak background and a strong source in a correspondingly stronger background.

To obtain the amplitude information due to variation in the background temperature as seen by the EW and NS groups, the self correlations were also measured separately by switching off the AGCs[8] in one EW (E16) and one NS (S15) groups. The self correlators of the MRT are wired in such a way that they measure the probability (P) that the input signal amplitude V, is in between the thresholds levels used for digitisation. This probability for a zero mean noise Gaussian signal with an rms fluctuation of σ and a symmetric 2-level digitizer with voltage threshold levels $\pm V_{th}$ is given by,

$$P = \frac{1}{\sigma\sqrt{2\pi}} \int_{-V_{th}}^{+V_{th}} e^{-(\frac{V}{\sqrt{2}\sigma})^2} dV = erf(\frac{V_{th}}{\sqrt{2}\sigma}) \tag{7.6}$$

Knowing P, the $\frac{V_{th}}{\sigma}$ of the signal can be obtained. The equivalent analog correlation, ρ_a, can be obtained using the relation,

$$\rho_a = \rho \times \sigma_1 \times \sigma_2 \tag{7.7}$$

where ρ is the normalized correlation coefficient (see Sec. 1.5.3, Eqn. 1.18), σ_1 and σ_2 are the rms of the signals being correlated and can be obtained from the channels where the AGCs have been switched off.

The measurements of the self correlation without the AGCs are carried out along with the measurement of the visibilities and are stored in the same data file. In an ideal situation the best desired course would have been to incorporate this information in each day's image as and when synthesized. In practice the non-AGC measurements are severely corrupted by interference and are also affected by DC level jumps due to which their reliable estimates on all the days of data used for imaging was not possible. In view of this, it was felt appropriate to incorporate the required correction in the full resolution images. Incorporating the required background correction at the level of each day or full resolution image is equivalent under the assumption that V_{th} is constant during the entire period of

[8]We also refer self correlations without AGC as total power measurements.

observations used for obtaining the full resolution images. We now discuss the procedure used to estimate and apply this correction to the images.

In the first step, all observations for which continuously observed data was available for the sidereal hour range 15:00 hrs to 04:00 hrs were selected. Since Sun is a strong radio source and the HPBWs of the EW (2°) and the NS (15°) groups are quite broad, it severely affects the total power measurements. Hence only those continuous stretches of observations when the Sun is in northern sky and its hour angle is at least more than four sidereal hours from the meridian during the entire stretch of observations were considered. This condition left us with only few continuous stretches of observations. After carefully examining 50 such continuous stretches of total power measurements, we chose six best stretches of observations which have minimum interference, no unexpected level shifts and measured counts of the EW and the NS groups consistent with each other and with the expected response[9].

Each of these stretches of total power measurements for the six days were processed separately. The measured counts were subjected to an upper and lower threshold cutoffs followed by recursive robust Hampel filtering (See Sec. 4.3.3) with various values of decreasing aggressiveness parameters (7,5,4 and 3). This minimised the effect of interference. Fig. 7.7 shows the self correlation counts with time for the EW and the NS groups for one stretch of observations before and after interference removal. The measured non-AGC self correlation counts for the EW and the NS groups after interference removal for all the six continuous stretch of observations is shown in Fig. 7.8.

The value of the corresponding power, $(\frac{\sigma}{V_{th}})^2$ was calculated using the counts for each of the EW and the NS groups (see Eqn. 7.6). We assume that the value of V_{th} is unchanged throughout the observations. The estimated total powers were convolved with the expected beam of the EW and the NS groups respectively (corresponding to δ=0°) to further suppress the effect of any remaining interference and also increase their signal to noise ratio. Fig. 7.9 shows the estimated total power as a function of RA for the EW and the NS groups after convolution.

Since the non-AGC self correlation measurements on the six days selected have no perceptible level shifts within EW and NS groups on the same day and from one day to another, the estimated corresponding total powers are also similar without significant level shifts as shown in Fig. 7.9. We averaged the measured total powers on the all the days at each RA to obtain one average profile for the EW and the NS groups. These are shown (red) in Fig. 7.9(a) (for EW) and Fig. 7.9(b) (for NS). The average total power for EW and NS groups

[9]Actually we had two sets of total power measurements (for six and five days) but with a DC level shift. We used the set which had minimum DC.

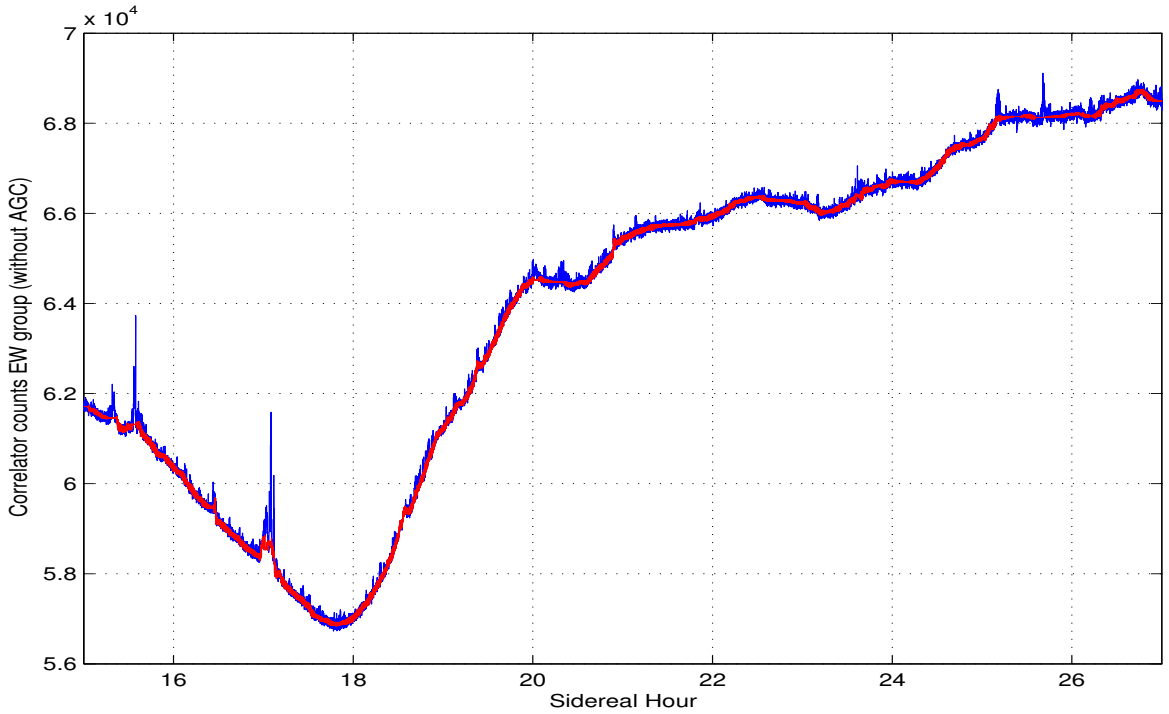

(a) EW group

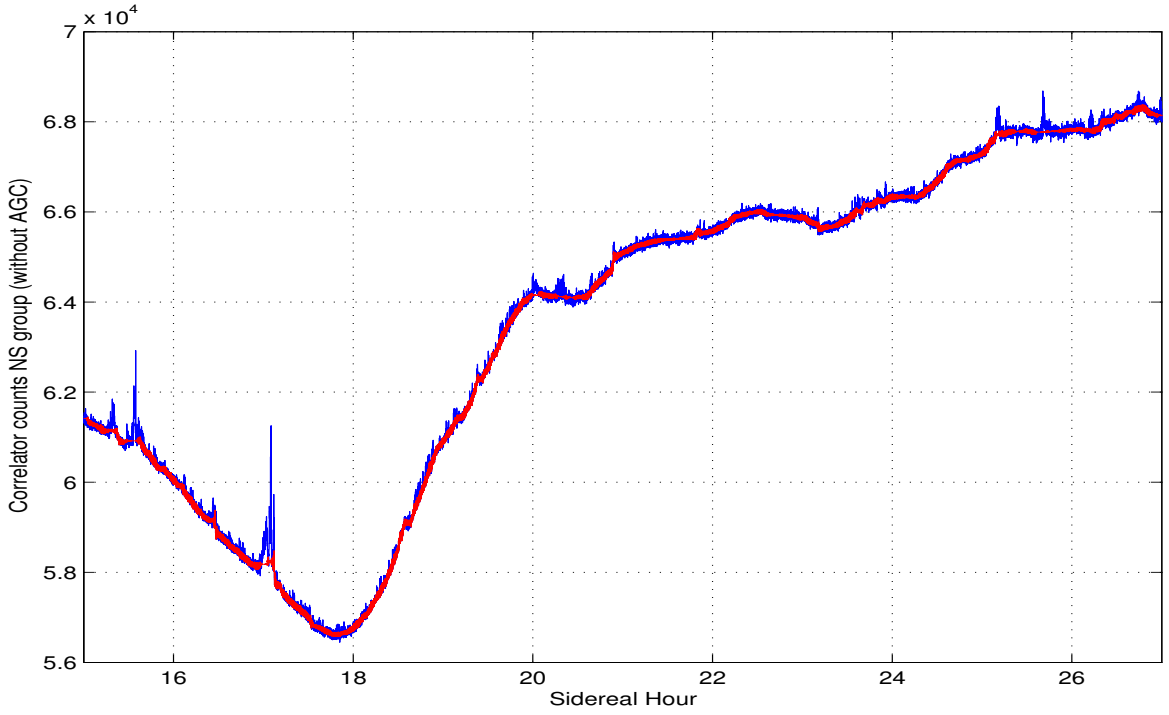

(b) NS group

Fig. 7.7: The plots show the measured non-AGC self correlation counts of the EW (upper plot) and the NS (lower plot) groups. The curve obtained after interference has been removed using Hampel filtering is also shown (red line) along with.

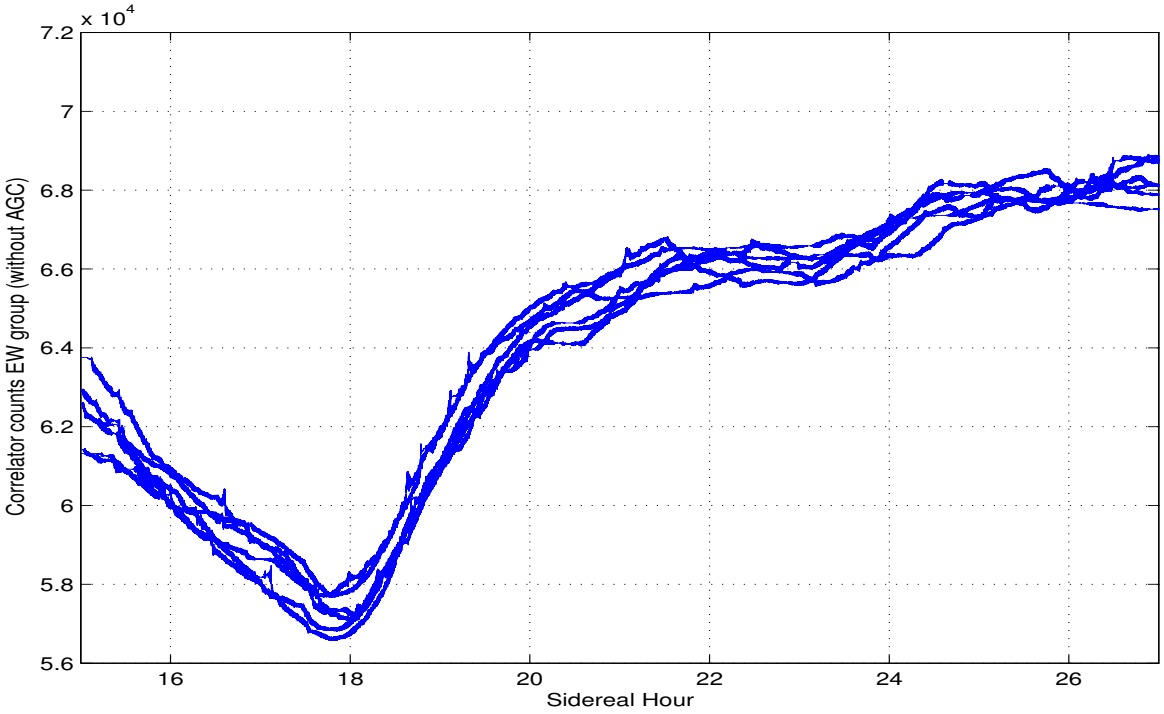

(a) EW group

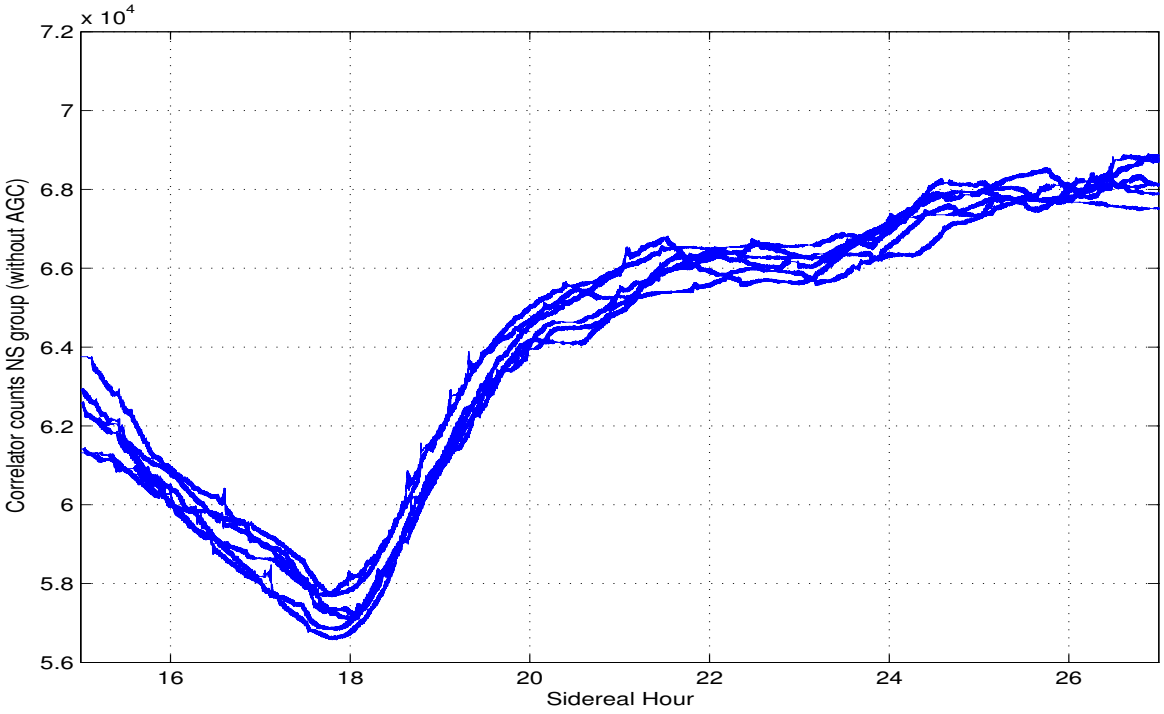

(b) NS group

Fig. 7.8: The plot shows the measured non-AGC self correlation counts of the EW (upper plot) and the NS (lower plot) groups of six sets of continuous observation stretches on different days (after excision of interference using Hampel filtering). The shapes obtained are self consistent within each group on different days and there are no significant perceptible level shifts.

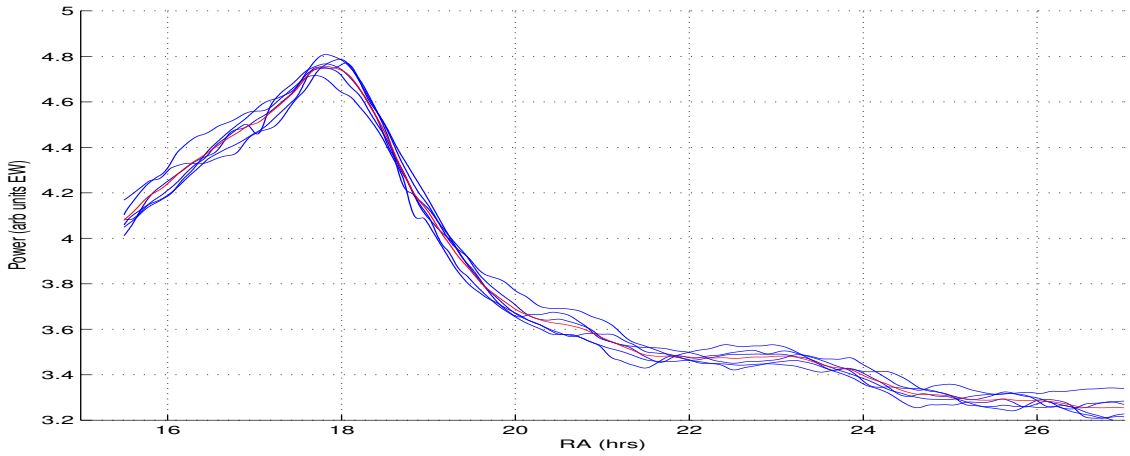

(a) EW group

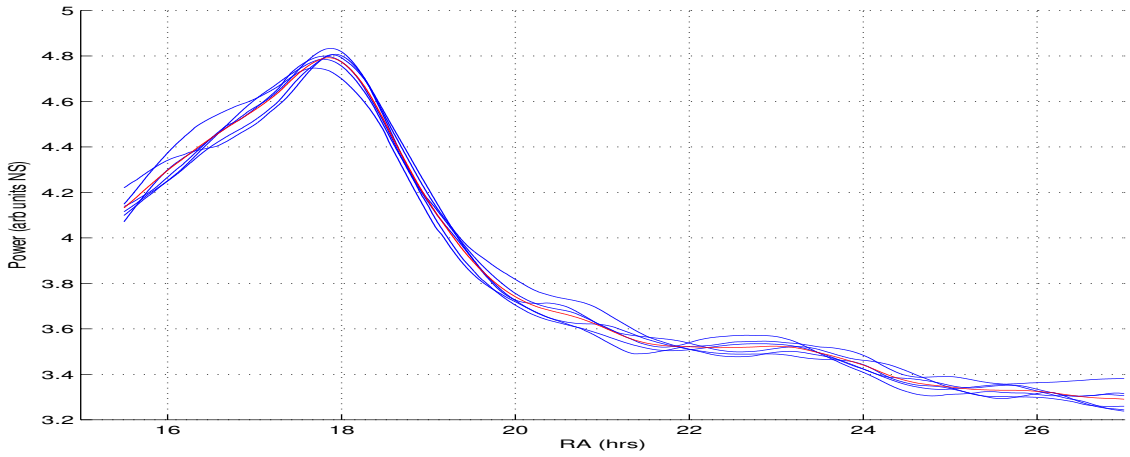

(b) NS group

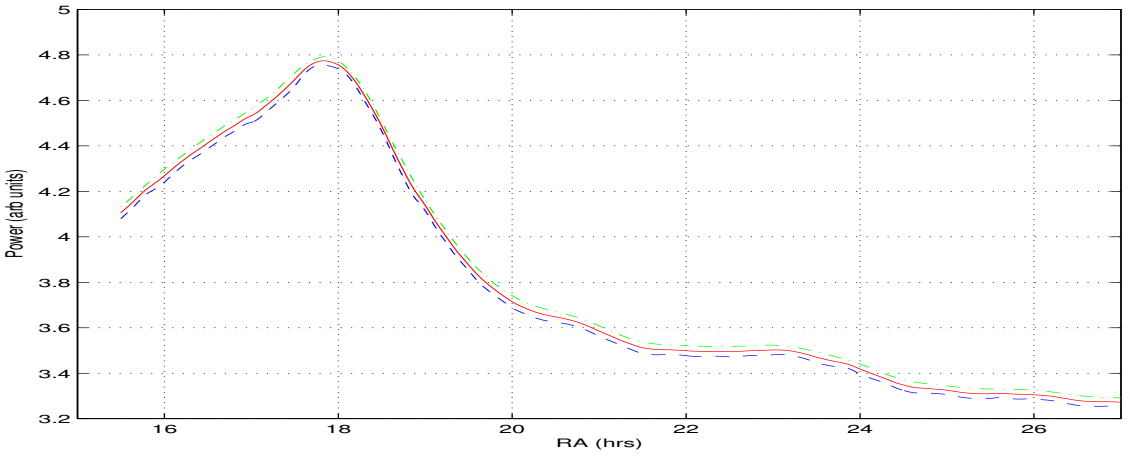

(c) EW×NS interferometer

Fig. 7.9: The total power estimated from the measured self correlation counts of the EW (upper plot) and the NS (middle plot) groups. The curve obtained by averaging the total powers estimated on different days is also shown in red for both the EW (upper) and the NS (middle) groups respectively. The lower plot shows the total power measured by an EW group (dashed dotted green), NS group (dashed blue) and by an EW×NS interferometer (red) as a function of RA. The scale on the y axis is in arbitrary units.

are also shown in Fig. 7.9(c). The total power seen by an EW×NS interferometer (given by $\sqrt{P_{EW}P_{NS}}$) using the average profiles of the total power of the EW and NS groups is shown in Fig. 7.9(c). We note that the total power for the NS group is slightly broader compared to that of an EW group and its peak value is also slightly lower as expected due to its broader beam. The total powers of both EW and the NS groups and the power as seen by an EW×NS interferometer as expected peak near the transit time of the Galactic center.

A rough estimate of the system temperature was obtained by convolving the 408 MHz all sky image (Haslam et. al., 1982) with the beams of the elements of the interferometer (EW group and a NS group) and using a temperature spectral index, α_T ($T \propto \nu^{-\alpha_T}$) of 2.7 for regions away from the Galactic plane and 2.5 towards the Galactic center. It is to be noted that the the regions from zenith angle (za), za=-69.°86 to za=-90°are circumpolar at MRT. These effects of circumpolarity were included while carrying out the convolution. The expected variation in system temperature with RA after taking into account the receiver temperature (400 K) is shown in Fig 1.4(b). We note that our measurements for the region of the sky under consideration (RA range 18:00 hrs to 24:00 hrs and 00:00 hrs to 03:00 hrs) are qualitatively similar.

The estimated total powers from the non-AGC self correlation measurements can be affected by a gain factor and a constant level shift. Let us say the true total power from the sky as seen by the EW and the NS groups respectively is P_{Tew} and P_{Tns}, then we can write ,

$$P_{Tew} = k_1 P_{ew} + C_1,$$

$$P_{Tns} = k_2 P_{ns} + C_2$$

where P_{ew} and P_{ns} are the estimated values of the total powers from the non-AGC self correlation measurements of the EW and the NS groups respectively and k_1, C_1, k_2, C_2 are some constants. From the analysis of 408 MHz all sky image (Haslam et. al., 1982), we know that $P_{Tns} \approx P_{Tew}$ for the region of the sky under consideration. The measured values of P_{ew} and P_{ns} from the non-AGC measurements are also nearly equal i.e. $P_{ew} \approx P_{ns}$. From this we can approximate $k_1 \approx k_2$ and $C_1 \approx C_2$. Thus the true power $P_{Tew\times Tns}$ as seen by an EW×NS interferometer can be written as,

$$P_{Tew\times Tns} \approx \sqrt{P_{Tew} \times P_{Tns}} \approx k\sqrt{P_{ew} \times P_{ns}} + C$$

where the constants k and C need to be estimated.

To estimate the values of the constant k and C, we used sources in the MS4[10] sample

[10]The Molonglo 4 Jy southern sky (MS4) sample. This is a flux density limited complete sample of sources brighter than 4 Jy at 408 MHz in the declination range -85°< δ <-30°, excluding the regions within the Galactic latitude $|b|$ <10° and the regions covered by the Magellanic cloud regions. There are total 229 sources covering 2.43 Sr of the sky in this sample.

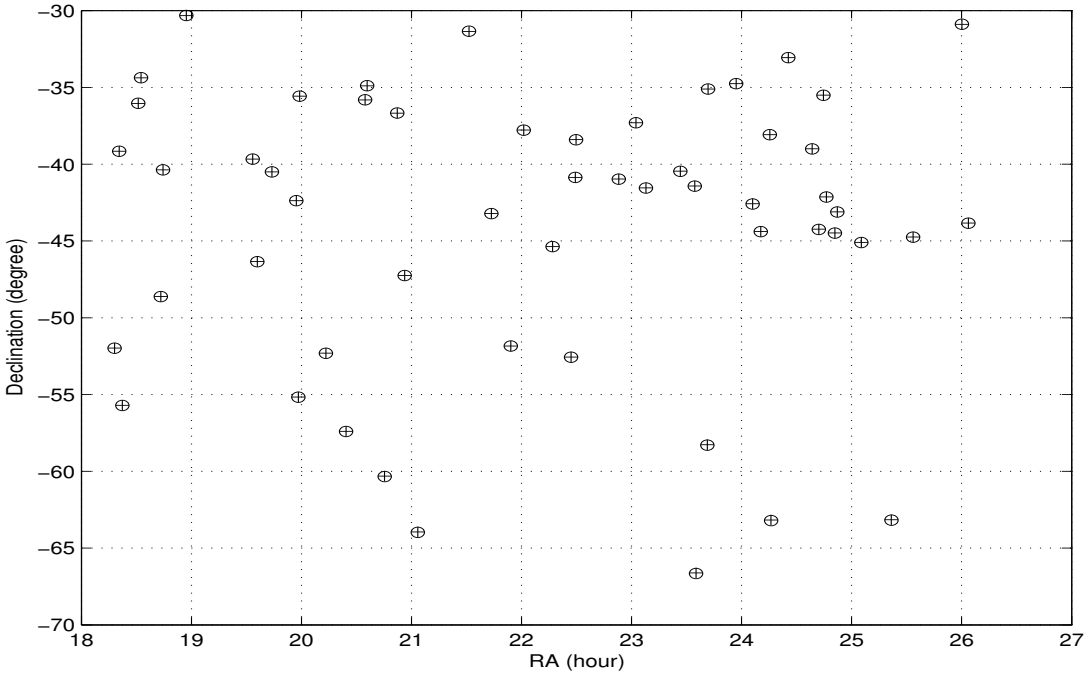

Fig. 7.10: The plot shows the distribution of 55 sources from the MS4 sample used to scale the total power estimated using the non-AGC measurements. The sources are well distributed across the entire RA range and are located away from the Galactic plane.

present in the region of the sky covered in our images. We selected from about 100 MS4 sources (which lie in region of the sky imaged), those which met the following criteria.

a. The source is detected with a fitted peak flux density of more than 10σ in the MRT image.

b. The source is unresolved in the MRT image and at 843 MHz in the MOST image (resolution$\approx$43″).

c. The flux density of the source is known at a good number of frequencies preferably around 151.5 MHz.

d. The fit to the measured spectra is good and the spectrum can be approximated by a single power law. The fitted flux density at 160 MHz should not differ by more than 20% with the measured value in culgoora catalogue (if available).

e. The source is away from the Galactic plane and lies in an empty field.

After subjecting these sources to the above mentioned criteria, 55 sources met our requirement and their distribution in the sky is shown in Fig. 7.10. The flux density for each one of them at 151.5 MHz can be accurately estimated because the fitted spectra matches well with the measured flux densities at a range of frequencies including the frequencies near 151.5 MHz (references for the flux densities obtained via private communication from

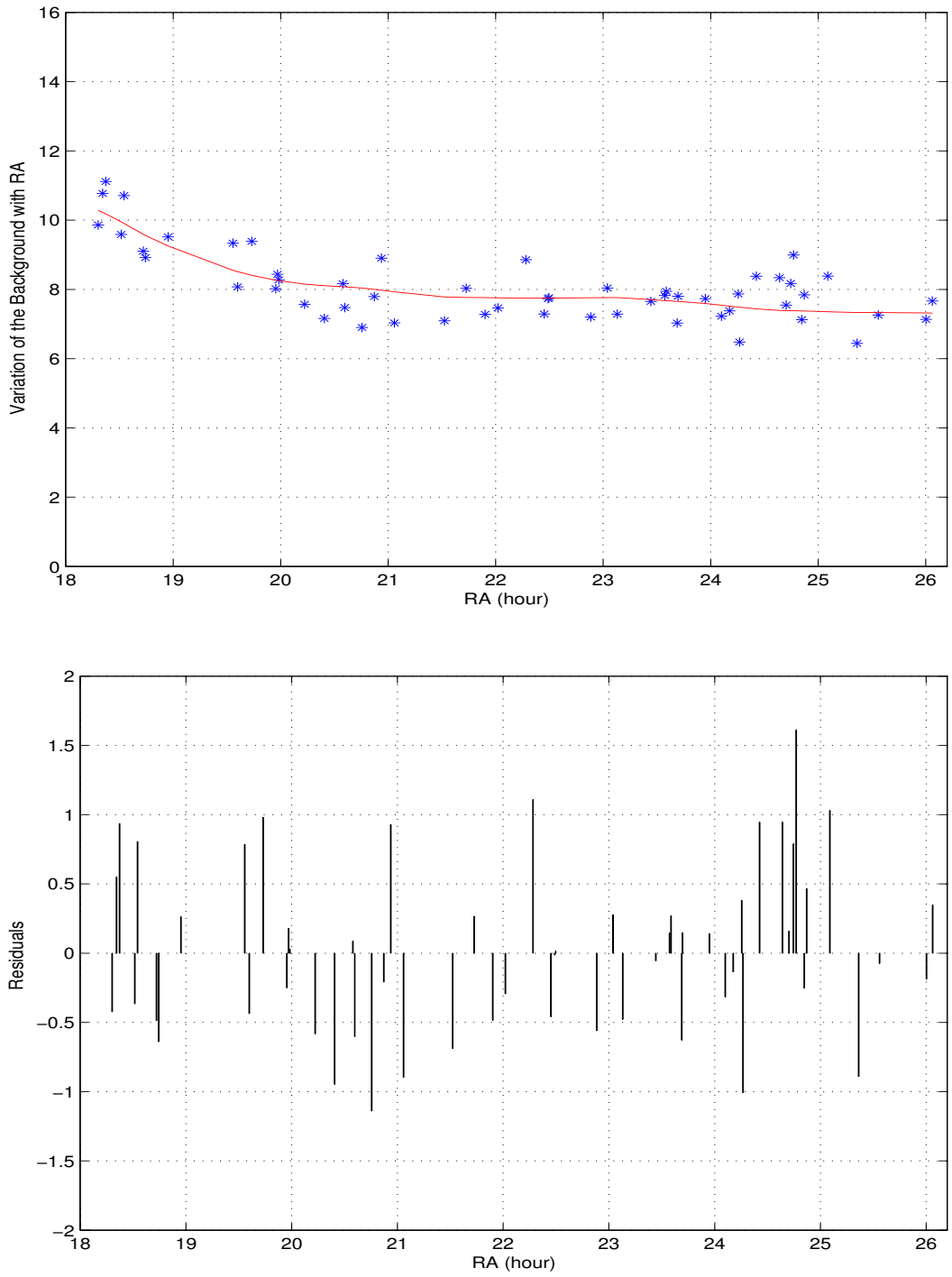

Fig. 7.11: The upper plot shows the ratios (shown by *) of the flux densities of the MS4 sources at 151.5 MHz with their peak fitted flux densities (arbitrary units) from the MRT images. The curve shown is the scaled version of the total power as seen by an EW×NS interferometer estimated using the non-AGC measurements to fit the ratio using Eqn. 7.8. The lower plot shows the residuals (difference in the actual ratios shown as * and the fitted curve) for each of these 55 sources. The rms difference in the actual ratio and the fitted curve is ≈6.3%.

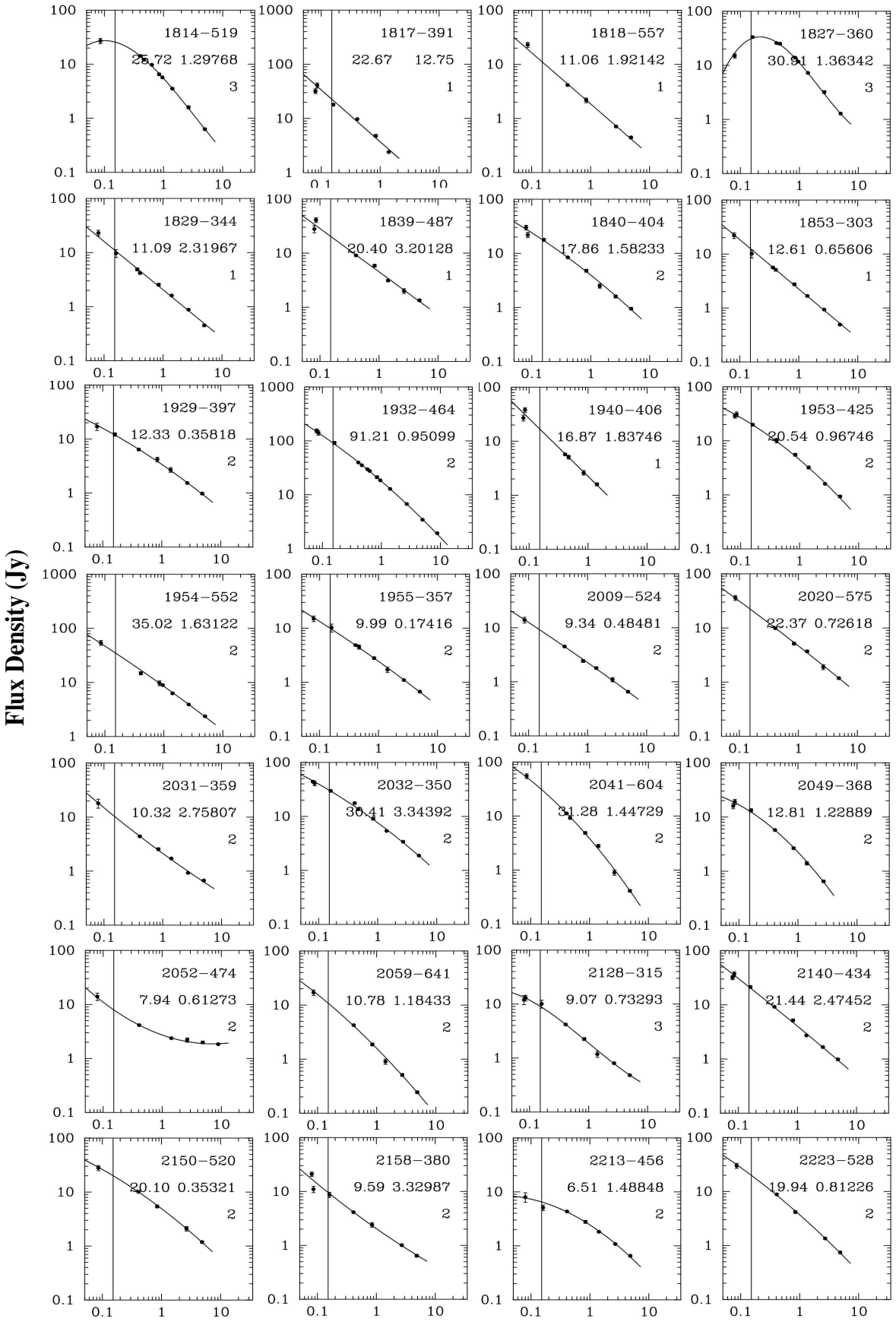

Fig. 7.12: Radio Spectra of the MS4 sources used to estimate the required scaling of the total power measurements. The spectra have been obtained from R. Hunstead and A. Burgess via private communication. Some details are in (Burgess, 1998). The vertical line shows the frequency of 151.5 MHz and the corresponding fitted flux density is shown on its immediate right side. The names of the individual sources are shown on the top right hand corner of each plot. On the X-axis frequency is in GHz. (contd...)

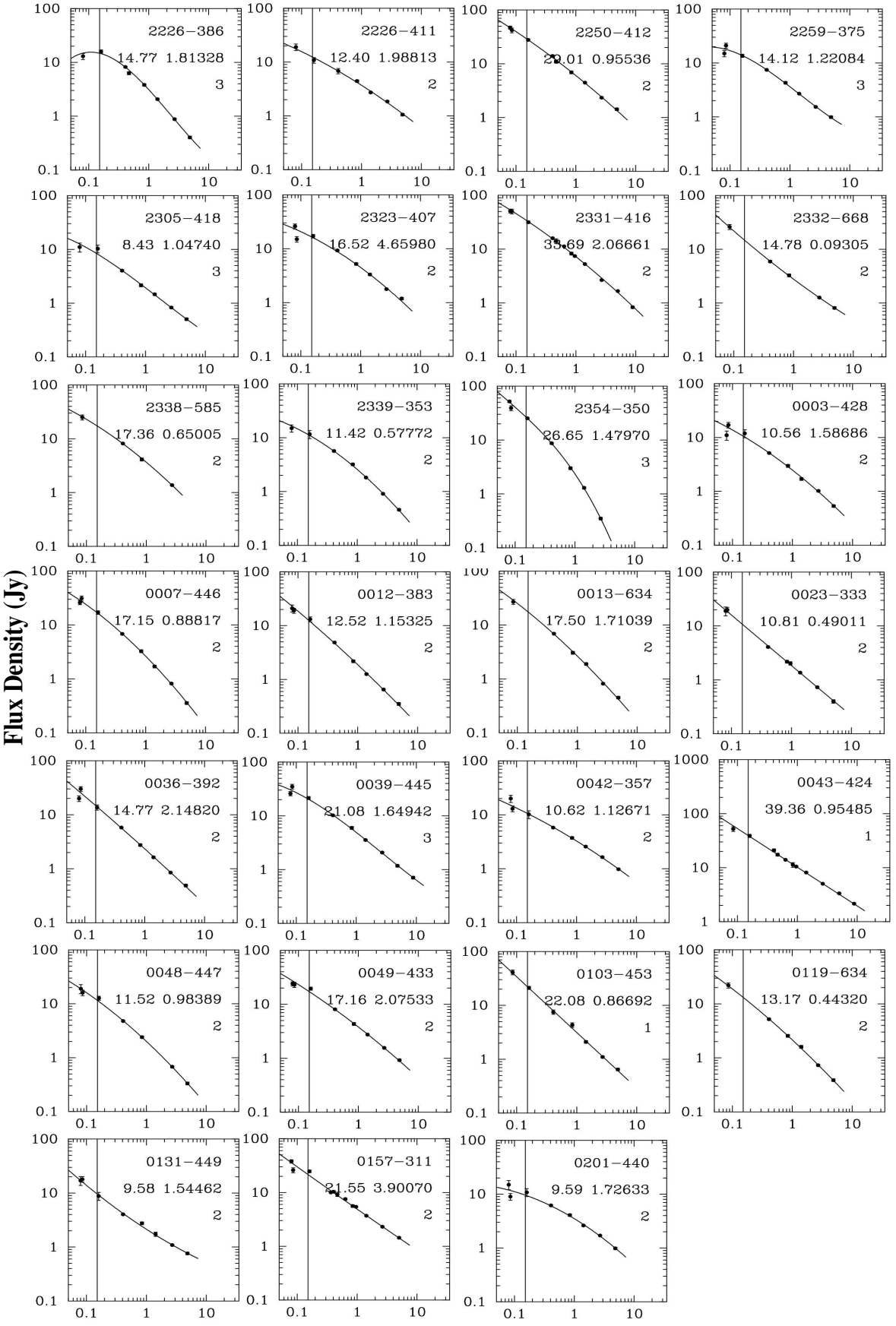

Fig. 7.12: Radio Spectra of the MS4 sources used to estimate the required scaling of the total power measurements. The spectra have been obtained from R. Hunstead and A. Burgess via private communication. Some details are in (Burgess, 1998). The vertical line shows the frequency of 151.5 MHz and the corresponding fitted flux density is shown on its immediate right side. The names of the individual sources are shown on the top right hand corner of each plot. On the X-axis frequency is in GHz.

R. Hunstead & Ann Burgess(Burgess, 1998)). The measured and the fitted spectra for each of these sources is shown in the Fig. 7.12.

After applying the correction for the derived primary beam of the helix (Sec. 7.2.1.2), we plotted the ratio of the estimated flux density of the 55 MS4 sources at 151.5 MHz from the fitted spectra to their fitted peak flux density in the MRT images as a function of RA as shown in the Fig. 7.11. The ratio is expected to follow the correction needed to be applied to incorporate the variation of the sky background in the MRT images with RA (Fig. 7.9(c)), in addition to a multiplicative constant (a) which basically is to scale the images from arbitrary units to the true flux density scale. Thus the required correction to be applied as a function of RA, say $f(RA)$, to bring the images to the true flux density scale and incorporate the variation of sky background can be written as,

$$f(RA) = a[k\ \sqrt{P_{Tew}\,P_{Tns}} + C] = k'\ \sqrt{P_{Tew}\,P_{Tns}} + C' \tag{7.8}$$

where k' and C' are some constants. In order to estimate the constants k' and C', we scaled the curve of the total power variation of the sky background estimated using the non-AGC measurements to fit to the ratio (using Eqn. 7.8), which is shown in Fig. 7.11(a). The values of the parameters obtained from the fit are k′=2.2518584 and C′=-0.1226518. A low value of c' indicates that the self correlation measurements used were not affected by any significant DC. The difference (residuals) between the flux density ratio of the 55 MS4 sources and the MRT peak amplitudes with the fitted curve is shown in Fig. 7.11(b). The rms difference is ≈6.3%.

Using the total power estimated and the Eqn. 7.8, all the images were transformed from arbitrary units to true flux density scale. The images which were not deconvolved (covering the sidereal hour range 15:06 hrs and 18:00 hrs and presented in the Appendix A) are also at the same reference scale as the deconvolved images, so they were also transformed using the total powers estimated and the expression in Eqn. 7.8.

The images at this stage are in true flux density units. However it is customary to refer to the true flux densities of sources in survey through a few well known primary calibrators. In view of this we discuss our choice of primary flux calibrator for the MRT images.

7.2.1.4 Primary flux calibrator

The Baars et. al. (1977) flux density scale is the most widely accepted for frequencies up to 30 GHz. It is based on the absolute flux density measurements of Cas A and has a list of several secondary calibrators distributed in RA. The calibrators however are all in the

northern hemisphere and cannot be used directly to calibrate the flux densities in the MRT survey.

The RBC[11] scale (Roger et. al., 1973) is another widely used flux density scale. This is based on the observations of 225 sources at 10 and 22 MHz by the Dominion Radio Astrophysical Observatory. The flux density scale of the Cambridge 6C survey at 151 MHz is based on the RBC scale. Since the sources for the RBC scale are all in the northern sky and 6C is also a northern sky survey ($\delta \geq 30°$), they cannot be used directly for the flux density calibration of the MRT sources.

Earlier attempts for flux calibration of MRT images : For partial resolution survey with the MRT (Golap, 1998), MRC1932-464 was used as a primary flux calibrator with a flux density of 87 Jy. The expected primary beam of the helix was used to correct for the estimated flux densities across the declination of the survey.

Choice of the primary flux calibrator : In order to look for potential sources as primary calibrators for the images presented in this dissertation, we investigated the possibility of using the calibrators used for the SUMSS survey and from the 55 MS4 sources discussed earlier. Among these sources which met the following conditions were selected.

1. The source should be non-variable.
2. The source is unresolved in the MRT image and the 843 MHz MOST image (SUMSS survey, resolution 43″). For ensuring that the sources is of much smaller size compared to the MRT beam higher resolution images at 4.8 GHz (ATCA) in the MS4 sample (Burgess, 1998) were also inspected.
3. The source has a minimum apparent strength of 50σ at 151.5 MHz in the MRT image.
4. The flux density of the source has been measured at a good number of frequencies including around 151.5 MHz. The fitted spectrum should be in good agreement with the measured flux densities. The fitted flux density at 160 MHz should not differ by more than 20% with the measured value in Culgoora catalogue (if available).
5. The source should be away from the Galactic plane and in a relatively empty region.

Long term monitoring of 55 sources used for calibration purposes by the MOST at a frequency of 843 MHz was carried out over a period of 13 years from 1984 to 1996 at irregular intervals by Gaensler & Hunstead (2000). They showed that 19 of these can be considered non-variable. The 843 MHz SUMSS survey was calibrated using seven of these non-variable calibrator sources having flux density >5 Jy (at 843 MHz). Only one source among these seven calibrators lies in the RA range 19 to 24 hrs (RA range 18 to 19 hrs was

[11] Roger, Bridle and Costain.

Source Name	RA (J2000)	DEC (J2000)	Flux density (true)	Flux density (attenuated)[$$]	$\left(\frac{peak}{rms}\right)^{\$}$	size	z (red shift)
MRC2140-434	21: 43: 33.4	-43: 12: 48	21.44	21.42	90	71.″2	0.650
MRC2323-407	23: 26: 33.8	-40: 27: 17	16.52	16.39	60	15.″6	1*
MRC2354-350	23: 57: 01.1	-34: 45: 39	26.65	26.30	95	17.″0	0.0487

Table 7.3: The sources in the RA range 19:00 to 24:00 hrs considered as potential primary flux calibrators for MRT for the images presented here. MRC2354-350 is detected in the images with highest signal to noise ratio and is used as the primary flux calibrator for the images. [$] indicates the ratio of fitted peak flux density in the MRT images with the rms noise, [$$] indicates the flux density after attenuation due to the helix response, * indicates most probable value.

excluded to avoid the Galactic plane) and declination range of MRT, which is MRC2323-407. It has a flux density of 5.21 Jy at 843 MHz and 16.52 Jy at 151.5 MHz. This is among one of the potential candidates considered for the primary flux calibrator at MRT.

Next we looked for possible calibrator sources in the MS4 sample. At metre wavelengths (80 and 160 MHz) detailed study of the intensity variation in the 412 extragalactic sources which were randomly selected from the 2,000 sources in the Culgoora list was carried out from 1970-1984 by Slee & Siegman (1988). Their measurements provided one of the very few extensive databases for studies of flux density variations at metre wavelengths. They classified the sources into two categories at 160 MHz as variable and non-variable sources. We looked for suitable sources in the non-variable category in the MS4 sample from RA 19:00 hrs to 24:00 hrs. Only three sources namely, MRC2140-430, MRC2323-407 and MRC 2354-350 satisfied all the desired criteria including non-variability and are listed in the Table. 7.3. Their measured and fitted spectra are also shown in Fig. 7.12.

Among the three calibrators mentioned above we chose MRC2354-350 as the primary flux calibrator for MRT. This source has maximum signal to noise ratio among the three sources. Fig. 7.13 shows the contour image of this source at 4.8 GHz and 151.5 MHz. The source has a size of 17″and is a point source for MRT. In view of this all the images were appropriately scaled up by 0.78% so as to be in confirmation with the flux density of the source MRC2354-350 being 26.30 Jy at 151.5 MHz. The details of its flux density measurements at various frequencies are given in Table. 7.4. The uncertainity in its flux density at 151.5 MHz is within 1.5%.

It may be noted that MRC1932-464 has been classified as a variable source in the studies of Slee & Siegman (1988). Due to this it was not preferred for primary flux calibrator for the images presented in this dissertation inspite of it being used as a primary flux calibrator in the earlier work.

We now present in the next section the MRT images and their analysis followed by catalogue construction. The obtained source list and some interesting aspects of the full resolution deconvolved images are also presented.

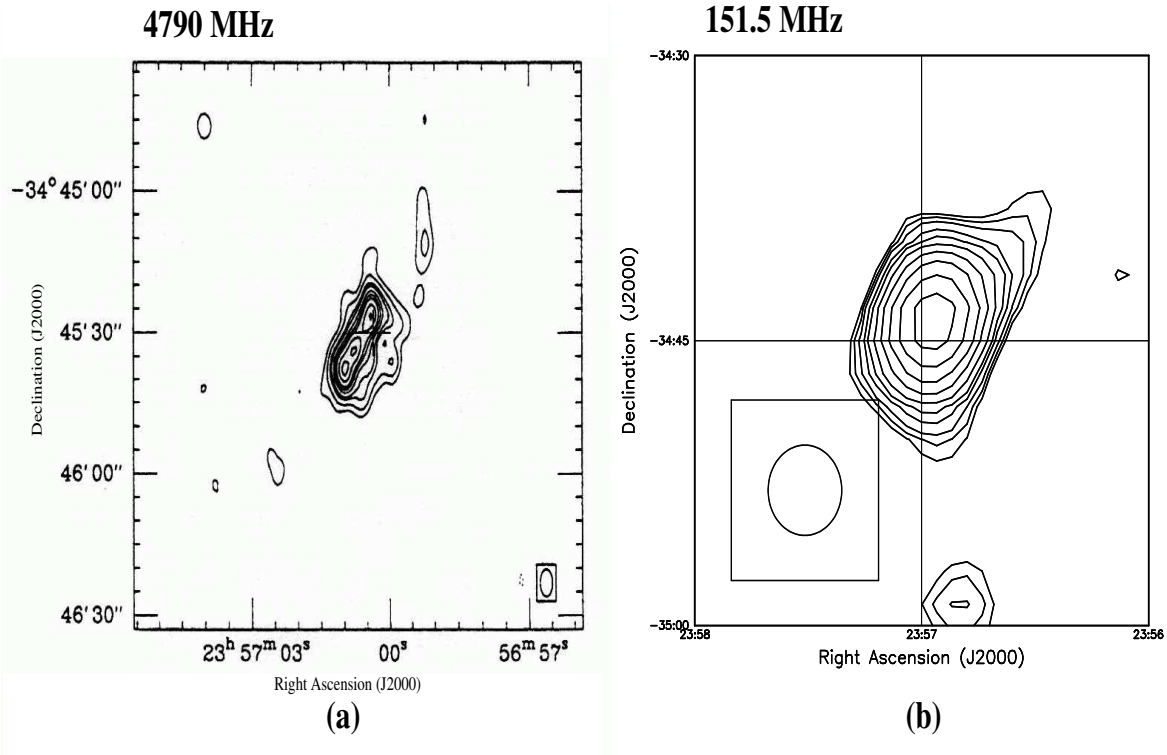

Fig. 7.13: The image of 2354-350 at (a) 4.79 GHz (using ATCA courtesy Burgess (1998)) and (b) 151.5 MHz (using MRT). The spectrum of the calibrator is also shown in Fig. 7.12. The high frequency image reveals that the source has a much smaller size compared to the MRT beam and also lies in an empty field, thus suited for being used as a primary flux calibrator. In the image (a) the contour levels (% of peak which is 16.9 mJy beam^{-1}) are -4, 4, 8, 15, 20, 30, 50, 70, 90. In the image (b) the contour levels are 1.0, 1.5, 2.0, 2.8, 3.6, 5.0, 7.2, 10.0, 14.4, 20.1, 28.8, 40 Jy beam^{-1}. The rms noise is ≈260 mJy beam^{-1}.

Frequency (MHz)	Flux density (Jy)	error (Jy)	Reference
80	52	2.4	CUL2354-350(Slee, 1995)
160	25.3	1.0	CUL2354-350(Slee, 1995)
408	8.70	0.35	MRC2354-350(Large et. al., 1981)
843	3.00	0.18	VOL2354-350(MOST 843 MHz)
1425	1.30	0.06	MOF2354-350(Fomalont & Moffet, 1971)
2700	0.35	0.02	PKS2354-350(Bolton et. al., 1964)
4850	0.117	0.014	PMNZ2354-350(Wright et. al., 1996)

Table 7.4: Flux densities of the MRT primary flux calibrator MRC2354-350 at different frequencies.

7.2.2 Images

We present the full resolution deconvolved images covering more than a steradian of the sky ($18^h \leq$RA$\leq 24^h30^m$, -75°$\leq \delta \leq$-10°) with a resolution 4′×4′.6sec(δ+20°.14) in J2000 coordinates. The images are given at the end of this chapter. Dirty images for an additional of about half a steradian of the sky ($15^h06^m \leq$RA$\leq 18^h$, -75°$\leq \delta \leq$-10°) which includes a large part of the southern Galactic plane including the Galactic center, with the same resolution are also presented in Appendix A. These form a part of the southern sky survey with the MRT at 151.5 MHz.

An image covering one sidereal hour range is referred by an alphabet from A (00:00 hrs-01:00 hrs) to X (23:00 hrs-24:00 hrs). The full declination range for each sidereal hour range is covered by four images made by co-adding images corresponding to different delay zones. These are so chosen to keep the net decorrelation minimum at any declination. The maximum decorrelation is less than 18% (Sec. 5.4.3). The four sets of images mentioned above to cover the entire declination range for each sidereal hour range are denoted by the number suffixes 1 to 4, after the alphabet denoting the sidereal hour range the image represents. For example an image referred as S2 covers sidereal hour range 18:00 hrs-19:00 hrs and declination range corresponding to the second declination zone.

The deconvolved images presented in this chapter have been split into 169 subimages for display as contour maps. The dirty images presented in the Appendix A have been split into 78 subimages for display. Each subimage spans 00:30 hrs (except the image covering 15:06 hrs to 15:30 hrs) in RA and 5° in declination. The RA and the declination coverage and the corresponding figure number of all the subimages is summarized in Fig. 7.14. The contour levels are -5, -3.6, -2.5, -1.8, 1, 1.4, 2, 2.8, 3.6, 5, 7, 10, 14, 20, 29, 40, 54, 72, 90, 100, 136, 180, 216, 252, 288 Jy beam^{-1}. The negative contour levels are represented using grey lines while the positive contours are represented by black solid lines. The average rms noise measured in each subimage is also shown at the bottom. The FWHM of the beam varies with declination. The FWHM in RA changes from 16.25 s (at δ=0°) to 61.8 s (δ=-75°) by a factor of ≈3.8. The FWHM along declination is constant in sin(za) coordinate system but changes as a function of declination in angular extent from 4′.6 (δ=-20°.14) to 8′ (δ=-75°) by a factor of ≈1.7. The FWHM corresponding to the center declination of each subimage are also shown on the individual maps in the bottom left corner.

***uv* coverage :** At the level of one allocation's image, all the 480 baselines are used as no baselines are rejected while imaging (except when there is interference). Thus the *uv* coverage of the full resolution images presented depends upon the availability of images for different allocations which have been used to obtain the full resolution image. Fig. 7.15

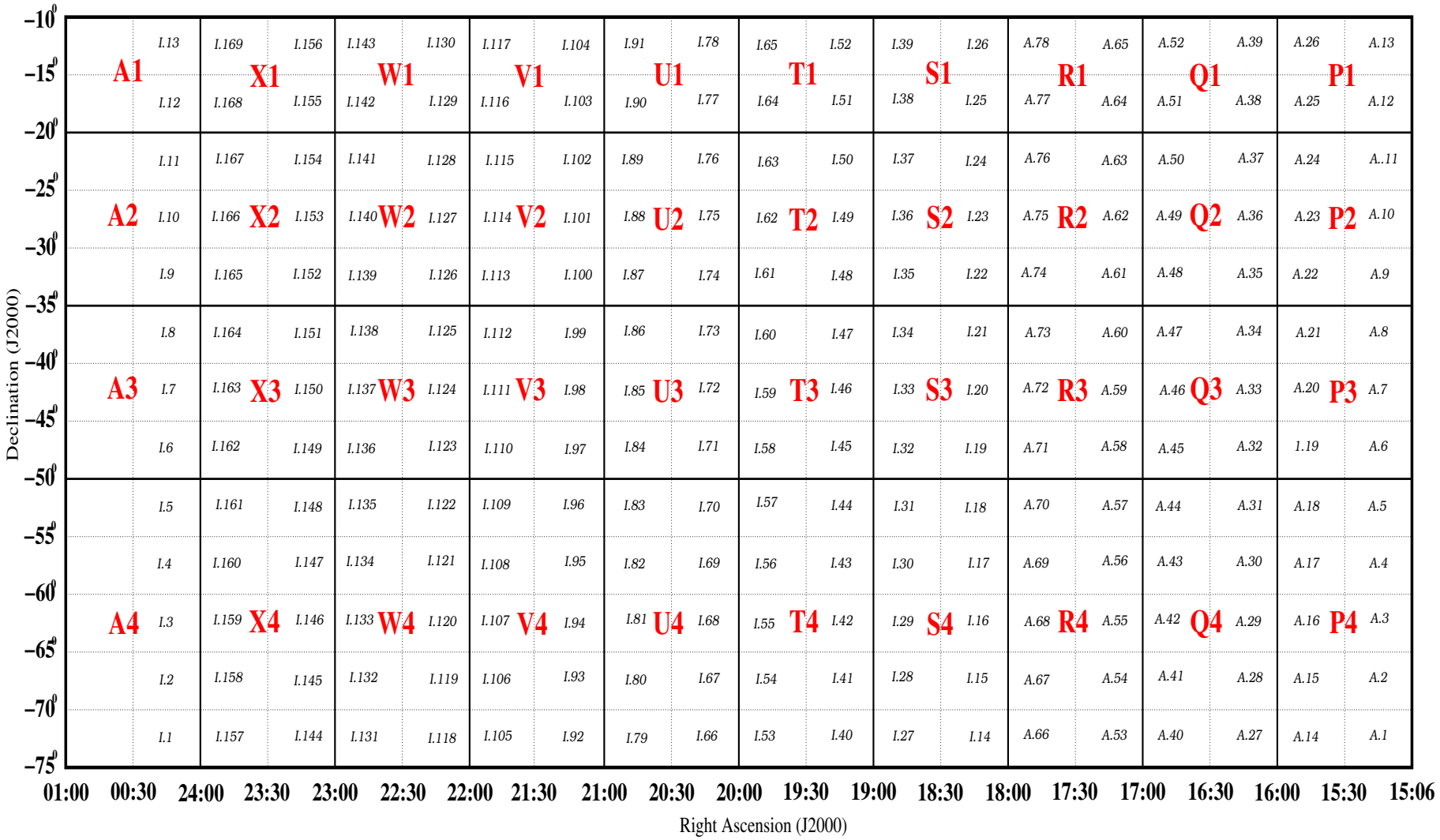

Fig. 7.14: Layout of images displayed in this thesis. An image covering each sidereal hour is referred by an alphabet suffixed by the declination zone (shown in red as P1,P2,... etc.). The figure number which displays the subimages is also shown along with the boundaries.

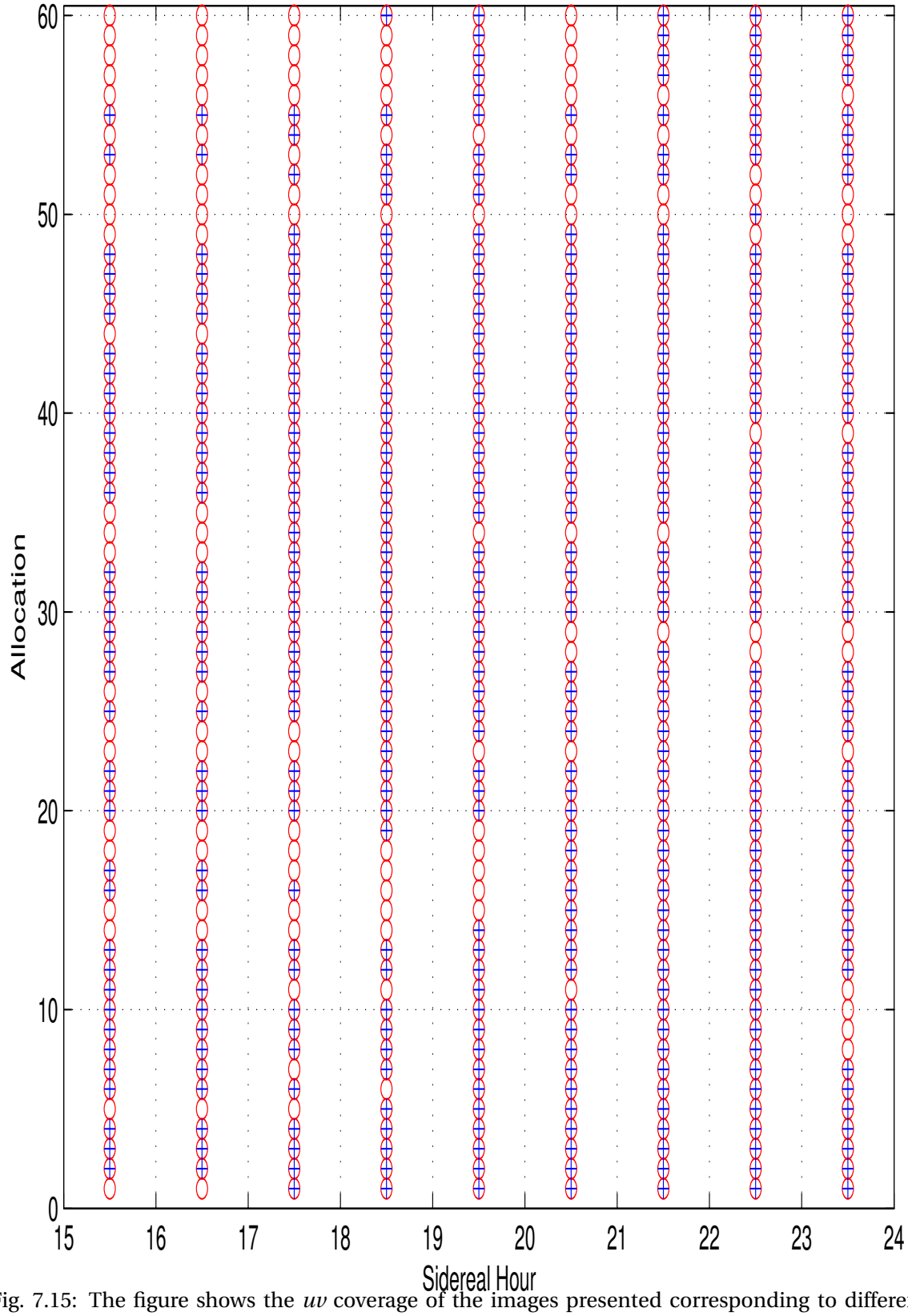

Fig. 7.15: The figure shows the *uv* coverage of the images presented corresponding to different sidereal hours. The '+' sign denotes the allocations which are present in the images synthesized while the hollow 'O' denote the missing allocations. It is clear from the plot that for most of the sidereal hours the *uv* coverage is nearly complete including the short spacings (allocations 1 to 12, See Sec. 2.1.1).

Frequency	151.5 MHz
Bandwidth	1 MHz
Declination Range	-75°≤ δ ≤-10°
RA span	18^h ≤RA≤24^h30^m
Typical image size	15°×15°
rms level (1σ)	≈260-390 mJy beam^{-1}
Resolution	$4' \times 4'.6$ sec (δ+20°.14)
Polarization	Right circular (IEEE)

Table 7.5: Characteristics of MRT images

shows the allocations for which the images were included to obtain the full resolution images covering the different sidereal hour ranges. For most of the images presented in this chapter the *uv* coverage is nearly complete and uniform. The number of allocations present[12] to obtain the full resolution images vary from 47 to 54 out of a total 60 allocations[13]. We also note that most of the allocations from 1-12 which contain short spacings are also present in all the images. Due to the good *uv* coverage the MRT images are sensitive to the extended structures and their morphologies is well represented in the images. The sidereal hour having the most complete and uniform *uv* coverage are the ones covering RA 21:00-22:00 hrs and RA 22:00-23:00 hrs while the most sparse coverage is for the image covering the sidereal hour 15:06-16:00 hrs and 16:00-17:00 hrs.

The maps : The maps presented here cover a large region of the sky and contain considerable amount of information. It is beyond the scope of this thesis to give complete analysis of all this data. However important conclusions which can be easily extracted from the deconvolved images presented in this chapter are also true about the images presented in the Appendix A. A detailed interpretation of the dirty images covering the Galactic plane need a separate treatment and is beyond the scope of this thesis.

The key characteristics of the images displayed here are summarized in the Table. 7.5. The rms noise varies[14] with RA due to changing brightness temperature of the sky, from 260 mJy beam^{-1} to 390 mJy beam^{-1}. Since the response of the helix varies along declination (due to meridian transit imaging there is no effect of helix response along RA except for the fact that it modulates the PSF), the sensitivity becomes progressively poorer in declination away from the direction of the peak response up to a factor of 2 at the ends of declination

[12]It is to be noted that for all the images presented in this thesis, visibilities with atleast one allocation from the tenth block have been used. This ensures that the length of the maximum baseline in the NS is nearly 880 m. Due to this the FWHM of all the images in declination corresponds to the maximum length of the baseline in the NS arm and same.

[13]For *uv* coverage only the first 60 allocations are important as the last 3 allocations mostly contain baselines which are repeated in allocations 55 to 60.

[14]The rms noise is also a function of declination due to the primary beam of the helix. During our discussion on rms noise, it would always imply rms noise without taking into account the helix beam unless specified. The rms noise at any declination can simply be computed by dividing it by the primary beam response of the helix at the concerned declination.

range of interest. There are fields which are simpler and contain mostly numerous small diameter sources while there are also fields which have the extended sources. We would describe general interpretation of the maps including highlighting some interesting features.

Unavoidably certain regions of the map have been affected due to various factors which can be broadly divided into sources appearing in grating lobes/aliased images and regions affected by residual DC along RA which could not be effectively removed from the images. The reliability in such areas is significantly affected and is best judged by the examination of the contour maps themselves. Another imperfection in the map is due to imperfect CLEANing of several strong sources. This problem gives rise to compact negative sidelobes which immediately straddle nearby individual sources. An example of this is the unrealistic negative contours which surround the source MRC2211-690. These sidelobes are unfortunate as they cause confusion in some areas with legitimate sources. These can generally be easily identified due to the proximity of the strong sources and being characteristically different from the genuine emission. The total region of the sky lost due to regions not considered reliable is ≈3.6%. For source searching the regions including the Galactic plane is also not considered, which makes a total 4.5% of the region covered not being included in the source list.

7.2.2.1 Noise in the images

The expected rms noise ΔS_{min}, in the images made with 4 s of integration is given by,

$$\Delta S_{min} = \sqrt{\left(\frac{\sqrt{2}\ 2k_B(\sqrt{T_{sys_{ew}} T_{sys_{ns}}})}{\eta_{eff}\ \sqrt{N_b} A_e\ \sqrt{\Delta \nu t}} \right)^2 + S_{conf}^2} \tag{7.9}$$

where the symbols have their usual meanings (as in Sec. 1.5.2). Since the estimated primary beam of the helix is wider from the theoretical response (Sec. 7.2.1.2), to conserve the total collecting area, the response of the helix in the direction of maximum response would be attenuated instead of assumed value of unity (no attenuation) as in the Eqn. 7.9. The factor (R) by which the response is attenuated is given by,

$$R = \frac{\int P_{theory}\, d\Omega}{\int P_{derived}\, d\Omega} \tag{7.10}$$

where P_{theory} and $P_{derived}$ are the theoretically expected and the estimated normalized power pattern response of the helix and Ω is the solid angle covered by the helix beam. The estimated value of R is 0.9 (using only the solid angle corresponding to the FWHM of the

Sidereal hour	T_{sys} (K)	No. of allocations	No. of days	rms noise (mJy beam^{-1}) expected	measured	ratio $\left(\frac{\text{measured}}{\text{expected}}\right)$
18.5	1680	48	81	310	390	1.3
19.5	1100	53	90	200	360	1.8
20.5	860	47	87	165	260	1.6
21.5	800	55	90	160	260	1.6
22.5	760	54	100	145	260	1.8
23.5	730	48	80	150	290	1.9

Table 7.6: The comparison of the measured rms noise with the expected rms noise in the images covering different sidereal hour ranges. The measured rms noise is typically 1.7 times the measured noise.

Sidereal hour	zone 1	zone 2	zone 3	zone 4	average
18:00-19:00	378	403	396	389	388
19:00-20:00	349	363	368	381	361
20:00-21:00	253	265	261	273	258
21:00-22:00	254	255	261	271	258
22:00-23:00	255	260	267	267	259
23:00-24:39	286	299	305	305	291

Table 7.7: The average measured noise (mJy beam^{-1}) in different delay zones of the images covering different sidereal hours.

power pattern). Thus the net effective thermal noise[15] would be higher and the expected rms noise is given by,

$$\Delta S'_{min} = \frac{1}{R}\sqrt{\left(\frac{\sqrt{2}\,2k_B(\sqrt{T_{sys_{ew}}T_{sys_{ns}}})}{R\,\eta_{eff}\sqrt{N_b}A_e\sqrt{\Delta\nu t}}\right)^2 + S^2_{conf}} \tag{7.11}$$

The expected confusion at 151.5 MHz at the resolution of MRT is ≈18 mJy (Sec. 1.5.2). In the above equation, to calculate the system noise one needs to know the system temperature and the number of days of data used to synthesize the image. Estimation of the system temperature has been discussed earlier (Sec. 1.5.2). The variation in system temperature with RA is shown in Fig. 1.4 assuming a receiver temperature of 400 K for the both EW and the NS groups. In addition the images across different allocations have been combined with weights equal to the inverse of the relative gains which results in increased thermal noise. Based on the relative gains in different allocation's image for one sidereal hour image the increase in the noise due to uniform weighting is typically about 15-20%. Taking this into account, using the system temperature and the number of days of data used we can calculate the expected noise as given in Table 7.6.

[15]We recall that the noise in the images is discussed without the primary beam of helix taken into account. At any declination the actual noise would be higher depending upon the corresponding attenuation due to helix primary beam response.

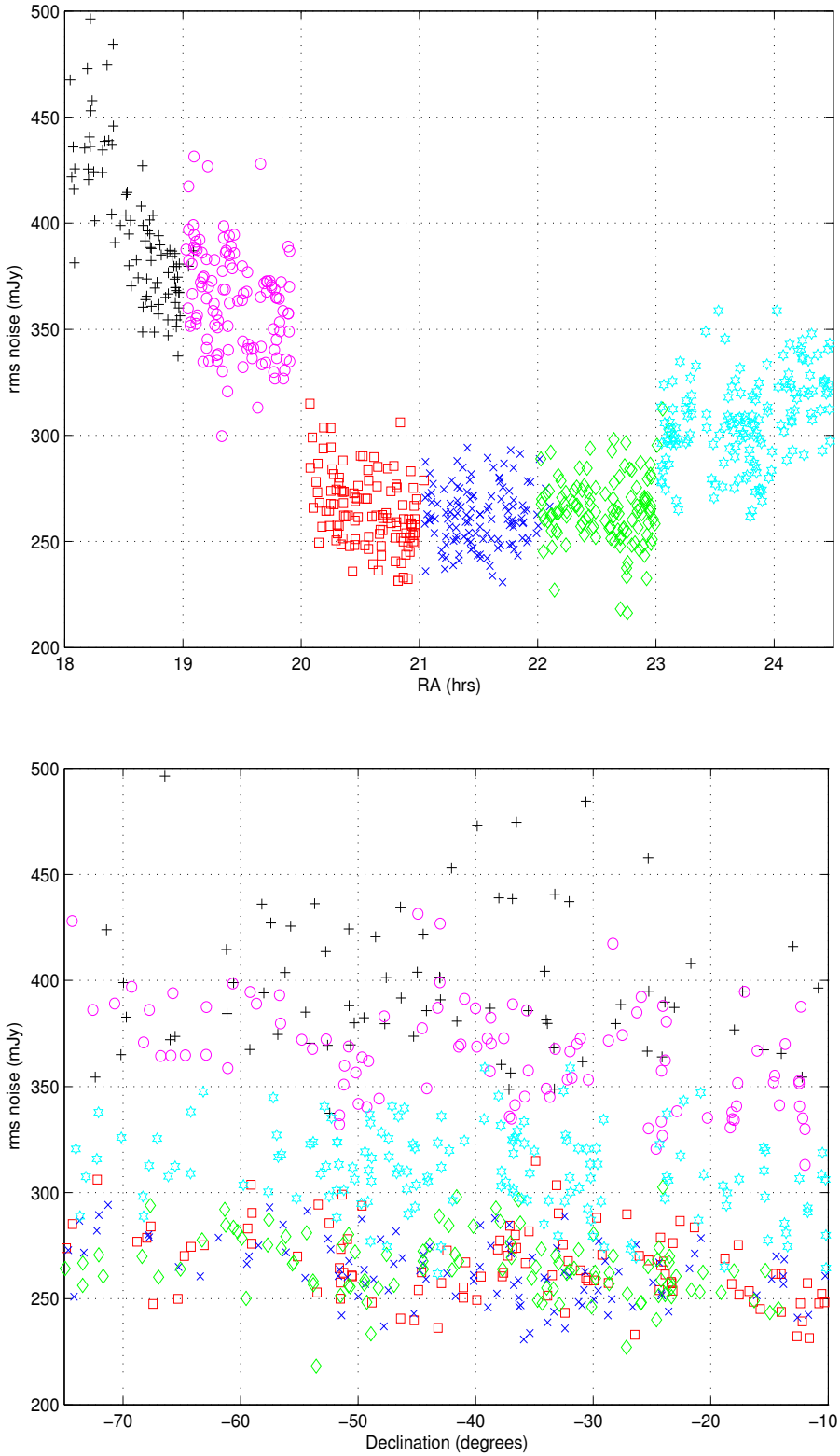

Fig. 7.16: The measured rms noise within individual regions devoid of strong sources for various sidereal hour ranges (shown by different symbols) as a function of RA (upper plot) and declination (lower plot) before applying the primary beam correction. The variation in the rms noise with RA is due to changing brightness temperature of the sky and the number of days of data used for each sidereal hour. The rms noise within each sidereal hour is nearly constant with declination as seen in the lower plot, which shows that the rms noise is dominantly thermal.

To estimate the noise in the images, we selected many regions which appeared to be devoid of strong sources[16]. Although images for each sidereal hour are made with guard zones on both sides in RA, only the region within the one sidereal hour range of interest is used for estimating the rms noise. Typically in an image covering one delay zone for a given sidereal hour range ≈20-25 such empty regions were selected for this purpose. The rms noise was estimated for each of these regions. The individual values of rms noise in these empty regions were averaged in quadrature (with weights being equal to the number of pixels used for individual values) to obtain the overall noise in the image. Fig. 7.16 shows the variation of rms noise in each of the empty regions selected in the different sidereal hour images as a function of RA. The rms noise varies with RA due to change in the brightness temperature of the sky. The rms noise in the images corresponding to different sidereal hours also varies with RA due to different number of one day images used to synthesize the full resolution image.

Fig. 7.16 also shows the variation of rms noise in each of the empty regions selected as a function of declination for different sidereal hour images. The rms noise in the images (without any primary beam correction) is expected to be independent of declination. The scatter in the rms noise at any given sidereal hour is likely due to region having contribution from weaker sources (confusion noise), sidelobes of nearby strong sources, region being affected due to sources in grating lobes/aliased images, bandwidth decorrelation and the accuracy with which the rms noise itself can be estimated. This scatter in the measured rms noise itself is typically 40 mJy beam^{-1}. Table 7.7 shows the rms noise measured within each delay zone and the overall noise for the images corresponding to various sidereal hours. The rms noise as expected is nearly constant in all the declination zones of each sidereal hour. This clearly indicates that the noise is dominantly thermal and confusion noise is negligible. If the images were confusion noise limited the noise variation would have followed the primary beam shape of the helix.

Table 7.6 shows the comparison between the expected and the measured rms noise. For the images covering each sidereal hour, the number of allocations used and the total number of days of data used (as for some allocations more than one days of data has been used) is given in Table 7.6. It also shows the system temperature of the sky at center RA of the each sidereal hour images presented here. We note that the rms noise estimated in the images is higher as compared to the expected theoretical noise on average by a factor of 1.7. There are various factors which may be the likely responsible for this higher rms than expected. Some of the most likely of them are higher receiver temperature than assumed value of 400 K, aliased images, possible residual sidelobes, residual DC, calibration

[16]At this stage the images are in true flux density units except for applying the primary beam correction.

errors and weak interference. It is likely to be a combination of many factors which may be responsible to give this higher value of rms noise. At the level of each allocation the visibilities corresponding to each baseline have been given uniform weighting due to which thermal noise suffers. Due to these reasons the expected thermal noise would be higher.

Aliased images of strong sources like MRC2152-699, MRC2356-611 are seen at multiple declinations and can be identified in the full resolution images. Since images of all sources will have their aliased images of diminished intensity it would contribute to the measured rms noise. In addition although the regions selected were taken away from the confused regions, artifacts and spurious sources, in the images for a few hours it is quite difficult and is likely that some contamination of the spurious features contributes to the rms noise. One such example is in image covering sidereal hour 19-20 hrs/20-21 hrs, the entire declination and a large part in RA is affected by the grating response of Cyg A. A quantitative estimate needs to be carried out to estimate the increase in the rms noise due to aliased images of all sources. We also need to consider the contribution due to undetected weak interference in the images. Sachdev (1999) showed that if one assumes that there is unidentified interference at each sidereal second in the data of only one day used to make the images, the ratio of undetected interference to noise in the images would be $2.83\sqrt{\frac{\tau_{integ}}{N}}$, where τ_{integ} is the integration time and N is the number of days of data used to obtain the full resolution images. Taking the total number of days of data used as typically 90, with an integration time 4 s this ratio is ≈0.6. Therefore the total noise expected would increase by ≈20%. This still leaves the measured noise 1.5 times the expected noise.

7.2.2.2 Surface brightness sensitivity

The surface brightness sensitivity in the synthesized images is given by,

$$B = \frac{S}{\Omega} = \frac{S}{(\frac{\pi}{4ln2})\Omega_{beam}} \mathrm{Wm^{-2}Hz^{-1}Sr^{-1}} \tag{7.12}$$

where S is the limiting point source sensitivity and Ω_{beam} is the solid angle of the two dimensional synthesized beam. Since the rms noise in the images changes with RA, the corresponding surface brightness sensitivity also changes. Taking the case for the mosaic covering RA range 18:00 hrs to 19:00 hrs where the rms noise is ≈390 mJy, the corresponding surface brightness sensitivity is $2.1\times10^{-21}\mathrm{Wm^{-2}Hz^{-1}Sr^{-1}}$ (1σ). This is a good surface brightness sensitivity limit to look for extended features. We now discuss the second part of this chapter related to source catalogue.

7.3 Source catalogue

In this part of the chapter, we first describe the algorithm developed for catalogue construction including source extraction and parametrization. Next we present a catalogue derived from the images presented. Our initial analysis of the catalogue and its cross comparison with the MRC catalogue at 408 MHz and Culgoora catalogue at 160 MHz are also presented.

Deriving a catalogue of sources from astronomical images is a common requirement and a number of algorithms have been developed for this purpose (like DAOPHOT[17]). However many of these program were developed specifically for extracting point sources from optical images. These are generally not well suited for radio images in which the noise has peculiar characteristics that causes trouble when the optical source finding procedures are used (as an example the rms noise may vary from region to region and there are large residual structures still remaining after the CLEANing is complete). Due to this source detection and parameterization algorithms were specifically developed for deriving catalogue of sources from radio images like the tasks SAD, VSAD, IMSAD, HAPPY etc. of standard data reduction packages AIPS and MIRIAD. The format of the images presented here is in RA and $\sin(za)$ coordinate system. The FWHM of the beam varies from one end to another by a factor of $\approx$3.8 in RA and $\approx$1.7 in declination. No such readily available software seemed to be easily adaptable to these conditions. Our initial attempts with packages for source extraction like SexTractor[18] were not encouraging.

Our images at present have not been converted into standard FITS format due to which we could not exploit the generalized sources detection algorithms like IMSAD. In view of this it was essential to develop our own catalogue construction software package, by adapting a few features from the well known source detection algorithms and adding new ones which were specifically required for our need. We describe the source detection and parameterization technique developed keeping in mind our specific requirements.

7.3.1 Source - detection, fitting and inspection

Our initial attempts for source detection and parameter extraction was based on similar approach as of the task SAD (Search And Destroy) in AIPS. In this mode the maximum of the image is detected and a fitting with an appropriate model beam (2-D elliptical Gaussian) is carried out. After a satisfactory fit the parameters of the fitted Gaussian are recorded in the source catalogue and the fitted Gaussian is subtracted from the image. In case the fit is found to be unsatisfactory i.e. the source needs to be rejected, a region is

[17] http://www.star.bris.ac.uk/~mbt/daophot
[18] http://sextractor.sourceforge.net

marked around the maximum position which is not considered for further source searching. The residual image is again searched for the maximum and the process is repeated till a user defined threshold is reached. In our case this approach did lead to a variety of problems. In case when the fit was poor, the subtraction of the Gaussian did not lead to proper removal of the source emission and the program after a few iterations repeatedly found the maximum in the residual image at the nearby positions where the source had been already detected. This led to detecting prohibitively a large number of spurious sources. In view of this we followed an approach on similar lines to the task HAPPY in AIPS for catalogue construction. HAPPY was written primarily for catalogue construction from the FIRST survey and was publicly not available in the AIPS distribution. Salient features of the algorithm are described by White et. al. (1997), some of which we have also adopted in design of our source detection algorithm.

Detection: Our source detection program starts by searching an image for a pixel with maximum value exceeding a given user provided threshold. A rectangle referred as an island of emission around the detected maximum is defined containing the contiguous set of pixels on the four sides along RA and declination axis, which exceed another lower user provided threshold. This is done by moving away from the detected maximum on both the sides along RA and declination axis and stopping when the first pixel with intensity below the lower user threshold is detected. The resulting rectangles or islands are padded with a border of one pixel on all the four sides. The two rectangles of different islands can overlap with each other at the maximum by this padded area. In addition an outer rectangle is defined around the island which has an extra width equivalent to the FWHM of the beam in respective directions on all the four sides. The pixels in the outer rectangle are not considered for any source fitting but are used to determine the background DC level which acts as an input parameter during the source fitting. During the search for next island all the pixels which are a part of the inner rectangle of the islands previously detected are not considered. The program is permitted to find maximum 2,000 islands but generally the typical islands in an images are about 300-400.

Fitting: At the start of the program all the possible islands of emission are detected before any source fitting is carried out. The individual islands are analysed in order of decreasing brightness. The program has provisions of fitting up to a user specified number of multiple Gaussian components to an island. The pixels in each island are searched for a specified number of local maxima whose coordinates are used as initial estimates of the parameters of two dimensional elliptical Gaussian being fitted. However practical experience showed no significant advantage and hence only a single 2-D Gaussian was fitted to each island in the analysis presented in this dissertation. The coordinates of the pixel with the maximum

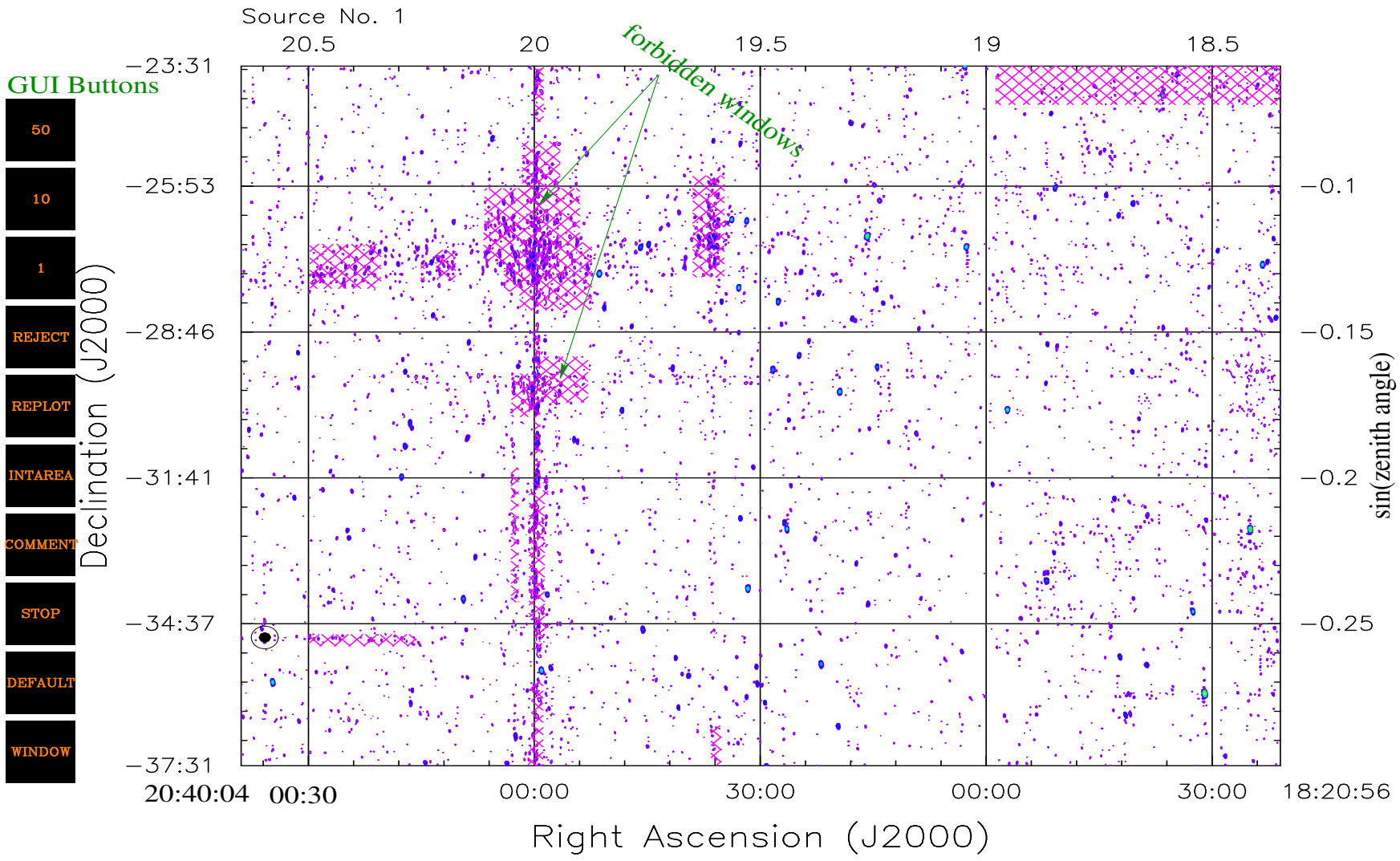

Fig. 7.17: A snapshot (second window) of the GUI based source extraction program including the contour image. The corrupted regions due to strong sources in grating lobes, aliased images, or regions of image which are not of interest are hatched as shown and are not considered for source extraction. The position of the source which is presently under analysis is shown encircled. The various actions desired can be carried out by using the GUI based buttons on the left or alternate keys. The regions near RA 20 hrs across the entire declination range is corrupted due to Cygnus A in grating lobes.

value in the island are used as initial guess for the fit. nonlinear fitting is carried out using the Levenburg Marquardt method. Only pixels with intensities above a user specified threshold in the inner rectangle are considered for fitting. The free parameters for a fit are the position of the source in RA and declination, the FWHM along the major and minor axis of the elliptical Gaussian, its position angle and the peak flux density. As mentioned earlier the DC (baseplane) is estimated from the background (pixels in the outer rectangle to the island) and kept constant during the fit. As each island is fitted, the results of the fitting algorithm must pass several acceptance criteria.

a. The fitted Gaussian must be positive.
b. The fitted position must be within the inner rectangle.
c. The peak flux density must not be more than twice the maximum value in the island.
d. The centroid position and the fitted peak position must not differ by more than expected FWHM.
e. The fitted FWHM of the Gaussian must be more than 0.75 times the expected width.

If any of these criteria is not met a visual inspection is carried out to check the source and a decision is taken accordingly. In case of a successful fit the emission due to fitted source is subtracted from the original image before the next island is fitted.

The source list program is a GUI based interactive software developed with a more general aim in addition to producing the source catalogue. The other purpose of the program is to confirm if the sources have been CLEANed properly. An external source list in the specified format can also be provided to the program and their positions and names are marked on the plots during the fitting as and when they are analysed. In addition it has option to display positions of known Galaxy clusters, sources in the MRC catalogue, superposed on the image to locate interesting sources. These features have not been exploited in the interpretation presented in this dissertation due to lack of time but would be subsequently used later.

Inspection : During the entire execution life time, the source extraction program has four display windows. The first window is stationary during the execution life time of the program while the other three are dynamic and change for each island and are described as follows.

a. The first window (stationary) contains the contour plot of the original dirty image. This acts as a reference image.
b. The second window (dynamic) contains the contour plot of the CLEANed image as shown in Fig. 7.17. This also contains the main GUI interface controls. The compar-

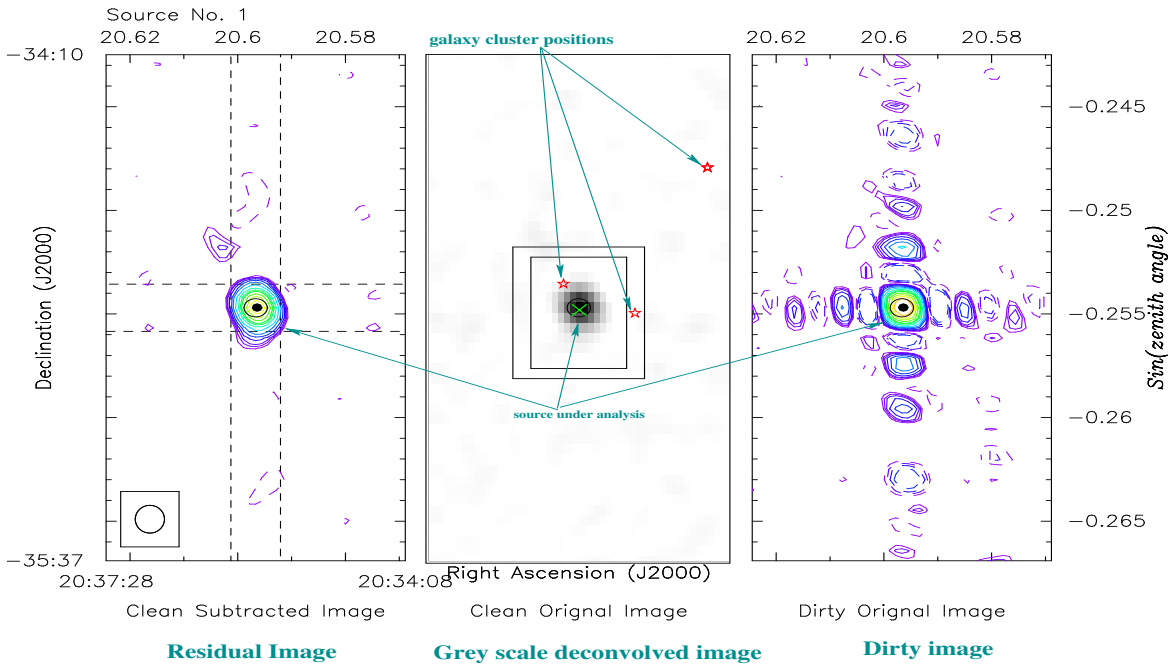

Fig. 7.18: A snapshot (third window) of the source extraction program displaying the image of the source presently under analysis. The leftmost subplot is a contour image of the region around the island under analysis in the residual image from which the emission due to all sources accepted and fitted earlier has been subtracted. The subplot in the middle is the grey scale image of the same region in the original CLEANed image. The rightmost subplot is the contour image of the same region in the original dirty image.

ison of the dirty and the CLEAN image helps to get an overall view about the effectiveness of the CLEAN. In this image the islands which have been fitted earlier, either accepted or rejected are displayed with the actual boundary of rectangles. The current island is indicated with a different symbol (a filled circle). These help us to check that the island search algorithm has correctly identified islands of emission and has not got stuck due to artifact or sidelobes of some strong source mistakingly identifying them as real sources.

c. The third window (dynamic) as shown in Fig. 7.18 has three sub plots. The first subplot on the left is the contour plot of the current island being fitted and the surrounding region in the residual image. Residual image is defined as the deconvolved image from which the emission due to all accepted sources fitted earlier has been subtracted. The subplot in the middle is the grey scale image of the same region in the original CLEANed image. The third subplot (on the right) is the contour image of the same region in the original dirty image. The three subimages help in rechecking the effectiveness of the CLEAN, checking whether the source is genuine or due to residual sidelobes of a nearby strong source or an artifact. In addition the first subimage helps

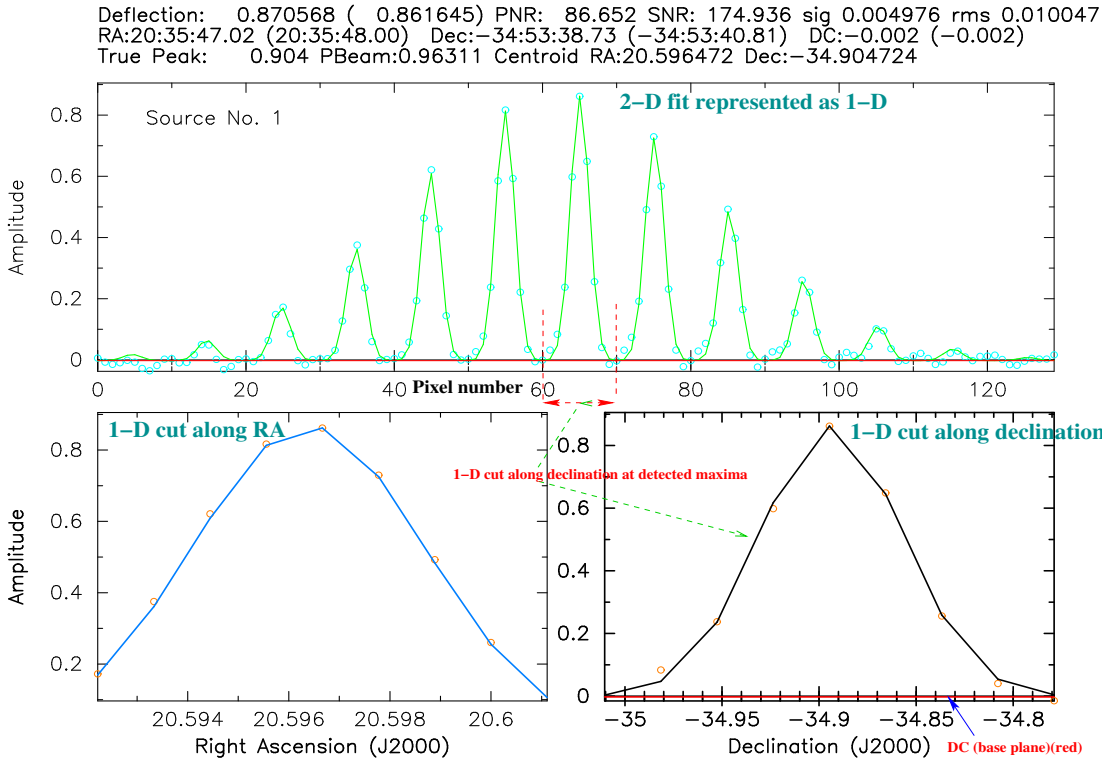

Fig. 7.19: A snapshot (fourth window) of the source extraction program displaying the measured intensity and the fitted 2-D Gaussian along with the fitted parameters. The plot on the bottom left corner shows a one dimensional cut or profile (o) in the residual image and the fitted curve (blue line) along RA at the located maximum. The plot on the bottom right shows the one dimensional cut or profile (o) in the residual image along declination and the corresponding fit (black line). The upper plot shows the measured intensity (o) and the fitted two dimensional elliptical Gaussian (green line) around the located maximum as a 1-D plot (see text for fourth window for details).

is analyzing whether the subtraction of the emission from the sources in the previous detected islands which are near by within the extent of the present display window has not produced any undesirable effects such as negative bowls etc.. The contour maps are best suited for displaying the actual intensities while the grey scale image is suited to see the contrast with the background due to which both forms of display have been used in this window.

d. The fourth window (dynamic) also consists of three subplots as shown in the Fig. 7.19. It displays the fit for the source in the present island under analysis. The plot on the bottom left corner shows a one dimensional cut/profile of the intensity in the residual image and the fitted curve along RA around the located maximum. The bottom right plot shows the one dimensional cut/profile of the intensity in the residual image and the fitted curve along declination around the located maximum.

   The plot on the top shows 2-D measured intensity profile in the residual image and the fitted 2-D elliptical Gaussian around the located maximum presented as a 1-D

plot. The 2-D fit is shown as a 1-D plot to make the fit more explicit. From the detected peak on both the sides a region in the image equivalent to FWHM of the synthesized beam is considered along RA and declination. The 1-D scans along declination at each RA pixel (in the 1-D scan along RA at the detected peak) starting from the first pixel to the last pixel in the region considered are plotted side by side one after another (next to each other) as shown by open circles. The corresponding value of the fitted elliptical Gaussian is shown by solid lines. Since the sampling (in the display) is exactly the same as measured image, the fitted profile may not appear as smooth as it may actually be. At the same time this way of displaying a 2-D fit gives a very explicit view to visually ascertain the quality of fit. Useful parameters like peak deflection, position in RA and declination of the detected peak in the measured image and after fitting are displayed. The rms noise, DC value, primary beam attenuation, centroid position along RA and declination are also displayed. In case of doubt this visual inspection and the information displayed helps in deciding whether a source is genuine or otherwise.

The end product of the source extraction program is a list of elliptically fitted Gaussian. For each island the source extraction program gives RA and declination of the fitted position of the source, the peak and integrated flux density, position angle of the fitted Gaussian and input DC estimated from the background. In addition the error estimate on each parameter is provided by the fit. The island number, fitted parameters and the initial guess parameters are saved as these quantities are often helpful in doubtful cases and identifying complex islands. Although some of this information is not included in the catalogue but it has not been discarded and would be used for rechecking in case any discrepancies are found later.

The goodness of the Gaussian fit parameters is additionally checked by comparing the obtained parameters with the reference values which are defined as follows. The position of the source is additionally characterized by two important parameters namely the centroid position and the position of the maximum. For any source significant departure of the fitted Gaussian position with both of them is manually examined and accordingly a decision is made on case to case basis. In cases when the fit position is poorly determined the centroid position has been used. Such instances of unresolved sources are very less (<2%).

For sources having their angular extent of the fitted Gaussian less than 0.75 times of the expected HPBW, they are most likely a result of being an artifact or occasionally the fitting algorithm has performed poorly. Such sources are also manually examined and a decision is made accordingly. For sources which are well resolved (angular size more than twice the expected beam) approximating the emission with an elliptical Gaussian

has been found to be inappropriate and the position was estimated using the centroid of emission. For such sources we integrate the emission to obtain the value of integrated flux. During the integration the background emission is subtracted from the individual pixel intensities. The region which is considered for estimating the integrated flux is the inner rectangle of the island which is automatically decided by the program (based on the lower user threshold). For those sources for which it was found to be inappropriate, using the interactive GUI feature an appropriate size rectangle is drawn by the user after visual inspection (taking into account the rms noise in the image) which is used to compute the integrated flux.

From the profile plot along RA and declination a visual inspection easily reveals whether the estimated DC is appropriate or not (shown as red line in Rig. 7.19). Generally the DC is nearly zero and always less than the rms noise. In any region where the estimated DC is comparable to the rms noise they are carefully analysed. Generally such regions are those where the DC removal along RA has not been very effective. There are no cases seen where the DC estimation from the background has been found to be significantly different from the actual value seen in the images.

Effect of rms noise on source extraction : The images are processed on sidereal hour basis. The rms noise is nearly constant in declination as mentioned earlier (without applying the primary beam correction of the helix). In order to have minimum change of detection threshold (ratio of detected peak to noise), the source detection is carried out before any background correction is applied to incorporate the variation in the brightness temperature of the sky. As explained earlier the rms noise was estimated by selecting regions which seemed to be devoid of strong sources. A weighted average of the rms noise in each individual regions are combined in quadrature (weights equal to the number of pixels in each selected region) to estimate the overall rms noise (global rms). The source detection program uses this single global rms noise for determining the detection threshold for the image. Careful measurements shows that the local noise varies by about 10-20% from this average value and hence will also decide the corresponding completeness of the catalogue.

Artifacts in images : As described in earlier section the images are also affected by artifacts which are non-astronomical in origin. During the island search and subsequent source fitting it is important to ensure that such regions are excluded to the maximum possible extent. During the deconvolution all such perceptible features suspected to be non-real were forbidden (Sec. 6.3.4.1). The information about the boundaries and locations of such regions is preserved and passed on to the source extraction program which are excluded during any source search. Still there are some problematic cases which we

did come across during the source extraction. The problematic cases can be broadly classified as follows.

a. Islands for which the automated algorithm provides poor parameters. Generally in such cases the fit gets stuck in some local minimum during the χ^2 minimization. These cases are handled by refitting with a single Gaussian with different initial conditions. In the first pass, fitting is carried out with initial guess parameters for a position estimated by the centroid of emission and each pixel is given a weight equal to the signal to noise ratio of the intensity of that pixel. The obtained values of fitted parameters are then used as guess parameters and then the fitting is carried out in the usual way in the second pass to obtain the fitted parameters.

b. Islands which cannot be described by single Gaussian fits. For these islands simply the integrated flux and the centroid positions were used. The regions for which the integrated emission is calculated is marked automatically and if required it is marked manually based on visual inspection by the user via the GUI interface.

c. Islands corresponding to nearby confused regions due to residual sidelobes of strong sources. All these appear real but definitive statements about them cannot be made. A decision is made based on visual inspection using the a priori knowledge of the rms noise.

d. Islands corresponding to obviously unreal sources, which are noise peaks, residual sidelobes of strong sources, image artifacts, residual DC along RA, sources appearing as grating lobes etc.. Such sources are summarily rejected. The examination reveals that generally such skinny sources are sidelobes of nearby strong sources.

Duplicate sources

Each image is mapped with guard zones covering sufficient region on either side in both RA and declination. During the source detection, apart from the region of interest in the image for a sidereal hour range and a given declination zone, in order not to miss any sources on the ends, about half degree overlap is chosen in declination on either side of the delay zone and a region covering about 36 s in RA is chosen on both the sides of the image[19]. Due to this a few sources are repeated in the adjacent images which need to be rejected. These overlap regions also help in cross checking the self consistency of detection. The number of sources which get repeated between images covering same RA range but adjacent delay zones is ≈4% while between two images with same delay zones but covering adjacent sidereal hours is ≈1%. Our analysis revealed that the sources detected in the

[19]The actual region of overlap between two adjacent images is much larger, but for source list purpose only a small overlap is considered.

overlapped regions have self consistency both in terms of their peak amplitudes and positions (Sec. 7.2.1.1). The catalogue creation process involves identification and removal of these duplicate sources.

Since the overlapping images in declination are nearly identical, having been formed from the same set of data except with different delay settings the identification of such sources is straight forward. In RA the two images having duplicate sources are made with the data of different days and the source parameters may be somewhat different. In both cases the source may wind up with slightly different set of parameters. In order to remove the duplicate sources in both cases first a list of all common sources in the overlapping images is prepared. Two sources are defined as common if the angular distance is less than 1′ and their flux density does not differ[20] from each other by more than 40%. The source corresponding to the image in which it has a higher signal to noise ratio is retained while it is rejected from the other image. We removed in total ≈3 to 4% of the sources as duplicates.

Estimation of systematics :

The systematics were identified by comparing the positions and flux densities of sources common[21] to MRC across the entire declination range of MRT for each sidereal hour. The result of comparison for a typical one sidereal hour image is shown in Fig. 7.20. From the plots we note that there are no systematics in position as a function of RA, but the difference in positions show a clear linear trend as a function of declination. The estimation of the systematics in the positions was carried by minimizing the sum of absolute discrepancies (using the function robustfit in Matlab and the form given in Eqn. 7.13 and Eqn. 7.14) as the least square minimization is sensitive to outliers. This further increases the accuracy of the estimation of the systematics.The positions had to be corrected for a systematic error in declination which has a magnitude of,

$$sin(za)_{true} = sin(za)_{measured} - \frac{2}{4095}[-1.8891957\,\delta + 1.3825375] \tag{7.13}$$

The error is zero for δ ≈-42°and increases for the sources away from this declination. The maximum value of this error is at δ=-10°, at which it is nearly 0.29 times the beam width. The systematic error in RA position with declination is much lesser and has a magnitude of,

[20]The integrated flux density accuracies were not estimated at this stage, so a substantially higher difference in the flux densities was allowed to pass through.

[21]The sources were labeled as common if they lie within 6′ of each other (See Eqn. 7.1). In case of more than one source present in the MRT image within 6′ of an MRC source, such sources were not considered for the present analysis. A large angular distance was allowed to accommodate systematics in positions if any. Since the MRC catalogue has source density of about 0.5 source deg^{-2}, the chances of considering two unrelated sources as common is extremely low.

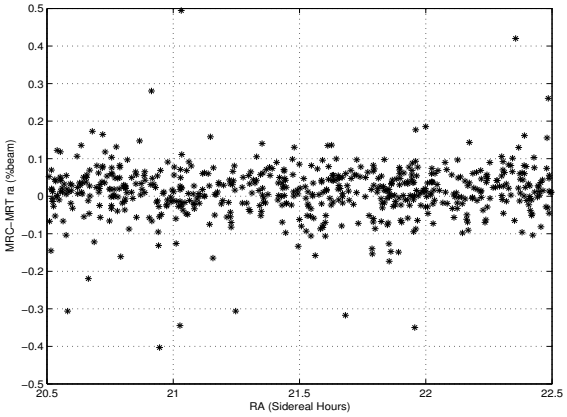

(a) Difference in RA position as a function of RA

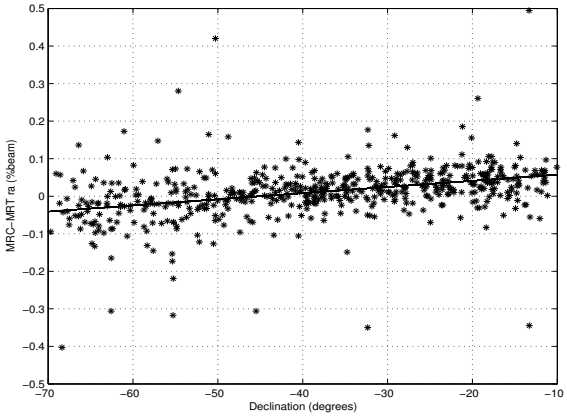

(b) Difference in RA position as a function of declination

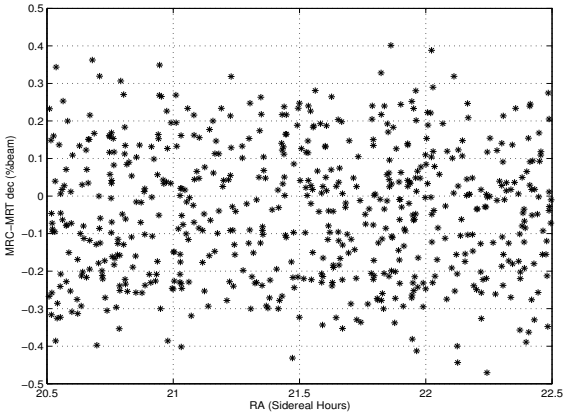

(c) Difference in declination position as a function of RA

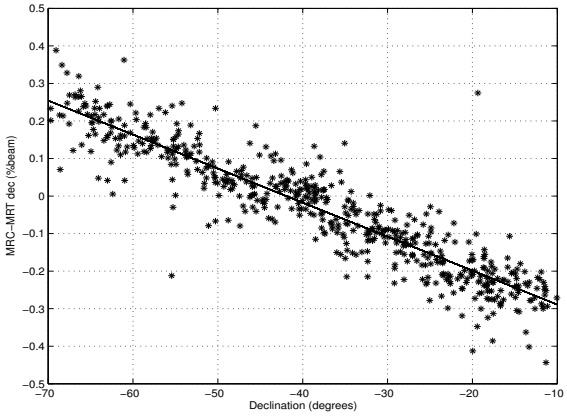

(d) Difference in declination position as a function of declination

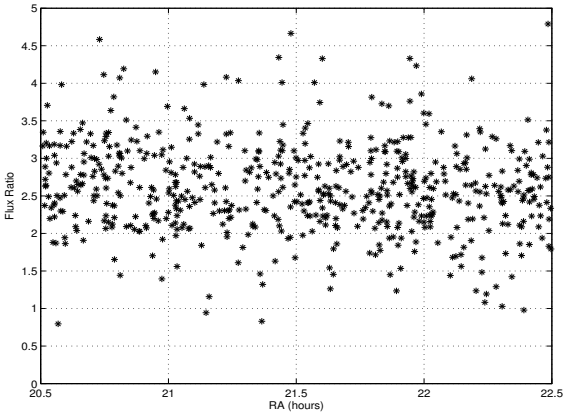

(e) Flux ratio as a function of RA position

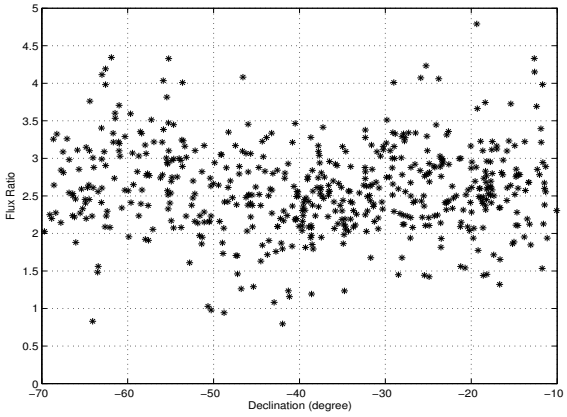

(f) Flux ratio as a function of declination position

Fig. 7.20: The plots show the difference in positions and comparison of flux density ratios of the common sources in MRT and MRC to estimate systematics in the images.

$$RA_{true} = RA_{measured} + 16\, sec(\delta)[0.12516979\,\delta + 0.09825329] \quad (7.14)$$

The error is zero at $\delta\approx$-45°and increases for sources away from this declination. The maximum value of this error is at δ=-10°at which it is 0.06 times the beam width. The estimation of the systematics is based on the assumption that the mean difference (with sign) between the positions of sources at 408 MHz and 151.5 MHz is zero for a sample of statistically large number of unresolved sources.

The flux ratio shows that there are no perceptible systematics in flux density estimates as a function of RA or declination. The systematics for all the images covering different sidereal hours were estimated and found to be having similar trend as in the above expression. The systematics in position mentioned above can be due to a combination of a variety of factors like wrongly assumed position of the phase calibrator, inaccuracies in sidereal time estimation, phase calibration errors (as a function of declination, geometry of the array) and ionospheric effects. We suspect that these systematics are mostly due to wrongly assumed position of the phase calibrator MRC1932-464. The accurate positions of the phase calibrators is not known at 151.5 MHz. We have assumed the same position as given in the MRC catalogue.

The images of MRC1932-464 at 4.74 GHz (from ATCA) and the 151.5MHz (from MRT) are shown in the Fig. 7.21. The high frequency image clearly shows that the size of this calibrator MRC1932-464 is ≈4 s in RA and ≈20″ in declination and hence it is a point source for us suitable for calibration. The position of this source from different frequency images is given in Table 7.8 and is also shown in Fig. 7.22. The position quoted at 408 MHz was the most appropriate choice as apart from being at a nearby frequency it is in between the positions quoted at 843 MHz and 4740 MHz. The Culgoora position was not preferred because it lies on one side of the all the other three measured positions as seen in the Fig. 7.22. In addition the positional accuracy of sources is much more precise in the 843 MHz and the 4.74 GHz images. In view of this, I assumed a position in between them as quoted in the MRC to be the most appropriate.

Frequency (ν)	Position(J2000) RA	Dec	Flux Density (Jy)	resolution	Telescope
4740 MHz	19:35:56.99	-46:20:41.5	3.86	$2\farcs3 \times 2\farcs2$	ATCA
843 MHz	19:35:57.17	-46:20:50.6	13.00	45″×45″ cosec(δ)	MOST
408 MHz	19:35:57.10	-46:20:44.0	39.6	$2\farcm62 \times 2\farcm86$ sec(δ+30.°5)	Molonglo cross
160 MHz	19:35:56.35	-46:20:11.93	91.6	$1\farcm9 \times 1\farcm9$ sec(δ+30.°3)	Culgoora

Table 7.8: The details of the phase calibrator MRC1932-464. It is clear that the position of the sources as quoted in Molonglo seems to be the most appropriate at 151.5 MHz.

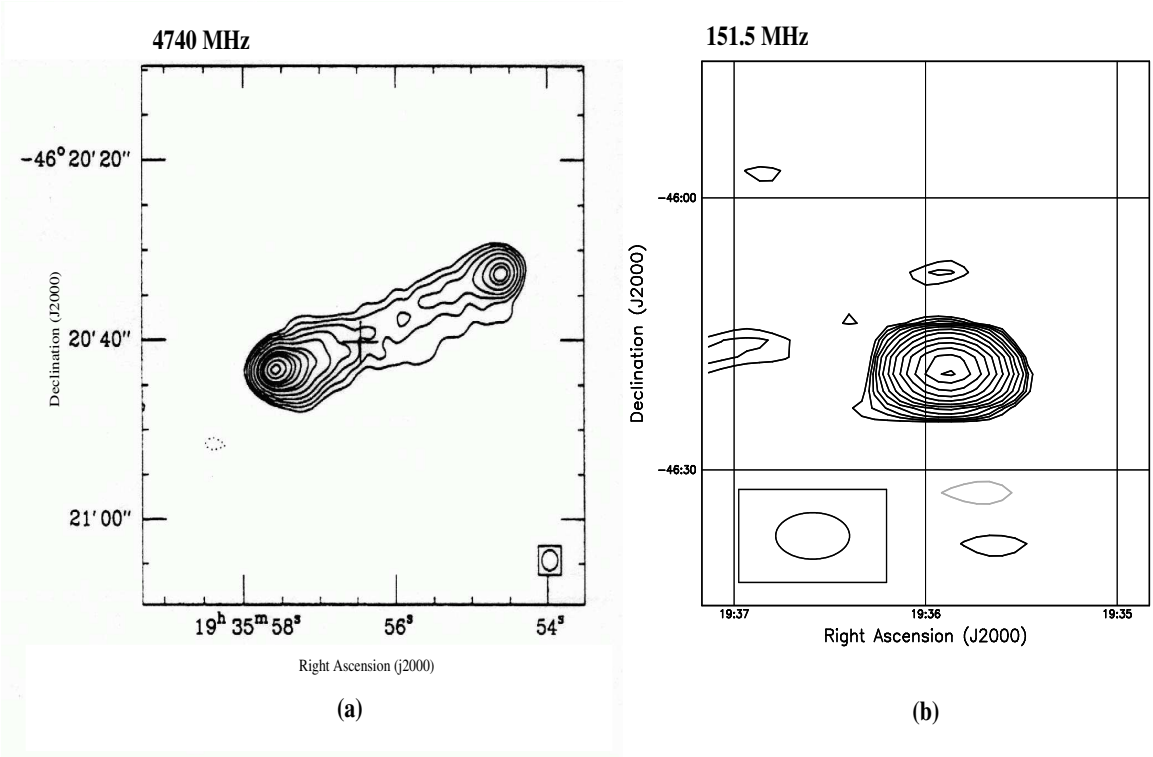

Fig. 7.21: The image of 1932-464 at (a) 4.74 GHz (using ATCA courtesy Burgess (1998)) and (b) 151.5 MHz (using MRT). The spectrum of the source is also shown in Fig. 7.12. The high frequency image reveals that the source has a much smaller size compared to the MRT beam and also lies in an empty field, thus suited for being used as a phase calibrator. In the image (a) the contour levels (% of peak which is 1080.0 mJy beam^{-1}) are -0.5, 0.5, 1, 2, 4, 8, 15, 20, 30, 40, 50, 70, 90. In the image (b) which has an rms noise of ≈360 mJy beam^{-1}, the contour levels are 1.5, 2.0, 2.8, 3.6, 5.0, 7.2, 10.0, 14.4, 20.1, 28.8, 39.6, 54.0, 72.0, 90.0 Jy beam^{-1}.

Since the systematics in the positional accuracies are much lesser than the beam width and can be accurately estimated owing to the large number of sources which are common to MRT and MRC and subsequently corrected for, it does not affect in anyway the scientific potential of the catalogue and neither any discussions hence forth regarding astronomical interpretation of the images (roughly the accuracy of estimation of the systematics is less than 3% of the beam width which is much less than the expected positional accuracies). Since systematics are similar for different images, it reconfirms that the systematics have been determined accurately. The entire source catalogue was corrected for the systematics in position on similar lines by estimating the systematics for each image of the form given in Eqn. 7.13. and Eqn. 7.14.

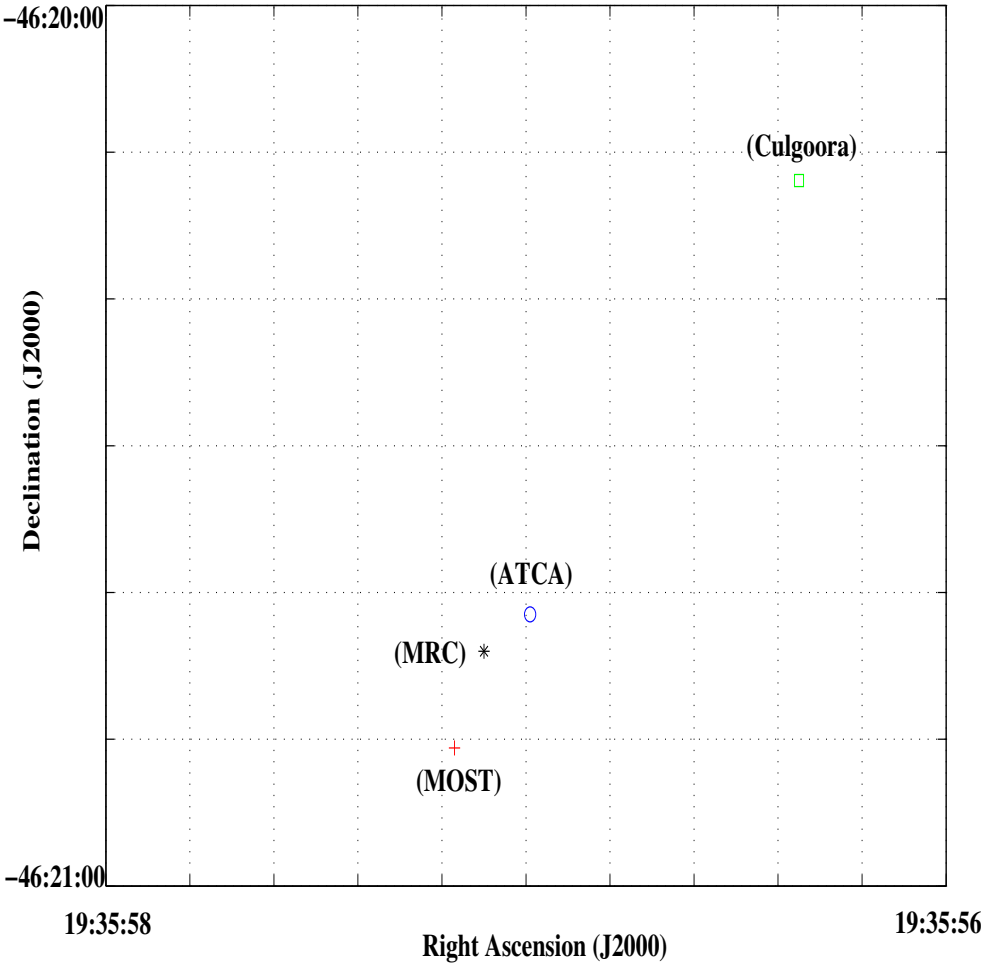

Fig. 7.22: MRC1932-464 positions at different frequencies. It is clear that the position quoted in MRC catalogue seems to be most appropriate as it lies in between the positions from the images made by MOST and ATCA. See (Table. 7.8) for details.

7.3.2 Source list/catalogue

The procedure described in the previous sections yielded a list of nearly 2,800 sources from the images covering[22] about a steradian of the sky ($18^h \leq$RA$\leq 24^h30^m$, $-75° \leq \delta \leq -10°$)[23]. Usually the rms noise in an image does not show much variation within one sidereal hour. The variation is generally less than 20% (except the images corresponding to the sidereal hour close to the Galactic plane). The detection threshold of 5σ was chosen after careful investigation of the behaviour of the rms noise, artifacts and remaing sidelobes, so as

[22] A few sources are also catalogued in the declination range -79° to -75°and -10° to-1°. The helix beam, significant bandwidth decorrelation and insufficient deconvolution do not permit accurate measurement of flux densities. So only those sources in these regions which appeared clearly genuine on visual inspection were accepted.

[23] Apart from regions which were avoided during source search, a small region covering the Galactic plane($18^h \leq$RA$\leq 19^h$, $-25° \leq \delta \leq -1°$) was also excluded except for a few sources which were manually picked up.

to minimize the incompleteness as the fluxes approach the detection threshold limit and keeping the source list reliable to maximum possible extent. Here reliability implies that all the sources which appear in the catalogue should be genuine. The format and the source catalogue is presented in the Appendix B.

7.3.3 Analysis

We have carried out preliminary analysis of our catalogue by comparing it with the two catalogues at nearby frequencies, MRC at 408 MHz and Culgoora at 160 MHz.

Comparison with the MRC :

The Molonglo Reference Catalogue (MRC) at 408 MHz has a resolution of 2.′62 in RA and 2.′86 sec(δ+30.°5) in declination. The pointing and the flux density calibrations of this catalogue are based on the measurements of Hunstead (1972) and an absolute scale of Wyllie (1969). It uniformly covers 7.85 steradians of the sky in the range (-85°< δ < +18.°5) and Galactic latitude $|b|$ >3. It is believed to be 99.9% complete above the flux density limit of 1 Jy. To this limit it contains 7301 sources, corresponding to an average surface density of 930 sources per steradian. In total there are 12,143 source down to a flux density limit of 0.6 Jy.

Fig. 7.23 shows the positions of all the sources in the MRT (denoted by o) and the MRC (denoted by +) in the region considered ($18^h \leq$RA$\leq 24^h39^m$, -75°$\leq \delta \leq$-10°) for comparison. The total number of MRT sources in the region considered is 2585, while the number of MRC sources is 2060. We carried out cross identification of sources in the two catalogues by identifying a unique MRC source within an angular distance of 2′ of an MRT source, which yielded 1,648 common sources. Thus about a thousand sources have been detected in the MRT catalogue which have not been detected in the MRC[24]. Fig. 7.24(a) shows plot of the difference in position (as a fraction of MRT beam width) along RA and declination of all common sources. The details of comparison of positions of common sources in the two catalogues are given in Table 7.9. Fig. 7.24(b) and Fig. 7.24(c) show the histogram of the absolute position difference in RA and declination in terms of the beam widths. Fig. 7.24(d) shows the histogram of the angular distance between the common sources in arc minutes.

From these plots shown we note that the discrepancies in the position along RA and declination are generally less than 0.07 times the MRT beam width (for more than 70% sources). The mean difference along RA and declination is close to zero. The angular distnace between the common sources is typically within 0.′3. Fig. 7.25(a) shows the angular

[24]This is based on the fact that even when the angular distance for sources to be considered as common was relaxed to 4′ there was hardly any increase in the number of common sources.

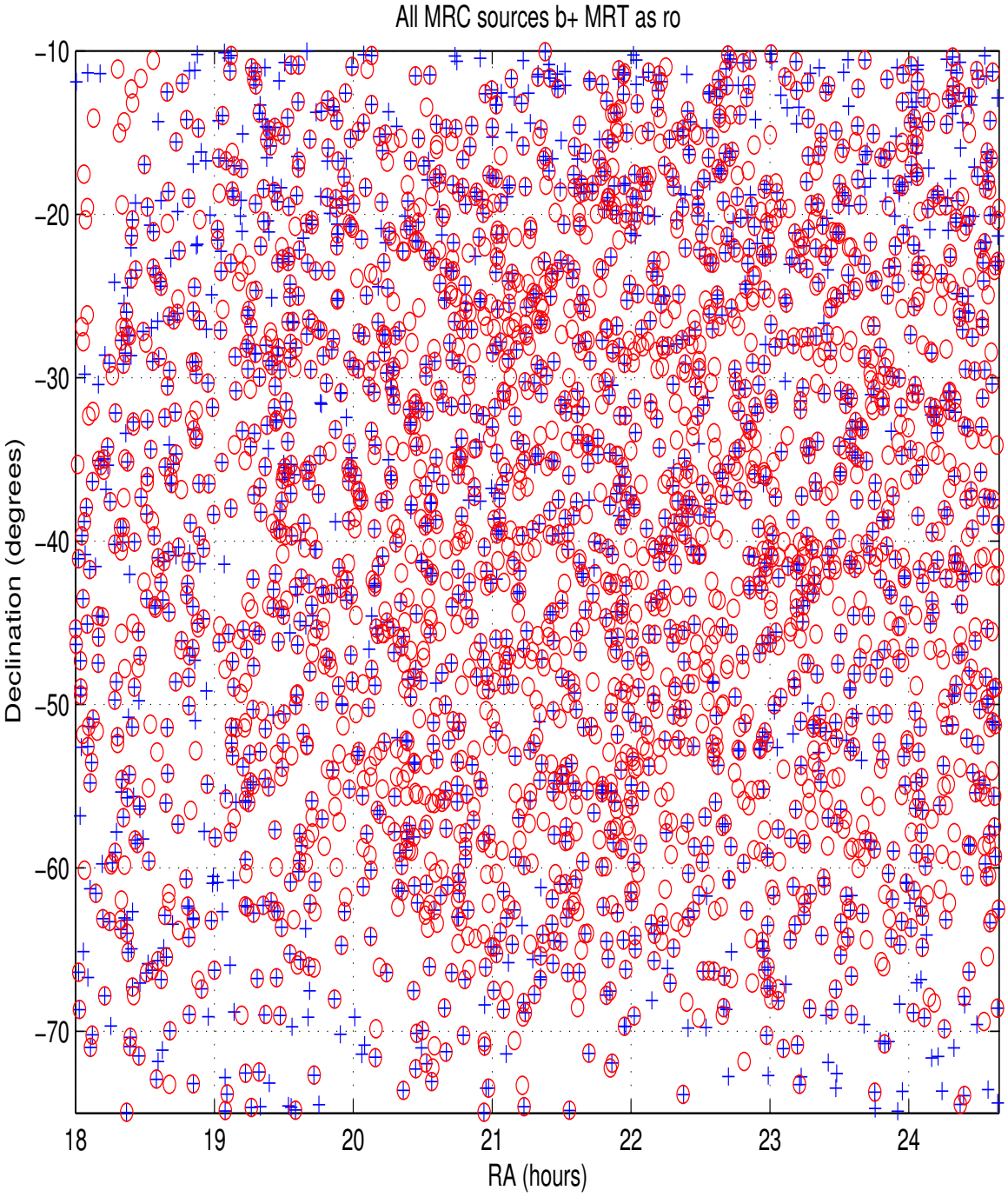

Fig. 7.23: The figure shows the positions of 2,585 sources detected in the MRT images marked by open circles (0) and 2,060 sources listed in the MRC marked by a + sign. There are 1,648 sources which are common. Among about 500 sources in the MRC which are not detected in the MRT image (with peak>5σ) most of them are at the ends of the declination range of MRT where the attenuation due to helix primary beam is maximum and the sources flux densities are lower than the MRT detection threshold. About 1,000 sources are detected in the MRT image which are not listed in the MRC.

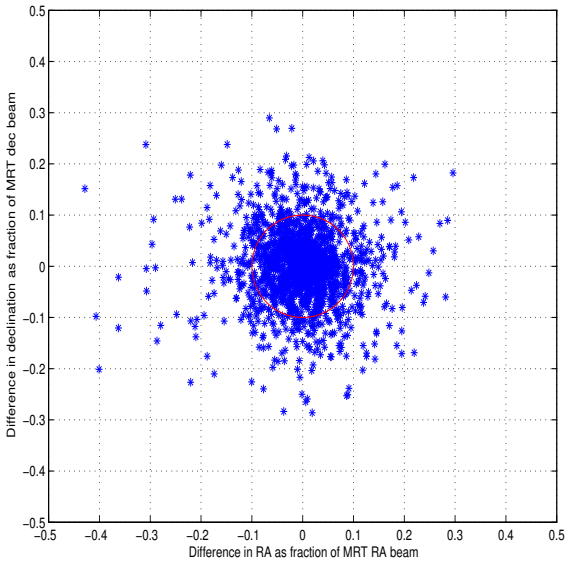

(a) Differences in RA and declination positions of common sources as a fraction of MRT beam width. The red circle shows the region within which the angular distance is less than 0.1 times the beam width.

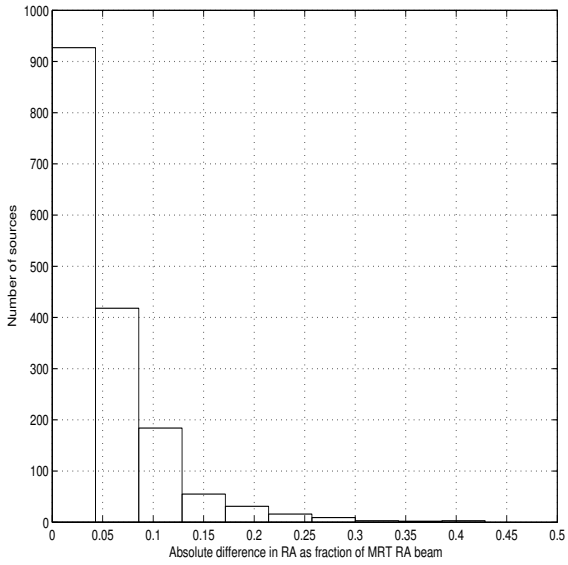

(b) Histogram of absolute difference in RA positions as fraction of MRT RA beam.

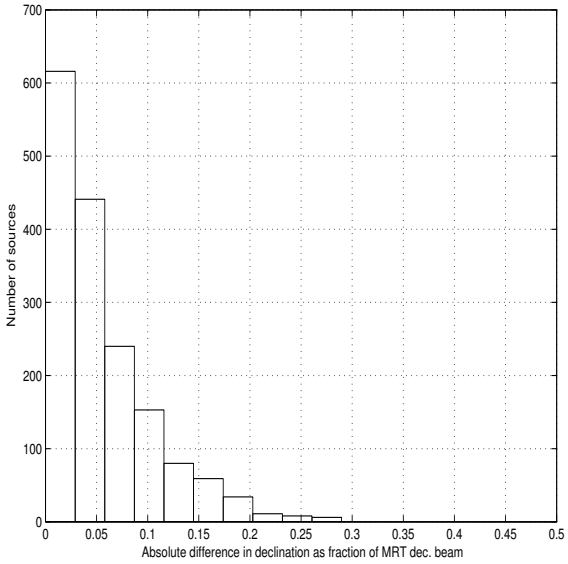

(c) Histogram of absolute difference in declination positions as a fraction of MRT declination beam.

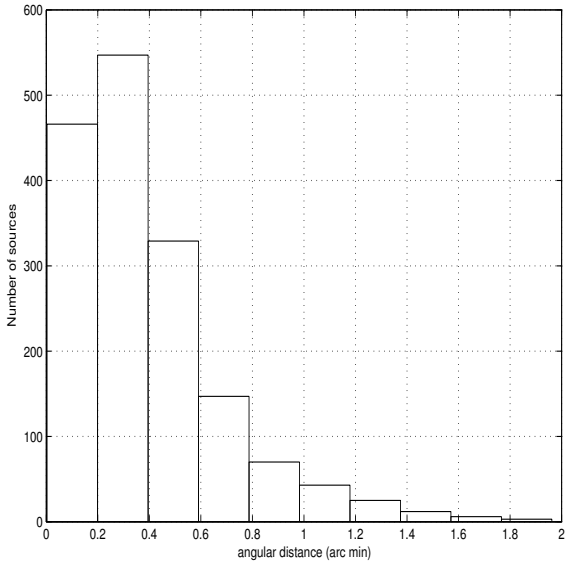

(d) Histogram of angular distance in the positions of common sources in arc minutes.

Fig. 7.24: Comparison of positions of sources common between MRC and MRT. Around 80% of the sources have their differences in RA and declination within 0.1 times the respective beam widths.

Position difference	mean (difference)	rms	mean (absolute difference)	rms
along RA [$]	0.0023	0.071	0.042	0.040
along dec.[$$]	0.0013	0.074	0.043	0.045
angular distance (′)	–	–	0.31	0.24

Table 7.9: The difference between the positions of 1,680 common sources in the MRT images and the MRC catalogue. [$] as fraction of MRT RA beam, [$$] as fraction of MRT declination beam. The mean difference in positions along RA and declination is very small as expected.

distance between the common sources as a function of their flux densities at 151.5 MHz. The angular distance for the common sources decreases with increasing flux density as expected due to the better positional accuracies in both MRT and MRC.

Fig. 7.25(b),Fig. 7.25(c) and Fig. 7.25(d) shows the ratio of flux densities at 151.5 MHz and 408 MHz of the common sources as a function of RA, declination and flux density at 151.5 MHz respectively. It does not show any systematic trend with RA or declination. The scatter in the ratio of flux densities shows a slightly decreasing trend with the flux densities which may also be probably due to the increased accuracy apart from any genuine behavior of spectral index distribution of strong sources.

Fig. 7.26(a) shows the histogram of spectral index[25] between 151.5 MHz and 408 MHz of all the common sources. The mean spectral index is ≈0.976 (median≈0.979) and the spectral index is distributed uniformly about the mean on both sides. The rms spread in the mean spectral index is ≈0.27.

As discussed earlier in this chapter (See Sec. 7.2.1.2) nearly 96.5% of the MRC sources above a flux density of 1.25 Jy at 408 MHz are also detected in MRT images. It is interesting to estimate the spectral index distribution of these sources which are a complete sample at 408 MHz. Fig. 7.26(b) shows the histogram of the spectral index distribution of 835 common sources. The mean spectral index in this case decreases to ≈0.89 (median≈0.90) which is expected as we would obviously have favourably detected sources with steeper spectral index near the detection threshold in the earlier case (Fig. 7.26(a)). This value for the mean spectral index between 151.5 MHz and 408 MHz agrees with the values quoted in the literature. The rms spread in the mean spectral index is ≈0.26.

The above comparison clearly reveals that there are no systematics in the final source list both in terms of positions and flux densities. The difference in positions between the common sources in MRT and the MRC are typically within 0.07 times the MRT beam width and within an angular distance of 0.′3.

Comparison with the Culgoora catalogue :

The updated Culgoora catalog (Slee, 1995) gives list of sources that were observed with

[25]We recall that spectral index α between two frequencies ν_1 and ν_2 is given by $\alpha_{\nu_1}^{\nu_2} = -\frac{log(S_2/S_1)}{log(\nu_2/\nu_1)}$.

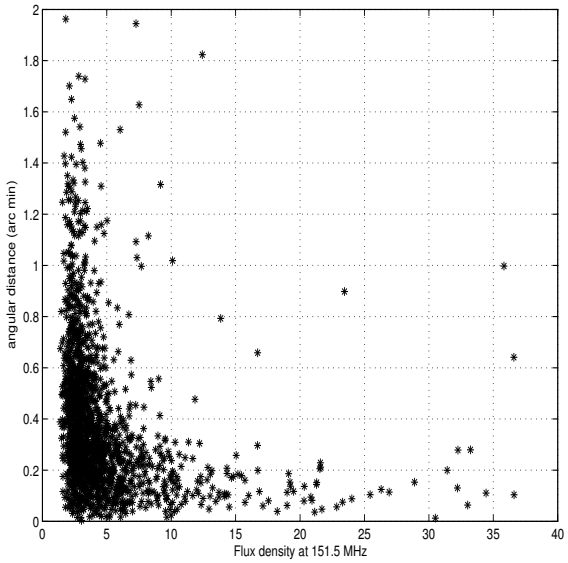

(a) The angular distance (arc minute) between common sources as a function of their flux densities at 151.5 MHz.

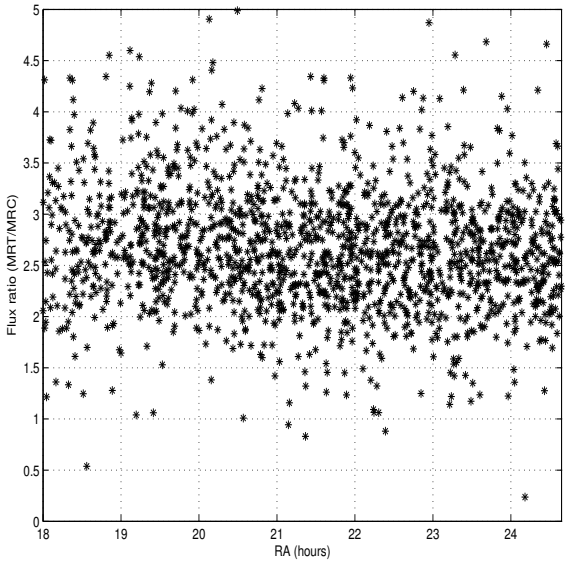

(b) Ratio of flux densities at 151.5 MHz and 408 MHz as a function of RA.

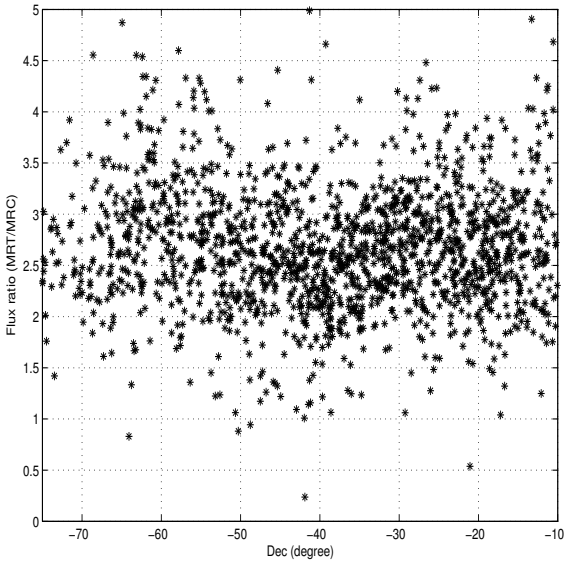

(c) Ratio of flux densities at 151.5 MHz and 408 MHz as a function of declination.

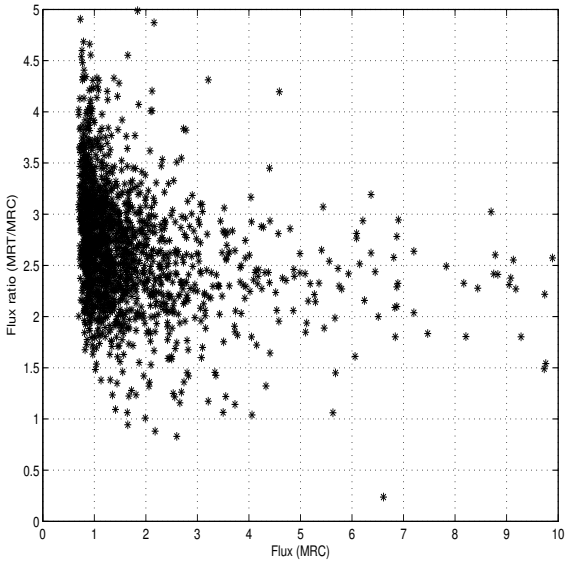

(d) Ratio of flux densities at 151.5 MHz and 408 MHz as a function of flux density at 151.5 MHz.

Fig. 7.25: A comparison of flux densities of sources common between MRC and MRT.

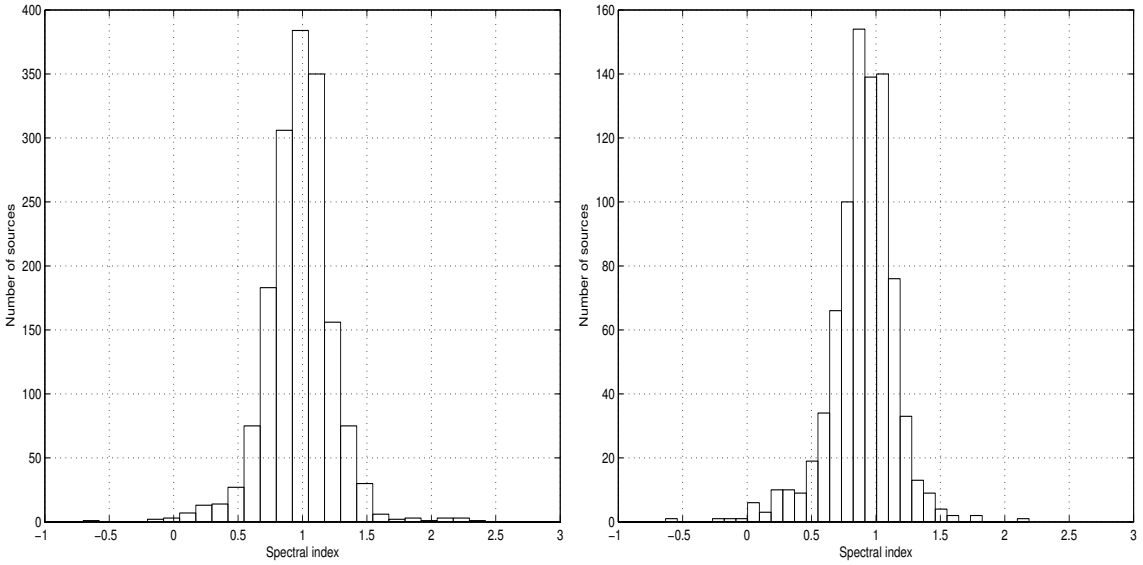

(a) Histogram of spectral index of all common sources between 151.5 MHz and 408 MHz.

(b) Histogram of spectral index between 151.5 MHz and 408 MHz of a flux density limited (>1.25Jy) complete sample at 408 MHz.

Fig. 7.26: Comparison of flux densities of common sources between MRC and MRT.

the Culgoora Circular Array (CCA) in the interval 1970-1984. The list contains all the sources that were published in the Culgoora-1,2,3 lists plus additional sources resulting from a survey of 353 Abell clusters of galaxies. The observations were made at 80 MHz and 160 MHz with HPBW in RA of $3\overset{'}{.}7$ and $1\overset{'}{.}85\sec(\delta+30\overset{\circ}{.}3)$ respectively. This list brings together all CCA measurements of flux density, position, spectral index and angular size, with limiting flux densities of 4 Jy at 80 MHz and 2 Jy at 160 MHz. The sources were selected for CCA observations from the Parkes, 4C and Ohio catalogues if an extrapolation of the then existing spectral data indicated that the 80 MHz flux density would be > 5 Jy.

A comparative study of MRT and Culgoora catalogue were carried out on similar lines as with the MRC. We cross identified common sources by identifying a unique Culgoora source with $2'$ of an MRT source. There are 221 Culgoora sources in the region of the sky considered. We considered only those sources for which the flux densities are given at both 160 MHz and 80 MHz. There are a total of 207 such sources. Their cross identification yielded a list of 198 common sources[26]. Fig. 7.27(a) shows plot of the difference in

[26]Out of 9 sources which were not detected as common, 4 are in regions which have been excluded during the source search. Among the five sources remaining CUL1905-190(3.4 Jy) and CUL2201-116 (2.4 Jy) were detected with a difference in position of $3'$. Finally the remaining three sources CUL1848-170(2.2 Jy), CUL2128-123(2.2 Jy), CUL2143-156 (3.9 Jy) were not detected by the source search program. All these three sources are weak and are near the end of declination range of interest of MRT where helix primary beam attenuation is maximum.

Position difference	mean (difference)	rms	mean (absolute difference)	rms
along RA[$]	0.006	0.068	0.041	0.045
along dec.[$$]	0.004	0.103	0.066	0.075
angular distance (′)	–	–	0.40	0.36

Table 7.10: The difference between the positions of 198 common sources in the MRT images and the Culgoora catalogue. [$] as fraction of MRT RA beam, [$$] as fraction of MRT declination beam.

positions (as a fraction of MRT beam width) of common sources along RA and declination. Fig. 7.27(b) and Fig. 7.27(c) show the histogram of the absolute difference in position along RA and declination in terms of the MRT beam widths. Fig. 7.27(d) shows the histogram of the angular distance between the common sources in arc minutes. The results of the comparison are also given in Table 7.10. In this case the difference in position between the common sources along RA is typically within 0.07 times the beam width in RA and along declination is typically within 0.011 times the beam width in declination. The differences in positions along declination are slightly higher compared to that along RA. The angular distance between the common sources is typically within 0.′40. From the comparison we conclude that the behavior of differences in position is on the expected lines and there are no systematics.

In order to have an independent method of comparing our flux densities with the flux densities of the common sources in the Culgoora list, using the spectral index quoted in the Culgoora catalogue we estimated the expected flux density at 151.5 MHz assuming a single power law behavior. Since the frequency 160 MHz is very close to 151.5 MHz, the estimation of flux densities at 151.5 MHz will have the same kind of uncertainties which are at 160 MHz in the Culgoora catalogue. Fig. 7.28 shows the histogram of the fractional difference between the flux density of common sources at 151.5 MHz in the MRT images and the interpolated flux density at 151.5 MHz from Culgoora list. The flux densities in the MRT images agree with the interpolated flux densities of culgoora within an rms difference of ≈20.1%.

Accuracy of flux densities and positions :

The uncertainties in the fitted peak brightness and the positions in the MRT images and the resulting catalogue depends upon the combined effect due to internal flux density calibration uncertainty, the local noise, accuracy of the source fitting algorithm and the accuracy of the derived helix primary beam shape. The comparison of flux densities with the 55 MS4 sources in the MS4 Jy sample revealed that the agreement in the flux density accuracies for strong sources is within 6.3%.

The comparison of positions with the MRC and the culgoora catalogue clearly revealed that the positional accuracies agree typically to about 0.07 times the MRT beam width.

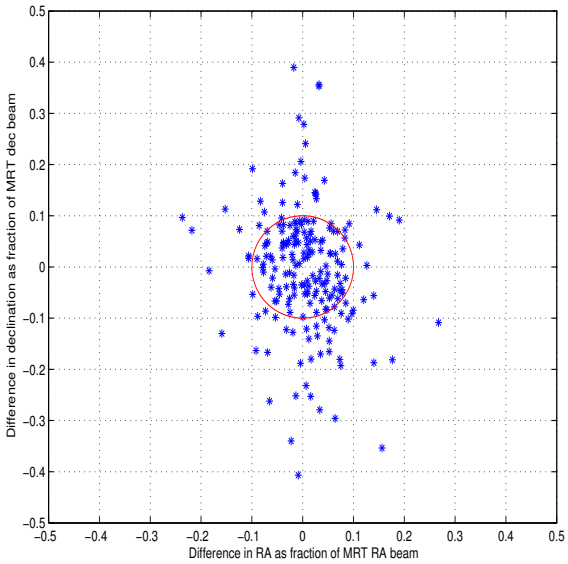

(a) Differences in RA and declination positions of common sources as a fraction of MRT beam width. The red circle shows the region within which the angular distance is less than 0.1 times the beam width.

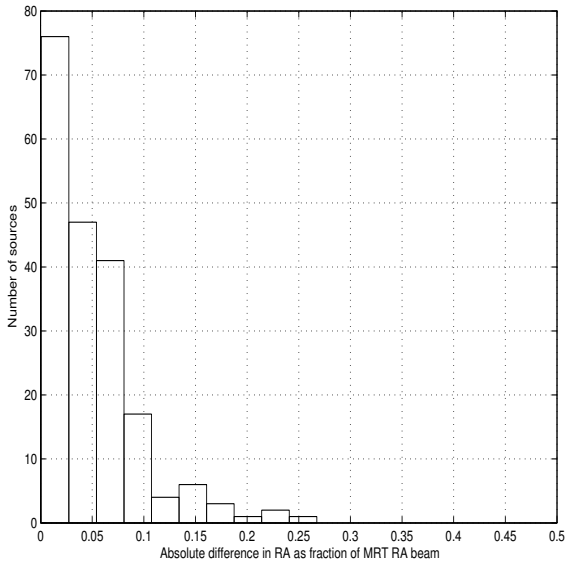

(b) Histogram of absolute difference in RA positions as fraction of MRT RA beam.

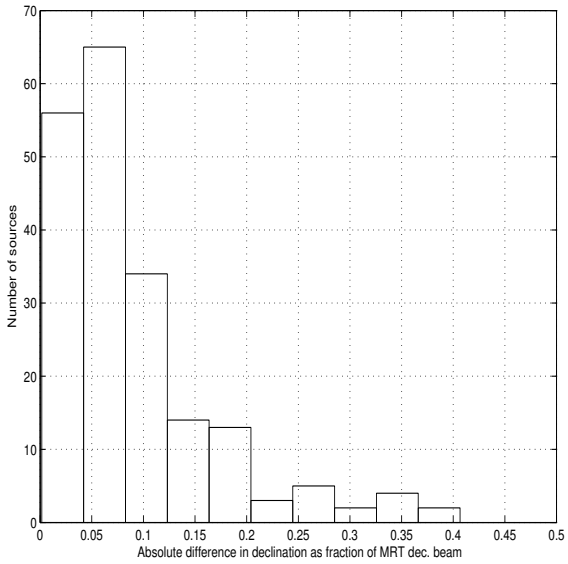

(c) Histogram of absolute difference in declination positions as a fraction of MRT declination beam.

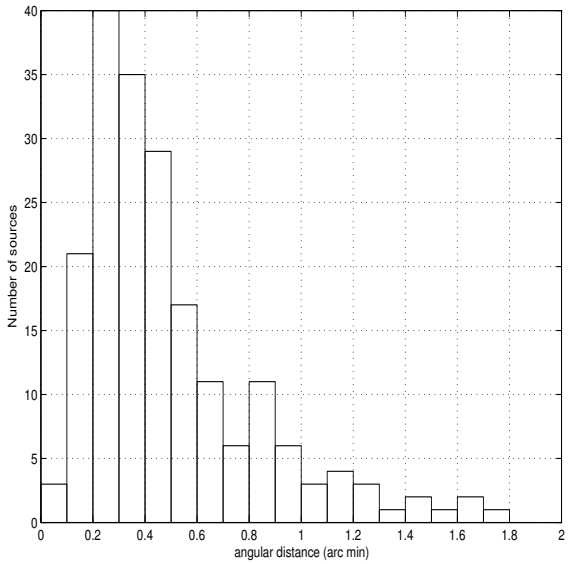

(d) Histogram of angular distance in the positions of common sources in arc minutes.

Fig. 7.27: Comparison of positions of sources common between Culgoora and MRT.

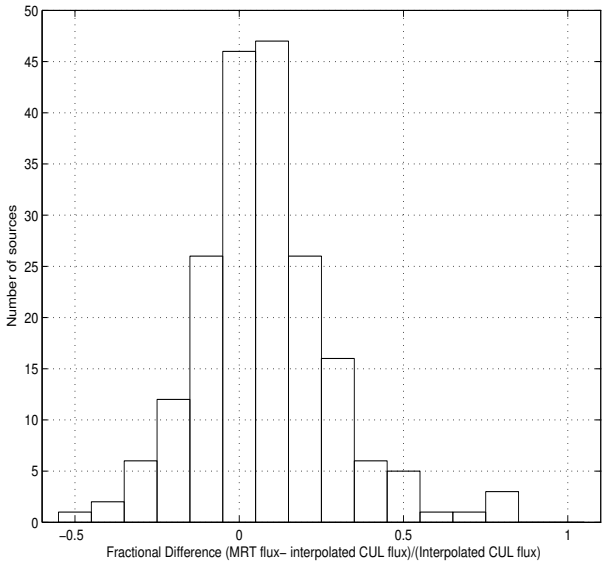

Fig. 7.28: Histogram of fractional difference in the flux densities between MRT and Culgoora catalogue flux density interpolated to 151.5 MHz.

Although the position of the sources at 151.5 MHz and 408 MHz is obviously expected to be close but there is no reason that the positions of all the sources should be exactly same. However the difference between the positions being small and random is expected to have a mean close to zero for a statistically large enough sample. This is clearly revealed in our comparative analysis (mean difference is about 0.002 times the beam width). In addition angular distance between the common sources is typically within 0.′3. These give a global overview of the accuracy of the flux densities and positions.

The flux density uncertainties of extended sources is difficult to predict. We have considered as described earlier the entire flux in the inner rectangle as due to emission from the source. In cases where the inner rectangle was not found to be appropriate using the GUI interface manual boxes were drawn for estimating the integrated flux density. At times for a few sources such as the cluster radio relic J2010-5628 (discussed in the Sec. 7.4) approximating the emission using a rectangular window is not appropriate and such cases have to handled manually. This has not been attempted in the present work.

Reliability and completeness :

The detection of a source with a given intrinsic (noise free) peak flux density depends upon the ratio of noise adjusted peak flux density (detected) over the local noise level. A source with an intrinsic peak flux density of 7σ will have a noise adjusted peak density between 5 and 9σ in 95% of the cases if we assume a normal distribution for the noise. From these numbers the completeness of a catalogue in different regions can be taken to be about 95% for a 7σ source depending upon the rms noise in each sidereal hour image.

The rms noise with a given sidereal hour image is more or less uniform across the declination before applying the primary beam correction, although it is slightly higher in the vicinity of bright sources. The rms noise changes with RA as the brightness distribution of the sky changes. There are regions where the source searching was not carried out as discussed earlier either due to unreliability of the regions or those which are close to the Galactic plane as shown in Fig. 7.29. The total sky area covered by these regions is ≈4.5% of the entire region of the images presented here. If the regions covered by Galactic plane are excluded the actual region which has not been included for source search due to being unreliable is 3.6%. Since the primary beam shape of the helix depends upon declination that has to be also taken into account while estimating the completeness limit.

In our catalogue making process each source was visually inspected for the background in both the raw and the deconvolved image, the fits obtained, the ratio of the fitted flux density to χ and the goodness of the fit parameter returned by the fitting routine. We believe that as far as the reliability of the sources is concerned the catalogue is reliable to more than 95%. Cases in which we were doubtful about the genuineness of a source were excluded. A monte-carlo simulations combined with the theoritical analysis for flux density accuracy, positional accuracies, completeness and reliability of the sources is still required and will be carried out in future.

7.4 Some interesting sources in the images

A steradian of the sky contains a wealth of information. Unfortunately due to lack of time it is beyond the scope of this dissertation to discuss it in a reasonable depth. As a representative of interesting sources in the images, we present a few steep spectrum sources, giant radio sources, double sources, cluster radio relics/fossil galaxies and report the structure of a few resolved supernova remnants. The examples presented here are by no means either comprehensive or complete. Point sources can be a study in themselves but we will restrict ourselves to the ones with steep spectrum.

Steep spectrum sources :

Steep spectrum radio sources are one of the most interesting objects in a low frequency survey. They facilitate study of astrophysically interesting objects like high redshift galaxies, pulsars and sometimes cluster halos.

One of the most interesting questions in observational cosmology is how do galaxies form and evolve and when did the first primeval galaxies appear. By observing galaxies which are at high redshift we can look back in time and observe the so called ancestors of the present day galaxies to address this question. Steep spectrum and small angular

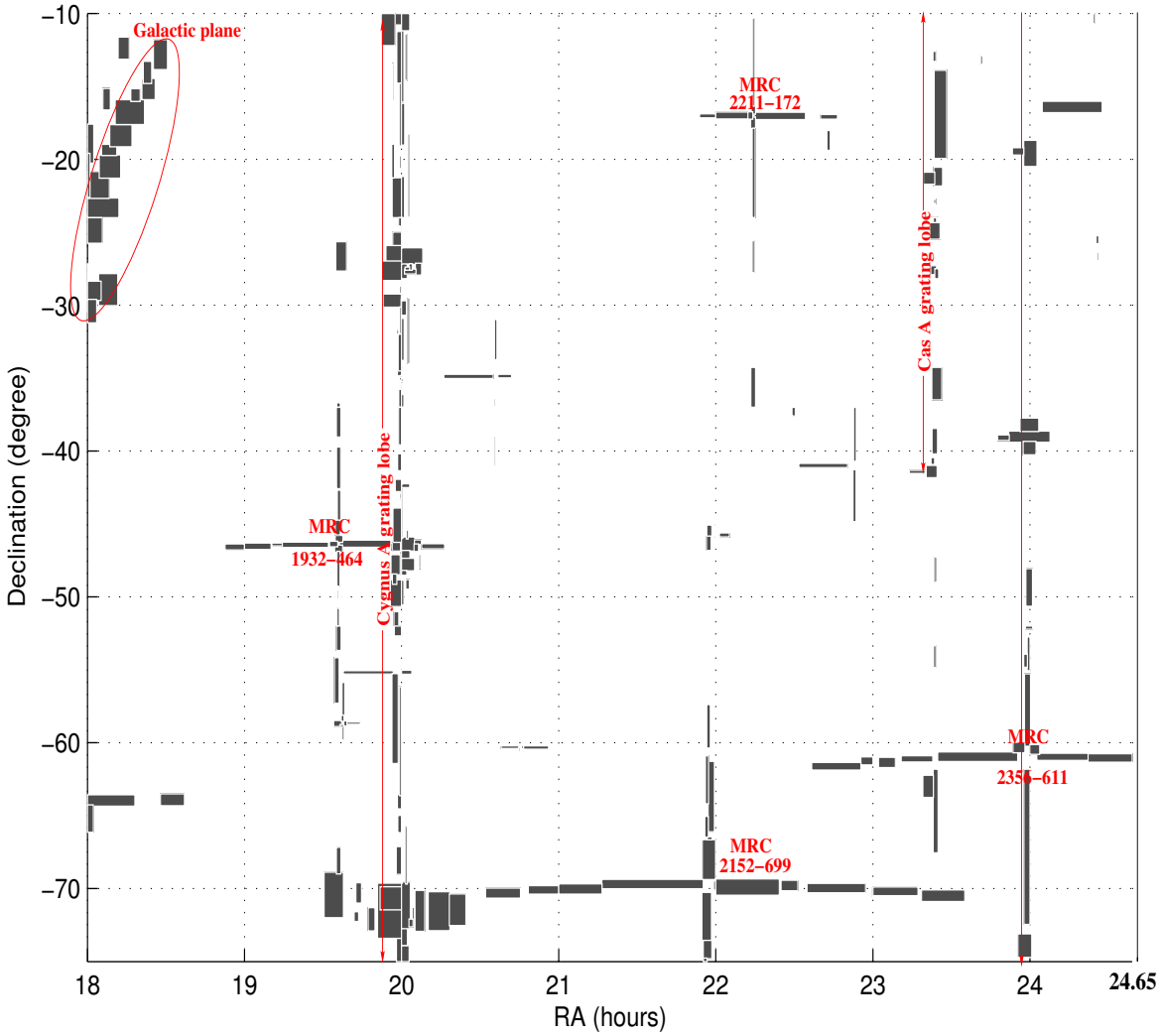

Fig. 7.29: Regions (shaded) of the image which were excluded during source search. Except the regions covered by the Galactic plane all other shaded regions were not included as they were not considered reliable enough due to various reasons. These regions are best investigated by looking at the image themselves. They cover a total area of 4.5% of the sky covered by the images. If the Galactic plane region is not taken into account the area of the sky corrupted is ≈3.6%.

size are the two features which are extensively and effectively used in filtering the sample of sources in low frequency radio surveys as potential candidates for high redshift galaxies (Rawlings et. al., 1996; De Breuck et. al., 2000, 2004; Van Breugel et. al., 1999). Many high redshift radio galaxies known including the most distant ones have been detected using searches based on steep spectrum sources. Although other techniques like color dropouts, deep spectroscopic observations of blank fields, narrow band Lyman α imaging are also popularly used, however selection techniques based on steep spectrum radio sources is still the one to find objects that can be selected uniformly and at all redshift ranges in a way that it does not suffer from optical biases such as dust extinction which is

Source Name	Counter part	redshift(z)	$S_{408\,MHZ}$ (Jy)	$S_{151.5\,MHz}$ (Jy)	α
MRT J2045-6019	MP2045-6018	1.464	11.6	36.61	1.2
MRT J2048-5750	MP2048-5750	1.262	2.8	8.78	1.16
MRT J2028-2140	MRC2052-218	2.63	1.28	3.03	0.87
MRT J2106-2405	MRC2104-242	2.49	1.8	6.20	1.25
MRT J2142-2858	MRC2139-292	1.326	1.66	5.24	1.16

Table 7.11: A few moderate high redshift galaxies known in the literature detected in the MRT. The references to the data are De Breuck et. al. (2000) and McCarthy et. al. (1990). α denotes the spectral index.

important at high redshifts.

We have used the 1,680 common sources between MRC and MRT to produce a list of about 120 sources which have their spectra steeper than 1.3. The list is by no means complete as there are about a thousand sources detected in the MRT images which are not listed in the MRC. Some of these arise due to the incompleteness of the MRC below 1 Jy and some of them are genuinely steep spectrum. These can be used to form a set of samples for such searches after referring the literature for excluding those which have already been used. Table 7.11 gives a few of the known galaxies (and having steep spectrum except one) at moderately high redshifts which have also been detected in the MRT images. We have also identified about a dozen sources which have not been detected in MRC catalogue and have spectra steeper than 1.37 (even if we assume they are just at the detection limit of 1 Jy, the completeness limit of the MRC catalogue and thus missed). A comparison with SUMSS and other high frequency surveys would be helpful to make a larger list of steep spectrum sources. It is not known how many of all these steep spectral index sources will actually be high redshift galaxies, however even a small fraction would be important to increase the number of known population.

Pulsars, especially millisecond pulsars, have steepest known radio spectra (generally rarely detected outside the Galactic plane) and are conspicuous continuum sources in low frequency surveys. The catalogue presented does not cover the Galactic plane. Analysis of the Galactic plane images should yield a few candidates suitable for pulsar searches.

The catalogue extends the radio spectra of source populations to 151.5 MHz which is important since below about 100 MHz, synchrotron self absorption and electron energy spectral cut-offs effects become more important. The catalogue can be used as a starting point for building complete samples like the MRC 1 Jy sample or MS4 sample. One of the main advantages of defining a flux density limited sample at the frequency of 151.5 MHz is that there is little contamination due to beamed sources[27]. Thus samples selected at 151.5 MHz would be virtually dominated by isotropic radio emission (contamination by

[27] At 178 MHz (4C survey) the contamination by beamed sources is only 10% (Wall & Jackson, 1997).

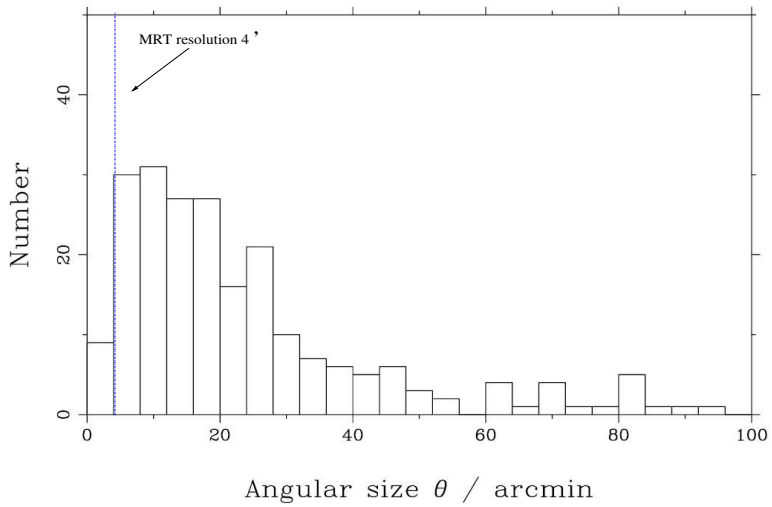

Fig. 7.30: Histogram of the angular size of all the Galactic SNRs known in the literature as a function of their angular size (courtesy (Green, 2004)). The typical size of the SNRs is 11′. It means that there are quite a few SNRs which would be well resolved in the MRT images.

beamed sources will be less than 10%) and would provide an unbiased view of the parent populations used in unification models. So 151.5 MHz is some kind of an optimal frequency for such flux density limited complete samples.

Supernova Remnants :

The expected point source sensitivity in the synthesized images in MRT changes depending upon the region of the sky under consideration. In view of this the corresponding surface brightness sensitivity also changes. Taking the worst case for rms noise as ≈390 mJy the surface brightness sensitivity is $\approx 2.1\times10^{-21}$ W m^{-2} Hz^{-1} Sr^{-1} (1σ at 151.5 MHz). Due to availability of short spacings and nearly complete uv coverage, our images are suited to study the morphology and spectra of Galactic supernova remnants (SNRs), which are used as primary signatures for their identification and classification. Fig. 7.30 shows the angular size distribution of the 219 Galactic SNRs. The typical size of SNRs is ≈11′ and quite a few of are well extended (≈25% of them having sizes exceeding 20′). Fig. 7.31 and Fig. 7.32 show the surface brightness distribution of all the 217 Galactic SNRs known in the literature (Green, 2004). The typical surface brightness of the SNRs is $\approx 1.5\times10^{-20}$ W m^{-2} Hz^{-1} Sr^{-1} (at 151.5 MHz) (Green, 2004). With our resolution of $4'\times4\farcm6\sec(\delta+20\fdg14)$ and achieved surface brightness sensitivity, these objects are generally resolved and detectable in our images. Images of very extended SNRs would also help in making up of spectral index variation maps by comparison with other high frequency images.

Our achieved surface brightness sensitivity $\approx 4.2\times10^{-22}$ W m^{-2} Hz^{-1} Sr^{-1} (1σ, at 1 GHz) is

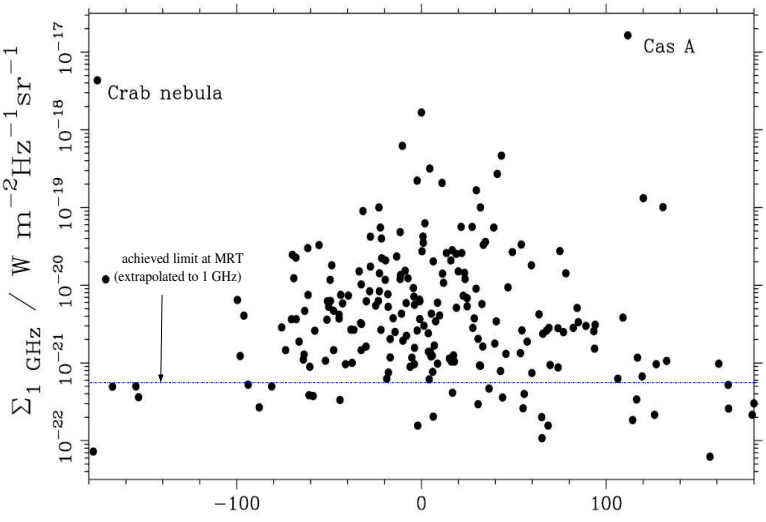

Fig. 7.31: The plot shows the surface brightness of all the Galactic SNRs known in the literature as a function of Galactic latitude (courtesy (Green, 2004)). The achieved surface brightness sensitivity in the MRT images (1σ) is also shown.

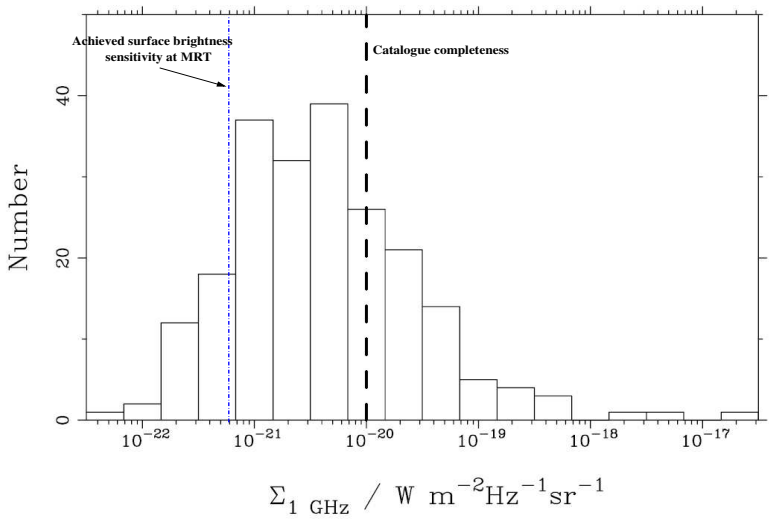

Fig. 7.32: Histogram of the surface brightness of all the Galactic SNRs known in the literature as a function of their surface brightness (courtesy (Green, 2004)). The dashed line shows the limit above which the SNR catalogue is believed to be complete. The achieved surface brightness sensitivity in the MRT images (1σ) is also shown.

significantly better than the surface brightness limit up to which the SNR catalogue is believed to be complete ($\approx 10^{-20}$W m^{-2} Hz^{-1} Sr^{-1} (at 1 GHz)). Thus it would be useful to look for new low surface brightness SNR candidates in the images especially the ones which are large sized and older and are believed to be missing from the known catalogues of SNRs due to selection effects.

Images covering an additional 0.5 steradian of the sky ($15^h06^m \leq$RA$\leq 18^h$, -75°$\leq \delta \leq$-10°) presented in the Appendix A include a large part of the southern Galactic plane including the Galactic center would be very interesting to investigate in this context. A cursory glance indicates that we have been able identify more than 50 SNRs out of 80 known in the literature in the region imaged. The images can be used to study their morphology, measure their integrated flux and estimate their spectra.

We now present images of a few of the resolved SNRs in Fig. 7.33 from the images presented in this chapter along with a few comments (See Green (2004) and (Kassim, 1989) for references). The names of the SNRs is also shown along with each image.

Comments on individual SNRs :

G011.2-00.3 : This is a shell type SNR having a symmetrical clumpy shell and is very marginally resolved in our image. Green et. al. (1988) describe this source as an evolved Cassiopeia A based on their high resolution VLA observations. This SNR is believed to be associated with the SNR of AD386. Its X-ray image shows that the shell has a hard spectrum. There is a pulsar located in the center. H I absorption indicates the distance of this source to be 5 Kpc.

G022.7-00.2 : This source shows a lot of structure in our image with a shell morphology. This is a ring shaped fairly complete shell type SNR in a complex region whose flux density is uncertain due to its overlap with the SNR G23.3-0.3 and the contribution from atleast one well known H II region.

G023.3-00.3 : This source is an asymmetric shell in a complex region having an overlap with the SNR G22.7-0.2 and the superposition of two small diameter H II regions. There have been suggestions of Pulsar associations with this source. In our image not much structure is revealed as compared to the 330 MHz image by Kassim (1989) which may indicate a flat spectrum.

G021.5-00.9 : This is a well known plerionic SNR which has been well studied especially at high frequencies. This source is unresolved in our image. This is having a filled center with a high frequency turnover. H I absorption indicates that this is more than 5.5 Kpc away. The central core has also been detected in X-ray with a faint halo.

G021.8-00.6 : This source shows is well extended and and shows a typical incomplete morphology like many Galactic SNRs. The nearby source is an H II region which is believed to

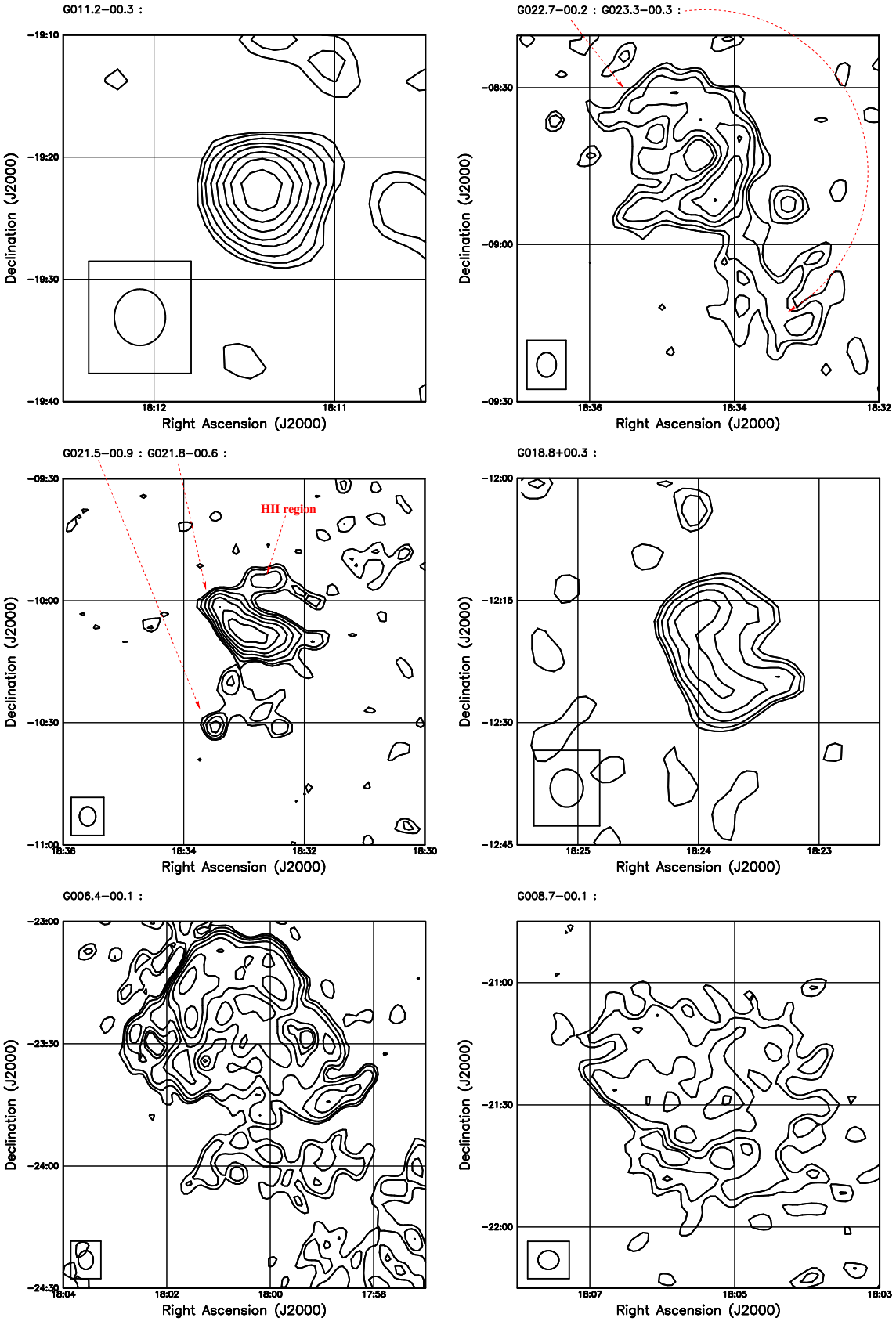

Fig. 7.33: Contour images of a few interesting extended SNRs in the MRT images. The contour levels for all the figures are -5, -3.00, 2.8, 3.6, 5, 7.2, 10.0, 14.4, 20.2, 28.8, 39.6, 54.0, 72.0, 100.1, 136.8, 180.0 Jy beam^{-1}. The rms noise in the individual image varies from 0.5 to 1 Jy beam^{-1}depending upon the declination (due to helix primary beam).

be unrelated to the SNR. H_2CO absorption lines indicate a distance of more than 6.3 Kpc to this SNR.

G018.8-00.3 : The image shows an incomplete shell type morphology of this source. HI I absorption indicates that the distance is between 9.5 to 19 Kpc. This is a steep spectrum source having a shell type spectrum.

G006.4-00.1 : This shows an edge brightened morphology in our image. Our image shows considerable extended low surface brightness emission features associated with the interior of the bright shell which is difficult to distinguish from the Galactic background at higher frequency maps. This SNR exhibits bright shell type emission from a nonthermal ring and possibly plerionic emission from a flat spectrum core and is classified as a composite in the Greens catalogue (Green, 2004). The bright extended source to the south is a known H II region (Lokmans 1989 catalog). This is also called as G007.06-0.12

G008.7-00.1 : This is a clumpy nonthermal shell, with a low frequency turnover. There is a Pulsar detected in the western edge and is believed that this pulsar PSR 1800-21 is associated with this SNR. This SNR is associated with the W30 complex. This has a spectrum typical of a shell type SNR. H II region in the W30 complex yields a distance of about 6 Kpc. At this distance, this is one of the most distant low surface brightness SNRs presently known in our galaxy. In our image it appears as a weak diffused structure but no very prominent features.

Extended extragalactic sources in the MRT Images :

Due to low frequency and surface brightness sensitivity, MRT is also suited for the study of extended extragalactic sources. In this part of the chapter, we first discuss a specific cluster radio relic/fossil galaxy. Later we present a few extended extragalactic sources seen in the images.

Cluster radio relic MRT J2010-5628(B2006-566)/MRT J 2011-5643(B2007-568)[28]

Cluster radio relics in the vicinity of clusters of galaxies are believed to be fossil galaxies, with shock accelerated relativistic electron population (Ensslin & Bierman, 1998). The necessary shock waves would be of Mpc scale and believed to be due to steady accretion of matter on to the cluster or due to merger event with another cluster. Recently observed sub-structures in X-ray temperature maps support the existence of extended shock waves at locations of several known cluster relics (Markevitch et. al., 1998; Donelly et. al., 1998). Fig. 7.34 shows extended radio emission from these proposed shocks around the X-ray cluster Abell 3667 in the MRT image. A contour image from the ROSAT overlaid on a grey scale radio image at 843 MHz from the MOST is also shown (Röttgering et. al., 1997). The emission from giant steep spectrum cluster radio relic MRT J2010-5628 has a Z shaped

[28]The names indicated in the parenthesis indicate the corresponding source name as in the MRC catalog.

structure and extends to about 2.6 Mpc with a constant spectral index along the main axis of the relic. The Z shape is believed to be the structure of the radio plasma (Röttgering et. al., 1997). The side more distant from the cluster center is sharply edged and the spectral index variation suggests presence of particle acceleration. Röttgering et. al. (1997) also report a pressure imbalance of one to two orders of magnitude between the gas pressure at the projected cluster radius of the relic and equipartition pressure. They show that the discrepancy could vanish if the lower gas pressure of the shock radius and higher radio plasma pressure of a compressed flattened structure is taken into account. The images also reveal a second cluster relic MRT J 2011-5643 on the other side of the cluster. Röttgering et. al. (1997) suggest that both the relics might be the two lobes of a former now inactive radio galaxy possibly a cD galaxy. If this is true it must be gigantic since the projected distance is about 5.2 Mpc. In addition the galaxy must have been very powerful and this should have happened during the early period of violent quasar activity when the intra cluster medium was thinner.

These reactivated fossil galaxies are powerful tools to investigate the properties of infalling matter onto the clusters of galaxies and a test ground of large scale structure formation. These are steep spectrum sources and we expect to detect quite a few such sources in the MRT survey.

Structures of a few extended sources

We report the structure of a few extended sources in the MRT images. Some of these sources are a group of unrelated sources confused in the MRT beam. A few straight forward comments on the individual sources are also mentioned (See (Jones & McAdam, 1979) and (Burgess, 1998) for detailed comments and references). The sample is a representative of the strong extragalactic radio sources in the region of the southern sky imaged, but is statistically not complete.

Fig. 7.35 to Fig. 7.38 show the structure of a few sources in the images which are generally well resolved[29]. We provide comments on the individual radio images and available in the literature. The names of these sources are also displayed along with their images[30].

MRT J 0116-4725(B0114-476) z=0.146 : (Fig. 7.35(a)) This is a giant complex radio source. The image clearly reveals two extended edge brightened lobes, both of which have inner hot spots. A faint core has also been seen in image of Subrahmanyan et. al. (1996).

MRT J 0127-6116(B0125-615) : (Fig. 7.35(b)) This source appears to have two asymmetric lobes in our image. It has not been marked as extended by Jones & McAdam (1979), but in our image it clearly appears extended.

[29] A few sources which necessarily do not form a part of a steradian of the sky presented in the images have also been included.

[30] The names indicated in the parenthesis indicate the corresponding source name as in the MRC catalog.

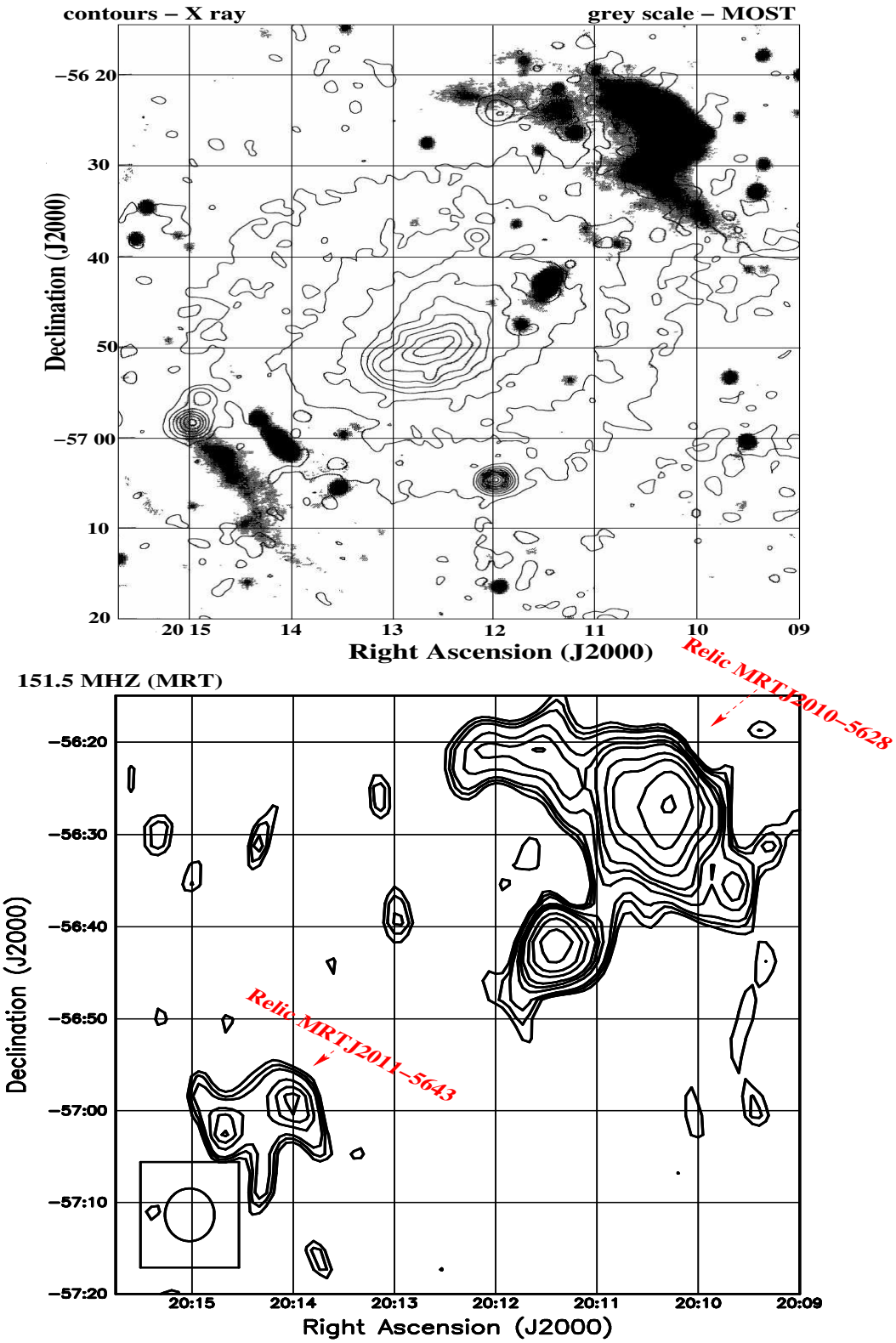

Fig. 7.34: Image of the region around the cluster Abell 3667. The figure on the left shows a contour representation of the ROSAT PSPC image (0.1-2 Kev), overlaid on a grey scale radio image at 843 MHz from the MOST. The X-ray contours are set at 2, 8, 18, 32, 50, 72, 98, 128, 162, 200 and 242 × the background noise (Röttgering et. al., 1997). The MRT image of the same region on the right shows the extended emission suspected to be due to the shocks formed between the infalling matter and the cluster core. The contour levels are $3, 4, 5, 7, 10, 14, 20, 28, 40, 56, 80 \times \mathrm{rms}(\sigma)$ which is $\approx$290 mJybeam^{-1}.

MRT J 0134-3629(B0131-367A/B0131-367B) z**=0.030 :** (Fig. 7.35(c)) This source is extended and shows edge brightened morphology. It is a double source having an FR II structure with a faint core. The optical counterpart is a SO galaxy. This source contains a prominent dust lane and is reported to be a rare example of a radio galaxy with a disk.

MRT J 0321-4510(B0319-453) z**=0.063 :** (Fig. 7.35(d)) This is a Giant complex edge brightened asymmetric double source. The image source very complex structure. This galaxy has a dust lane and coincides with a weak core in the image of Saripalli et. al. (1994). This is one of the largest sources in the sample of large extragalactic sources of Jones & McAdam (1979).

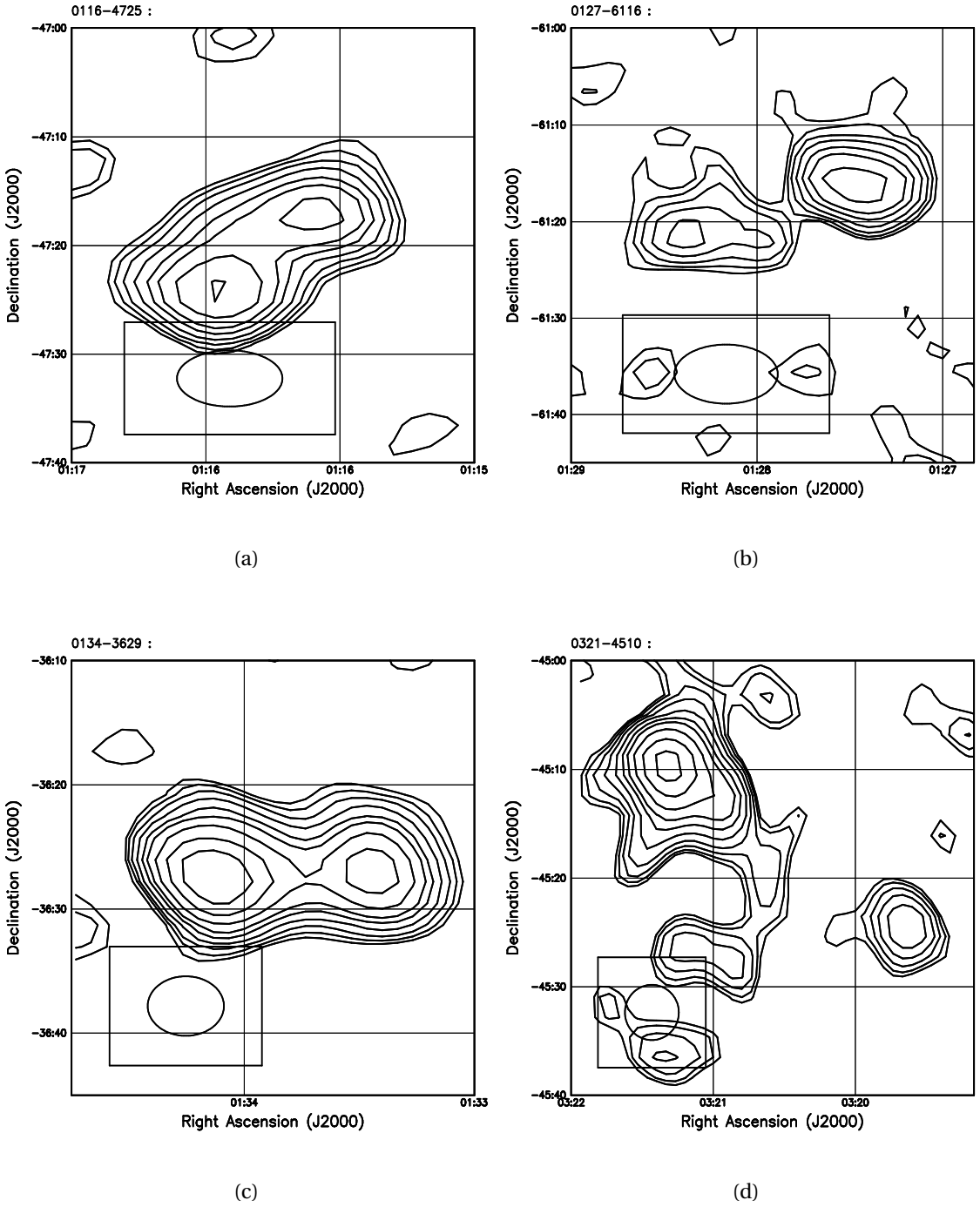

Fig. 7.35: Contour images of a few extended sources in the MRT images. The contour levels are -5, -3, 0.7, 1, 1.4, 2, 2.8, 3.6, 5, 7.2, 10, 14.4, 20, 29, 40, 54, 72, 100 Jy beam^{-1} for all the images. Source names as detected in MRT are shown on the top of each image.

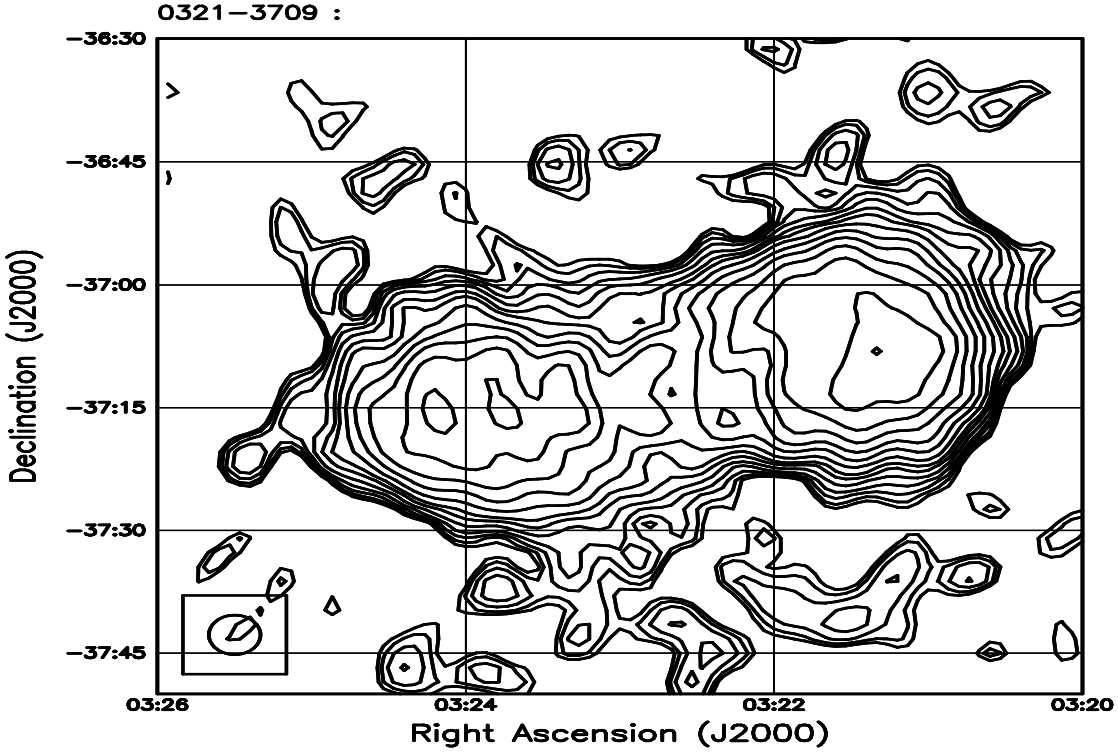

(a)

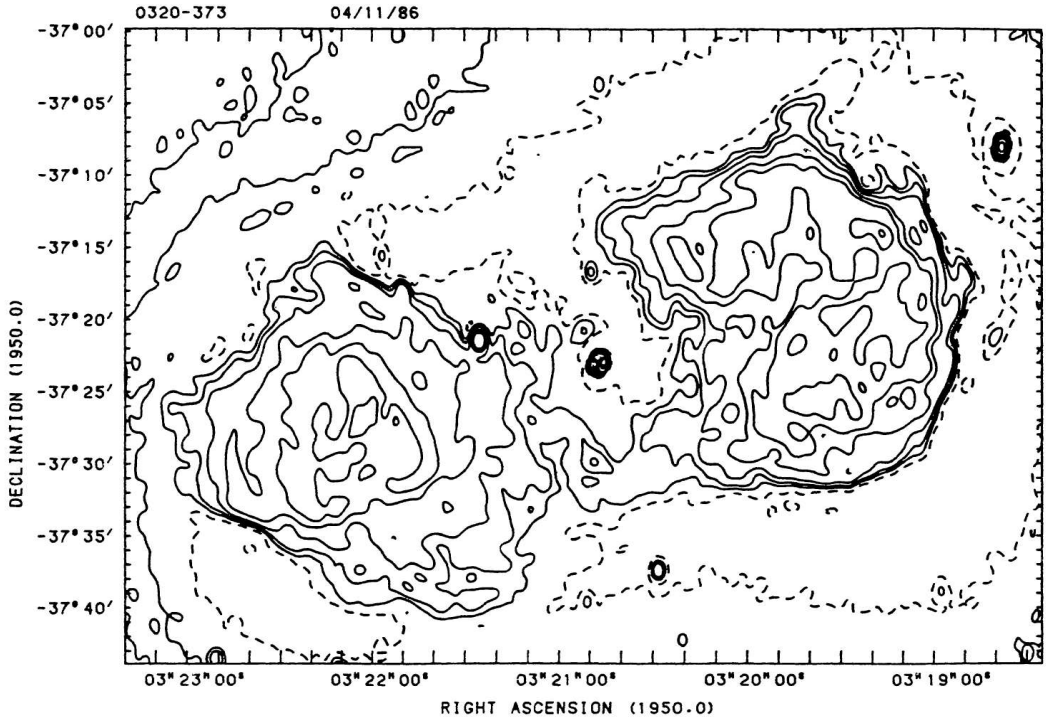

(b)

Fig. 7.36: Contour images of galaxy FORNAX A in (a) MRT and (b) 843 MHz MOST. The contour levels in the MRT image are -5, -3, 0.7, 1, 1.4, 2, 2.8, 3.6, 5, 7.2, 10, 14.4, 20, 29, 40, 54, 72, 100 Jy beam^{-1}. The contour levels in the MOST image are at ± 2%, 5%, 10%, 20%, 30%, 50%, 70%, 90% of the peak brightness. The dahsed contours show the negative bowl. The maximum peak brightness in the image is 0.36 Jy beam^{-1}. Due to availability of short spacing, the MRT images are not affected by negative bowl.

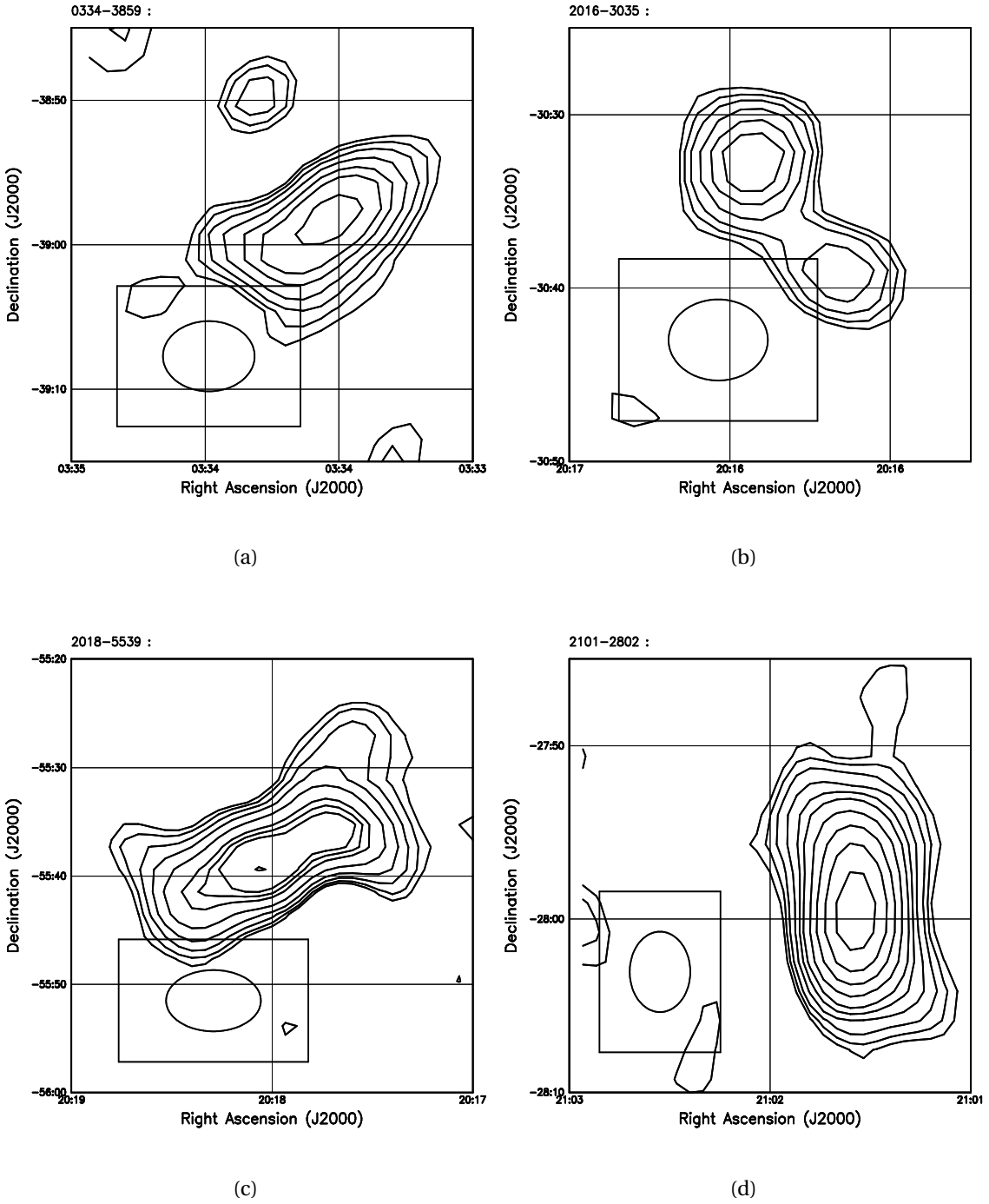

(a) (b)

(c) (d)

Fig. 7.37: Contour images of a few extended sources in the MRT images. The contour levels are -5, -3, 0.7, 1, 1.4, 2, 2.8, 3.6, 5, 7.2, 10, 14.4, 20, 29, 40, 54, 72, 100 Jy beam^{-1} for all the images. Source names as detected in MRT are shown on the top of each image.

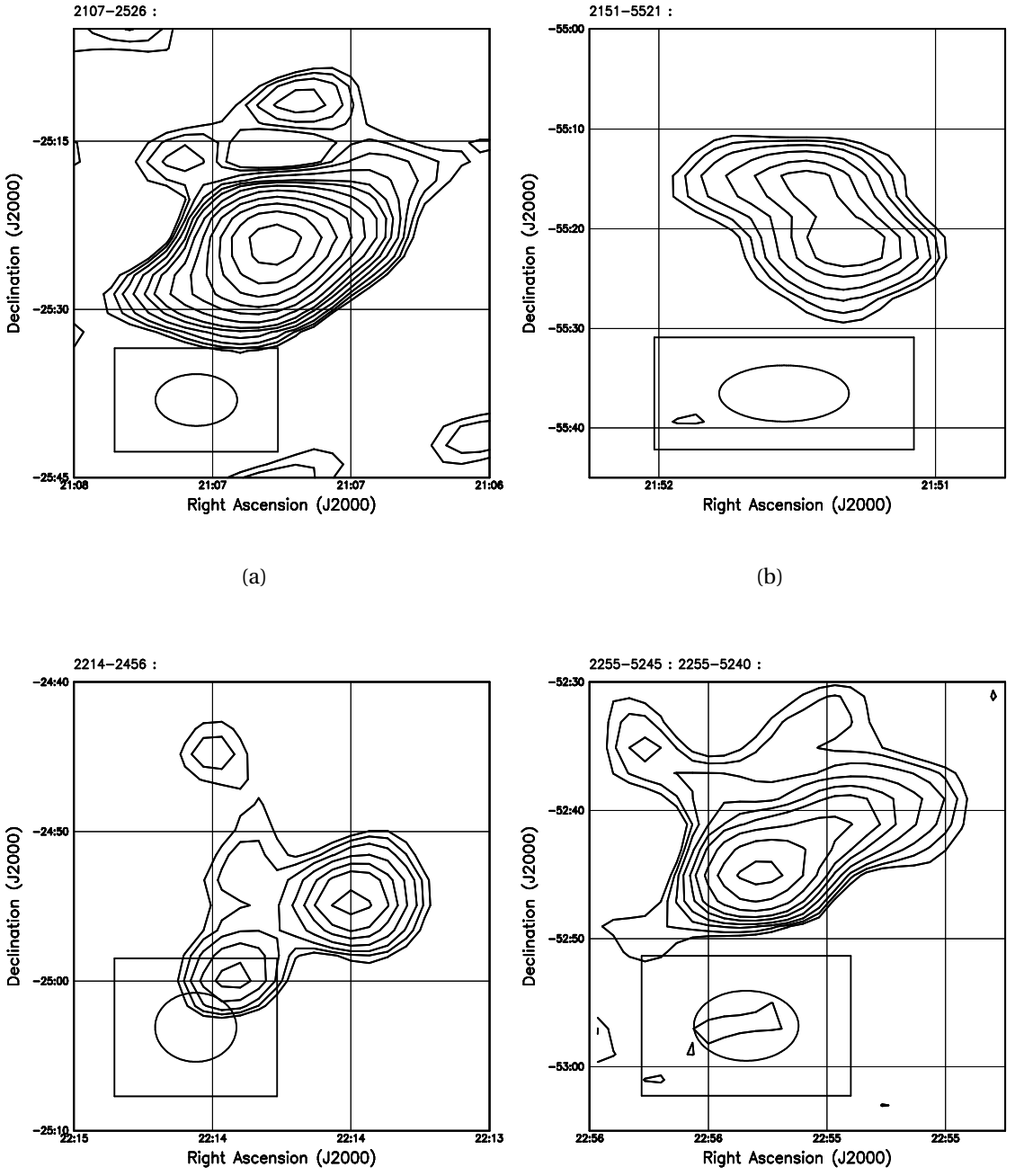

Fig. 7.38: Contour images of a few extended sources in the MRT images. The contour levels are -5, -3, 0.7, 1, 1.4, 2, 2.8, 3.6, 5, 7.2, 10, 14.4, 20, 29, 40, 54, 72, 100 Jy beam^{-1} for all the images. Source names as detected in MRT are shown on the top of each image.

MRT J 0321-3709(B0320-373) z**=0.0061 :** (Fig. 7.36(a), Fig. 7.36(b)) This is well studied elliptical radio galaxy Fornax A which shows evidence of recent merger events. It is a double source with a compact core component and large, diffuse edge brightened lobes. In our deconvolved image due to availability of short spacings, the morphology is well revealed without negative bowls as compared to the MOST image of Jones & McAdam (1979). The ROSAT X-ray image shows presence of hot gas component.

MRT J 0334-3859(B0332-391A/B0332-391B) z**=0.063 :** (Fig. 7.37(a)) This is a bent wide angle tail source in the cluster A3135, with two edge brightened and a core component. In our image although the source is not very well resolved the bent structure can be easily seen.

MRT J 2016-3035(B2013-308/B2013-307) : (Fig. 7.37(b)) There are two unrelated sources detected separately in the MRC but here appear like connected double source due to confused MRT beam.

MRT J 2018-5539(B2013-557) z**=0.0608 :** (Fig. 7.37(c)) This is a giant extended edge brightened source with strong core and diffuse lobes. The structure of this source shows rotational symmetry. In our images the external lobes seem to be very extended as if expanding perpendicular to the axis of the two lobes.

MRT J 2101-2802(B2058-282) : (Fig. 7.37(d)) This source appears to be a well extended single source in our image. It is difficult to conclude from the image whether there are two lobes of a single source or two sources close to each other are actually confused in the MRT beam.

MRT J 2107-2526(B2104-256) : (Fig. 7.38(a)) This source appears to be a well extended source with a very complex morphology in our image. There seem to be two small weak connected structures close to it and may be a part of the same source. The bent structure of this source is also seen.

MRT J 2151-5521(B2147-555/B2148-555) z**=0.035 :** (Fig. 7.38(b)) This is a complex edge darkened source in the cluster A3816, with a slightly bent shaped S structure.

MRT J 2214-2456(B2211-251/B2211-252) : (Fig. 7.38(c)) There are two separate sources which are detected as a single source in our image looking like a double source.

MRT J 2255-5245(B2252-530)/MRT J 2255-5240(B2252-529) : (Fig. 7.38(d)) This also is a pair of unrelated point sources which appear as a single extended source in the image.

In the next chapter we provide consolidated conclusions of the work carried out in this thesis.

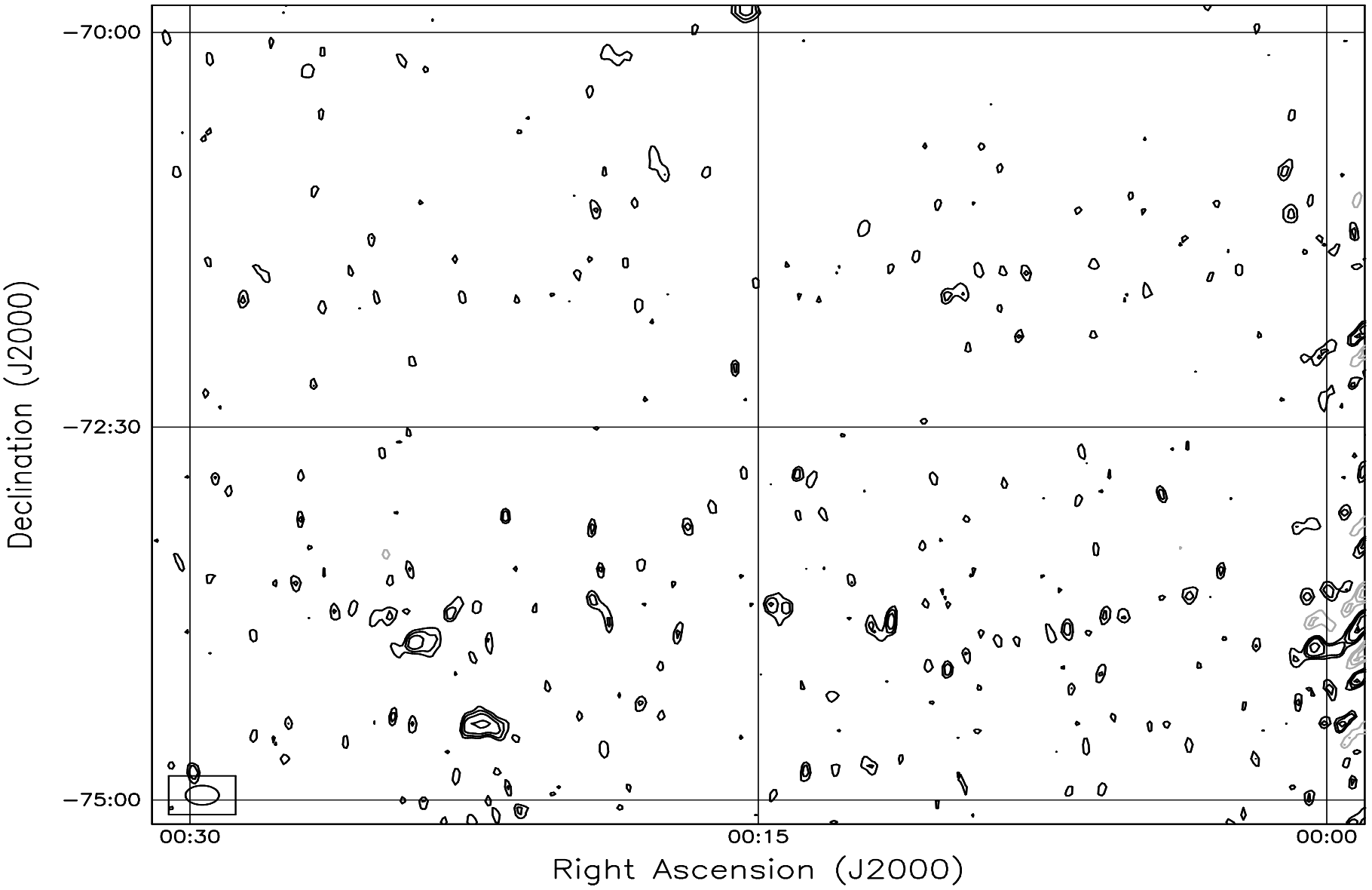

Fig. 7.39: Contour map covering the right ascension range 00h00m to 00h30m and declination range -75° to -70 °. The contour levels are -5, -3.6, -2.5, -1.8, 1, 1.4, 2, 2.8, 3.6, 5, 7, 10, 14, 20, 29, 40, 54, 72, 90, 100, 136, 180, 216, 252, 288 Jy beam^{-1}. The rms noise in the image is ≈425 mJy beam^{-1}.

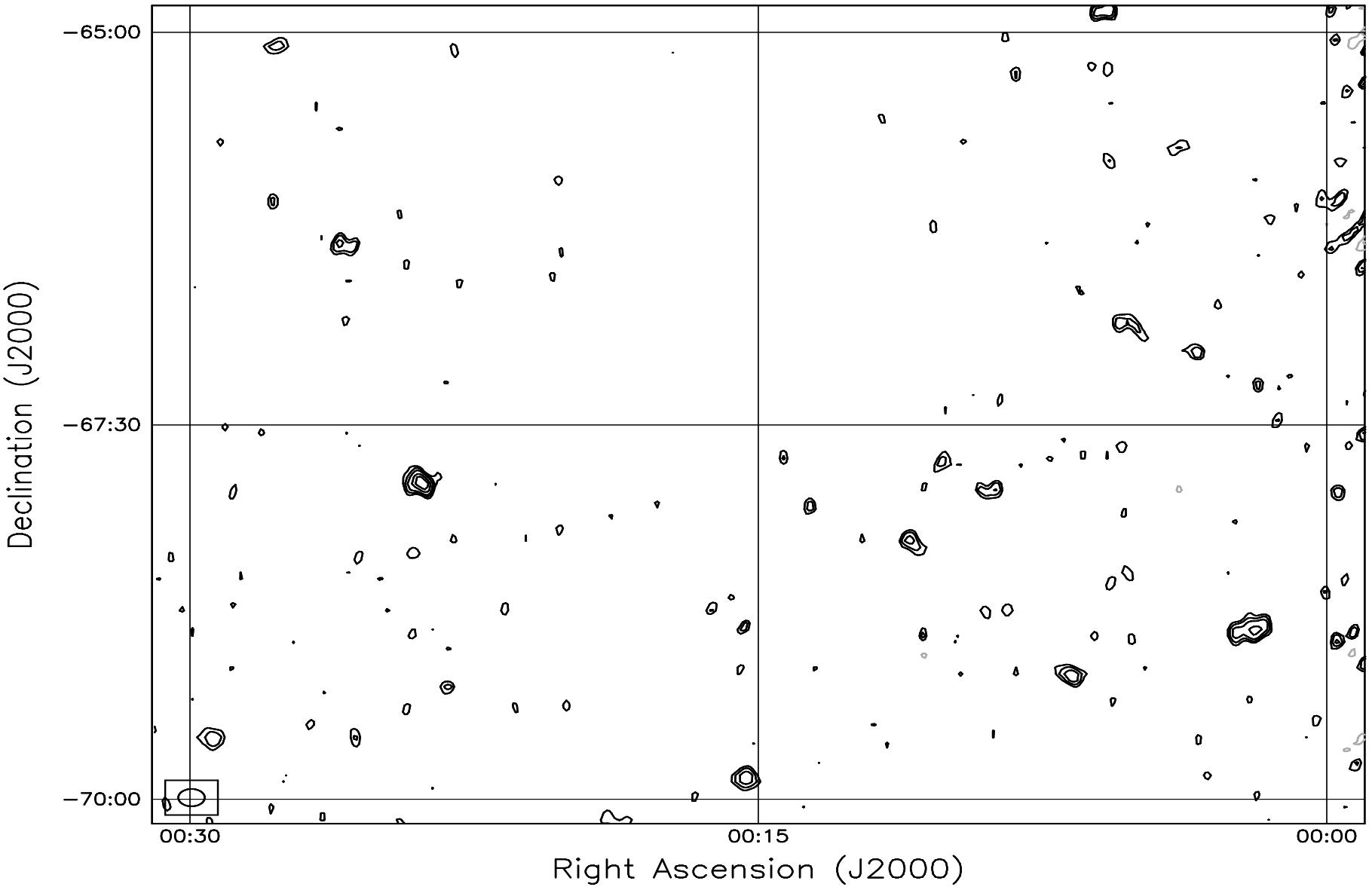

Fig. 7.40: Contour map covering the right ascension range 00h00m to 00h30m and declination range -70° to -65 °. The contour levels are -5, -3.6, -2.5, -1.8, 1, 1.4, 2, 2.8, 3.6, 5, 7, 10, 14, 20, 29, 40, 54, 72, 90, 100, 136, 180, 216, 252, 288 Jy beam^{-1}. The rms noise in the image is ≈370 mJy beam^{-1}.

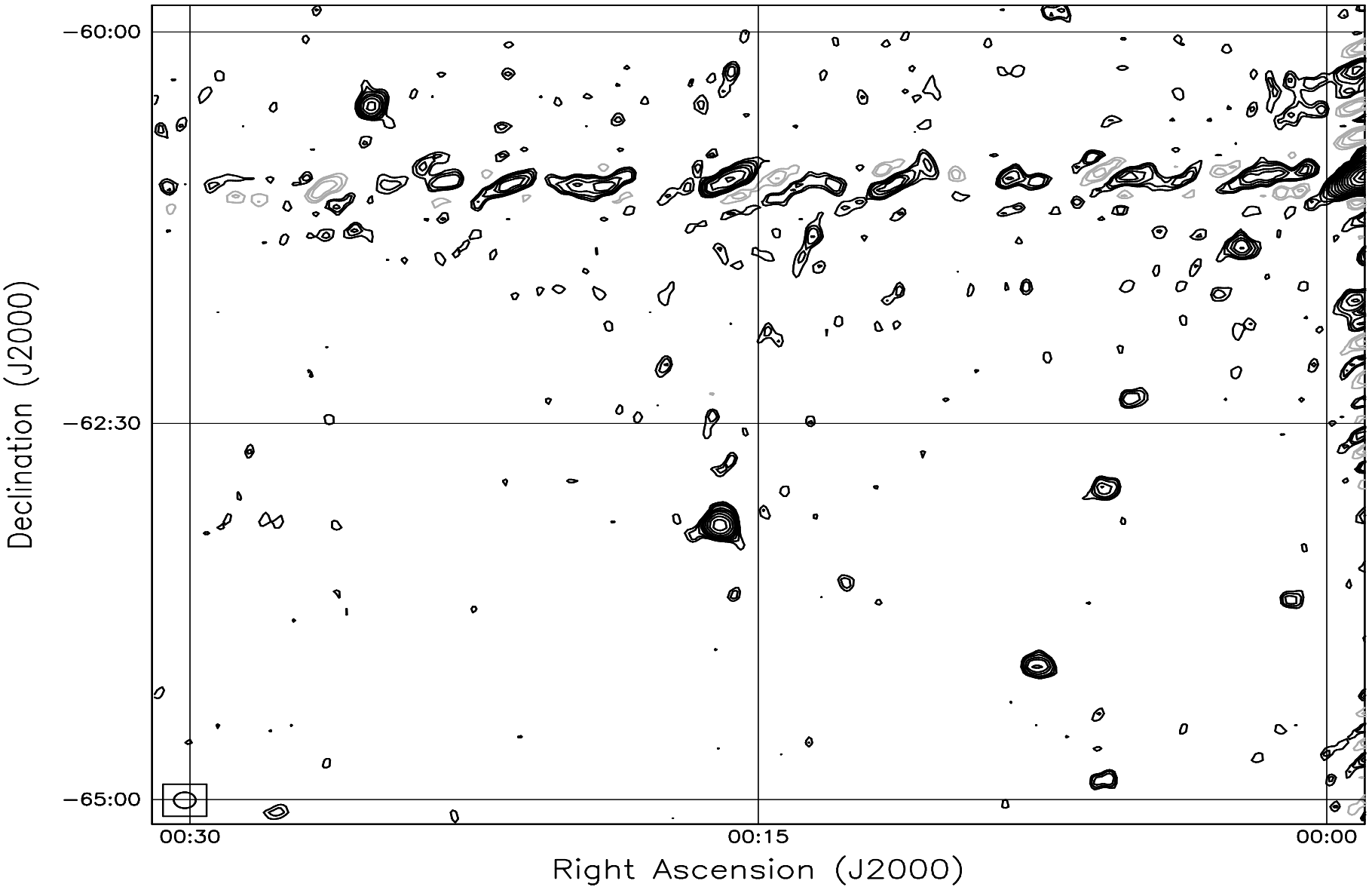

Fig. 7.41: Contour map covering the right ascension range 00h00m to 00h30m and declination range -65° to -60 °. The contour levels are -5, -3.6, -2.5, -1.8, 1, 1.4, 2, 2.8, 3.6, 5, 7, 10, 14, 20, 29, 40, 54, 72, 90, 100, 136, 180, 216, 252, 288 Jy beam^{-1}. The rms noise in the image is ≈330 mJy beam^{-1}.

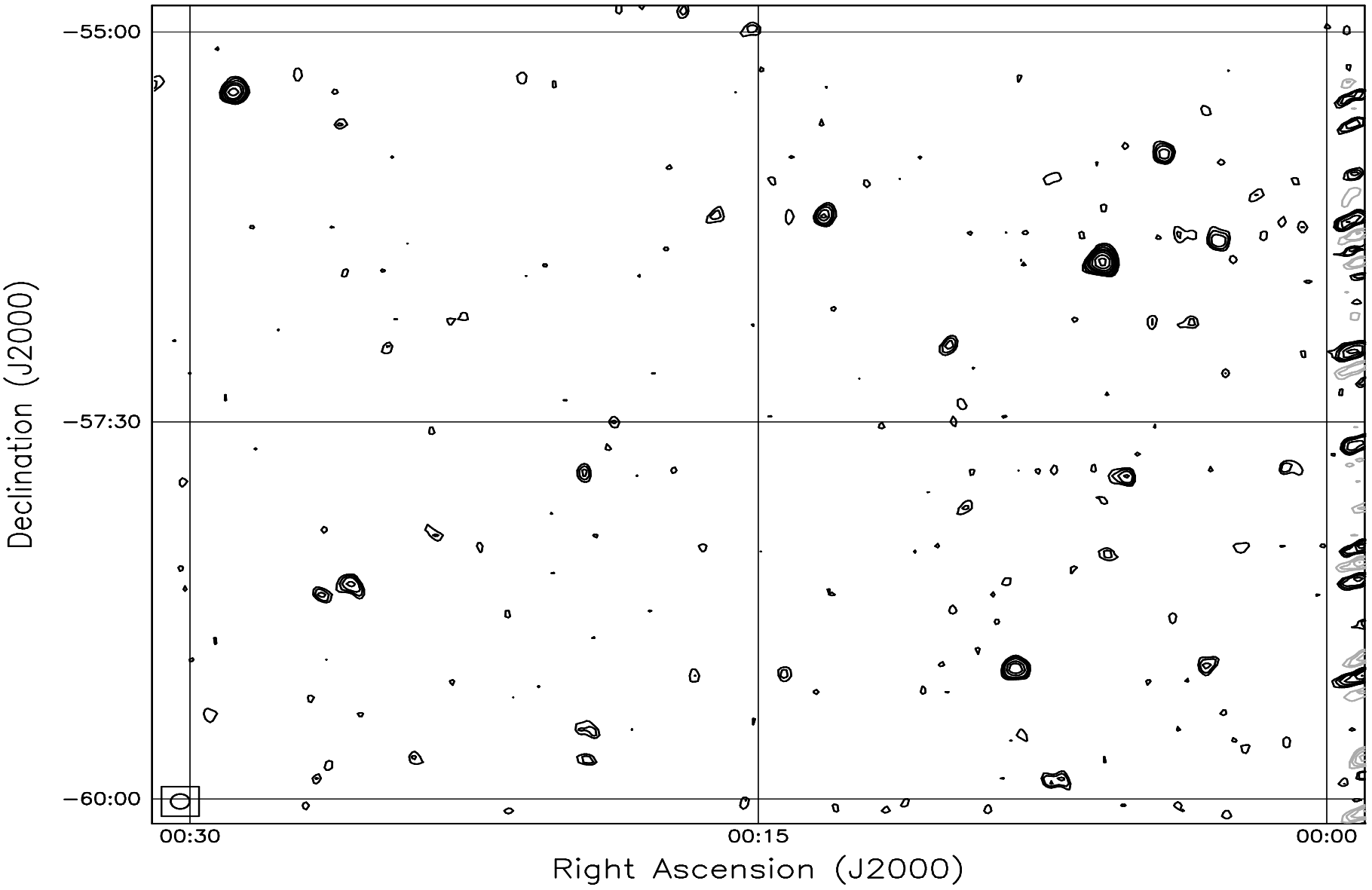

Fig. 7.42: Contour map covering the right ascension range 00h00m to 00h30m and declination range -60° to -55 °. The contour levels are -5, -3.6, -2.5, -1.8, 1, 1.4, 2, 2.8, 3.6, 5, 7, 10, 14, 20, 29, 40, 54, 72, 90, 100, 136, 180, 216, 252, 288 Jy beam^{-1}. The rms noise in the image is ≈310 mJy beam^{-1}.

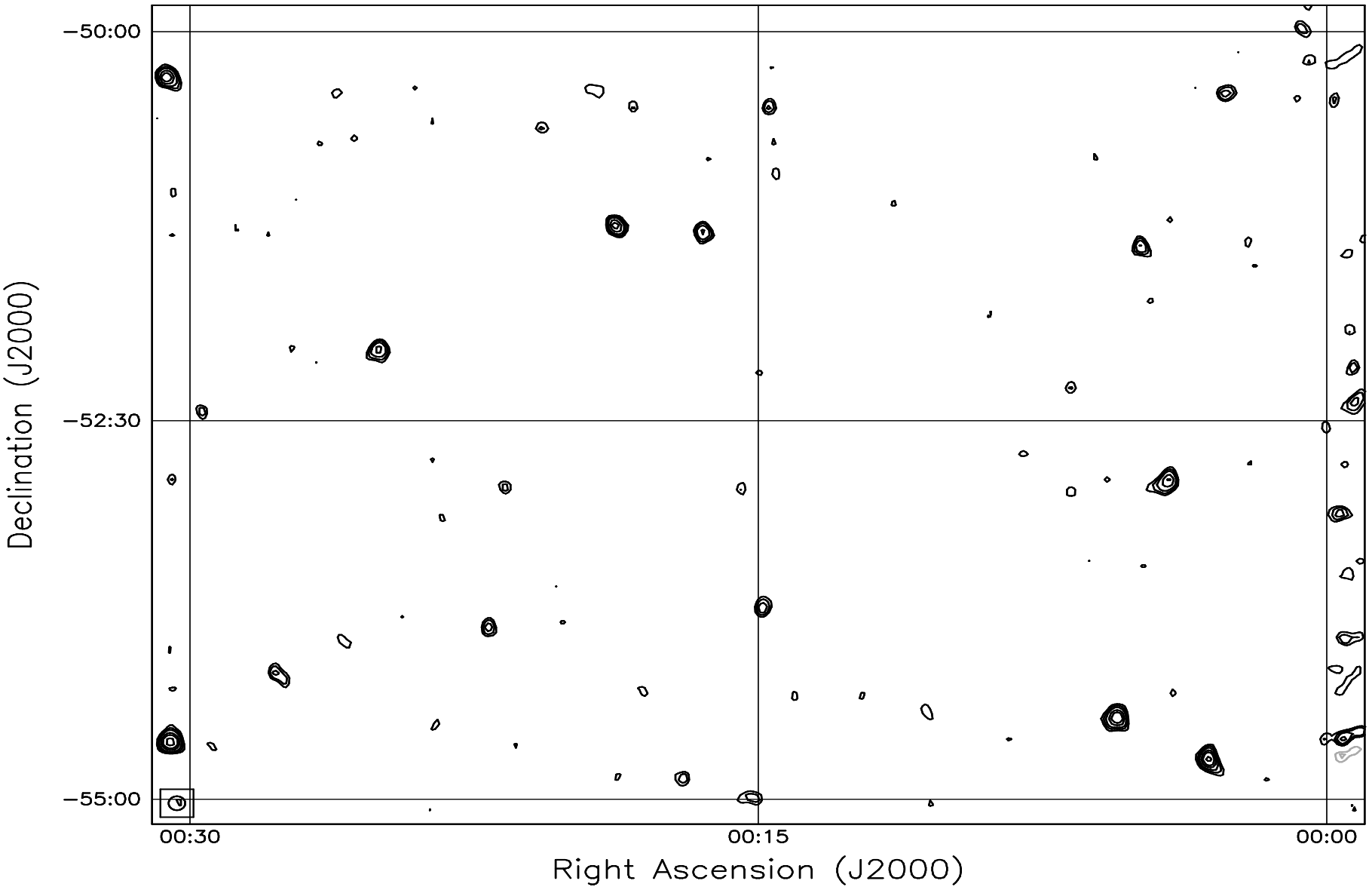

Fig. 7.43: Contour map covering the right ascension range 00h00m to 00h30m and declination range -55° to -50 °. The contour levels are -5, -3.6, -2.5, -1.8, 1, 1.4, 2, 2.8, 3.6, 5, 7, 10, 14, 20, 29, 40, 54, 72, 90, 100, 136, 180, 216, 252, 288 Jy beam^{-1}. The rms noise in the image is ≈300 mJy beam^{-1}.

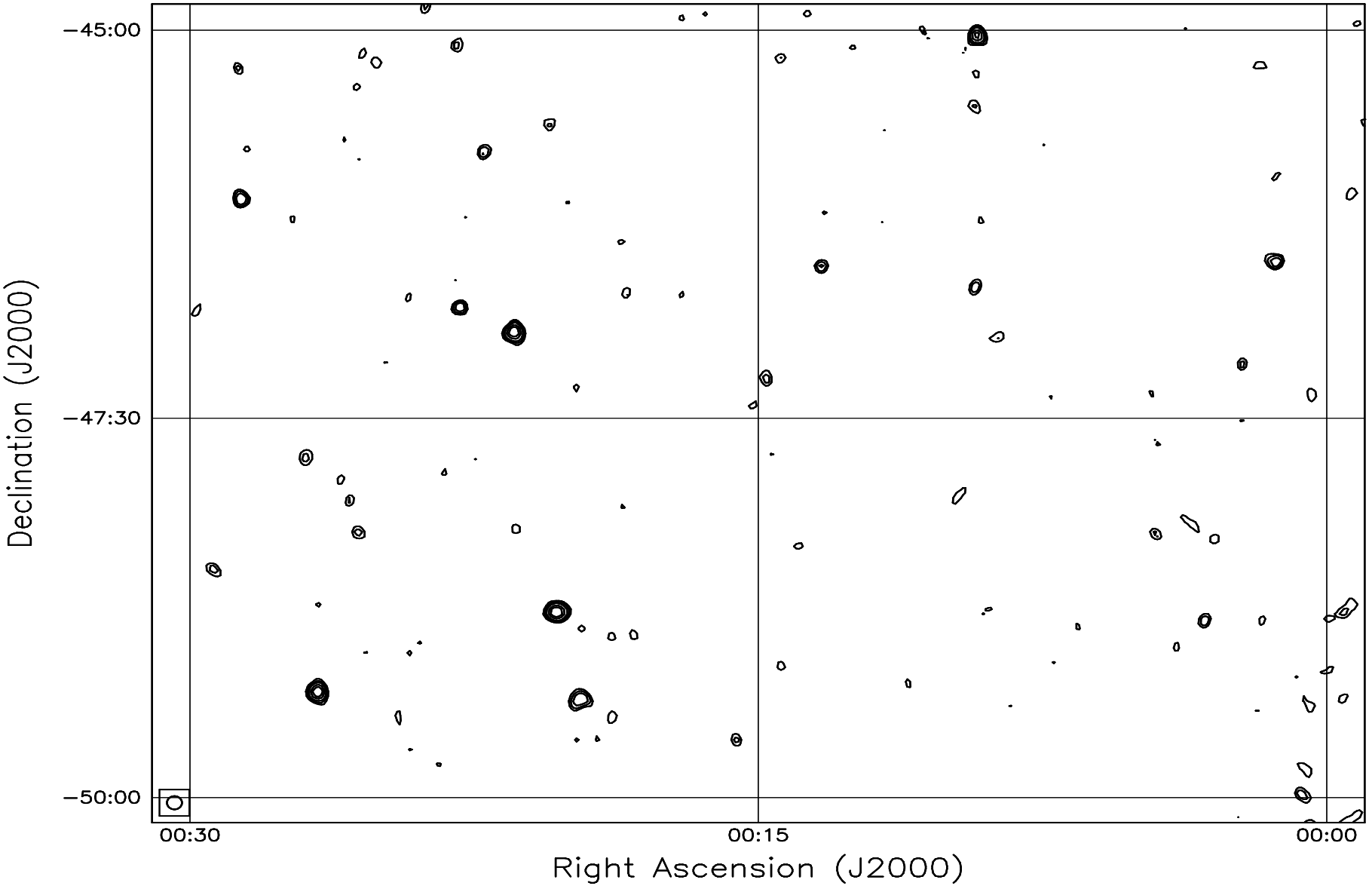

Fig. 7.44: Contour map covering the right ascension range 00h00m to 00h30m and declination range -50° to -45 °. The contour levels are -5, -3.6, -2.5, -1.8, 1, 1.4, 2, 2.8, 3.6, 5, 7, 10, 14, 20, 29, 40, 54, 72, 90, 100, 136, 180, 216, 252, 288 Jy beam^{-1}. The rms noise in the image is ≈290 mJy beam^{-1}.

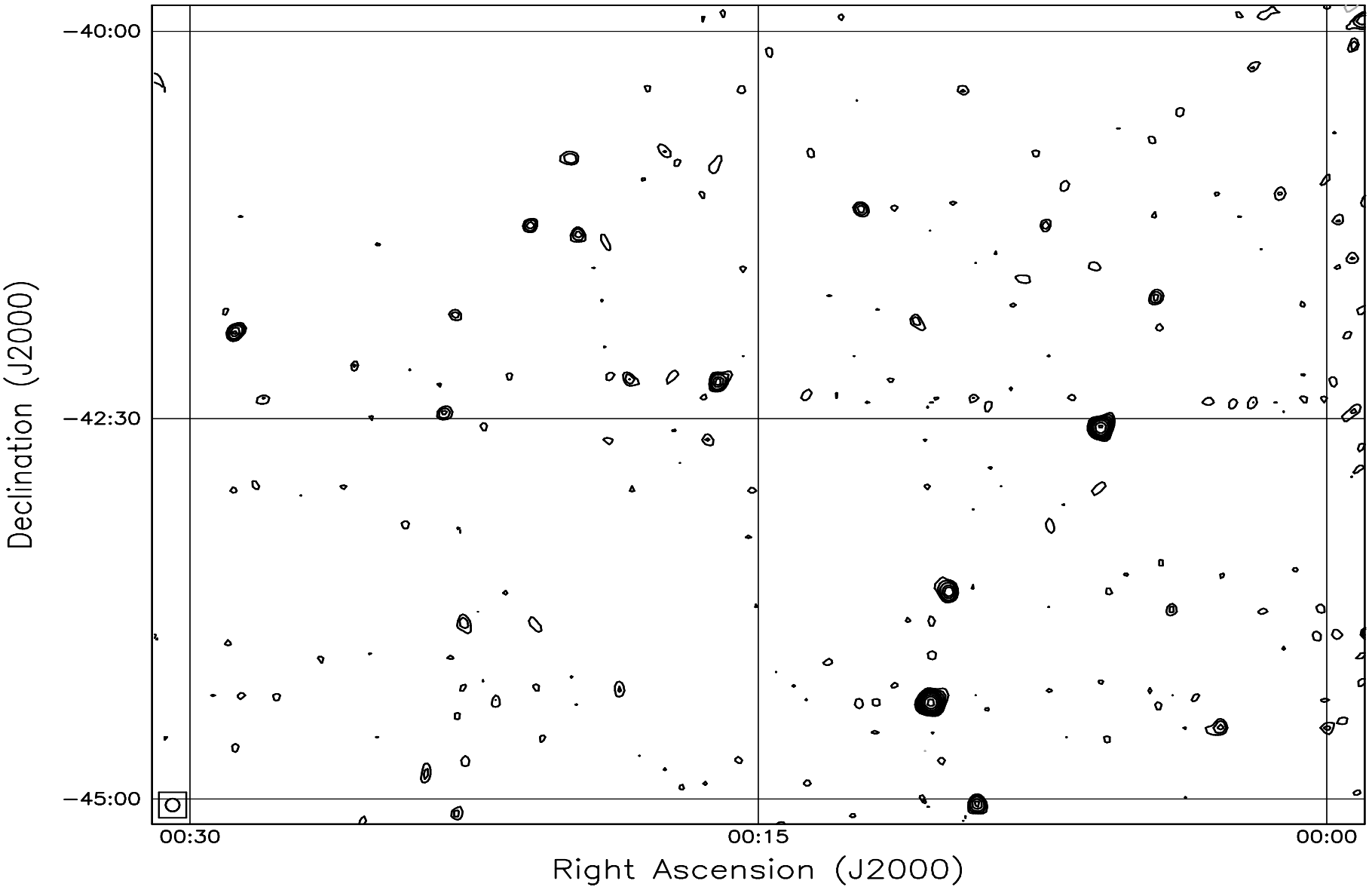

Fig. 7.45: Contour map covering the right ascension range 00h00m to 00h30m and declination range -45° to -40 °. The contour levels are -5, -3.6, -2.5, -1.8, 1, 1.4, 2, 2.8, 3.6, 5, 7, 10, 14, 20, 29, 40, 54, 72, 90, 100, 136, 180, 216, 252, 288 Jy beam^{-1}. The rms noise in the image is ≈290 mJy beam^{-1}.

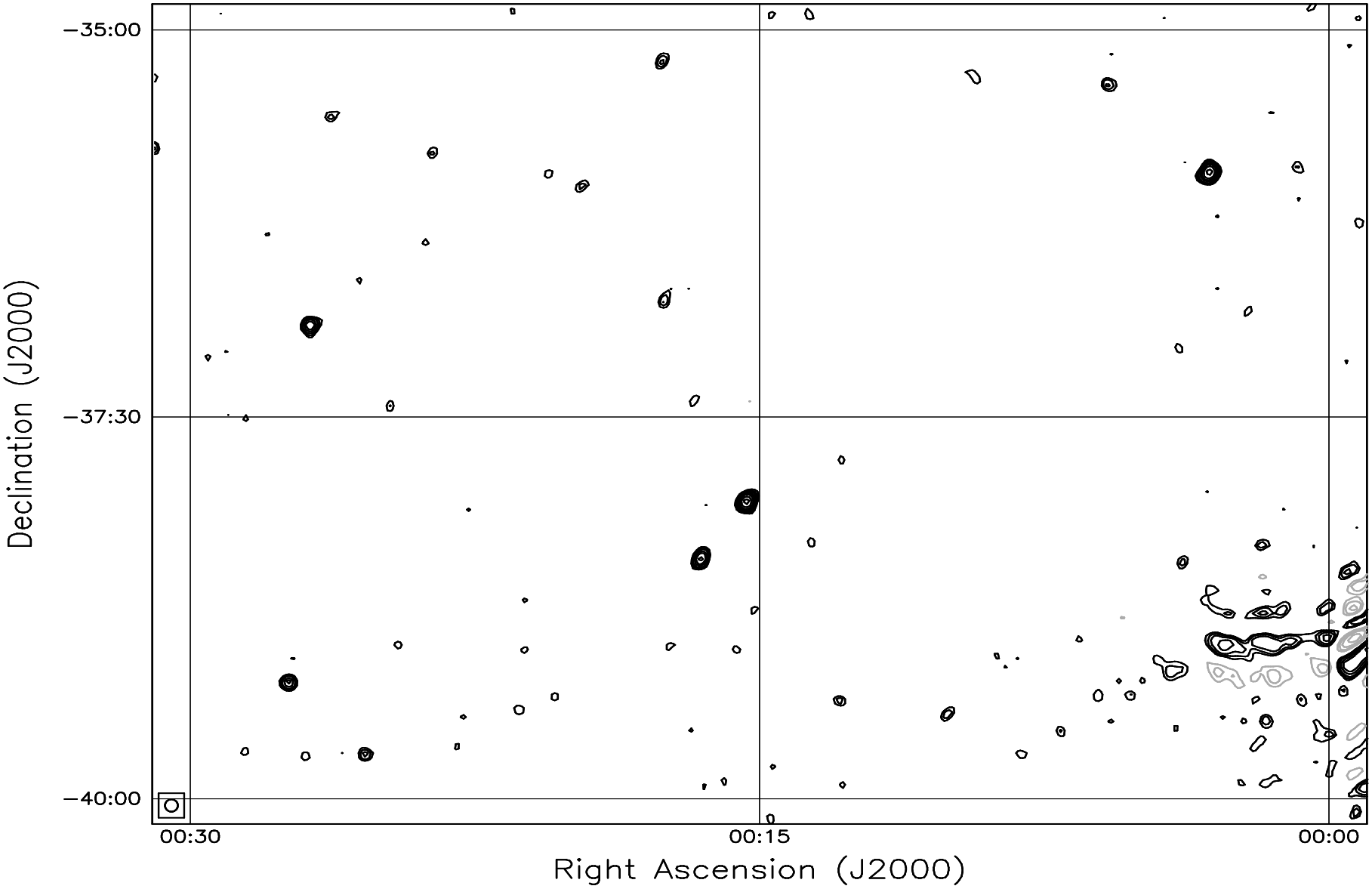

Fig. 7.46: Contour map covering the right ascension range 00h00m to 00h30m and declination range -40° to -35 °. The contour levels are -5, -3.6, -2.5, -1.8, 1, 1.4, 2, 2.8, 3.6, 5, 7, 10, 14, 20, 29, 40, 54, 72, 90, 100, 136, 180, 216, 252, 288 Jy beam^{-1}. The rms noise in the image is ≈300 mJy beam^{-1}.

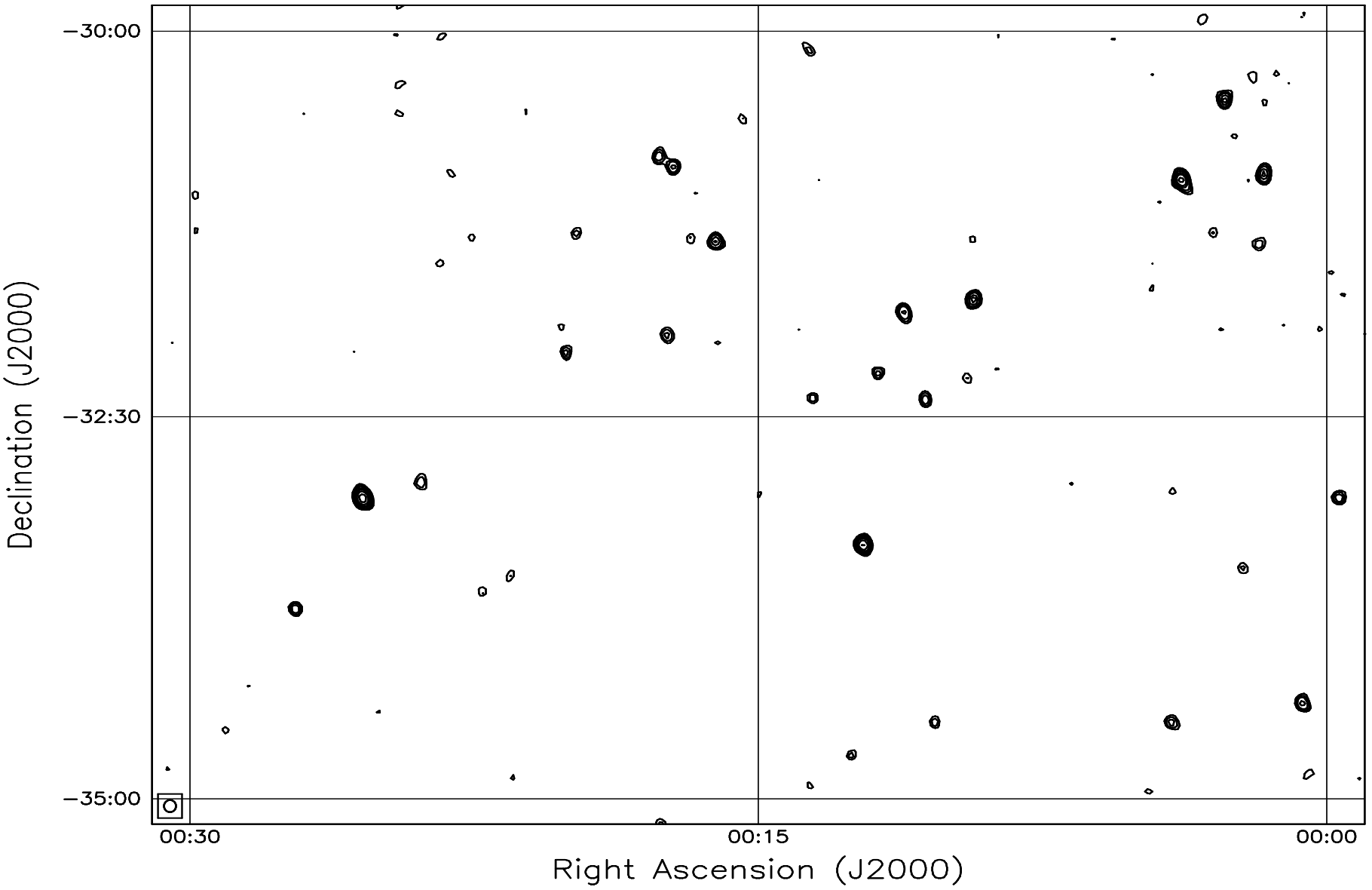

Fig. 7.47: Contour map covering the right ascension range 00h00m to 00h30m and declination range -35° to -30 °. The contour levels are -5, -3.6, -2.5, -1.8, 1, 1.4, 2, 2.8, 3.6, 5, 7, 10, 14, 20, 29, 40, 54, 72, 90, 100, 136, 180, 216, 252, 288 Jy beam^{-1}. The rms noise in the image is ≈310 mJy beam^{-1}.

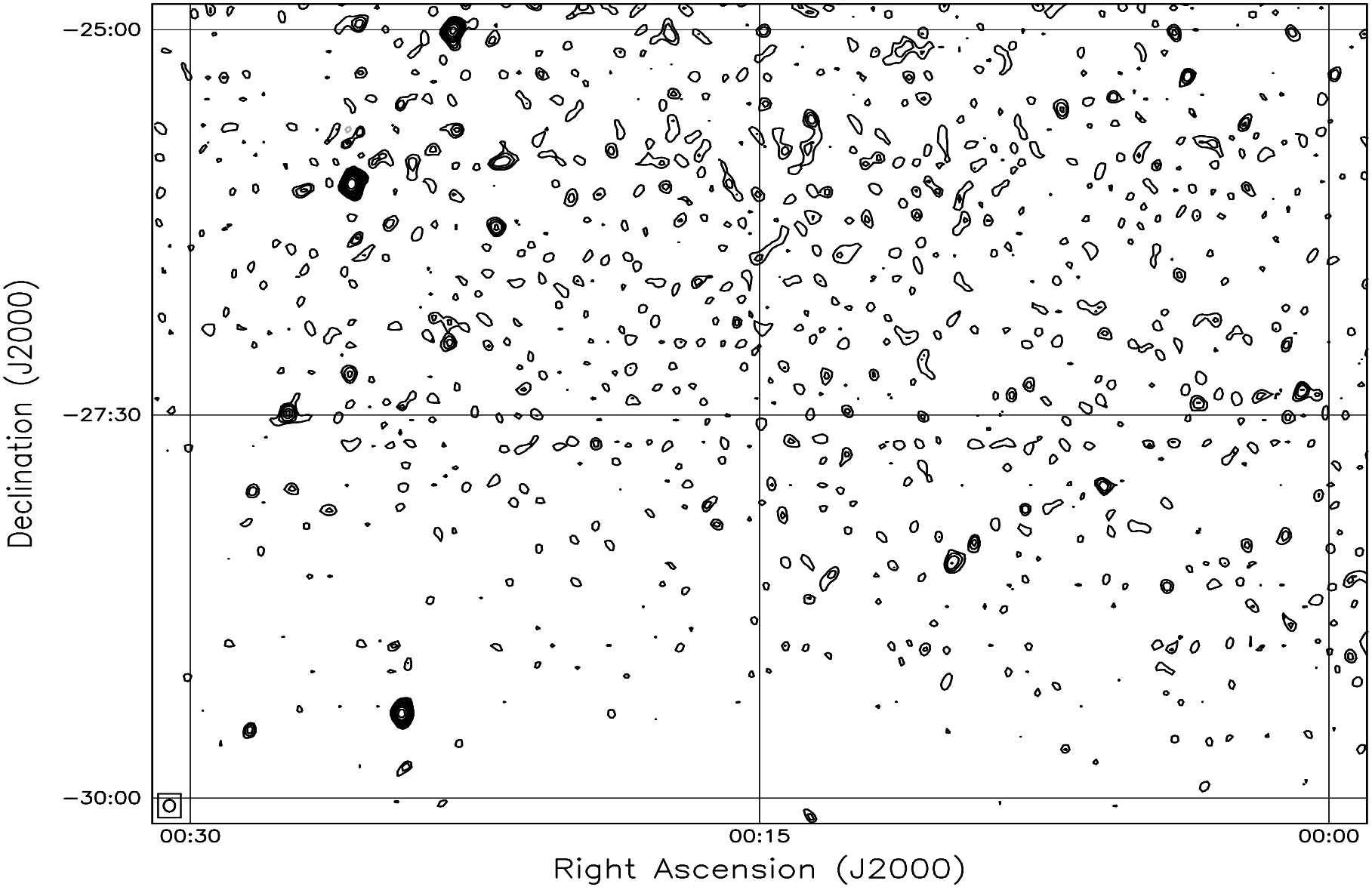

Fig. 7.48: Contour map covering the right ascension range 00h00m to 00h30m and declination range -30° to -25 °. The contour levels are -5, -3.6, -2.5, -1.8, 1, 1.4, 2, 2.8, 3.6, 5, 7, 10, 14, 20, 29, 40, 54, 72, 90, 100, 136, 180, 216, 252, 288 Jy beam^{-1}. The rms noise in the image is ≈330 mJy beam^{-1}.

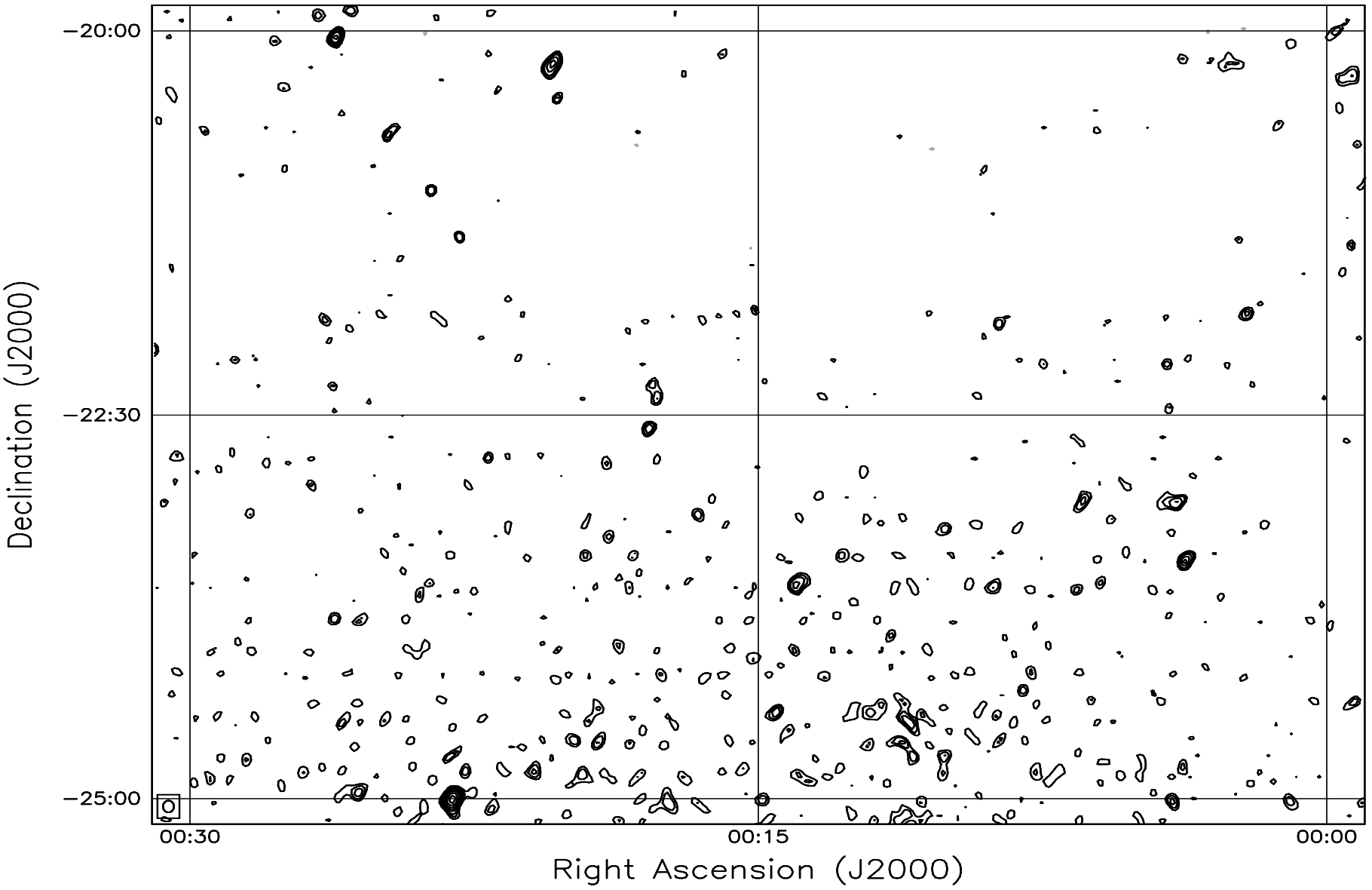

Fig. 7.49: Contour map covering the right ascension range 00h00m to 00h30m and declination range -25° to -20 °. The contour levels are -5, -3.6, -2.5, -1.8, 1, 1.4, 2, 2.8, 3.6, 5, 7, 10, 14, 20, 29, 40, 54, 72, 90, 100, 136, 180, 216, 252, 288 Jy beam^{-1}. The rms noise in the image is ≈365 mJy beam^{-1}.

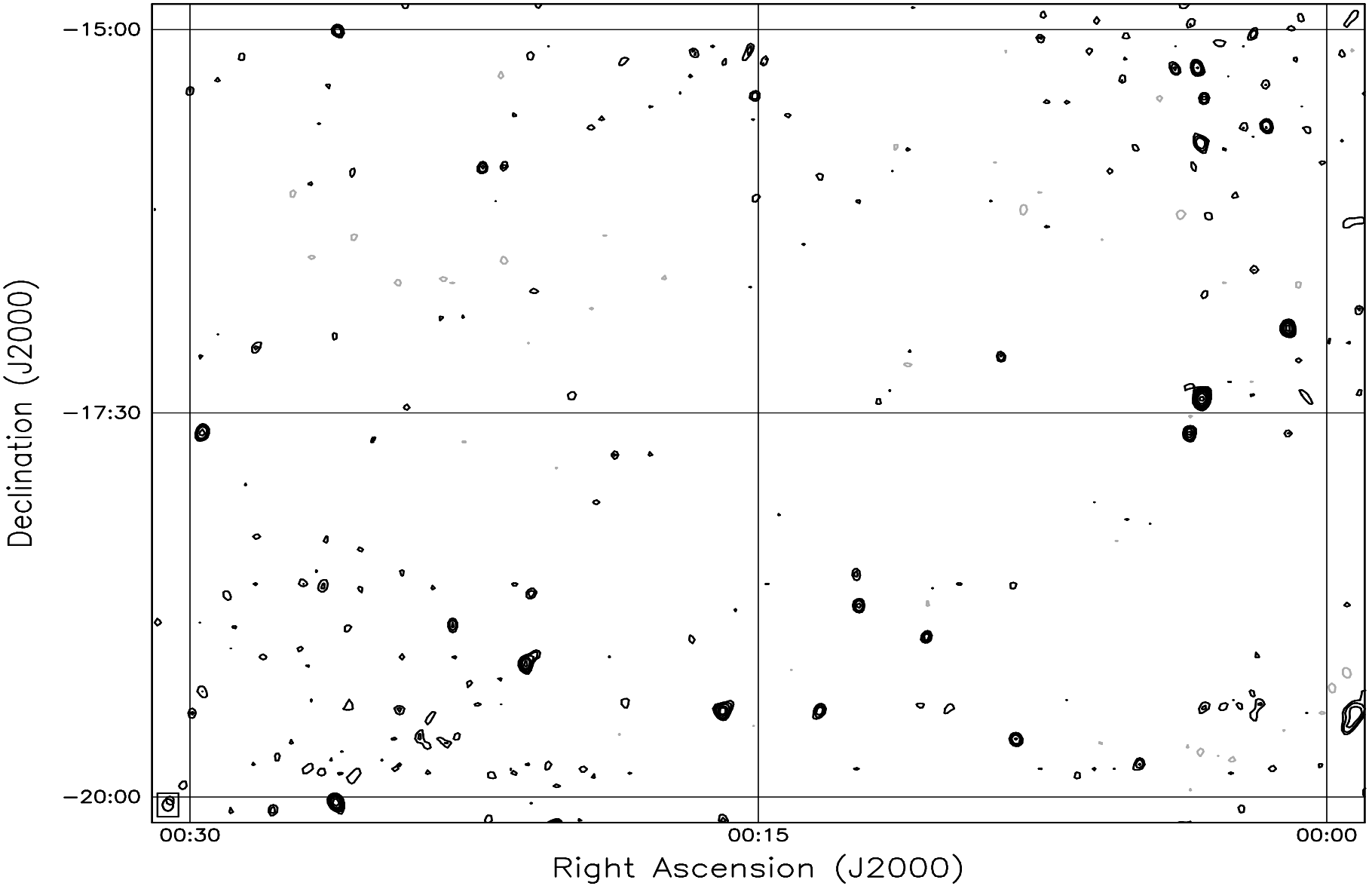

Fig. 7.50: Contour map covering the right ascension range 00h00m to 00h30m and declination range -20° to -15 °. The contour levels are -5, -3.6, -2.5, -1.8, 1, 1.4, 2, 2.8, 3.6, 5, 7, 10, 14, 20, 29, 40, 54, 72, 90, 100, 136, 180, 216, 252, 288 Jy beam^{-1}. The rms noise in the image is ≈420 mJy beam^{-1}.

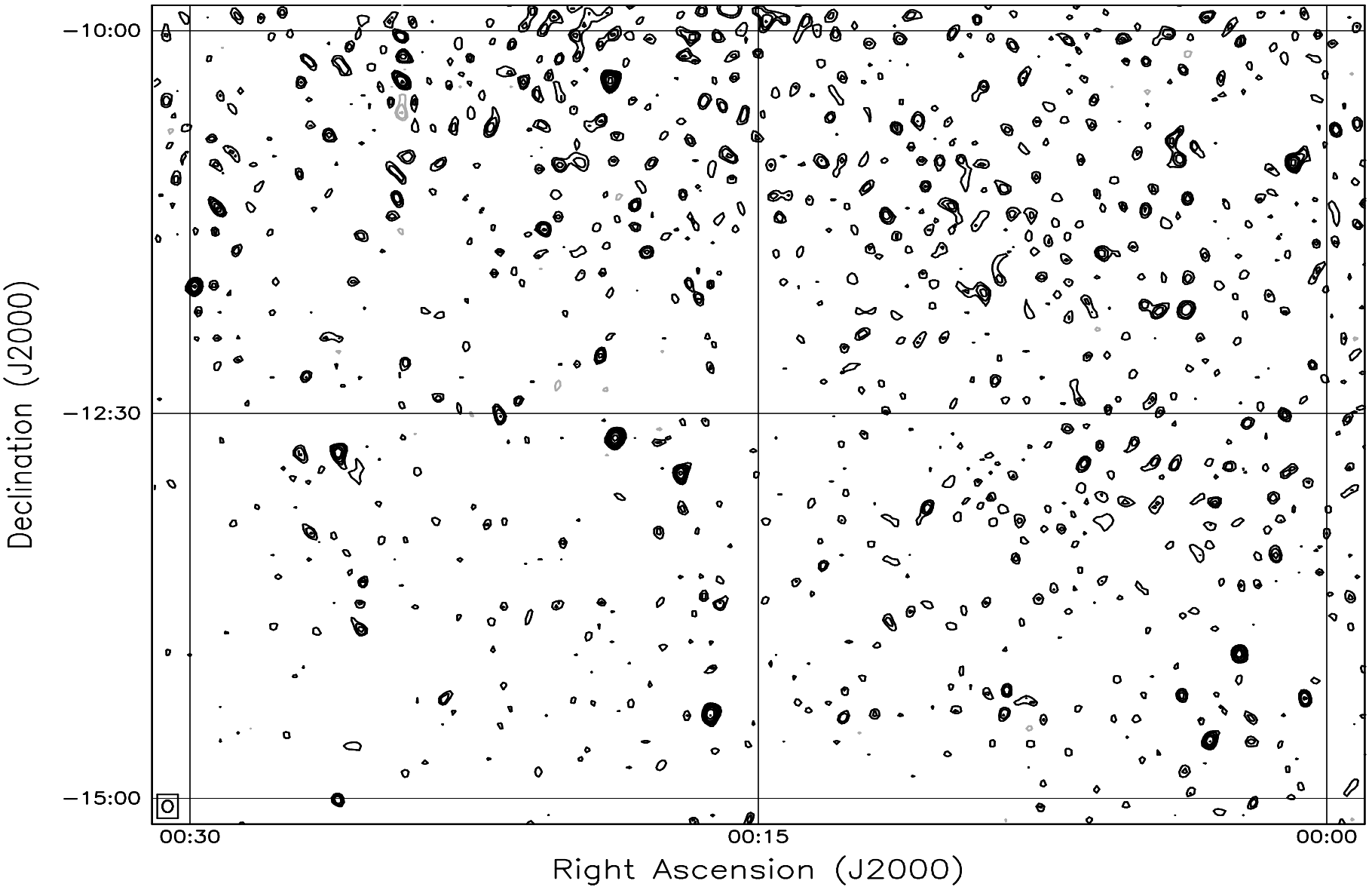

Fig. 7.51: Contour map covering the right ascension range 00h00m to 00h30m and declination range -15° to -10 °. The contour levels are -5, -3.6, -2.5, -1.8, 1, 1.4, 2, 2.8, 3.6, 5, 7, 10, 14, 20, 29, 40, 54, 72, 90, 100, 136, 180, 216, 252, 288 Jy beam^{-1}. The rms noise in the image is ≈510 mJy beam^{-1}.

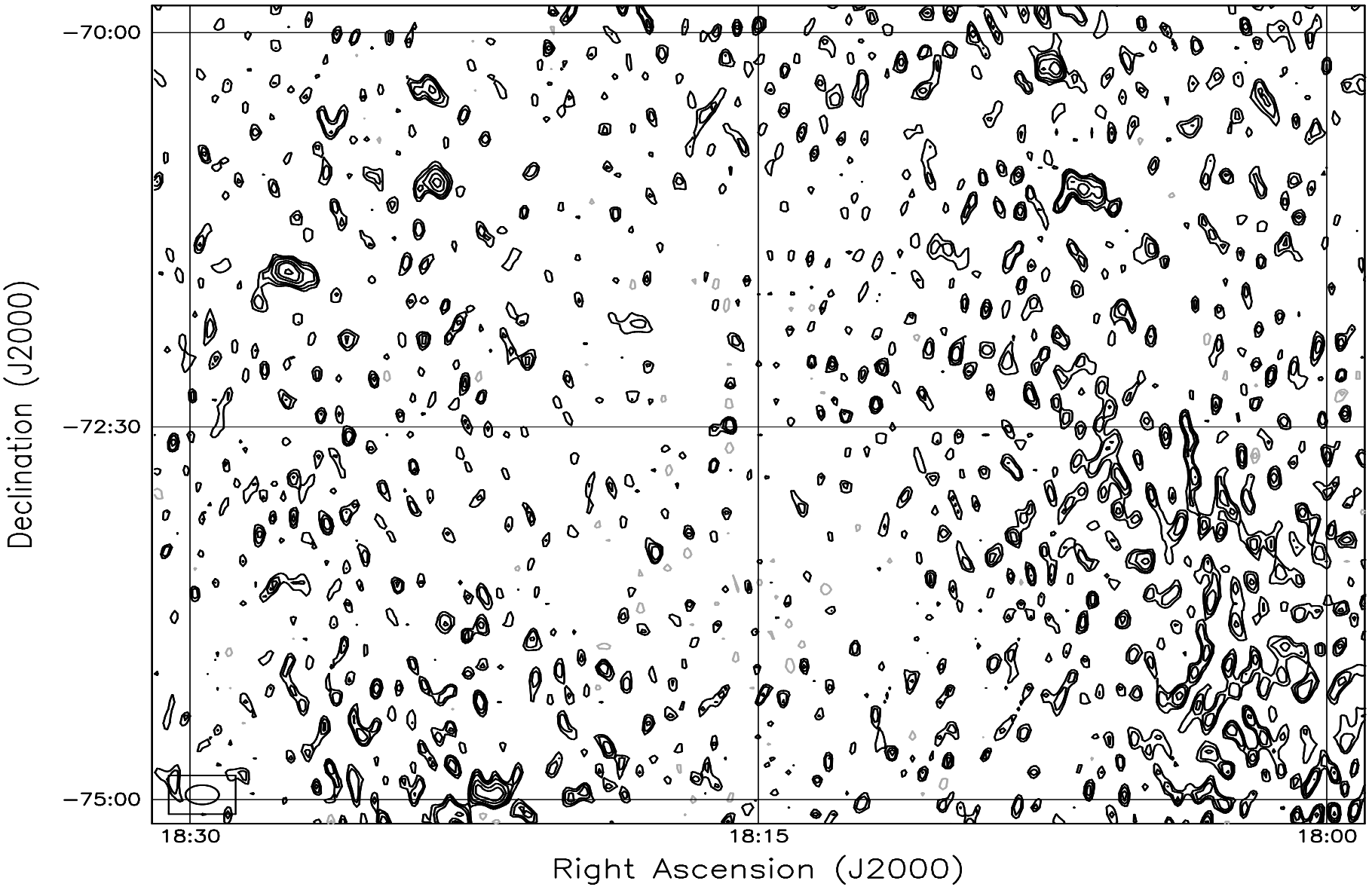

Fig. 7.52: Contour map covering the right ascension range 18h00m to 18h30m and declination range -75° to -70 °. The contour levels are -5, -3.6, -2.5, -1.8, 1, 1.4, 2, 2.8, 3.6, 5, 7, 10, 14, 20, 29, 40, 54, 72, 90, 100, 136, 180, 216, 252, 288 Jy beam^{-1}. The rms noise in the image is ≈570 mJy beam^{-1}.

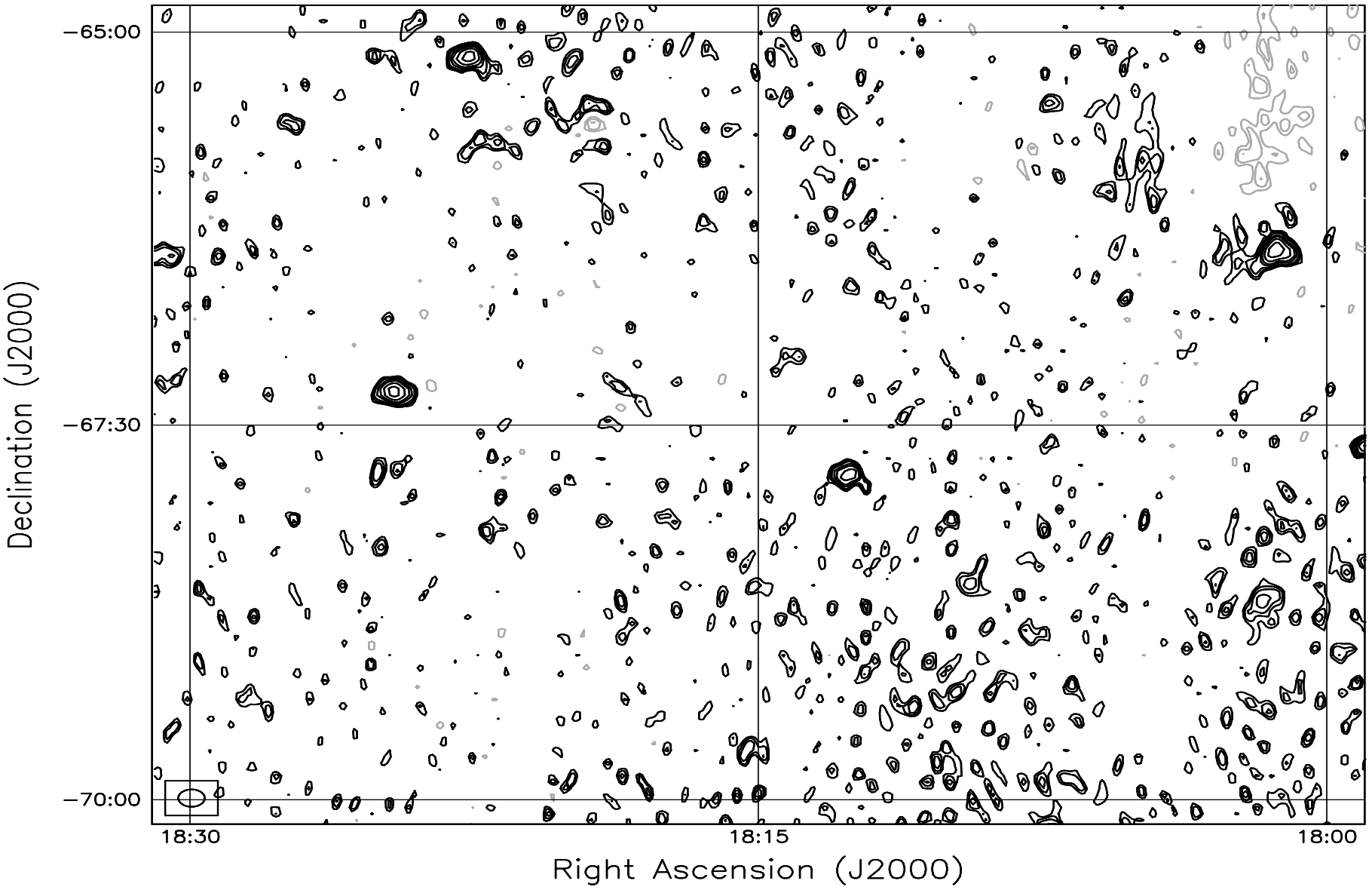

Fig. 7.53: Contour map covering the right ascension range 18h00m to 18h30m and declination range -70° to -65 °. The contour levels are -5, -3.6, -2.5, -1.8, 1, 1.4, 2, 2.8, 3.6, 5, 7, 10, 14, 20, 29, 40, 54, 72, 90, 100, 136, 180, 216, 252, 288 Jy beam^{-1}. The rms noise in the image is ≈500 mJy beam^{-1}.

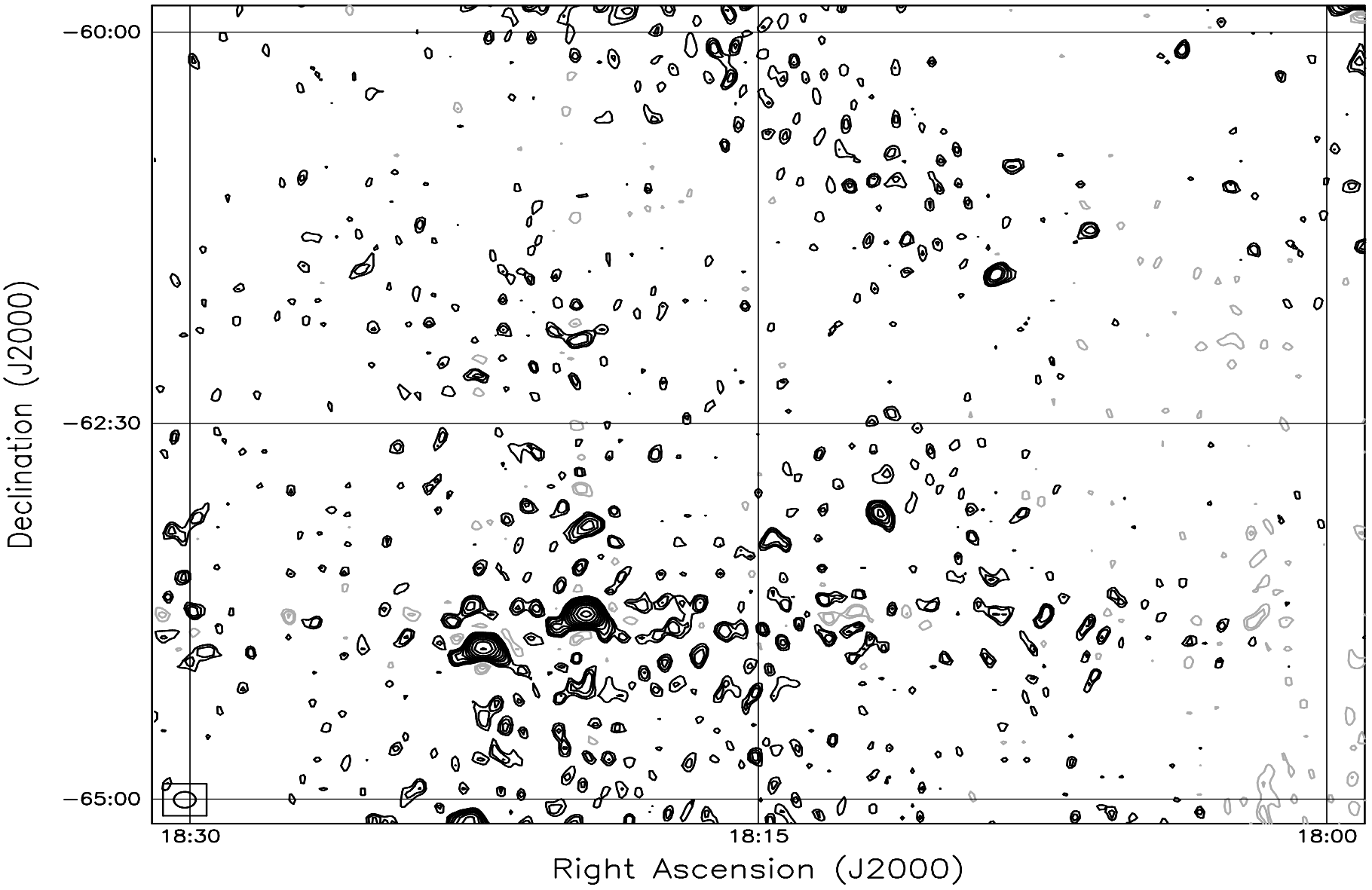

Fig. 7.54: Contour map covering the right ascension range 18h00m to 18h30m and declination range -65° to -60 °. The contour levels are -5, -3.6, -2.5, -1.8, 1, 1.4, 2, 2.8, 3.6, 5, 7, 10, 14, 20, 29, 40, 54, 72, 90, 100, 136, 180, 216, 252, 288 Jy beam^{-1}. The rms noise in the image is ≈450 mJy beam^{-1}.

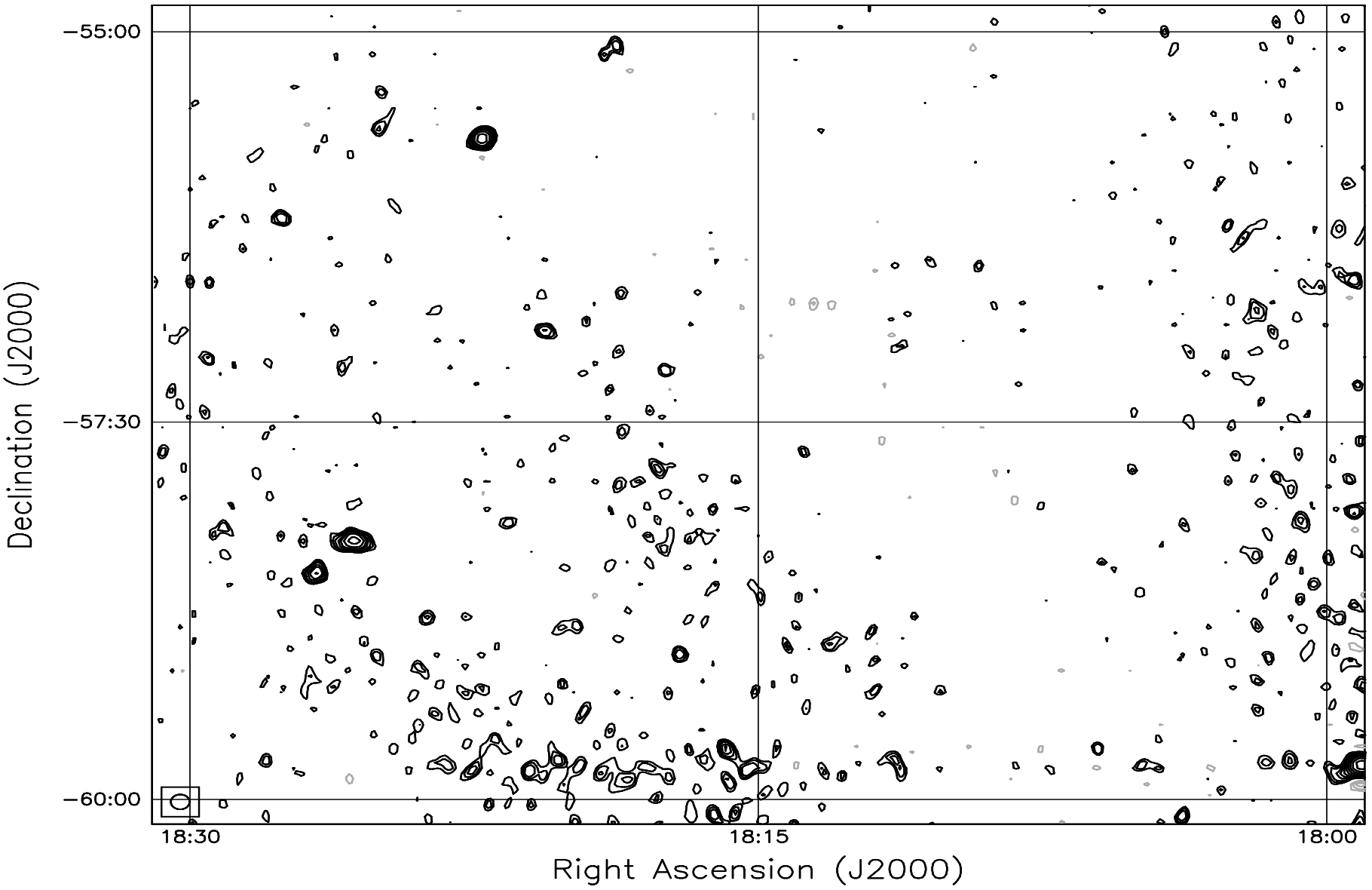

Fig. 7.55: Contour map covering the right ascension range 18h00m to 18h30m and declination range -60° to -55 °. The contour levels are -5, -3.6, -2.5, -1.8, 1, 1.4, 2, 2.8, 3.6, 5, 7, 10, 14, 20, 29, 40, 54, 72, 90, 100, 136, 180, 216, 252, 288 Jy beam^{-1}. The rms noise in the image is ≈420 mJy beam^{-1}.

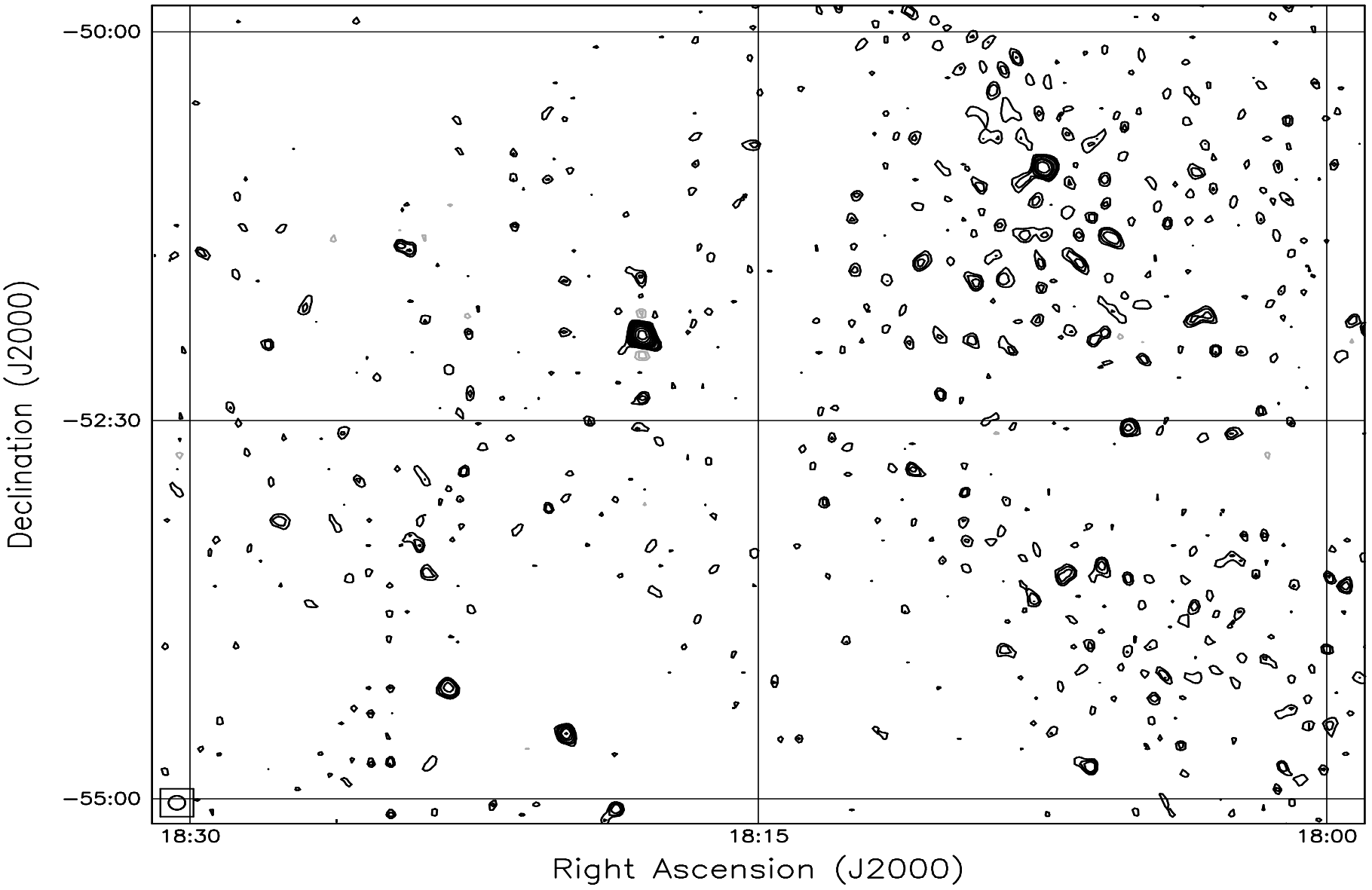

Fig. 7.56: Contour map covering the right ascension range 18h00m to 18h30m and declination range -55° to -50 °. The contour levels are -5, -3.6, -2.5, -1.8, 1, 1.4, 2, 2.8, 3.6, 5, 7, 10, 14, 20, 29, 40, 54, 72, 90, 100, 136, 180, 216, 252, 288 Jy beam^{-1}. The rms noise in the image is ≈400 mJy beam^{-1}.

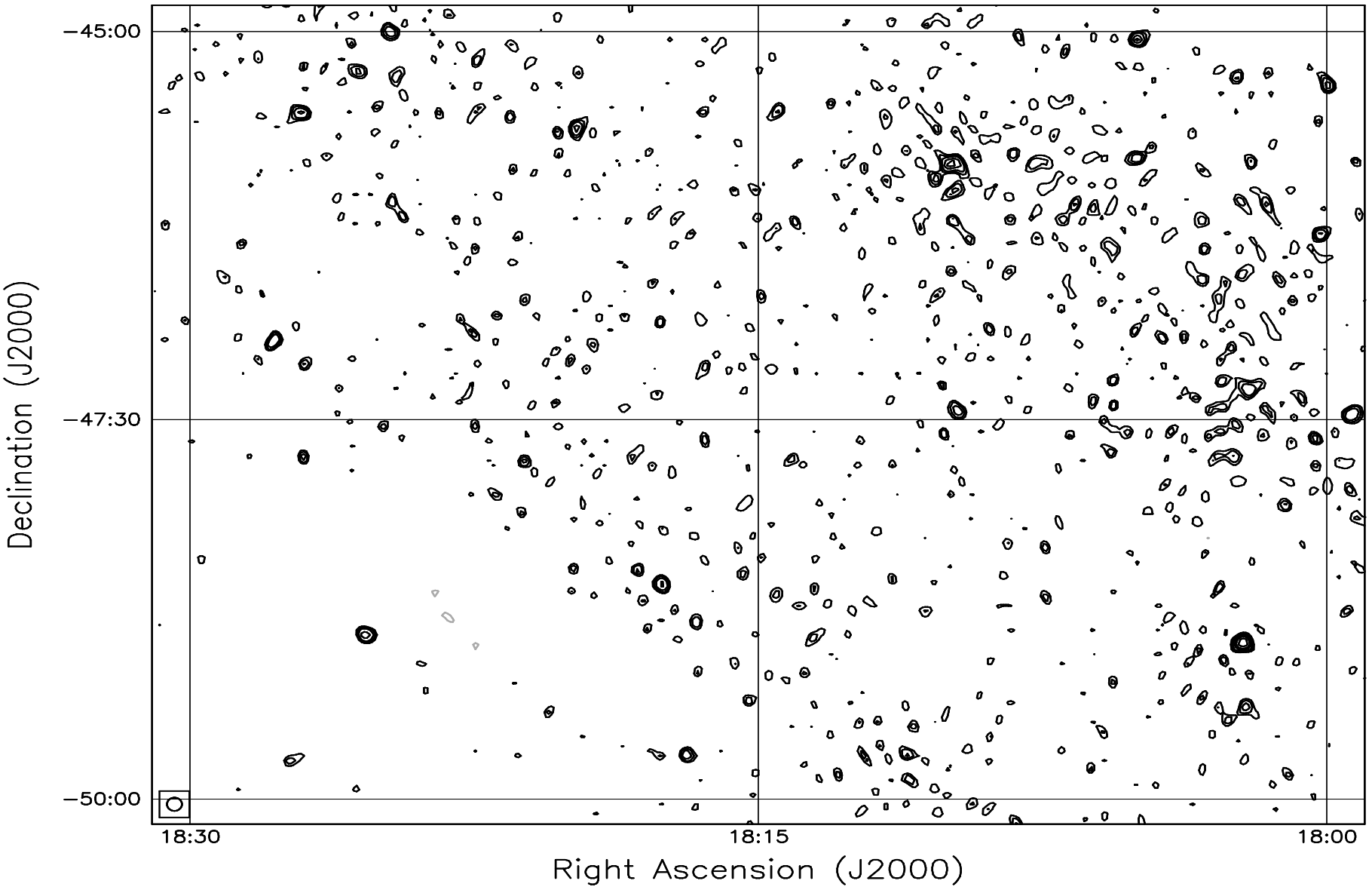

Fig. 7.57: Contour map covering the right ascension range 18h00m to 18h30m and declination range -50° to -45 °. The contour levels are -5, -3.6, -2.5, -1.8, 1, 1.4, 2, 2.8, 3.6, 5, 7, 10, 14, 20, 29, 40, 54, 72, 90, 100, 136, 180, 216, 252, 288 Jy beam^{-1}. The rms noise in the image is ≈390 mJy beam^{-1}.

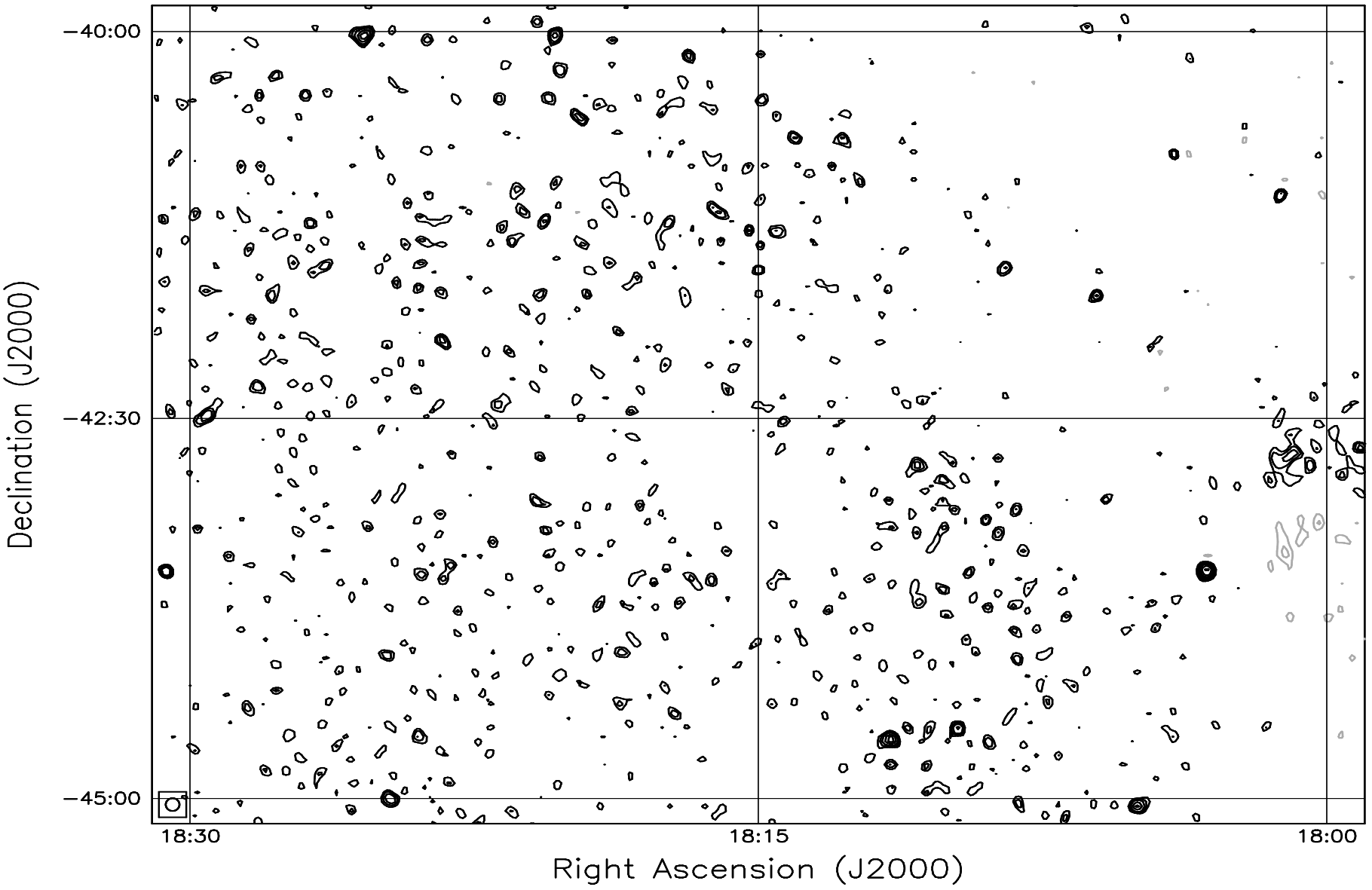

Fig. 7.58: Contour map covering the right ascension range 18h00m to 18h30m and declination range -45° to -40 °. The contour levels are -5, -3.6, -2.5, -1.8, 1, 1.4, 2, 2.8, 3.6, 5, 7, 10, 14, 20, 29, 40, 54, 72, 90, 100, 136, 180, 216, 252, 288 Jy beam^{-1}. The rms noise in the image is ≈390 mJy beam^{-1}.

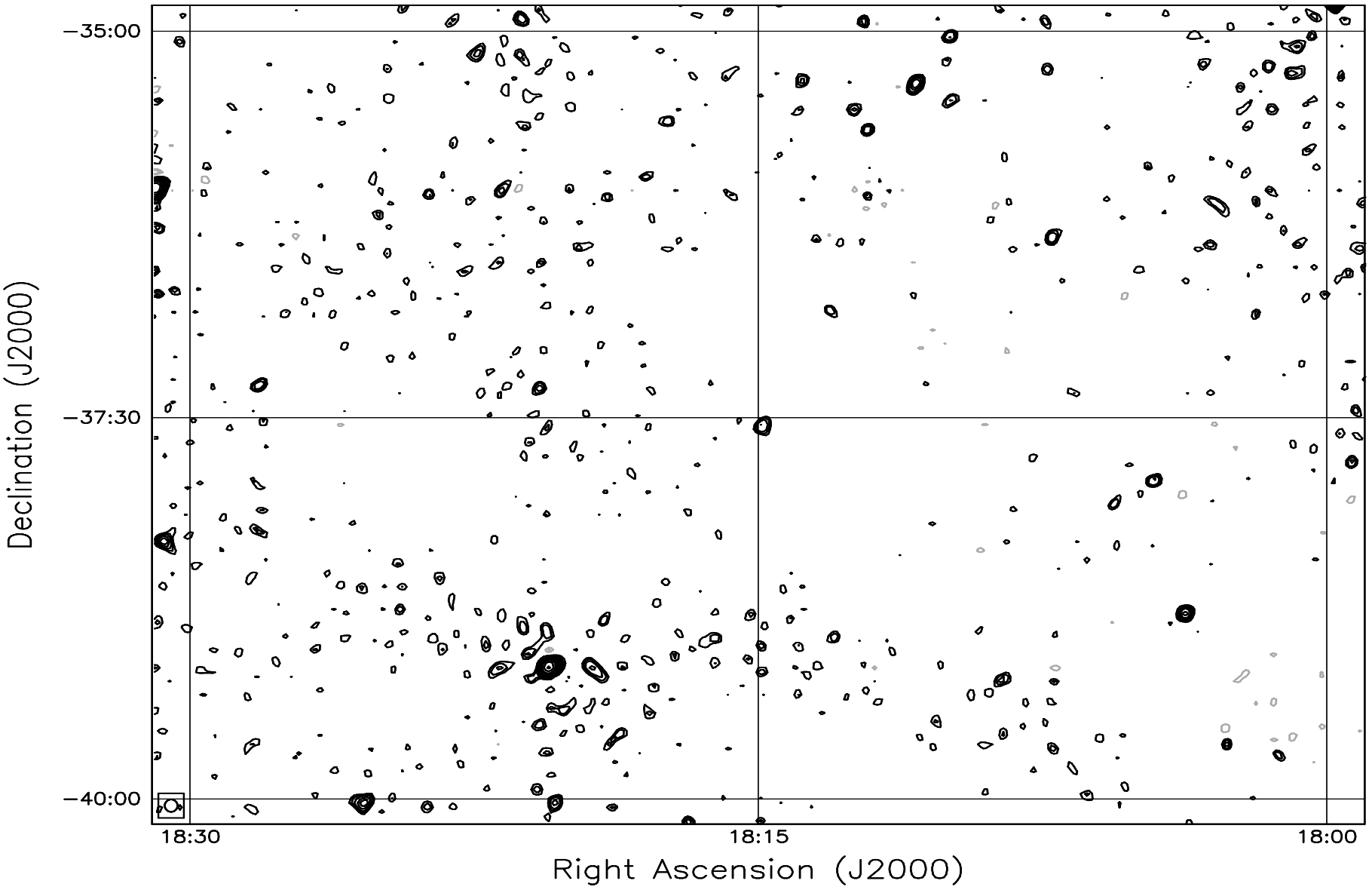

Fig. 7.59: Contour map covering the right ascension range 18h00m to 18h30m and declination range -40° to -35 °. The contour levels are -5, -3.6, -2.5, -1.8, 1, 1.4, 2, 2.8, 3.6, 5, 7, 10, 14, 20, 29, 40, 54, 72, 90, 100, 136, 180, 216, 252, 288 Jy beam^{-1}. The rms noise in the image is ≈400 mJy beam^{-1}.

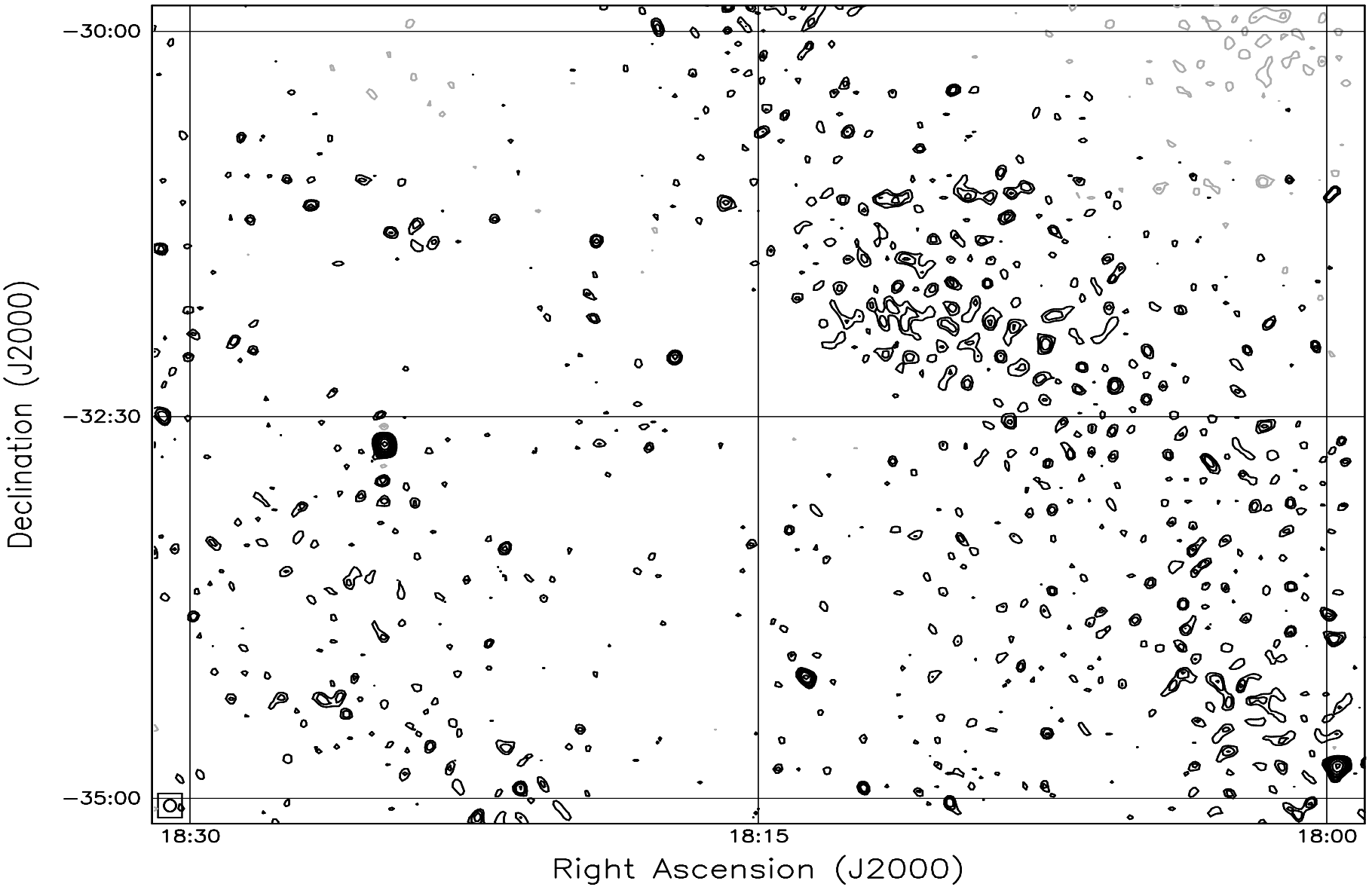

Fig. 7.60: Contour map covering the right ascension range 18h00m to 18h30m and declination range -35° to -30 °. The contour levels are -5, -3.6, -2.5, -1.8, 1, 1.4, 2, 2.8, 3.6, 5, 7, 10, 14, 20, 29, 40, 54, 72, 90, 100, 136, 180, 216, 252, 288 Jy beam^{-1}. The rms noise in the image is ≈420 mJy beam^{-1}.

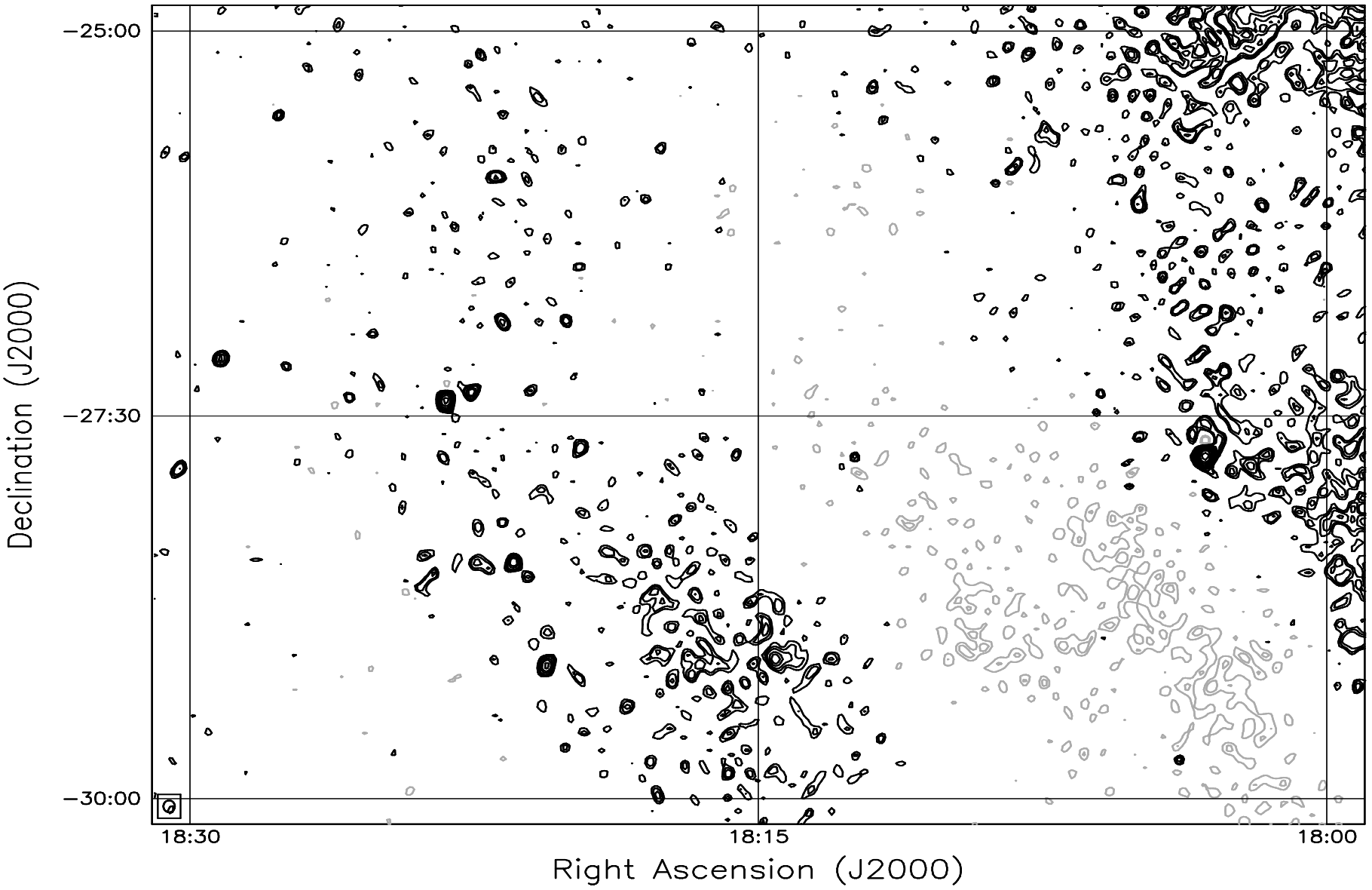

Fig. 7.61: Contour map covering the right ascension range 18h00m to 18h30m and declination range -30° to -25 °. The contour levels are -5, -3.6, -2.5, -1.8, 1, 1.4, 2, 2.8, 3.6, 5, 7, 10, 14, 20, 29, 40, 54, 72, 90, 100, 136, 180, 216, 252, 288 Jy beam^{-1}. The rms noise in the image is ≈445 mJy beam^{-1}.

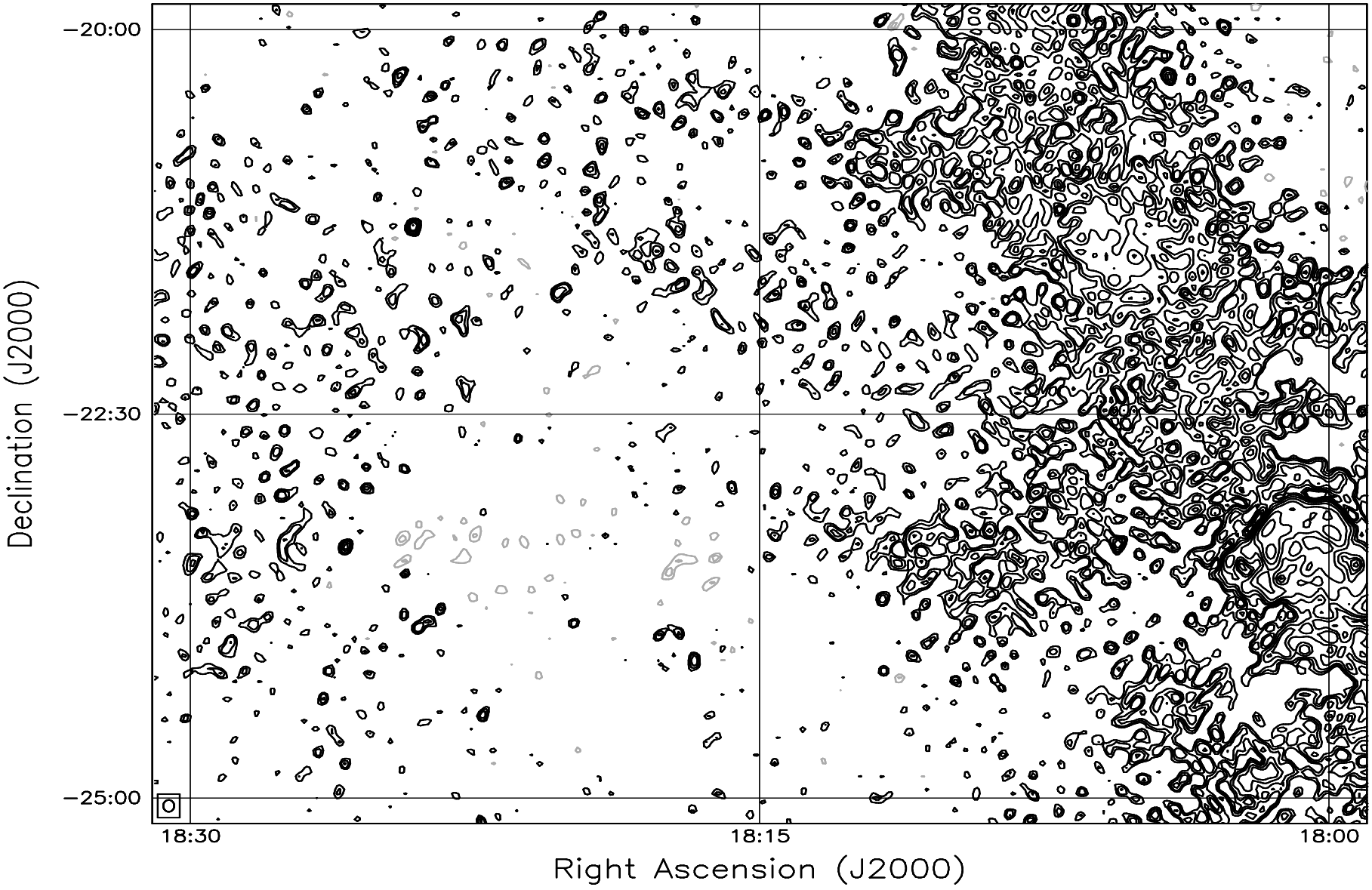

Fig. 7.62: Contour map covering the right ascension range 18h00m to 18h30m and declination range -25° to -20 °. The contour levels are -5, -3.6, -2.5, -1.8, 1, 1.4, 2, 2.8, 3.6, 5, 7, 10, 14, 20, 29, 40, 54, 72, 90, 100, 136, 180, 216, 252, 288 Jy beam^{-1}. The rms noise in the image is ≈490 mJy beam^{-1}.

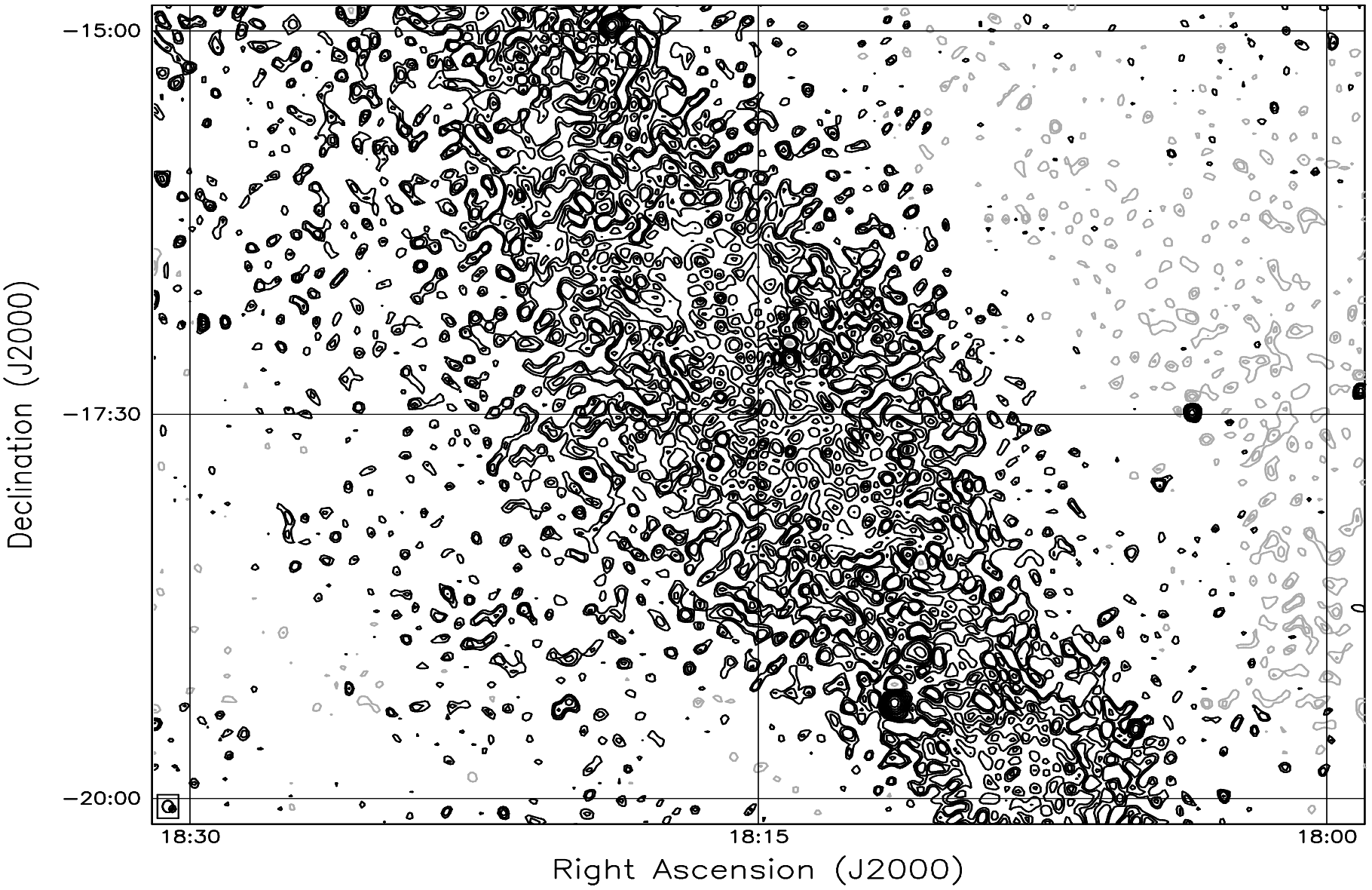

Fig. 7.63: Contour map covering the right ascension range 18h00m to 18h30m and declination range -20° to -15 °. The contour levels are -5, -3.6, -2.5, -1.8, 1, 1.4, 2, 2.8, 3.6, 5, 7, 10, 14, 20, 29, 40, 54, 72, 90, 100, 136, 180, 216, 252, 288 Jy beam^{-1}. The rms noise in the image is ≈560 mJy beam^{-1}.

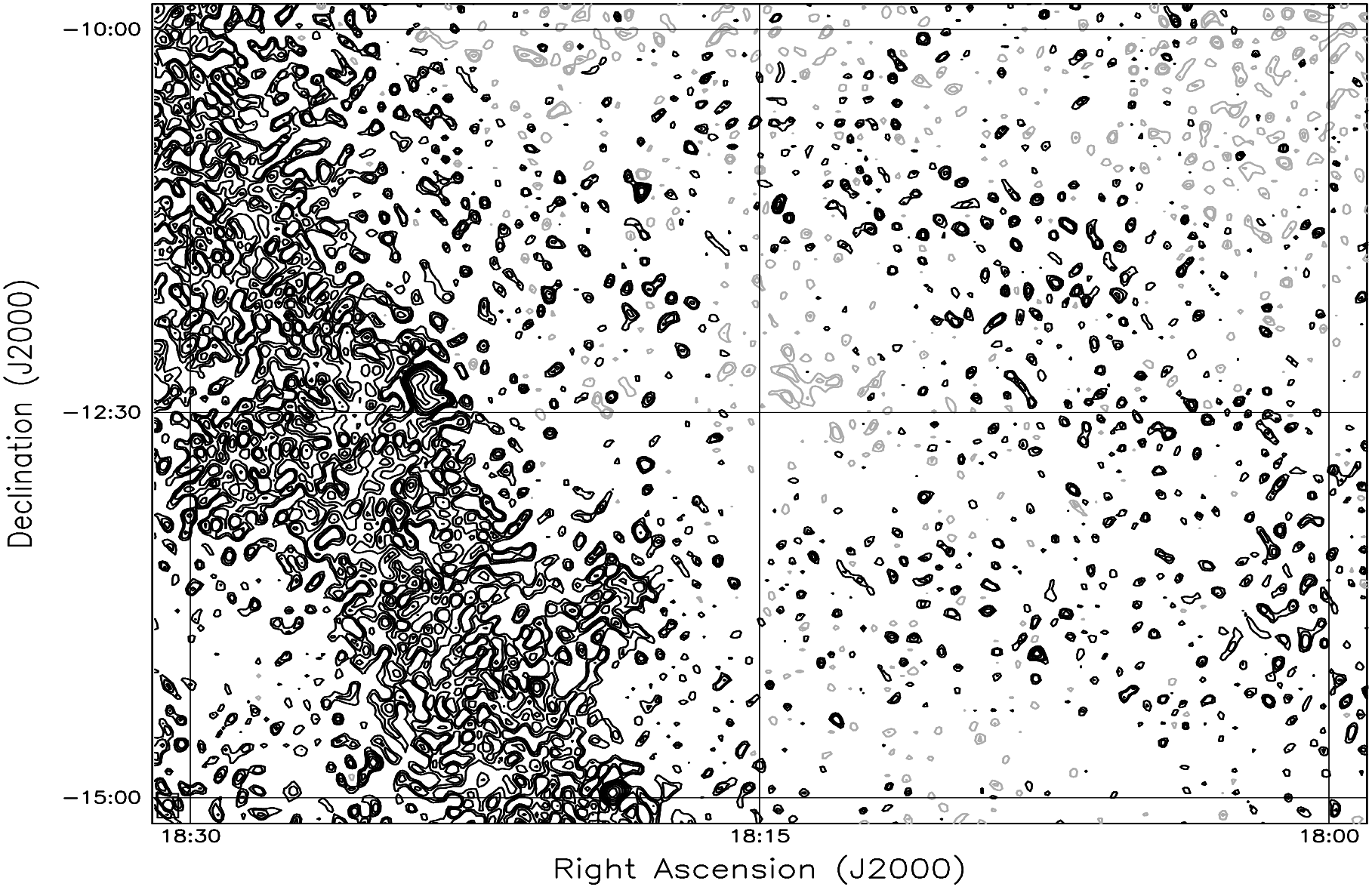

Fig. 7.64: Contour map covering the right ascension range 18h00m to 18h30m and declination range -15° to -10 °. The contour levels are -5, -3.6, -2.5, -1.8, 1, 1.4, 2, 2.8, 3.6, 5, 7, 10, 14, 20, 29, 40, 54, 72, 90, 100, 136, 180, 216, 252, 288 Jy beam^{-1}. The rms noise in the image is ≈680 mJy beam^{-1}.

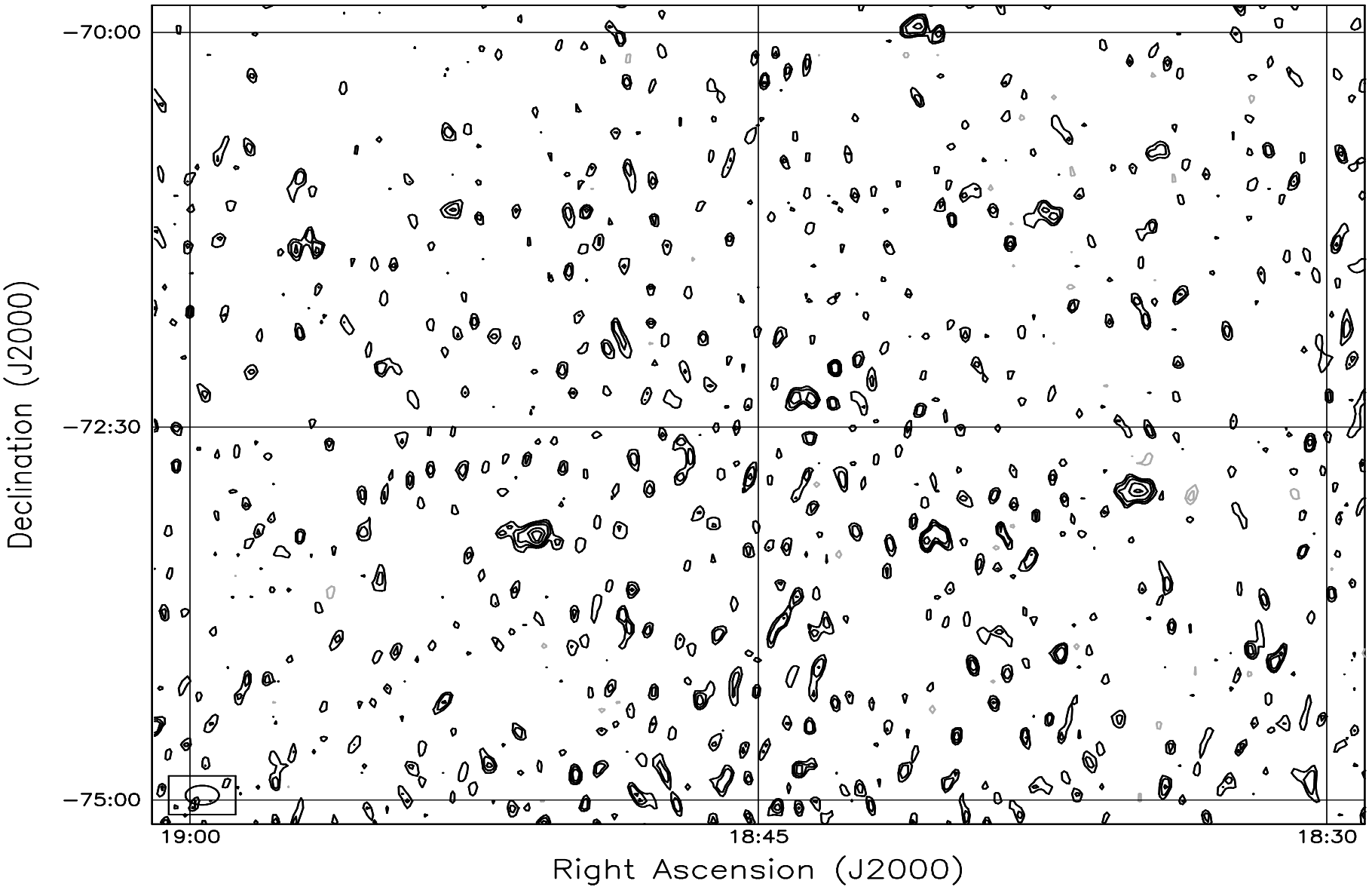

Fig. 7.65: Contour map covering the right ascension range 18h30m to 19h00m and declination range -75° to -70 °. The contour levels are -5, -3.6, -2.5, -1.8, 1, 1.4, 2, 2.8, 3.6, 5, 7, 10, 14, 20, 29, 40, 54, 72, 90, 100, 136, 180, 216, 252, 288 Jy beam^{-1}. The rms noise in the image is ≈570 mJy beam^{-1}.

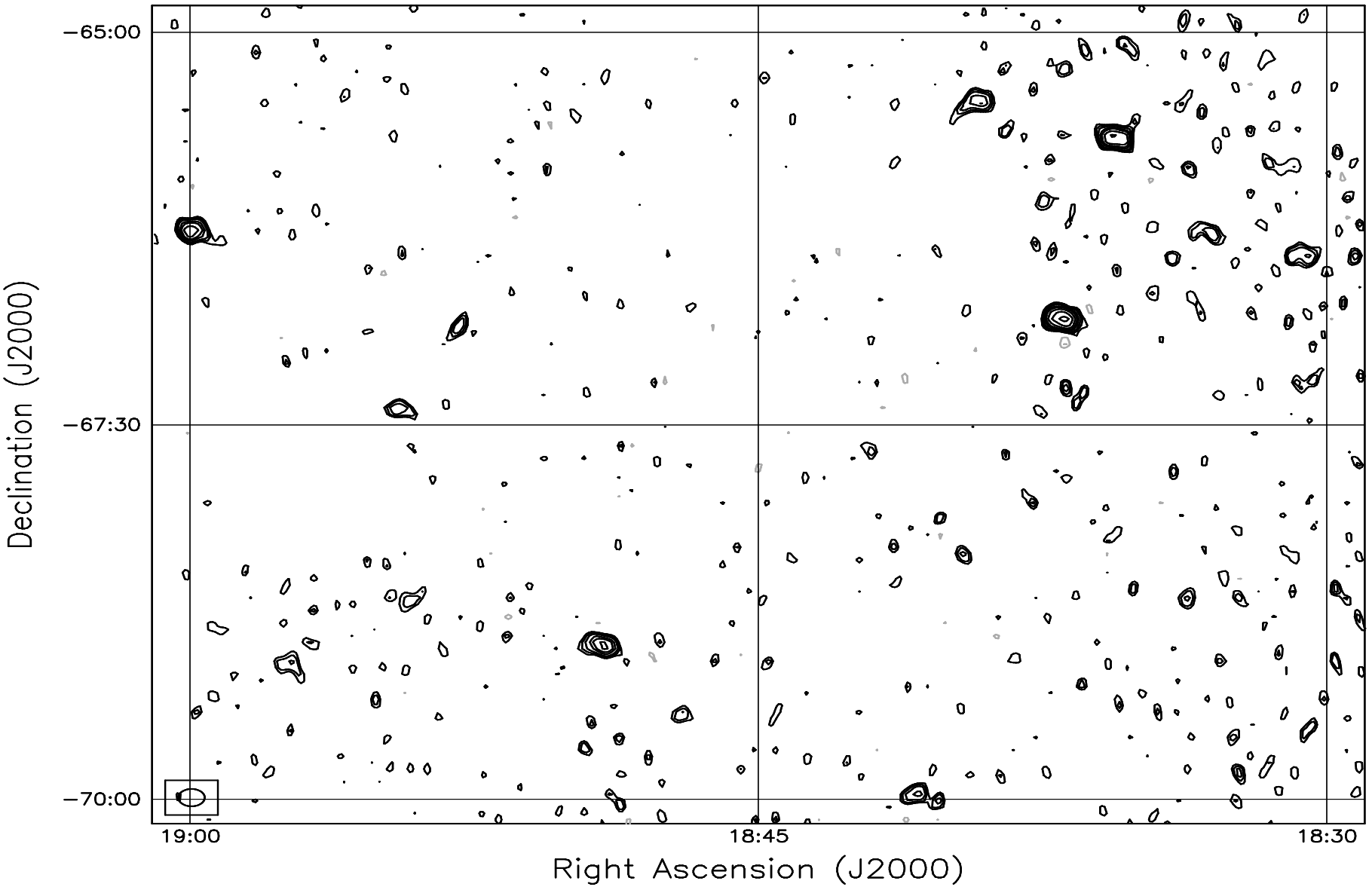

Fig. 7.66: Contour map covering the right ascension range 18h30m to 19h00m and declination range -70° to -65 °. The contour levels are -5, -3.6, -2.5, -1.8, 1, 1.4, 2, 2.8, 3.6, 5, 7, 10, 14, 20, 29, 40, 54, 72, 90, 100, 136, 180, 216, 252, 288 Jy beam^{-1}. The rms noise in the image is ≈500 mJy beam^{-1}.

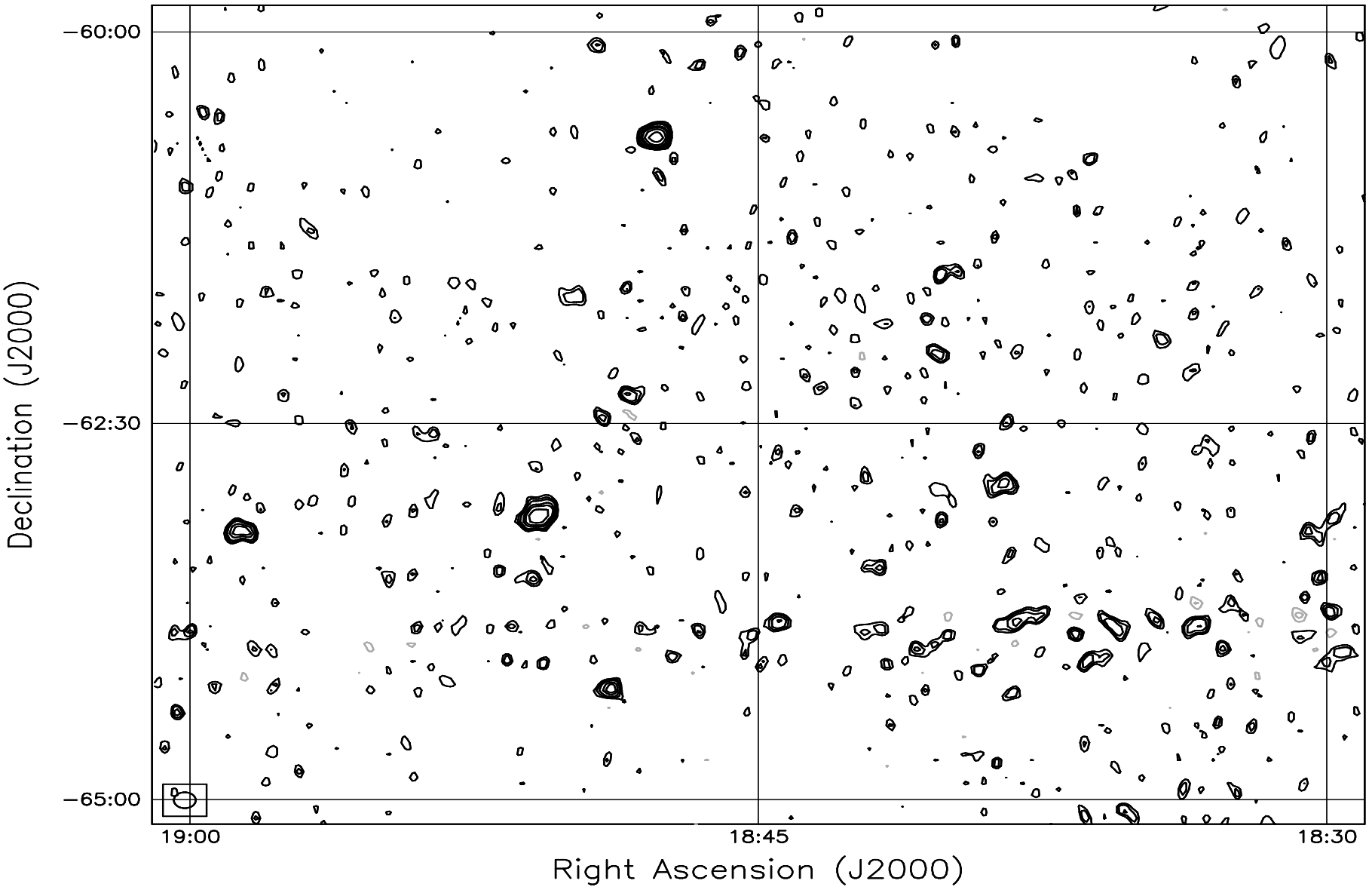

Fig. 7.67: Contour map covering the right ascension range 18h30m to 19h00m and declination range -65° to -60 °. The contour levels are -5, -3.6, -2.5, -1.8, 1, 1.4, 2, 2.8, 3.6, 5, 7, 10, 14, 20, 29, 40, 54, 72, 90, 100, 136, 180, 216, 252, 288 Jy beam^{-1}. The rms noise in the image is ≈450 mJy beam^{-1}.

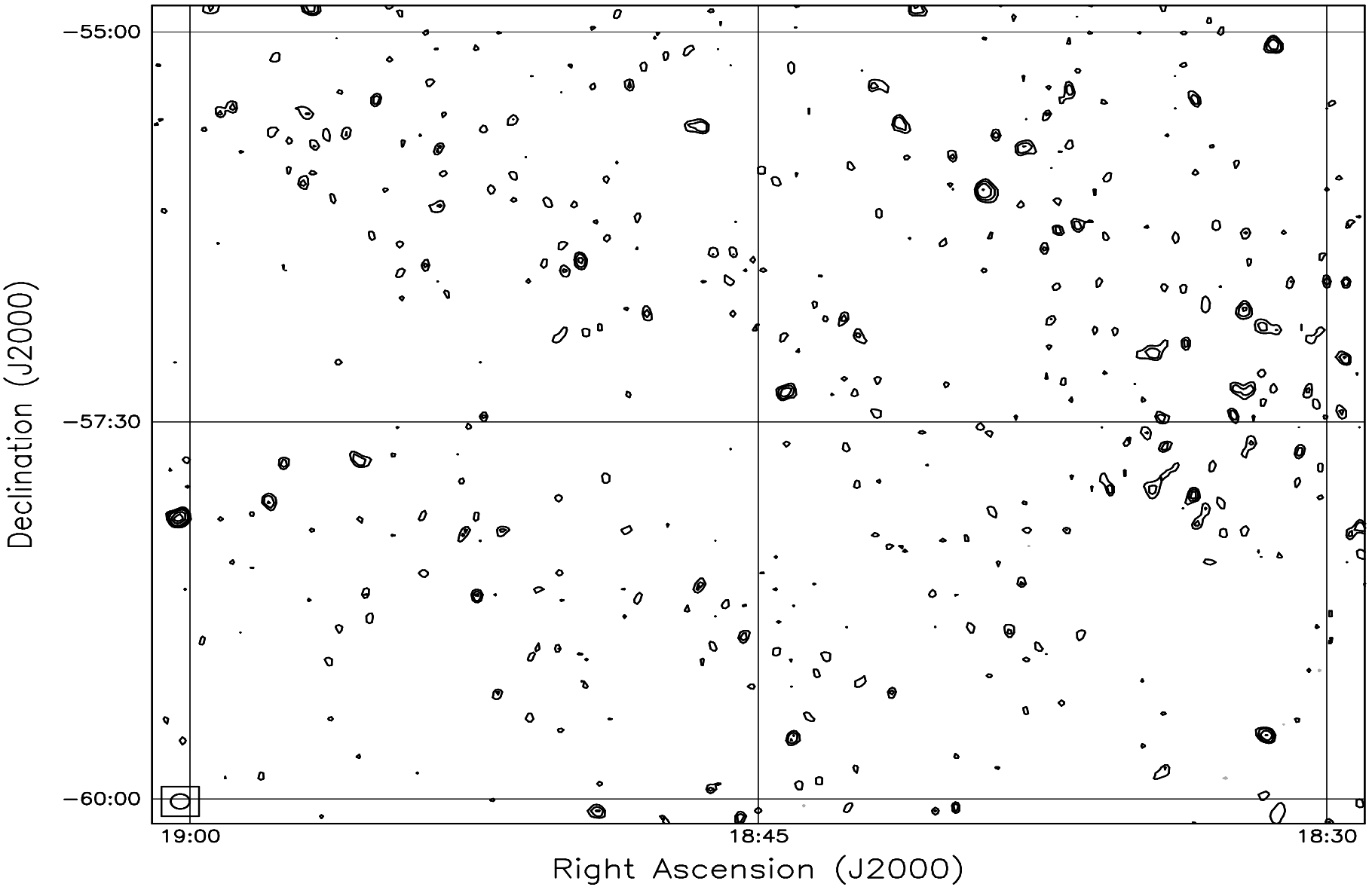

Fig. 7.68: Contour map covering the right ascension range 18h30m to 19h00m and declination range -60° to -55 °. The contour levels are -5, -3.6, -2.5, -1.8, 1, 1.4, 2, 2.8, 3.6, 5, 7, 10, 14, 20, 29, 40, 54, 72, 90, 100, 136, 180, 216, 252, 288 Jy beam^{-1}. The rms noise in the image is ≈420 mJy beam^{-1}.

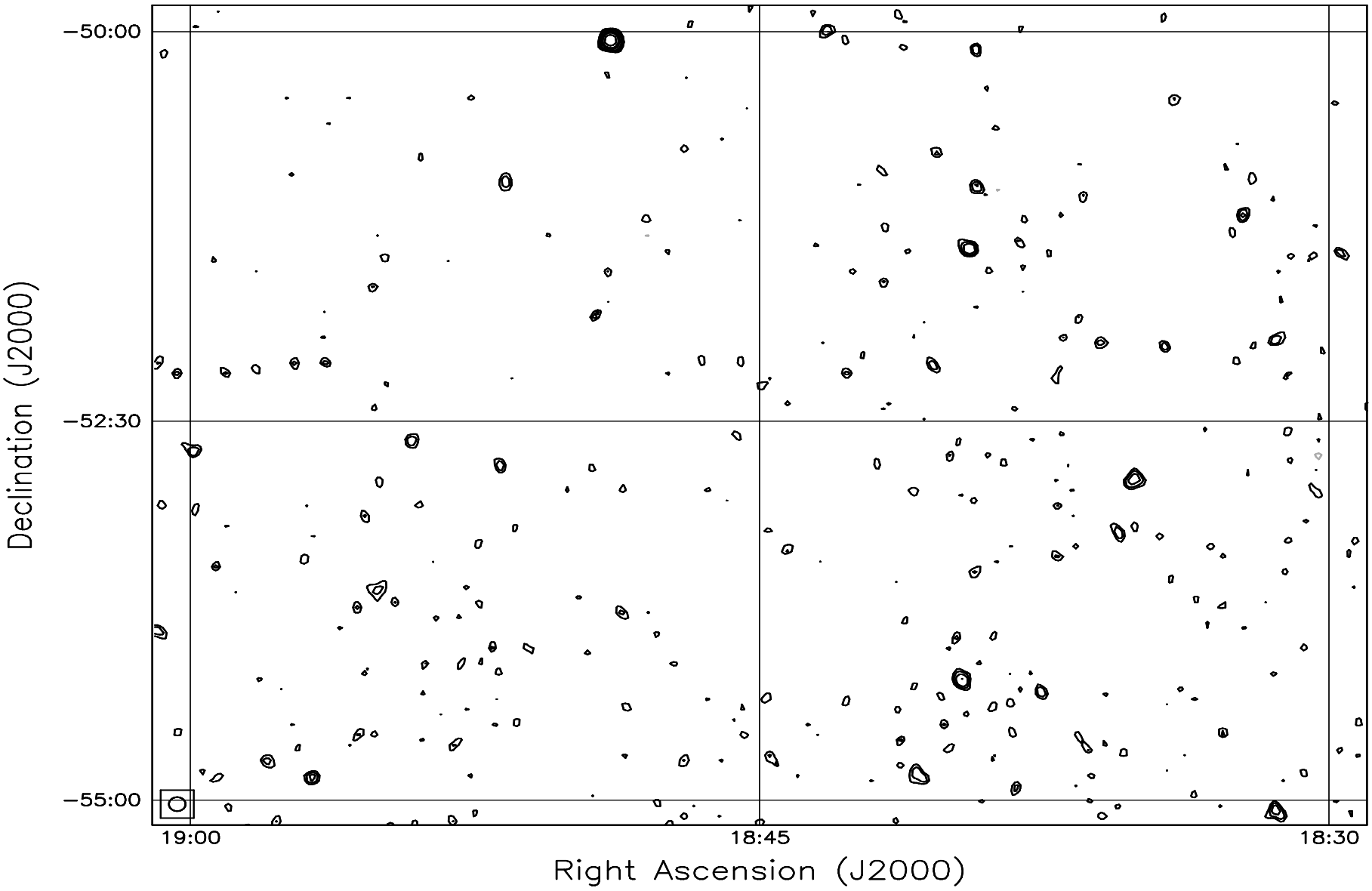

Fig. 7.69: Contour map covering the right ascension range 18h30m to 19h00m and declination range -55° to -50 °. The contour levels are -5, -3.6, -2.5, -1.8, 1, 1.4, 2, 2.8, 3.6, 5, 7, 10, 14, 20, 29, 40, 54, 72, 90, 100, 136, 180, 216, 252, 288 Jy beam^{-1}. The rms noise in the image is ≈400 mJy beam^{-1}.

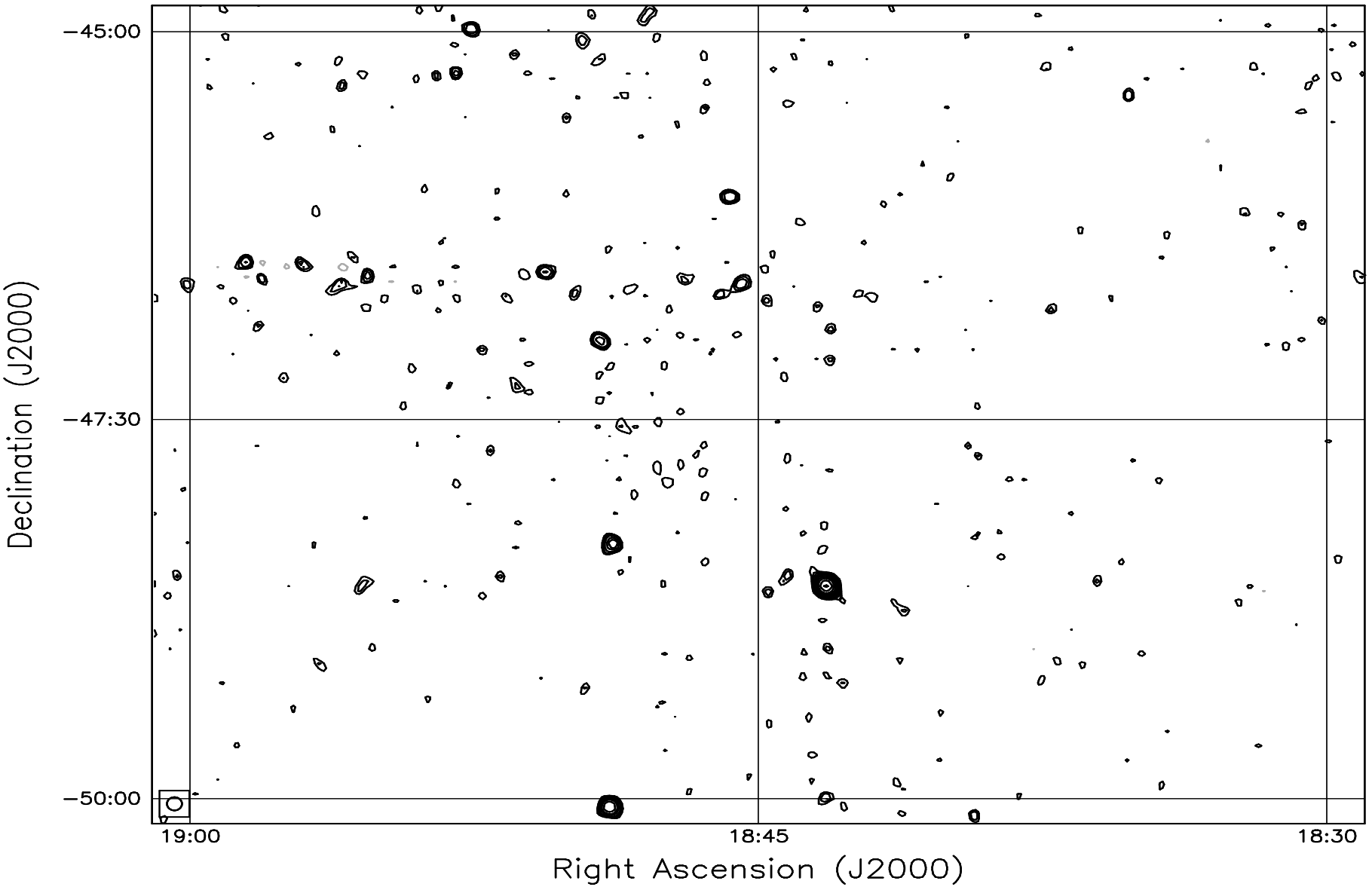

Fig. 7.70: Contour map covering the right ascension range 18h30m to 19h00m and declination range -50° to -45 °. The contour levels are -5, -3.6, -2.5, -1.8, 1, 1.4, 2, 2.8, 3.6, 5, 7, 10, 14, 20, 29, 40, 54, 72, 90, 100, 136, 180, 216, 252, 288 Jy beam^{-1}. The rms noise in the image is ≈390 mJy beam^{-1}.

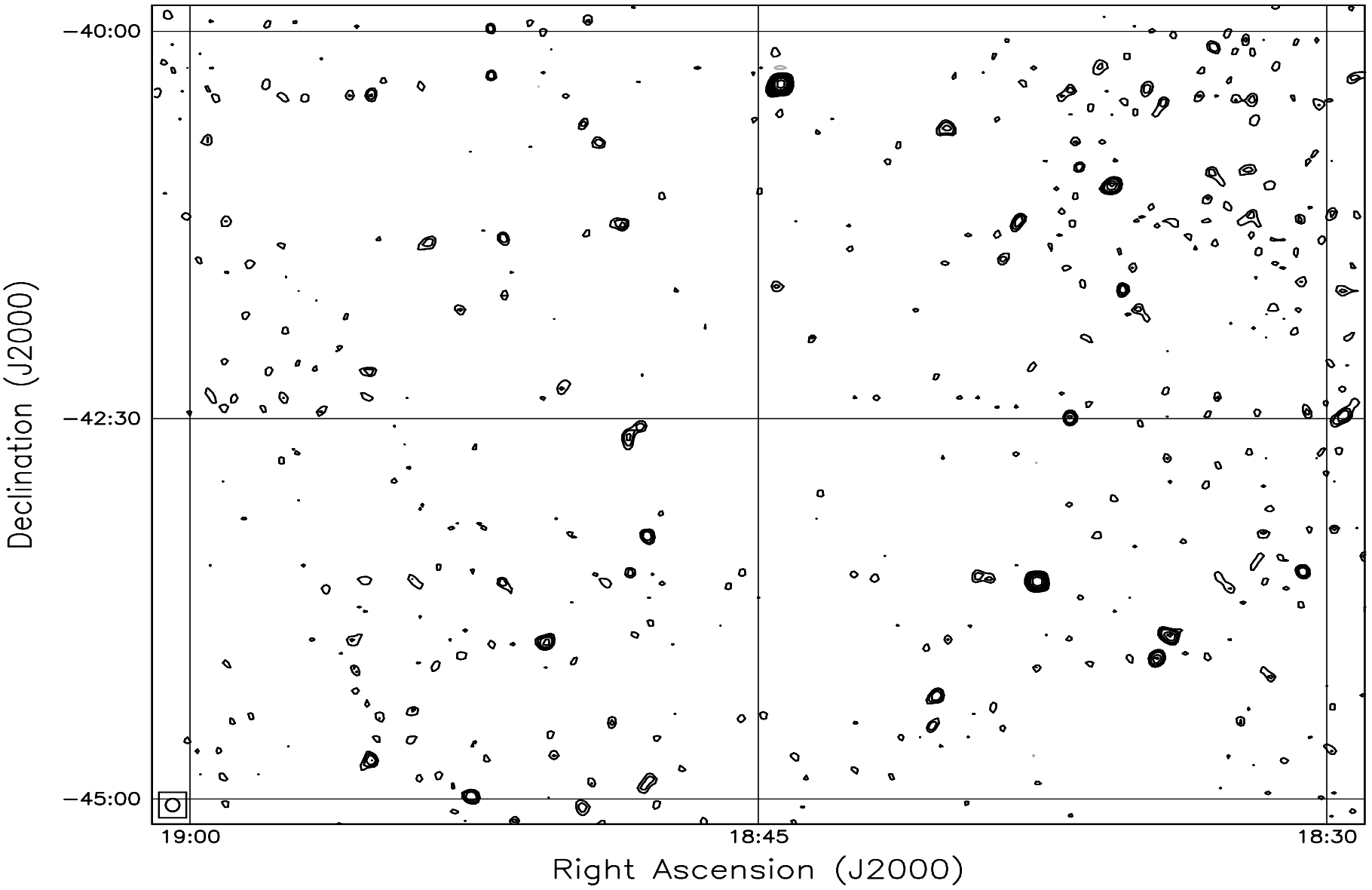

Fig. 7.71: Contour map covering the right ascension range 18h30m to 19h00m and declination range -45° to -40 °. The contour levels are -5, -3.6, -2.5, -1.8, 1, 1.4, 2, 2.8, 3.6, 5, 7, 10, 14, 20, 29, 40, 54, 72, 90, 100, 136, 180, 216, 252, 288 Jy beam^{-1}. The rms noise in the image is ≈390 mJy beam^{-1}.

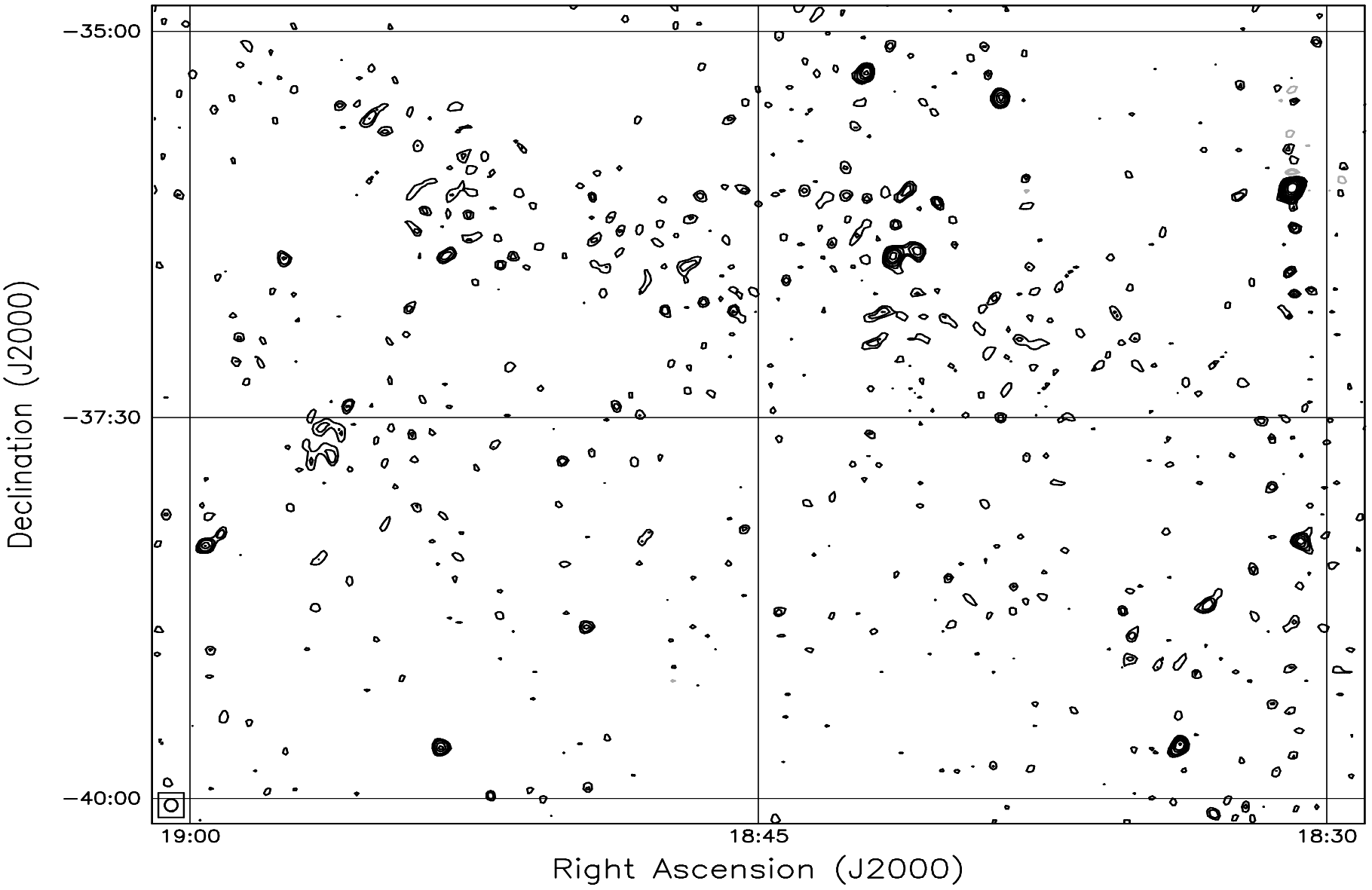

Fig. 7.72: Contour map covering the right ascension range 18h30m to 19h00m and declination range -40° to -35 °. The contour levels are -5, -3.6, -2.5, -1.8, 1, 1.4, 2, 2.8, 3.6, 5, 7, 10, 14, 20, 29, 40, 54, 72, 90, 100, 136, 180, 216, 252, 288 Jy beam^{-1}. The rms noise in the image is ≈400 mJy beam^{-1}.

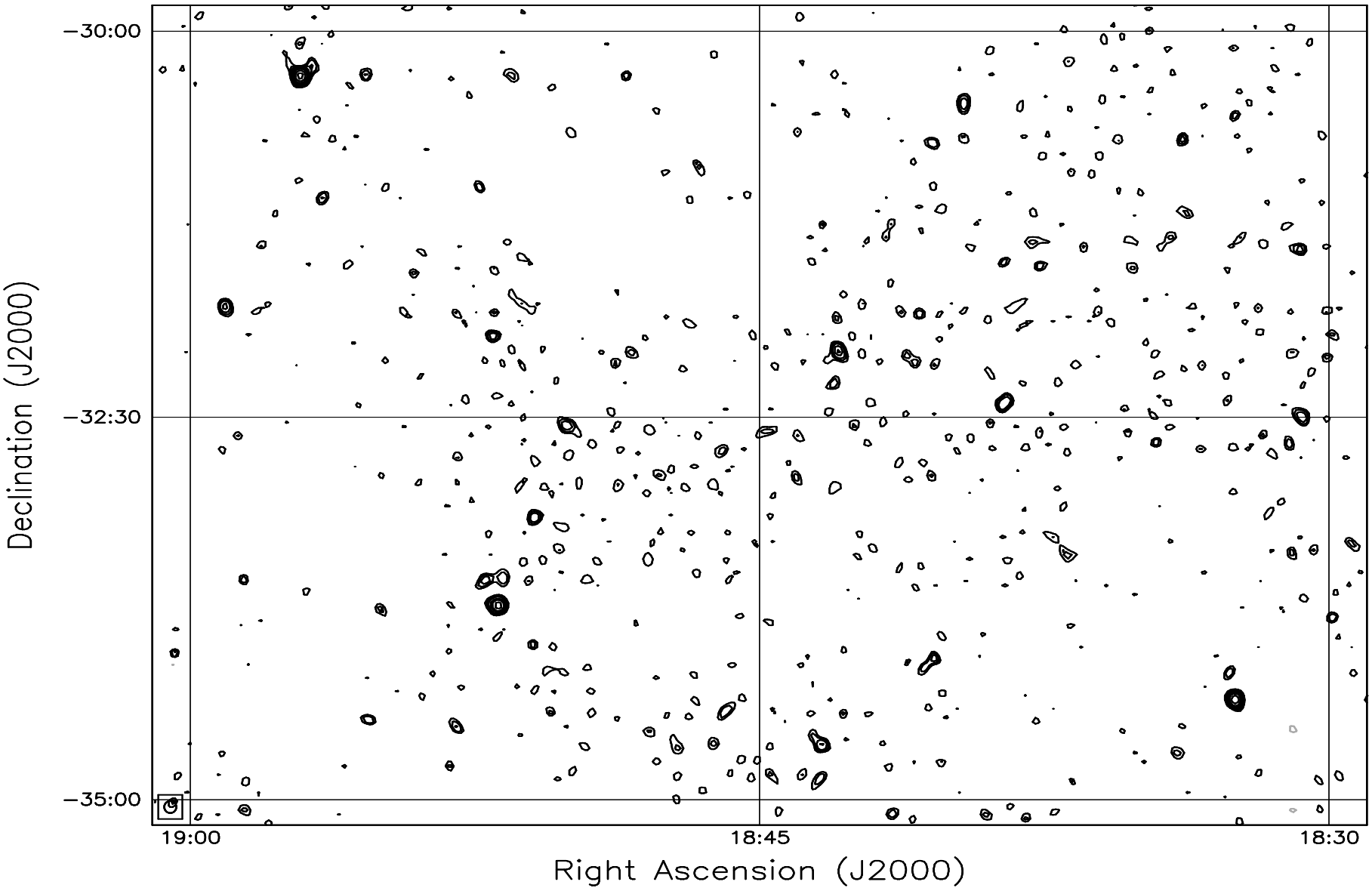

Fig. 7.73: Contour map covering the right ascension range 18h30m to 19h00m and declination range -35° to -30 °. The contour levels are -5, -3.6, -2.5, -1.8, 1, 1.4, 2, 2.8, 3.6, 5, 7, 10, 14, 20, 29, 40, 54, 72, 90, 100, 136, 180, 216, 252, 288 Jy beam^{-1}. The rms noise in the image is ≈420 mJy beam^{-1}.

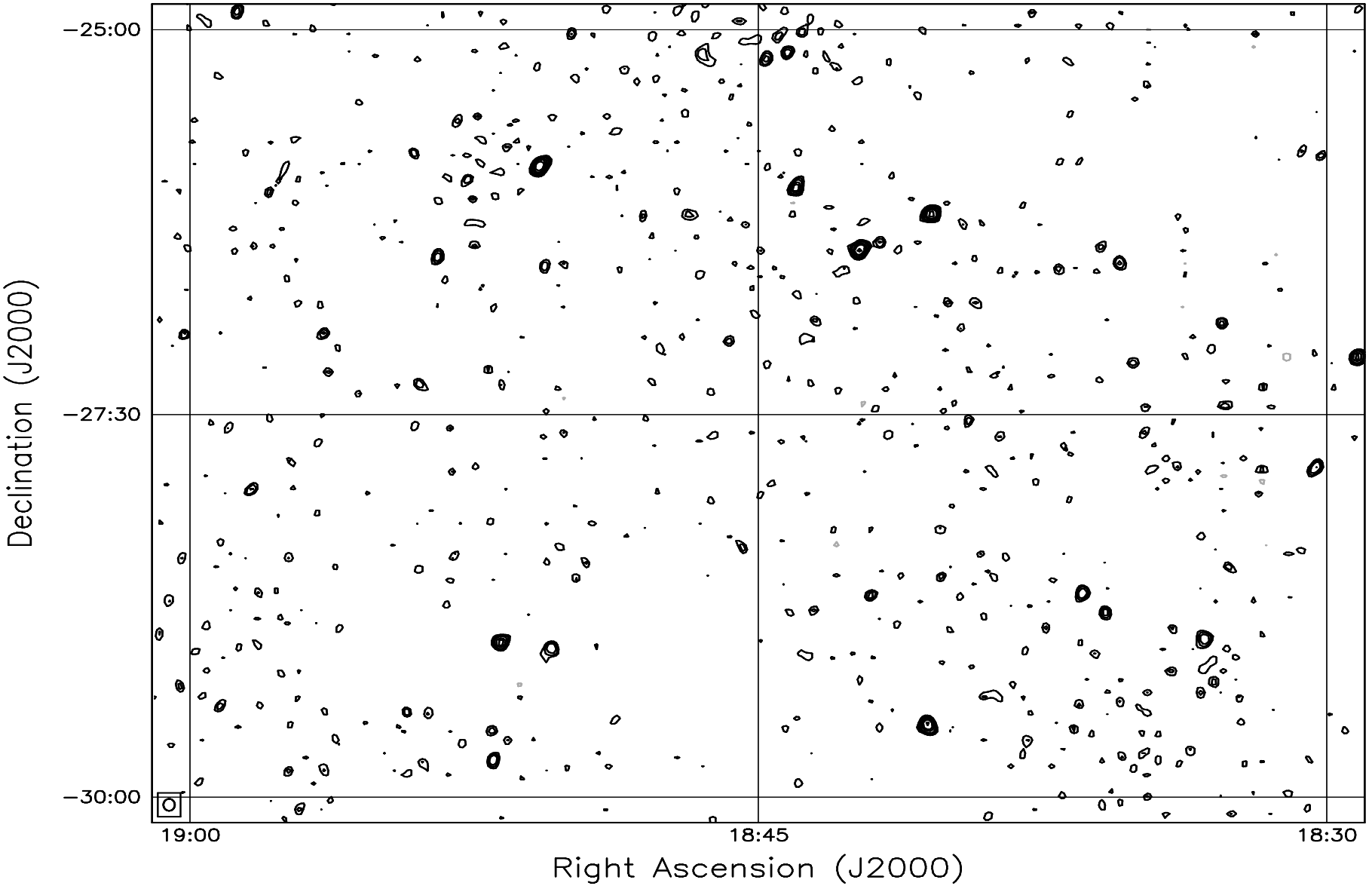

Fig. 7.74: Contour map covering the right ascension range 18h30m to 19h00m and declination range -30° to -25 °. The contour levels are -5, -3.6, -2.5, -1.8, 1, 1.4, 2, 2.8, 3.6, 5, 7, 10, 14, 20, 29, 40, 54, 72, 90, 100, 136, 180, 216, 252, 288 Jy beam^{-1}. The rms noise in the image is ≈445 mJy beam^{-1}.

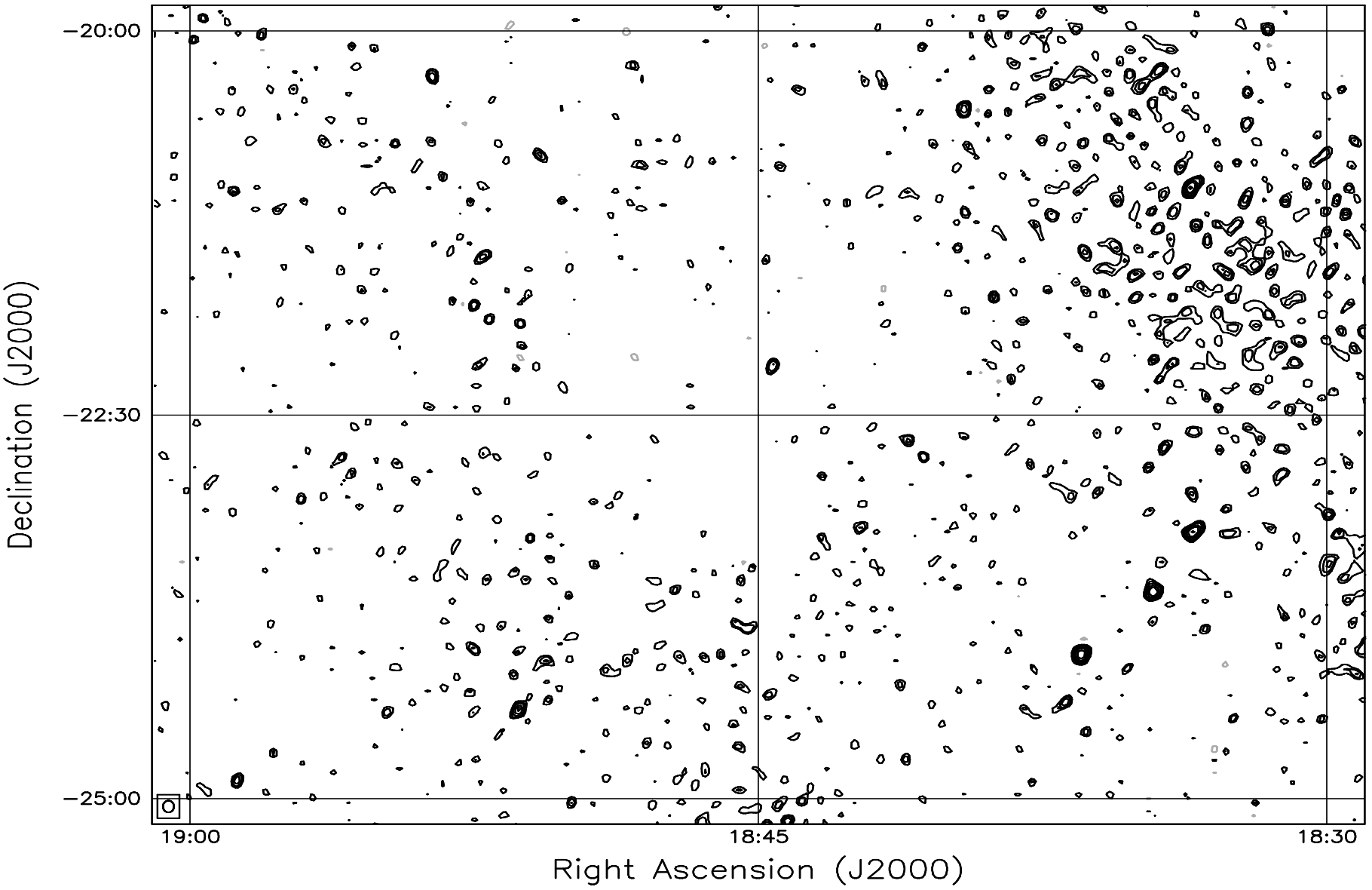

Fig. 7.75: Contour map covering the right ascension range 18h30m to 19h00m and declination range -25° to -20 °. The contour levels are -5, -3.6, -2.5, -1.8, 1, 1.4, 2, 2.8, 3.6, 5, 7, 10, 14, 20, 29, 40, 54, 72, 90, 100, 136, 180, 216, 252, 288 Jy beam^{-1}. The rms noise in the image is ≈490 mJy beam^{-1}.

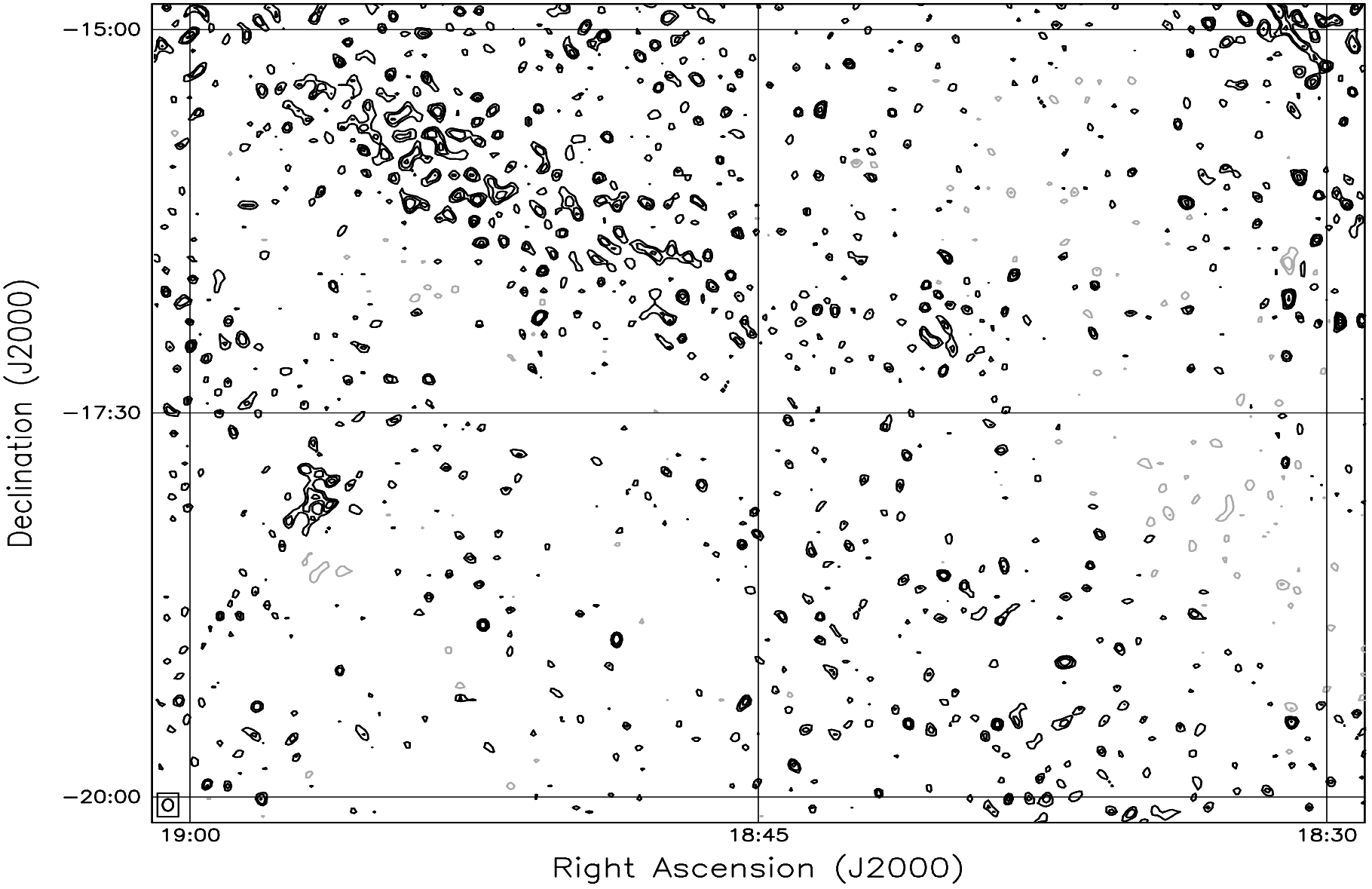

Fig. 7.76: Contour map covering the right ascension range 18h30m to 19h00m and declination range -20° to -15 °. The contour levels are -5, -3.6, -2.5, -1.8, 1, 1.4, 2, 2.8, 3.6, 5, 7, 10, 14, 20, 29, 40, 54, 72, 90, 100, 136, 180, 216, 252, 288 Jy beam^{-1}. The rms noise in the image is ≈560 mJy beam^{-1}.

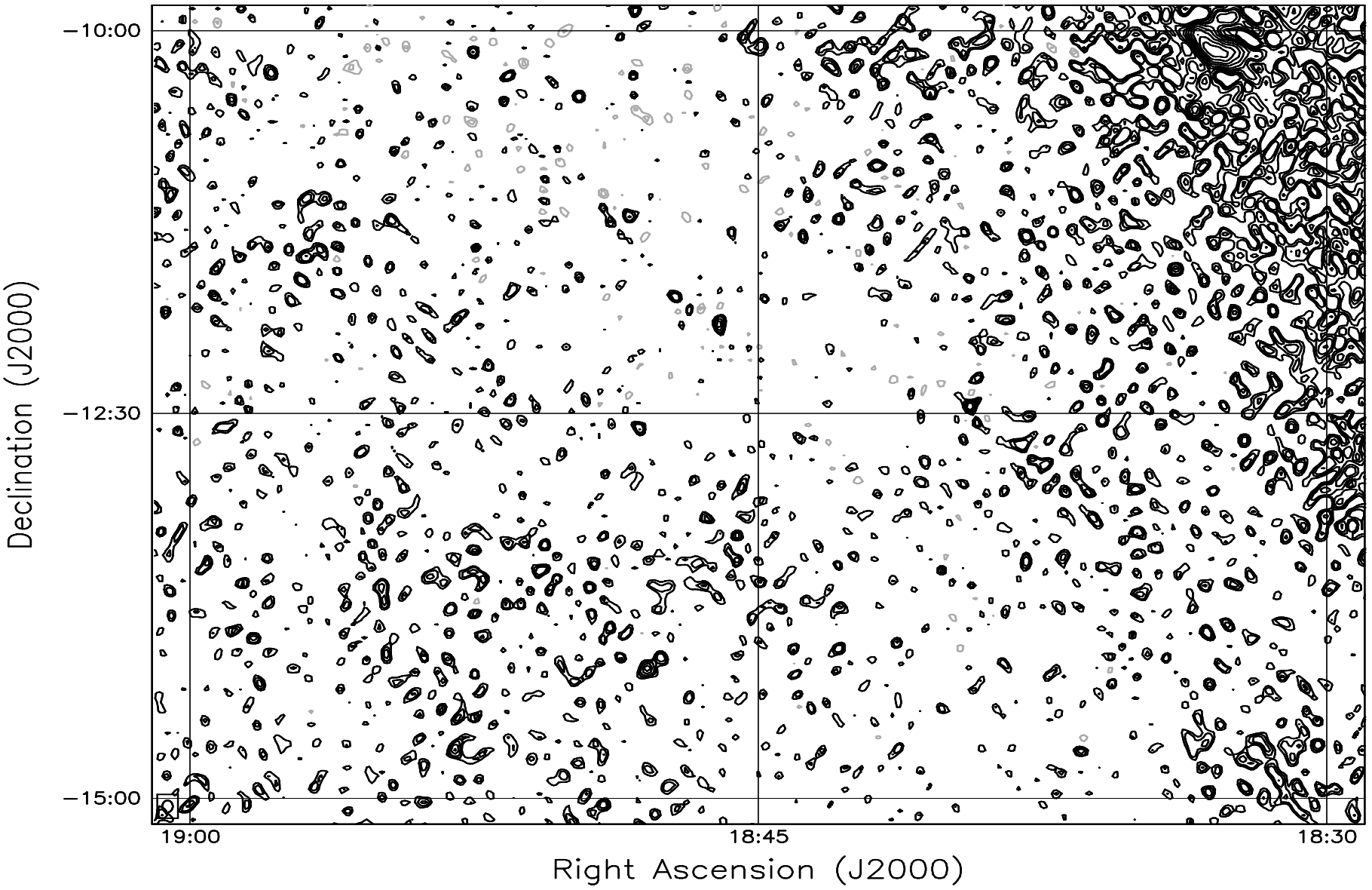

Fig. 7.77: Contour map covering the right ascension range 18h30m to 19h00m and declination range -15° to -10 °. The contour levels are -5, -3.6, -2.5, -1.8, 1, 1.4, 2, 2.8, 3.6, 5, 7, 10, 14, 20, 29, 40, 54, 72, 90, 100, 136, 180, 216, 252, 288 Jy beam^{-1}. The rms noise in the image is ≈680 mJy beam^{-1}.

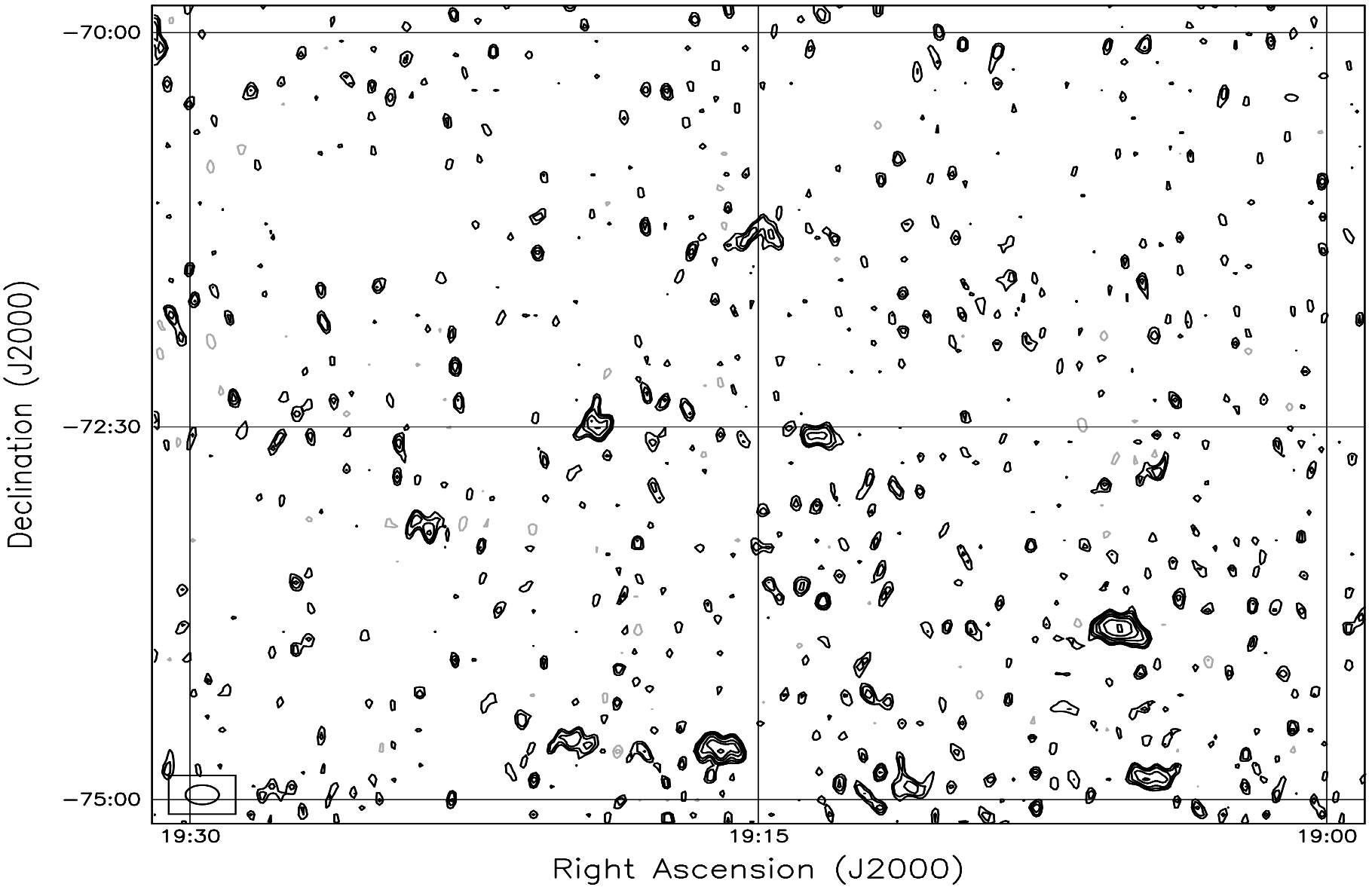

Fig. 7.78: Contour map covering the right ascension range 19h00m to 19h30m and declination range -75° to -70 °. The contour levels are -5, -3.6, -2.5, -1.8, 1, 1.4, 2, 2.8, 3.6, 5, 7, 10, 14, 20, 29, 40, 54, 72, 90, 100, 136, 180, 216, 252, 288 Jy beam^{-1}. The rms noise in the image is ≈530 mJy beam^{-1}.

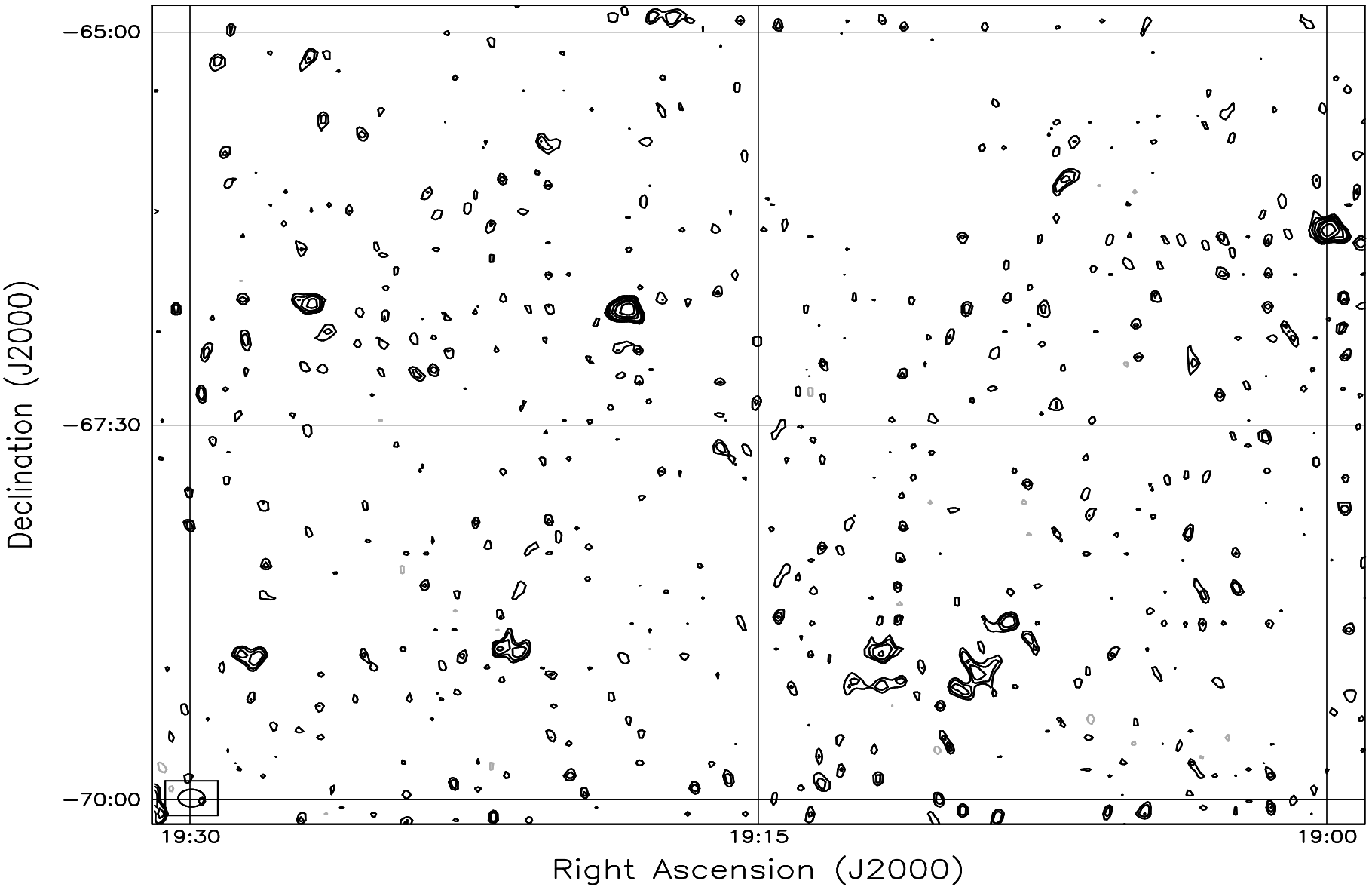

Fig. 7.79: Contour map covering the right ascension range 19h00m to 19h30m and declination range -70° to -65 °. The contour levels are -5, -3.6, -2.5, -1.8, 1, 1.4, 2, 2.8, 3.6, 5, 7, 10, 14, 20, 29, 40, 54, 72, 90, 100, 136, 180, 216, 252, 288 Jy beam^{-1}. The rms noise in the image is ≈460 mJy beam^{-1}.

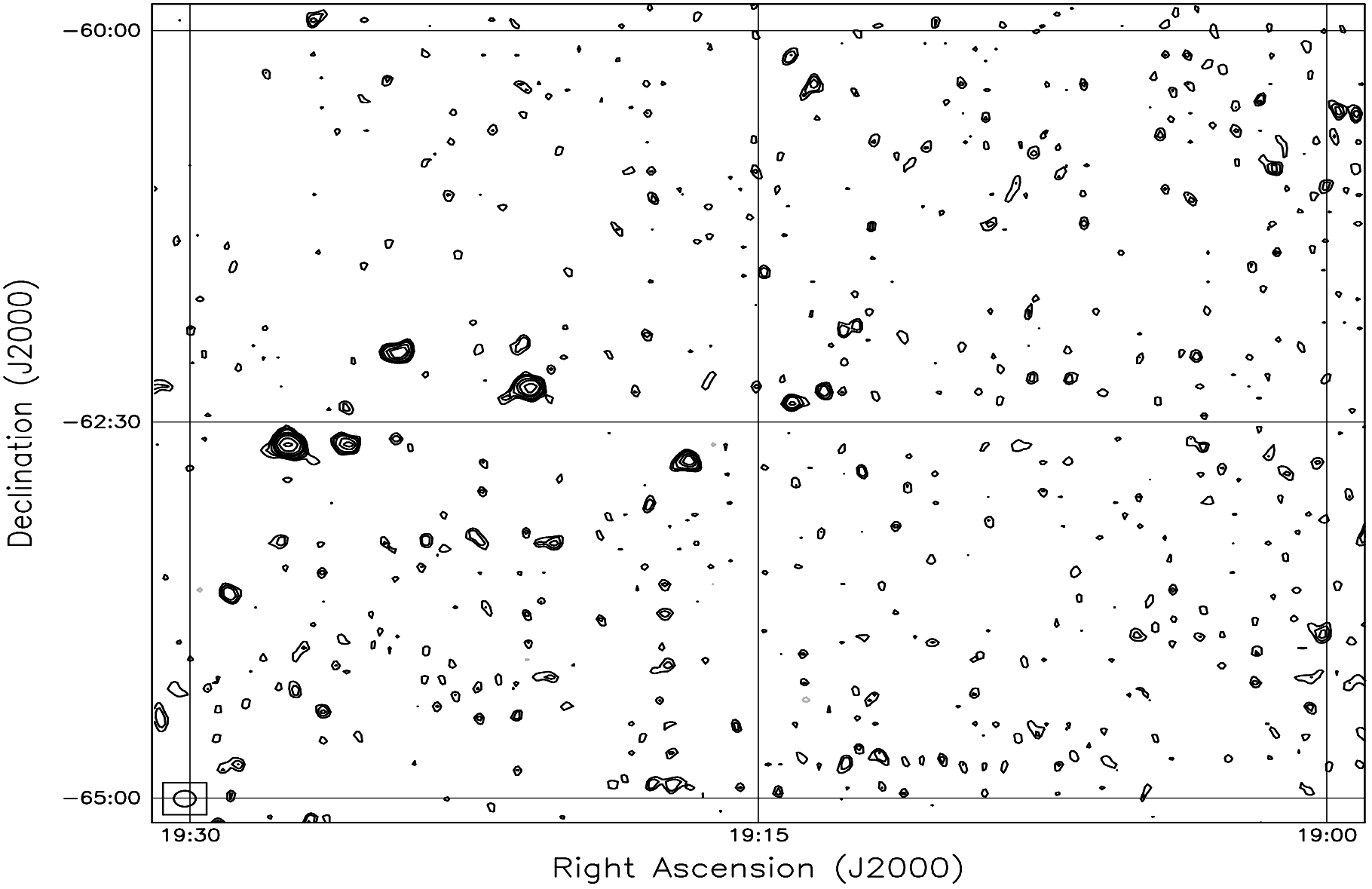

Fig. 7.80: Contour map covering the right ascension range 19h00m to 19h30m and declination range -65° to -60 °. The contour levels are -5, -3.6, -2.5, -1.8, 1, 1.4, 2, 2.8, 3.6, 5, 7, 10, 14, 20, 29, 40, 54, 72, 90, 100, 136, 180, 216, 252, 288 Jy beam^{-1}. The rms noise in the image is ≈415 mJy beam^{-1}.

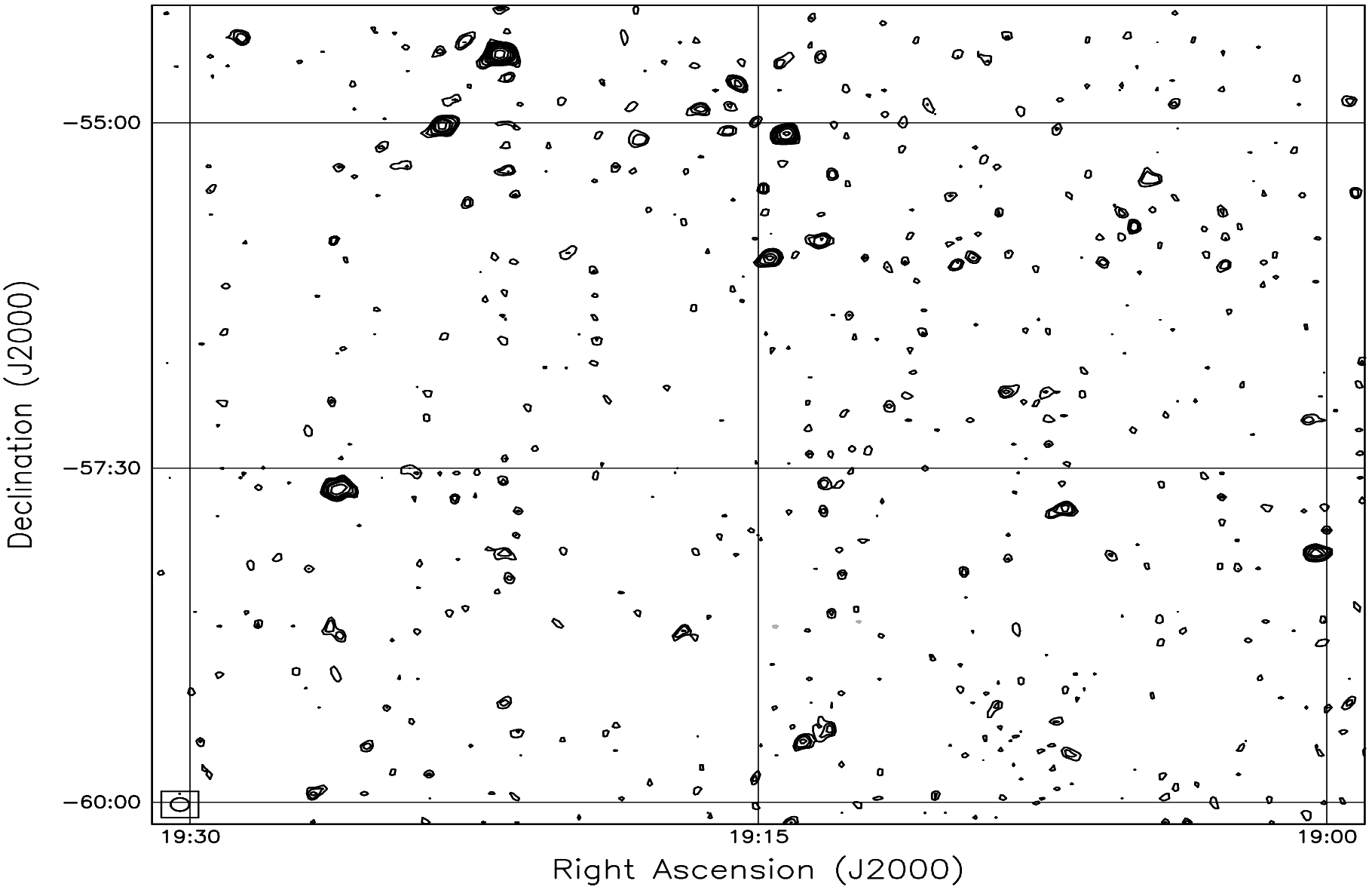

Fig. 7.81: Contour map covering the right ascension range 19h00m to 19h30m and declination range -60° to -55 °. The contour levels are -5, -3.6, -2.5, -1.8, 1, 1.4, 2, 2.8, 3.6, 5, 7, 10, 14, 20, 29, 40, 54, 72, 90, 100, 136, 180, 216, 252, 288 Jy beam^{-1}. The rms noise in the image is ≈390 mJy beam^{-1}.

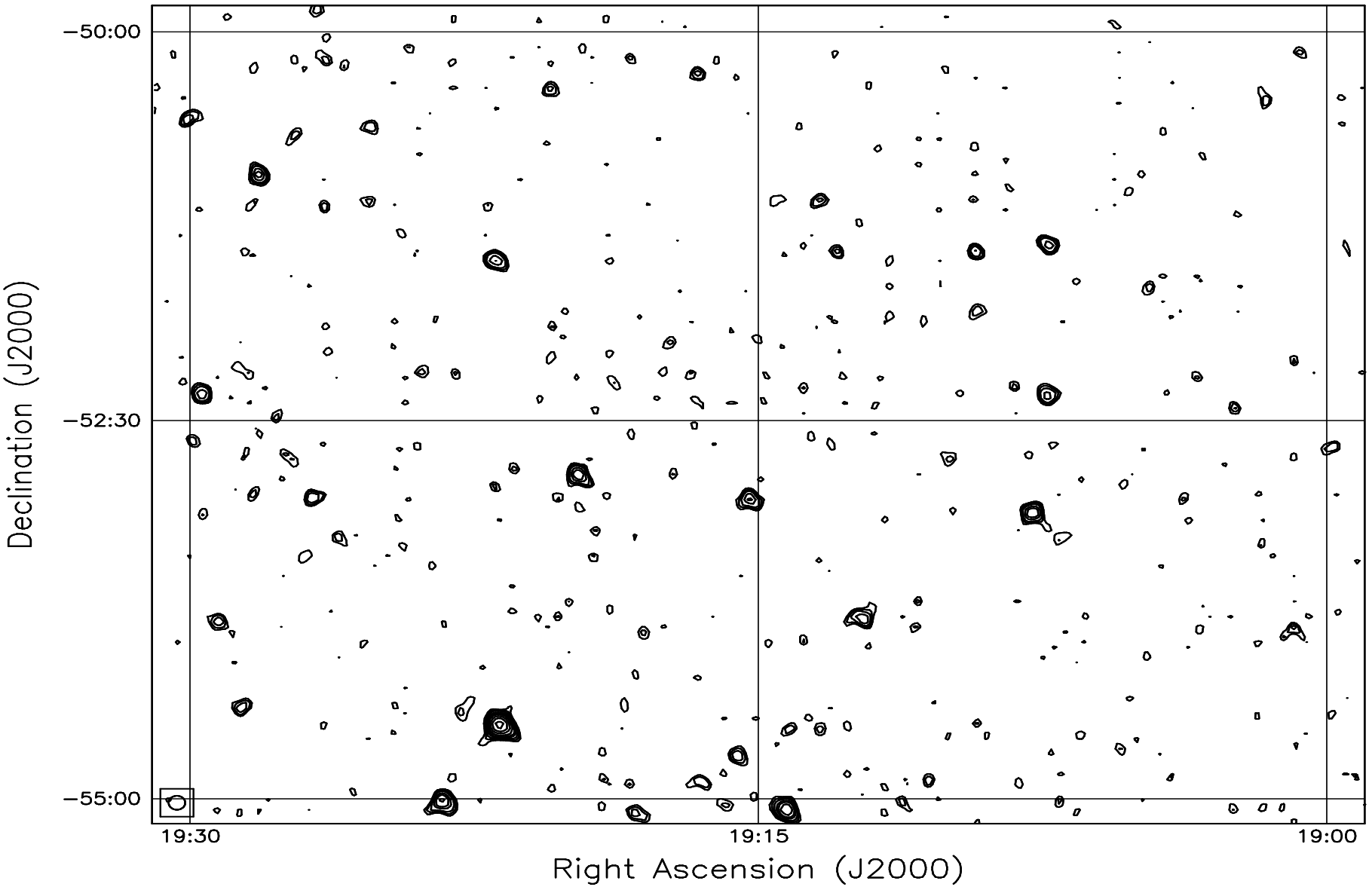

Fig. 7.82: Contour map covering the right ascension range 19h00m to 19h30m and declination range -55° to -50 °. The contour levels are -5, -3.6, -2.5, -1.8, 1, 1.4, 2, 2.8, 3.6, 5, 7, 10, 14, 20, 29, 40, 54, 72, 90, 100, 136, 180, 216, 252, 288 Jy beam^{-1}. The rms noise in the image is ≈370 mJy beam^{-1}.

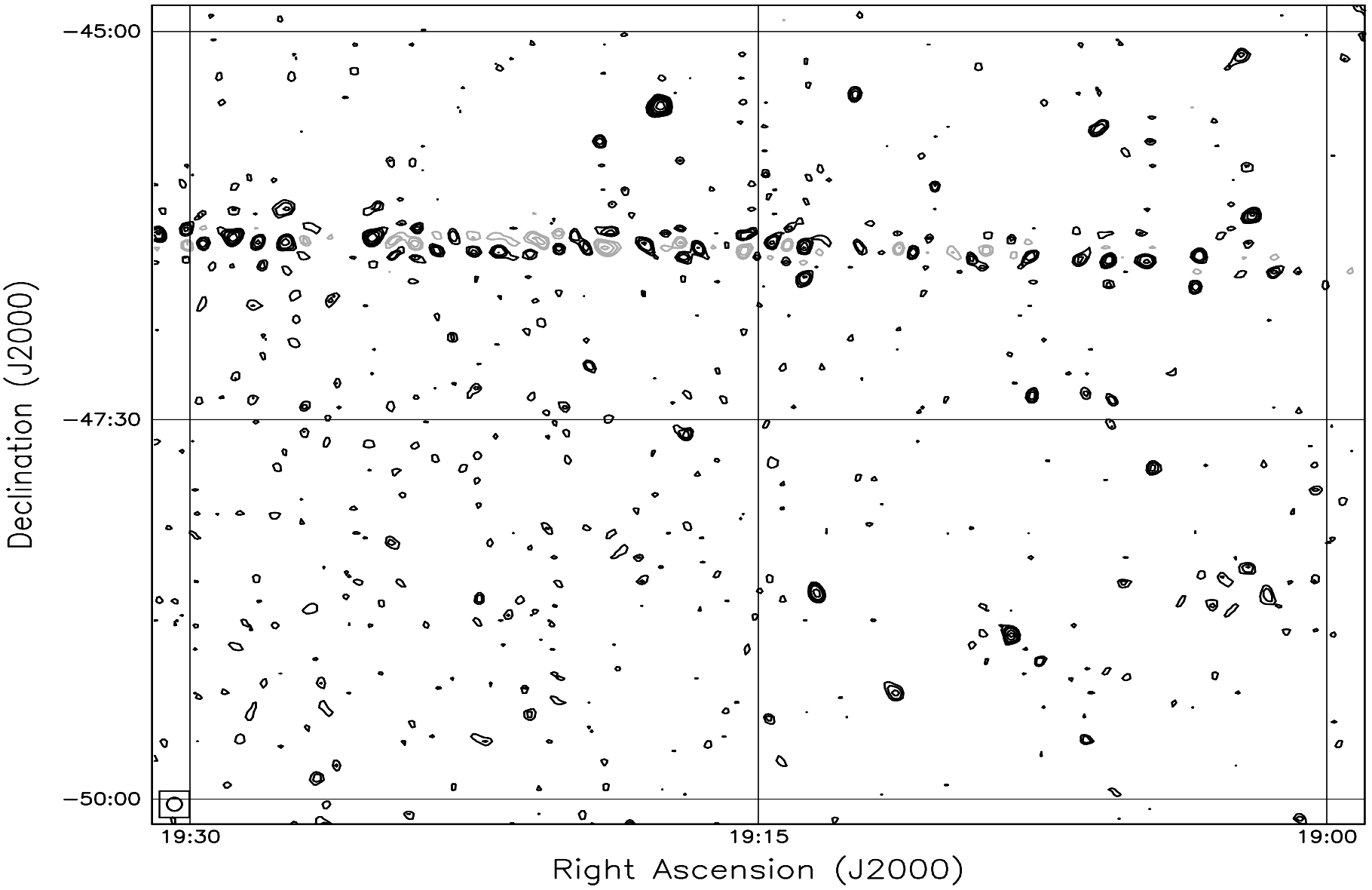

Fig. 7.83: Contour map covering the right ascension range 19h00m to 19h30m and declination range -50° to -45 °. The contour levels are -5, -3.6, -2.5, -1.8, 1, 1.4, 2, 2.8, 3.6, 5, 7, 10, 14, 20, 29, 40, 54, 72, 90, 100, 136, 180, 216, 252, 288 Jy beam^{-1}. The rms noise in the image is ≈360 mJy beam^{-1}.

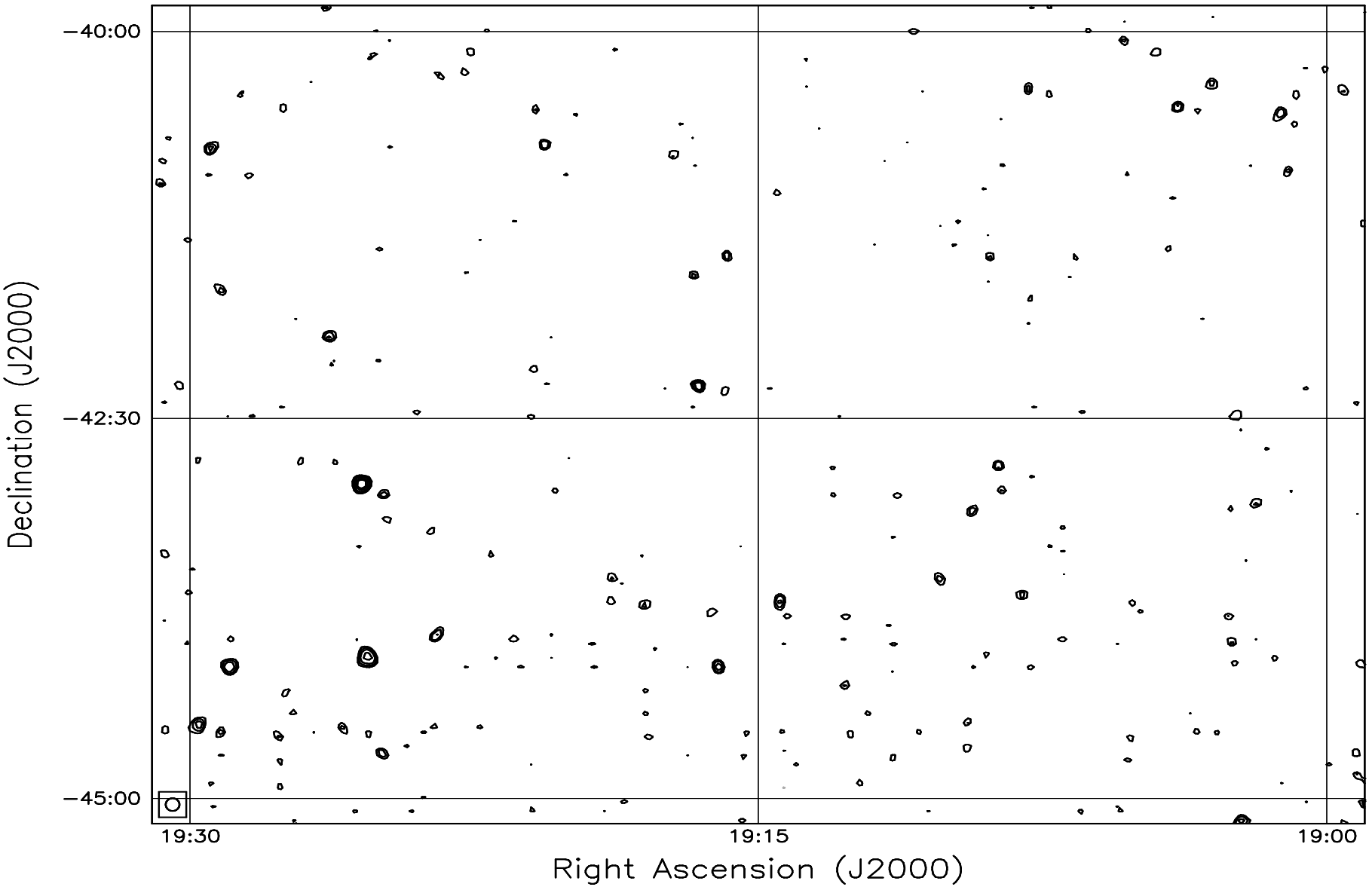

Fig. 7.84: Contour map covering the right ascension range 19h00m to 19h30m and declination range -45° to -40 °. The contour levels are -5, -3.6, -2.5, -1.8, 1, 1.4, 2, 2.8, 3.6, 5, 7, 10, 14, 20, 29, 40, 54, 72, 90, 100, 136, 180, 216, 252, 288 Jy beam^{-1}. The rms noise in the image is ≈360 mJy beam^{-1}.

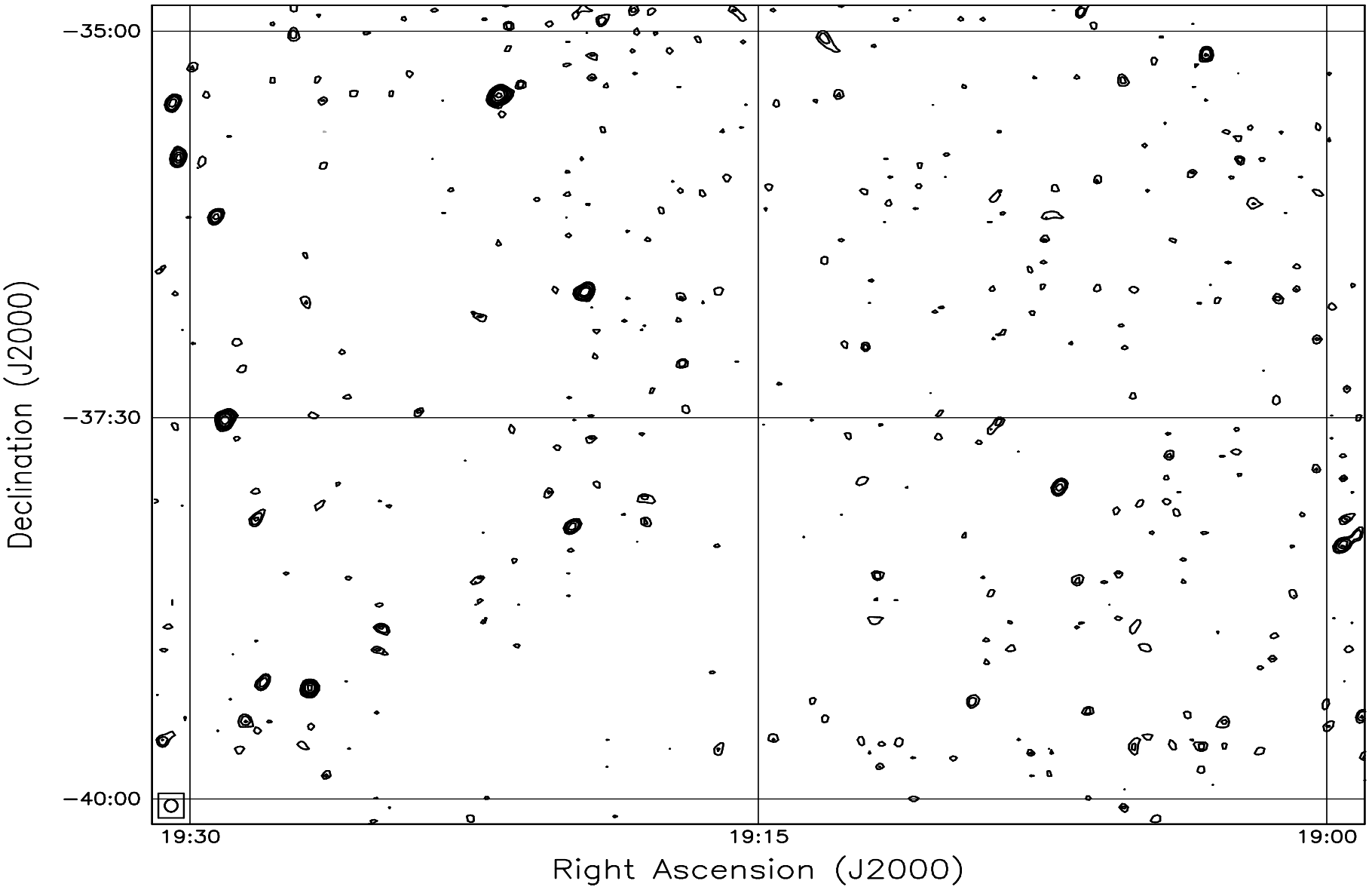

Fig. 7.85: Contour map covering the right ascension range 19h00m to 19h30m and declination range -40° to -35 °. The contour levels are -5, -3.6, -2.5, -1.8, 1, 1.4, 2, 2.8, 3.6, 5, 7, 10, 14, 20, 29, 40, 54, 72, 90, 100, 136, 180, 216, 252, 288 Jy beam^{-1}. The rms noise in the image is ≈370 mJy beam^{-1}.

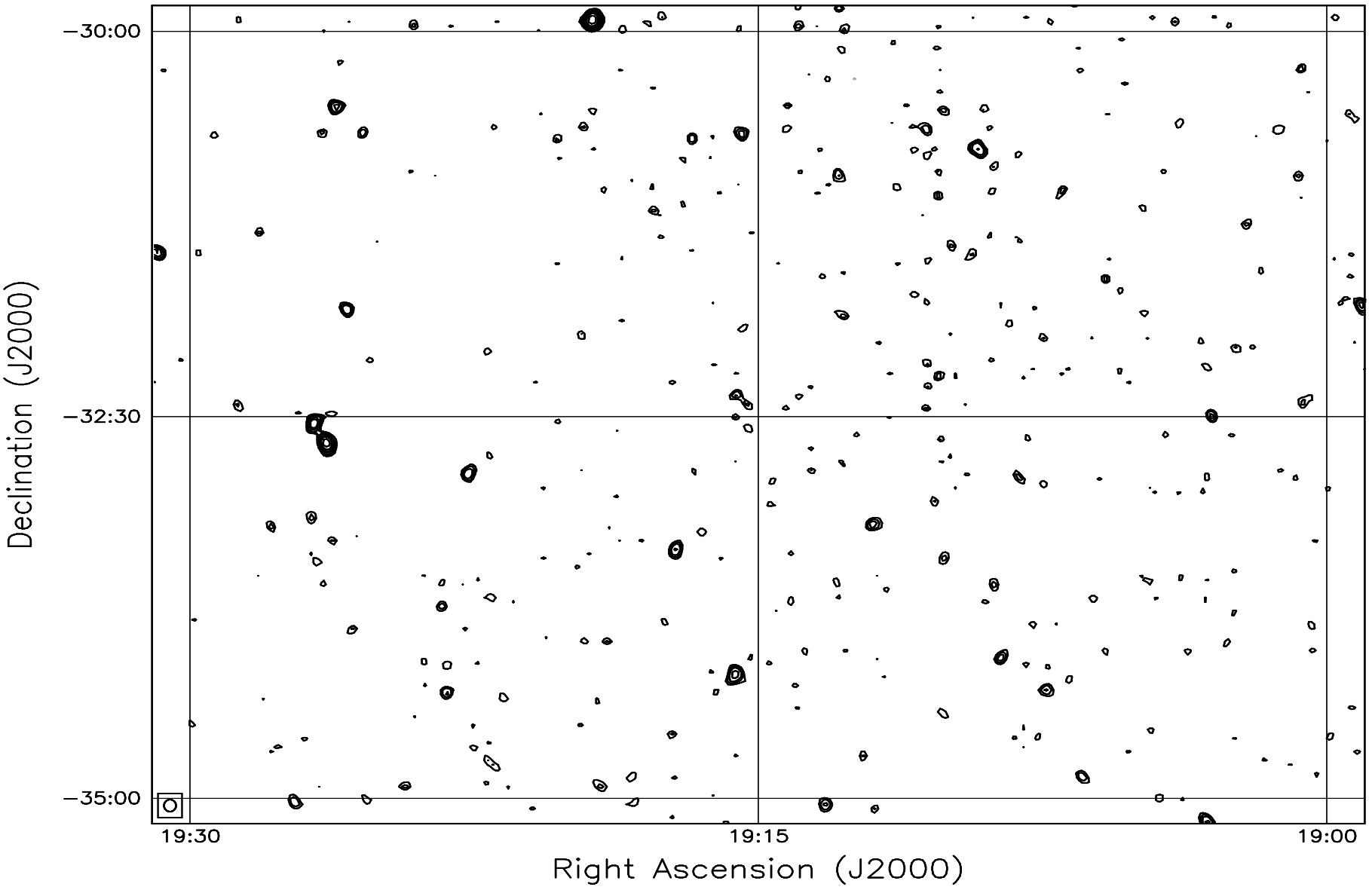

Fig. 7.86: Contour map covering the right ascension range 19h00m to 19h30m and declination range -35° to -30 °. The contour levels are -5, -3.6, -2.5, -1.8, 1, 1.4, 2, 2.8, 3.6, 5, 7, 10, 14, 20, 29, 40, 54, 72, 90, 100, 136, 180, 216, 252, 288 Jy beam^{-1}. The rms noise in the image is ≈385 mJy beam^{-1}.

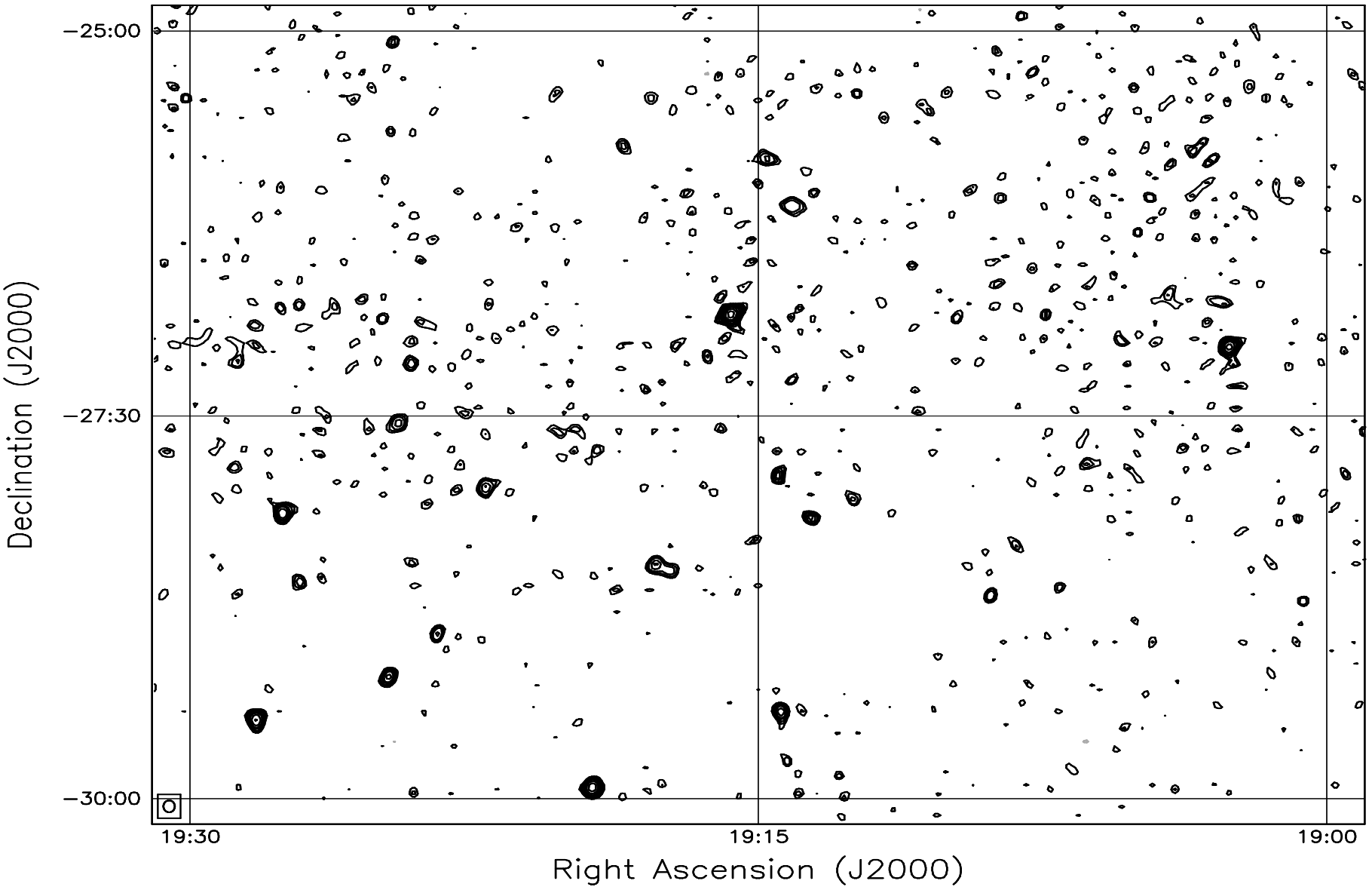

Fig. 7.87: Contour map covering the right ascension range 19h00m to 19h30m and declination range -30° to -25 °. The contour levels are -5, -3.6, -2.5, -1.8, 1, 1.4, 2, 2.8, 3.6, 5, 7, 10, 14, 20, 29, 40, 54, 72, 90, 100, 136, 180, 216, 252, 288 Jy beam^{-1}. The rms noise in the image is ≈410 mJy beam^{-1}.

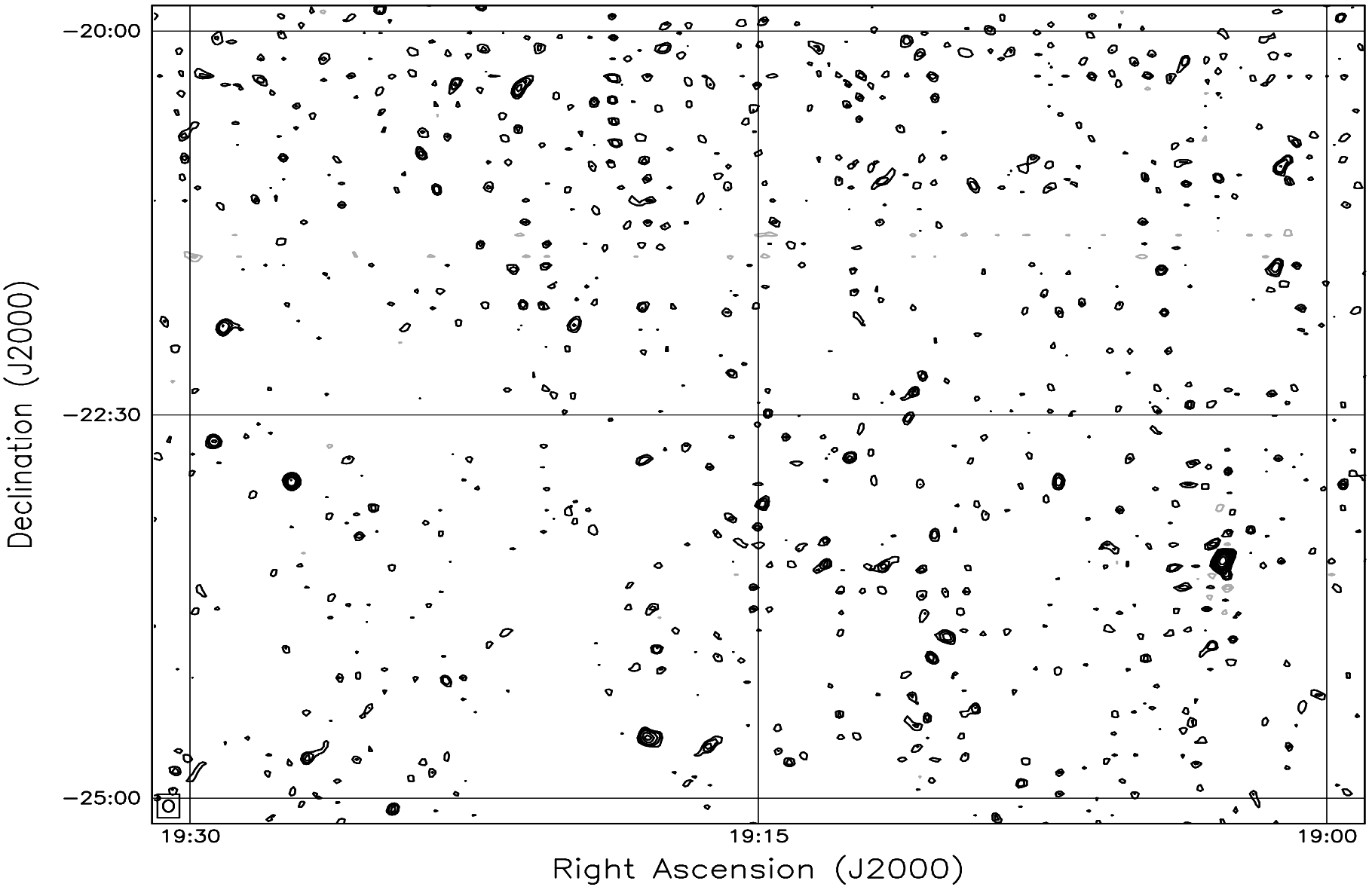

Fig. 7.88: Contour map covering the right ascension range 19h00m to 19h30m and declination range -25° to -20 °. The contour levels are -5, -3.6, -2.5, -1.8, 1, 1.4, 2, 2.8, 3.6, 5, 7, 10, 14, 20, 29, 40, 54, 72, 90, 100, 136, 180, 216, 252, 288 Jy beam^{-1}. The rms noise in the image is ≈450 mJy beam^{-1}.

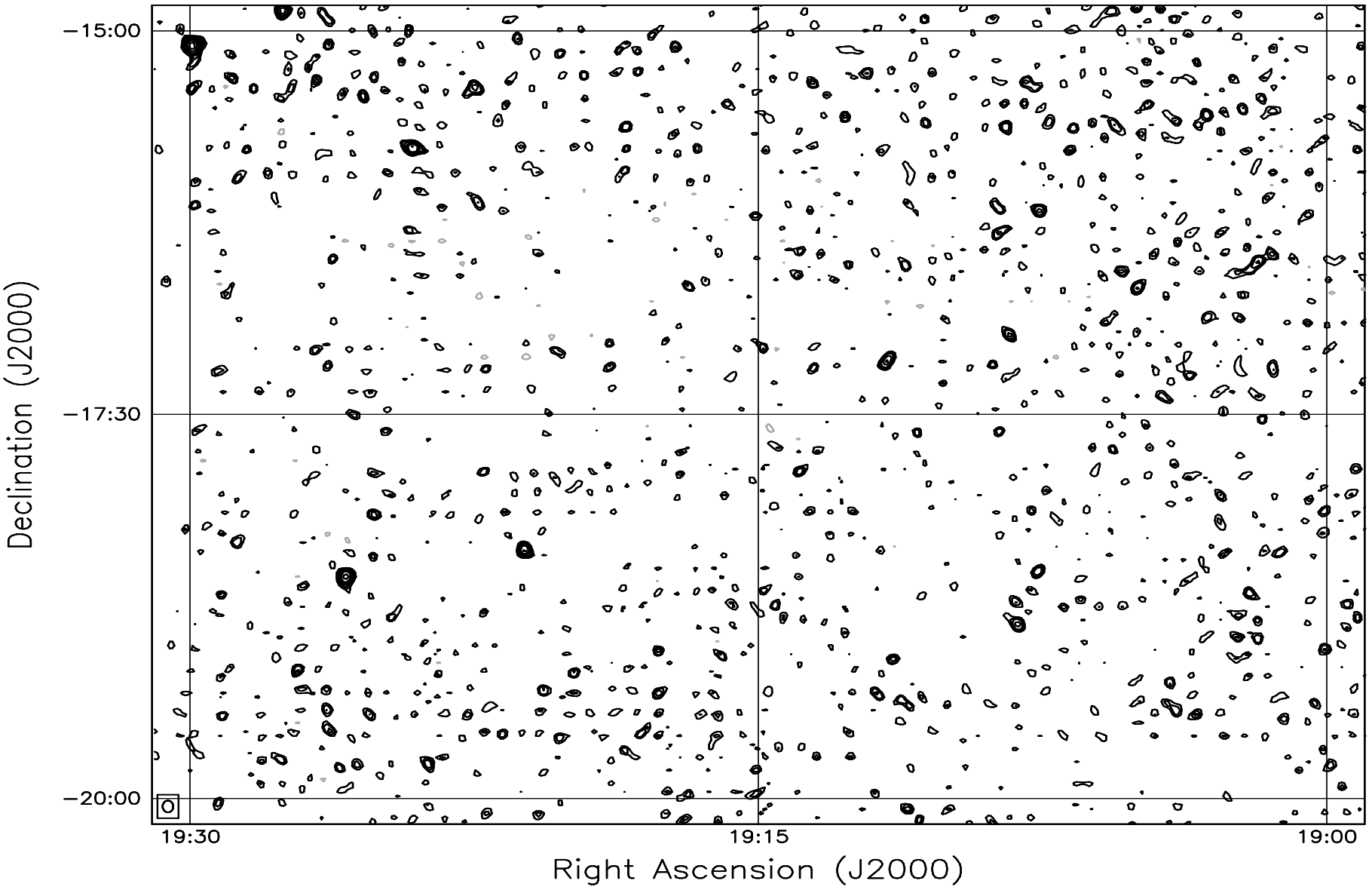

Fig. 7.89: Contour map covering the right ascension range 19h00m to 19h30m and declination range -20° to -15 °. The contour levels are -5, -3.6, -2.5, -1.8, 1, 1.4, 2, 2.8, 3.6, 5, 7, 10, 14, 20, 29, 40, 54, 72, 90, 100, 136, 180, 216, 252, 288 Jy beam^{-1}. The rms noise in the image is ≈520 mJy beam^{-1}.

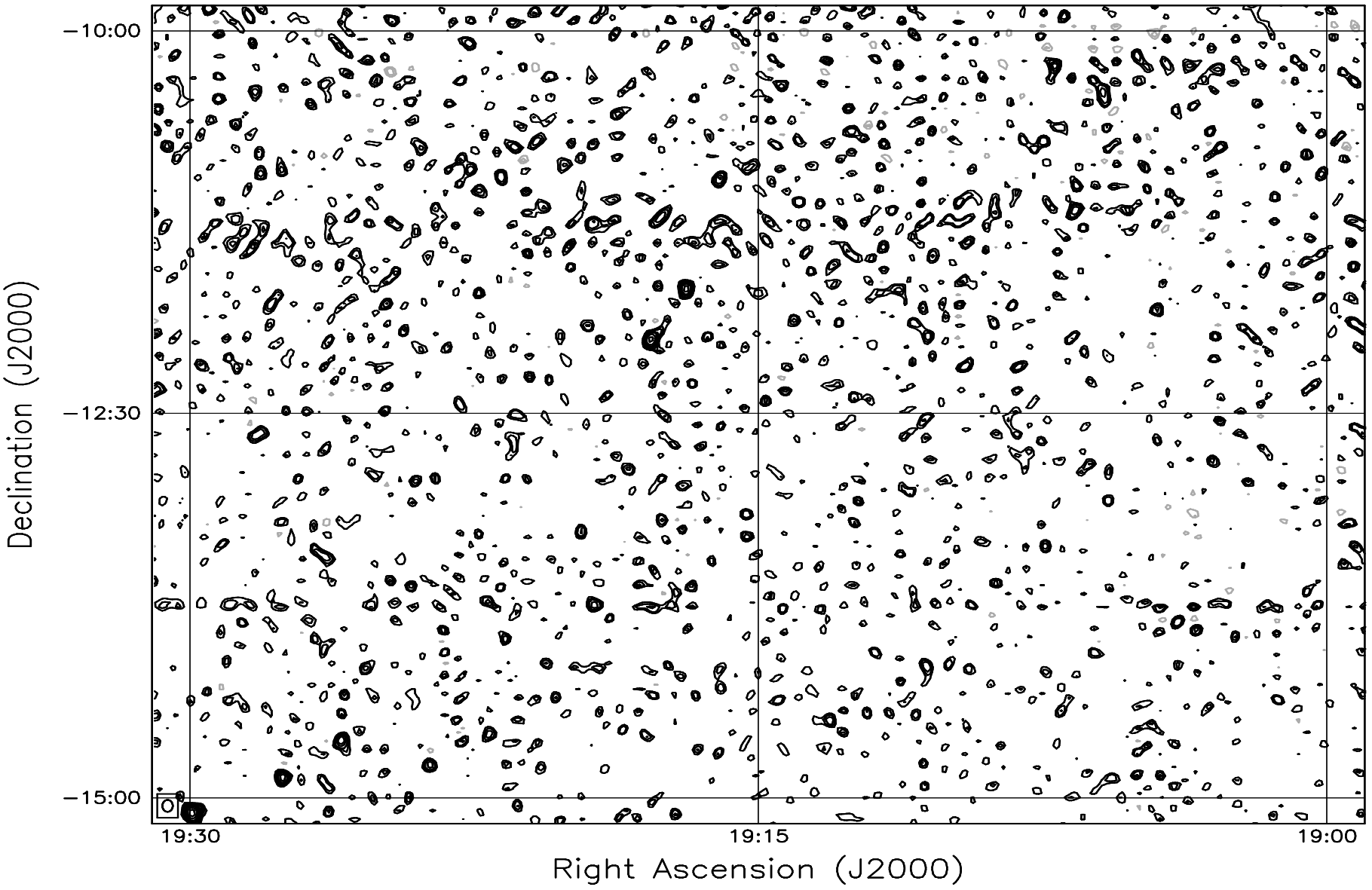

Fig. 7.90: Contour map covering the right ascension range 19h00m to 19h30m and declination range -15° to -10 °. The contour levels are -5, -3.6, -2.5, -1.8, 1, 1.4, 2, 2.8, 3.6, 5, 7, 10, 14, 20, 29, 40, 54, 72, 90, 100, 136, 180, 216, 252, 288 Jy beam^{-1}. The rms noise in the image is ≈630 mJy beam^{-1}.

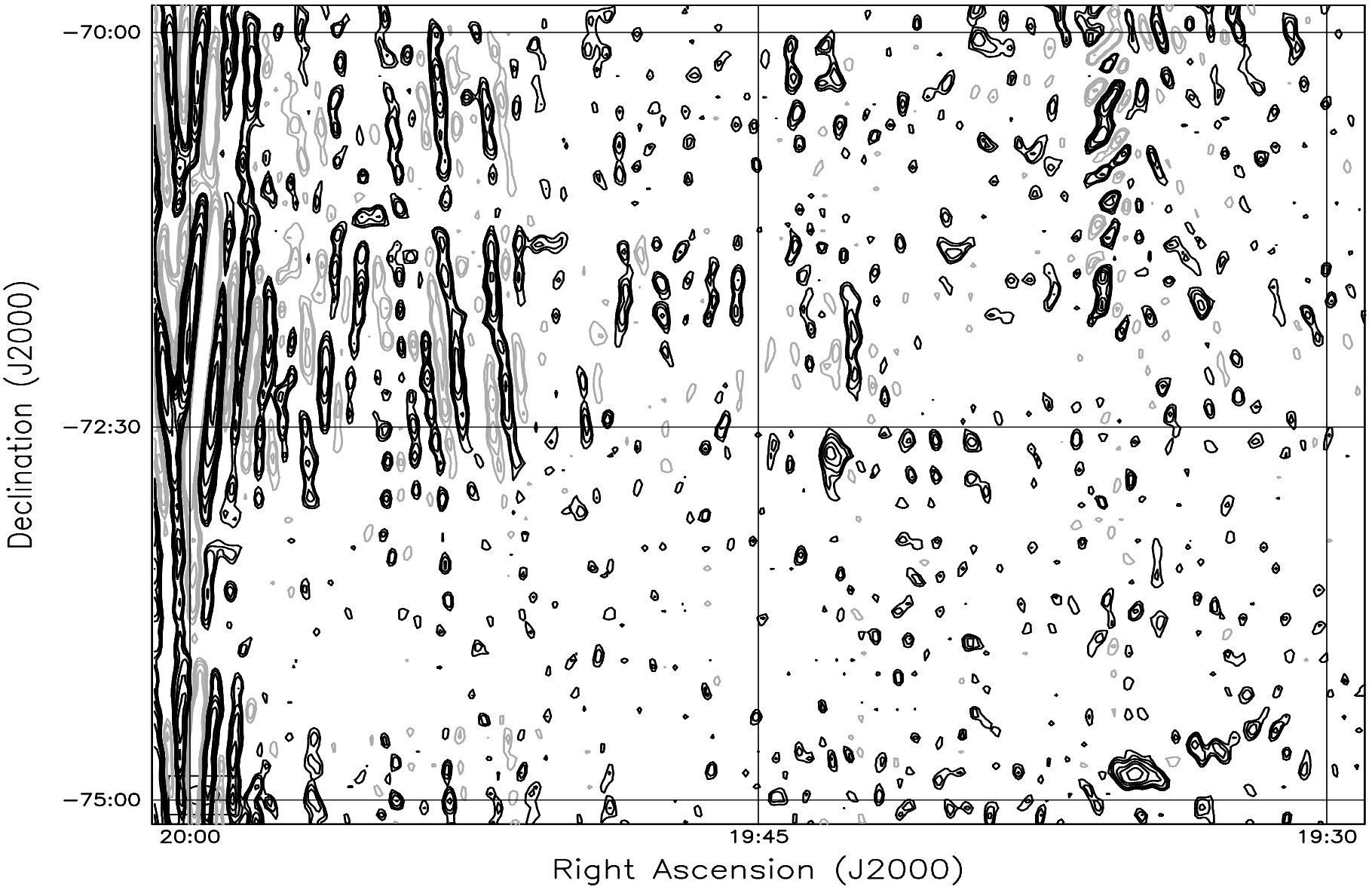

Fig. 7.91: Contour map covering the right ascension range 19h30m to 20h00m and declination range -75° to -70 °. The contour levels are -5, -3.6, -2.5, -1.8, 1, 1.4, 2, 2.8, 3.6, 5, 7, 10, 14, 20, 29, 40, 54, 72, 90, 100, 136, 180, 216, 252, 288 Jy beam^{-1}. The rms noise in the image is ≈530 mJy beam^{-1}.

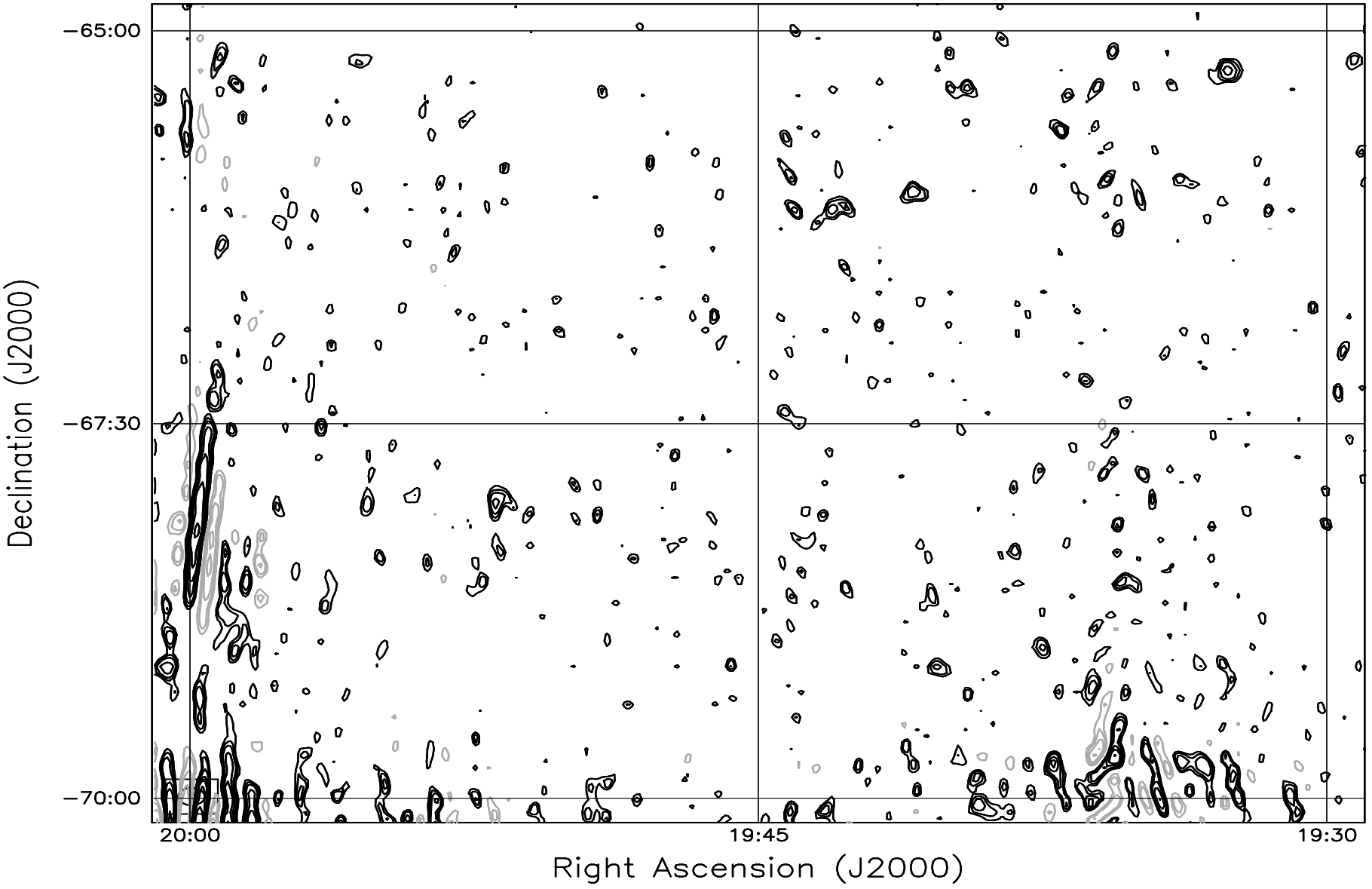

Fig. 7.92: Contour map covering the right ascension range 19h30m to 20h00m and declination range -70° to -65 °. The contour levels are -5, -3.6, -2.5, -1.8, 1, 1.4, 2, 2.8, 3.6, 5, 7, 10, 14, 20, 29, 40, 54, 72, 90, 100, 136, 180, 216, 252, 288 Jy beam^{-1}. The rms noise in the image is ≈460 mJy beam^{-1}.

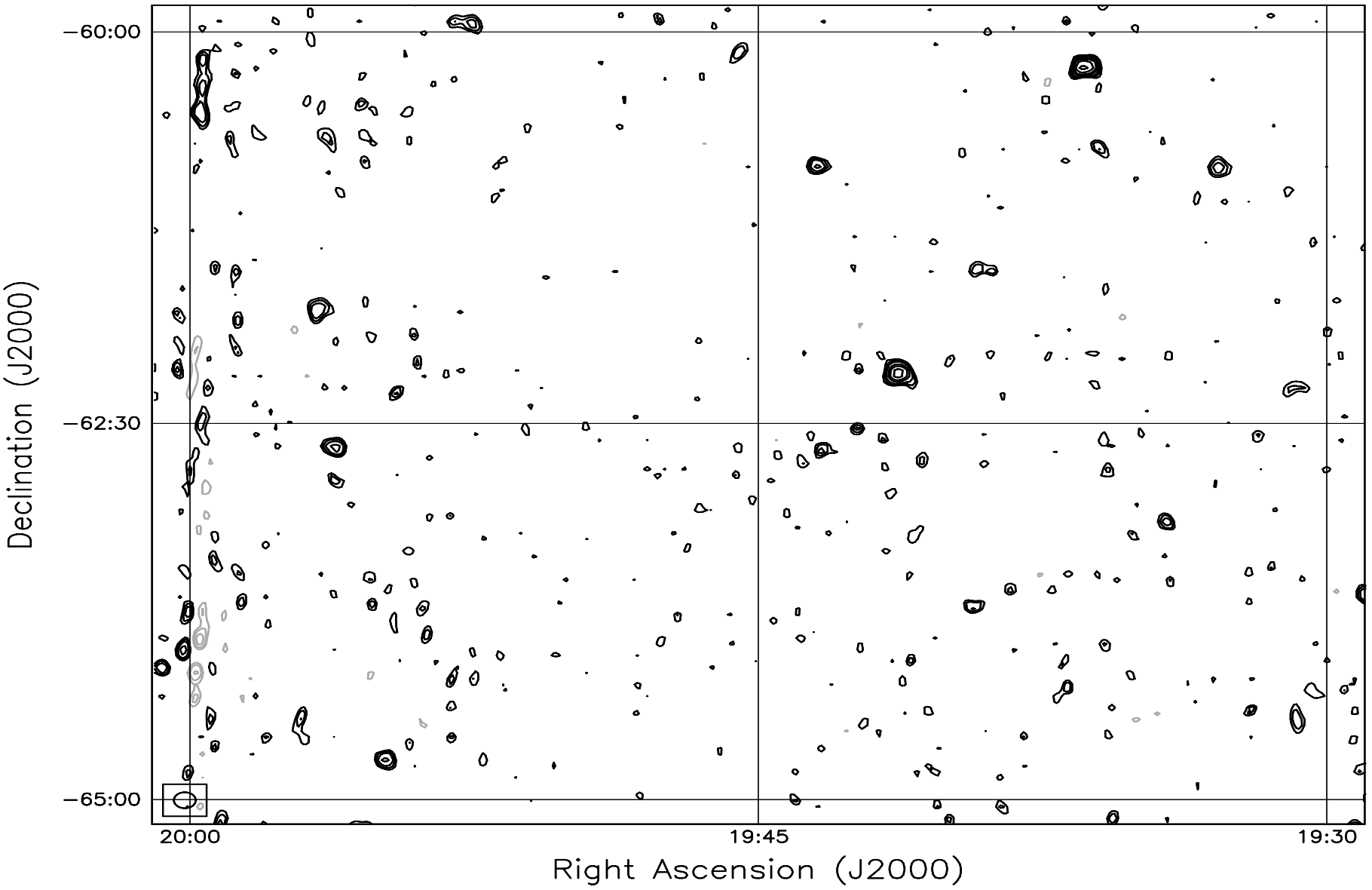

Fig. 7.93: Contour map covering the right ascension range 19h30m to 20h00m and declination range -65° to -60 °. The contour levels are -5, -3.6, -2.5, -1.8, 1, 1.4, 2, 2.8, 3.6, 5, 7, 10, 14, 20, 29, 40, 54, 72, 90, 100, 136, 180, 216, 252, 288 Jy beam^{-1}. The rms noise in the image is ≈415 mJy beam^{-1}.

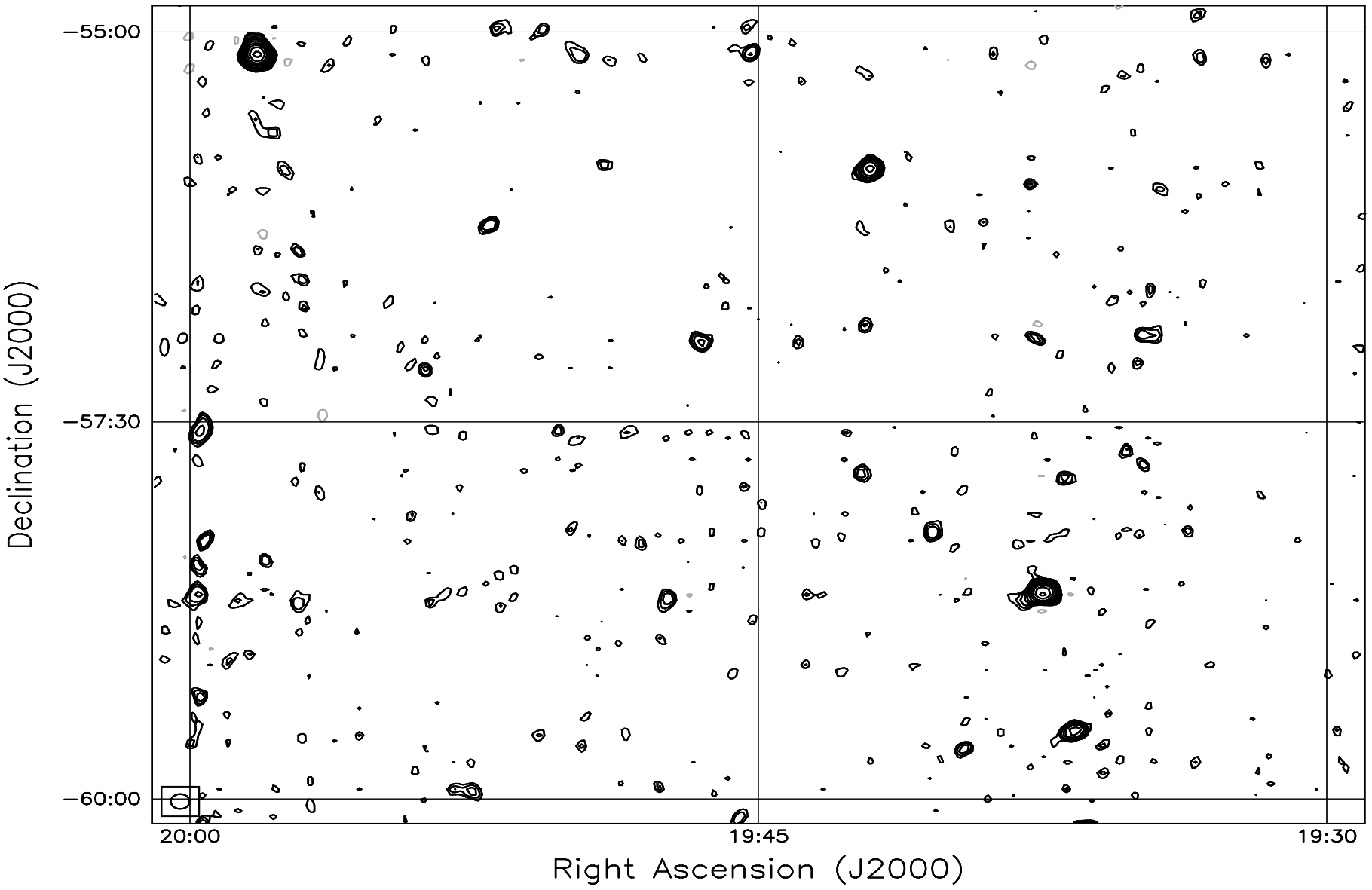

Fig. 7.94: Contour map covering the right ascension range 19h30m to 20h00m and declination range -60° to -55 °. The contour levels are -5, -3.6, -2.5, -1.8, 1, 1.4, 2, 2.8, 3.6, 5, 7, 10, 14, 20, 29, 40, 54, 72, 90, 100, 136, 180, 216, 252, 288 Jy beam^{-1}. The rms noise in the image is ≈390 mJy beam^{-1}.

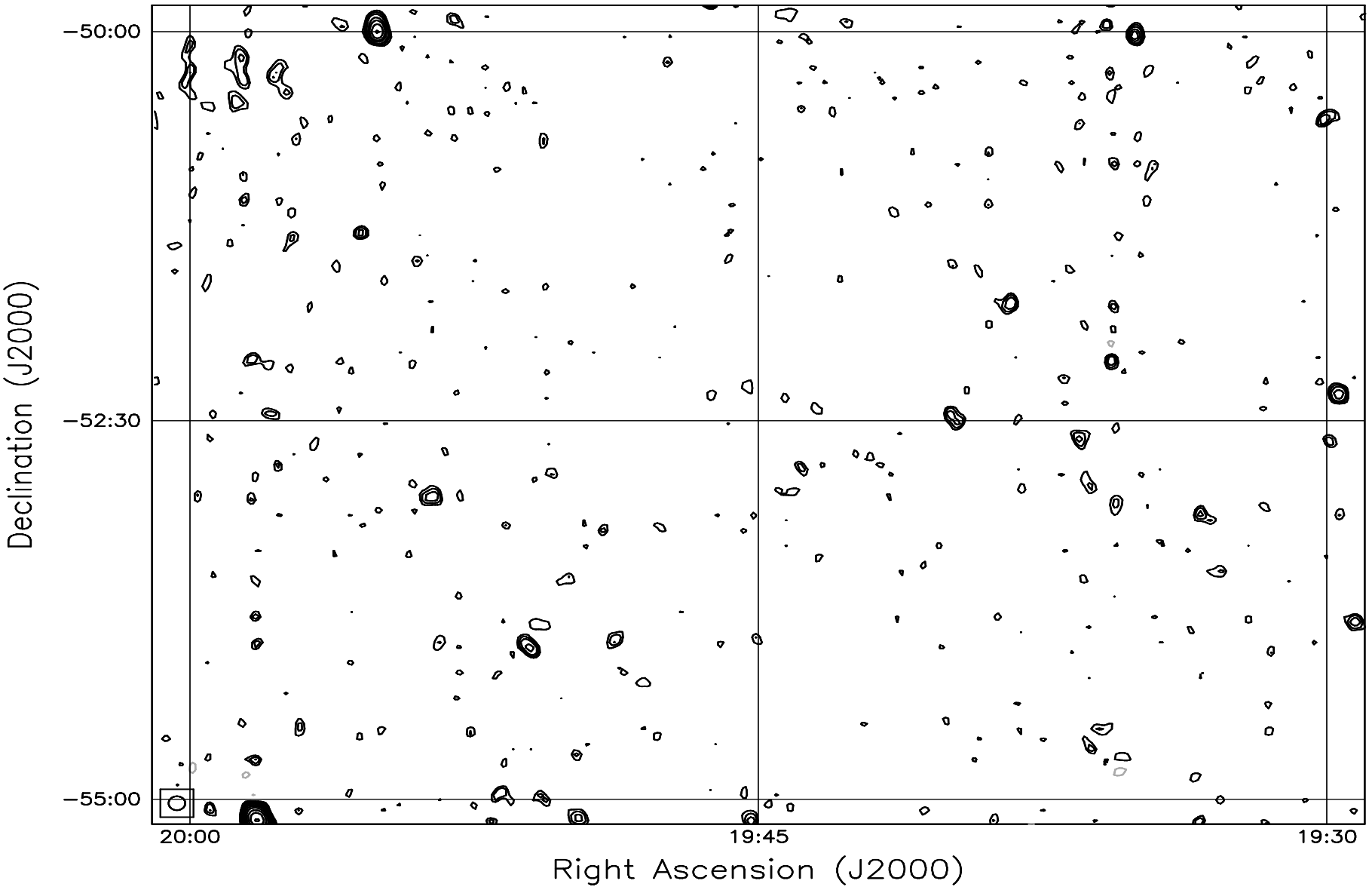

Fig. 7.95: Contour map covering the right ascension range 19h30m to 20h00m and declination range -55° to -50 °. The contour levels are -5, -3.6, -2.5, -1.8, 1, 1.4, 2, 2.8, 3.6, 5, 7, 10, 14, 20, 29, 40, 54, 72, 90, 100, 136, 180, 216, 252, 288 Jy beam^{-1}. The rms noise in the image is ≈370 mJy beam^{-1}.

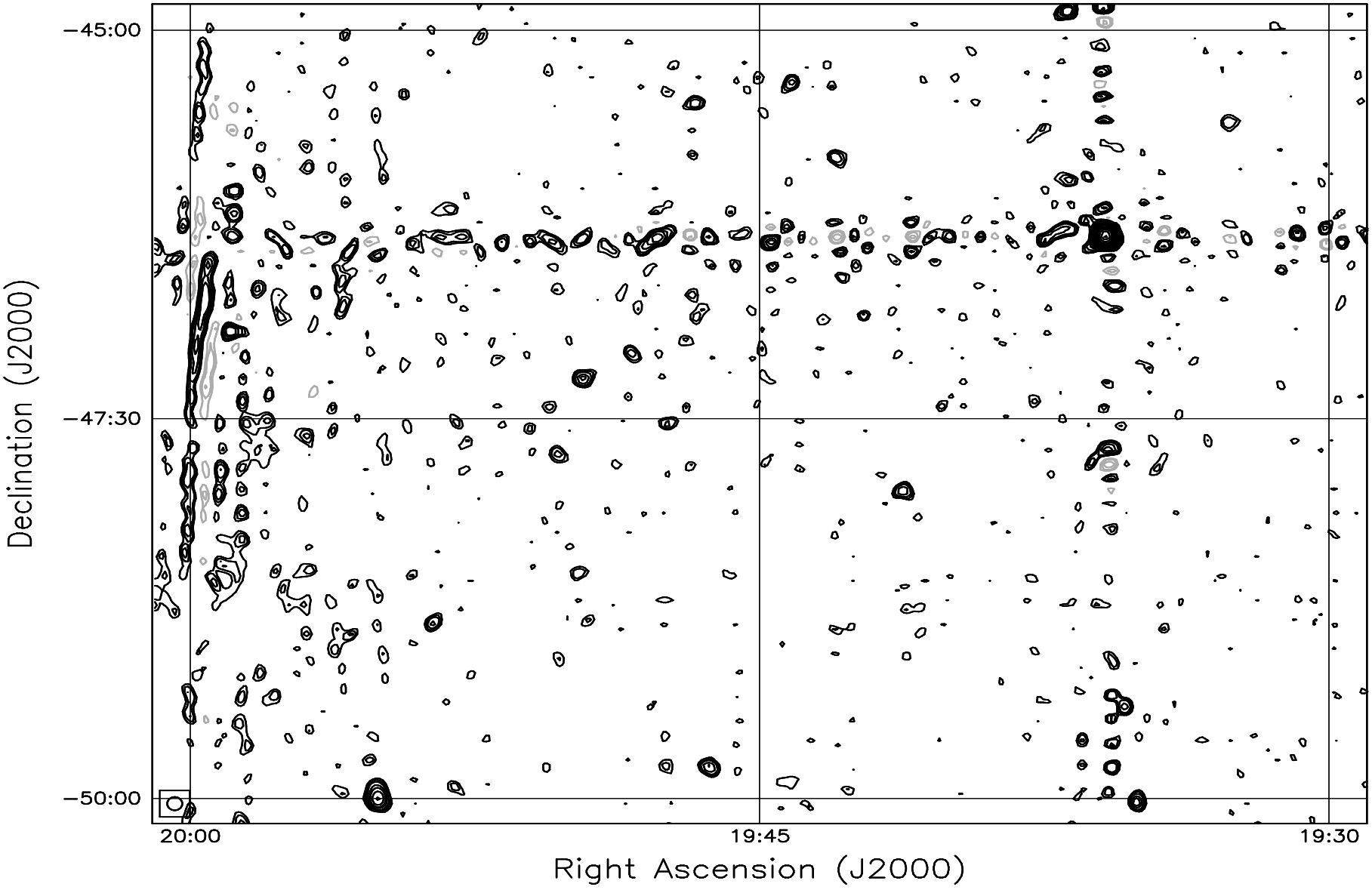

Fig. 7.96: Contour map covering the right ascension range 19h30m to 20h00m and declination range -50° to -45 °. The contour levels are -5, -3.6, -2.5, -1.8, 1, 1.4, 2, 2.8, 3.6, 5, 7, 10, 14, 20, 29, 40, 54, 72, 90, 100, 136, 180, 216, 252, 288 Jy beam^{-1}. The rms noise in the image is ≈360 mJy beam^{-1}.

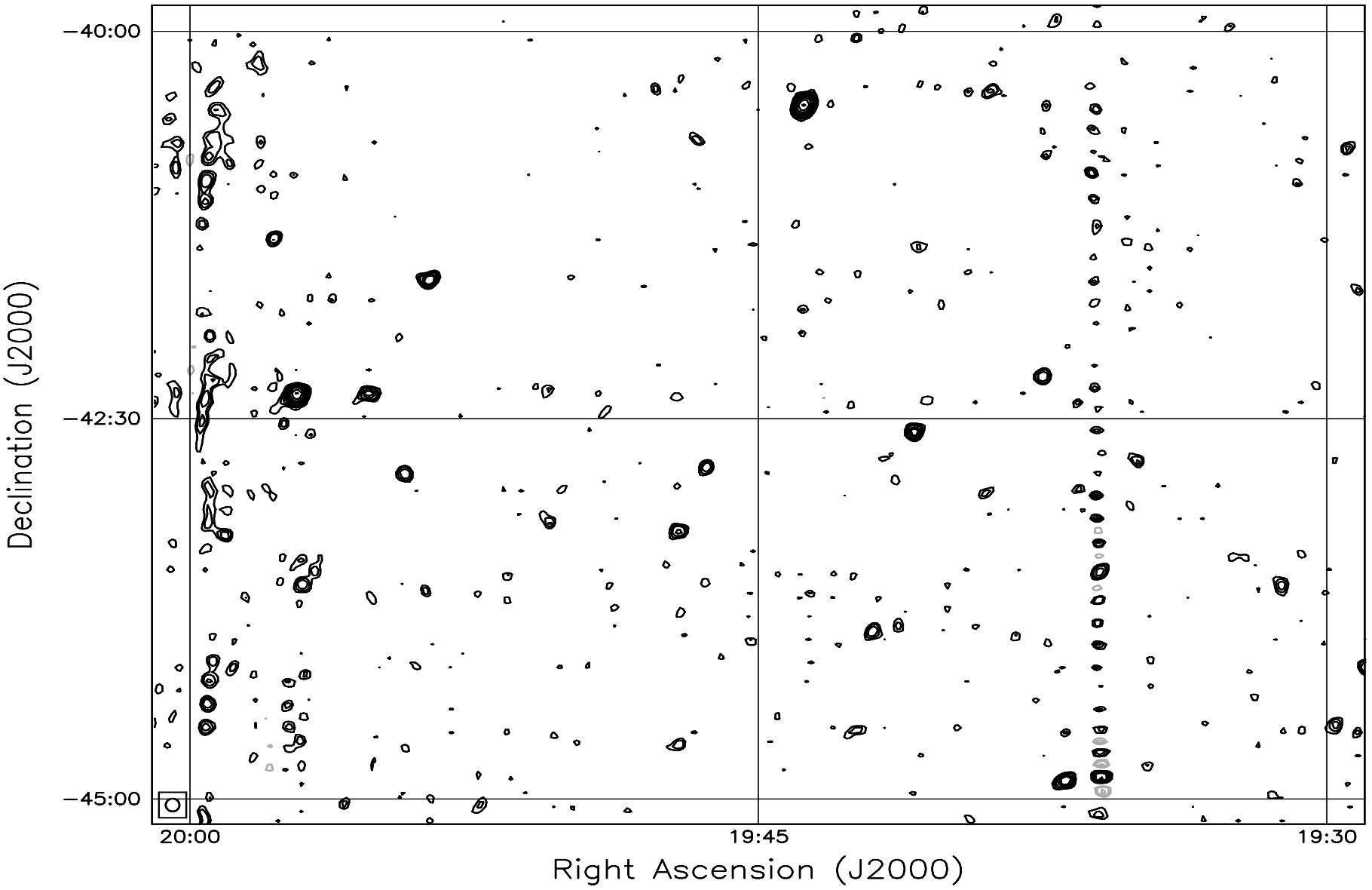

Fig. 7.97: Contour map covering the right ascension range 19h30m to 20h00m and declination range -45° to -40 °. The contour levels are -5, -3.6, -2.5, -1.8, 1, 1.4, 2, 2.8, 3.6, 5, 7, 10, 14, 20, 29, 40, 54, 72, 90, 100, 136, 180, 216, 252, 288 Jy beam^{-1}. The rms noise in the image is ≈360 mJy beam^{-1}.

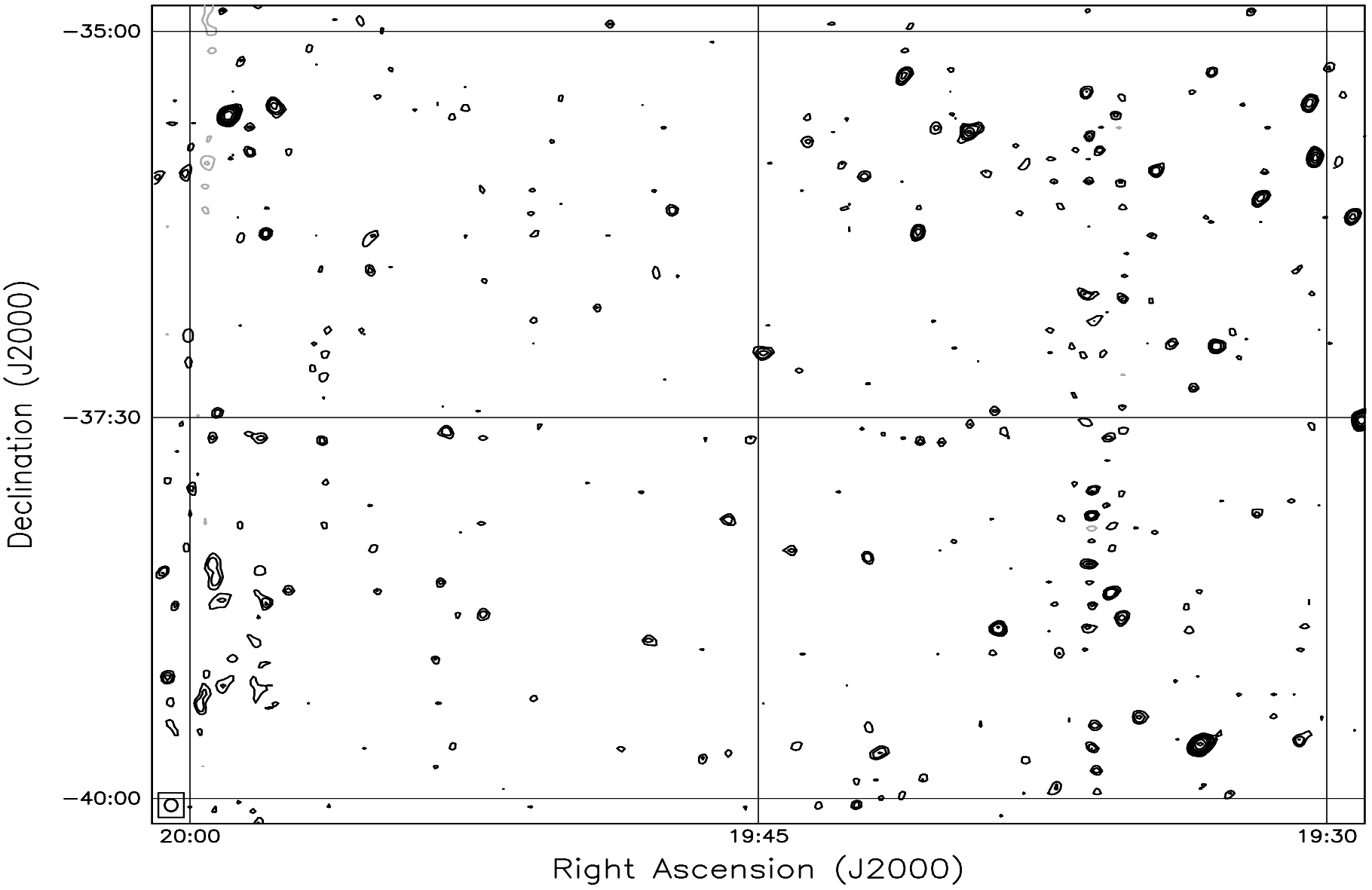

Fig. 7.98: Contour map covering the right ascension range 19h30m to 20h00m and declination range -40° to -35 °. The contour levels are -5, -3.6, -2.5, -1.8, 1, 1.4, 2, 2.8, 3.6, 5, 7, 10, 14, 20, 29, 40, 54, 72, 90, 100, 136, 180, 216, 252, 288 Jy beam^{-1}. The rms noise in the image is ≈370 mJy beam^{-1}.

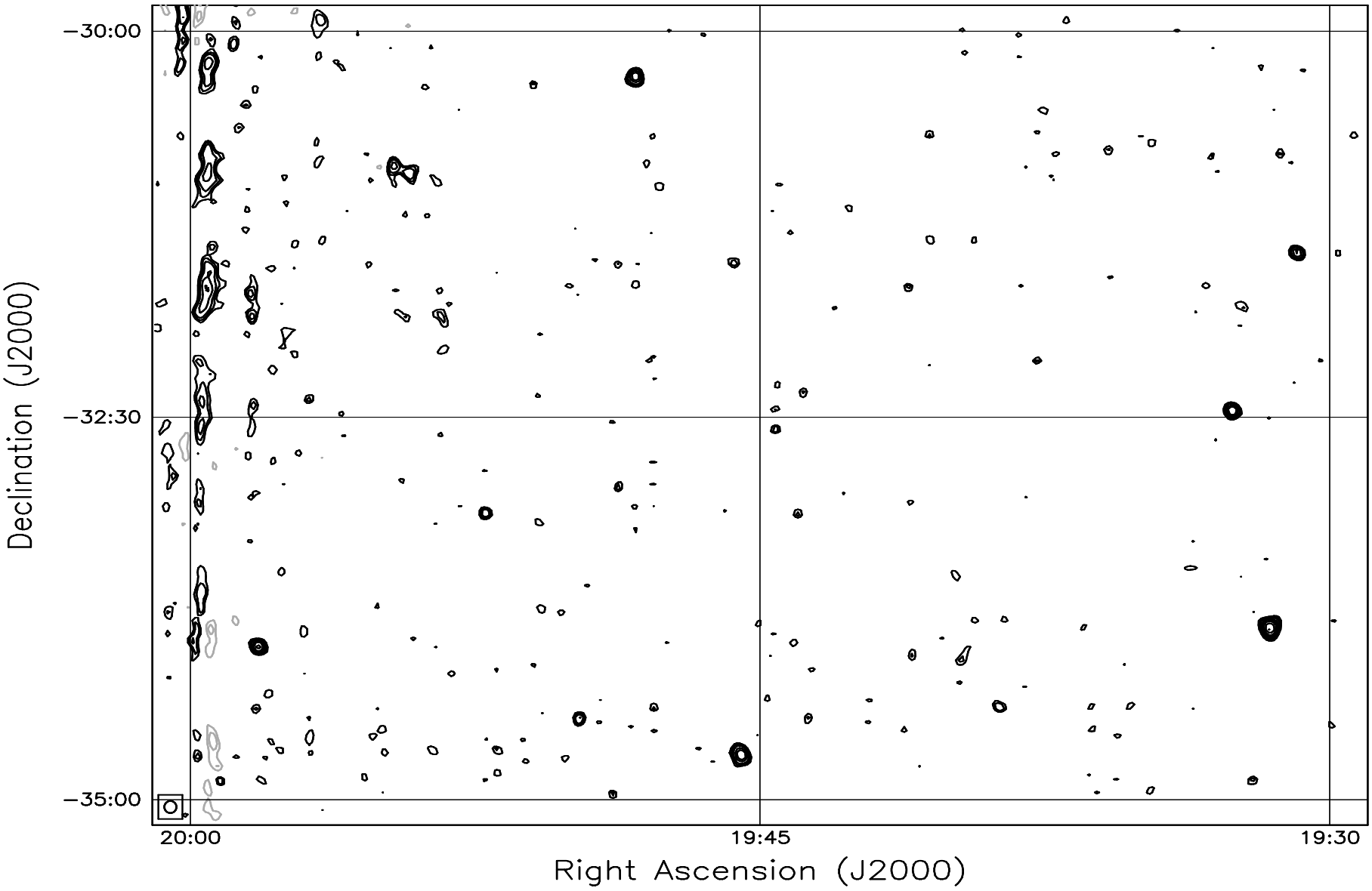

Fig. 7.99: Contour map covering the right ascension range 19h30m to 20h00m and declination range -35° to -30 °. The contour levels are -5, -3.6, -2.5, -1.8, 1, 1.4, 2, 2.8, 3.6, 5, 7, 10, 14, 20, 29, 40, 54, 72, 90, 100, 136, 180, 216, 252, 288 Jy beam^{-1}. The rms noise in the image is ≈385 mJy beam^{-1}.

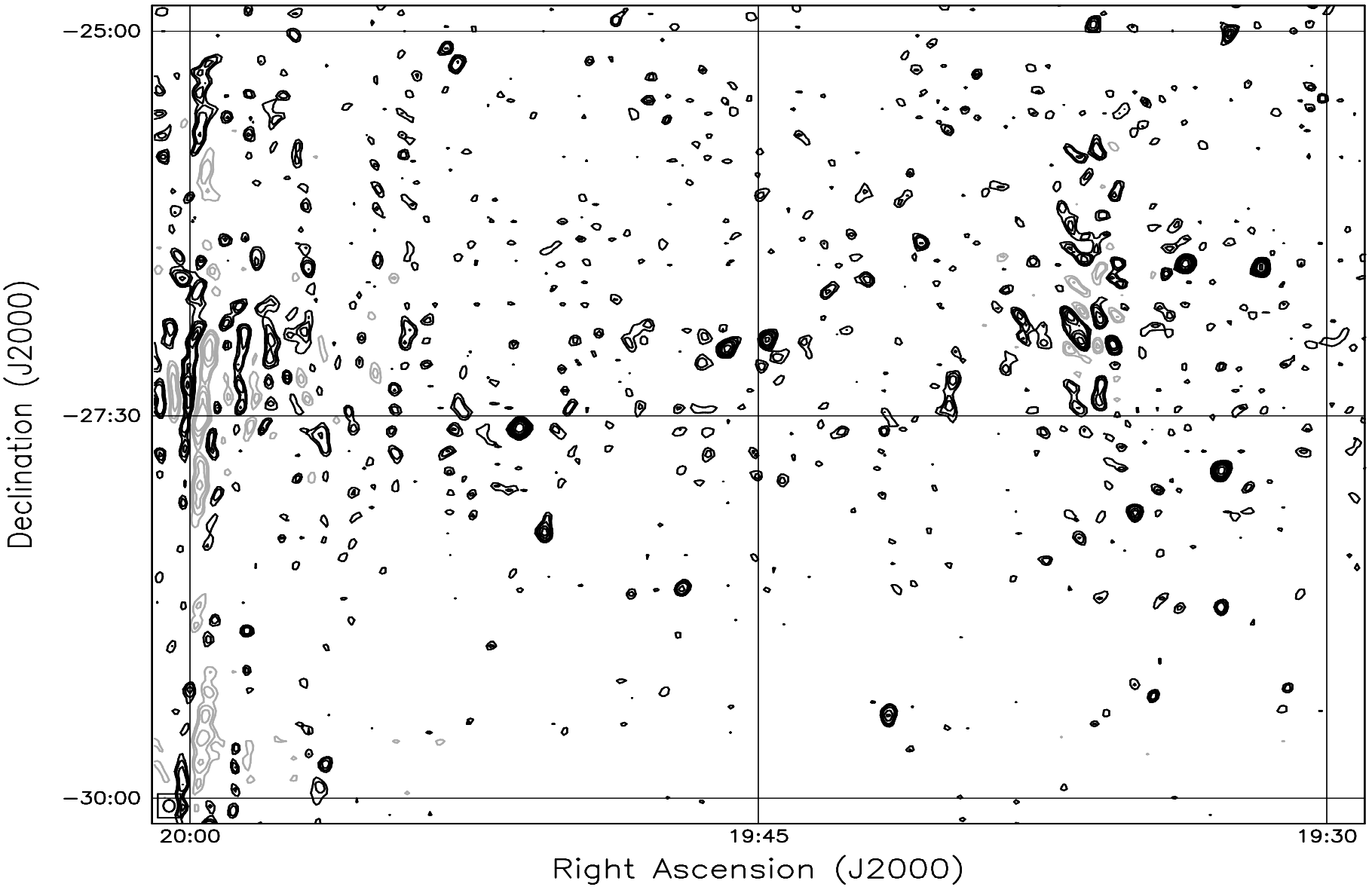

Fig. 7.100: Contour map covering the right ascension range 19h30m to 20h00m and declination range -30° to -25 °. The contour levels are -5, -3.6, -2.5, -1.8, 1, 1.4, 2, 2.8, 3.6, 5, 7, 10, 14, 20, 29, 40, 54, 72, 90, 100, 136, 180, 216, 252, 288 Jy beam^{-1}. The rms noise in the image is ≈410 mJy beam^{-1}.

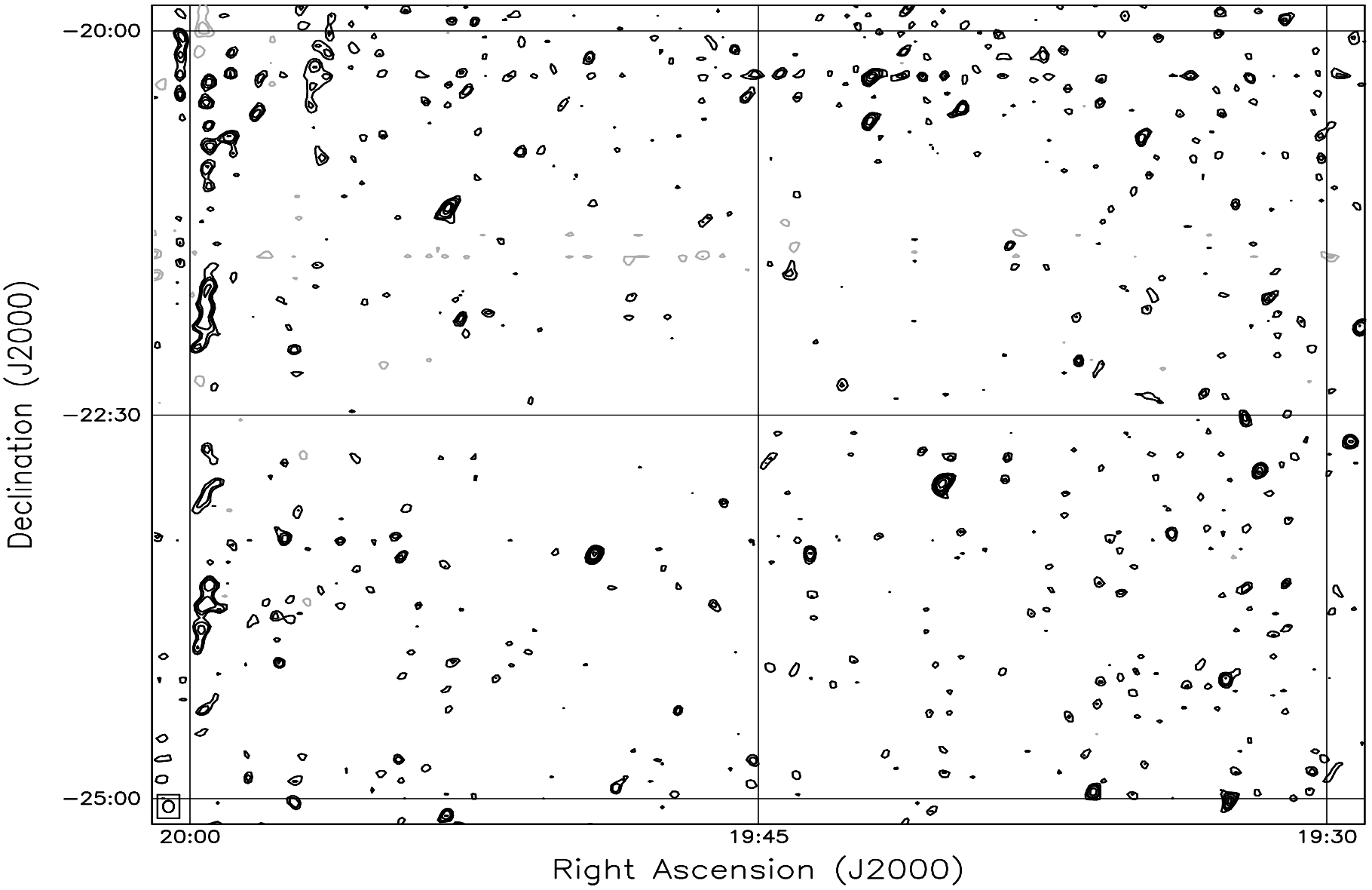

Fig. 7.101: Contour map covering the right ascension range 19h30m to 20h00m and declination range -25° to -20 °. The contour levels are -5, -3.6, -2.5, -1.8, 1, 1.4, 2, 2.8, 3.6, 5, 7, 10, 14, 20, 29, 40, 54, 72, 90, 100, 136, 180, 216, 252, 288 Jy beam^{-1}. The rms noise in the image is ≈450 mJy beam^{-1}.

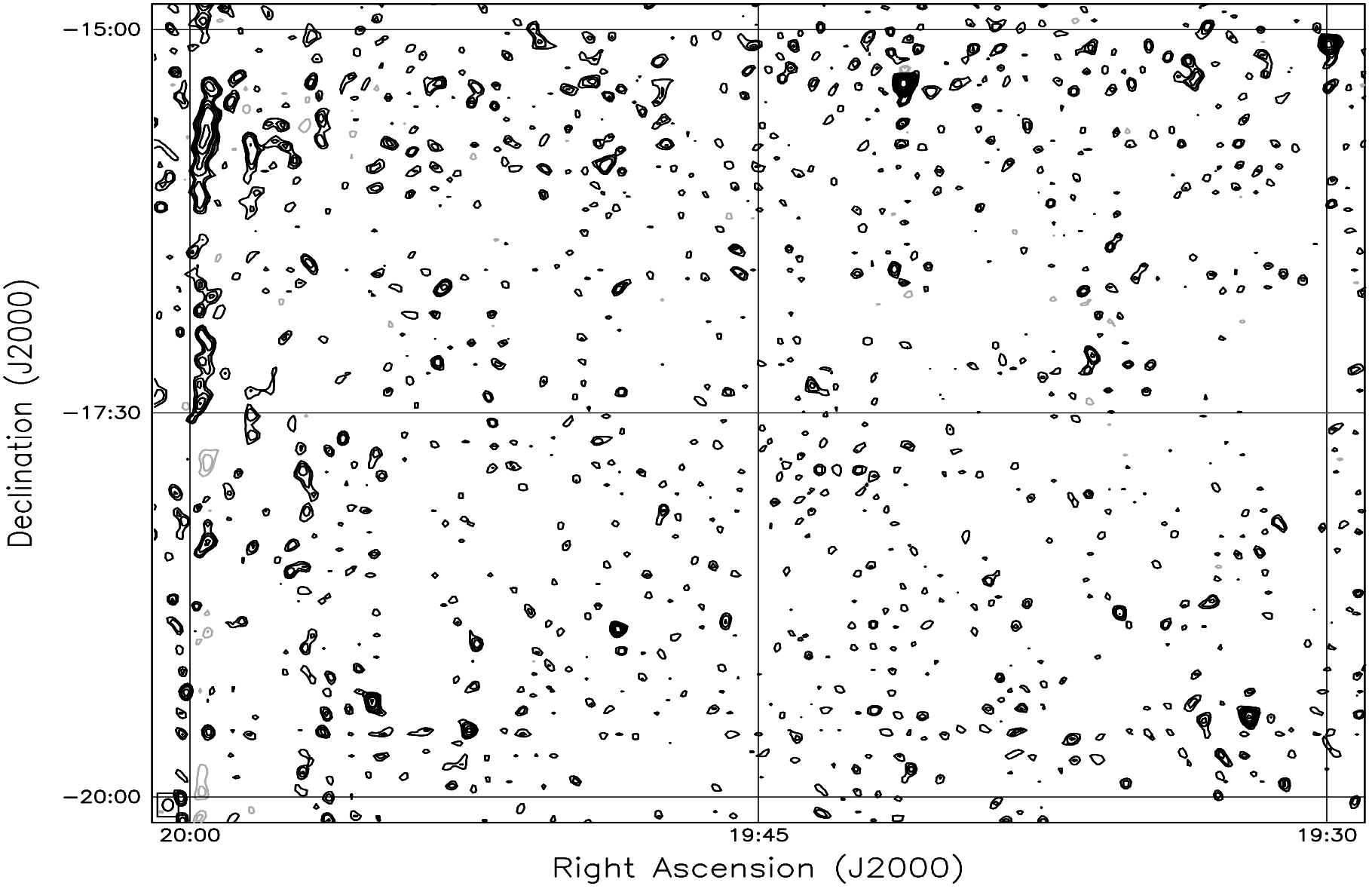

Fig. 7.102: Contour map covering the right ascension range 19h30m to 20h00m and declination range -20° to -15 °. The contour levels are -5, -3.6, -2.5, -1.8, 1, 1.4, 2, 2.8, 3.6, 5, 7, 10, 14, 20, 29, 40, 54, 72, 90, 100, 136, 180, 216, 252, 288 Jy beam^{-1}. The rms noise in the image is ≈520 mJy beam^{-1}.

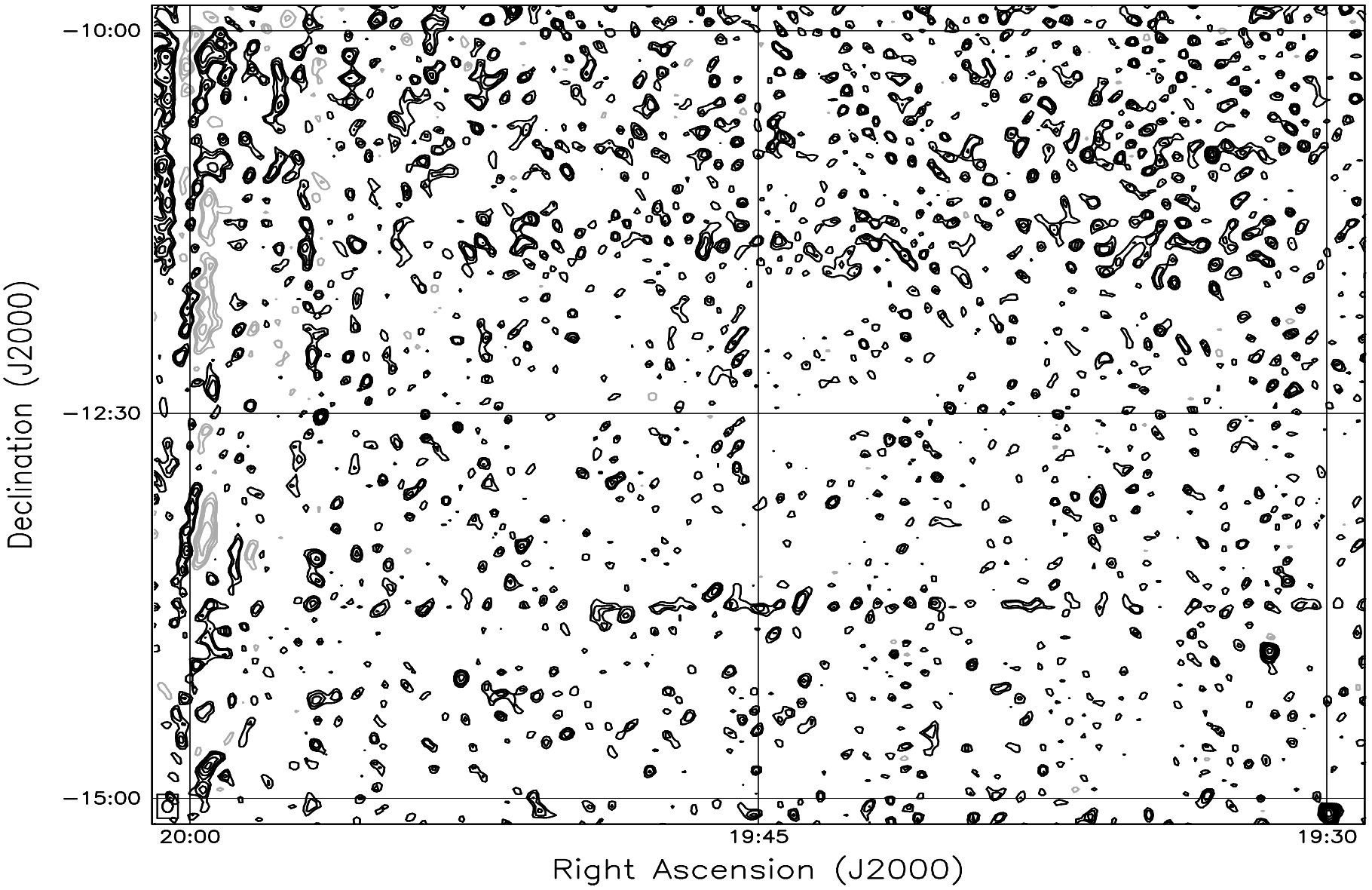

Fig. 7.103: Contour map covering the right ascension range 19h30m to 20h00m and declination range -15° to -10 °. The contour levels are -5, -3.6, -2.5, -1.8, 1, 1.4, 2, 2.8, 3.6, 5, 7, 10, 14, 20, 29, 40, 54, 72, 90, 100, 136, 180, 216, 252, 288 Jy beam^{-1}. The rms noise in the image is ≈630 mJy beam^{-1}.

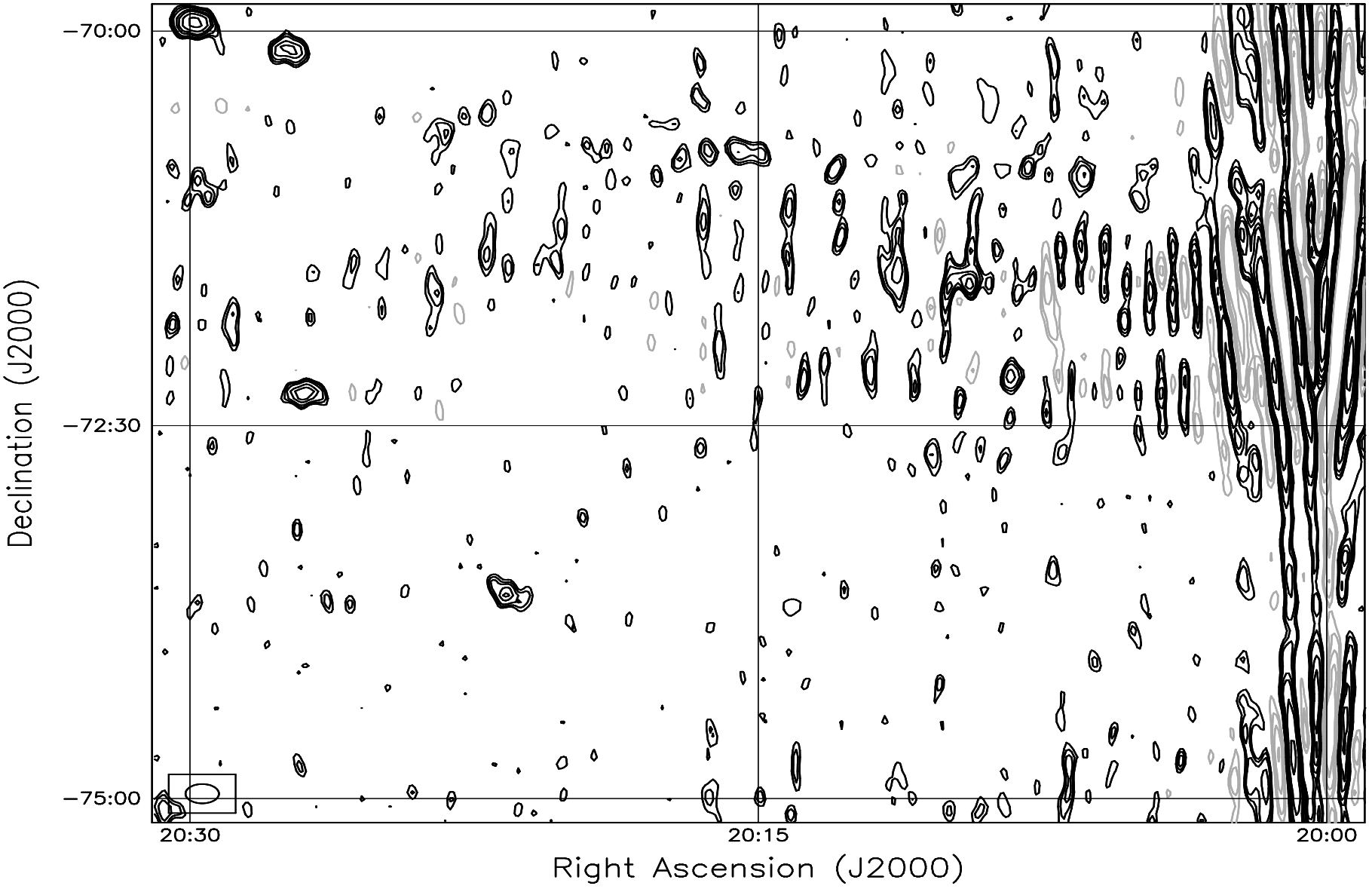

Fig. 7.104: Contour map covering the right ascension range 20h00m to 20h30m and declination range -75° to -70 °. The contour levels are -5, -3.6, -2.5, -1.8, 1, 1.4, 2, 2.8, 3.6, 5, 7, 10, 14, 20, 29, 40, 54, 72, 90, 100, 136, 180, 216, 252, 288 Jy beam^{-1}. The rms noise in the image is ≈380 mJy beam^{-1}.

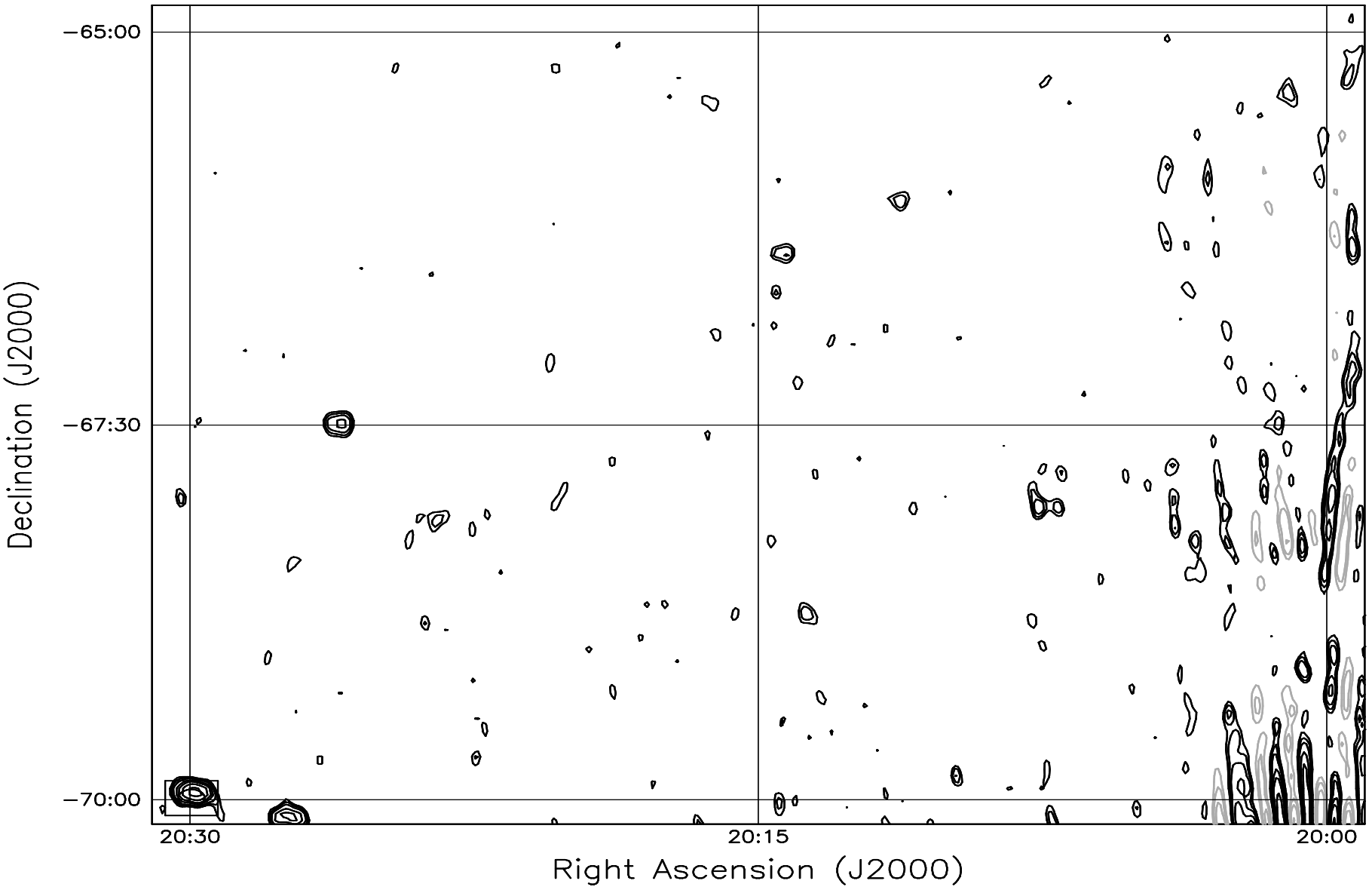

Fig. 7.105: Contour map covering the right ascension range 20h00m to 20h30m and declination range -70° to -65 °. The contour levels are -5, -3.6, -2.5, -1.8, 1, 1.4, 2, 2.8, 3.6, 5, 7, 10, 14, 20, 29, 40, 54, 72, 90, 100, 136, 180, 216, 252, 288 Jy beam^{-1}. The rms noise in the image is ≈330 mJy beam^{-1}.

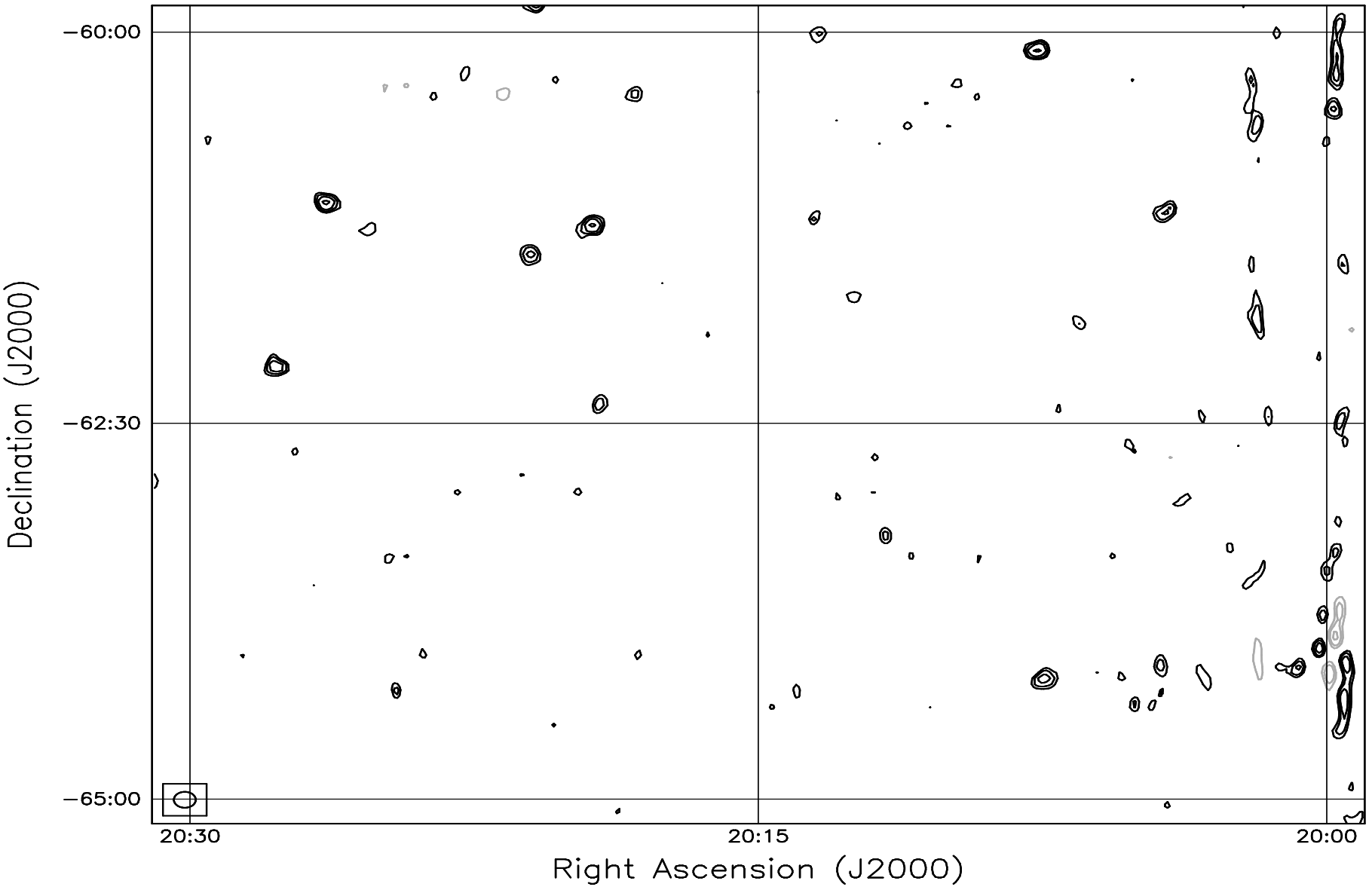

Fig. 7.106: Contour map covering the right ascension range 20h00m to 20h30m and declination range -65° to -60 °. The contour levels are -5, -3.6, -2.5, -1.8, 1, 1.4, 2, 2.8, 3.6, 5, 7, 10, 14, 20, 29, 40, 54, 72, 90, 100, 136, 180, 216, 252, 288 Jy beam^{-1}. The rms noise in the image is ≈300 mJy beam^{-1}.

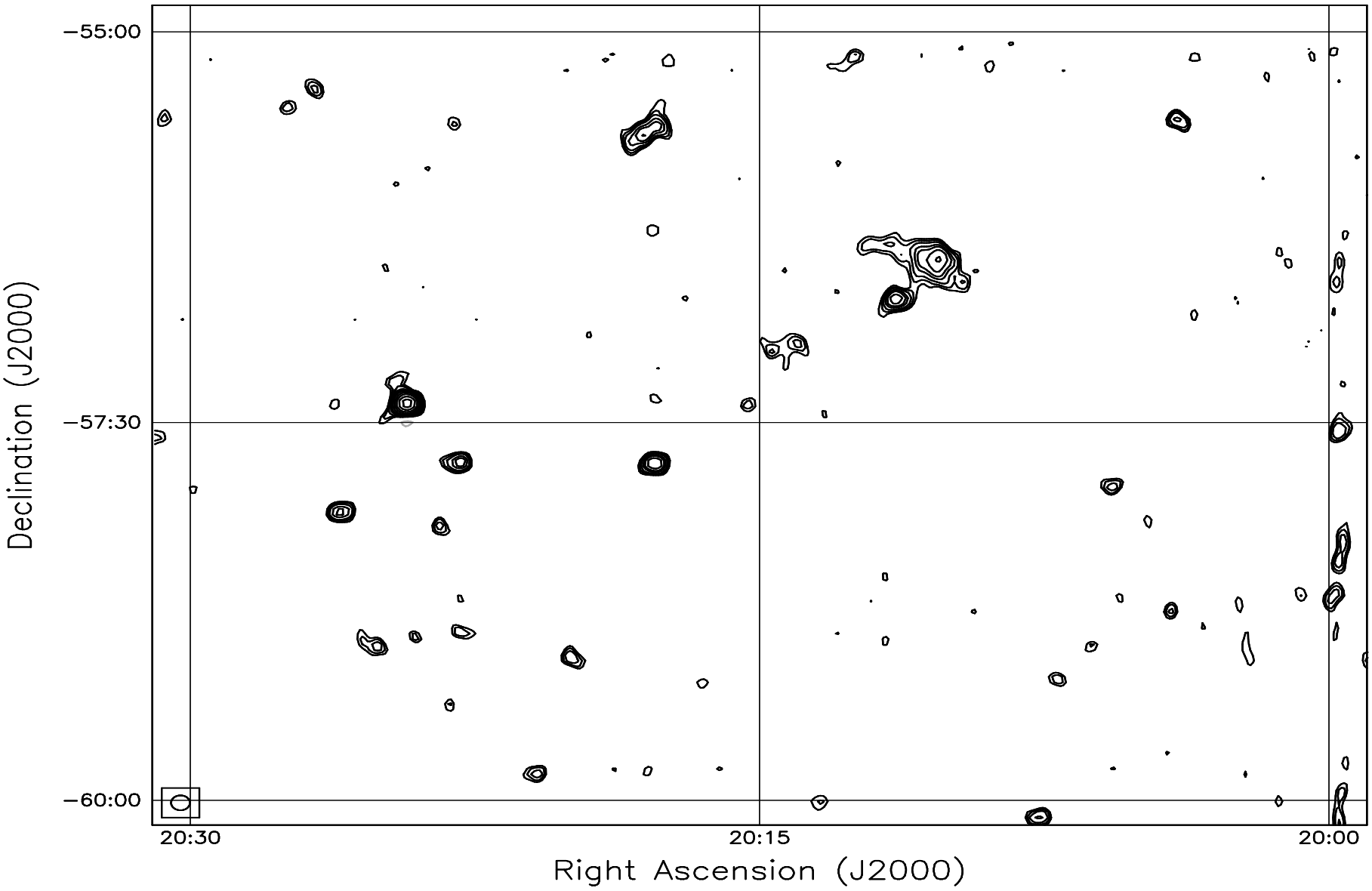

Fig. 7.107: Contour map covering the right ascension range 20h00m to 20h30m and declination range -60° to -55 °. The contour levels are -5, -3.6, -2.5, -1.8, 1, 1.4, 2, 2.8, 3.6, 5, 7, 10, 14, 20, 29, 40, 54, 72, 90, 100, 136, 180, 216, 252, 288 Jy beam^{-1}. The rms noise in the image is ≈280 mJy beam^{-1}.

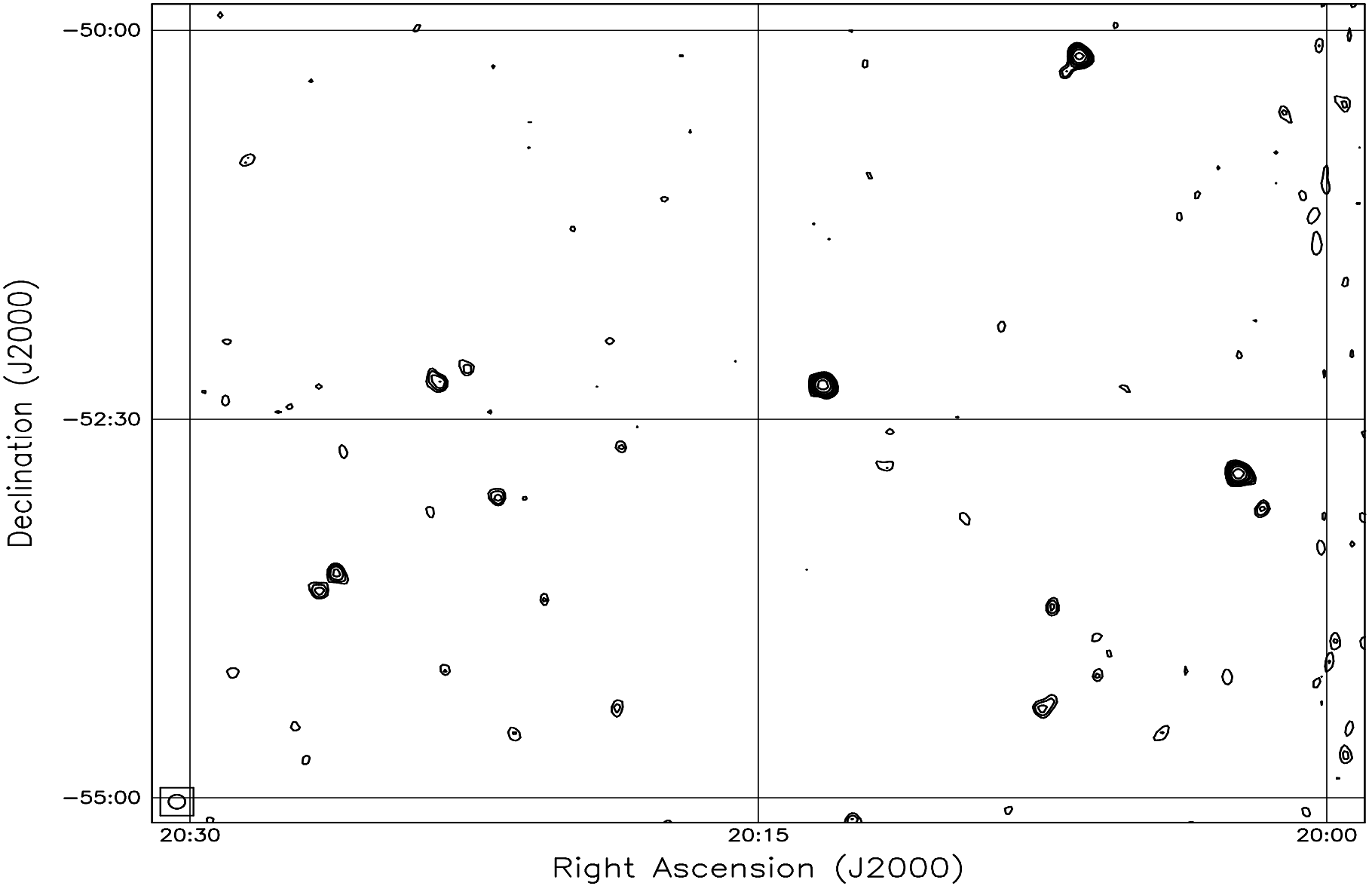

Fig. 7.108: Contour map covering the right ascension range 20h00m to 20h30m and declination range -55° to -50 °. The contour levels are -5, -3.6, -2.5, -1.8, 1, 1.4, 2, 2.8, 3.6, 5, 7, 10, 14, 20, 29, 40, 54, 72, 90, 100, 136, 180, 216, 252, 288 Jy beam^{-1}. The rms noise in the image is ≈270 mJy beam^{-1}.

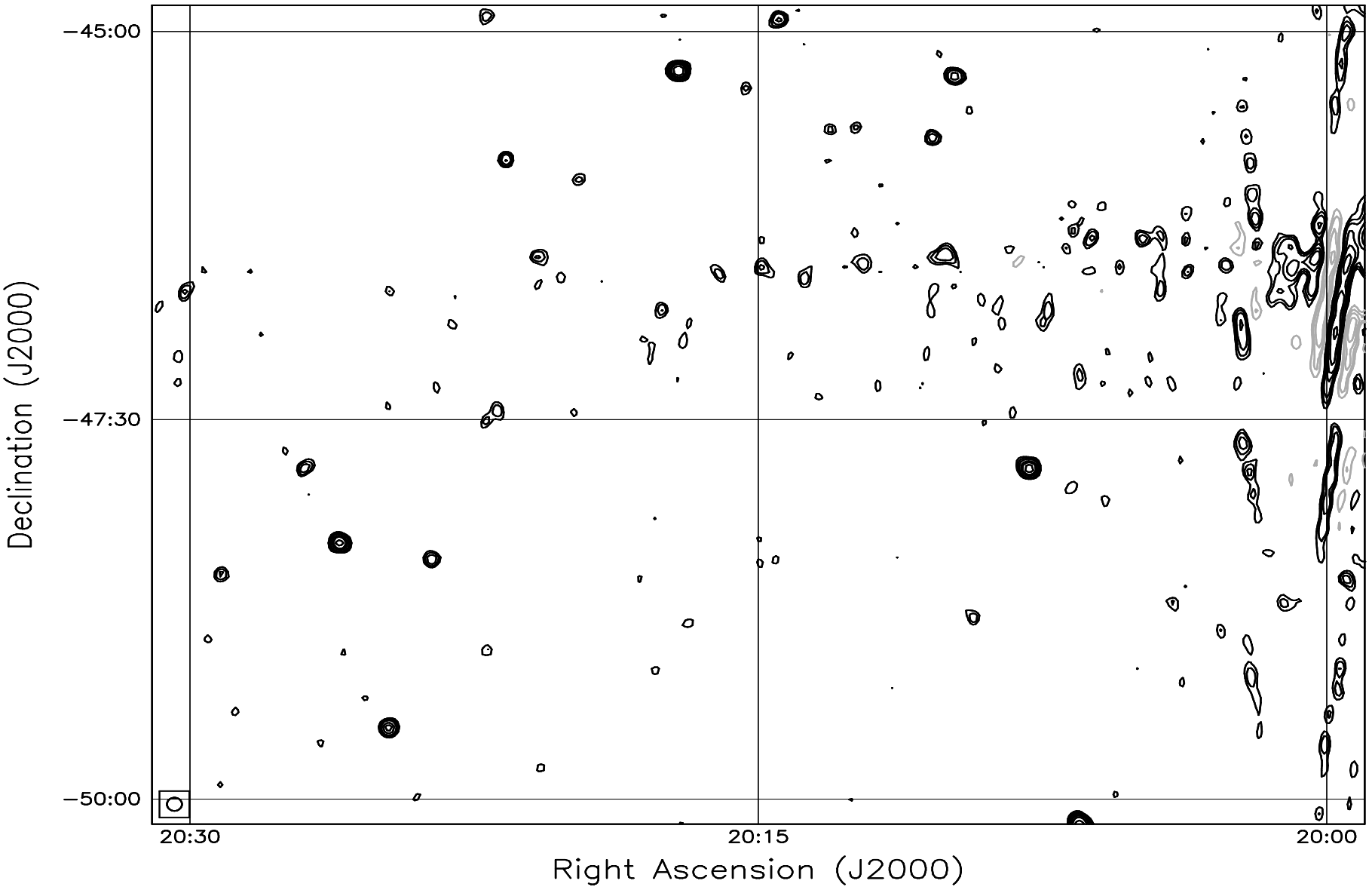

Fig. 7.109: Contour map covering the right ascension range 20h00m to 20h30m and declination range -50° to -45 °. The contour levels are -5, -3.6, -2.5, -1.8, 1, 1.4, 2, 2.8, 3.6, 5, 7, 10, 14, 20, 29, 40, 54, 72, 90, 100, 136, 180, 216, 252, 288 Jy beam^{-1}. The rms noise in the image is ≈260 mJy beam^{-1}.

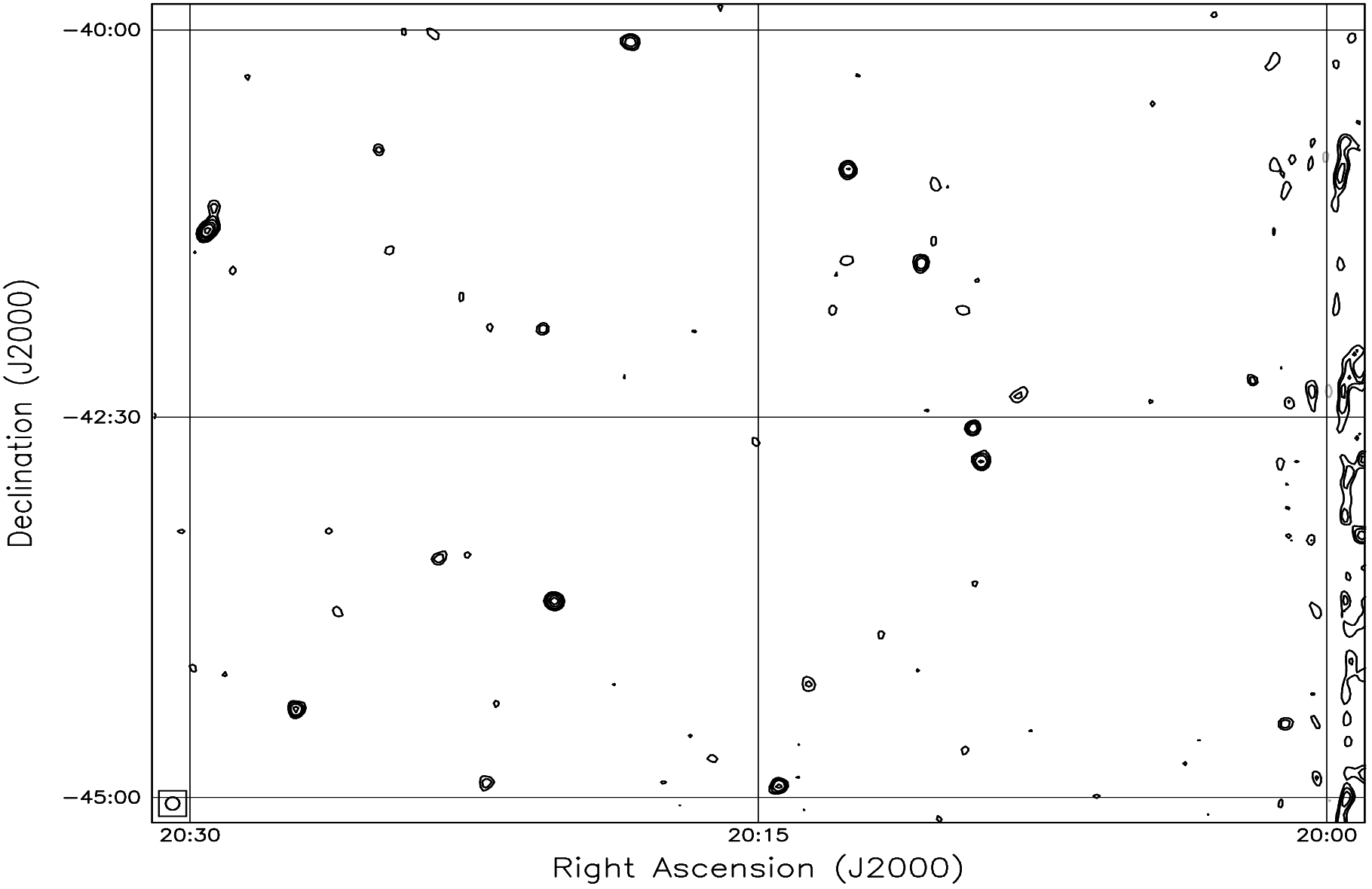

Fig. 7.110: Contour map covering the right ascension range 20h00m to 20h30m and declination range -45° to -40 °. The contour levels are -5, -3.6, -2.5, -1.8, 1, 1.4, 2, 2.8, 3.6, 5, 7, 10, 14, 20, 29, 40, 54, 72, 90, 100, 136, 180, 216, 252, 288 Jy beam^{-1}. The rms noise in the image is ≈260 mJy beam^{-1}.

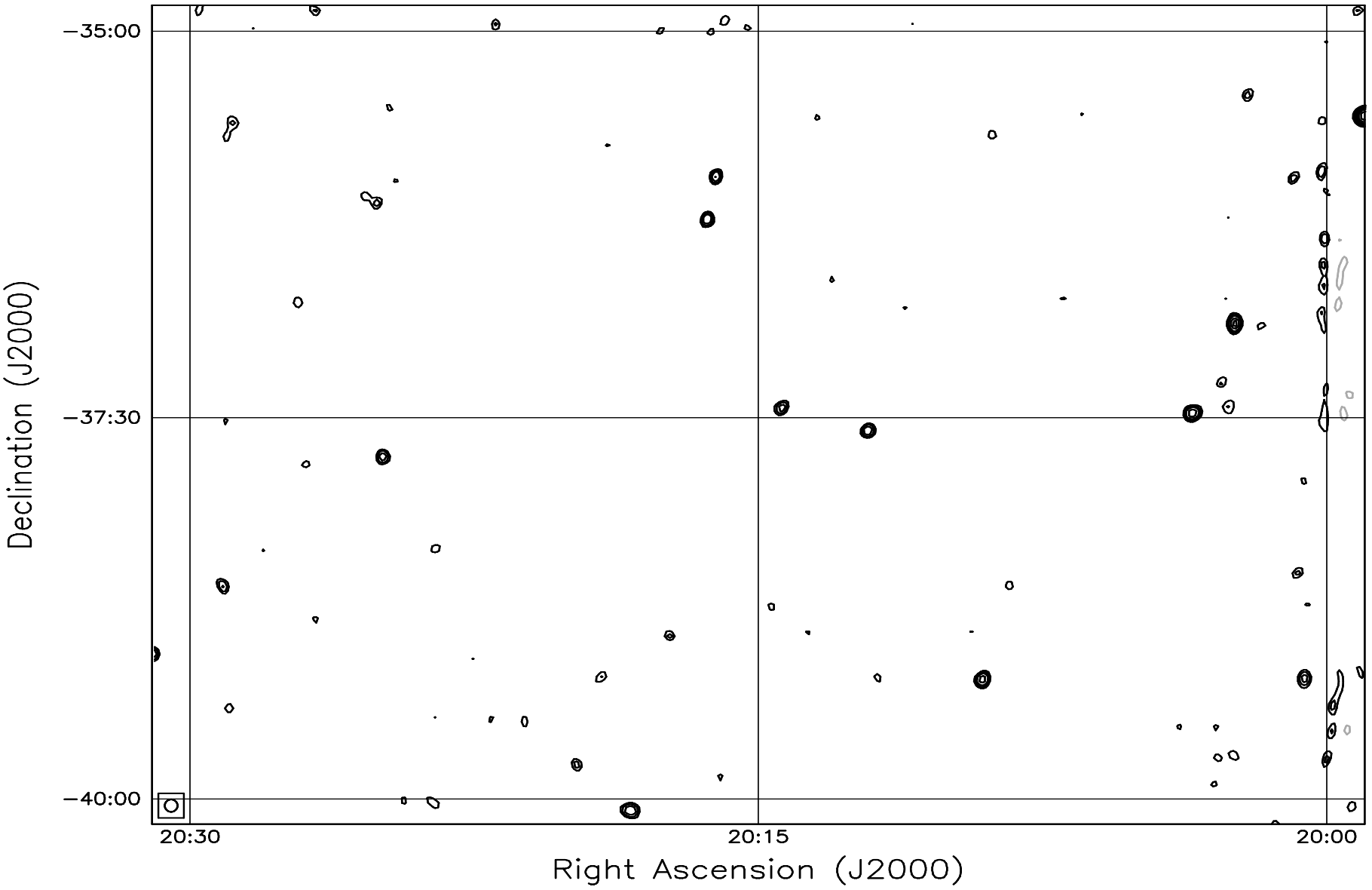

Fig. 7.111: Contour map covering the right ascension range 20h00m to 20h30m and declination range -40° to -35 °. The contour levels are -5, -3.6, -2.5, -1.8, 1, 1.4, 2, 2.8, 3.6, 5, 7, 10, 14, 20, 29, 40, 54, 72, 90, 100, 136, 180, 216, 252, 288 Jy beam^{-1}. The rms noise in the image is ≈270 mJy beam^{-1}.

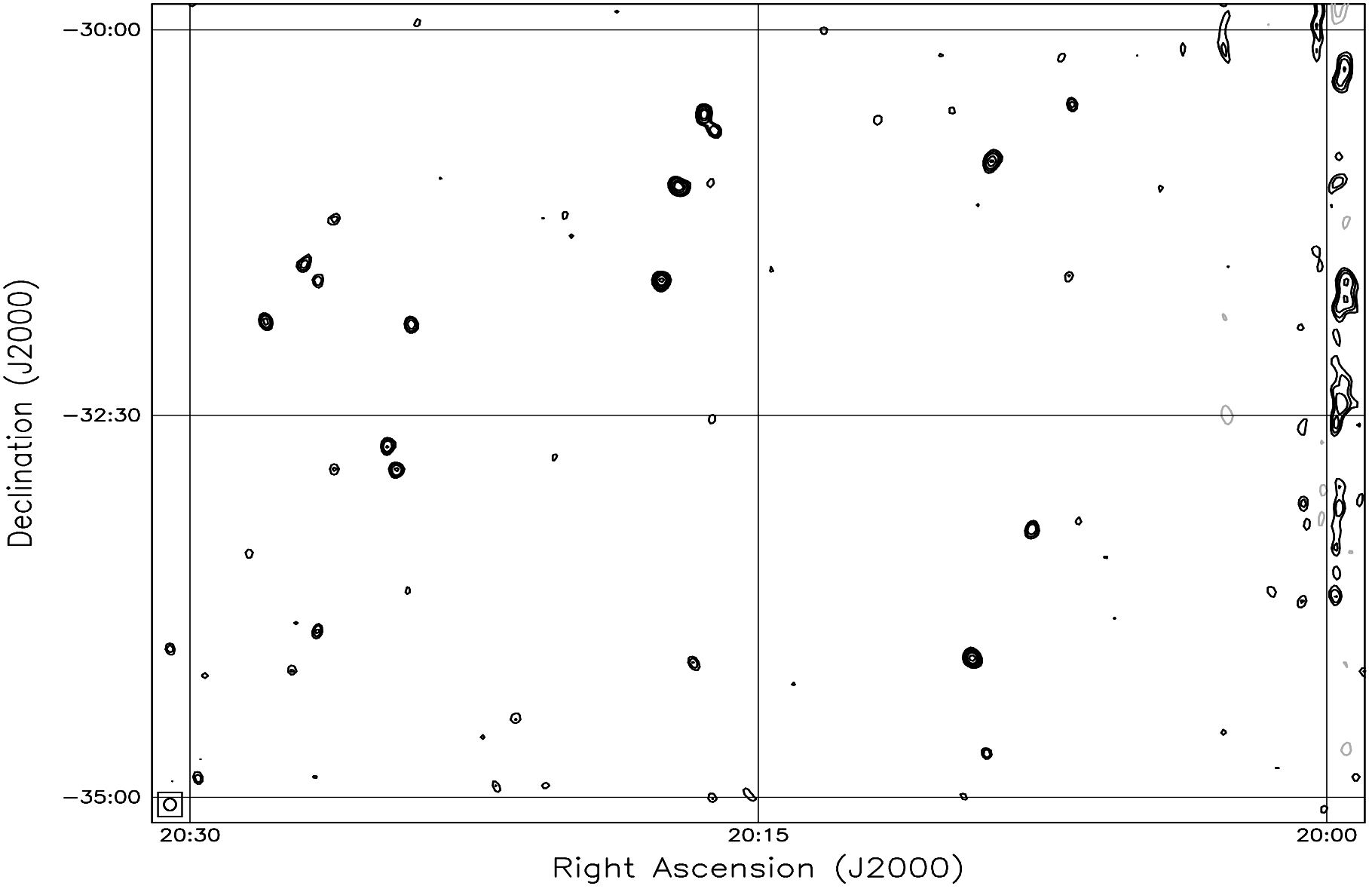

Fig. 7.112: Contour map covering the right ascension range 20h00m to 20h30m and declination range -35° to -30 °. The contour levels are -5, -3.6, -2.5, -1.8, 1, 1.4, 2, 2.8, 3.6, 5, 7, 10, 14, 20, 29, 40, 54, 72, 90, 100, 136, 180, 216, 252, 288 Jy beam^{-1}. The rms noise in the image is ≈280 mJy beam^{-1}.

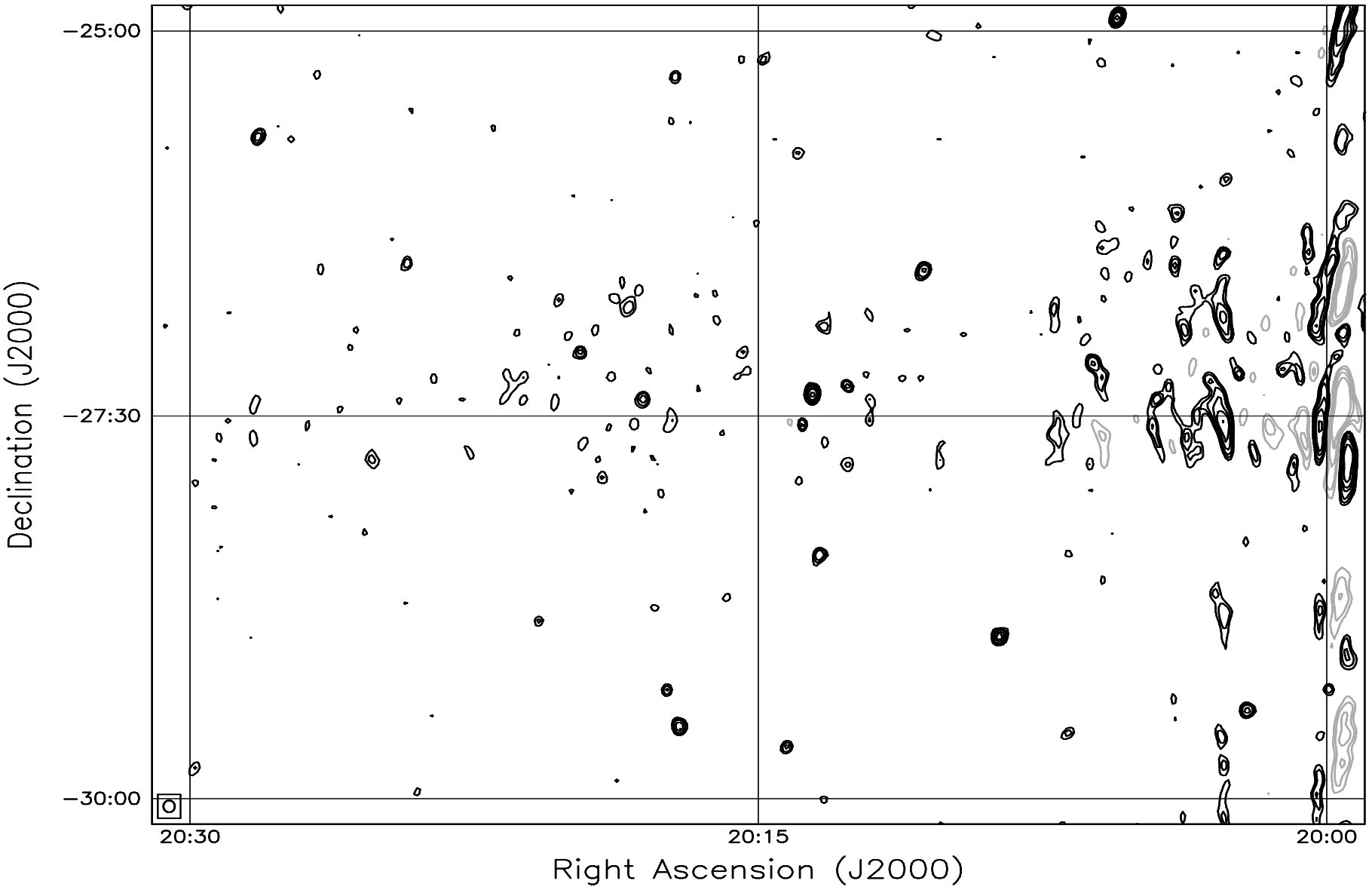

Fig. 7.113: Contour map covering the right ascension range 20h00m to 20h30m and declination range -30° to -25 °. The contour levels are -5, -3.6, -2.5, -1.8, 1, 1.4, 2, 2.8, 3.6, 5, 7, 10, 14, 20, 29, 40, 54, 72, 90, 100, 136, 180, 216, 252, 288 Jy beam^{-1}. The rms noise in the image is ≈300 mJy beam^{-1}.

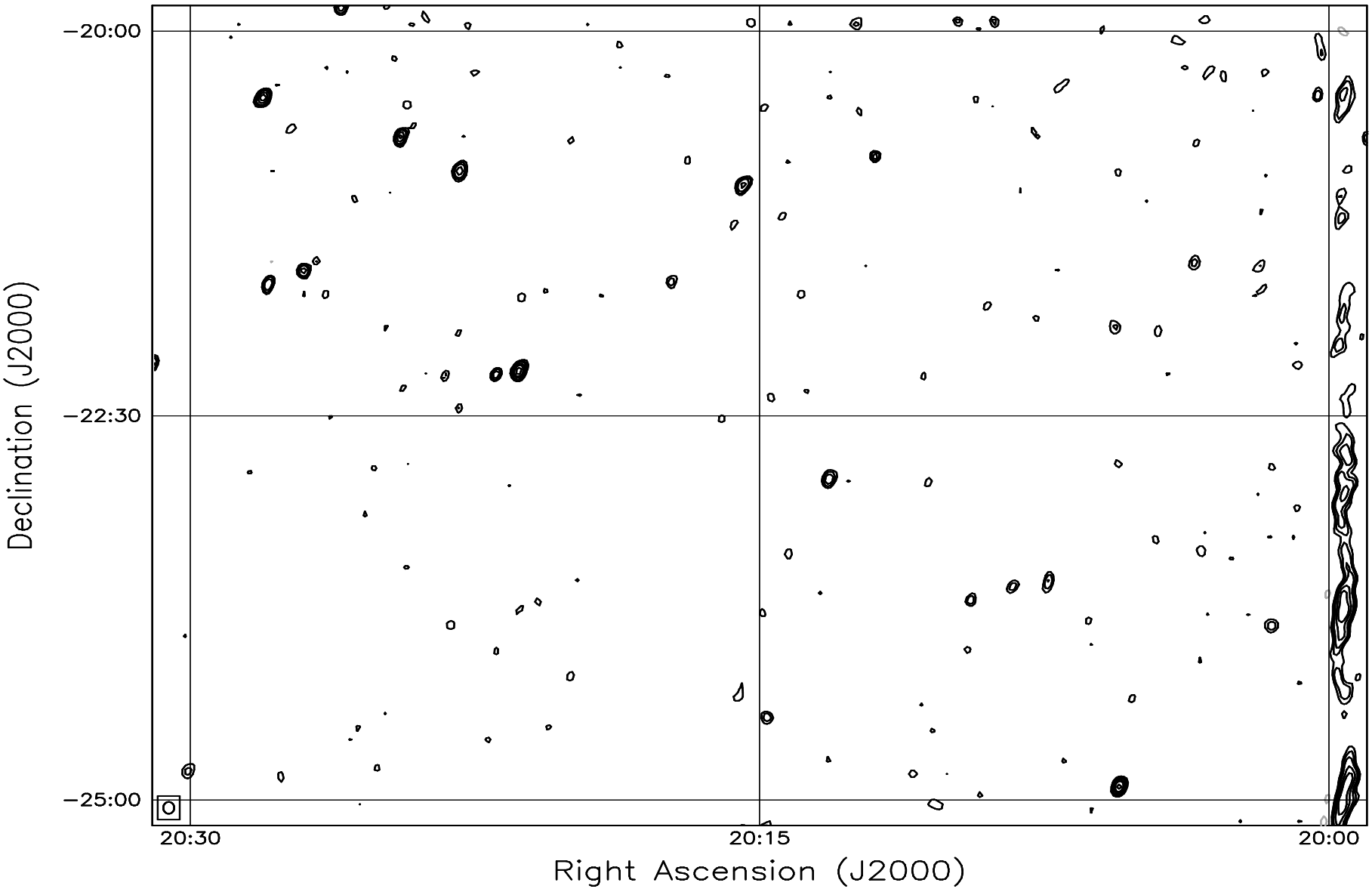

Fig. 7.114: Contour map covering the right ascension range 20h00m to 20h30m and declination range -25° to -20 °. The contour levels are -5, -3.6, -2.5, -1.8, 1, 1.4, 2, 2.8, 3.6, 5, 7, 10, 14, 20, 29, 40, 54, 72, 90, 100, 136, 180, 216, 252, 288 Jy beam^{-1}. The rms noise in the image is ≈330 mJy beam^{-1}.

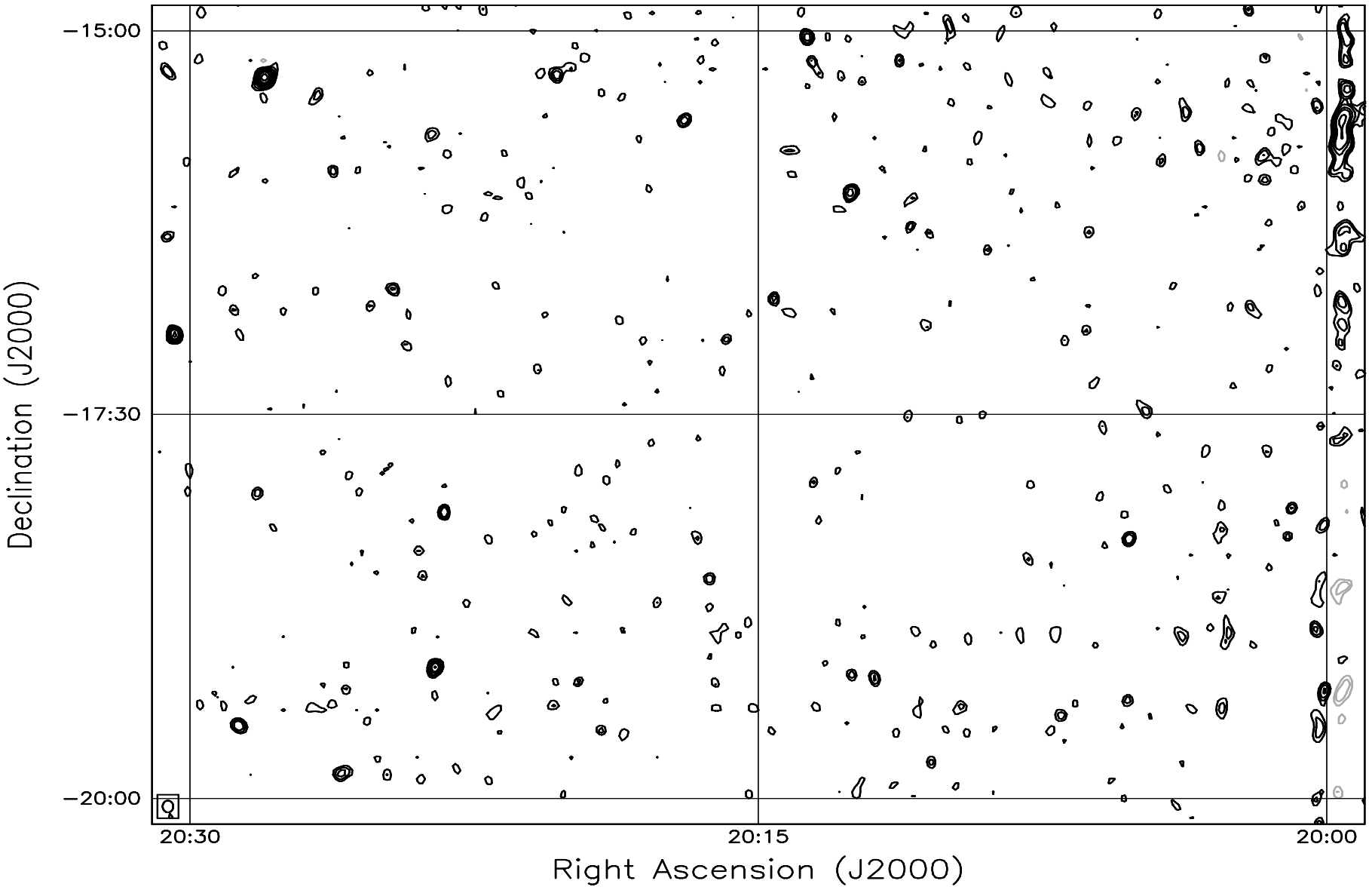

Fig. 7.115: Contour map covering the right ascension range 20h00m to 20h30m and declination range -20° to -15 °. The contour levels are -5, -3.6, -2.5, -1.8, 1, 1.4, 2, 2.8, 3.6, 5, 7, 10, 14, 20, 29, 40, 54, 72, 90, 100, 136, 180, 216, 252, 288 Jy beam^{-1}. The rms noise in the image is ≈375 mJy beam^{-1}.

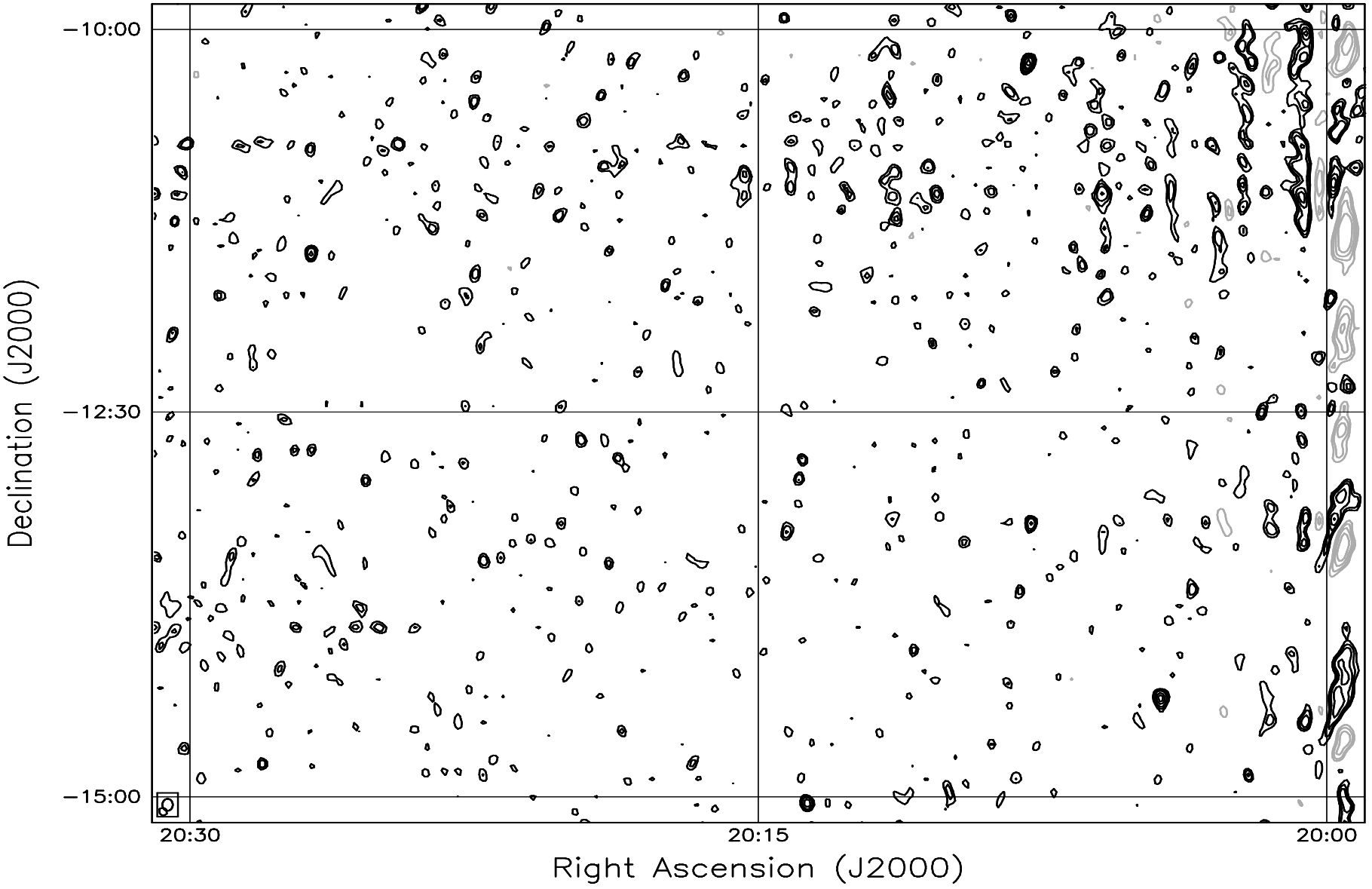

Fig. 7.116: Contour map covering the right ascension range 20h00m to 20h30m and declination range -15° to -10 °. The contour levels are -5, -3.6, -2.5, -1.8, 1, 1.4, 2, 2.8, 3.6, 5, 7, 10, 14, 20, 29, 40, 54, 72, 90, 100, 136, 180, 216, 252, 288 Jy beam^{-1}. The rms noise in the image is ≈460 mJy beam^{-1}.

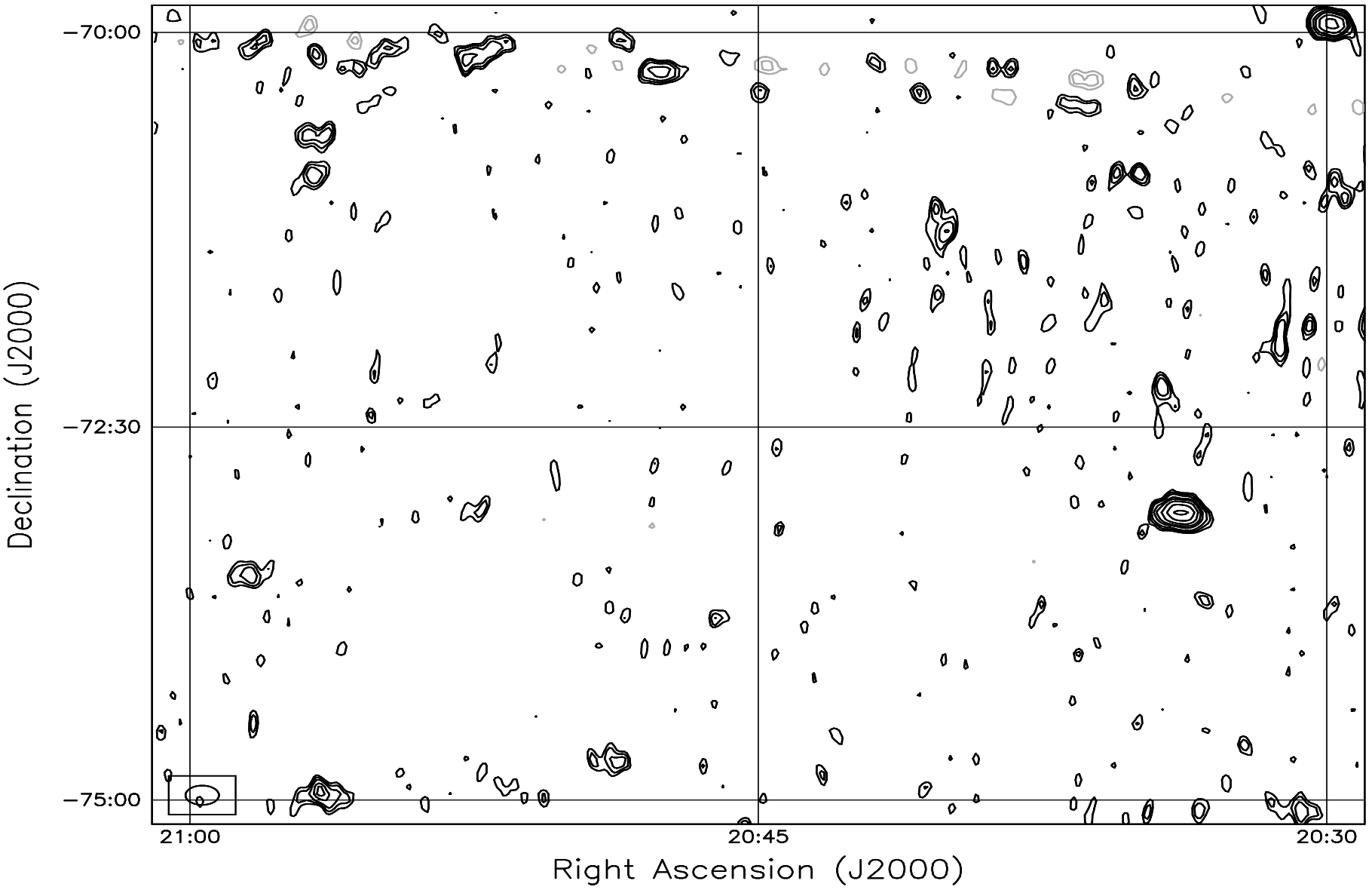

Fig. 7.117: Contour map covering the right ascension range 20h30m to 21h00m and declination range -75° to -70 °. The contour levels are -5, -3.6, -2.5, -1.8, 1, 1.4, 2, 2.8, 3.6, 5, 7, 10, 14, 20, 29, 40, 54, 72, 90, 100, 136, 180, 216, 252, 288 Jy beam^{-1}. The rms noise in the image is ≈380 mJy beam^{-1}.

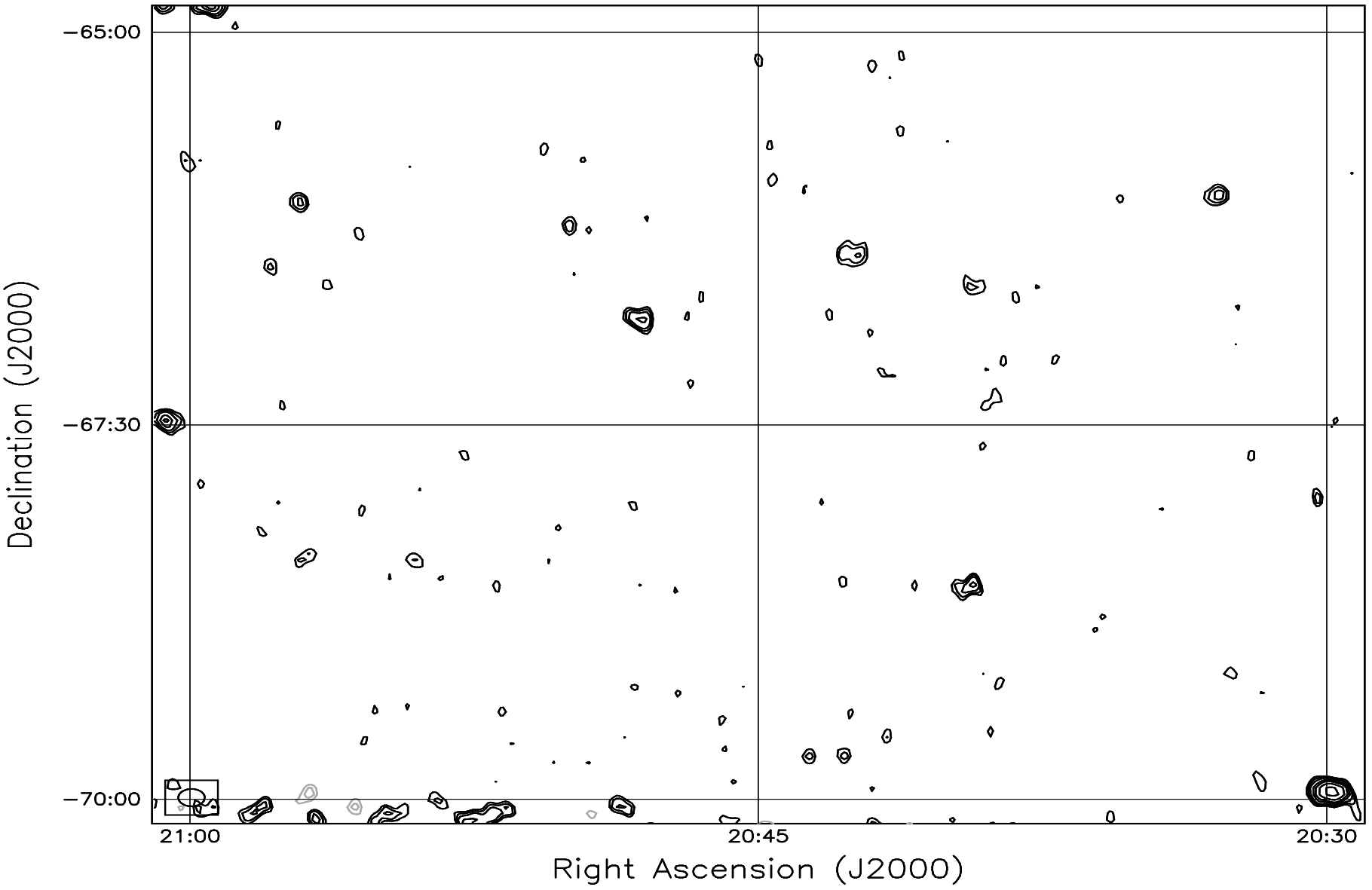

Fig. 7.118: Contour map covering the right ascension range 20h30m to 21h00m and declination range -70° to -65 °. The contour levels are -5, -3.6, -2.5, -1.8, 1, 1.4, 2, 2.8, 3.6, 5, 7, 10, 14, 20, 29, 40, 54, 72, 90, 100, 136, 180, 216, 252, 288 Jy beam^{-1}. The rms noise in the image is ≈330 mJy beam^{-1}.

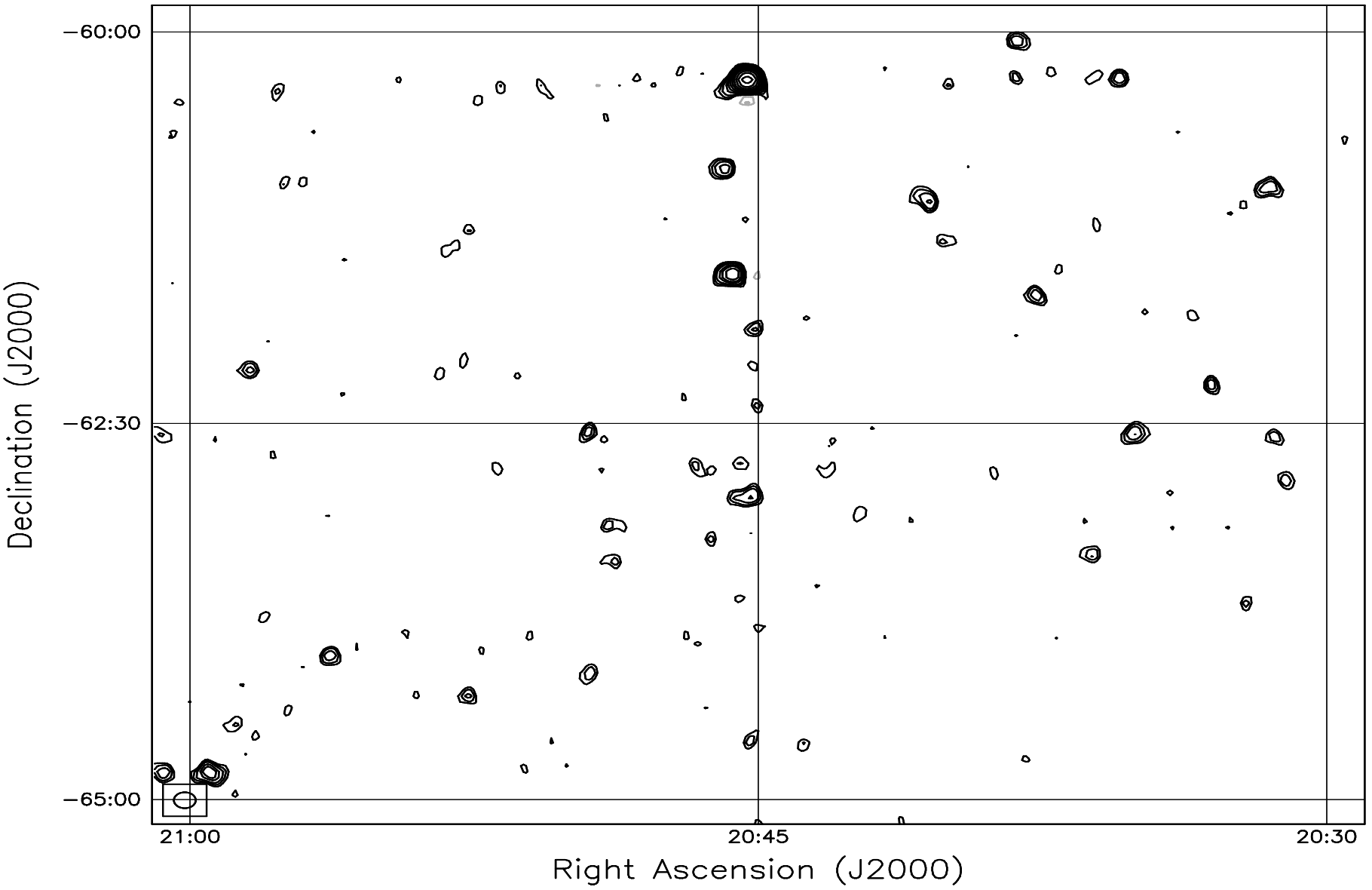

Fig. 7.119: Contour map covering the right ascension range 20h30m to 21h00m and declination range -65° to -60 °. The contour levels are -5, -3.6, -2.5, -1.8, 1, 1.4, 2, 2.8, 3.6, 5, 7, 10, 14, 20, 29, 40, 54, 72, 90, 100, 136, 180, 216, 252, 288 Jy beam^{-1}. The rms noise in the image is ≈300 mJy beam^{-1}.

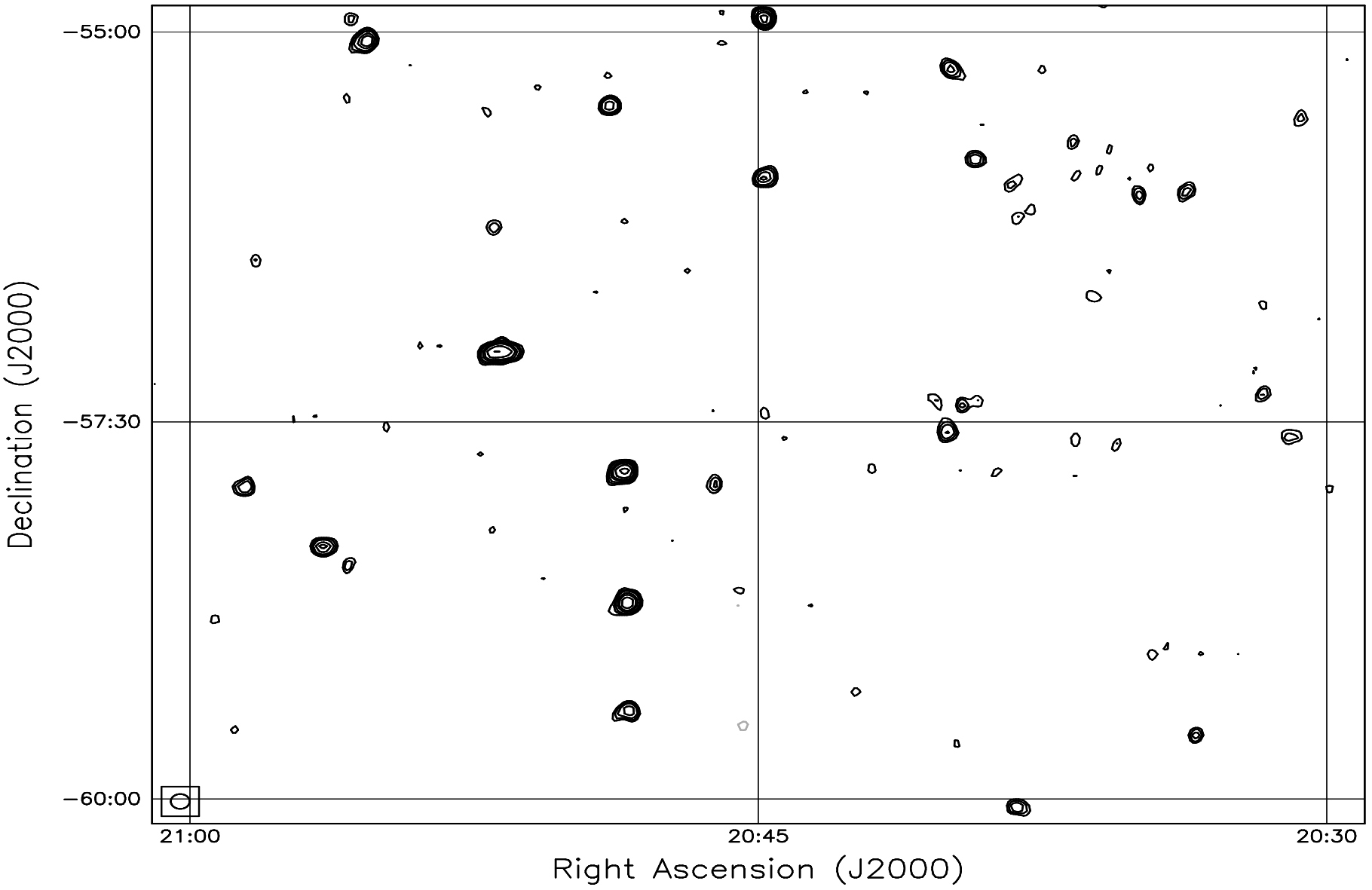

Fig. 7.120: Contour map covering the right ascension range 20h30m to 21h00m and declination range -60° to -55 °. The contour levels are -5, -3.6, -2.5, -1.8, 1, 1.4, 2, 2.8, 3.6, 5, 7, 10, 14, 20, 29, 40, 54, 72, 90, 100, 136, 180, 216, 252, 288 Jy beam^{-1}. The rms noise in the image is ≈280 mJy beam^{-1}.

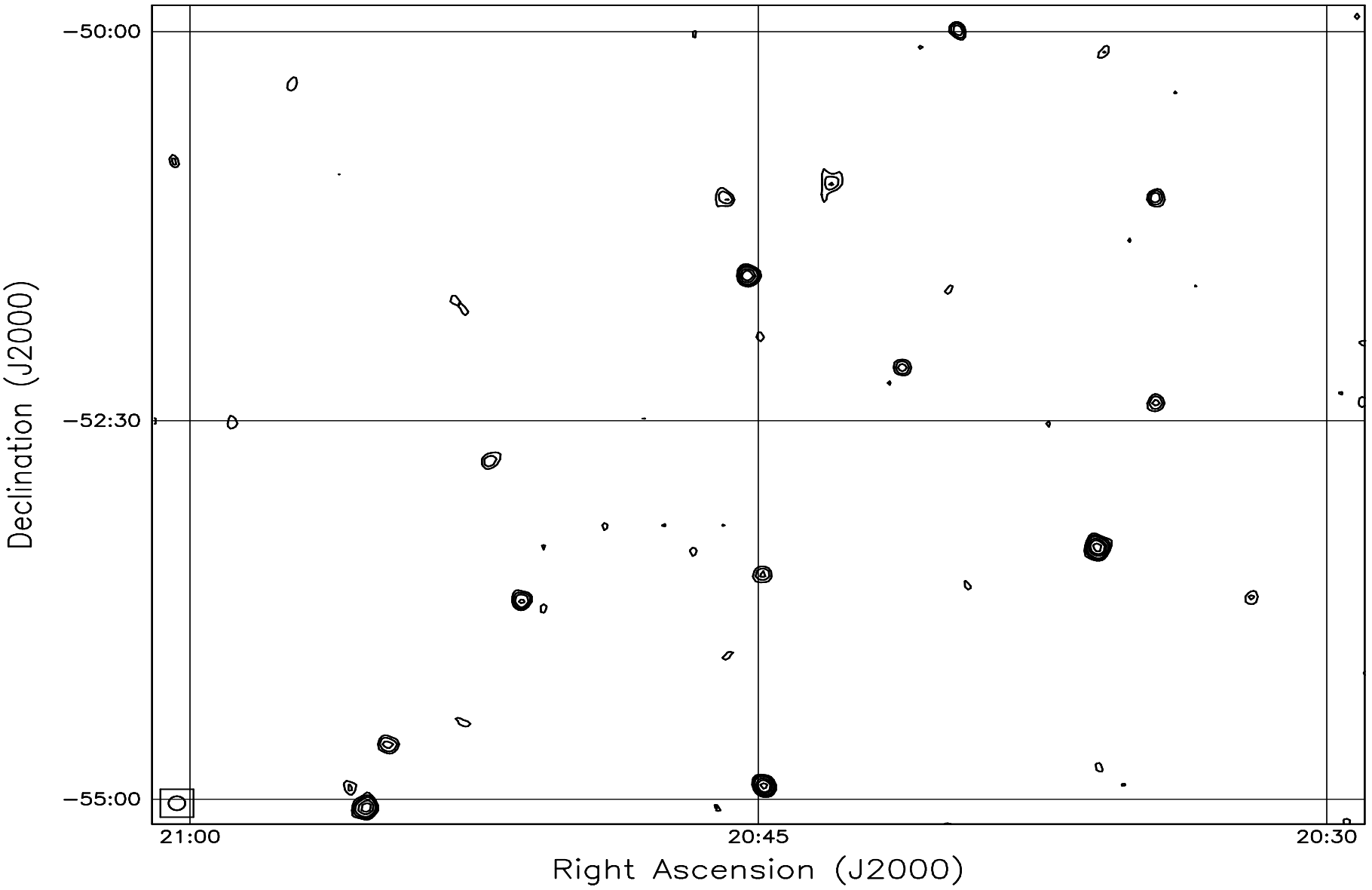

Fig. 7.121: Contour map covering the right ascension range 20h30m to 21h00m and declination range -55° to -50 °. The contour levels are -5, -3.6, -2.5, -1.8, 1, 1.4, 2, 2.8, 3.6, 5, 7, 10, 14, 20, 29, 40, 54, 72, 90, 100, 136, 180, 216, 252, 288 Jy beam^{-1}. The rms noise in the image is ≈270 mJy beam^{-1}.

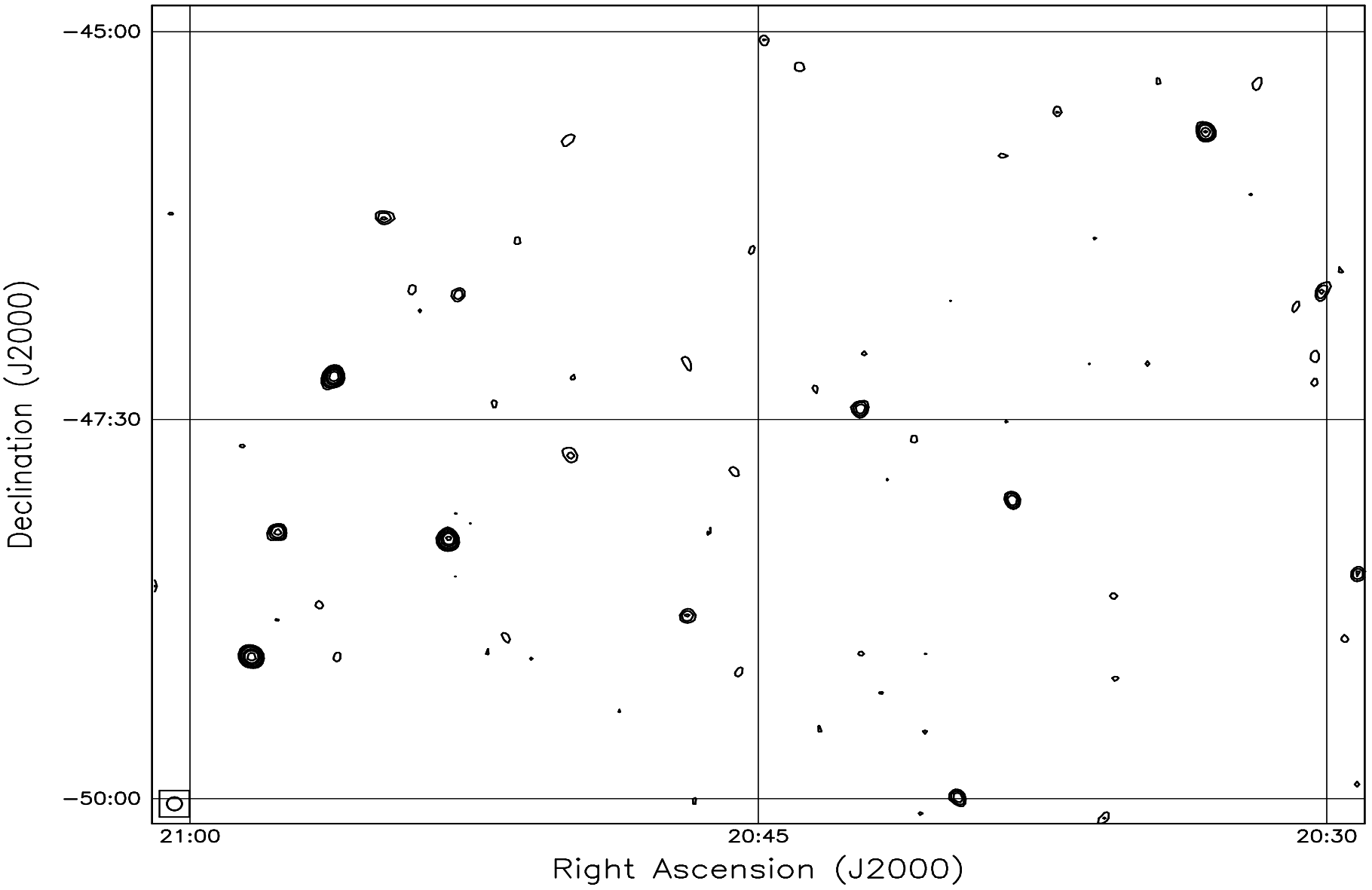

Fig. 7.122: Contour map covering the right ascension range 20h30m to 21h00m and declination range -50° to -45 °. The contour levels are -5, -3.6, -2.5, -1.8, 1, 1.4, 2, 2.8, 3.6, 5, 7, 10, 14, 20, 29, 40, 54, 72, 90, 100, 136, 180, 216, 252, 288 Jy beam^{-1}. The rms noise in the image is ≈260 mJy beam^{-1}.

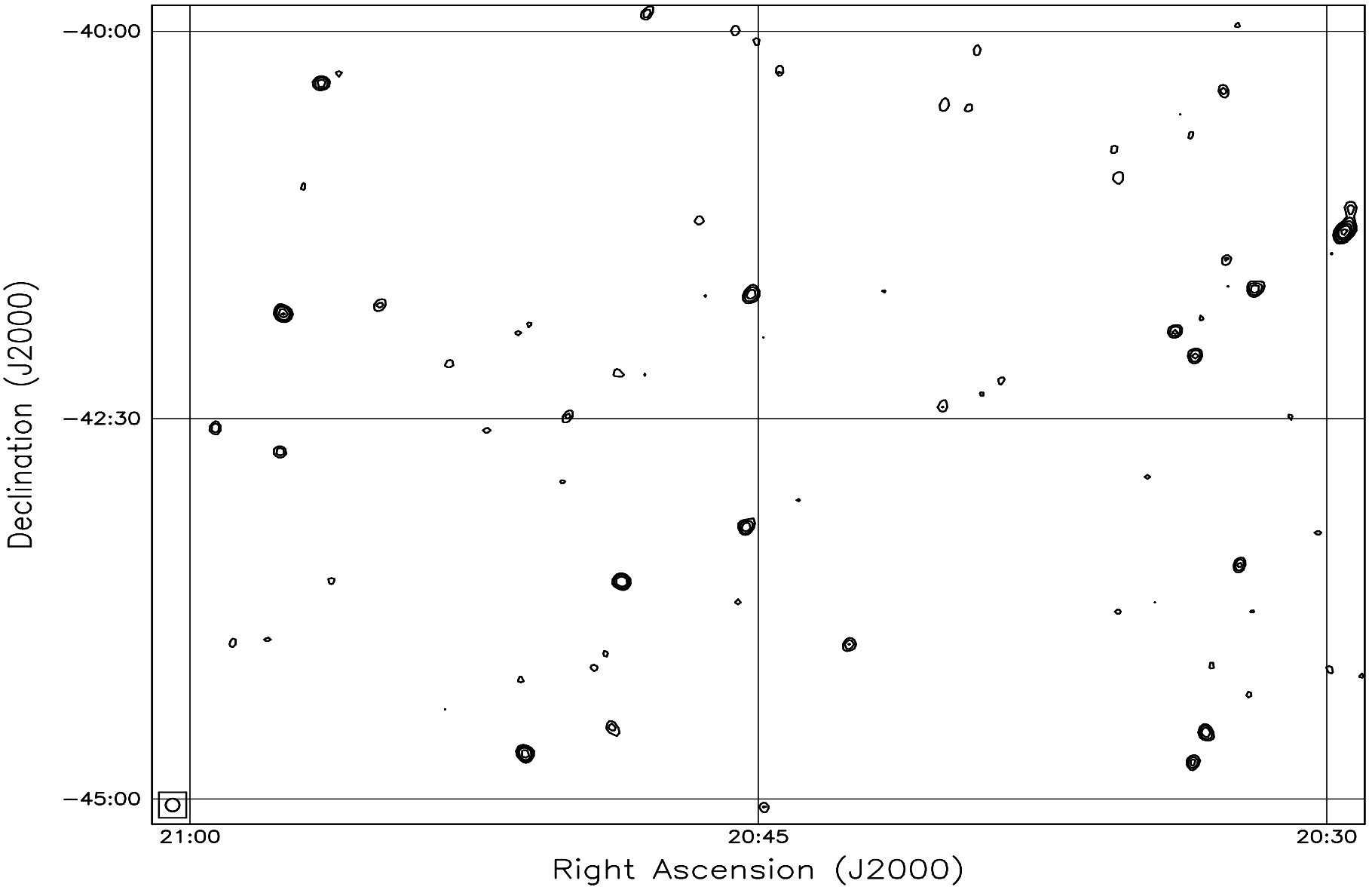

Fig. 7.123: Contour map covering the right ascension range 20h30m to 21h00m and declination range -45° to -40 °. The contour levels are -5, -3.6, -2.5, -1.8, 1, 1.4, 2, 2.8, 3.6, 5, 7, 10, 14, 20, 29, 40, 54, 72, 90, 100, 136, 180, 216, 252, 288 Jy beam^{-1}. The rms noise in the image is ≈260 mJy beam^{-1}.

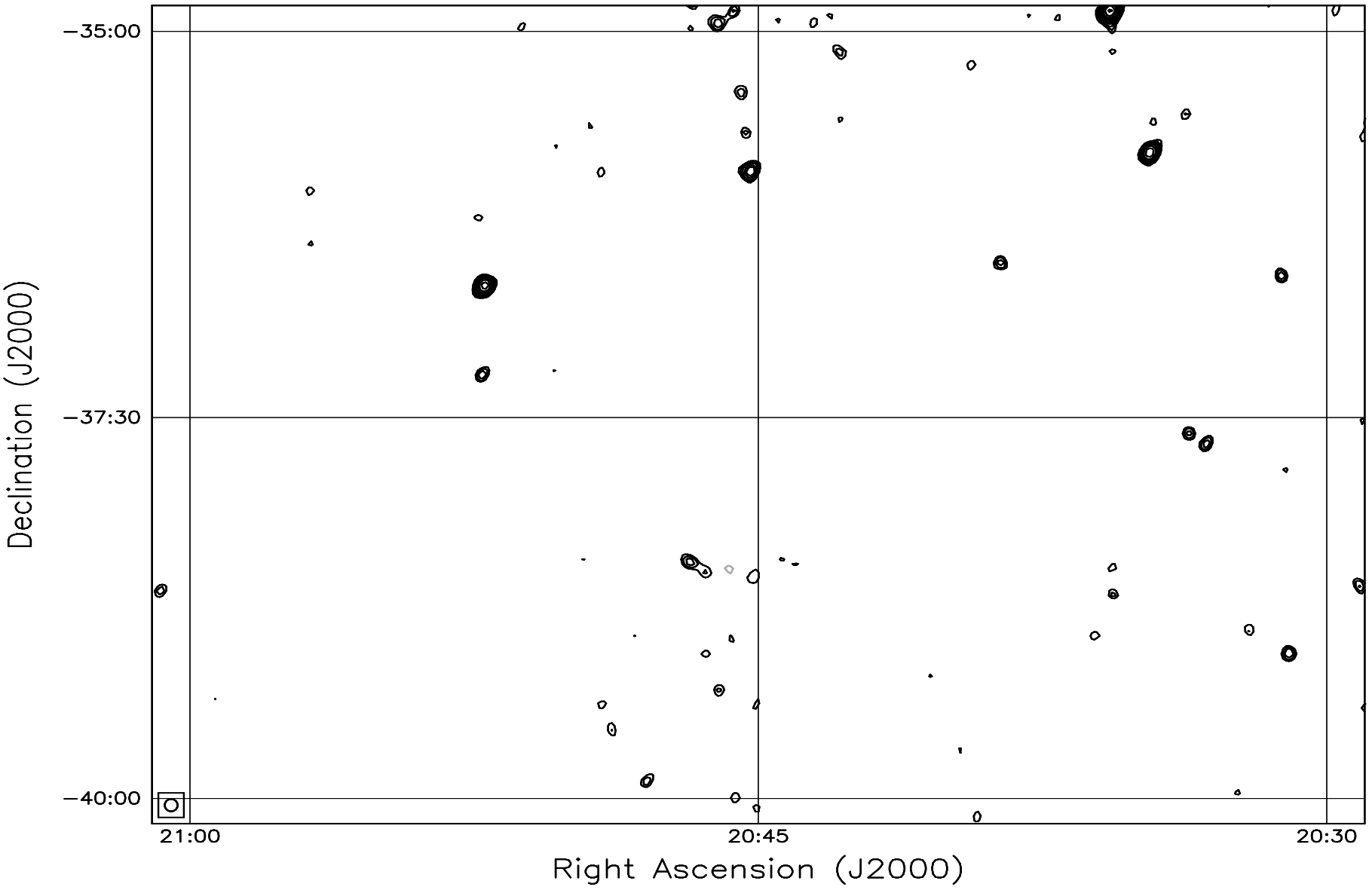

Fig. 7.124: Contour map covering the right ascension range 20h30m to 21h00m and declination range -40° to -35 °. The contour levels are -5, -3.6, -2.5, -1.8, 1, 1.4, 2, 2.8, 3.6, 5, 7, 10, 14, 20, 29, 40, 54, 72, 90, 100, 136, 180, 216, 252, 288 Jy beam^{-1}. The rms noise in the image is ≈270 mJy beam^{-1}.

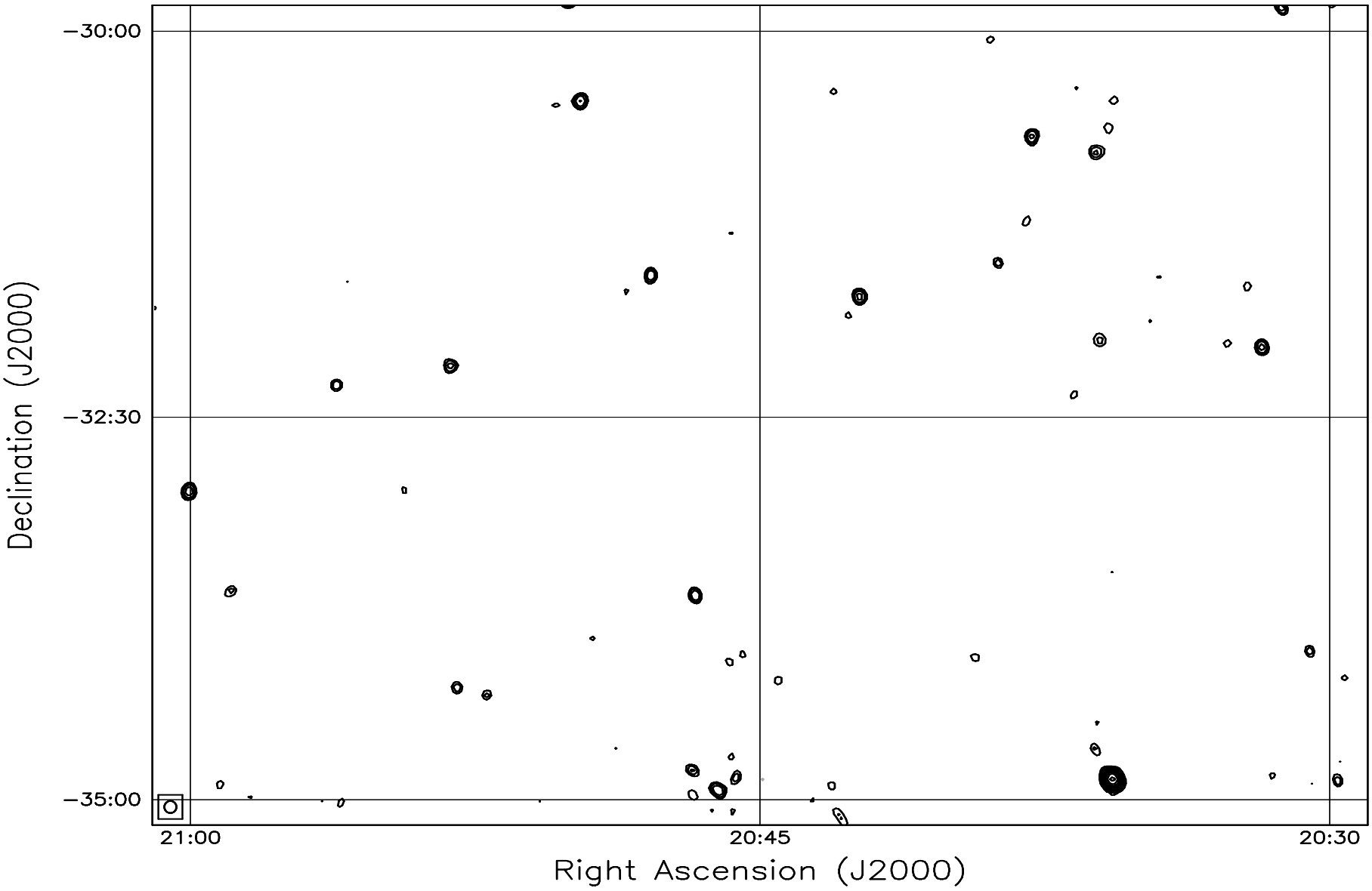

Fig. 7.125: Contour map covering the right ascension range 20h30m to 21h00m and declination range -35° to -30 °. The contour levels are -5, -3.6, -2.5, -1.8, 1, 1.4, 2, 2.8, 3.6, 5, 7, 10, 14, 20, 29, 40, 54, 72, 90, 100, 136, 180, 216, 252, 288 Jy beam^{-1}. The rms noise in the image is ≈280 mJy beam^{-1}.

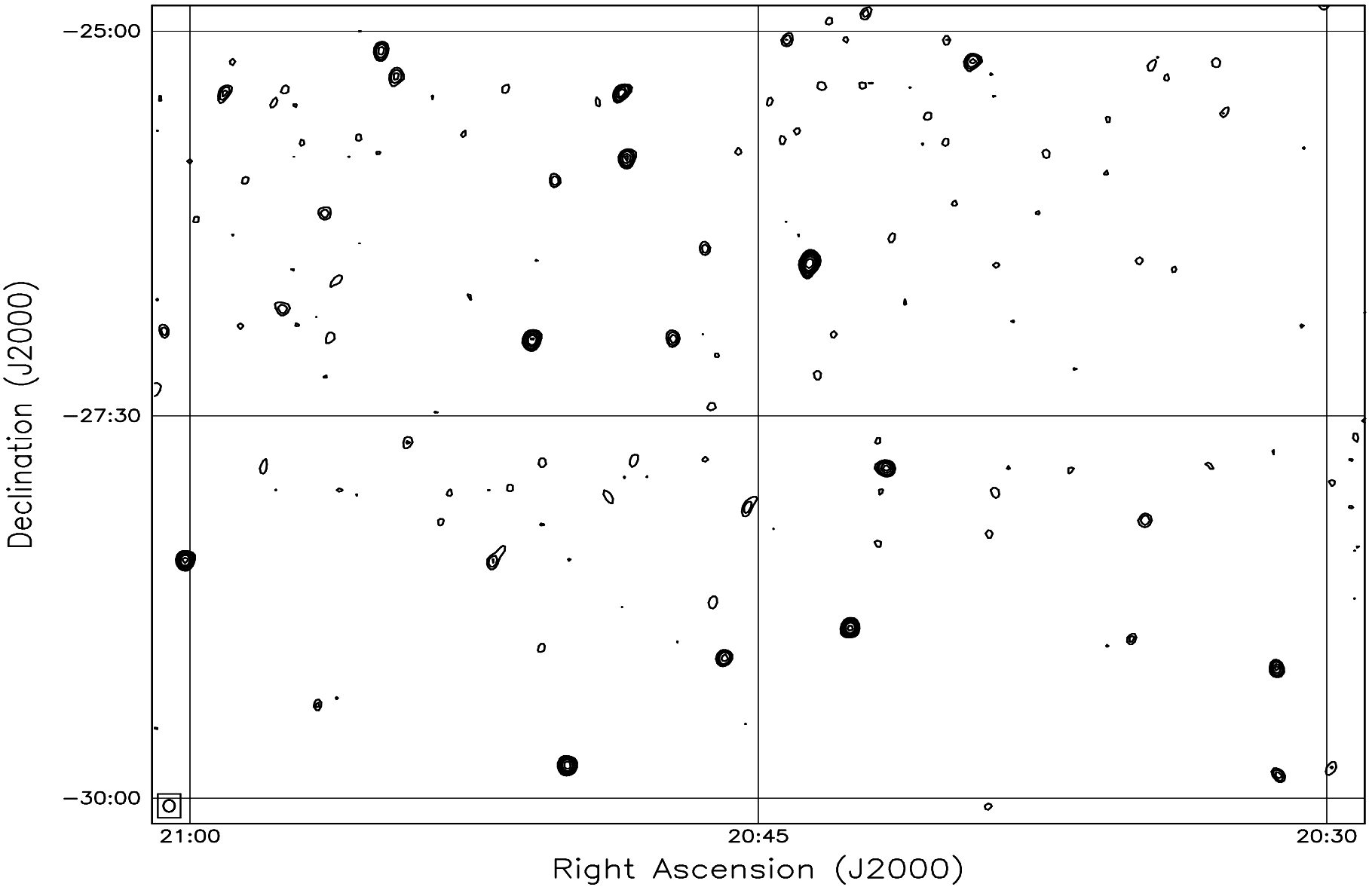

Fig. 7.126: Contour map covering the right ascension range 20h30m to 21h00m and declination range -30° to -25 °. The contour levels are -5, -3.6, -2.5, -1.8, 1, 1.4, 2, 2.8, 3.6, 5, 7, 10, 14, 20, 29, 40, 54, 72, 90, 100, 136, 180, 216, 252, 288 Jy beam^{-1}. The rms noise in the image is ≈300 mJy beam^{-1}.

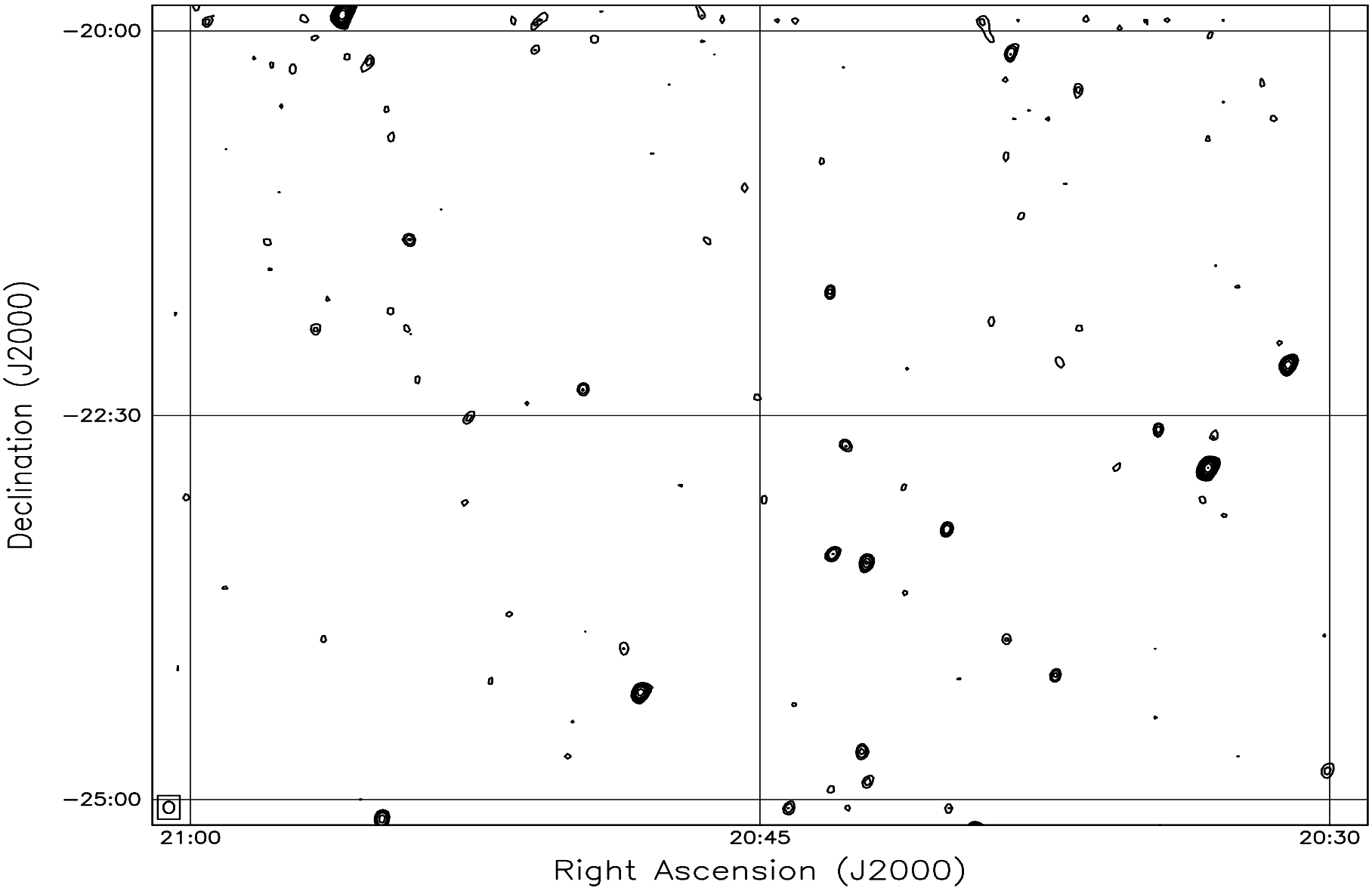

Fig. 7.127: Contour map covering the right ascension range 20h30m to 21h00m and declination range -25° to -20 °. The contour levels are -5, -3.6, -2.5, -1.8, 1, 1.4, 2, 2.8, 3.6, 5, 7, 10, 14, 20, 29, 40, 54, 72, 90, 100, 136, 180, 216, 252, 288 Jy beam^{-1}. The rms noise in the image is ≈330 mJy beam^{-1}.

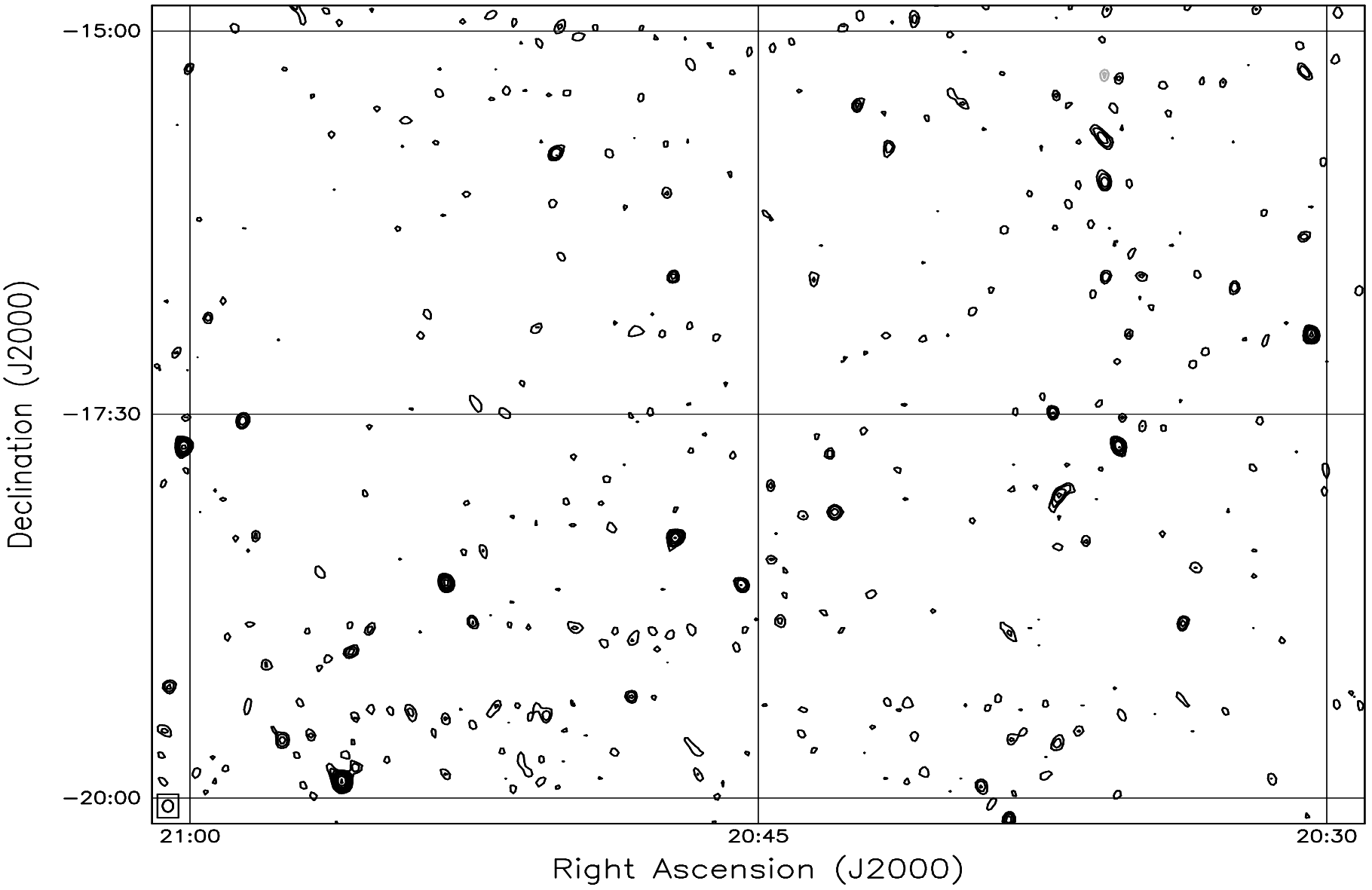

Fig. 7.128: Contour map covering the right ascension range 20h30m to 21h00m and declination range -20° to -15 °. The contour levels are -5, -3.6, -2.5, -1.8, 1, 1.4, 2, 2.8, 3.6, 5, 7, 10, 14, 20, 29, 40, 54, 72, 90, 100, 136, 180, 216, 252, 288 Jy beam^{-1}. The rms noise in the image is ≈375 mJy beam^{-1}.

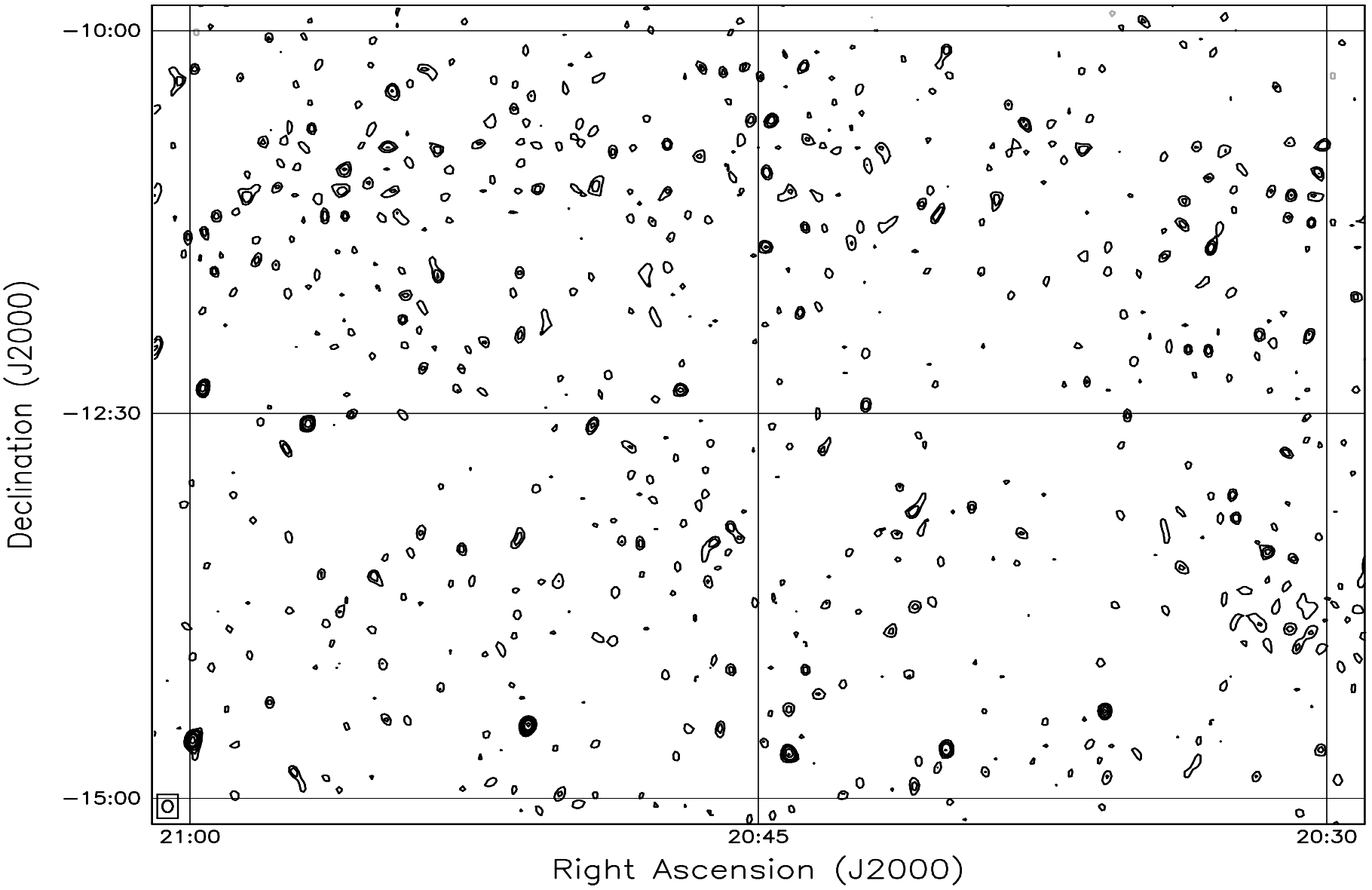

Fig. 7.129: Contour map covering the right ascension range 20h30m to 21h00m and declination range -15° to -10 °. The contour levels are -5, -3.6, -2.5, -1.8, 1, 1.4, 2, 2.8, 3.6, 5, 7, 10, 14, 20, 29, 40, 54, 72, 90, 100, 136, 180, 216, 252, 288 Jy beam^{-1}. The rms noise in the image is ≈460 mJy beam^{-1}.

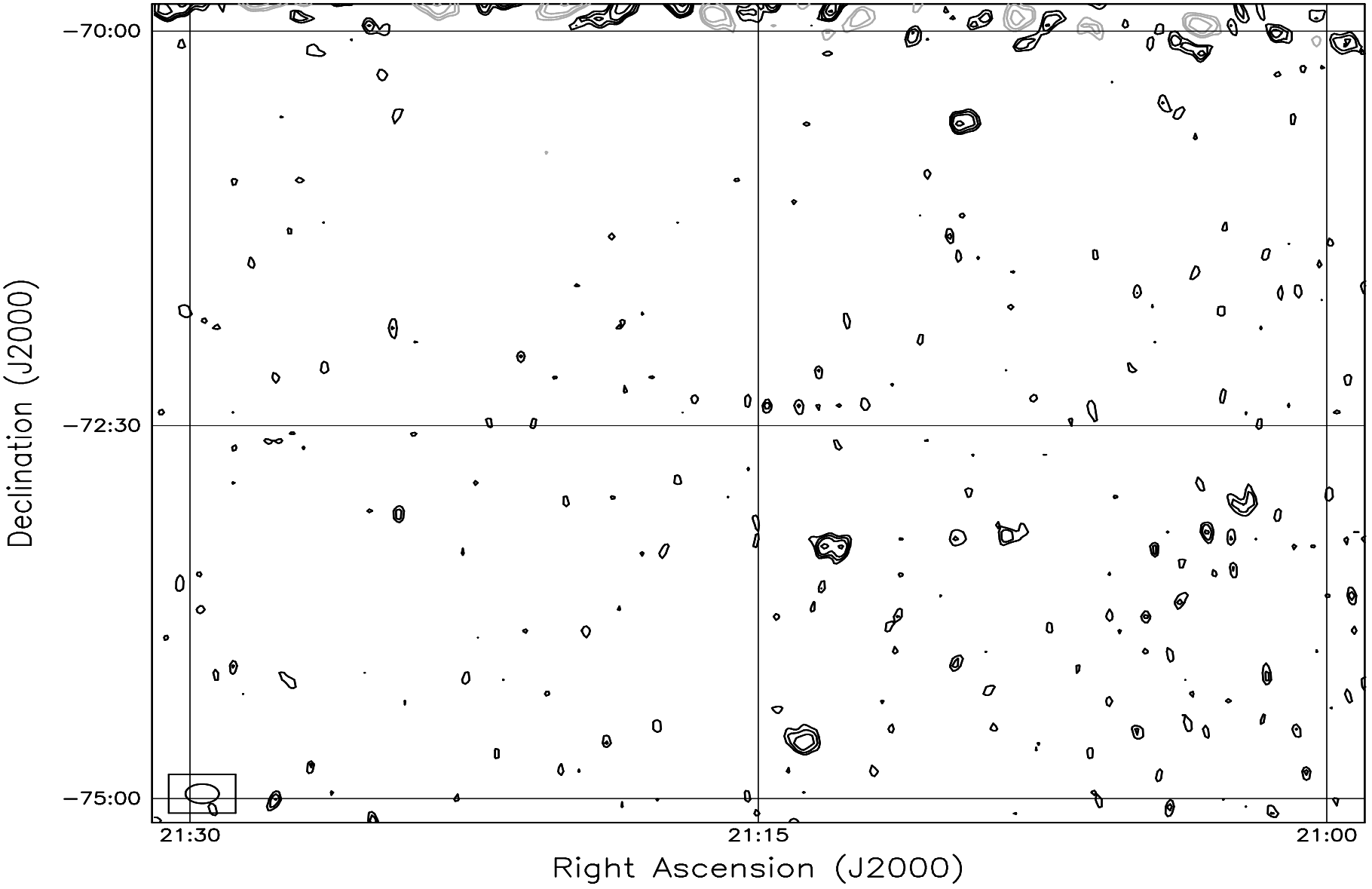

Fig. 7.130: Contour map covering the right ascension range 21h00m to 21h30m and declination range -75° to -70 °. The contour levels are -5, -3.6, -2.5, -1.8, 1, 1.4, 2, 2.8, 3.6, 5, 7, 10, 14, 20, 29, 40, 54, 72, 90, 100, 136, 180, 216, 252, 288 Jy beam^{-1}. The rms noise in the image is ≈380 mJy beam^{-1}.

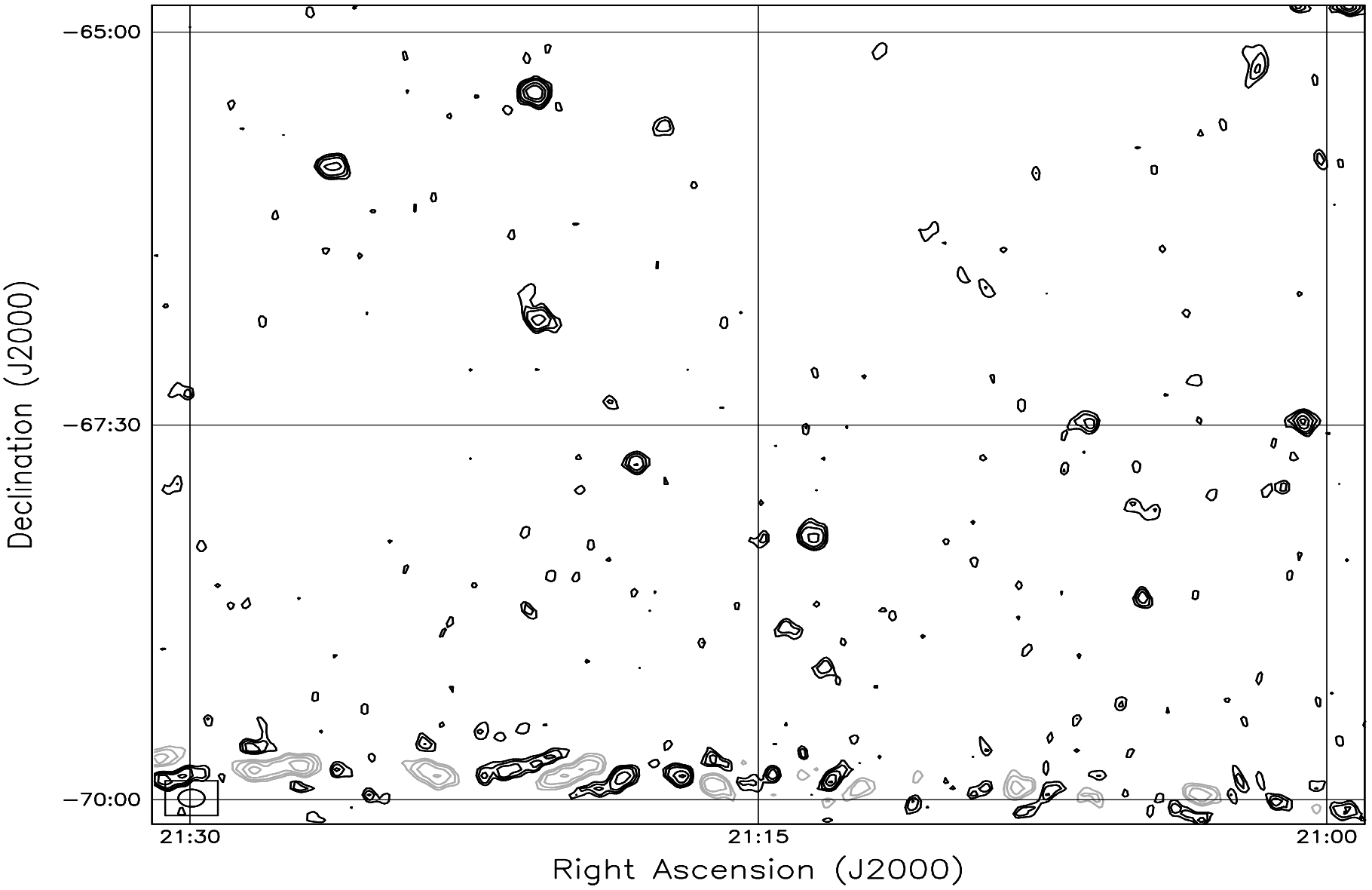

Fig. 7.131: Contour map covering the right ascension range 21h00m to 21h30m and declination range -70° to -65 °. The contour levels are -5, -3.6, -2.5, -1.8, 1, 1.4, 2, 2.8, 3.6, 5, 7, 10, 14, 20, 29, 40, 54, 72, 90, 100, 136, 180, 216, 252, 288 Jy beam^{-1}. The rms noise in the image is ≈330 mJy beam^{-1}.

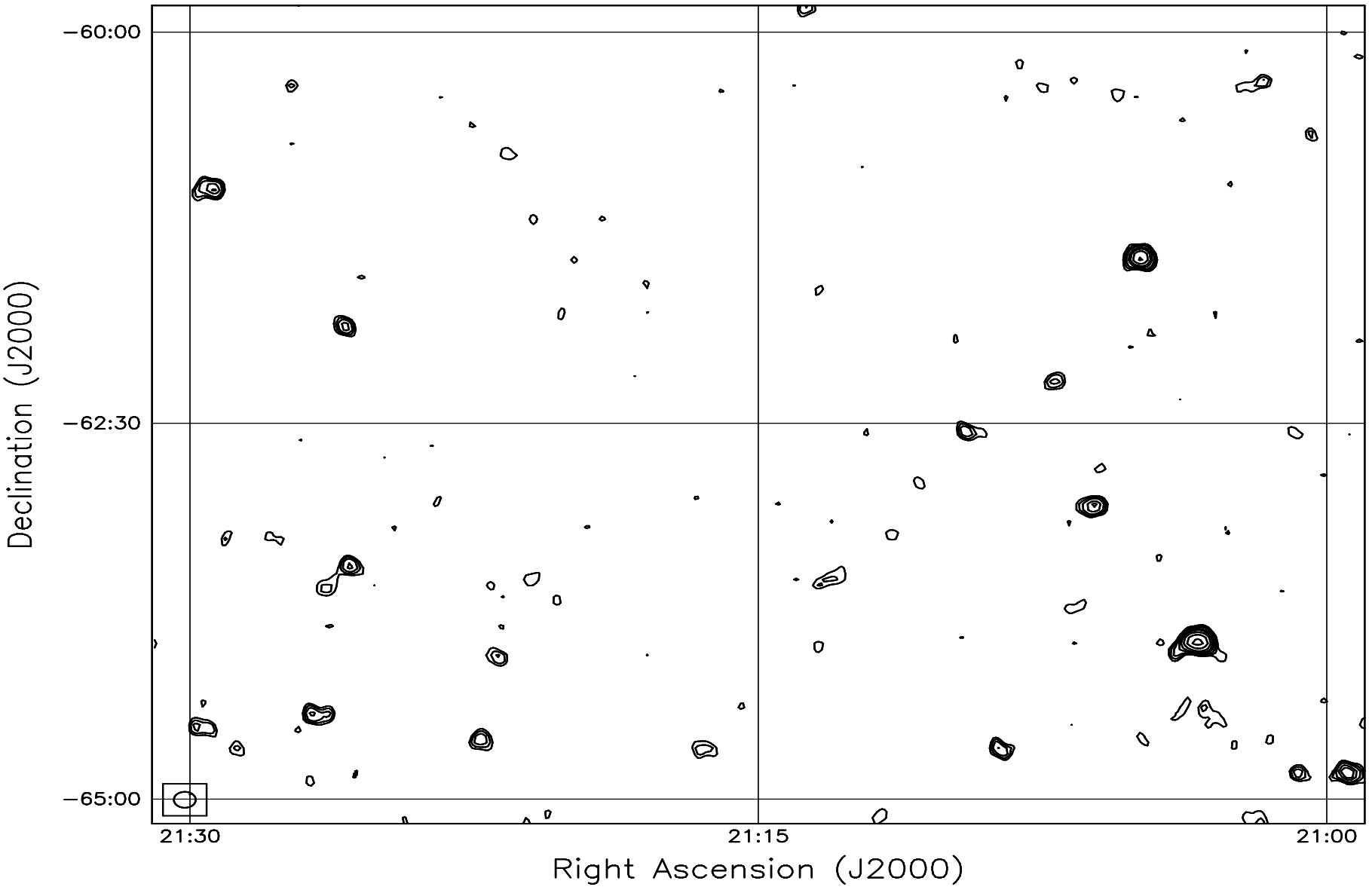

Fig. 7.132: Contour map covering the right ascension range 21h00m to 21h30m and declination range -65° to -60 °. The contour levels are -5, -3.6, -2.5, -1.8, 1, 1.4, 2, 2.8, 3.6, 5, 7, 10, 14, 20, 29, 40, 54, 72, 90, 100, 136, 180, 216, 252, 288 Jy beam^{-1}. The rms noise in the image is ≈300 mJy beam^{-1}.

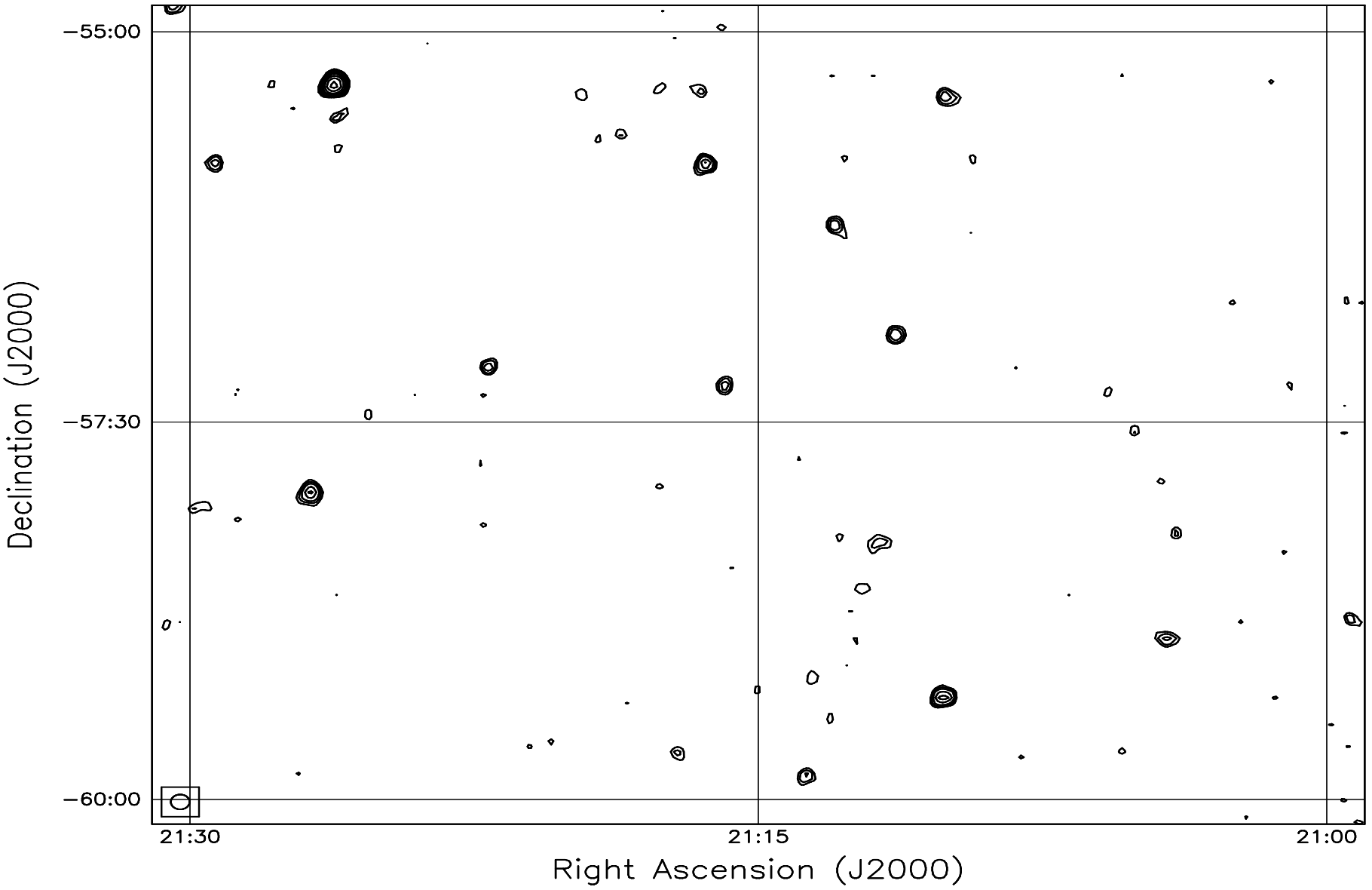

Fig. 7.133: Contour map covering the right ascension range 21h00m to 21h30m and declination range -60° to -55 °. The contour levels are -5, -3.6, -2.5, -1.8, 1, 1.4, 2, 2.8, 3.6, 5, 7, 10, 14, 20, 29, 40, 54, 72, 90, 100, 136, 180, 216, 252, 288 Jy beam^{-1}. The rms noise in the image is ≈280 mJy beam^{-1}.

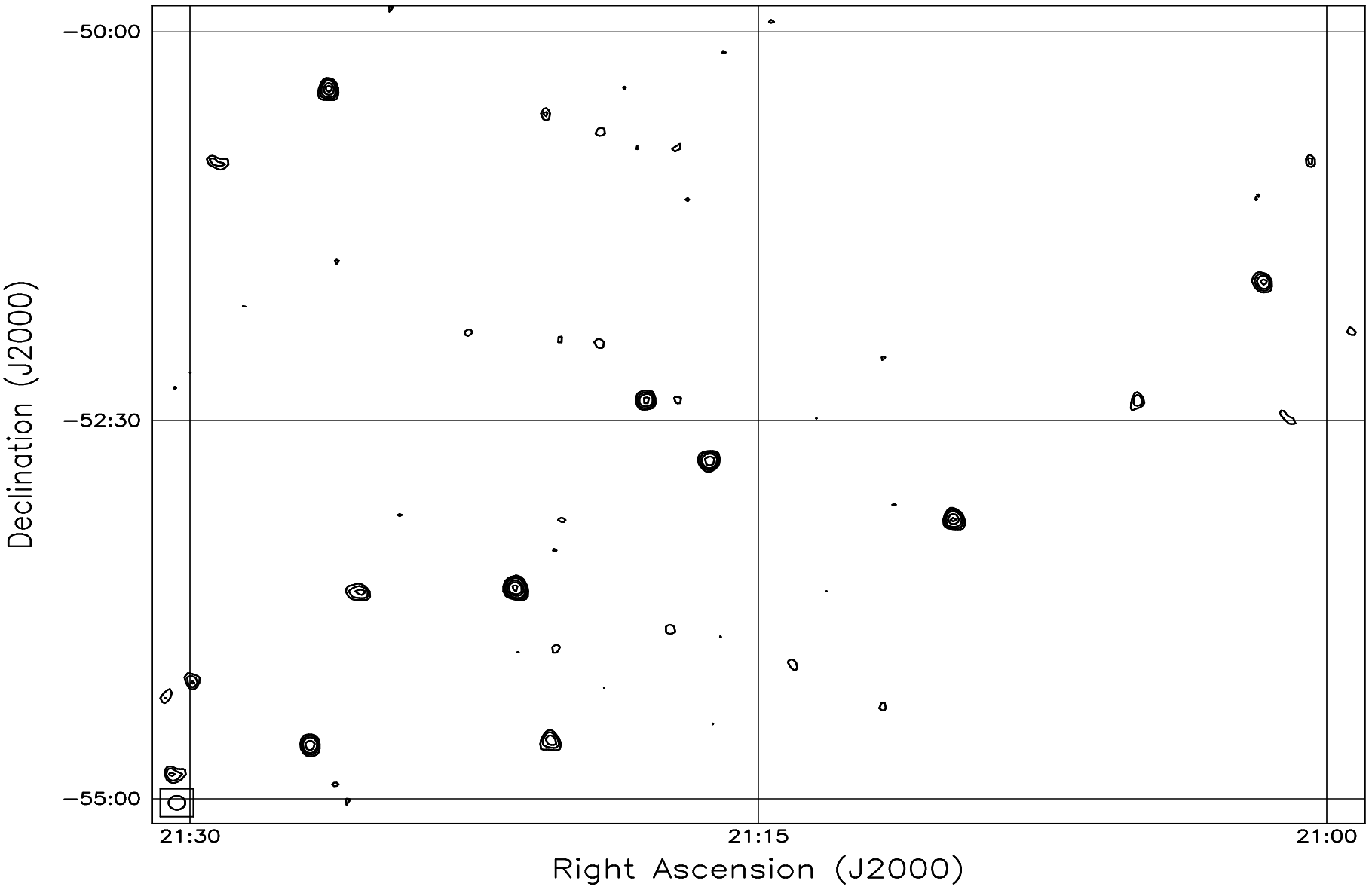

Fig. 7.134: Contour map covering the right ascension range 21h00m to 21h30m and declination range -55° to -50 °. The contour levels are -5, -3.6, -2.5, -1.8, 1, 1.4, 2, 2.8, 3.6, 5, 7, 10, 14, 20, 29, 40, 54, 72, 90, 100, 136, 180, 216, 252, 288 Jy beam^{-1}. The rms noise in the image is ≈270 mJy beam^{-1}.

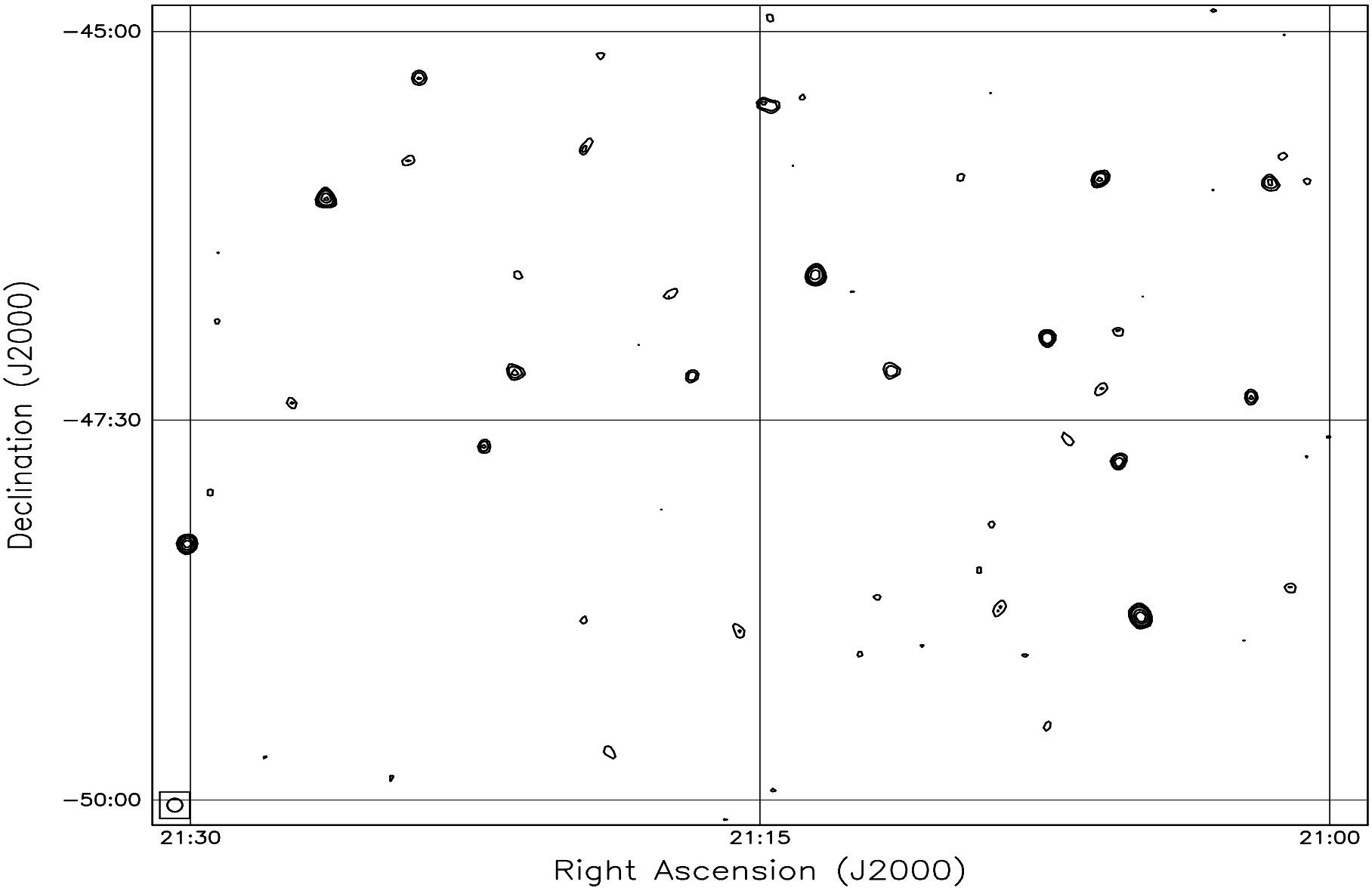

Fig. 7.135: Contour map covering the right ascension range 21h00m to 21h30m and declination range -50° to -45 °. The contour levels are -5, -3.6, -2.5, -1.8, 1, 1.4, 2, 2.8, 3.6, 5, 7, 10, 14, 20, 29, 40, 54, 72, 90, 100, 136, 180, 216, 252, 288 Jy beam^{-1}. The rms noise in the image is ≈260 mJy beam^{-1}.

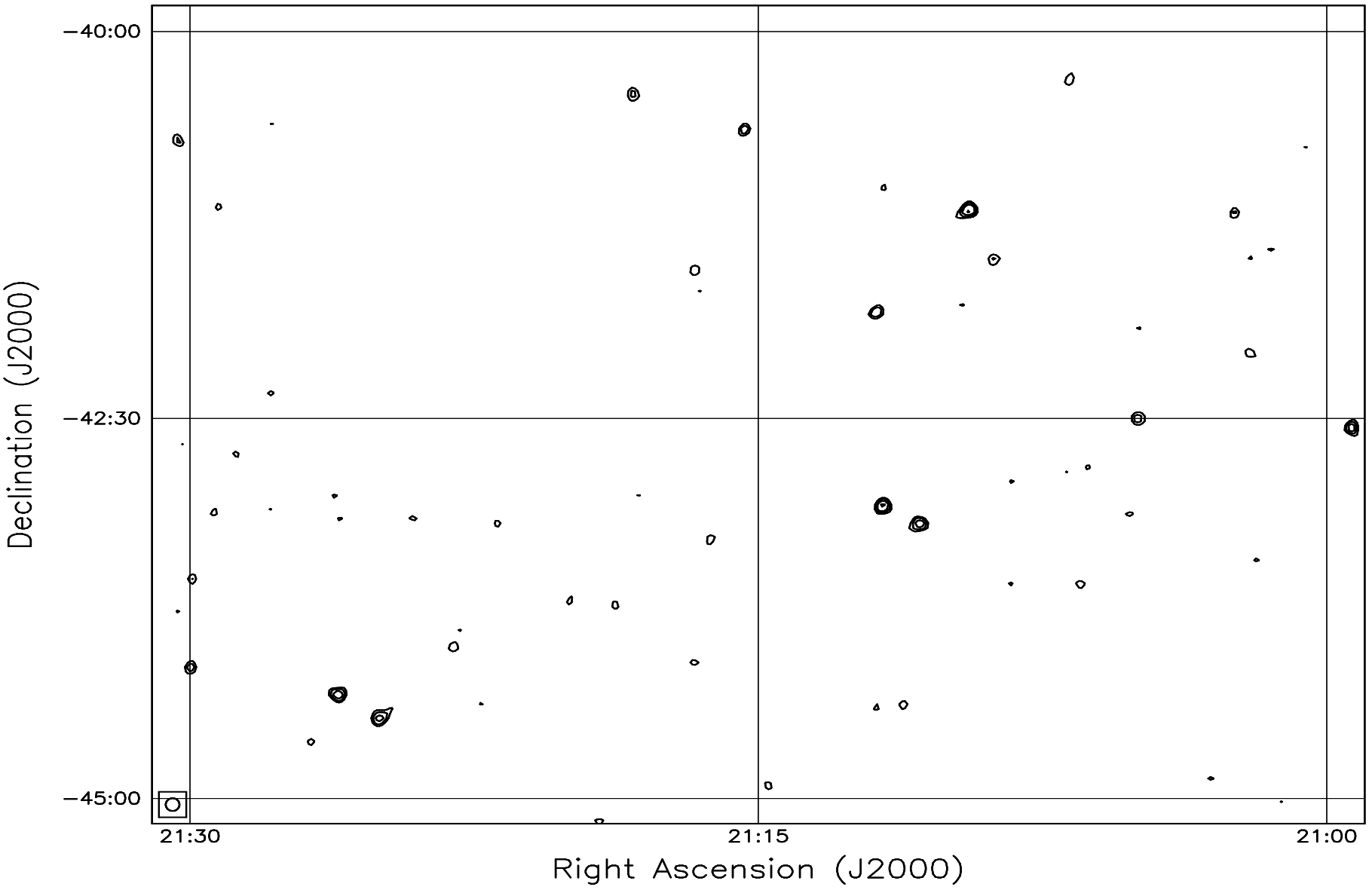

Fig. 7.136: Contour map covering the right ascension range 21h00m to 21h30m and declination range -45° to -40 °. The contour levels are -5, -3.6, -2.5, -1.8, 1, 1.4, 2, 2.8, 3.6, 5, 7, 10, 14, 20, 29, 40, 54, 72, 90, 100, 136, 180, 216, 252, 288 Jy beam^{-1}. The rms noise in the image is ≈260 mJy beam^{-1}.

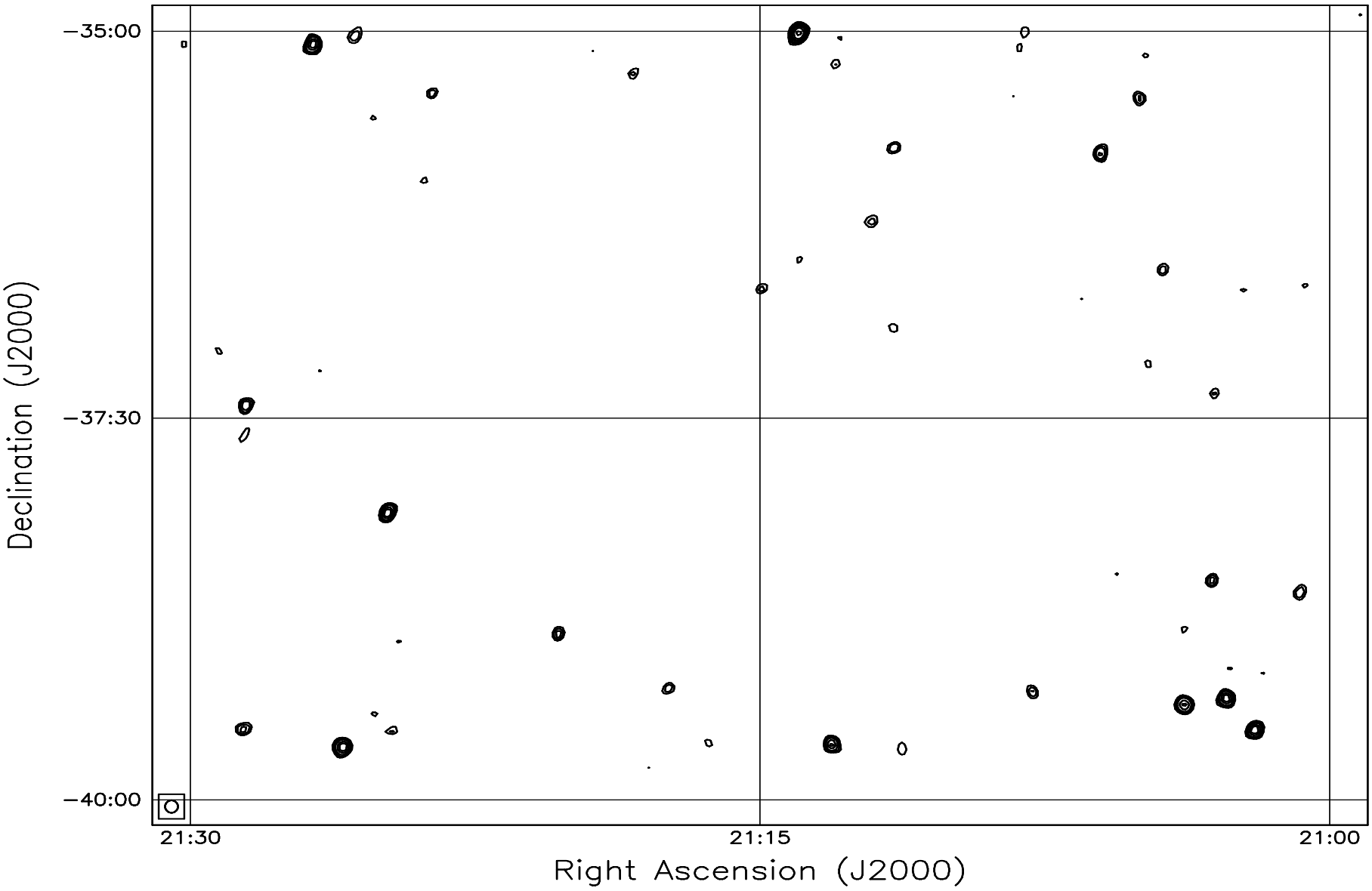

Fig. 7.137: Contour map covering the right ascension range 21h00m to 21h30m and declination range -40° to -35 °. The contour levels are -5, -3.6, -2.5, -1.8, 1, 1.4, 2, 2.8, 3.6, 5, 7, 10, 14, 20, 29, 40, 54, 72, 90, 100, 136, 180, 216, 252, 288 Jy beam^{-1}. The rms noise in the image is ≈270 mJy beam^{-1}.

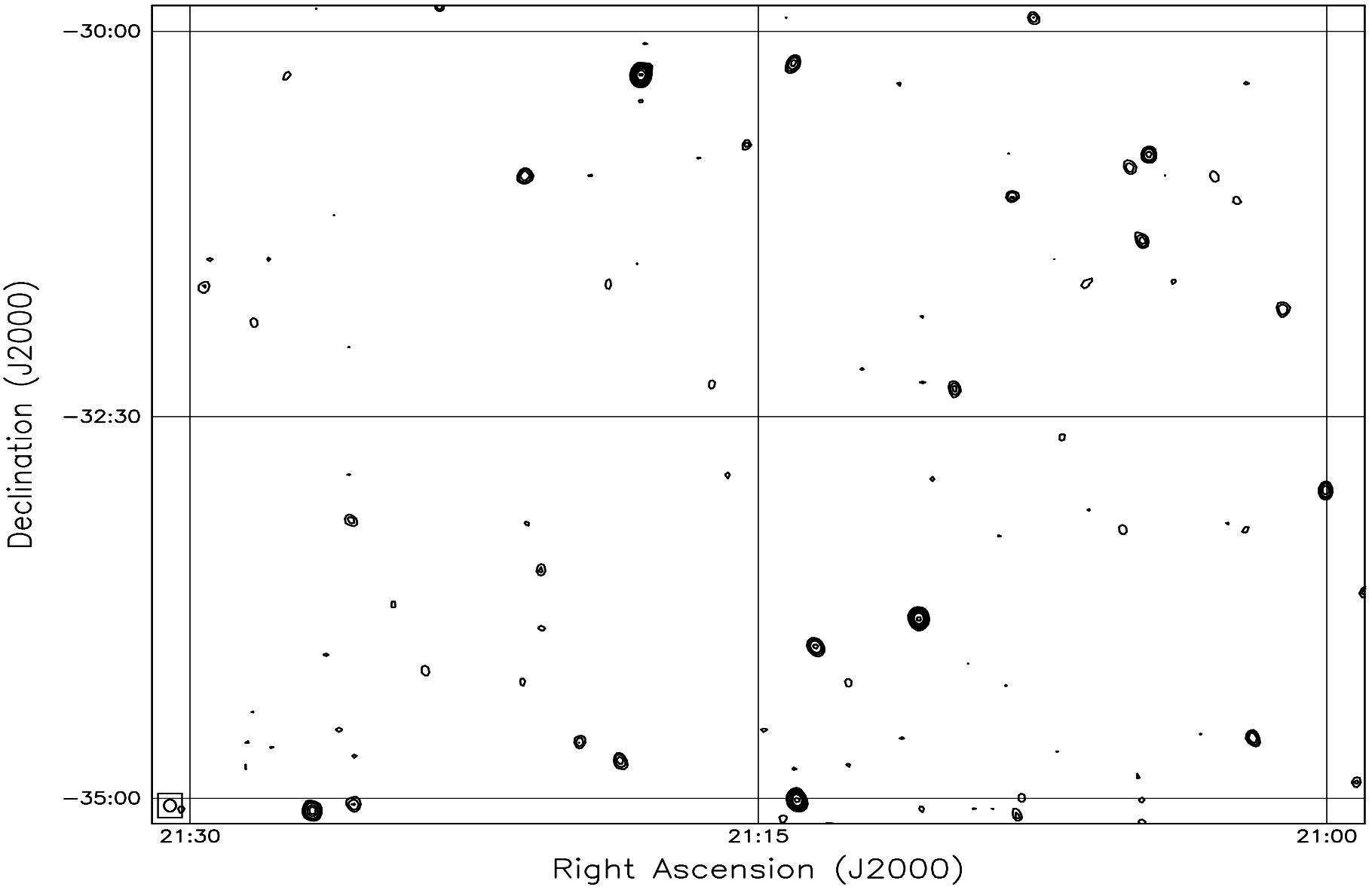

Fig. 7.138: Contour map covering the right ascension range 21h00m to 21h30m and declination range -35° to -30 °. The contour levels are -5, -3.6, -2.5, -1.8, 1, 1.4, 2, 2.8, 3.6, 5, 7, 10, 14, 20, 29, 40, 54, 72, 90, 100, 136, 180, 216, 252, 288 Jy beam^{-1}. The rms noise in the image is ≈280 mJy beam^{-1}.

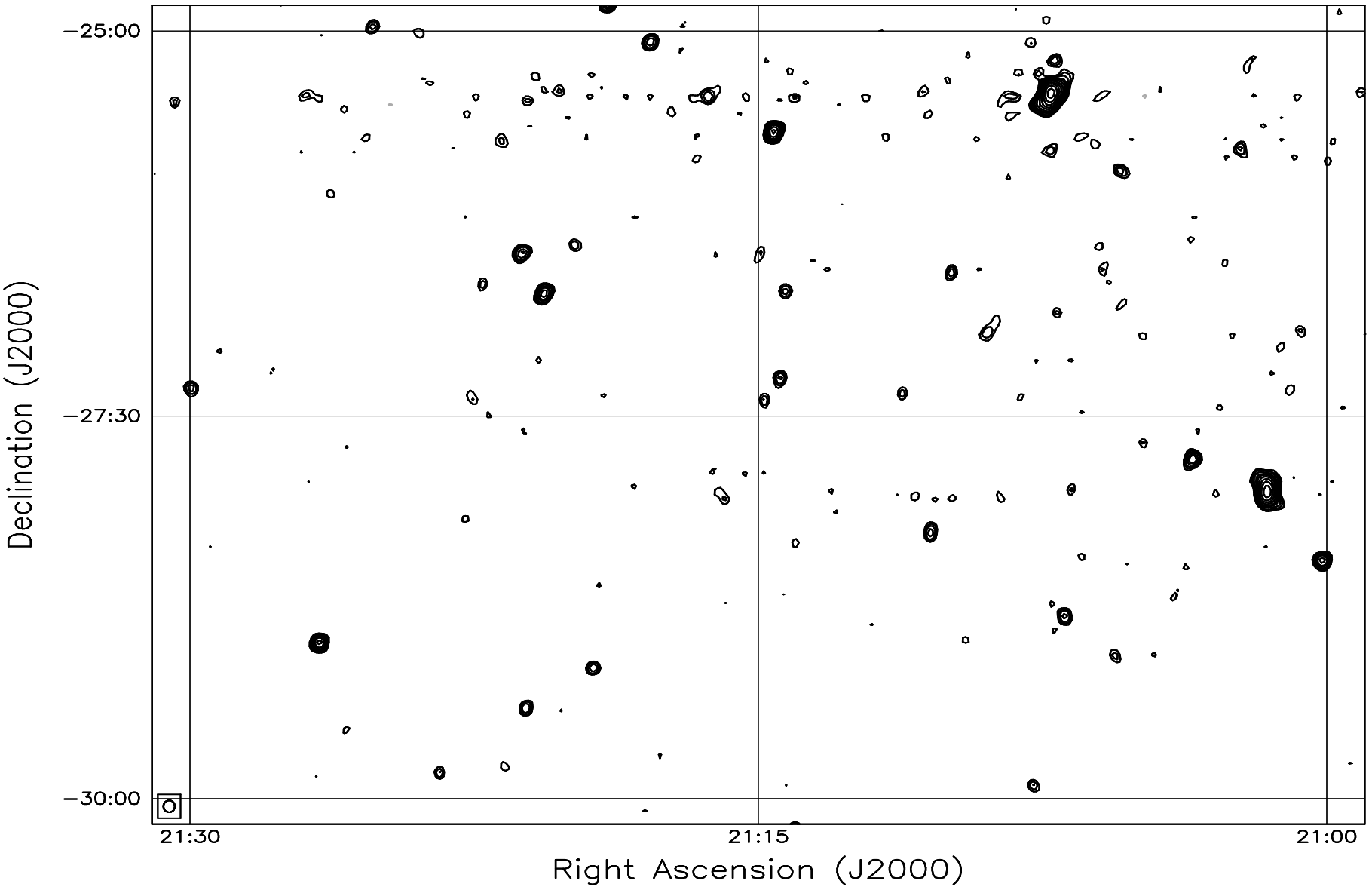

Fig. 7.139: Contour map covering the right ascension range 21h00m to 21h30m and declination range -30° to -25 °. The contour levels are -5, -3.6, -2.5, -1.8, 1, 1.4, 2, 2.8, 3.6, 5, 7, 10, 14, 20, 29, 40, 54, 72, 90, 100, 136, 180, 216, 252, 288 Jy beam^{-1}. The rms noise in the image is ≈300 mJy beam^{-1}.

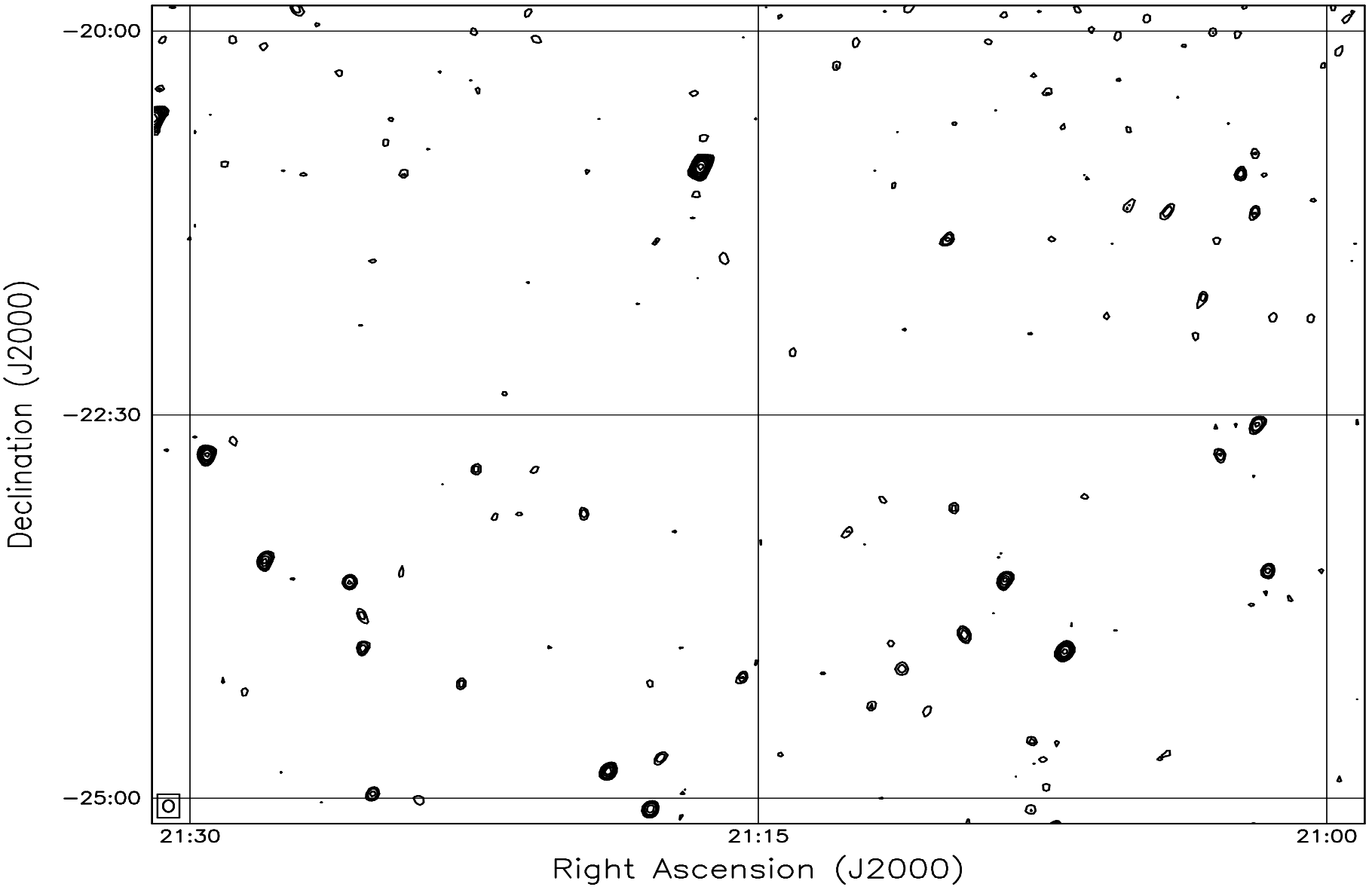

Fig. 7.140: Contour map covering the right ascension range 21h00m to 21h30m and declination range -25° to -20 °. The contour levels are -5, -3.6, -2.5, -1.8, 1, 1.4, 2, 2.8, 3.6, 5, 7, 10, 14, 20, 29, 40, 54, 72, 90, 100, 136, 180, 216, 252, 288 Jy beam^{-1}. The rms noise in the image is ≈330 mJy beam^{-1}.

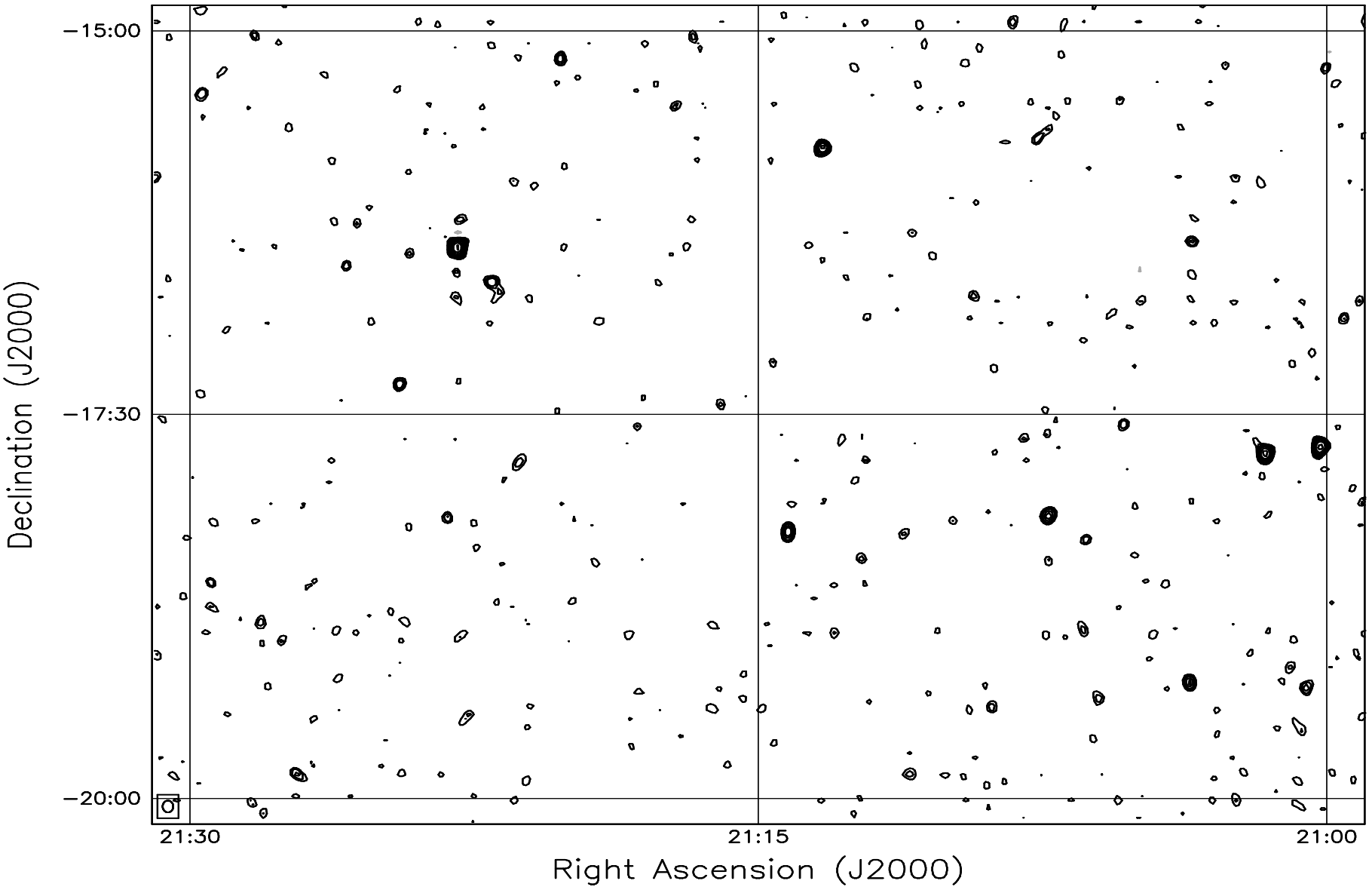

Fig. 7.141: Contour map covering the right ascension range 21h00m to 21h30m and declination range -20° to -15 °. The contour levels are -5, -3.6, -2.5, -1.8, 1, 1.4, 2, 2.8, 3.6, 5, 7, 10, 14, 20, 29, 40, 54, 72, 90, 100, 136, 180, 216, 252, 288 Jy beam^{-1}. The rms noise in the image is ≈375 mJy beam^{-1}.

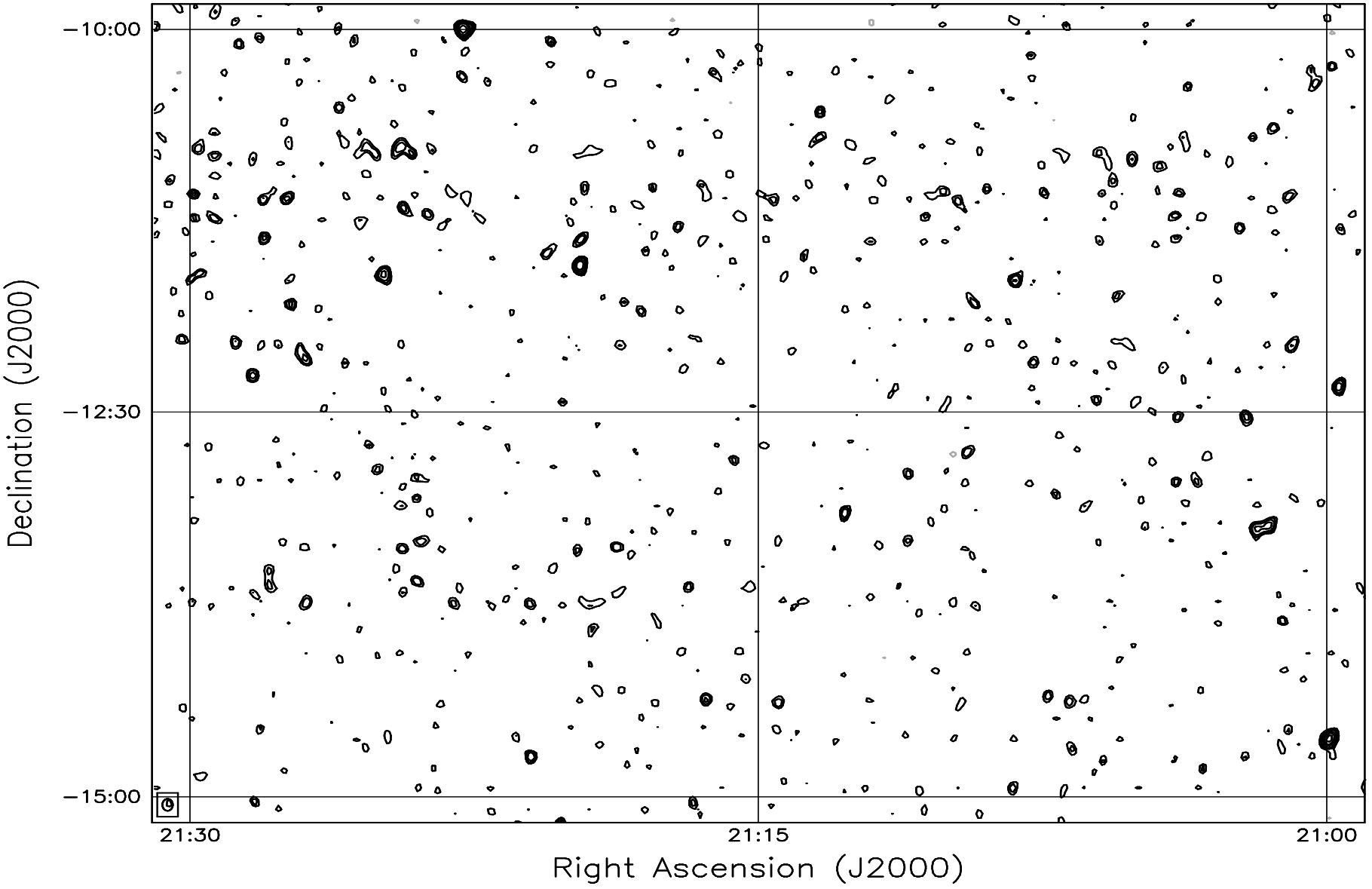

Fig. 7.142: Contour map covering the right ascension range 21h00m to 21h30m and declination range -15° to -10 °. The contour levels are -5, -3.6, -2.5, -1.8, 1, 1.4, 2, 2.8, 3.6, 5, 7, 10, 14, 20, 29, 40, 54, 72, 90, 100, 136, 180, 216, 252, 288 Jy beam^{-1}. The rms noise in the image is ≈460 mJy beam^{-1}.

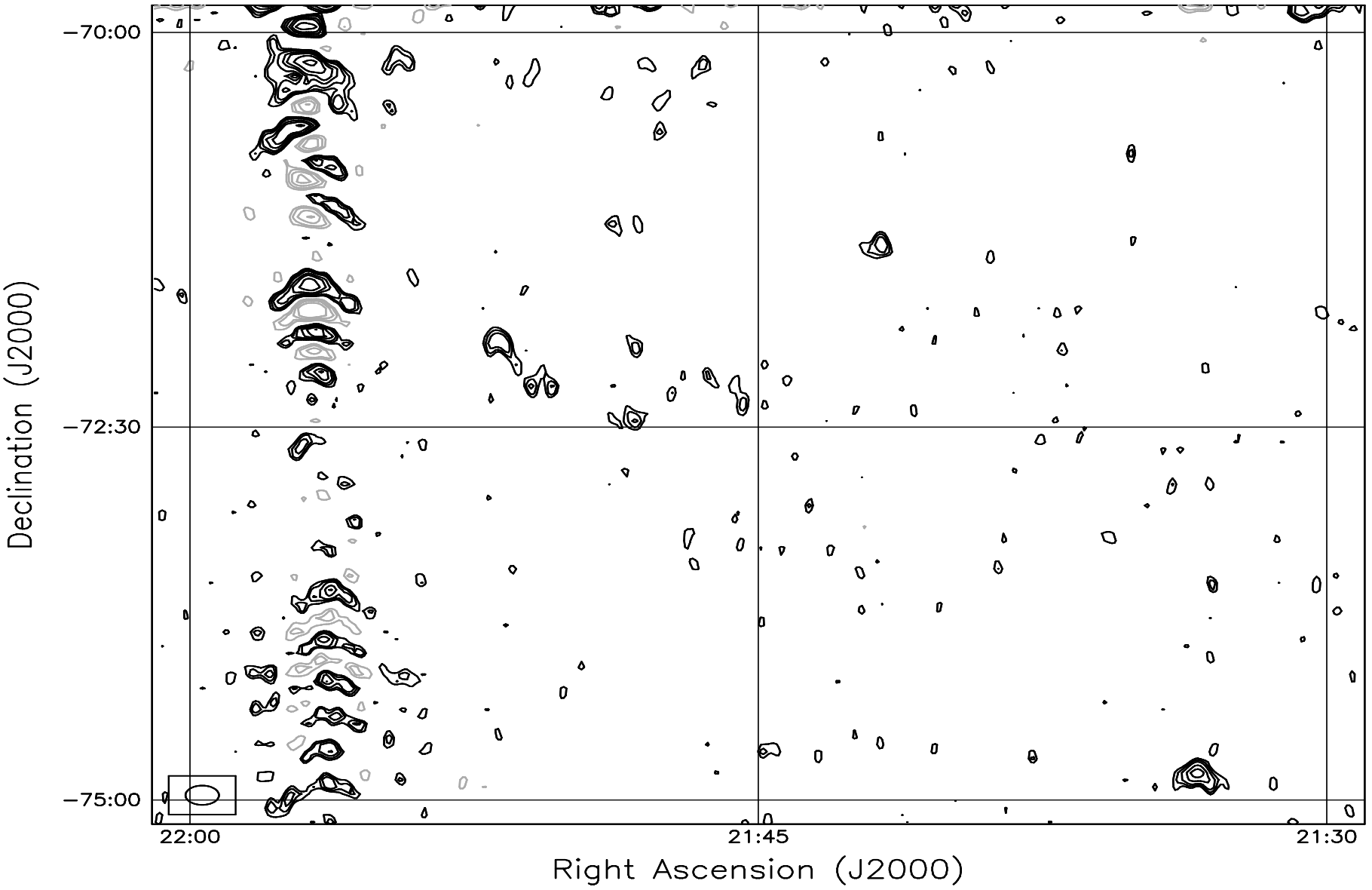

Fig. 7.143: Contour map covering the right ascension range 21h30m to 22h00m and declination range -75° to -70 °. The contour levels are -5, -3.6, -2.5, -1.8, 1, 1.4, 2, 2.8, 3.6, 5, 7, 10, 14, 20, 29, 40, 54, 72, 90, 100, 136, 180, 216, 252, 288 Jy beam^{-1}. The rms noise in the image is ≈380 mJy beam^{-1}.

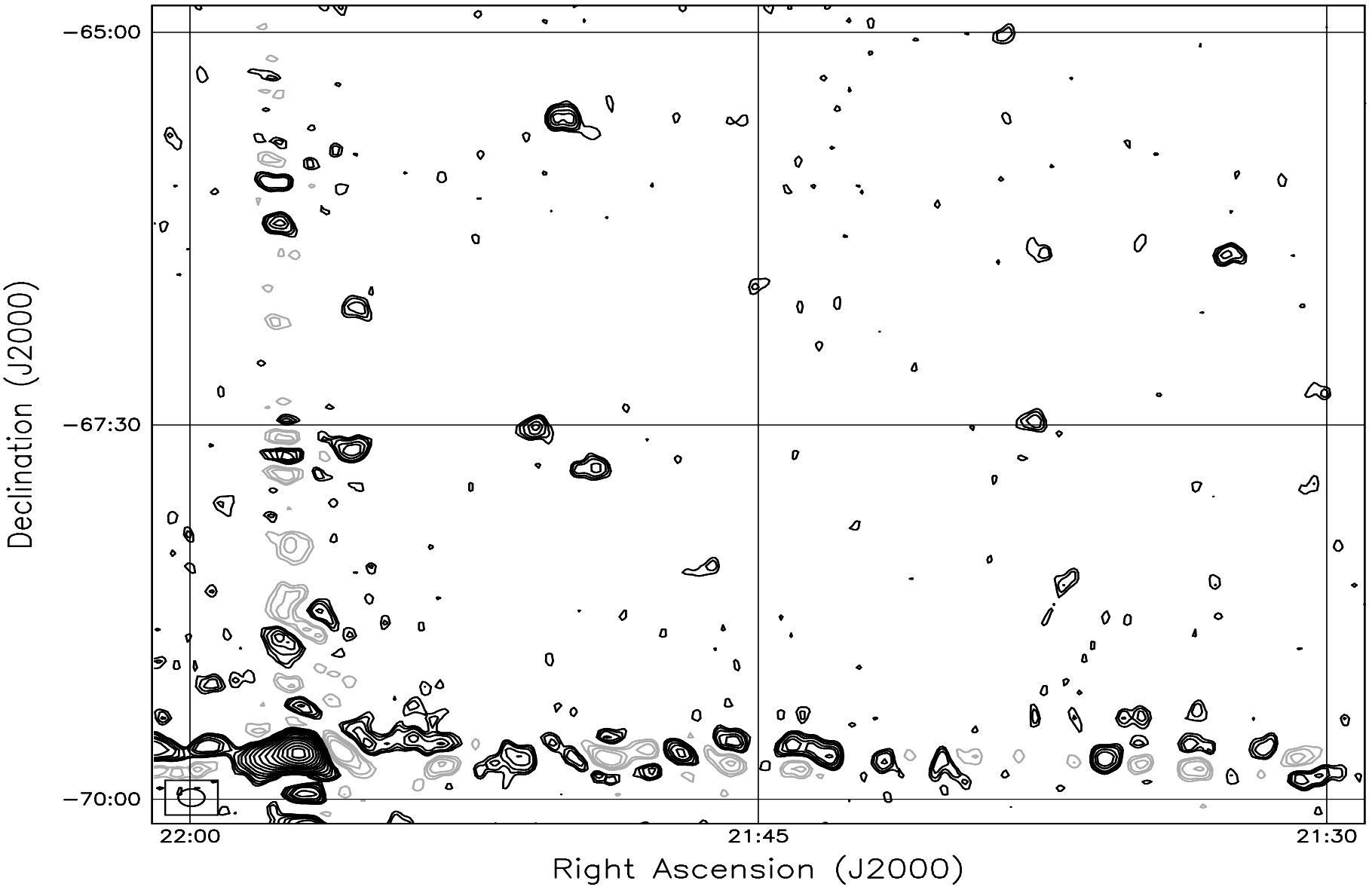

Fig. 7.144: Contour map covering the right ascension range 21h30m to 22h00m and declination range -70° to -65 °. The contour levels are -5, -3.6, -2.5, -1.8, 1, 1.4, 2, 2.8, 3.6, 5, 7, 10, 14, 20, 29, 40, 54, 72, 90, 100, 136, 180, 216, 252, 288 Jy beam^{-1}. The rms noise in the image is ≈330 mJy beam^{-1}.

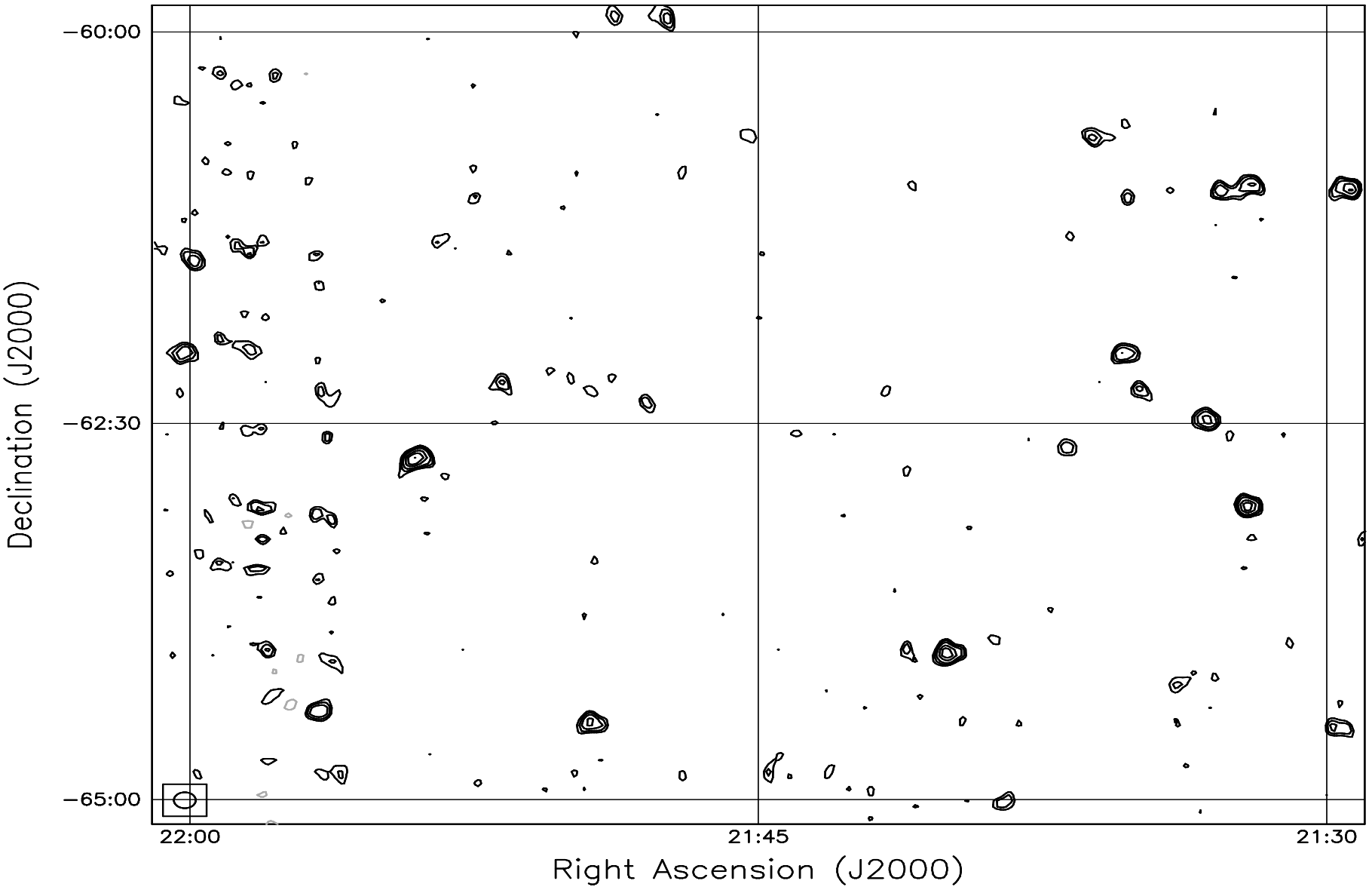

Fig. 7.145: Contour map covering the right ascension range 21h30m to 22h00m and declination range -65° to -60 °. The contour levels are -5, -3.6, -2.5, -1.8, 1, 1.4, 2, 2.8, 3.6, 5, 7, 10, 14, 20, 29, 40, 54, 72, 90, 100, 136, 180, 216, 252, 288 Jy beam^{-1}. The rms noise in the image is ≈300 mJy beam^{-1}.

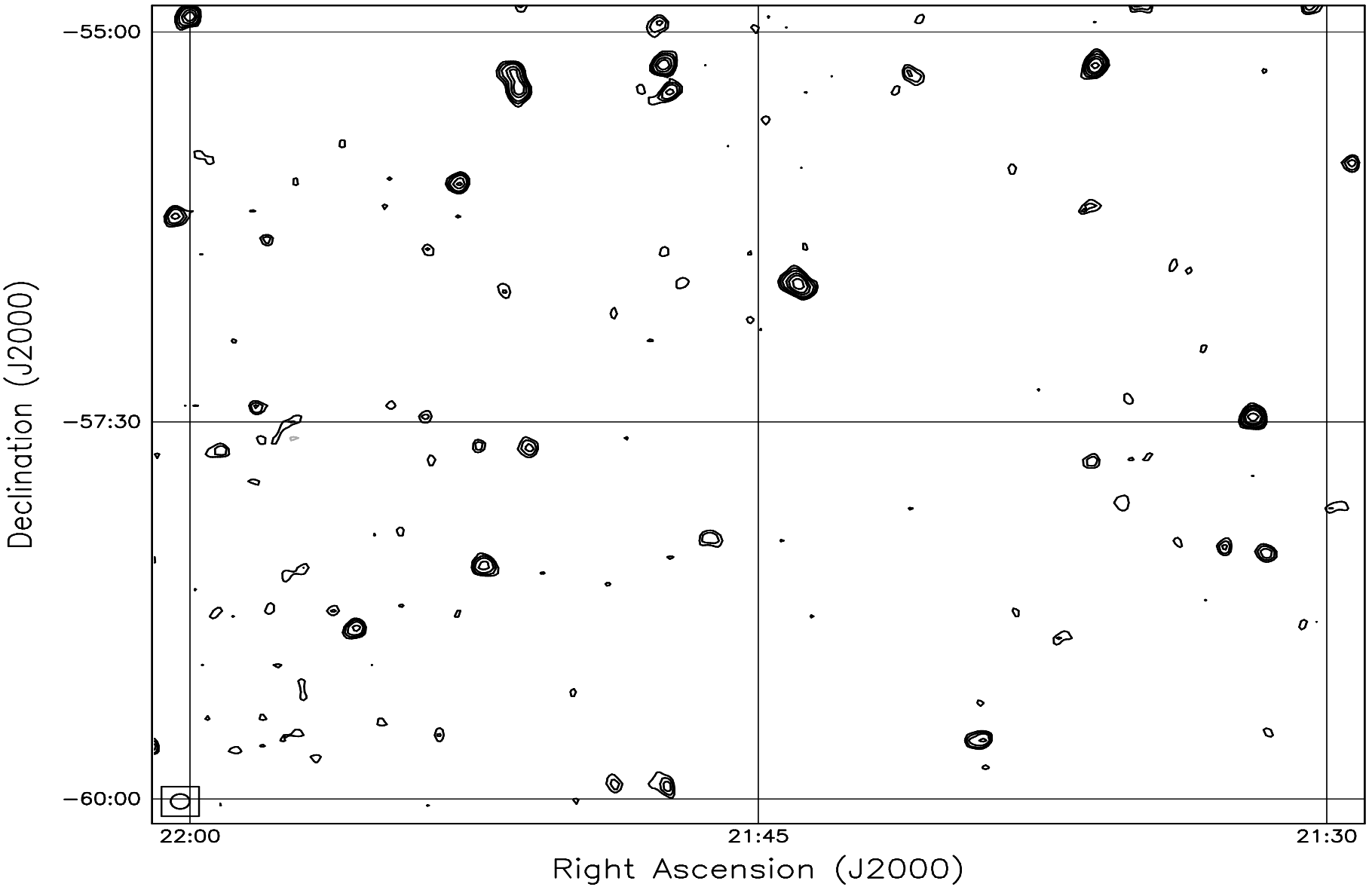

Fig. 7.146: Contour map covering the right ascension range 21h30m to 22h00m and declination range -60° to -55 °. The contour levels are -5, -3.6, -2.5, -1.8, 1, 1.4, 2, 2.8, 3.6, 5, 7, 10, 14, 20, 29, 40, 54, 72, 90, 100, 136, 180, 216, 252, 288 Jy beam^{-1}. The rms noise in the image is ≈280 mJy beam^{-1}.

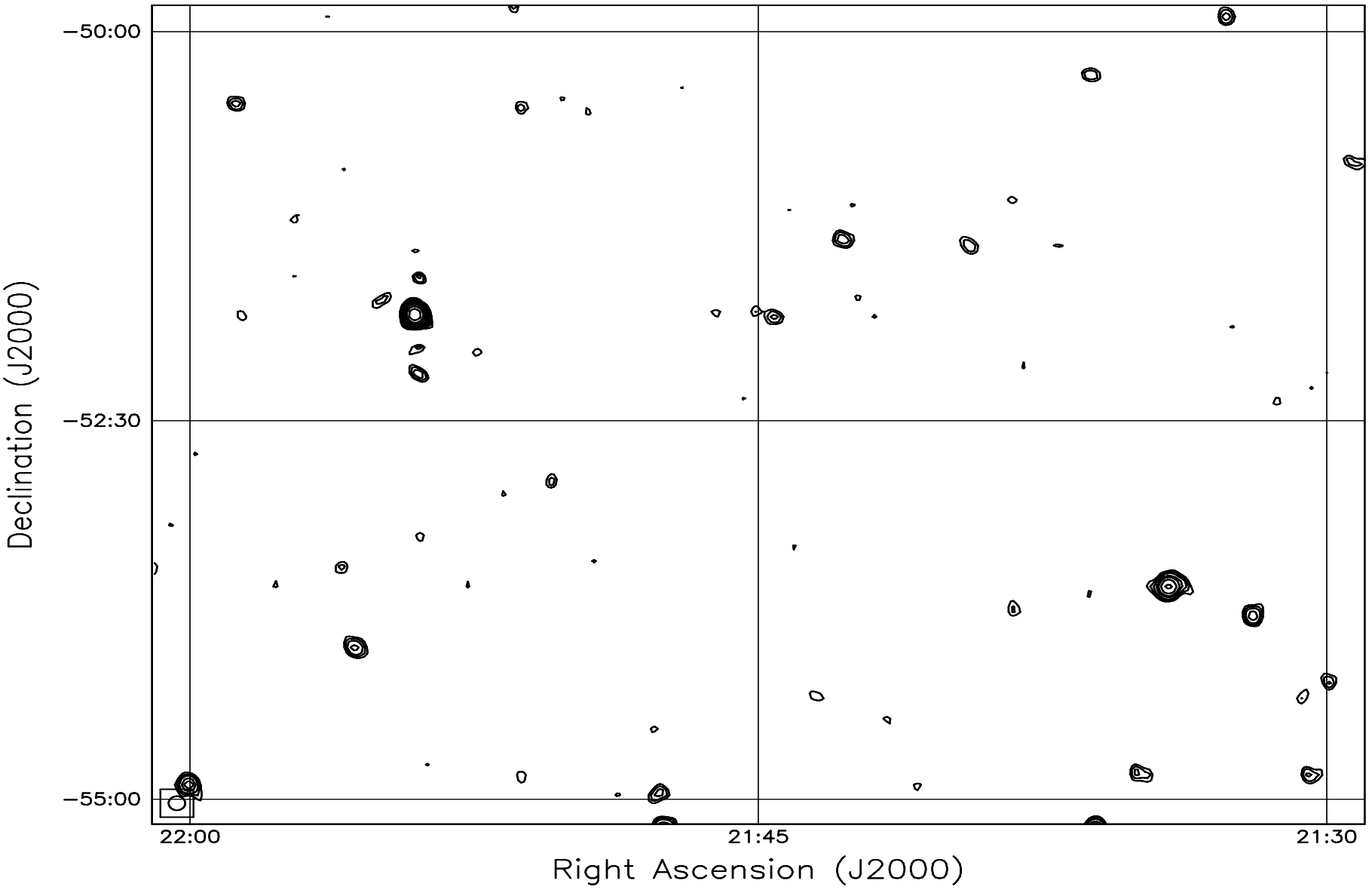

Fig. 7.147: Contour map covering the right ascension range 21h30m to 22h00m and declination range -55° to -50 °. The contour levels are -5, -3.6, -2.5, -1.8, 1, 1.4, 2, 2.8, 3.6, 5, 7, 10, 14, 20, 29, 40, 54, 72, 90, 100, 136, 180, 216, 252, 288 Jy beam^{-1}. The rms noise in the image is ≈270 mJy beam^{-1}.

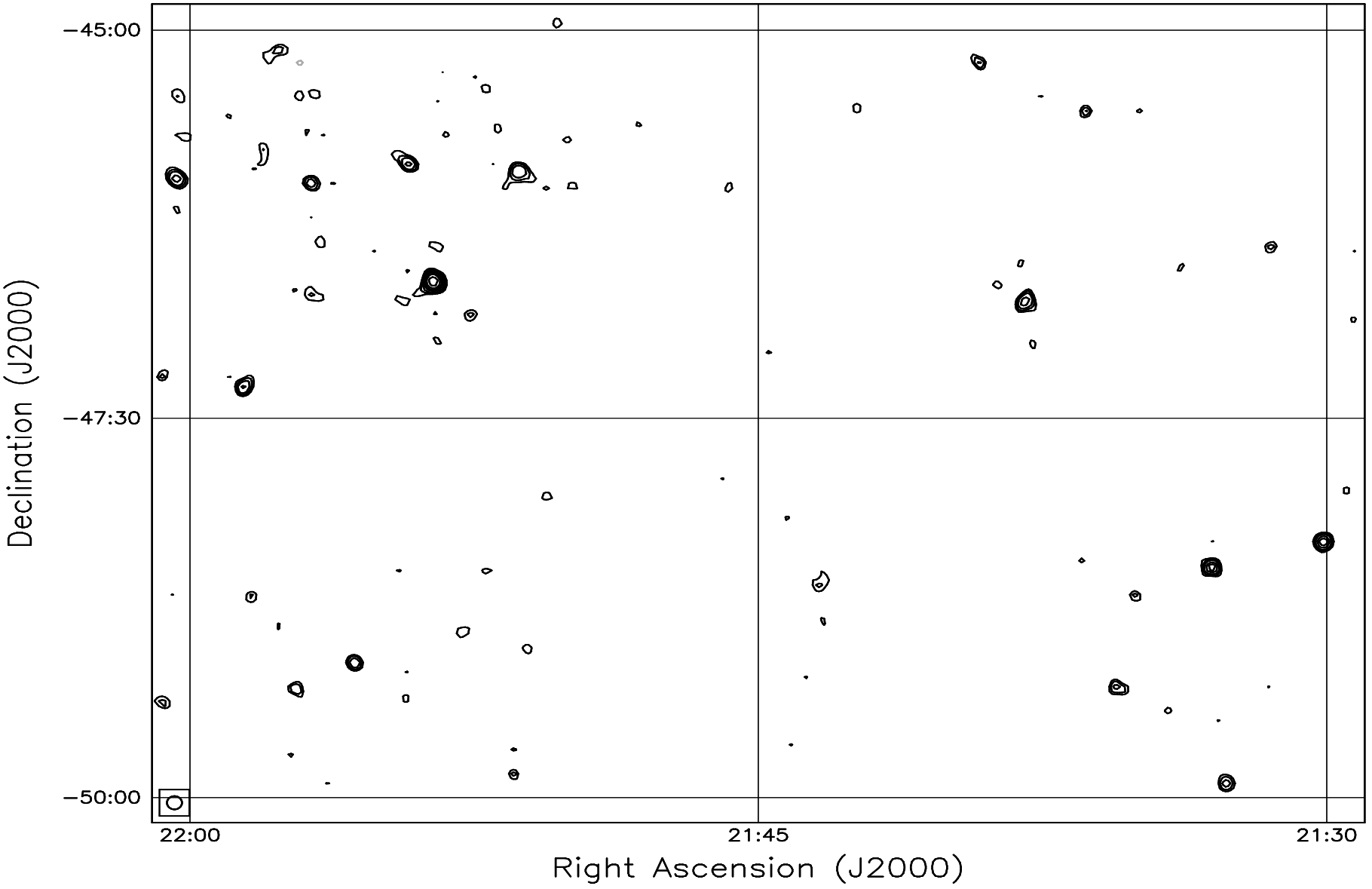

Fig. 7.148: Contour map covering the right ascension range 21h30m to 22h00m and declination range -50° to -45 °. The contour levels are -5, -3.6, -2.5, -1.8, 1, 1.4, 2, 2.8, 3.6, 5, 7, 10, 14, 20, 29, 40, 54, 72, 90, 100, 136, 180, 216, 252, 288 Jy beam^{-1}. The rms noise in the image is ≈260 mJy beam^{-1}.

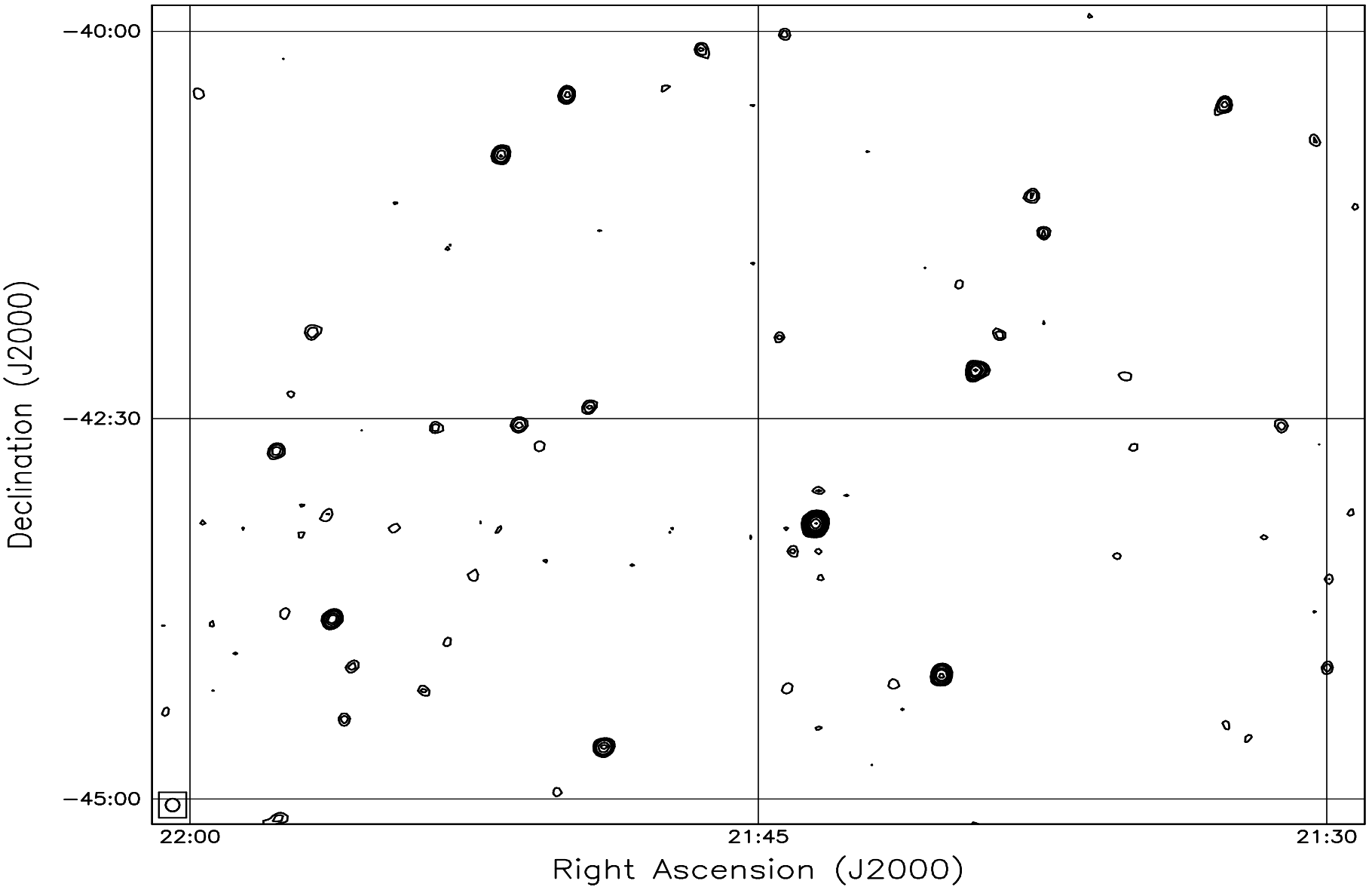

Fig. 7.149: Contour map covering the right ascension range 21h30m to 22h00m and declination range -45° to -40 °. The contour levels are -5, -3.6, -2.5, -1.8, 1, 1.4, 2, 2.8, 3.6, 5, 7, 10, 14, 20, 29, 40, 54, 72, 90, 100, 136, 180, 216, 252, 288 Jy beam^{-1}. The rms noise in the image is ≈260 mJy beam^{-1}.

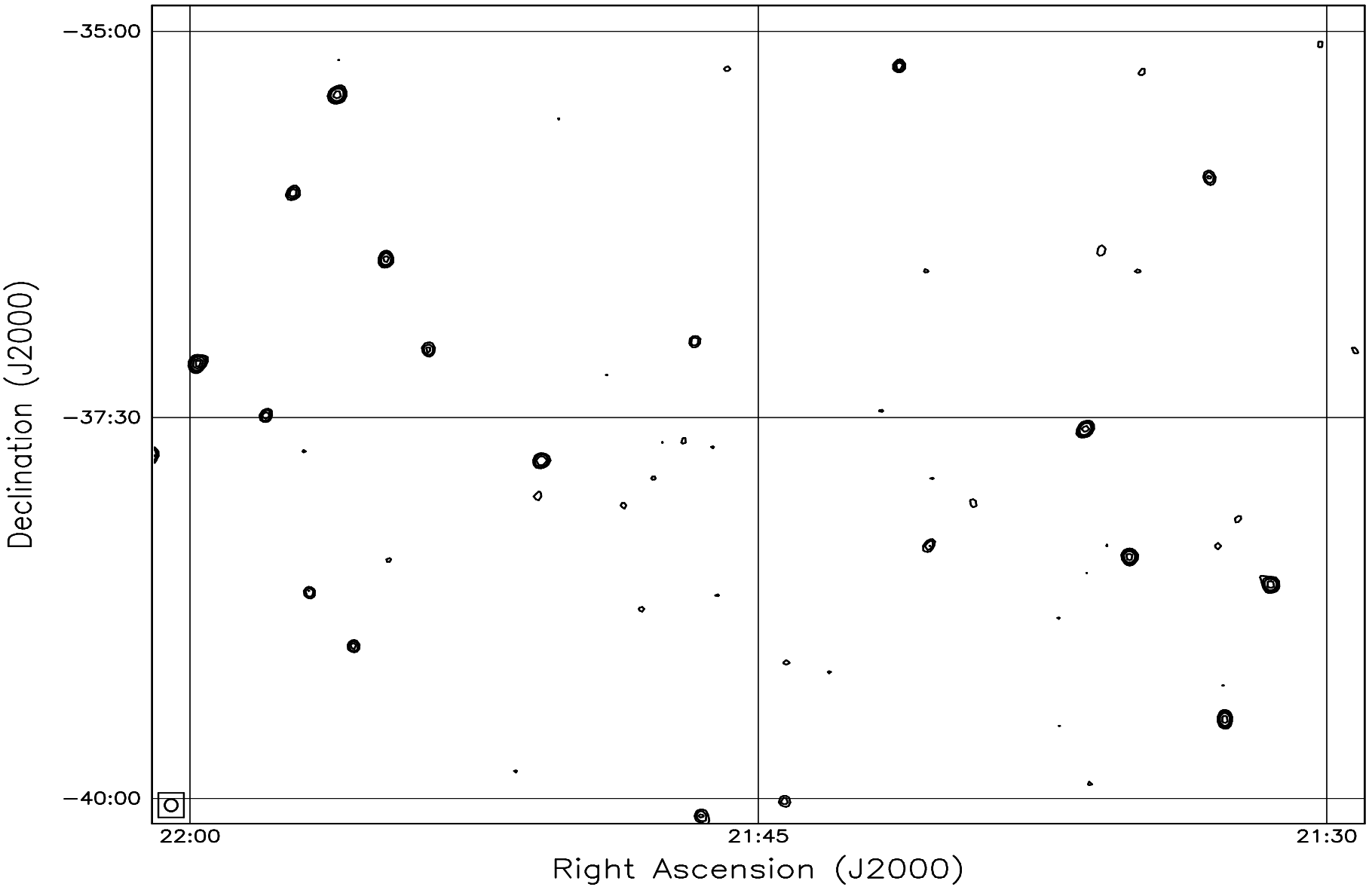

Fig. 7.150: Contour map covering the right ascension range 21h30m to 22h00m and declination range -40° to -35 °. The contour levels are -5, -3.6, -2.5, -1.8, 1, 1.4, 2, 2.8, 3.6, 5, 7, 10, 14, 20, 29, 40, 54, 72, 90, 100, 136, 180, 216, 252, 288 Jy beam^{-1}. The rms noise in the image is ≈270 mJy beam^{-1}.

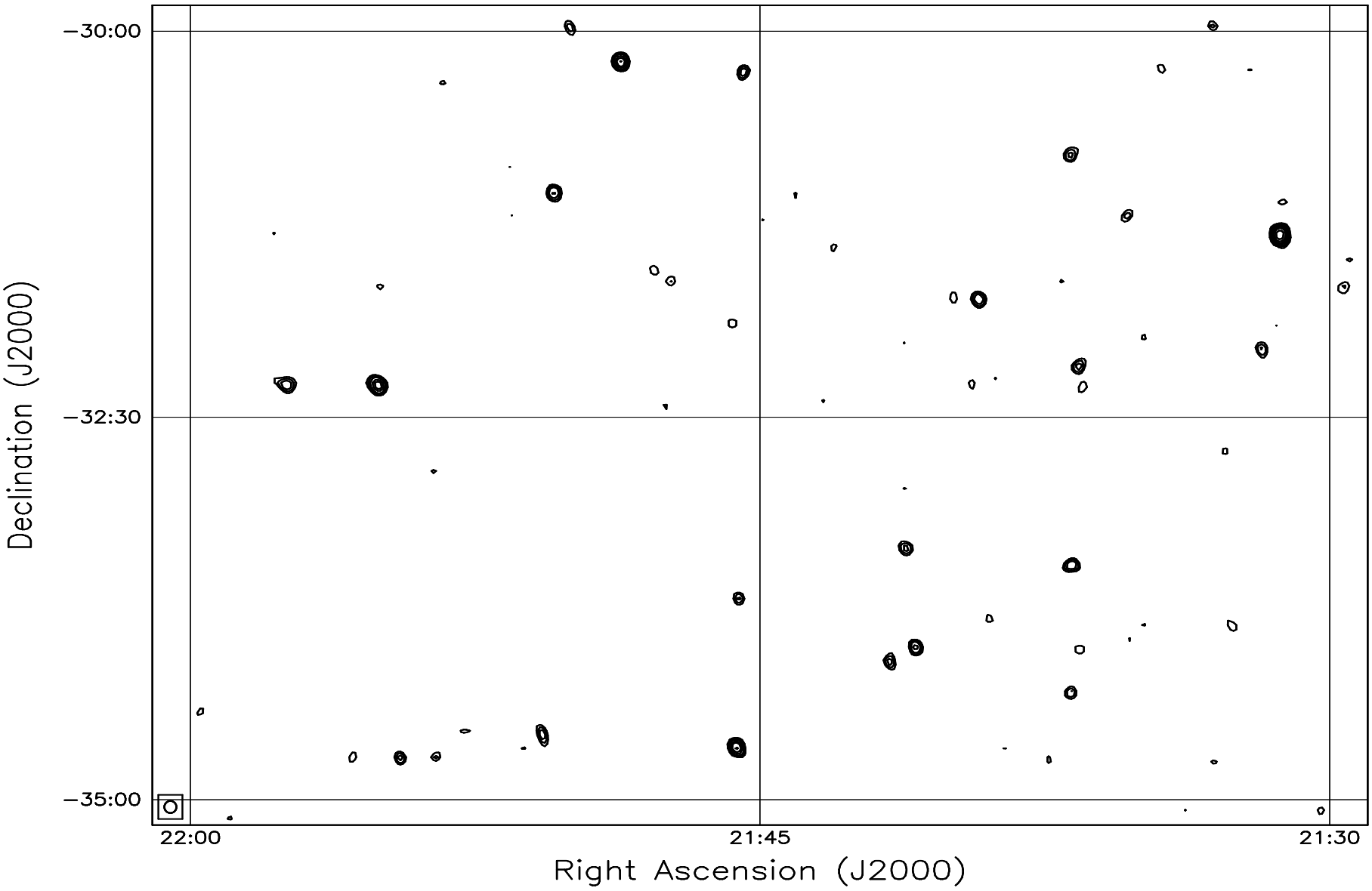

Fig. 7.151: Contour map covering the right ascension range 21h30m to 22h00m and declination range -35° to -30 °. The contour levels are -5, -3.6, -2.5, -1.8, 1, 1.4, 2, 2.8, 3.6, 5, 7, 10, 14, 20, 29, 40, 54, 72, 90, 100, 136, 180, 216, 252, 288 Jy beam^{-1}. The rms noise in the image is ≈280 mJy beam^{-1}.

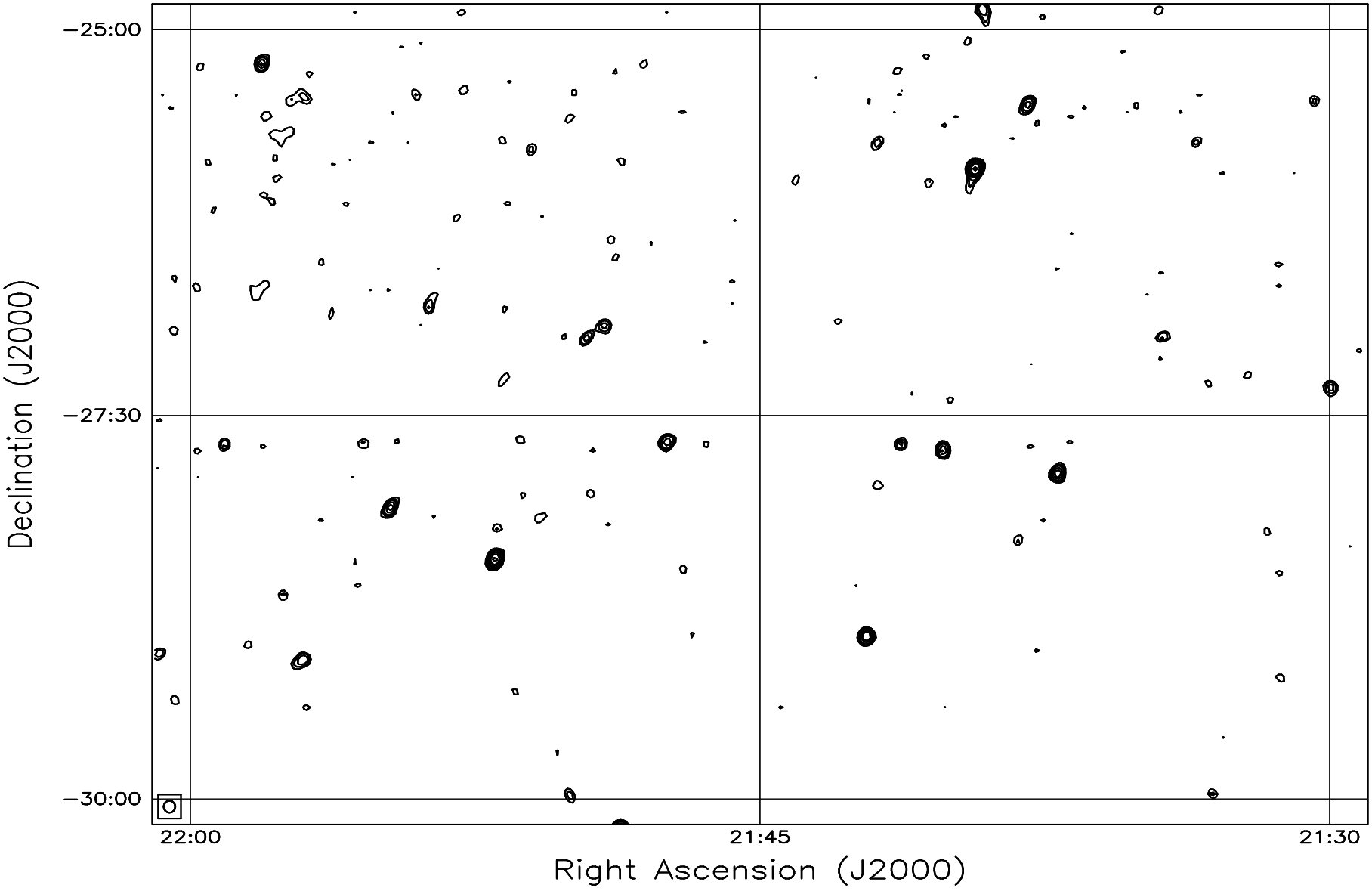

Fig. 7.152: Contour map covering the right ascension range 21h30m to 22h00m and declination range -30° to -25 °. The contour levels are -5, -3.6, -2.5, -1.8, 1, 1.4, 2, 2.8, 3.6, 5, 7, 10, 14, 20, 29, 40, 54, 72, 90, 100, 136, 180, 216, 252, 288 Jy beam^{-1}. The rms noise in the image is ≈300 mJy beam^{-1}.

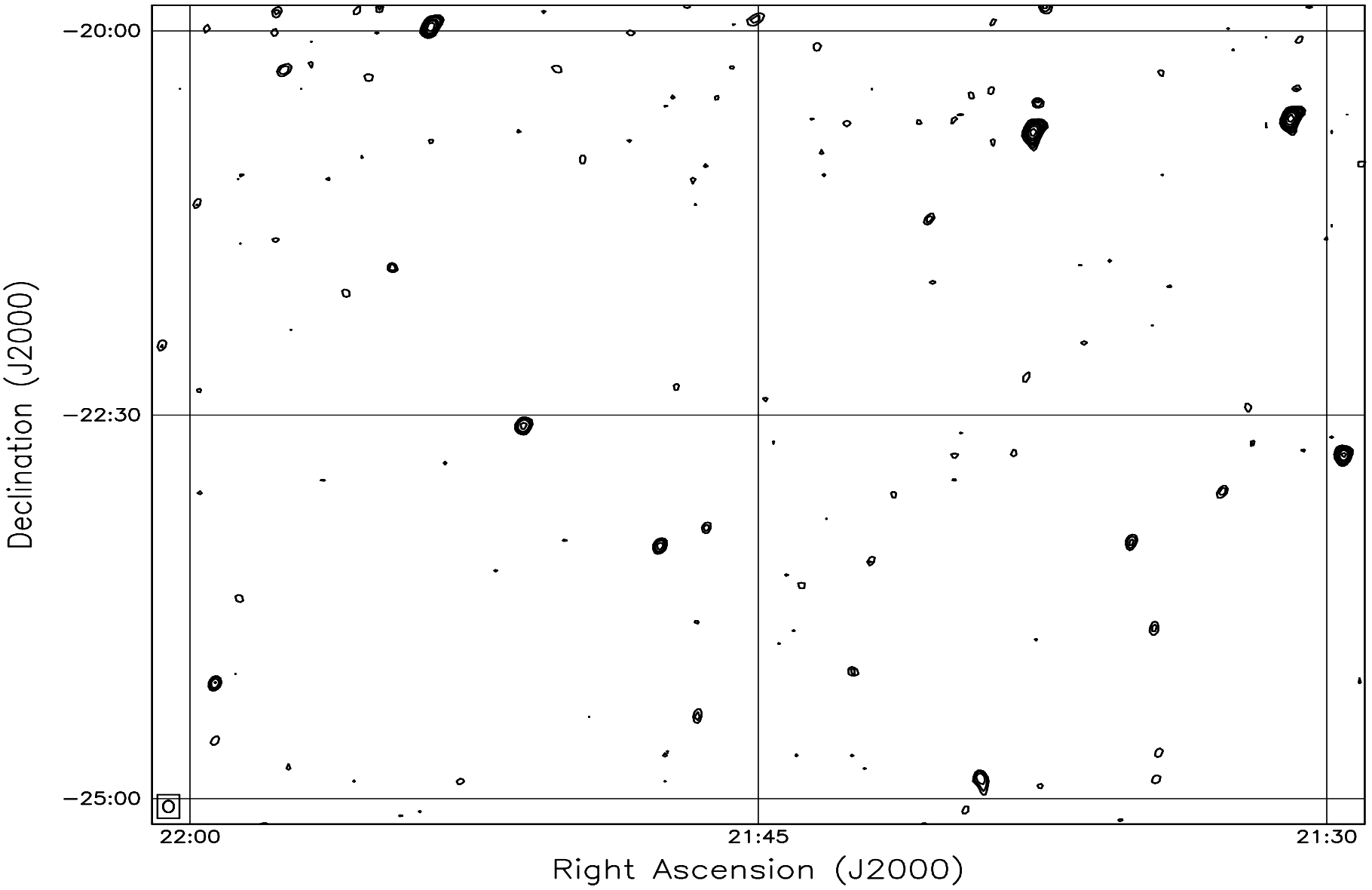

Fig. 7.153: Contour map covering the right ascension range 21h30m to 22h00m and declination range -25° to -20 °. The contour levels are -5, -3.6, -2.5, -1.8, 1, 1.4, 2, 2.8, 3.6, 5, 7, 10, 14, 20, 29, 40, 54, 72, 90, 100, 136, 180, 216, 252, 288 Jy beam^{-1}. The rms noise in the image is ≈330 mJy beam^{-1}.

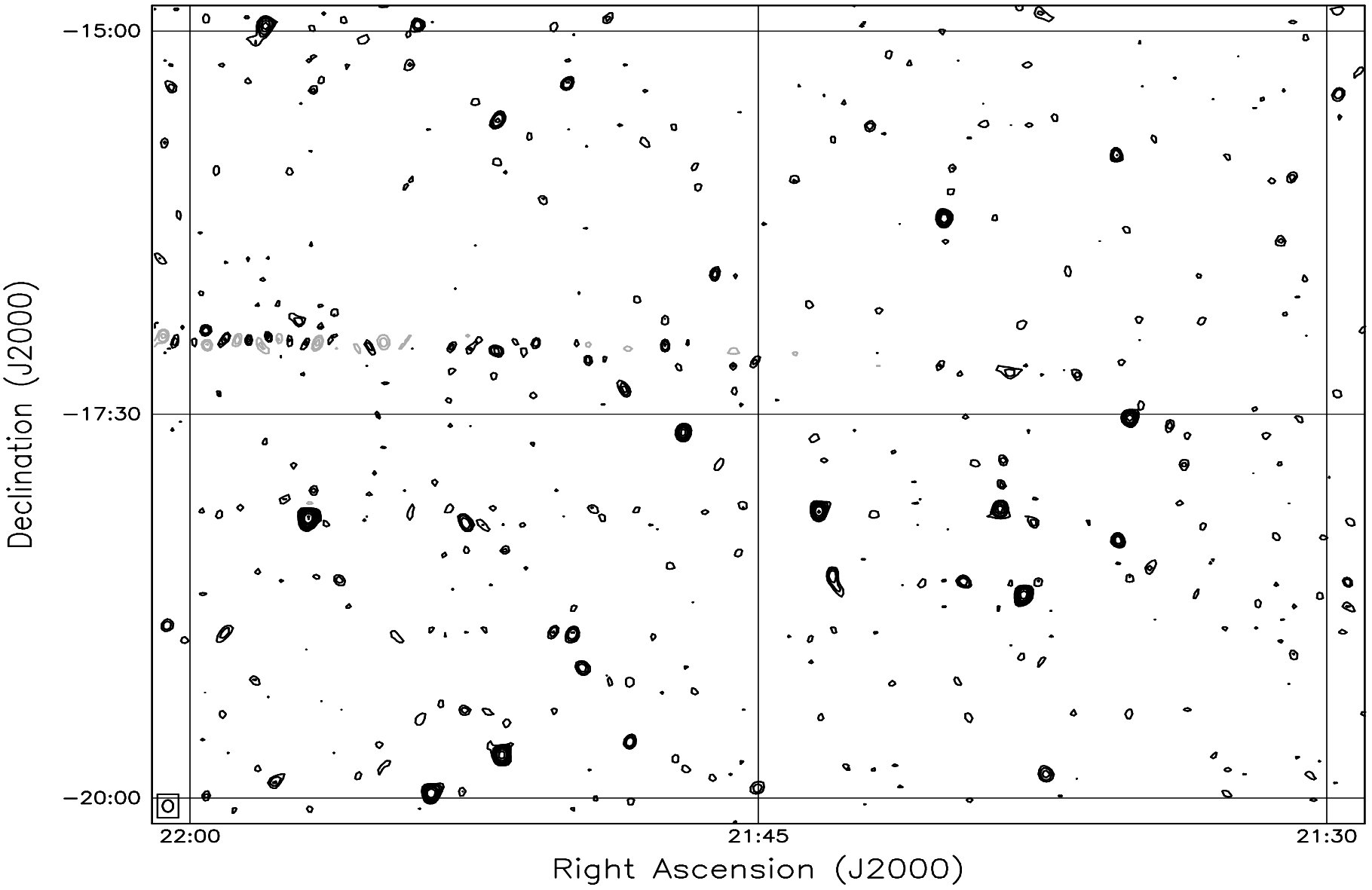

Fig. 7.154: Contour map covering the right ascension range 21h30m to 22h00m and declination range -20° to -15 °. The contour levels are -5, -3.6, -2.5, -1.8, 1, 1.4, 2, 2.8, 3.6, 5, 7, 10, 14, 20, 29, 40, 54, 72, 90, 100, 136, 180, 216, 252, 288 Jy beam^{-1}. The rms noise in the image is ≈375 mJy beam^{-1}.

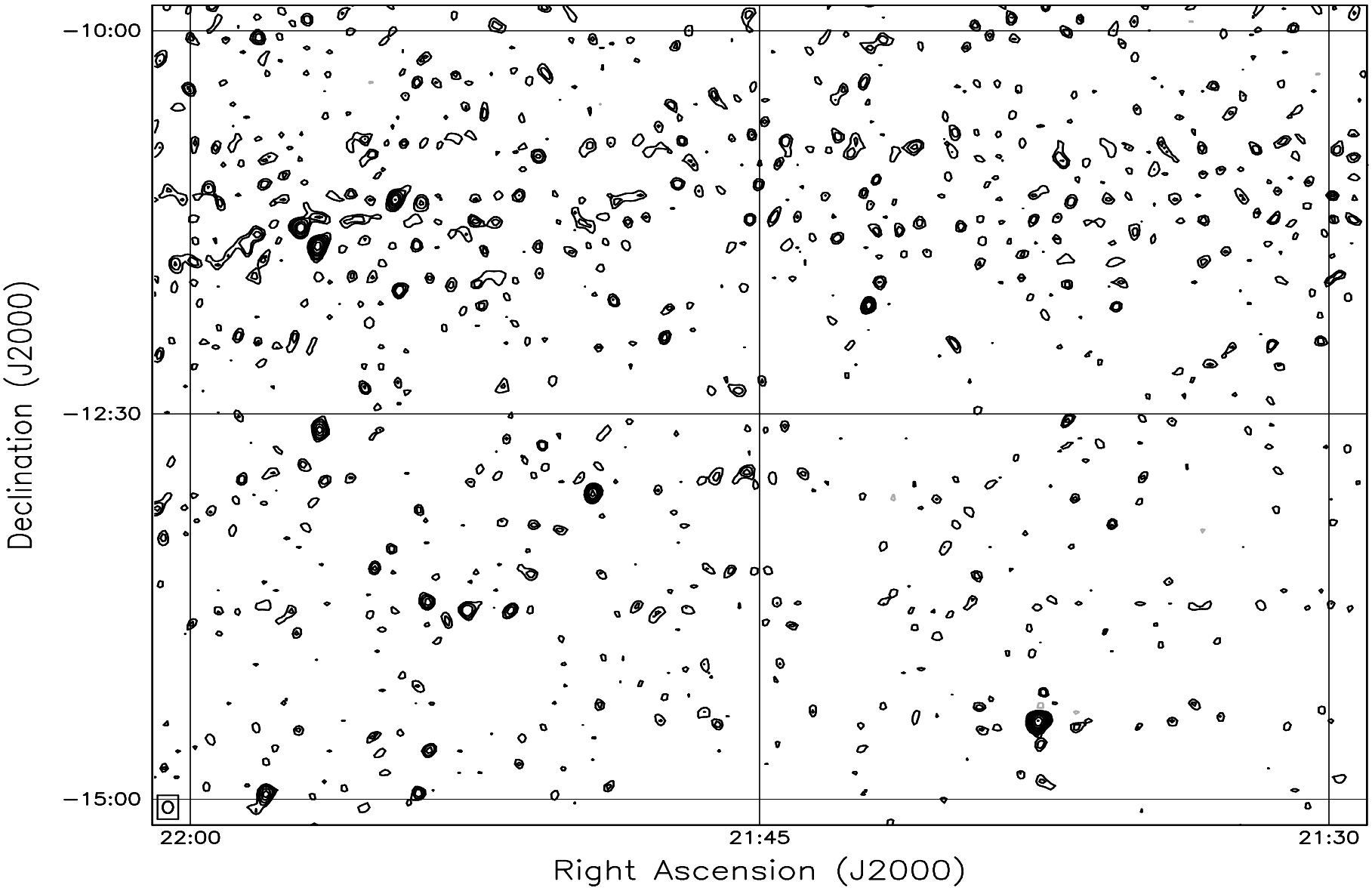

Fig. 7.155: Contour map covering the right ascension range 21h30m to 22h00m and declination range -15° to -10 °. The contour levels are -5, -3.6, -2.5, -1.8, 1, 1.4, 2, 2.8, 3.6, 5, 7, 10, 14, 20, 29, 40, 54, 72, 90, 100, 136, 180, 216, 252, 288 Jy beam^{-1}. The rms noise in the image is ≈460 mJy beam^{-1}.

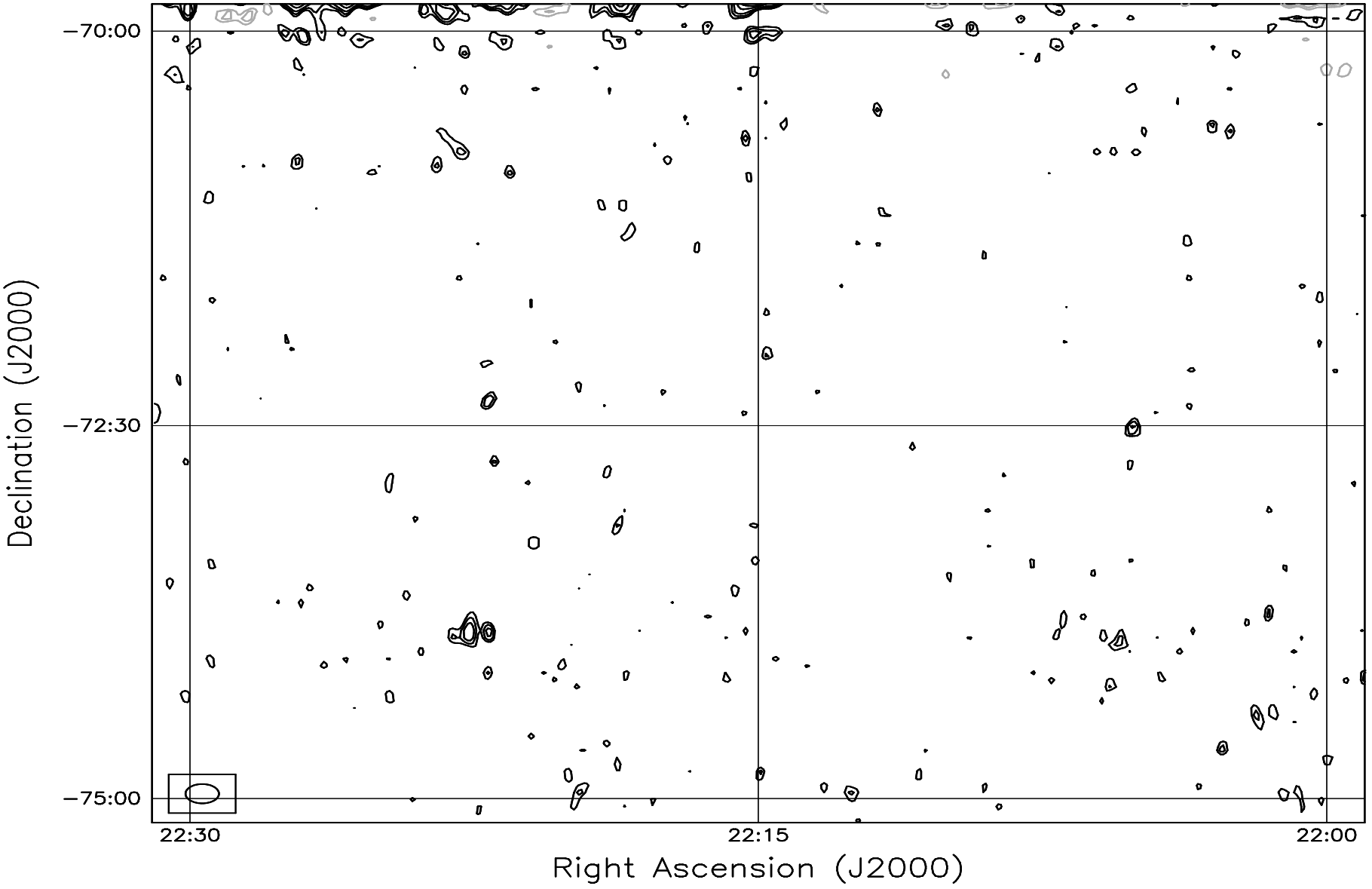

Fig. 7.156: Contour map covering the right ascension range 22h00m to 22h30m and declination range -75° to -70 °. The contour levels are -5, -3.6, -2.5, -1.8, 1, 1.4, 2, 2.8, 3.6, 5, 7, 10, 14, 20, 29, 40, 54, 72, 90, 100, 136, 180, 216, 252, 288 Jy beam^{-1}. The rms noise in the image is ≈380 mJy beam^{-1}.

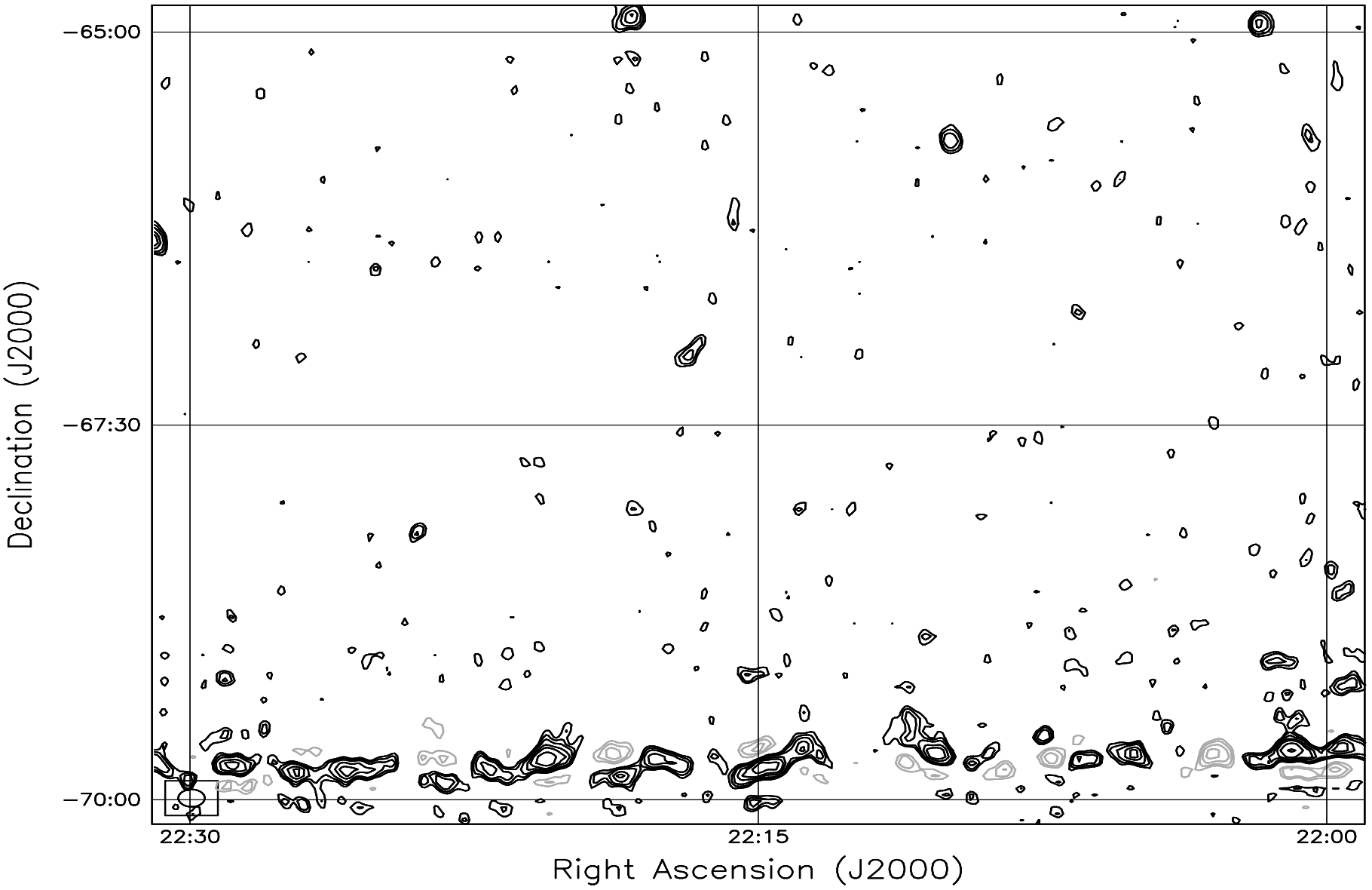

Fig. 7.157: Contour map covering the right ascension range 22h00m to 22h30m and declination range -70° to -65 °. The contour levels are -5, -3.6, -2.5, -1.8, 1, 1.4, 2, 2.8, 3.6, 5, 7, 10, 14, 20, 29, 40, 54, 72, 90, 100, 136, 180, 216, 252, 288 Jy beam^{-1}. The rms noise in the image is ≈330 mJy beam^{-1}.

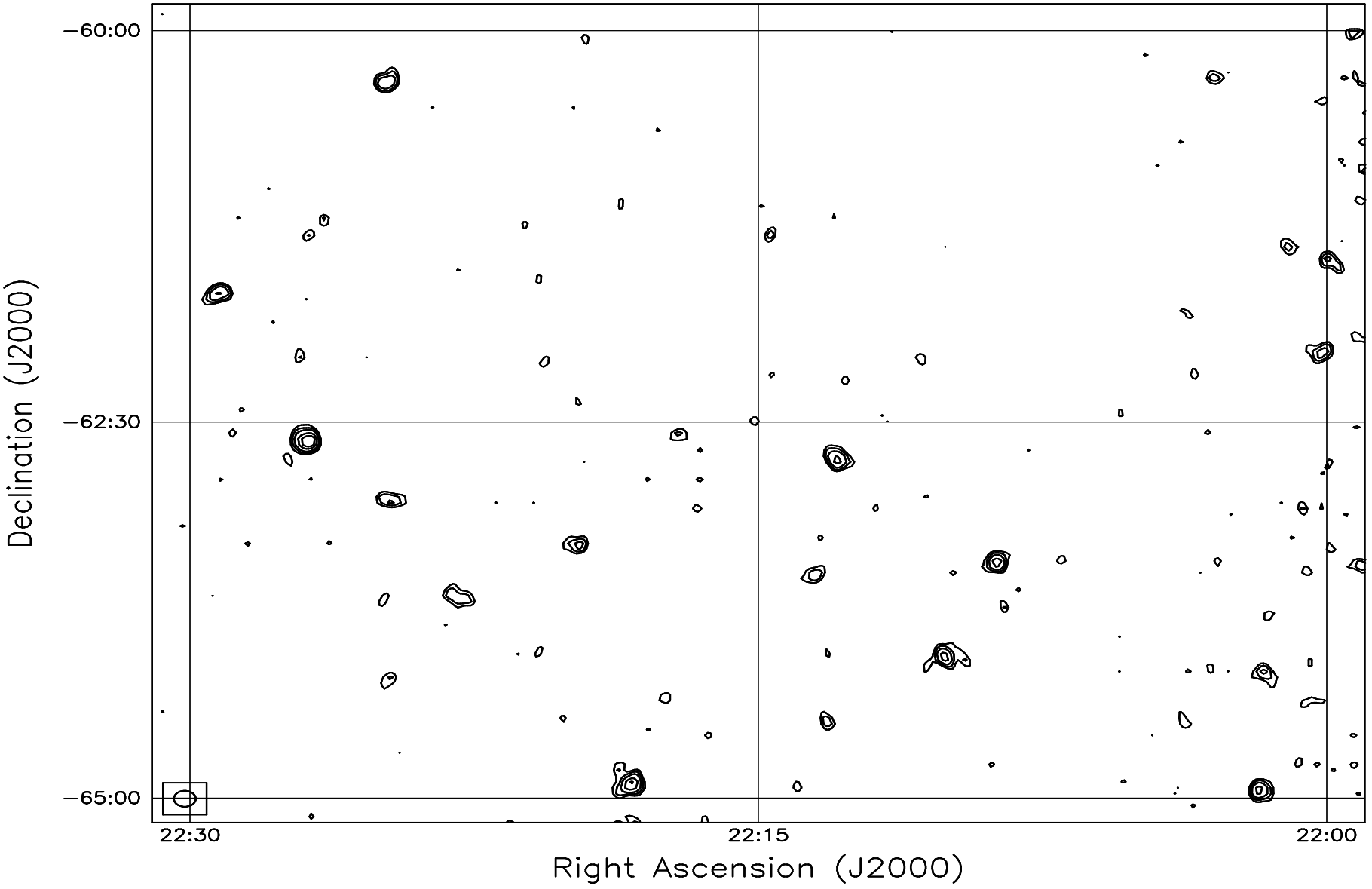

Fig. 7.158: Contour map covering the right ascension range 22h00m to 22h30m and declination range -65° to -60 °. The contour levels are -5, -3.6, -2.5, -1.8, 1, 1.4, 2, 2.8, 3.6, 5, 7, 10, 14, 20, 29, 40, 54, 72, 90, 100, 136, 180, 216, 252, 288 Jy beam^{-1}. The rms noise in the image is ≈300 mJy beam^{-1}.

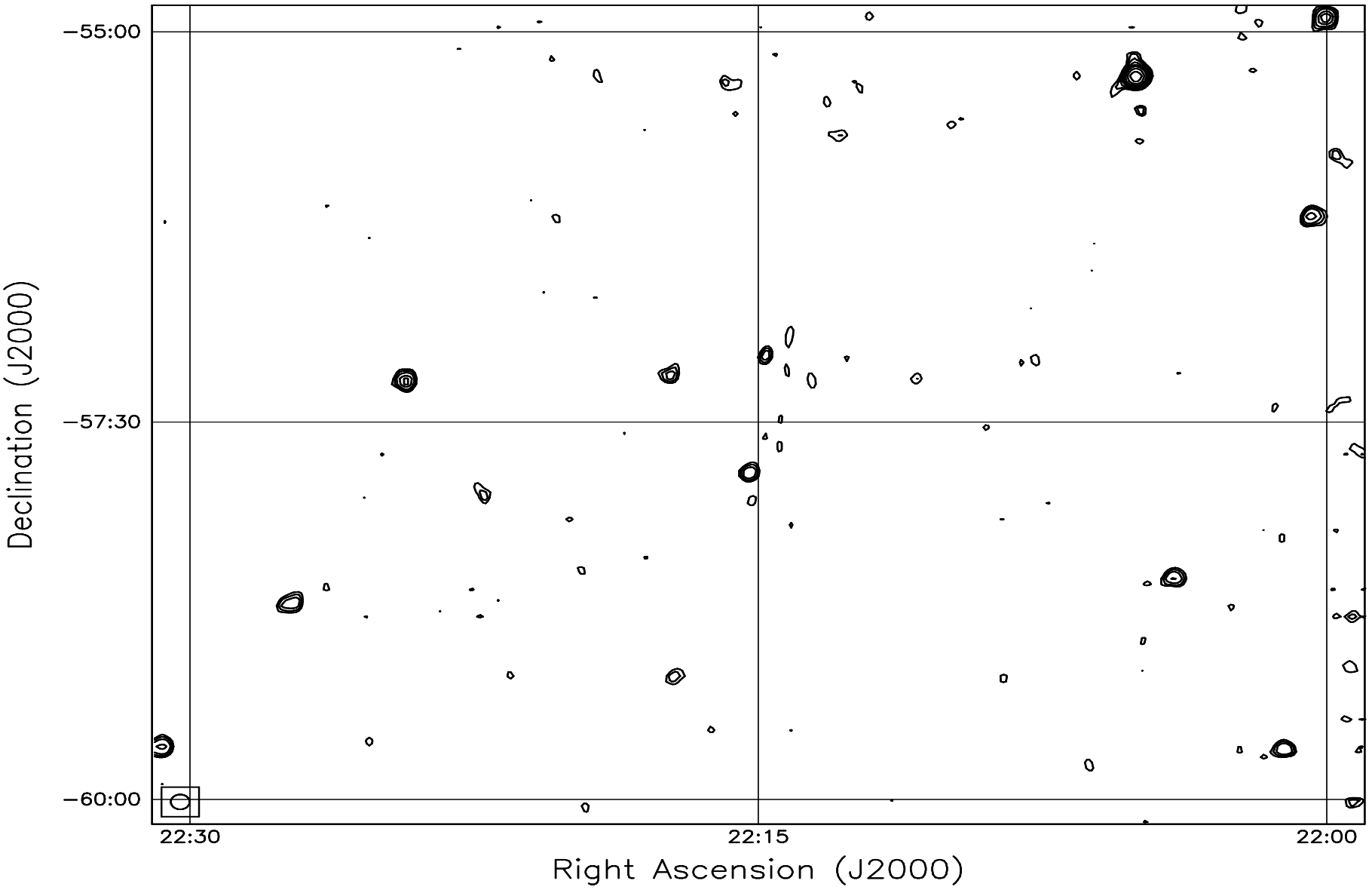

Fig. 7.159: Contour map covering the right ascension range 22h00m to 22h30m and declination range -60° to -55 °. The contour levels are -5, -3.6, -2.5, -1.8, 1, 1.4, 2, 2.8, 3.6, 5, 7, 10, 14, 20, 29, 40, 54, 72, 90, 100, 136, 180, 216, 252, 288 Jy beam^{-1}. The rms noise in the image is ≈280 mJy beam^{-1}.

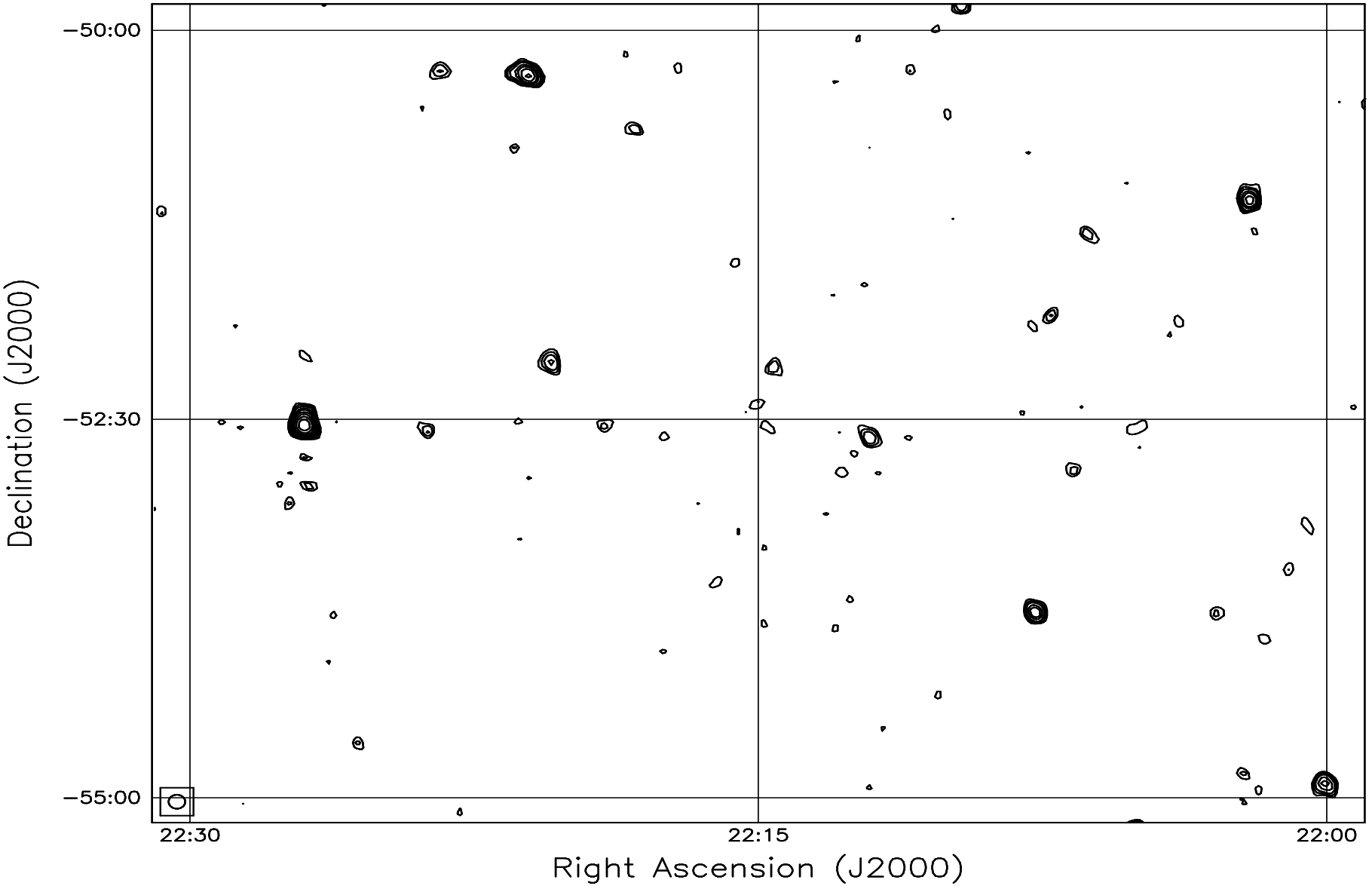

Fig. 7.160: Contour map covering the right ascension range 22h00m to 22h30m and declination range -55° to -50 °. The contour levels are -5, -3.6, -2.5, -1.8, 1, 1.4, 2, 2.8, 3.6, 5, 7, 10, 14, 20, 29, 40, 54, 72, 90, 100, 136, 180, 216, 252, 288 Jy beam^{-1}. The rms noise in the image is ≈270 mJy beam^{-1}.

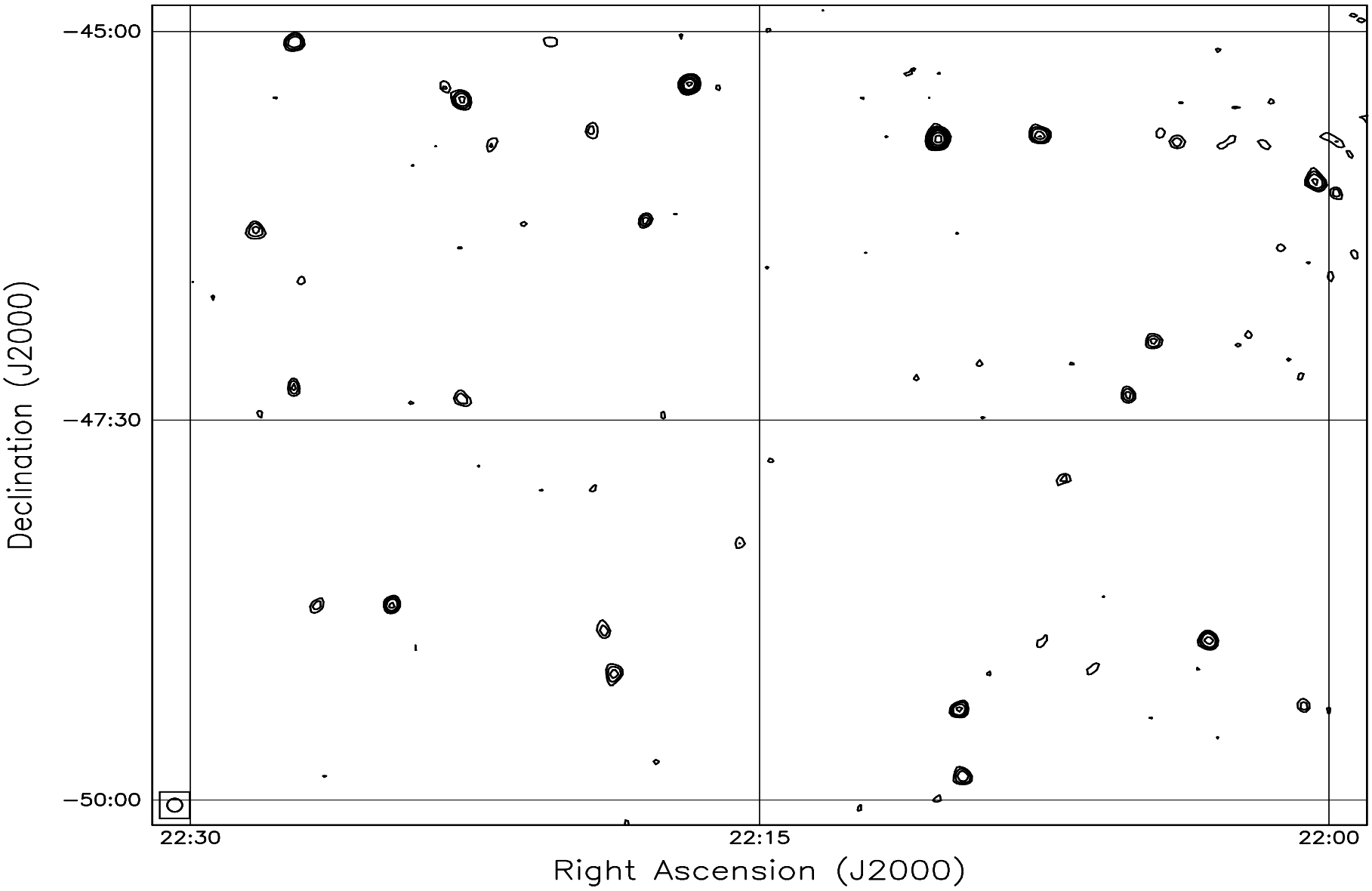

Fig. 7.161: Contour map covering the right ascension range 22h00m to 22h30m and declination range -50° to -45 °. The contour levels are -5, -3.6, -2.5, -1.8, 1, 1.4, 2, 2.8, 3.6, 5, 7, 10, 14, 20, 29, 40, 54, 72, 90, 100, 136, 180, 216, 252, 288 Jy beam^{-1}. The rms noise in the image is ≈260 mJy beam^{-1}.

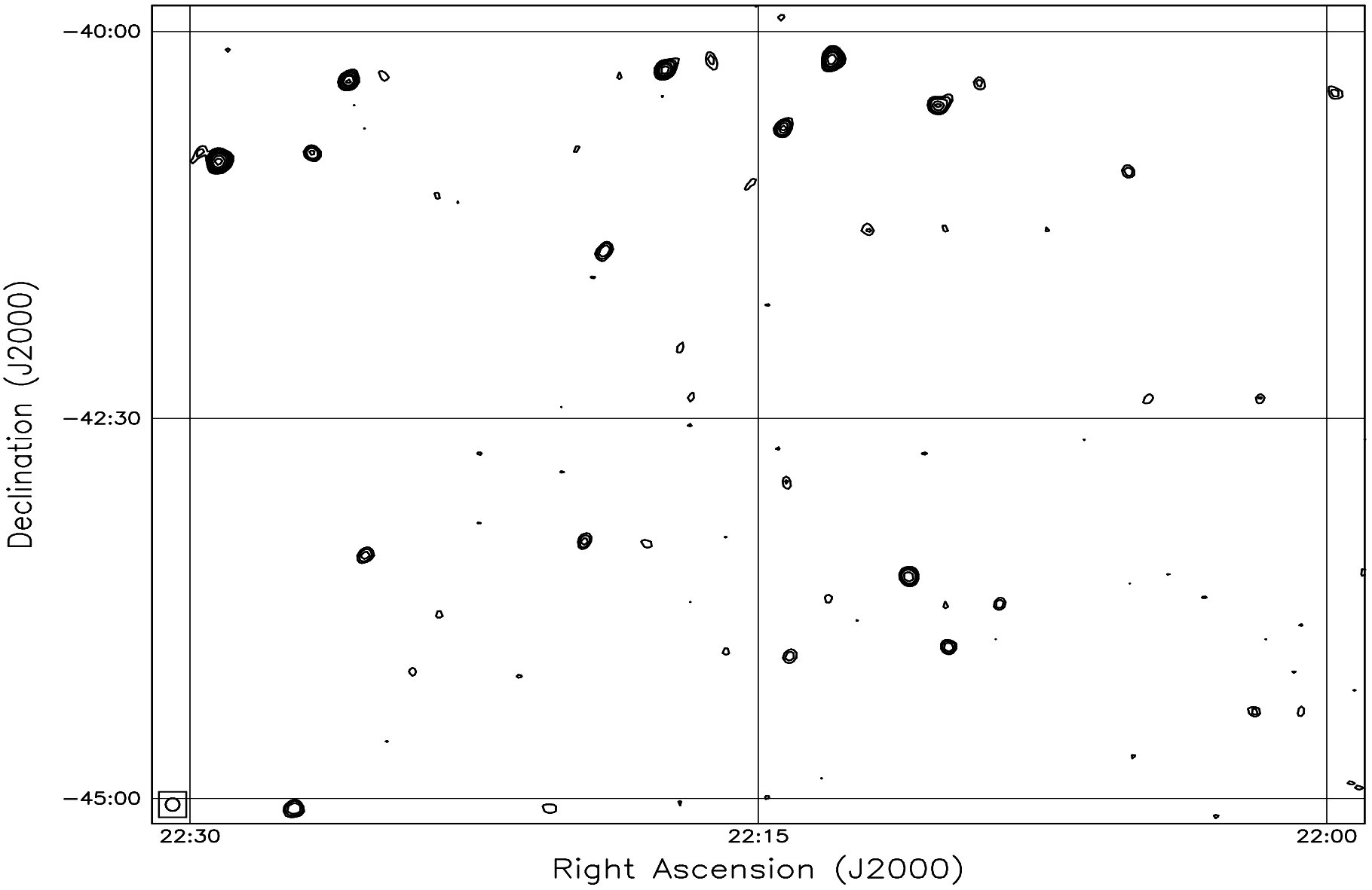

Fig. 7.162: Contour map covering the right ascension range 22h00m to 22h30m and declination range -45° to -40 °. The contour levels are -5, -3.6, -2.5, -1.8, 1, 1.4, 2, 2.8, 3.6, 5, 7, 10, 14, 20, 29, 40, 54, 72, 90, 100, 136, 180, 216, 252, 288 Jy beam^{-1}. The rms noise in the image is ≈260 mJy beam^{-1}.

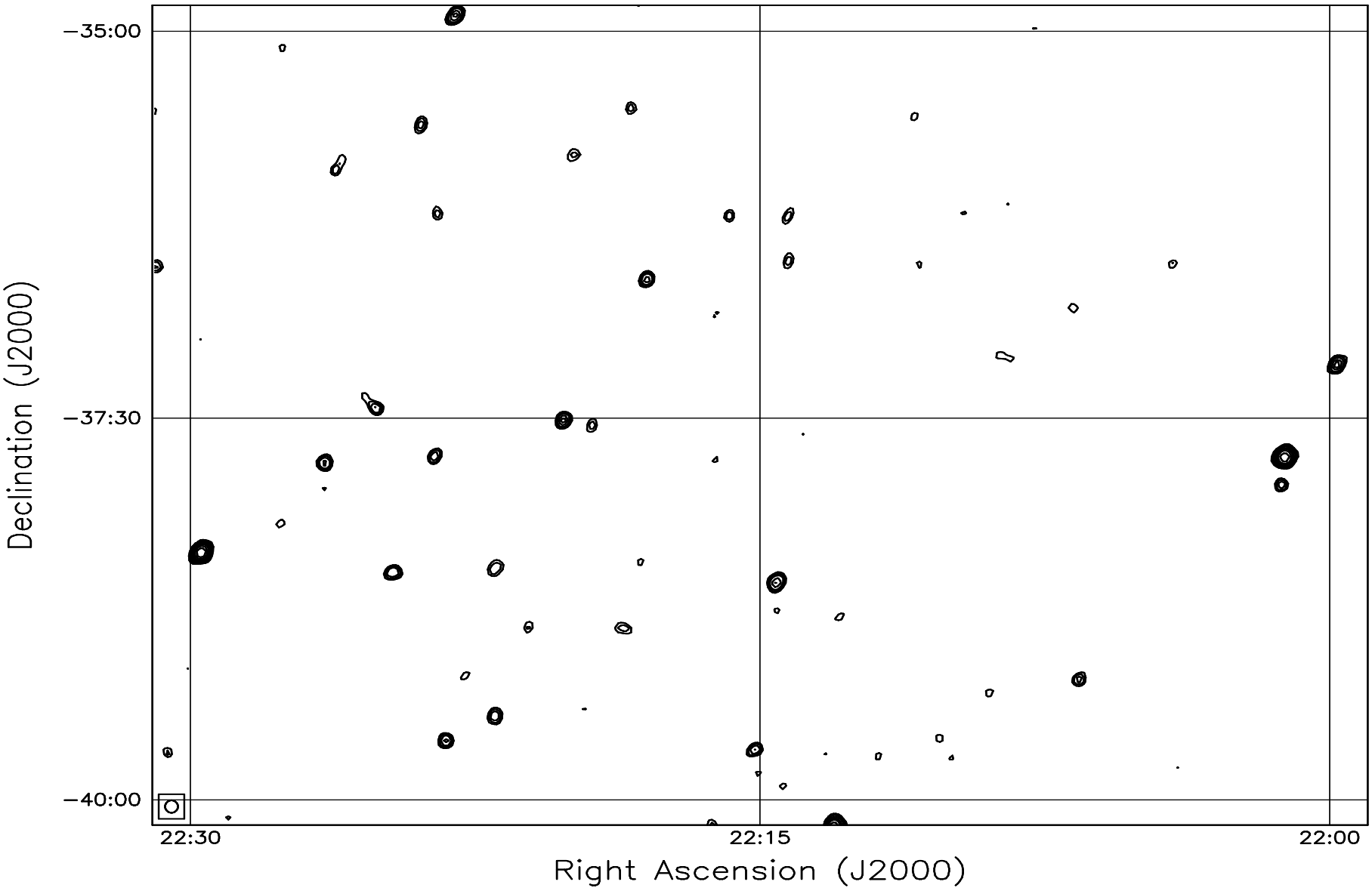

Fig. 7.163: Contour map covering the right ascension range 22h00m to 22h30m and declination range -40° to -35 °. The contour levels are -5, -3.6, -2.5, -1.8, 1, 1.4, 2, 2.8, 3.6, 5, 7, 10, 14, 20, 29, 40, 54, 72, 90, 100, 136, 180, 216, 252, 288 Jy beam^{-1}. The rms noise in the image is ≈270 mJy beam^{-1}.

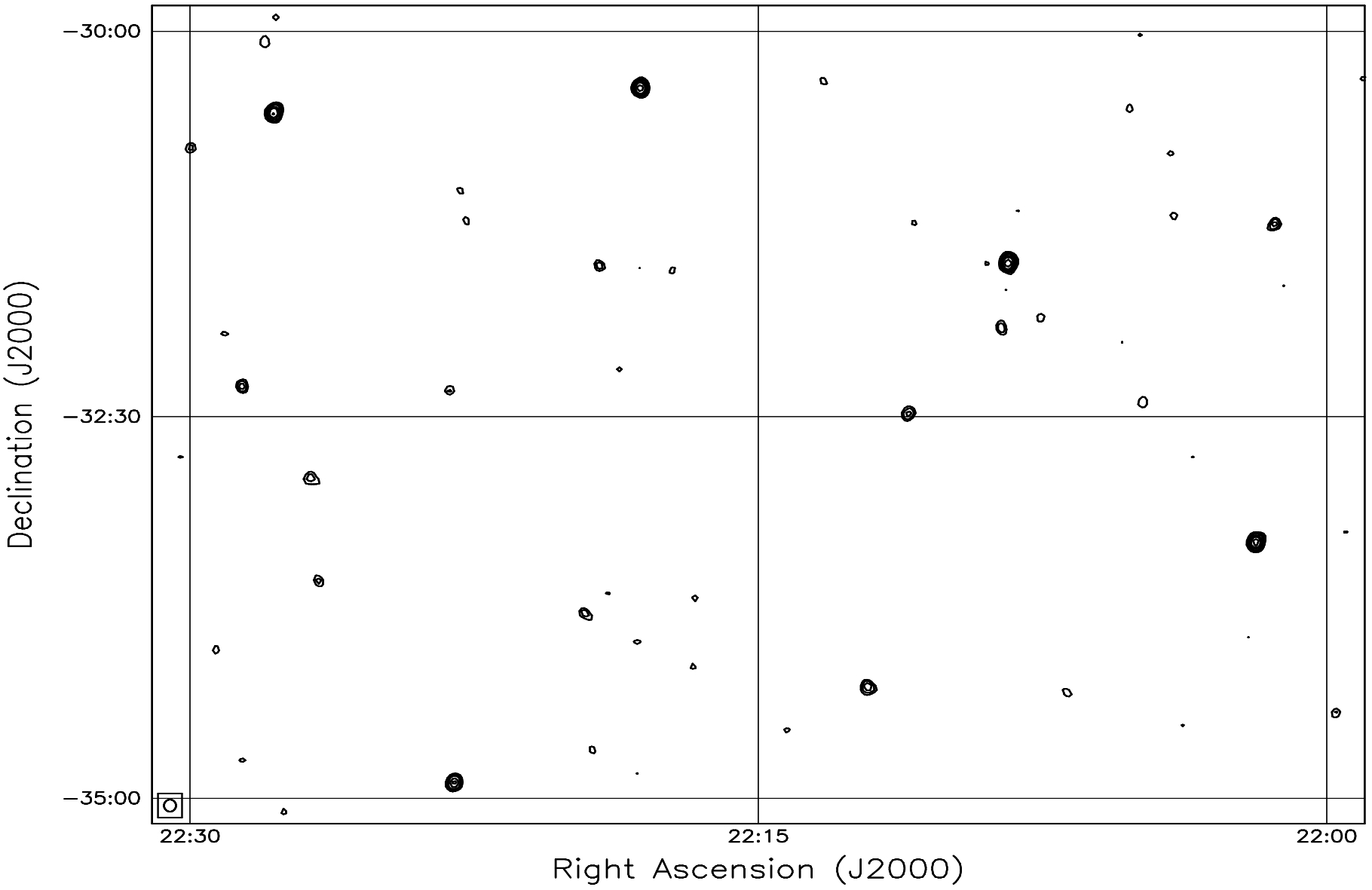

Fig. 7.164: Contour map covering the right ascension range 22h00m to 22h30m and declination range -35° to -30 °. The contour levels are -5, -3.6, -2.5, -1.8, 1, 1.4, 2, 2.8, 3.6, 5, 7, 10, 14, 20, 29, 40, 54, 72, 90, 100, 136, 180, 216, 252, 288 Jy beam^{-1}. The rms noise in the image is ≈280 mJy beam^{-1}.

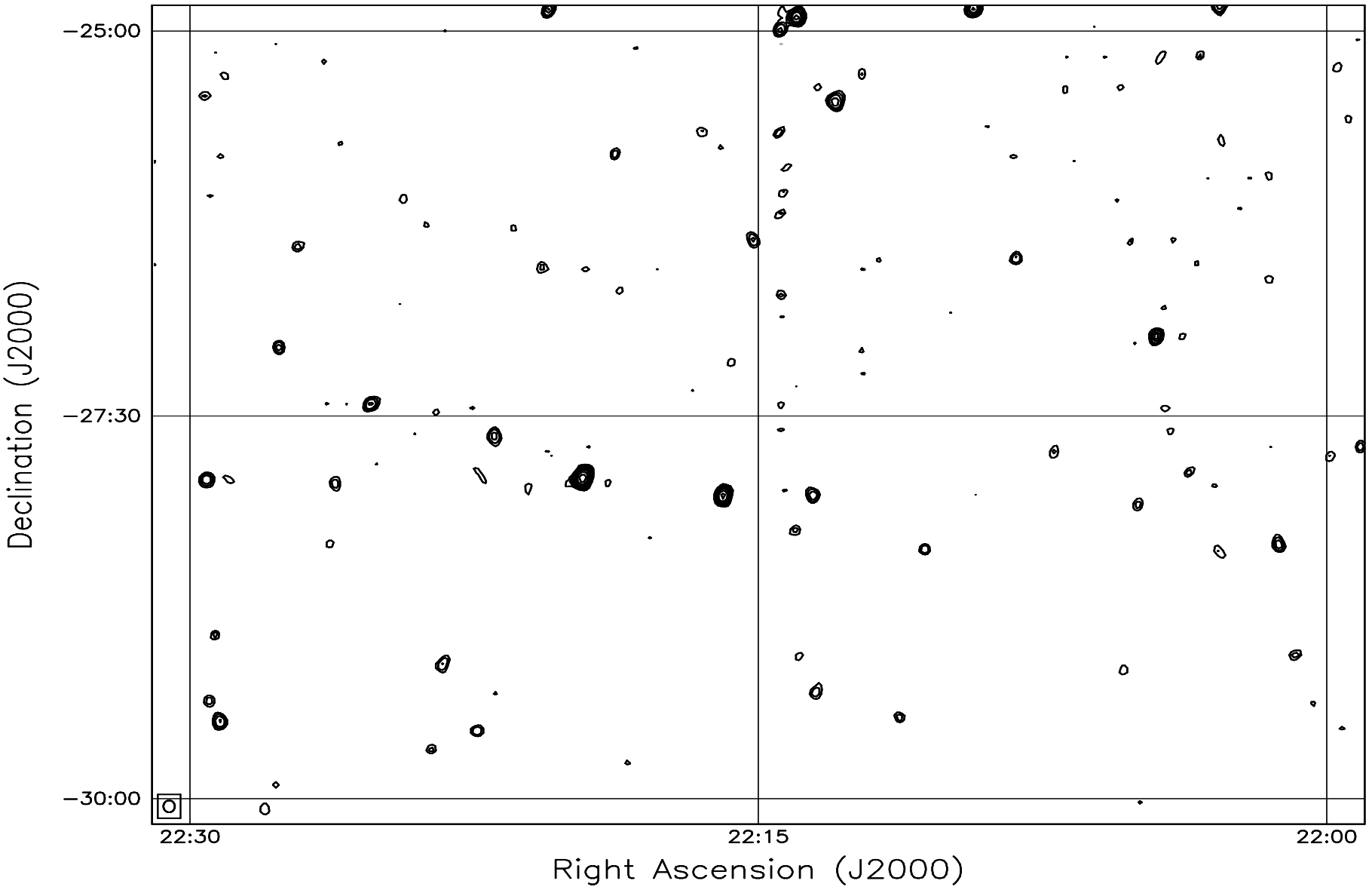

Fig. 7.165: Contour map covering the right ascension range 22h00m to 22h30m and declination range -30° to -25 °. The contour levels are -5, -3.6, -2.5, -1.8, 1, 1.4, 2, 2.8, 3.6, 5, 7, 10, 14, 20, 29, 40, 54, 72, 90, 100, 136, 180, 216, 252, 288 Jy beam^{-1}. The rms noise in the image is ≈300 mJy beam^{-1}.

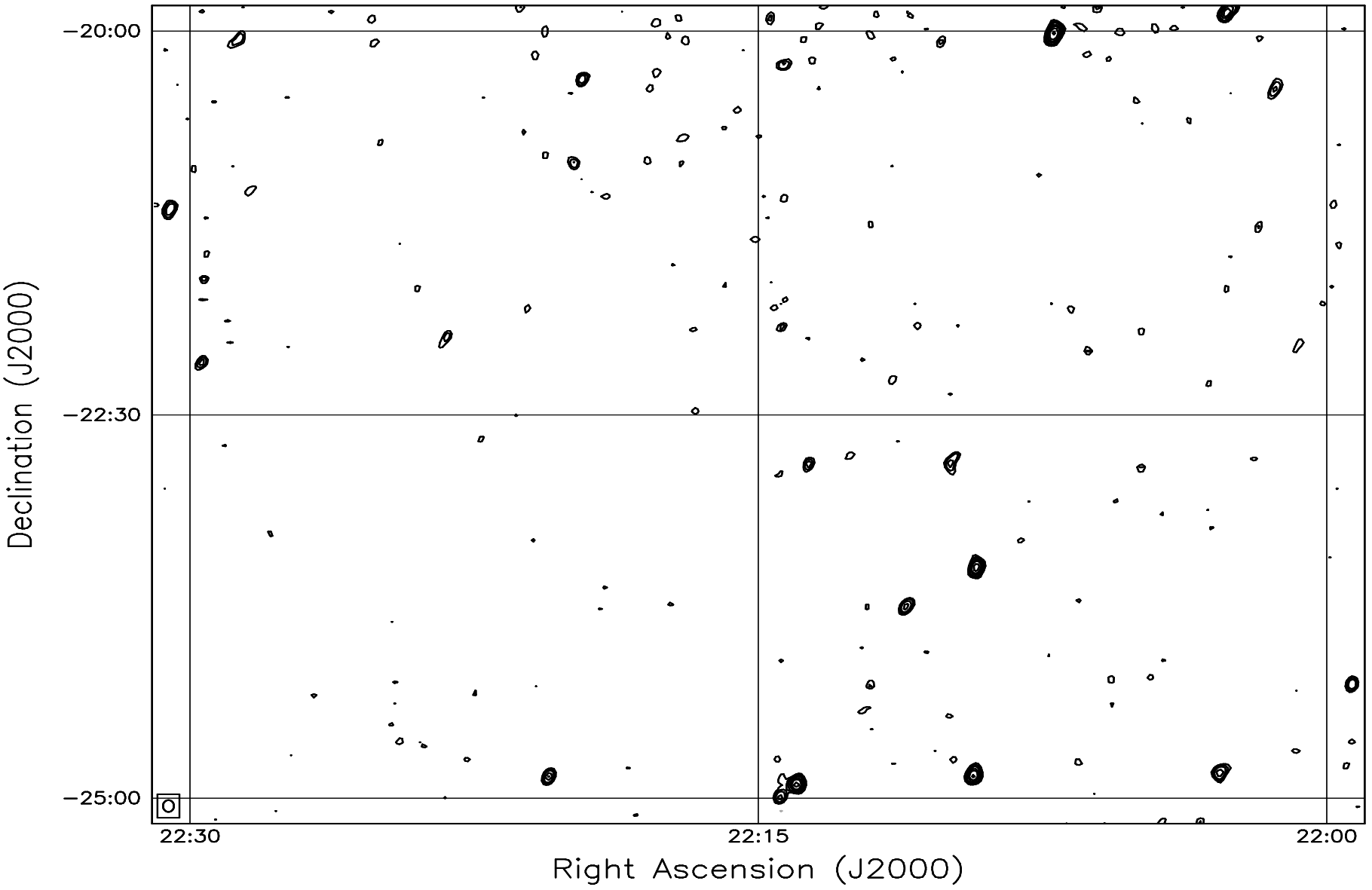

Fig. 7.166: Contour map covering the right ascension range 22h00m to 22h30m and declination range -25° to -20 °. The contour levels are -5, -3.6, -2.5, -1.8, 1, 1.4, 2, 2.8, 3.6, 5, 7, 10, 14, 20, 29, 40, 54, 72, 90, 100, 136, 180, 216, 252, 288 Jy beam^{-1}. The rms noise in the image is ≈330 mJy beam^{-1}.

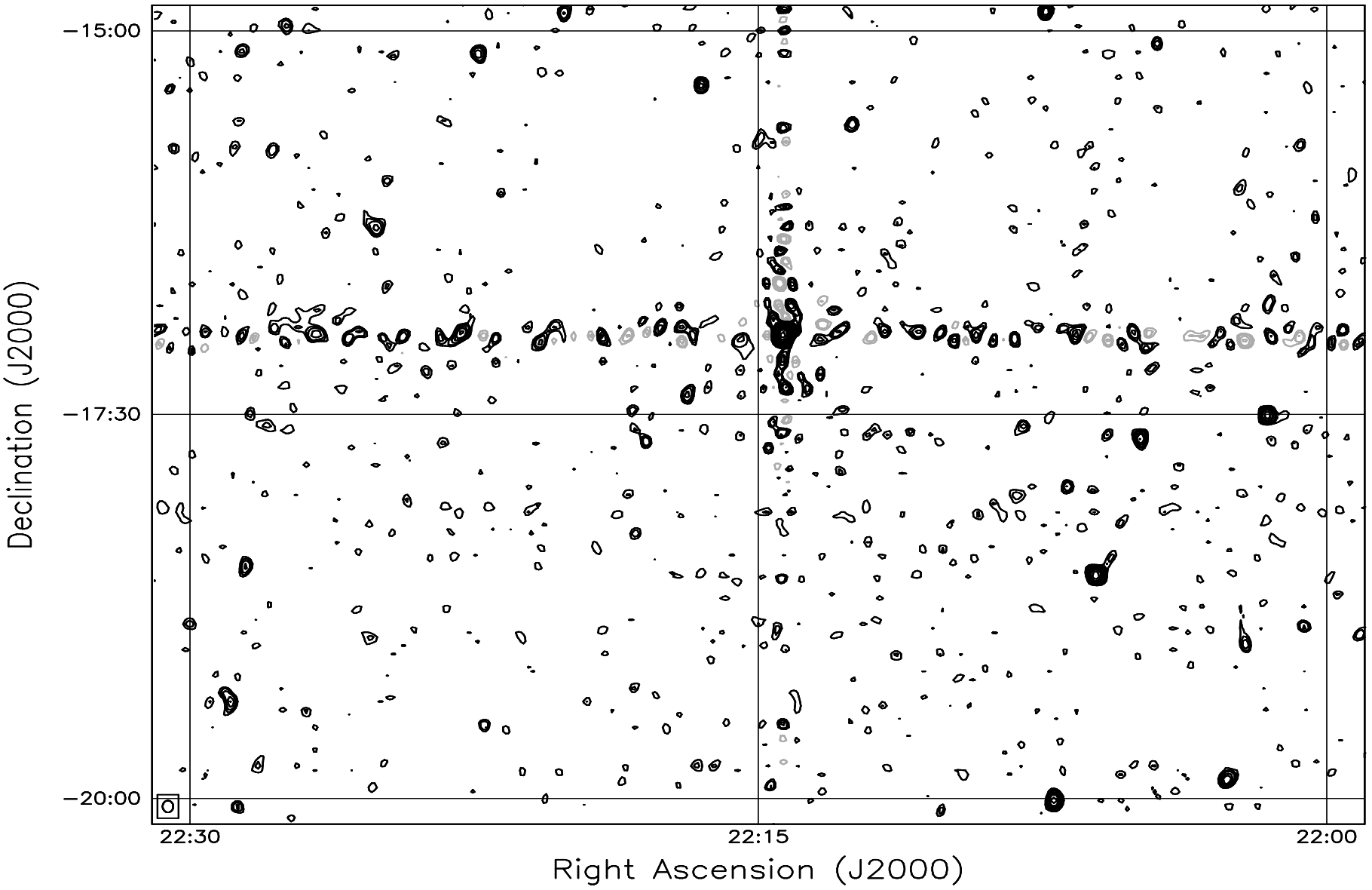

Fig. 7.167: Contour map covering the right ascension range 22h00m to 22h30m and declination range -20° to -15 °. The contour levels are -5, -3.6, -2.5, -1.8, 1, 1.4, 2, 2.8, 3.6, 5, 7, 10, 14, 20, 29, 40, 54, 72, 90, 100, 136, 180, 216, 252, 288 Jy beam^{-1}. The rms noise in the image is ≈375 mJy beam^{-1}.

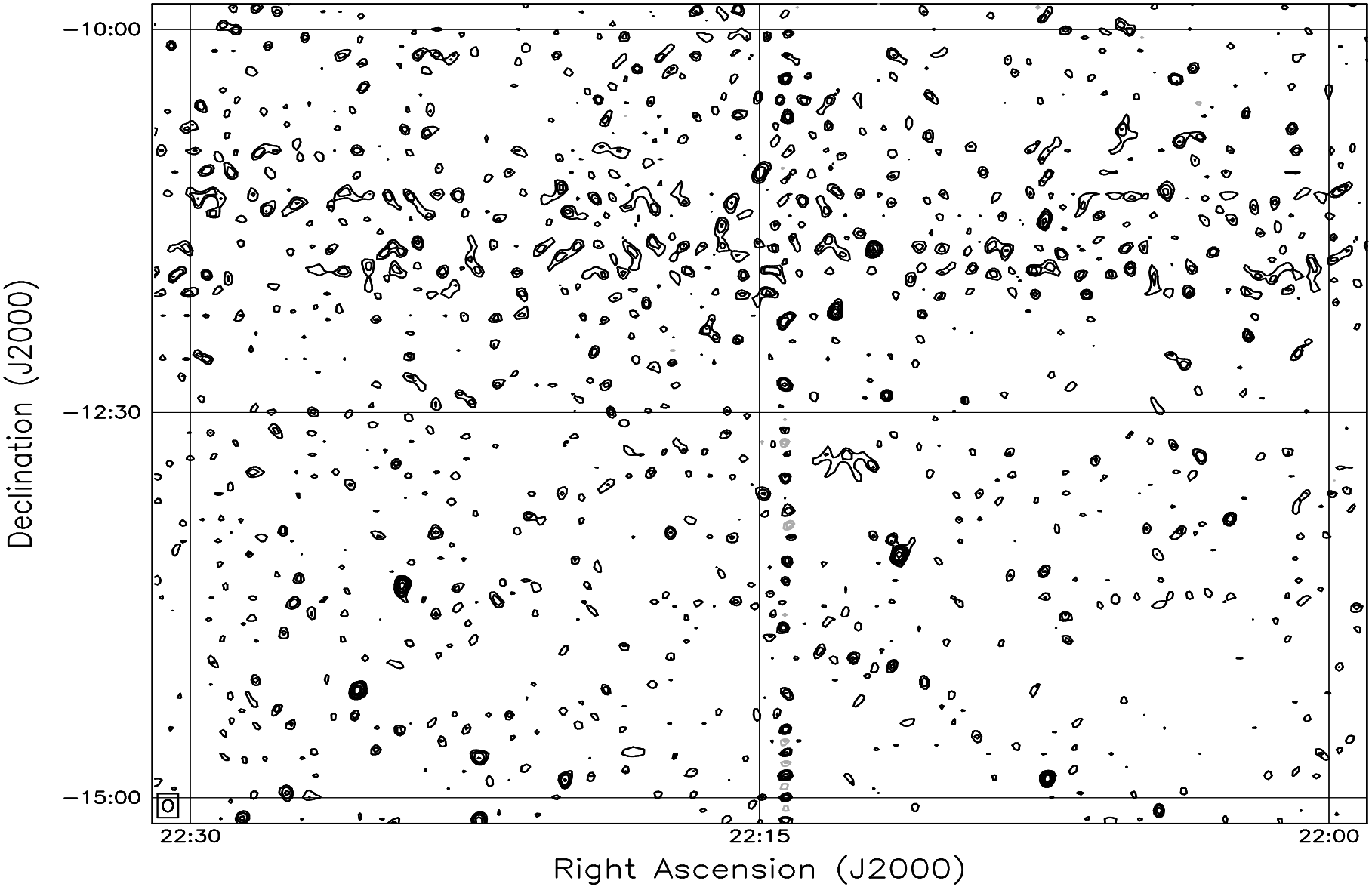

Fig. 7.168: Contour map covering the right ascension range 22h00m to 22h30m and declination range -15° to -10 °. The contour levels are -5, -3.6, -2.5, -1.8, 1, 1.4, 2, 2.8, 3.6, 5, 7, 10, 14, 20, 29, 40, 54, 72, 90, 100, 136, 180, 216, 252, 288 Jy beam^{-1}. The rms noise in the image is ≈460 mJy beam^{-1}.

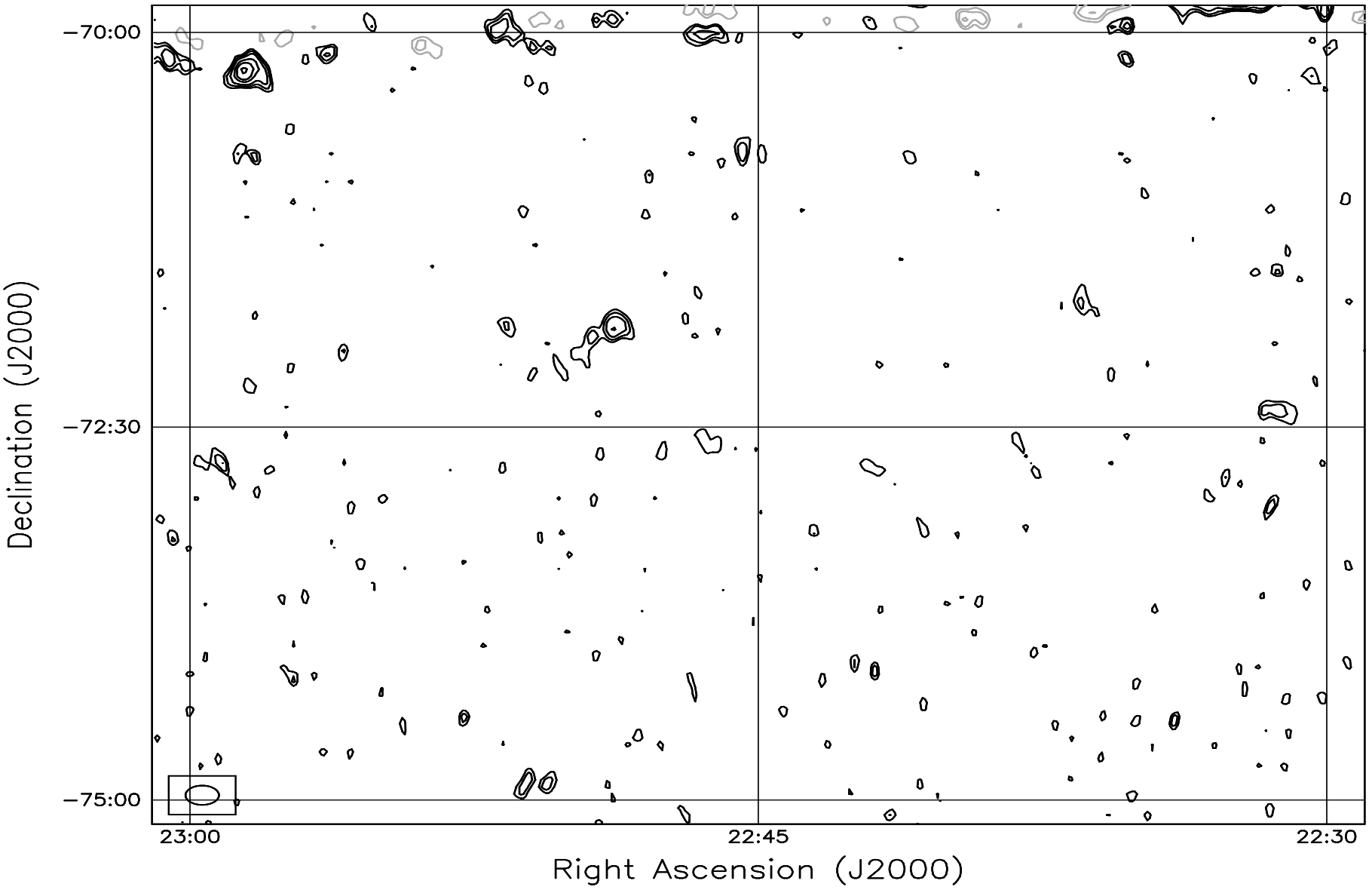

Fig. 7.169: Contour map covering the right ascension range 22h30m to 23h00m and declination range -75° to -70 °. The contour levels are -5, -3.6, -2.5, -1.8, 1, 1.4, 2, 2.8, 3.6, 5, 7, 10, 14, 20, 29, 40, 54, 72, 90, 100, 136, 180, 216, 252, 288 Jy beam^{-1}. The rms noise in the image is ≈380 mJy beam^{-1}.

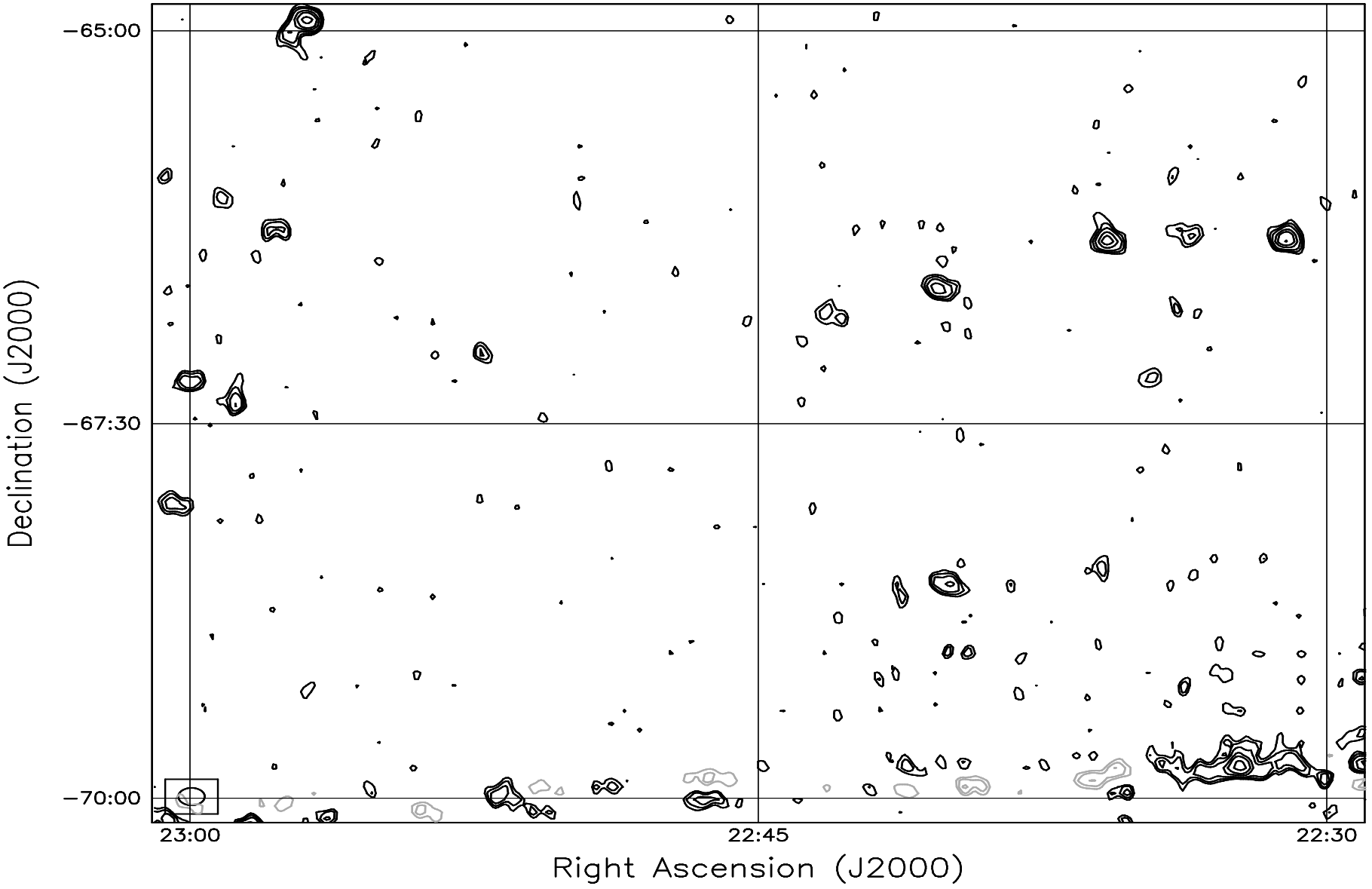

Fig. 7.170: Contour map covering the right ascension range 22h30m to 23h00m and declination range -70° to -65 °. The contour levels are -5, -3.6, -2.5, -1.8, 1, 1.4, 2, 2.8, 3.6, 5, 7, 10, 14, 20, 29, 40, 54, 72, 90, 100, 136, 180, 216, 252, 288 Jy beam^{-1}. The rms noise in the image is ≈330 mJy beam^{-1}.

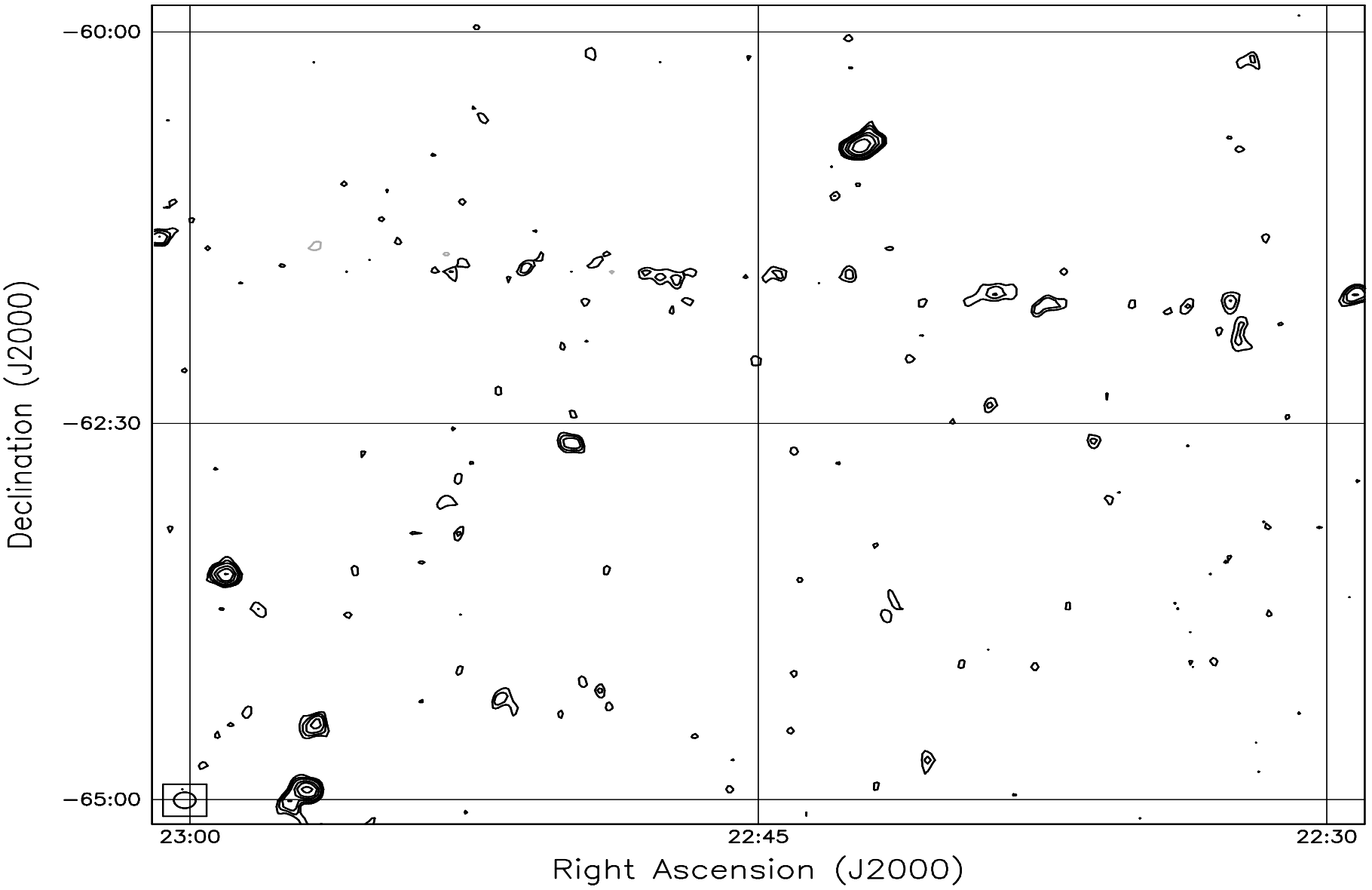

Fig. 7.171: Contour map covering the right ascension range 22h30m to 23h00m and declination range -65° to -60 °. The contour levels are -5, -3.6, -2.5, -1.8, 1, 1.4, 2, 2.8, 3.6, 5, 7, 10, 14, 20, 29, 40, 54, 72, 90, 100, 136, 180, 216, 252, 288 Jy beam^{-1}. The rms noise in the image is ≈300 mJy beam^{-1}.

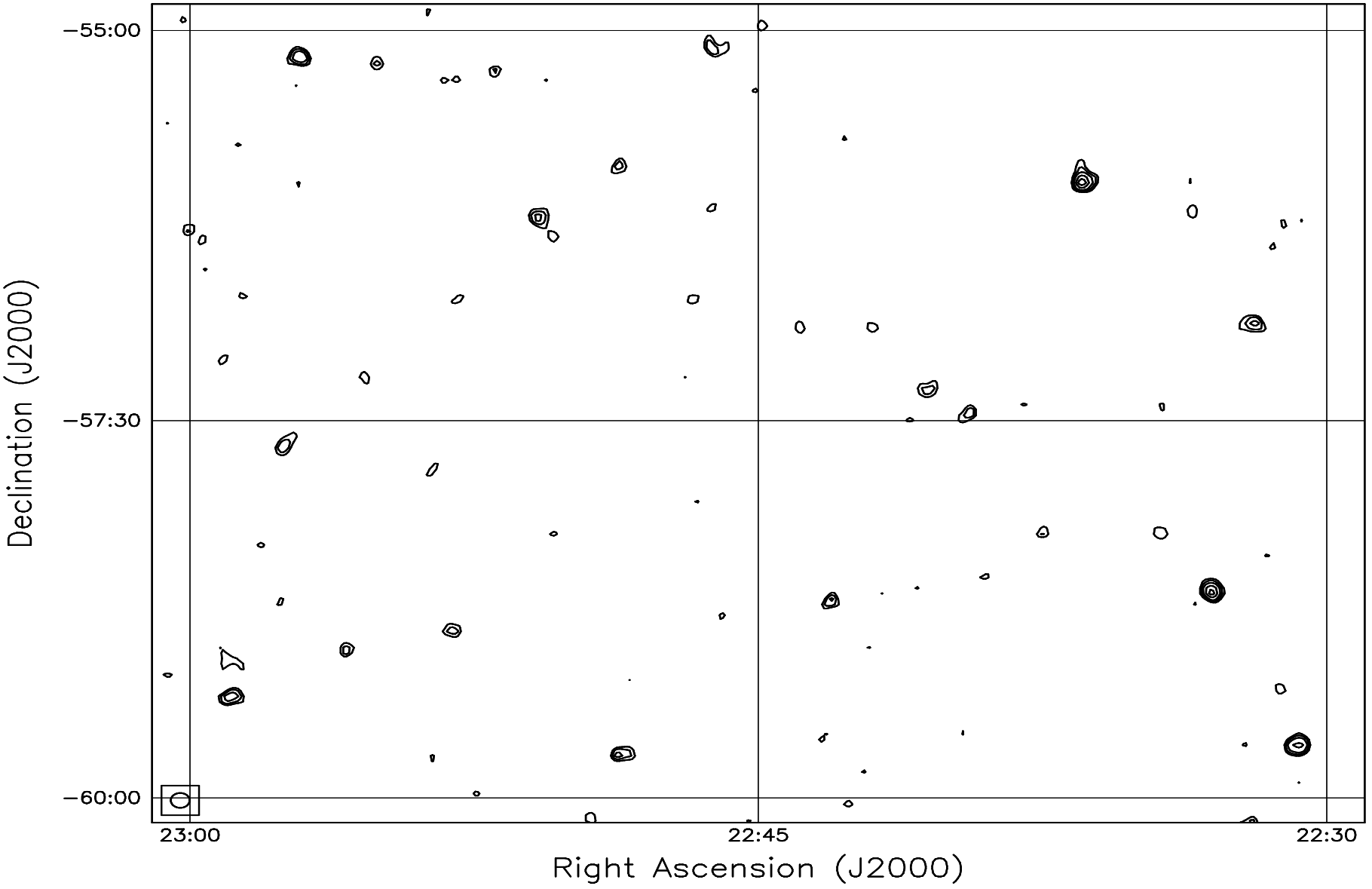

Fig. 7.172: Contour map covering the right ascension range 22h30m to 23h00m and declination range -60° to -55 °. The contour levels are -5, -3.6, -2.5, -1.8, 1, 1.4, 2, 2.8, 3.6, 5, 7, 10, 14, 20, 29, 40, 54, 72, 90, 100, 136, 180, 216, 252, 288 Jy beam^{-1}. The rms noise in the image is ≈280 mJy beam^{-1}.

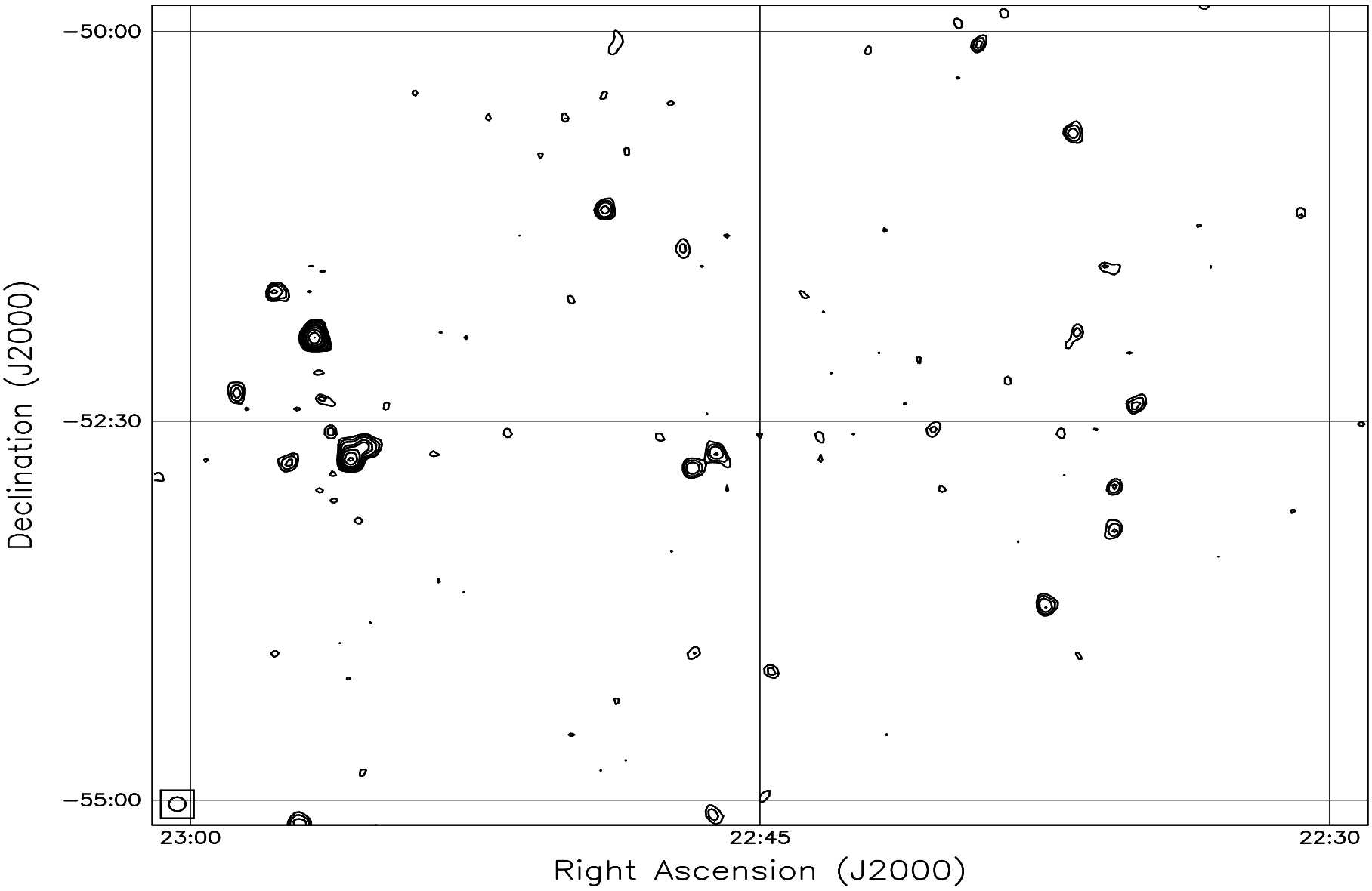

Fig. 7.173: Contour map covering the right ascension range 22h30m to 23h00m and declination range -55° to -50 °. The contour levels are -5, -3.6, -2.5, -1.8, 1, 1.4, 2, 2.8, 3.6, 5, 7, 10, 14, 20, 29, 40, 54, 72, 90, 100, 136, 180, 216, 252, 288 Jy beam^{-1}. The rms noise in the image is ≈270 mJy beam^{-1}.

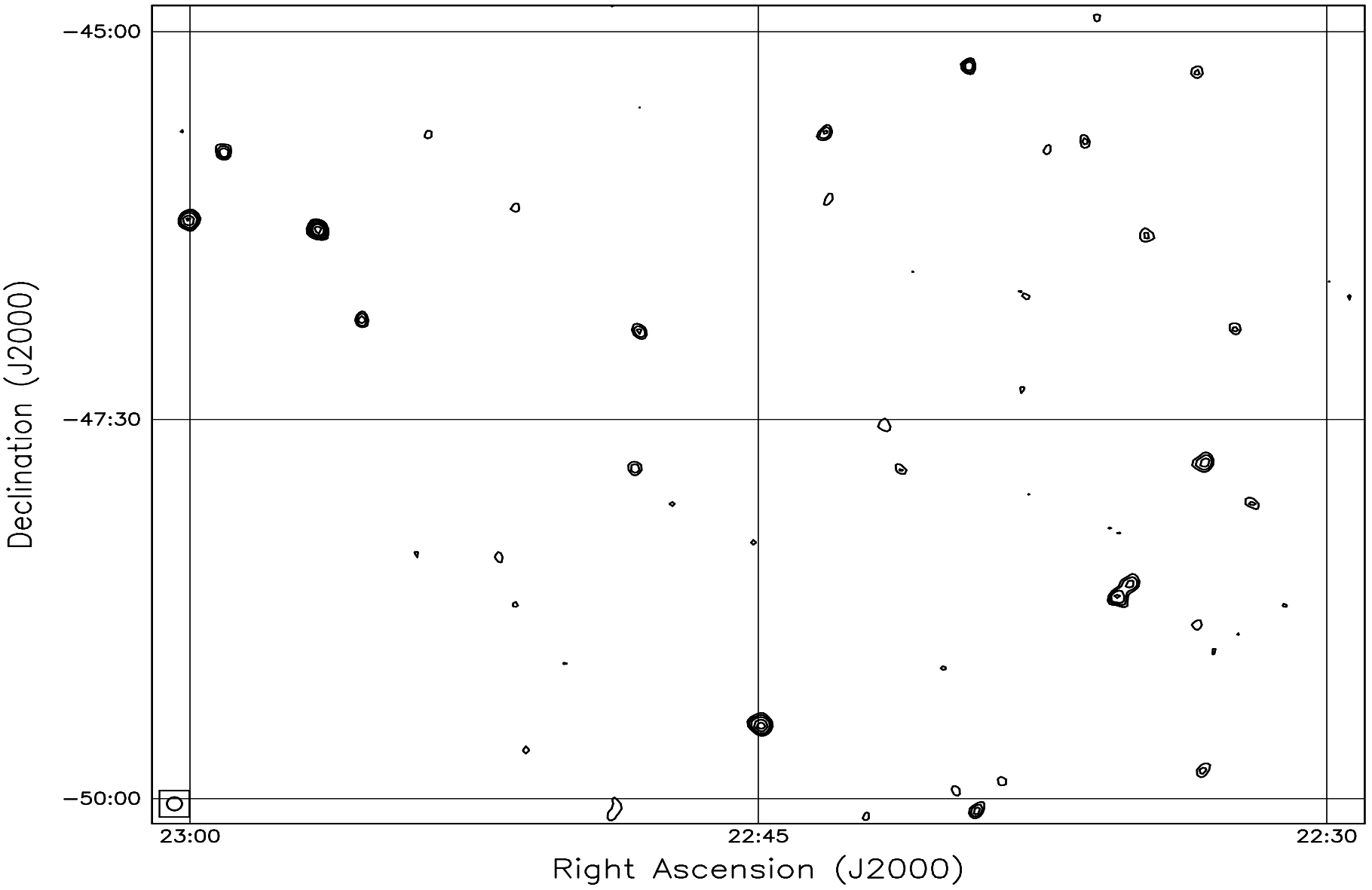

Fig. 7.174: Contour map covering the right ascension range 22h30m to 23h00m and declination range -50° to -45 °. The contour levels are -5, -3.6, -2.5, -1.8, 1, 1.4, 2, 2.8, 3.6, 5, 7, 10, 14, 20, 29, 40, 54, 72, 90, 100, 136, 180, 216, 252, 288 Jy beam^{-1}. The rms noise in the image is ≈260 mJy beam^{-1}.

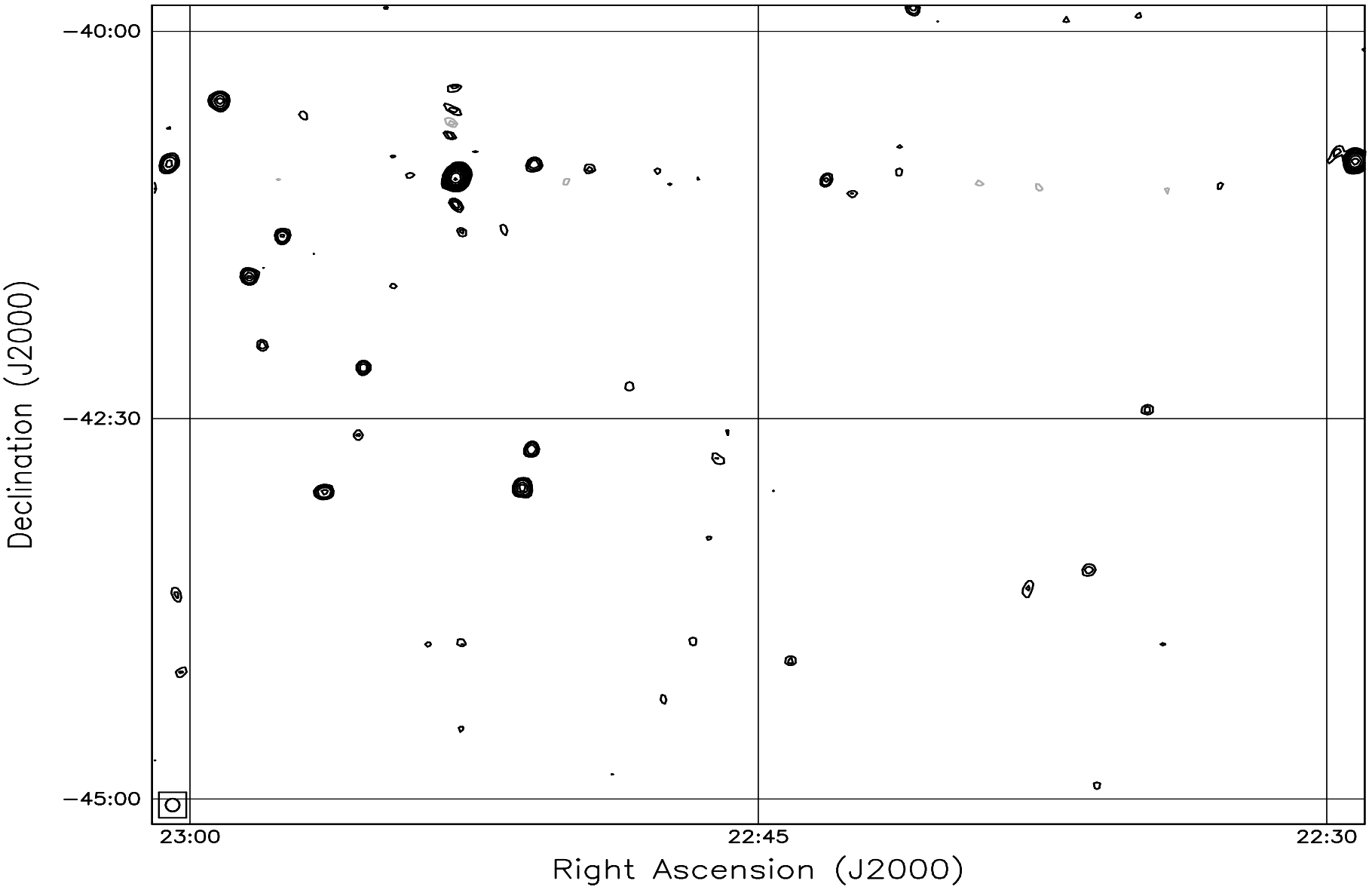

Fig. 7.175: Contour map covering the right ascension range 22h30m to 23h00m and declination range -45° to -40 °. The contour levels are -5, -3.6, -2.5, -1.8, 1, 1.4, 2, 2.8, 3.6, 5, 7, 10, 14, 20, 29, 40, 54, 72, 90, 100, 136, 180, 216, 252, 288 Jy beam^{-1}. The rms noise in the image is ≈260 mJy beam^{-1}.

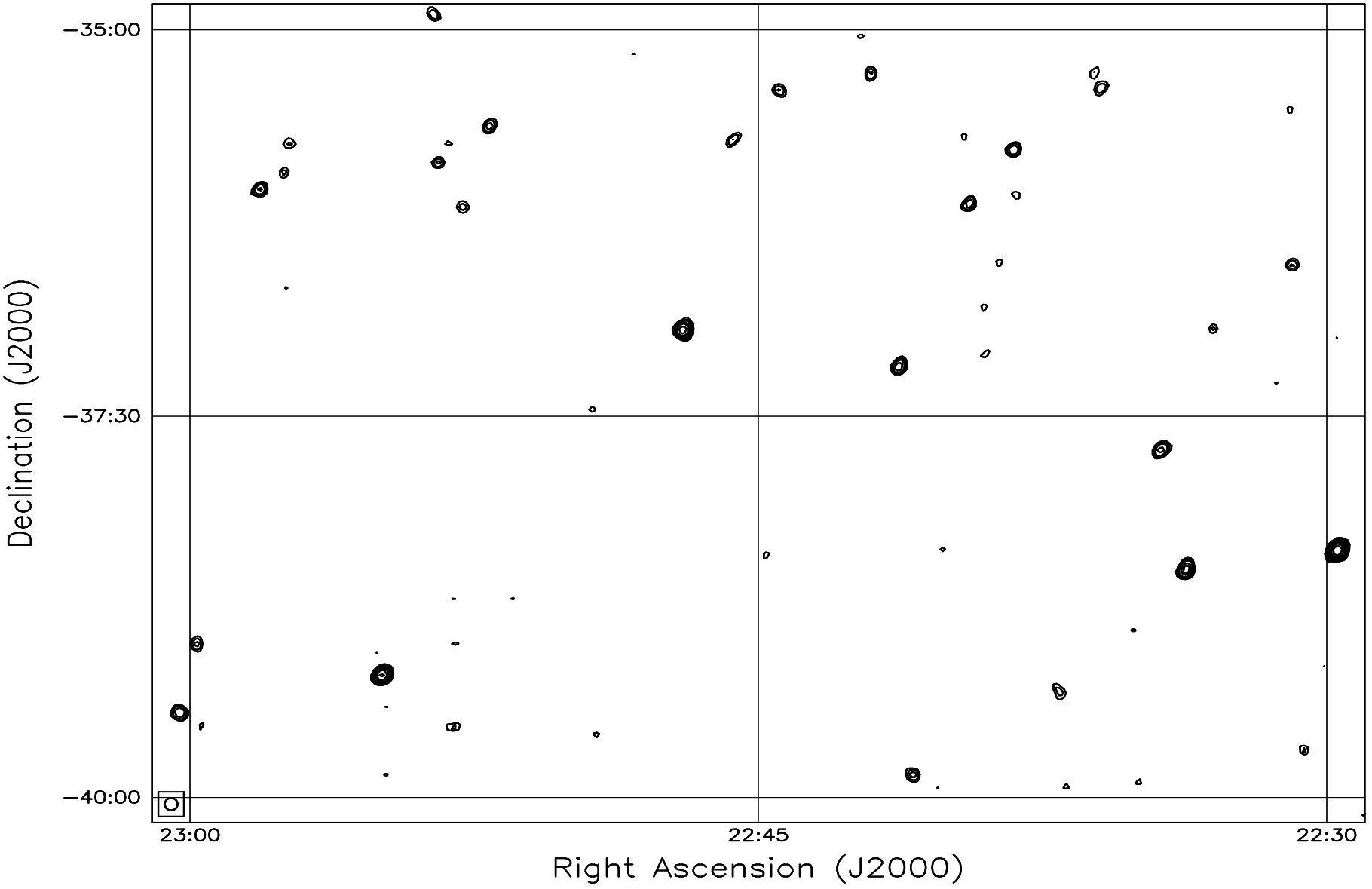

Fig. 7.176: Contour map covering the right ascension range 22h30m to 23h00m and declination range -40° to -35 °. The contour levels are -5, -3.6, -2.5, -1.8, 1, 1.4, 2, 2.8, 3.6, 5, 7, 10, 14, 20, 29, 40, 54, 72, 90, 100, 136, 180, 216, 252, 288 Jy beam^{-1}. The rms noise in the image is ≈270 mJy beam^{-1}.

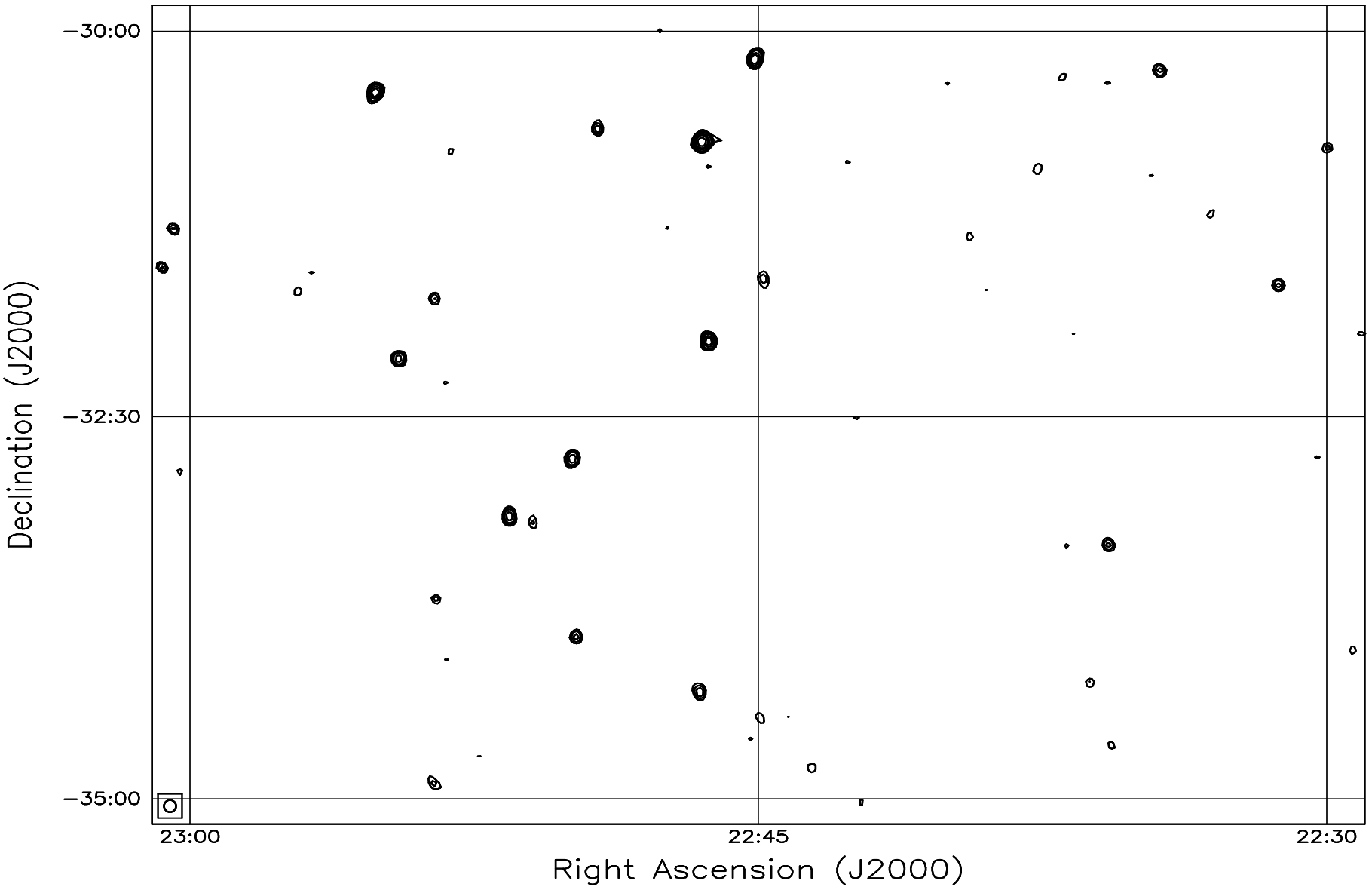

Fig. 7.177: Contour map covering the right ascension range 22h30m to 23h00m and declination range -35° to -30 °. The contour levels are -5, -3.6, -2.5, -1.8, 1, 1.4, 2, 2.8, 3.6, 5, 7, 10, 14, 20, 29, 40, 54, 72, 90, 100, 136, 180, 216, 252, 288 Jy beam^{-1}. The rms noise in the image is ≈280 mJy beam^{-1}.

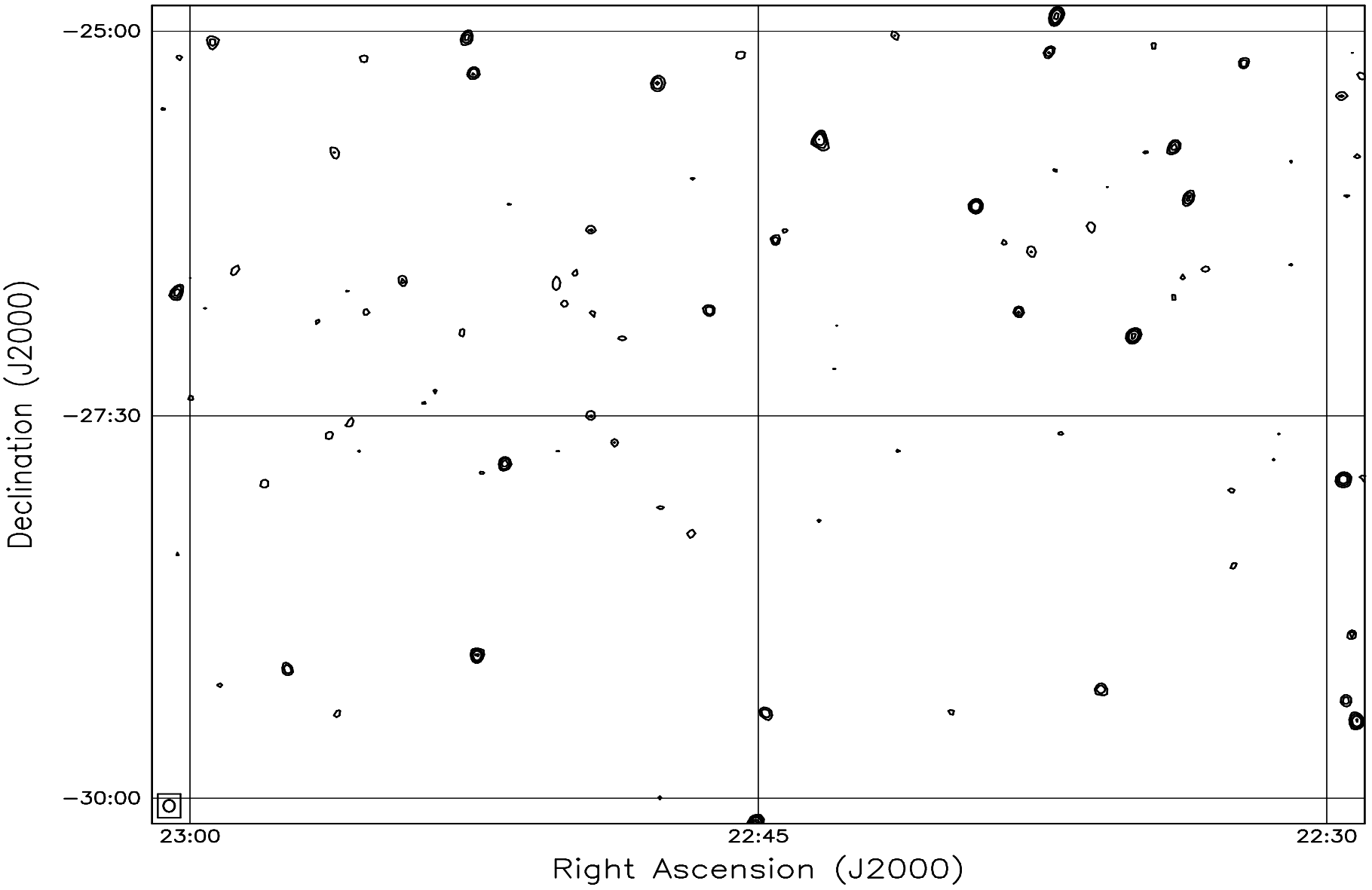

Fig. 7.178: Contour map covering the right ascension range 22h30m to 23h00m and declination range -30° to -25 °. The contour levels are -5, -3.6, -2.5, -1.8, 1, 1.4, 2, 2.8, 3.6, 5, 7, 10, 14, 20, 29, 40, 54, 72, 90, 100, 136, 180, 216, 252, 288 Jy beam^{-1}. The rms noise in the image is ≈300 mJy beam^{-1}.

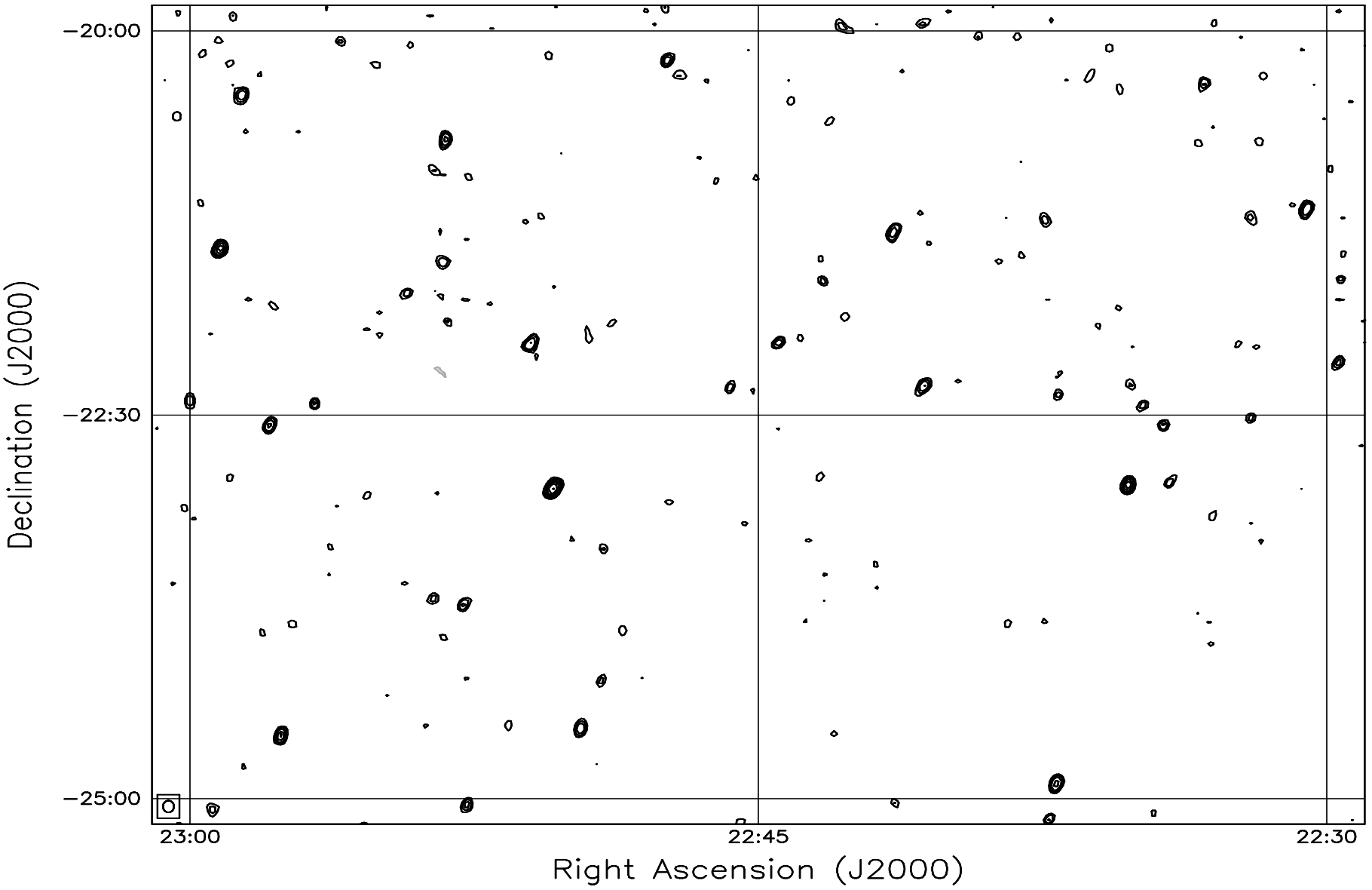

Fig. 7.179: Contour map covering the right ascension range 22h30m to 23h00m and declination range -25° to -20 °. The contour levels are -5, -3.6, -2.5, -1.8, 1, 1.4, 2, 2.8, 3.6, 5, 7, 10, 14, 20, 29, 40, 54, 72, 90, 100, 136, 180, 216, 252, 288 Jy beam^{-1}. The rms noise in the image is ≈330 mJy beam^{-1}.

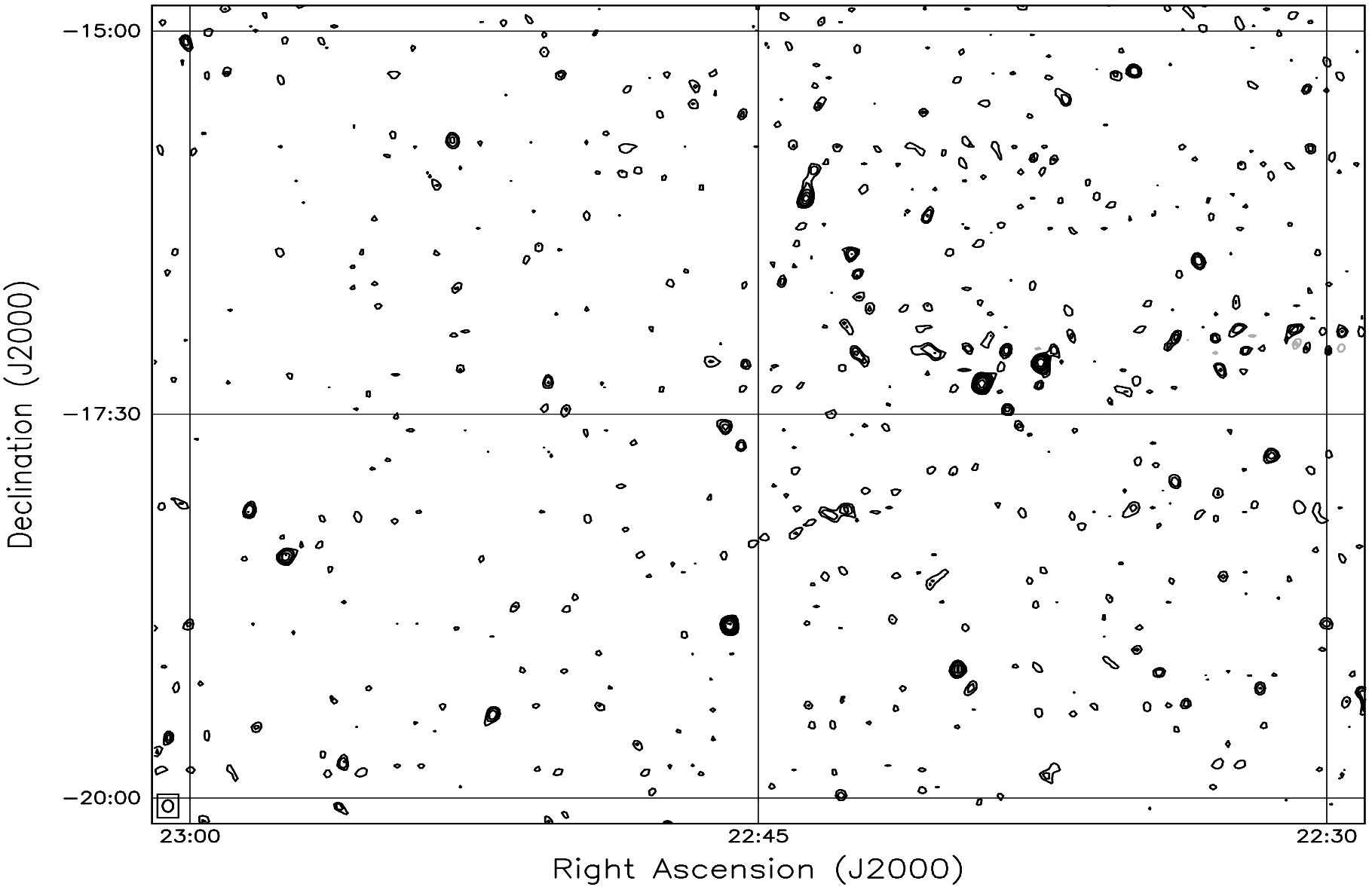

Fig. 7.180: Contour map covering the right ascension range 22h30m to 23h00m and declination range -20° to -15 °. The contour levels are -5, -3.6, -2.5, -1.8, 1, 1.4, 2, 2.8, 3.6, 5, 7, 10, 14, 20, 29, 40, 54, 72, 90, 100, 136, 180, 216, 252, 288 Jy beam^{-1}. The rms noise in the image is ≈375 mJy beam^{-1}.

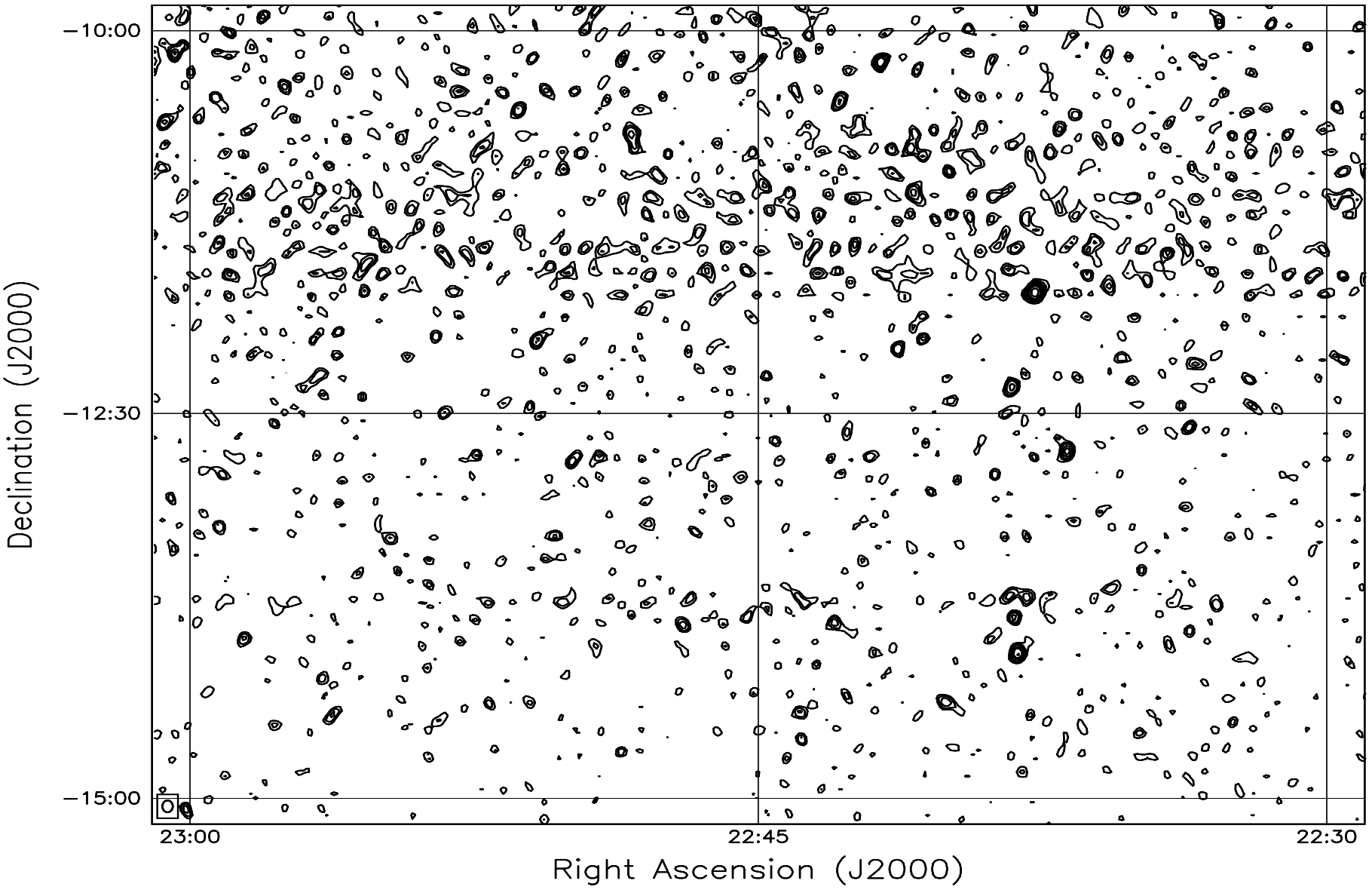

Fig. 7.181: Contour map covering the right ascension range 22h30m to 23h00m and declination range -15° to -10 °. The contour levels are -5, -3.6, -2.5, -1.8, 1, 1.4, 2, 2.8, 3.6, 5, 7, 10, 14, 20, 29, 40, 54, 72, 90, 100, 136, 180, 216, 252, 288 Jy beam^{-1}. The rms noise in the image is ≈460 mJy beam^{-1}.

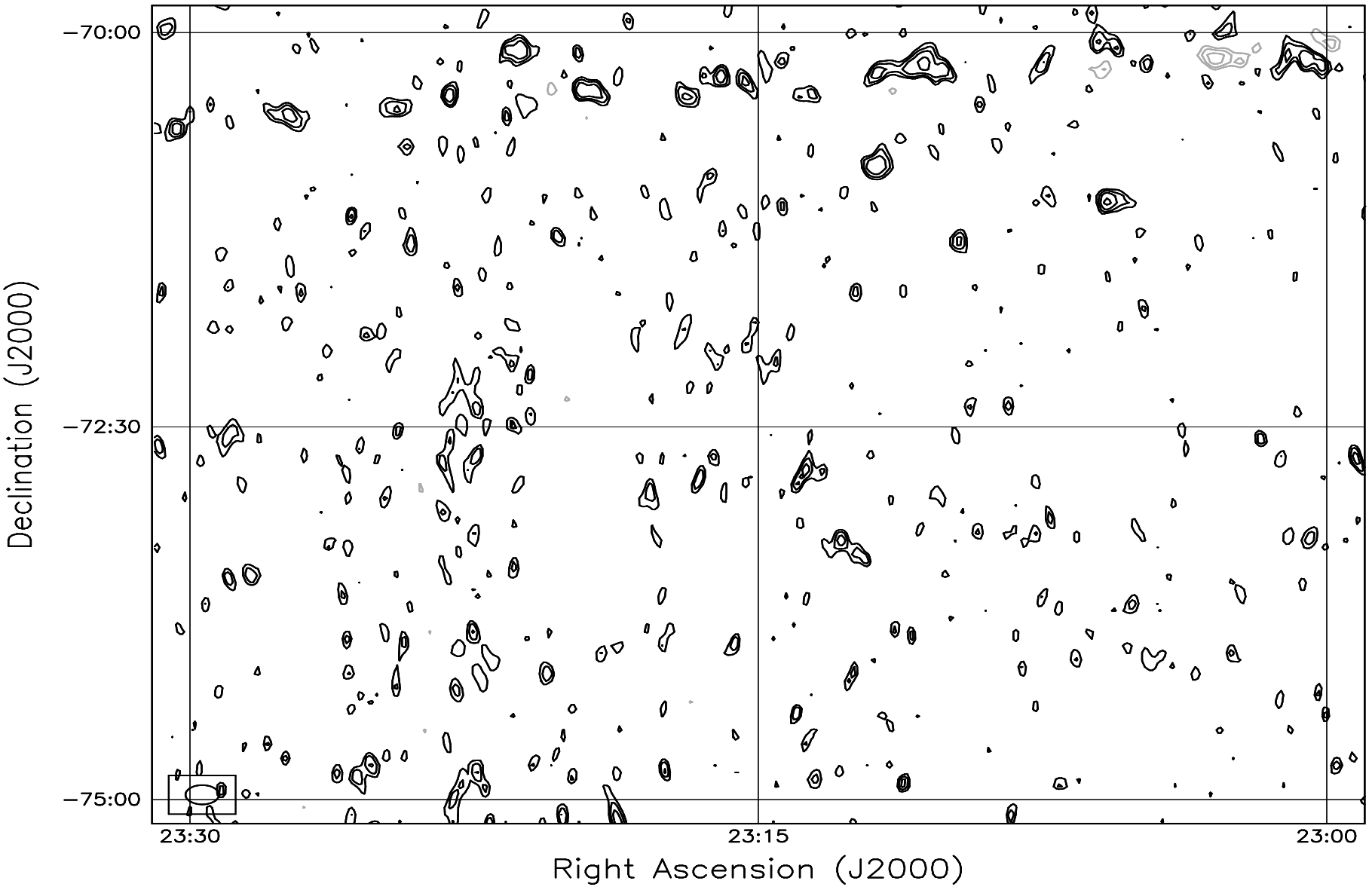

Fig. 7.182: Contour map covering the right ascension range 23h00m to 23h30m and declination range -75° to -70 °. The contour levels are -5, -3.6, -2.5, -1.8, 1, 1.4, 2, 2.8, 3.6, 5, 7, 10, 14, 20, 29, 40, 54, 72, 90, 100, 136, 180, 216, 252, 288 Jy beam^{-1}. The rms noise in the image is ≈425 mJy beam^{-1}.

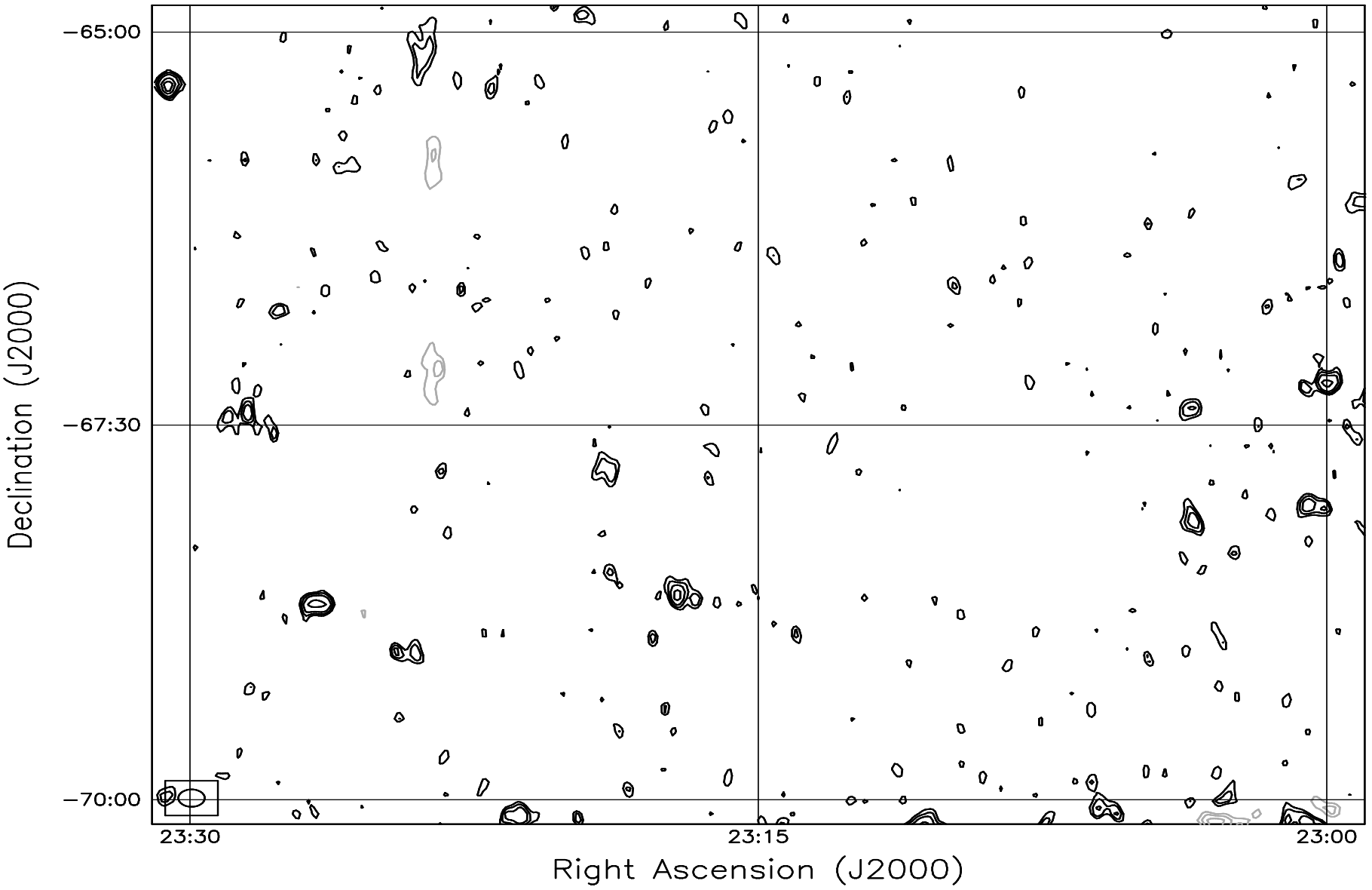

Fig. 7.183: Contour map covering the right ascension range 23h00m to 23h30m and declination range -70° to -65 °. The contour levels are -5, -3.6, -2.5, -1.8, 1, 1.4, 2, 2.8, 3.6, 5, 7, 10, 14, 20, 29, 40, 54, 72, 90, 100, 136, 180, 216, 252, 288 Jy beam^{-1}. The rms noise in the image is ≈370 mJy beam^{-1}.

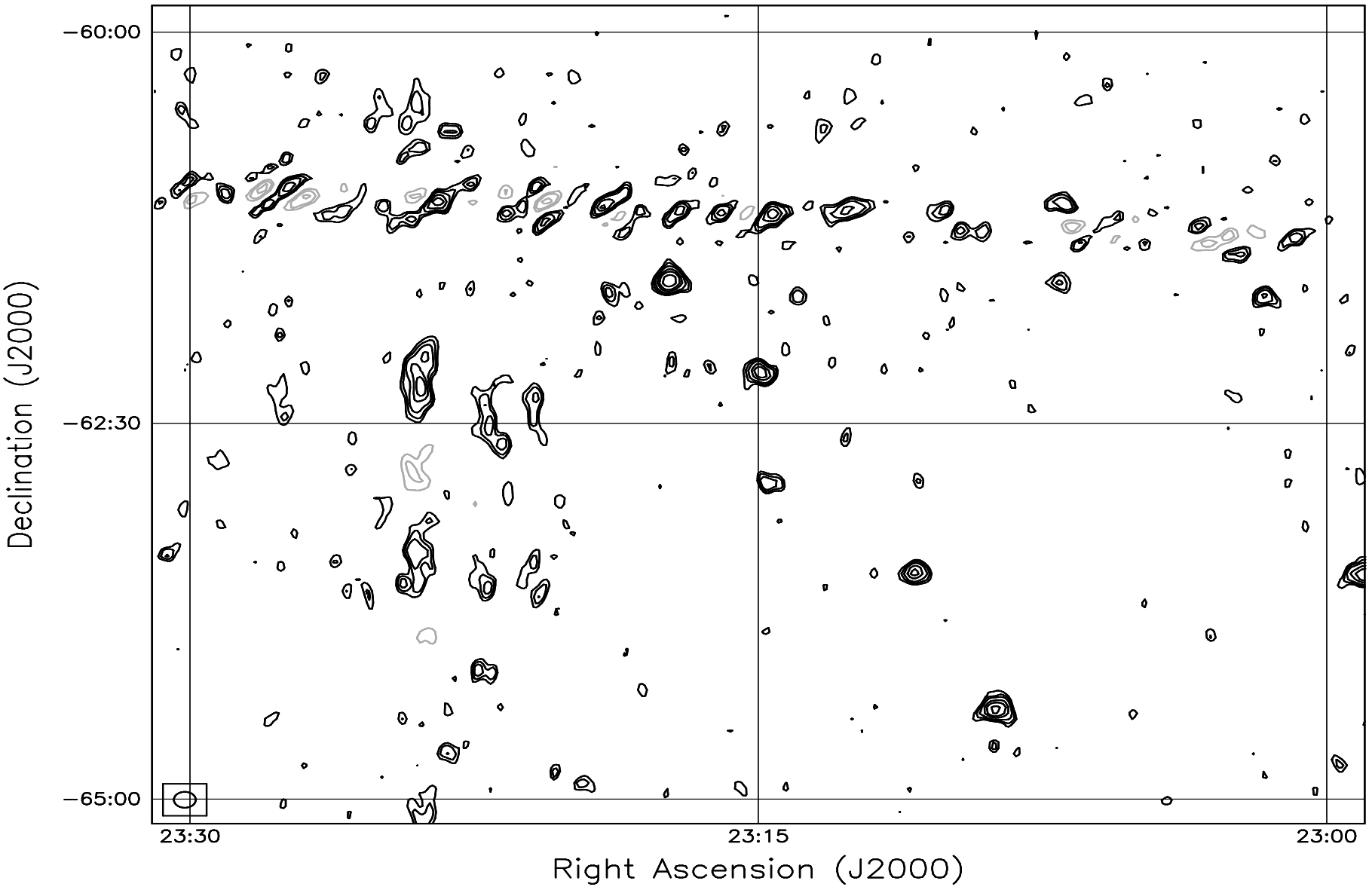

Fig. 7.184: Contour map covering the right ascension range 23h00m to 23h30m and declination range -65° to -60 °. The contour levels are -5, -3.6, -2.5, -1.8, 1, 1.4, 2, 2.8, 3.6, 5, 7, 10, 14, 20, 29, 40, 54, 72, 90, 100, 136, 180, 216, 252, 288 Jy beam^{-1}. The rms noise in the image is ≈330 mJy beam^{-1}.

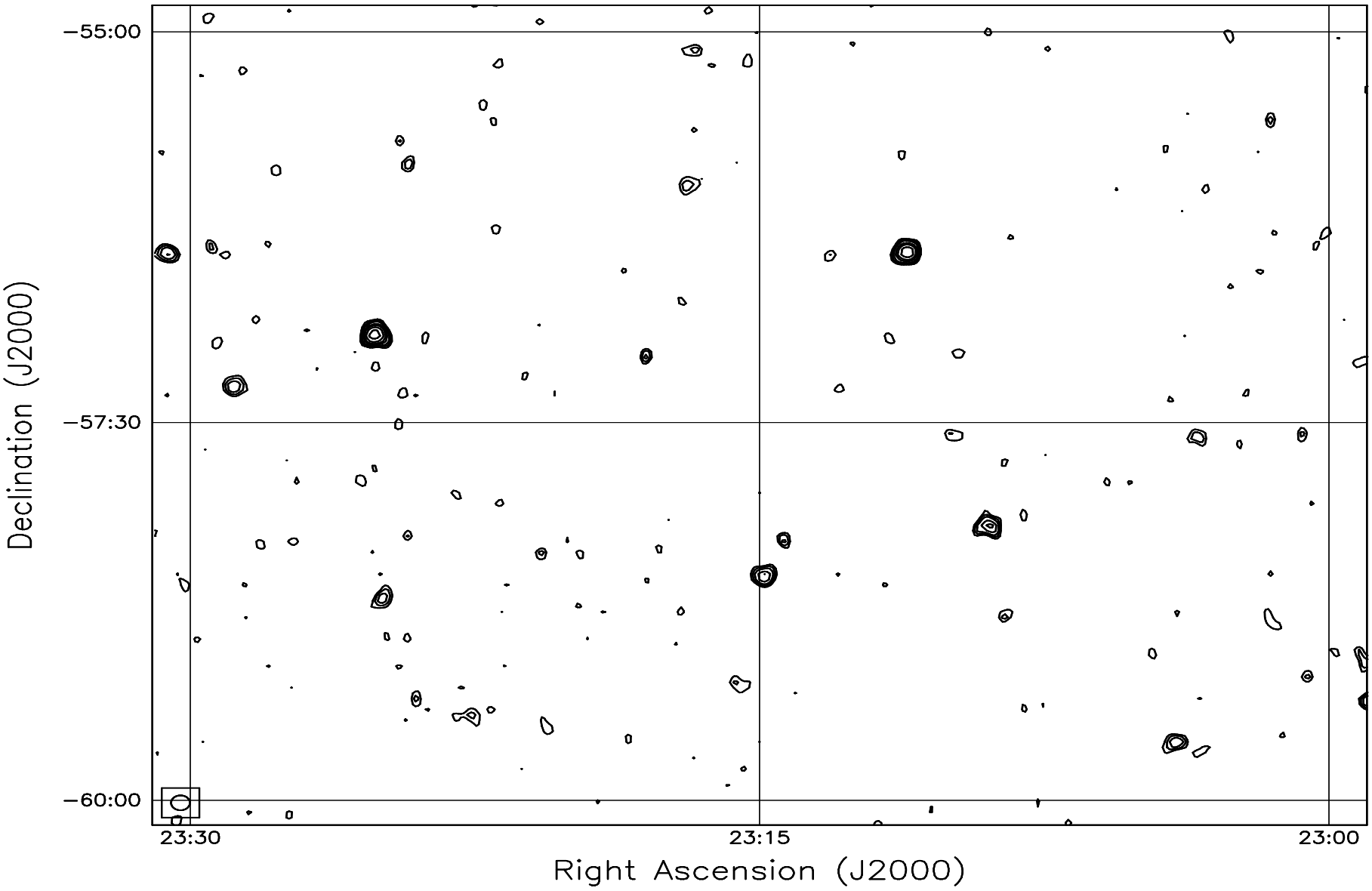

Fig. 7.185: Contour map covering the right ascension range 23h00m to 23h30m and declination range -60° to -55 °. The contour levels are -5, -3.6, -2.5, -1.8, 1, 1.4, 2, 2.8, 3.6, 5, 7, 10, 14, 20, 29, 40, 54, 72, 90, 100, 136, 180, 216, 252, 288 Jy beam^{-1}. The rms noise in the image is ≈310 mJy beam^{-1}.

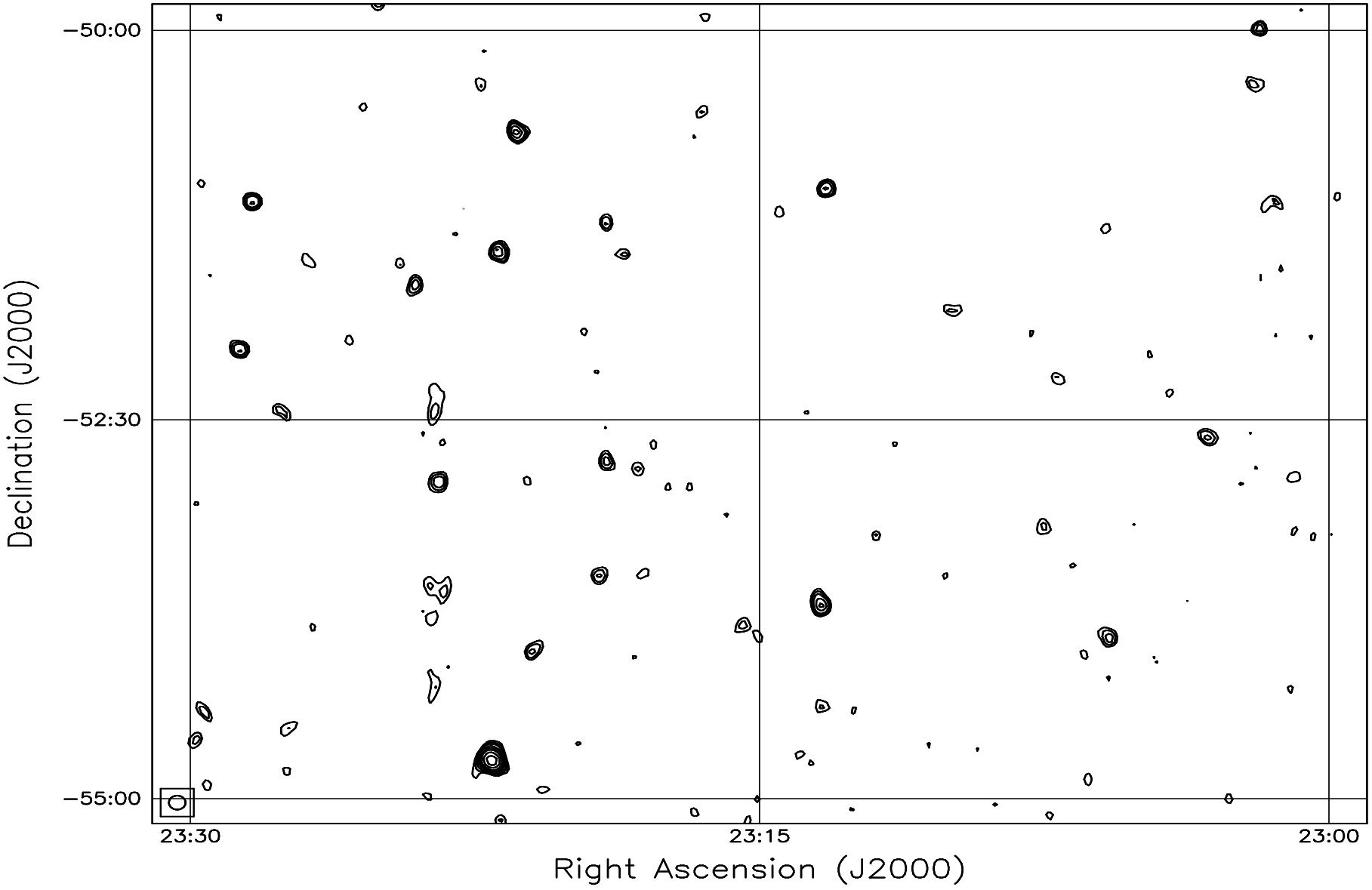

Fig. 7.186: Contour map covering the right ascension range 23h00m to 23h30m and declination range -55° to -50 °. The contour levels are -5, -3.6, -2.5, -1.8, 1, 1.4, 2, 2.8, 3.6, 5, 7, 10, 14, 20, 29, 40, 54, 72, 90, 100, 136, 180, 216, 252, 288 Jy beam^{-1}. The rms noise in the image is ≈300 mJy beam^{-1}.

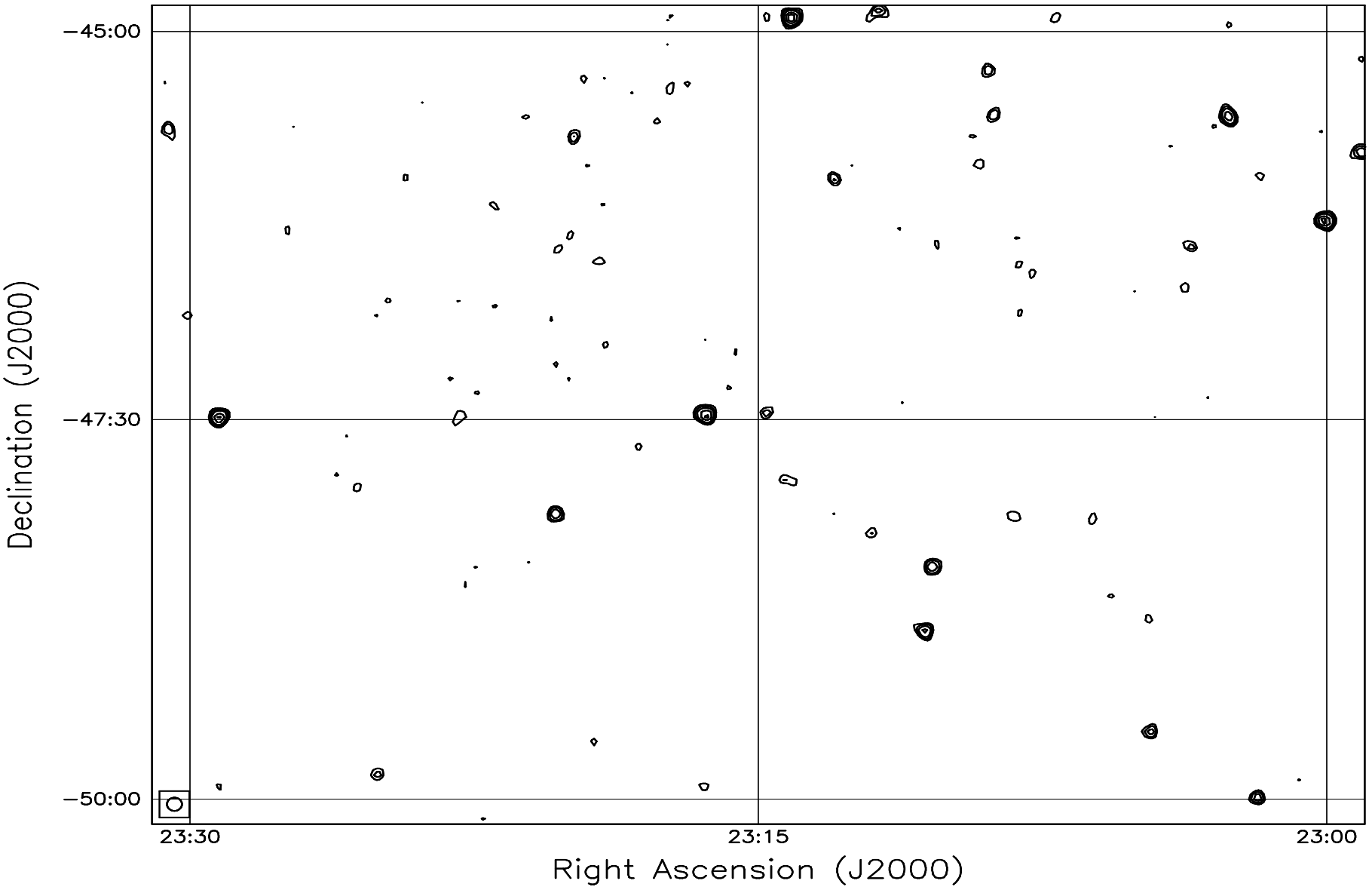

Fig. 7.187: Contour map covering the right ascension range 23h00m to 23h30m and declination range -50° to -45 °. The contour levels are -5, -3.6, -2.5, -1.8, 1, 1.4, 2, 2.8, 3.6, 5, 7, 10, 14, 20, 29, 40, 54, 72, 90, 100, 136, 180, 216, 252, 288 Jy beam^{-1}. The rms noise in the image is ≈290 mJy beam^{-1}.

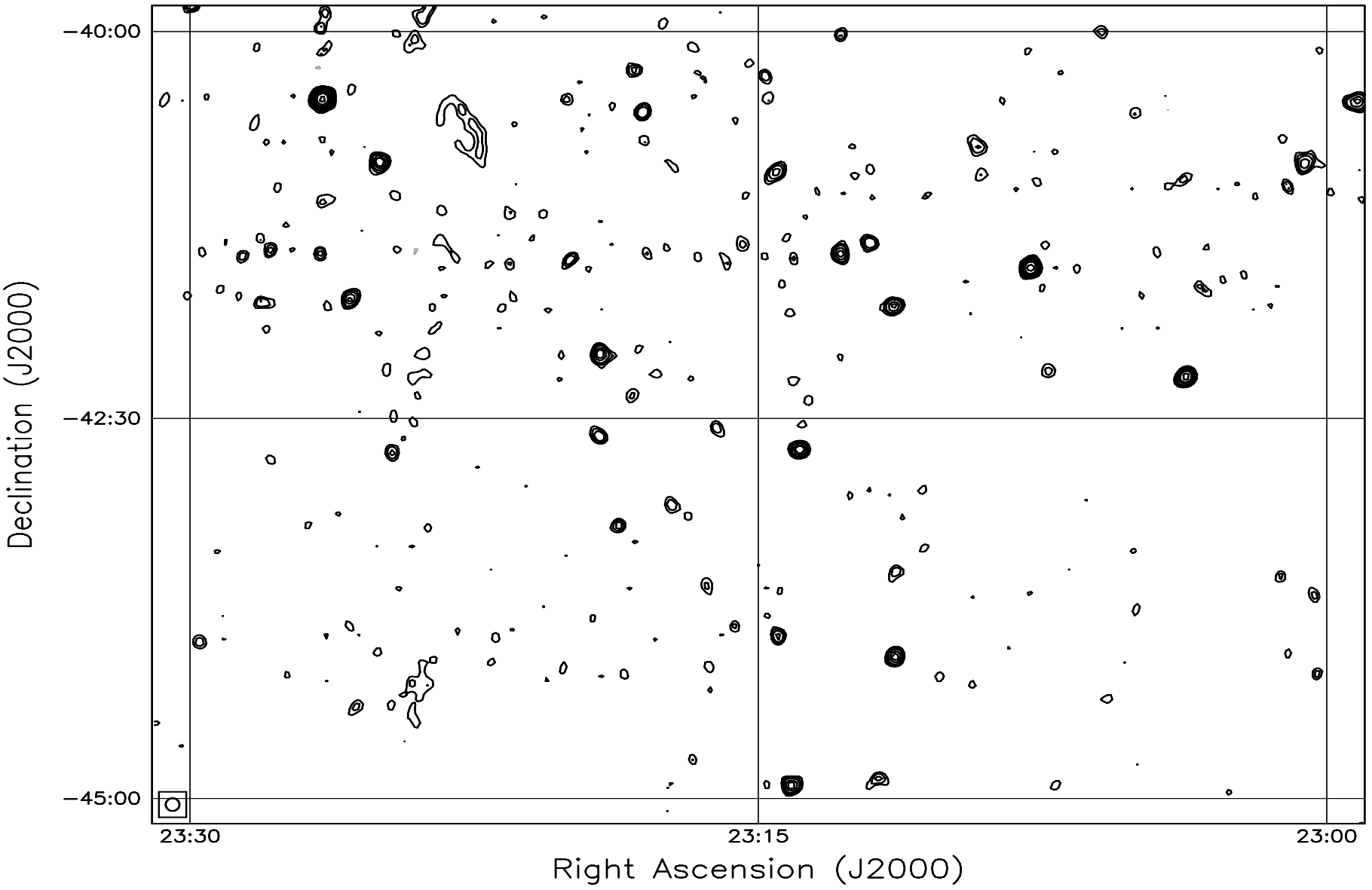

Fig. 7.188: Contour map covering the right ascension range 23h00m to 23h30m and declination range -45° to -40 °. The contour levels are -5, -3.6, -2.5, -1.8, 1, 1.4, 2, 2.8, 3.6, 5, 7, 10, 14, 20, 29, 40, 54, 72, 90, 100, 136, 180, 216, 252, 288 Jy beam^{-1}. The rms noise in the image is ≈290 mJy beam^{-1}.

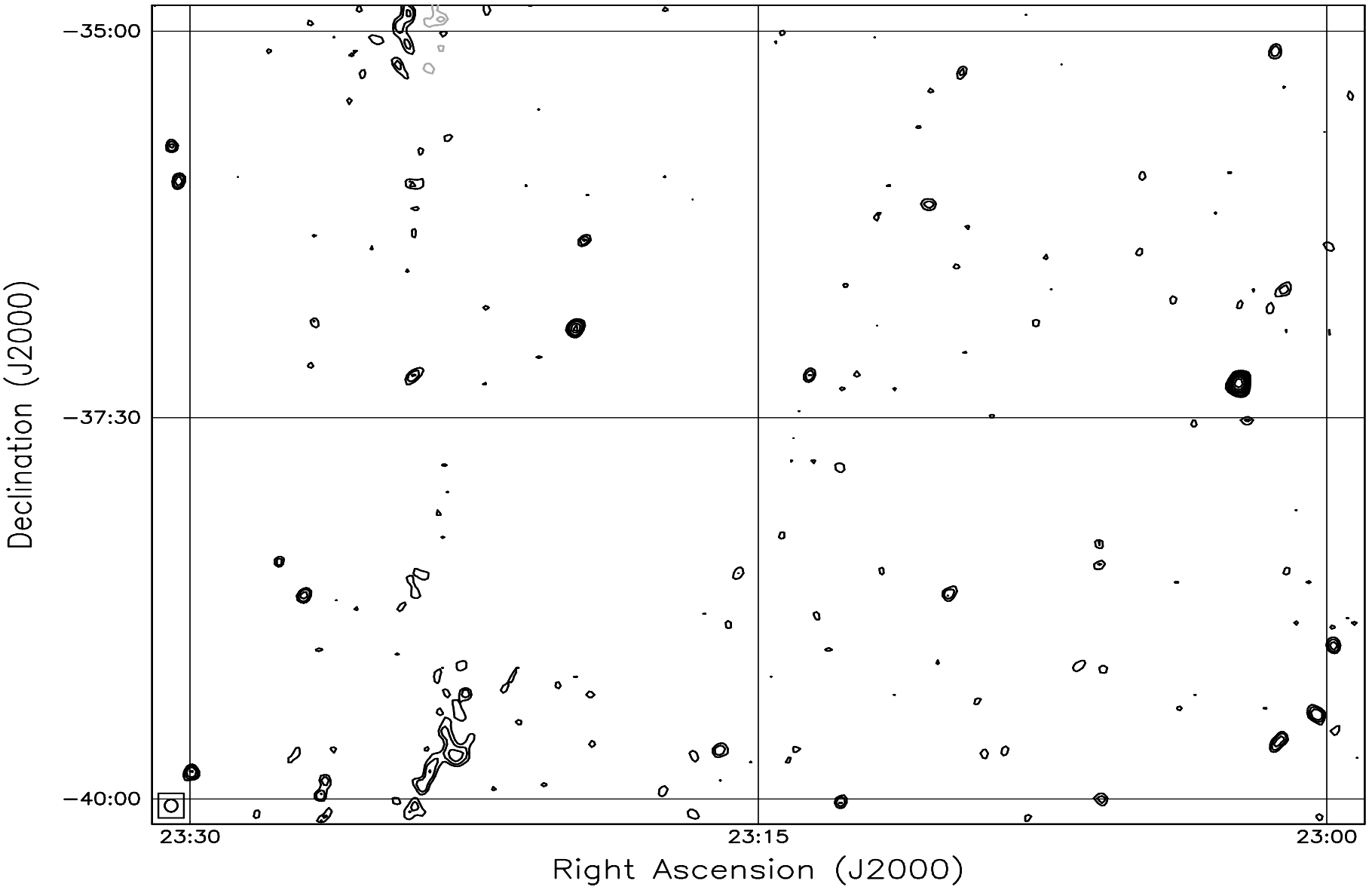

Fig. 7.189: Contour map covering the right ascension range 23h00m to 23h30m and declination range -40° to -35 °. The contour levels are -5, -3.6, -2.5, -1.8, 1, 1.4, 2, 2.8, 3.6, 5, 7, 10, 14, 20, 29, 40, 54, 72, 90, 100, 136, 180, 216, 252, 288 Jy beam^{-1}. The rms noise in the image is ≈300 mJy beam^{-1}.

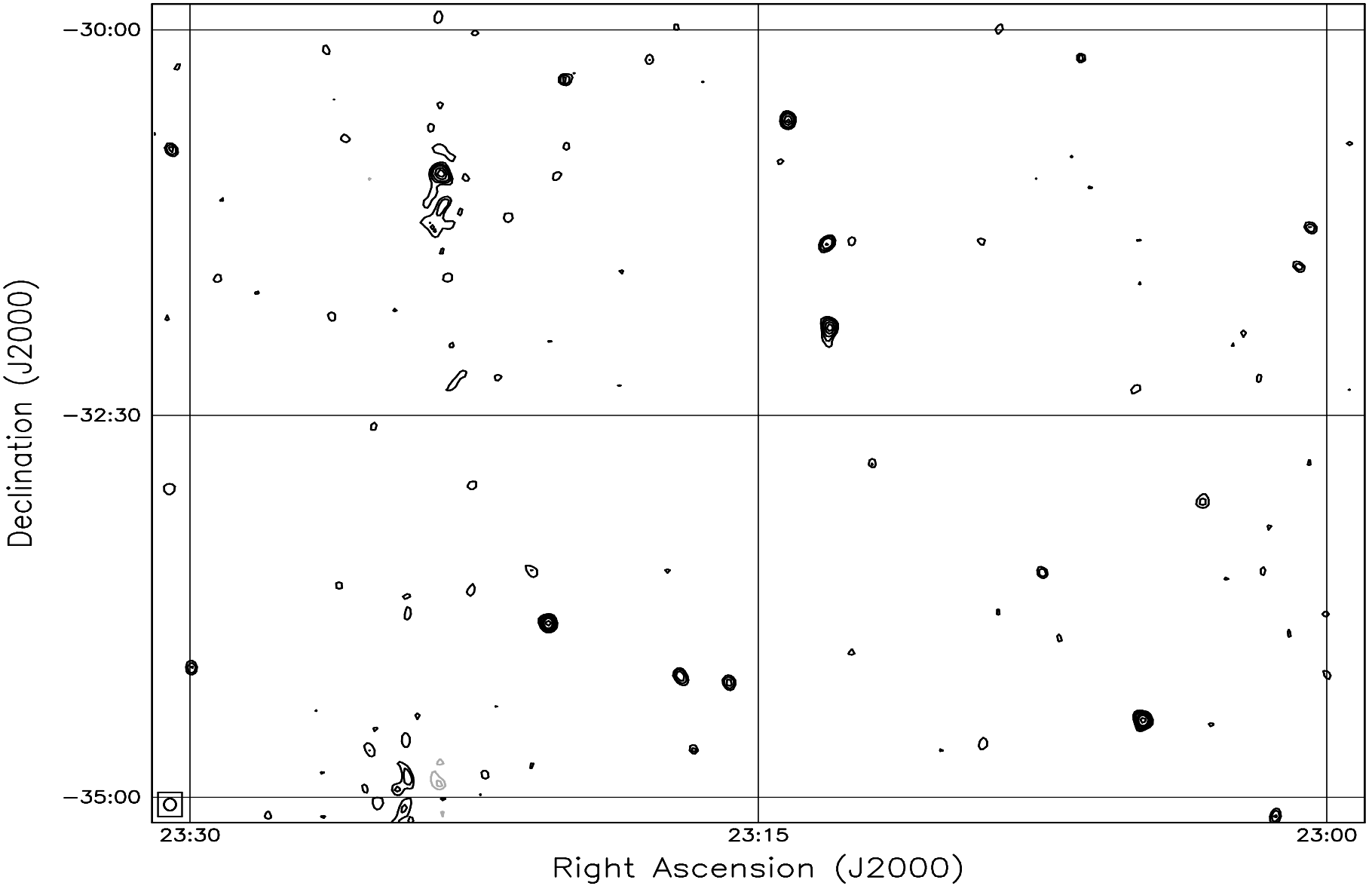

Fig. 7.190: Contour map covering the right ascension range 23h00m to 23h30m and declination range -35° to -30 °. The contour levels are -5, -3.6, -2.5, -1.8, 1, 1.4, 2, 2.8, 3.6, 5, 7, 10, 14, 20, 29, 40, 54, 72, 90, 100, 136, 180, 216, 252, 288 Jy beam^{-1}. The rms noise in the image is ≈310 mJy beam^{-1}.

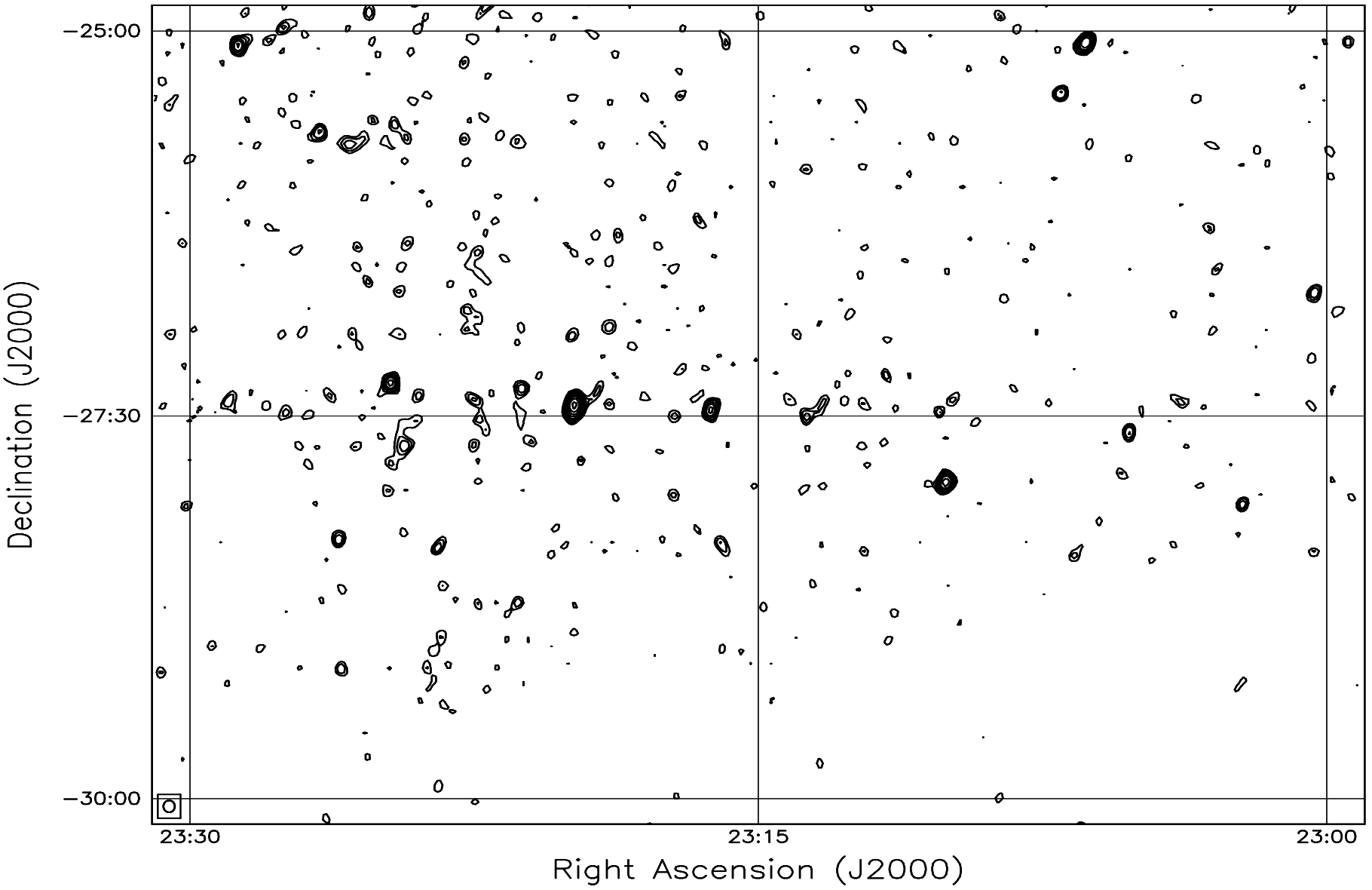

Fig. 7.191: Contour map covering the right ascension range 23h00m to 23h30m and declination range -30° to -25 °. The contour levels are -5, -3.6, -2.5, -1.8, 1, 1.4, 2, 2.8, 3.6, 5, 7, 10, 14, 20, 29, 40, 54, 72, 90, 100, 136, 180, 216, 252, 288 Jy beam^{-1}. The rms noise in the image is ≈330 mJy beam^{-1}.

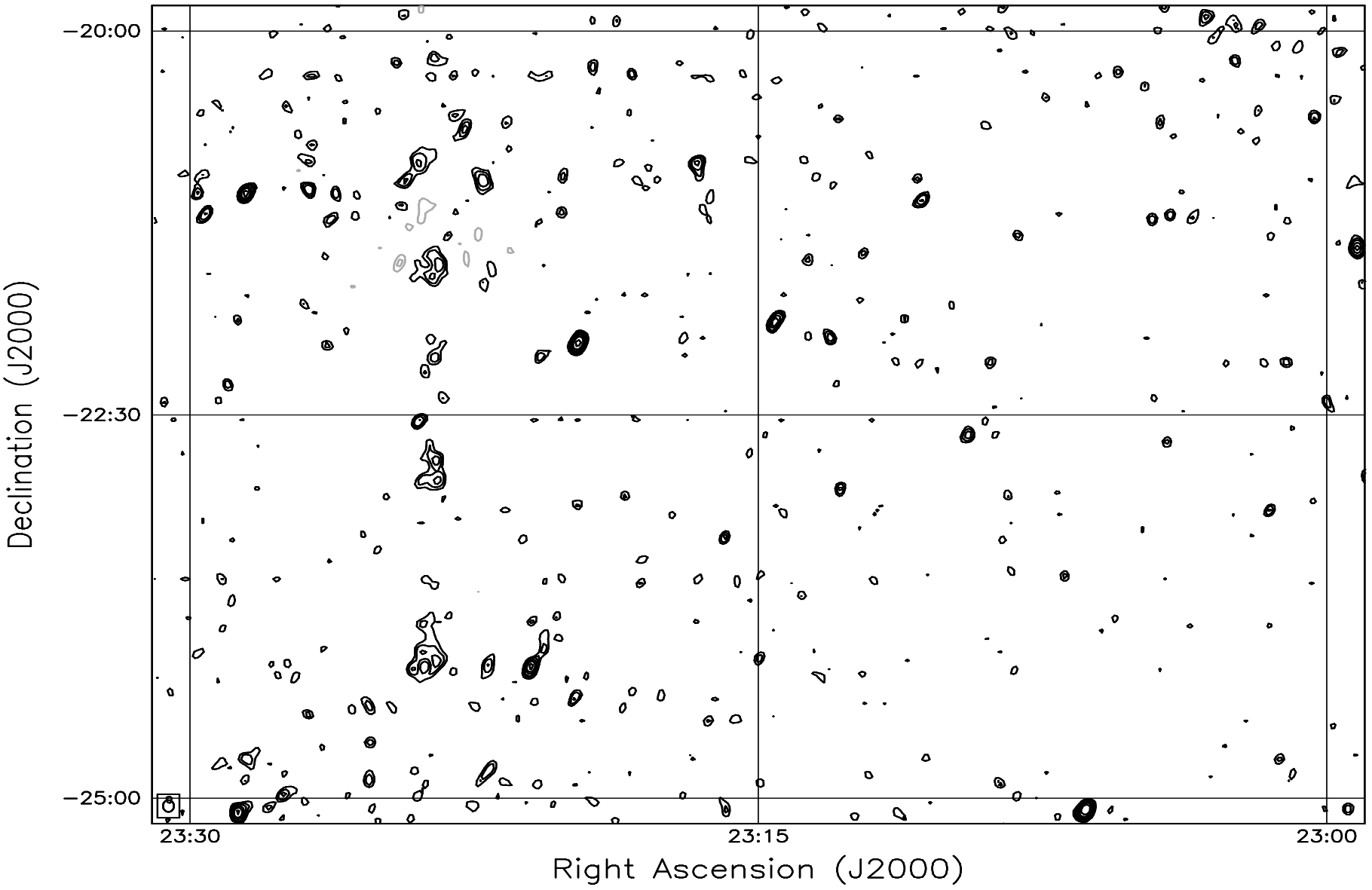

Fig. 7.192: Contour map covering the right ascension range 23h00m to 23h30m and declination range -25° to -20 °. The contour levels are -5, -3.6, -2.5, -1.8, 1, 1.4, 2, 2.8, 3.6, 5, 7, 10, 14, 20, 29, 40, 54, 72, 90, 100, 136, 180, 216, 252, 288 Jy beam^{-1}. The rms noise in the image is ≈365 mJy beam^{-1}.

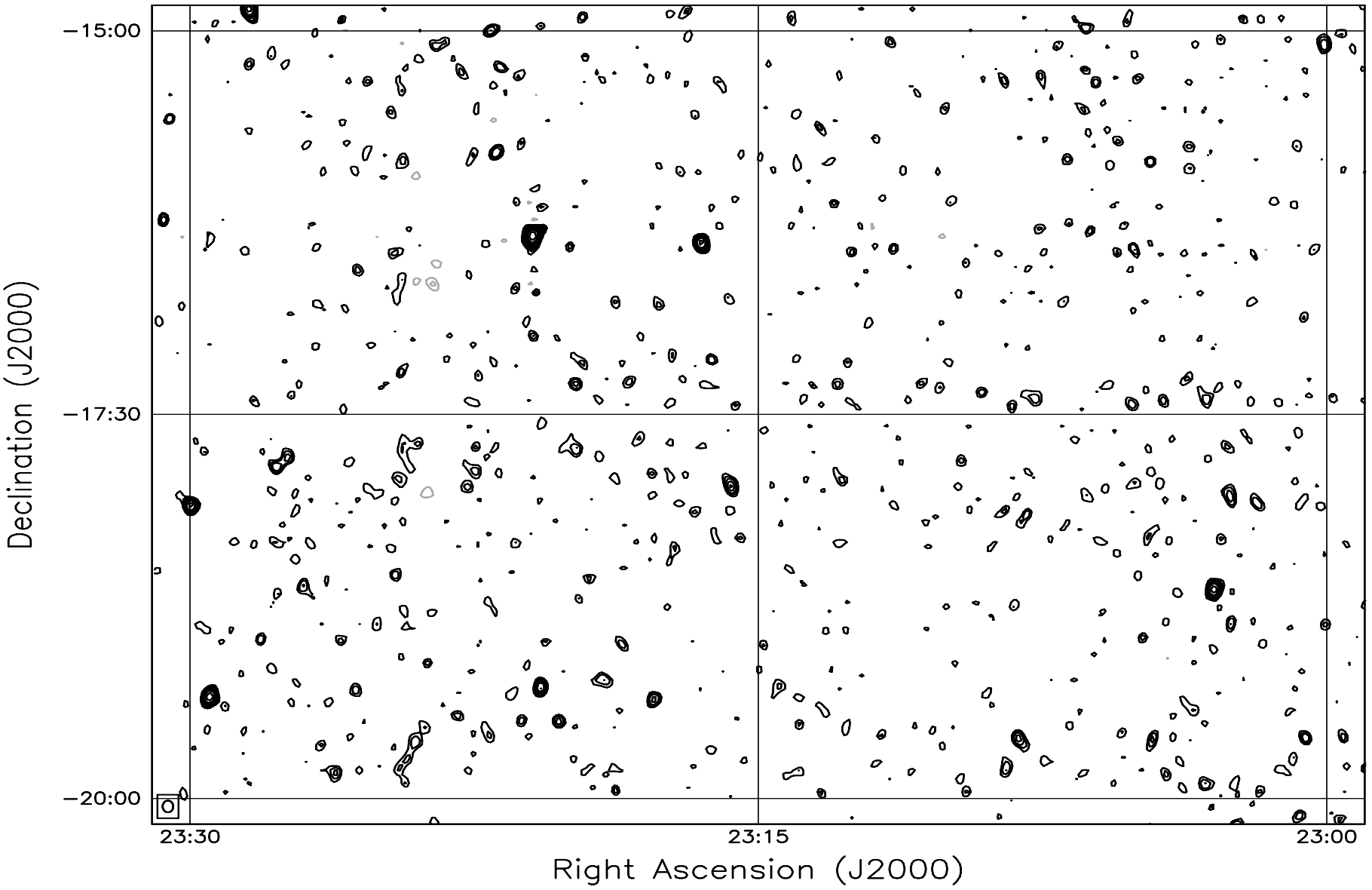

Fig. 7.193: Contour map covering the right ascension range 23h00m to 23h30m and declination range -20° to -15 °. The contour levels are -5, -3.6, -2.5, -1.8, 1, 1.4, 2, 2.8, 3.6, 5, 7, 10, 14, 20, 29, 40, 54, 72, 90, 100, 136, 180, 216, 252, 288 Jy beam^{-1}. The rms noise in the image is ≈420 mJy beam^{-1}.

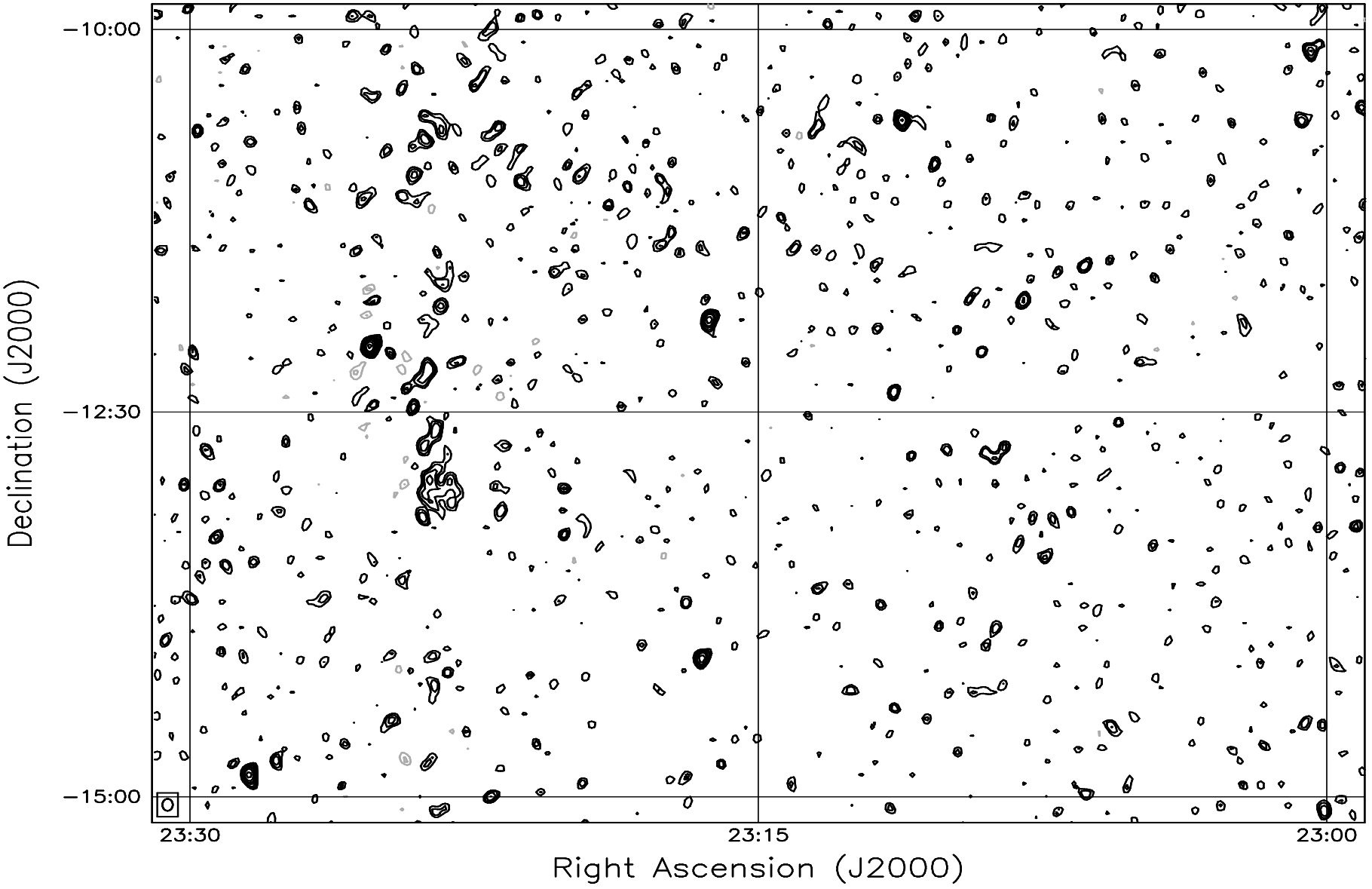

Fig. 7.194: Contour map covering the right ascension range 23h00m to 23h30m and declination range -15° to -10 °. The contour levels are -5, -3.6, -2.5, -1.8, 1, 1.4, 2, 2.8, 3.6, 5, 7, 10, 14, 20, 29, 40, 54, 72, 90, 100, 136, 180, 216, 252, 288 Jy beam^{-1}. The rms noise in the image is ≈510 mJy beam^{-1}.

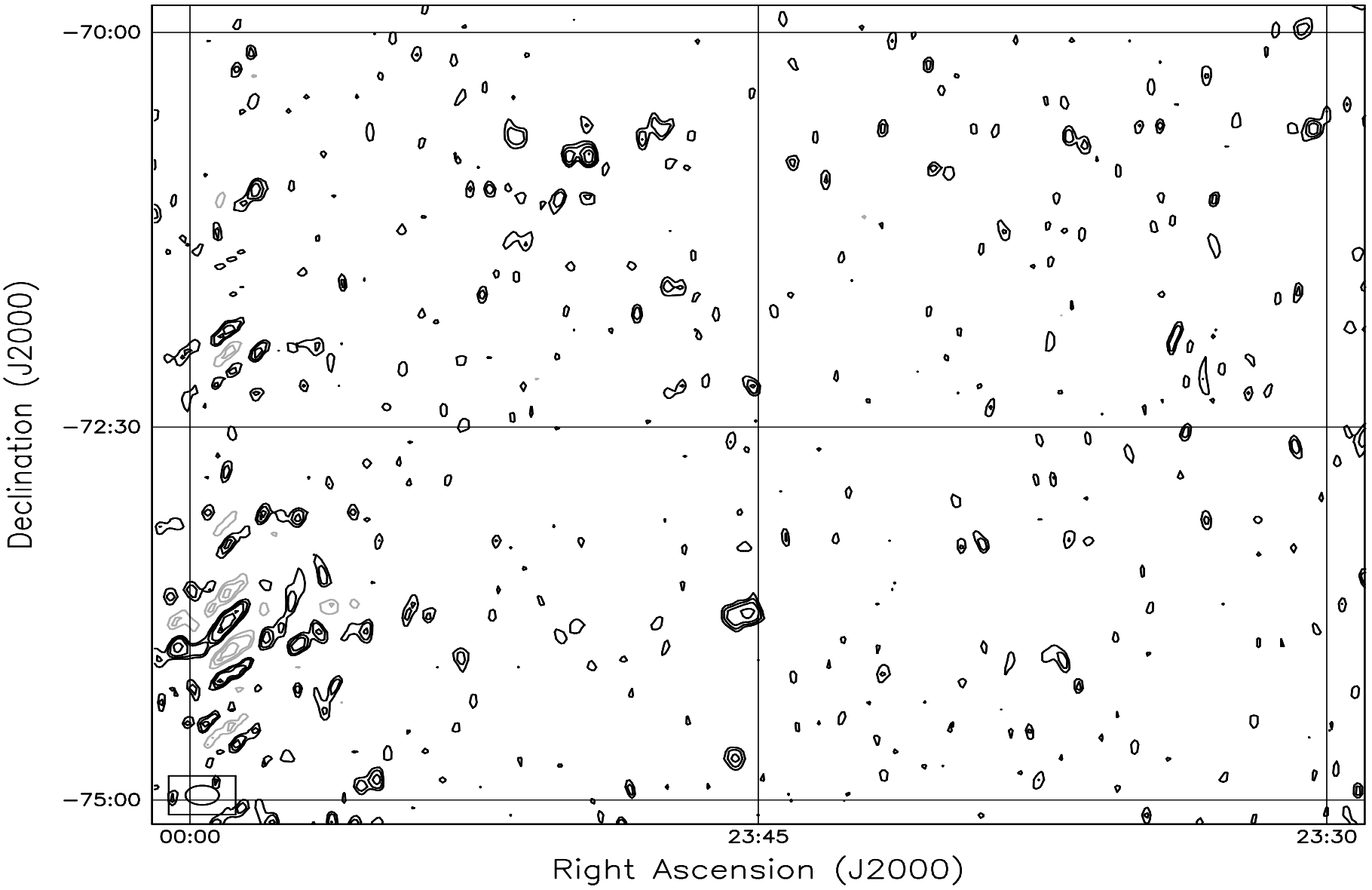

Fig. 7.195: Contour map covering the right ascension range 23h30m to 00h00m and declination range -75° to -70 °. The contour levels are -5, -3.6, -2.5, -1.8, 1, 1.4, 2, 2.8, 3.6, 5, 7, 10, 14, 20, 29, 40, 54, 72, 90, 100, 136, 180, 216, 252, 288 Jy beam^{-1}. The rms noise in the image is ≈425 mJy beam^{-1}.

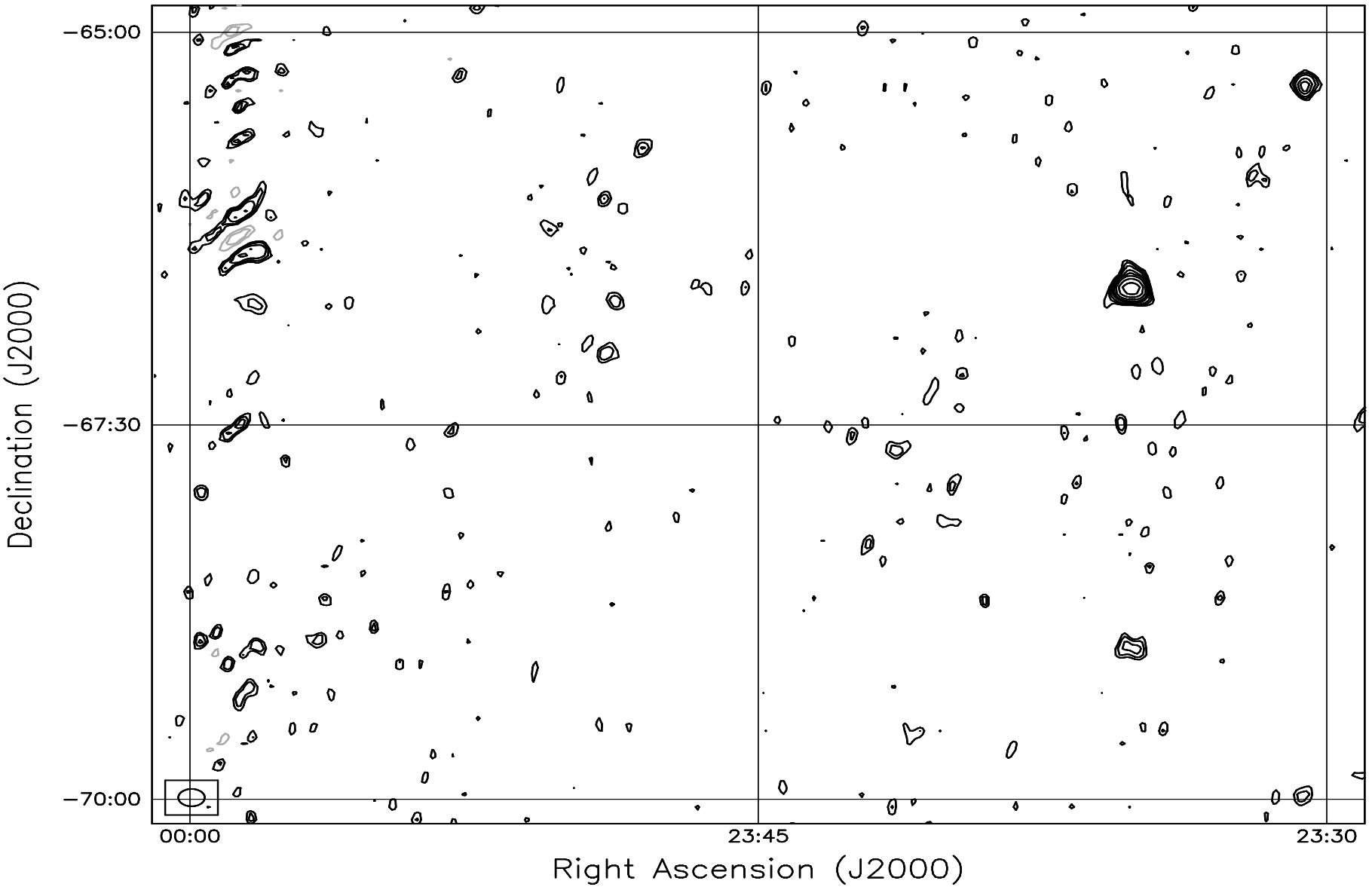

Fig. 7.196: Contour map covering the right ascension range 23h30m to 00h00m and declination range -70° to -65 °. The contour levels are -5, -3.6, -2.5, -1.8, 1, 1.4, 2, 2.8, 3.6, 5, 7, 10, 14, 20, 29, 40, 54, 72, 90, 100, 136, 180, 216, 252, 288 Jy beam^{-1}. The rms noise in the image is ≈370 mJy beam^{-1}.

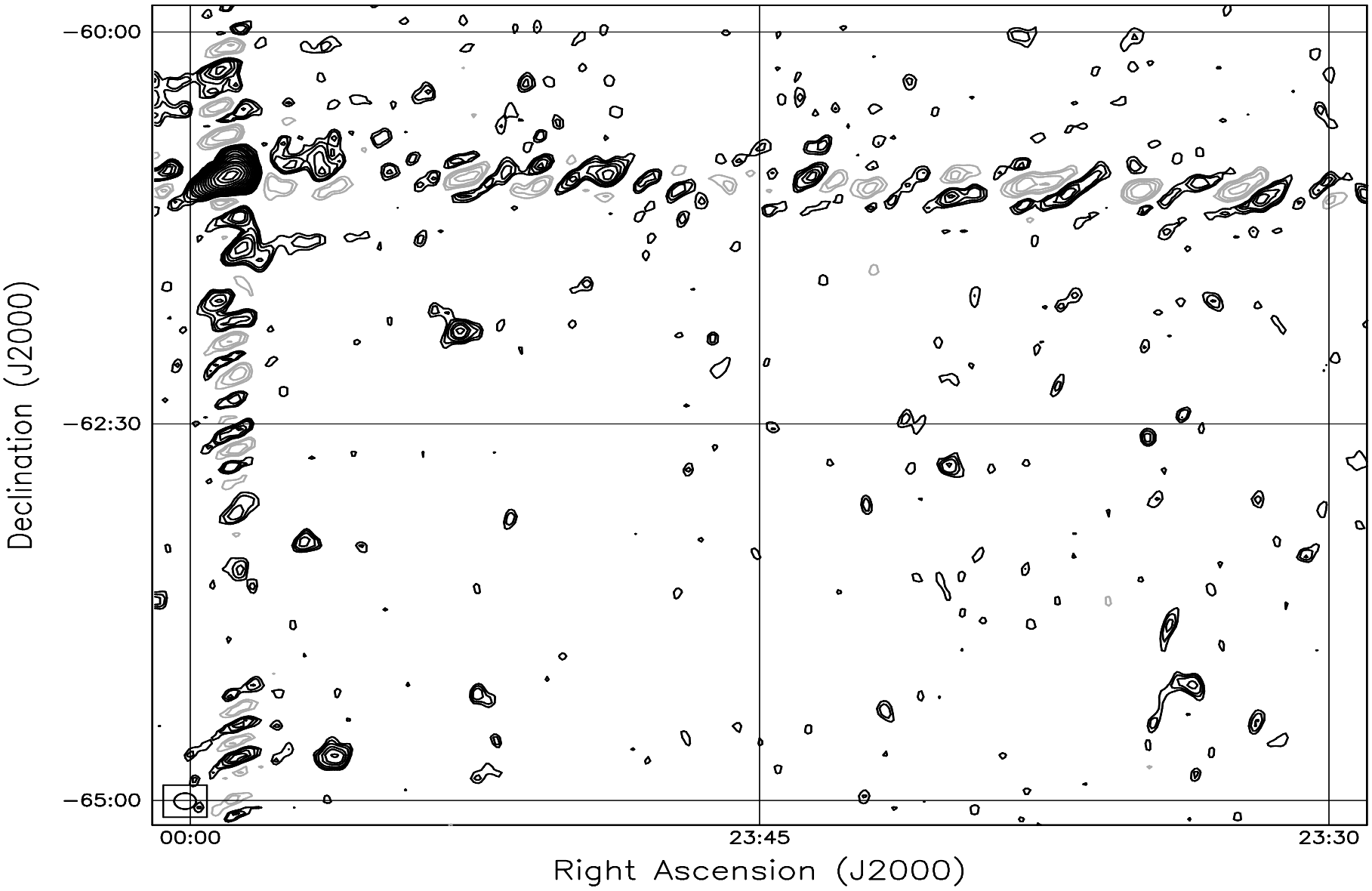

Fig. 7.197: Contour map covering the right ascension range 23h30m to 00h00m and declination range -65° to -60 °. The contour levels are -5, -3.6, -2.5, -1.8, 1, 1.4, 2, 2.8, 3.6, 5, 7, 10, 14, 20, 29, 40, 54, 72, 90, 100, 136, 180, 216, 252, 288 Jy beam^{-1}. The rms noise in the image is ≈330 mJy beam^{-1}.

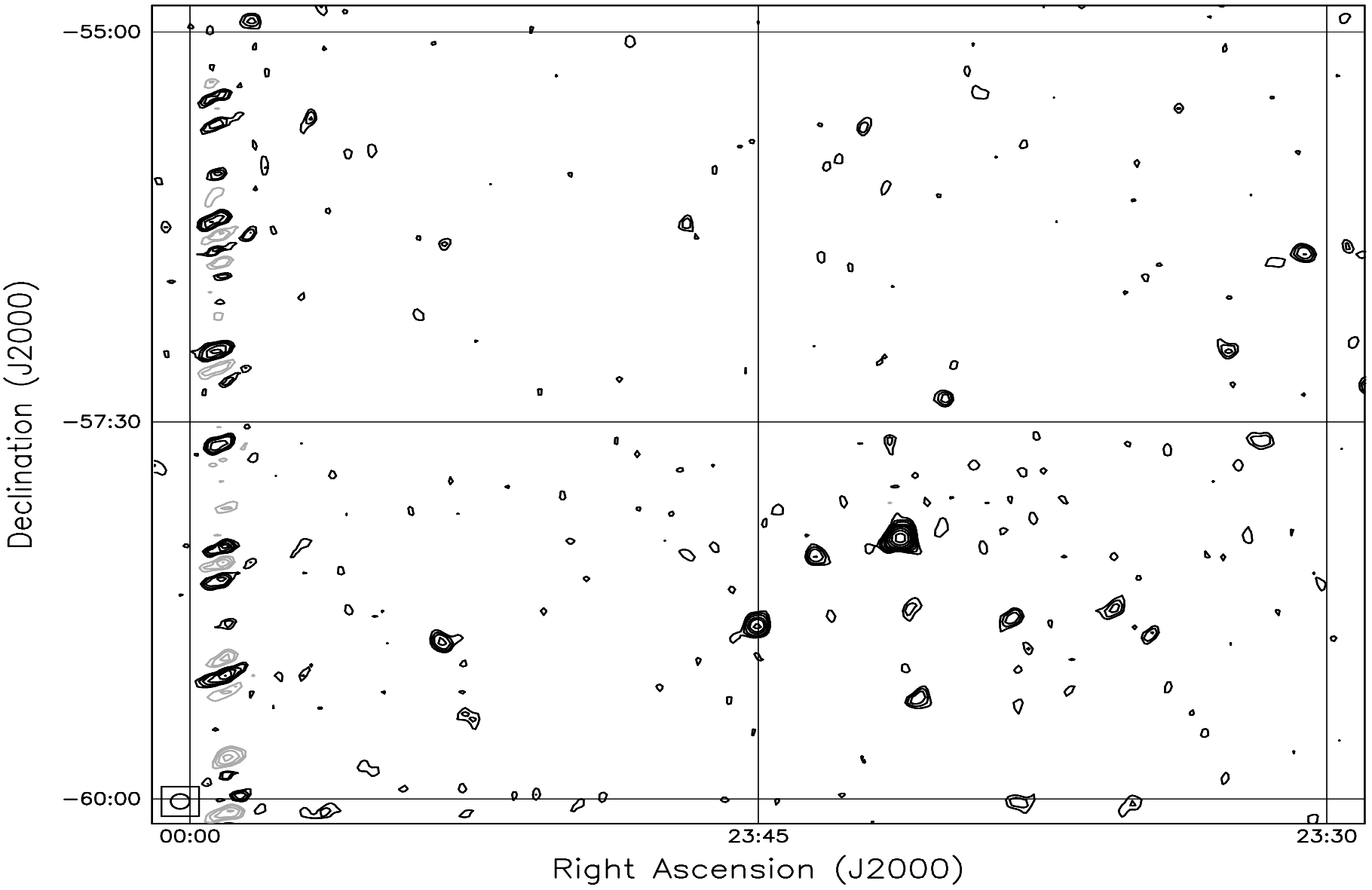

Fig. 7.198: Contour map covering the right ascension range 23h30m to 00h00m and declination range -60° to -55 °. The contour levels are -5, -3.6, -2.5, -1.8, 1, 1.4, 2, 2.8, 3.6, 5, 7, 10, 14, 20, 29, 40, 54, 72, 90, 100, 136, 180, 216, 252, 288 Jy beam^{-1}. The rms noise in the image is ≈310 mJy beam^{-1}.

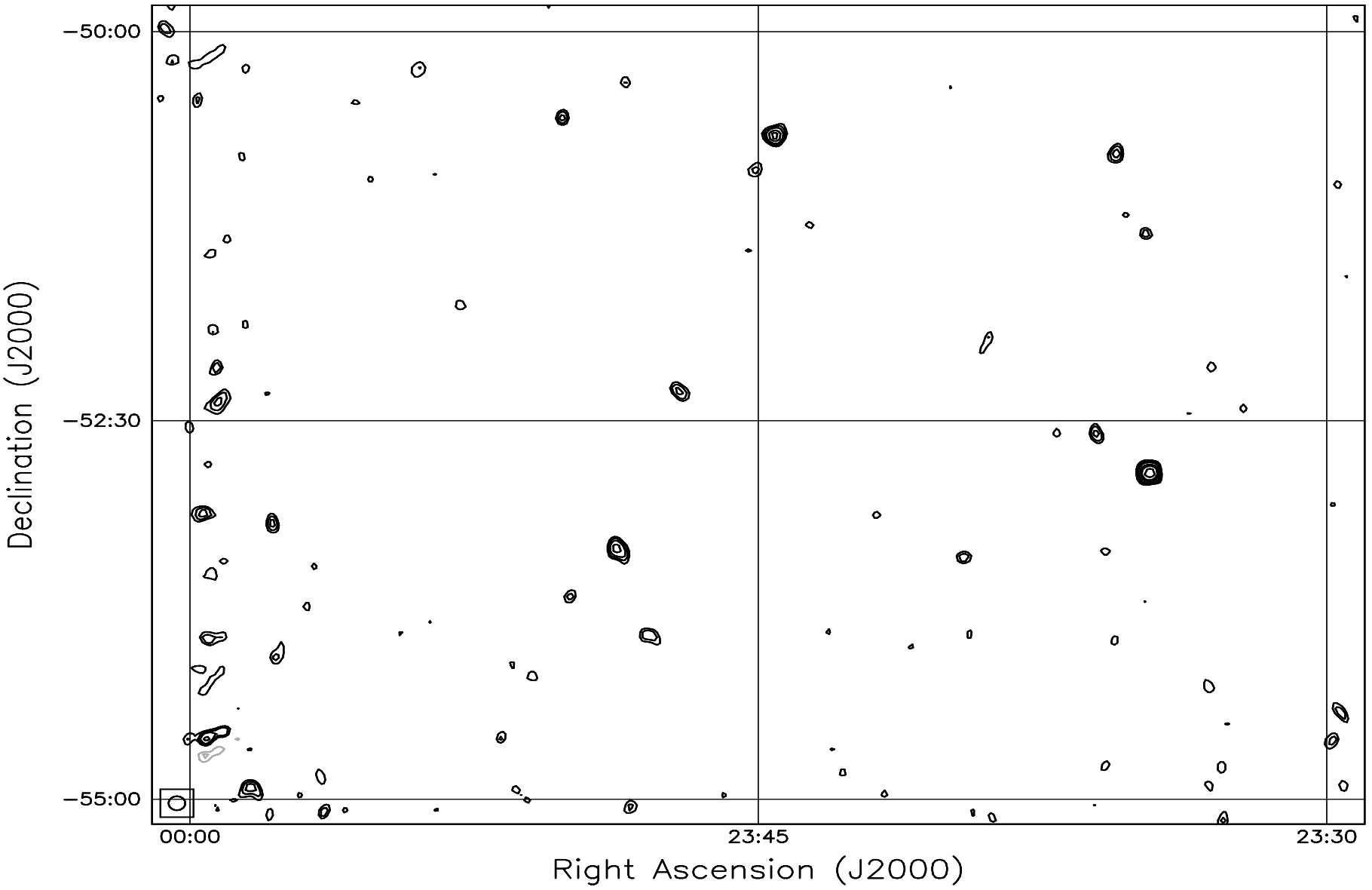

Fig. 7.199: Contour map covering the right ascension range 23h30m to 00h00m and declination range -55° to -50 °. The contour levels are -5, -3.6, -2.5, -1.8, 1, 1.4, 2, 2.8, 3.6, 5, 7, 10, 14, 20, 29, 40, 54, 72, 90, 100, 136, 180, 216, 252, 288 Jy beam^{-1}. The rms noise in the image is ≈300 mJy beam^{-1}.

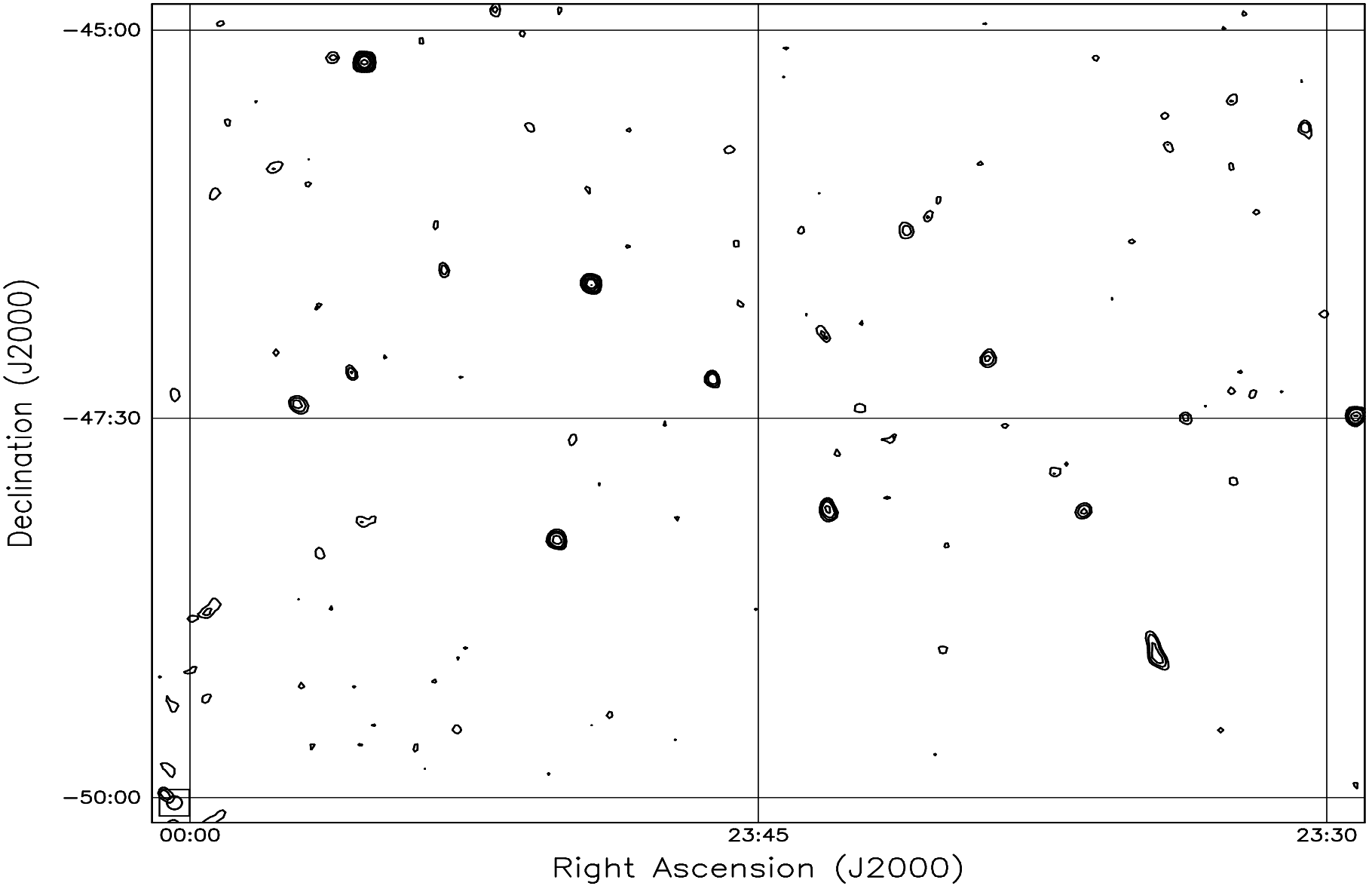

Fig. 7.200: Contour map covering the right ascension range 23h30m to 00h00m and declination range -50° to -45 °. The contour levels are -5, -3.6, -2.5, -1.8, 1, 1.4, 2, 2.8, 3.6, 5, 7, 10, 14, 20, 29, 40, 54, 72, 90, 100, 136, 180, 216, 252, 288 Jy beam^{-1}. The rms noise in the image is ≈290 mJy beam^{-1}.

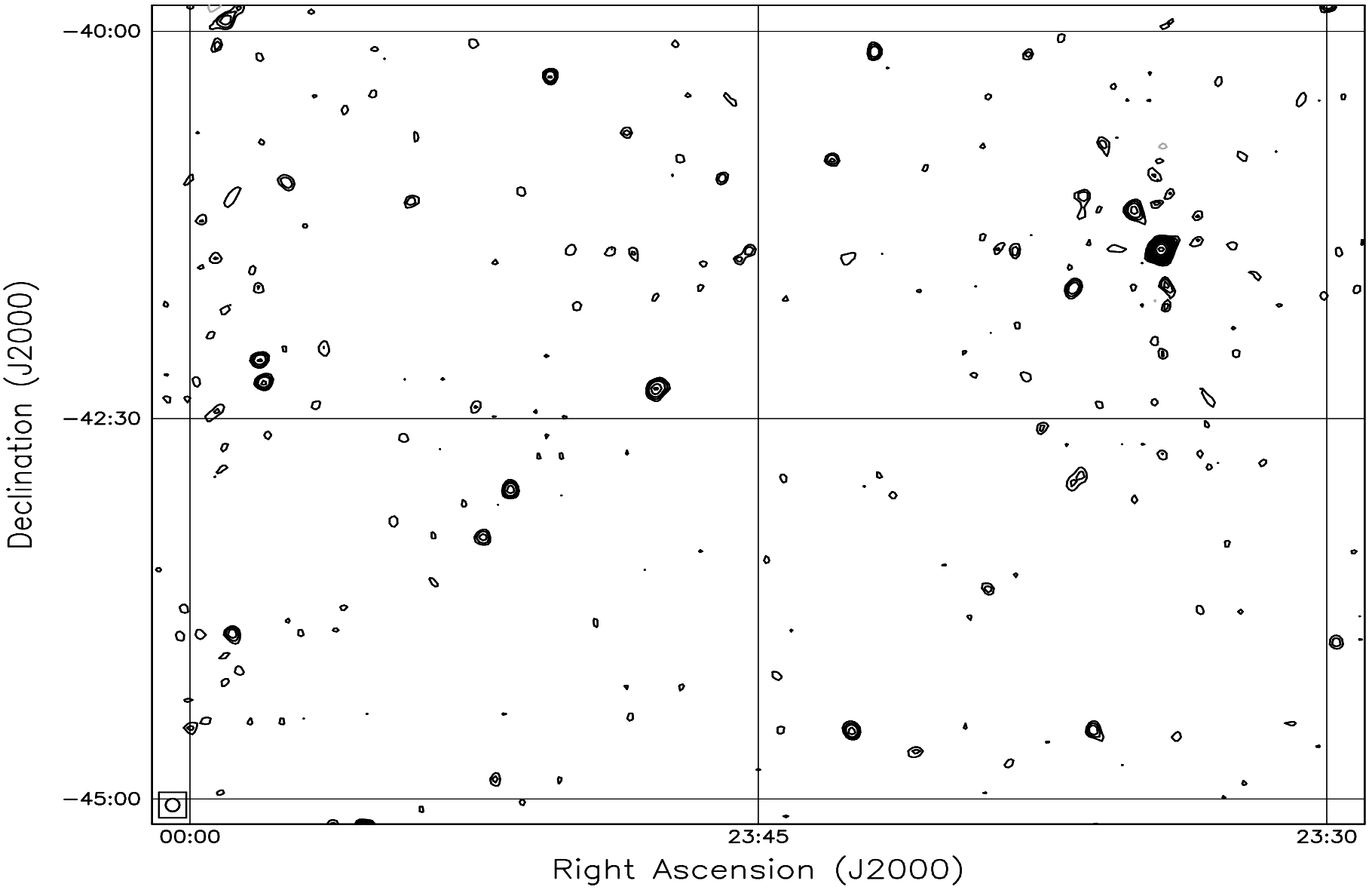

Fig. 7.201: Contour map covering the right ascension range 23h30m to 00h00m and declination range -45° to -40 °. The contour levels are -5, -3.6, -2.5, -1.8, 1, 1.4, 2, 2.8, 3.6, 5, 7, 10, 14, 20, 29, 40, 54, 72, 90, 100, 136, 180, 216, 252, 288 Jy beam^{-1}. The rms noise in the image is ≈290 mJy beam^{-1}.

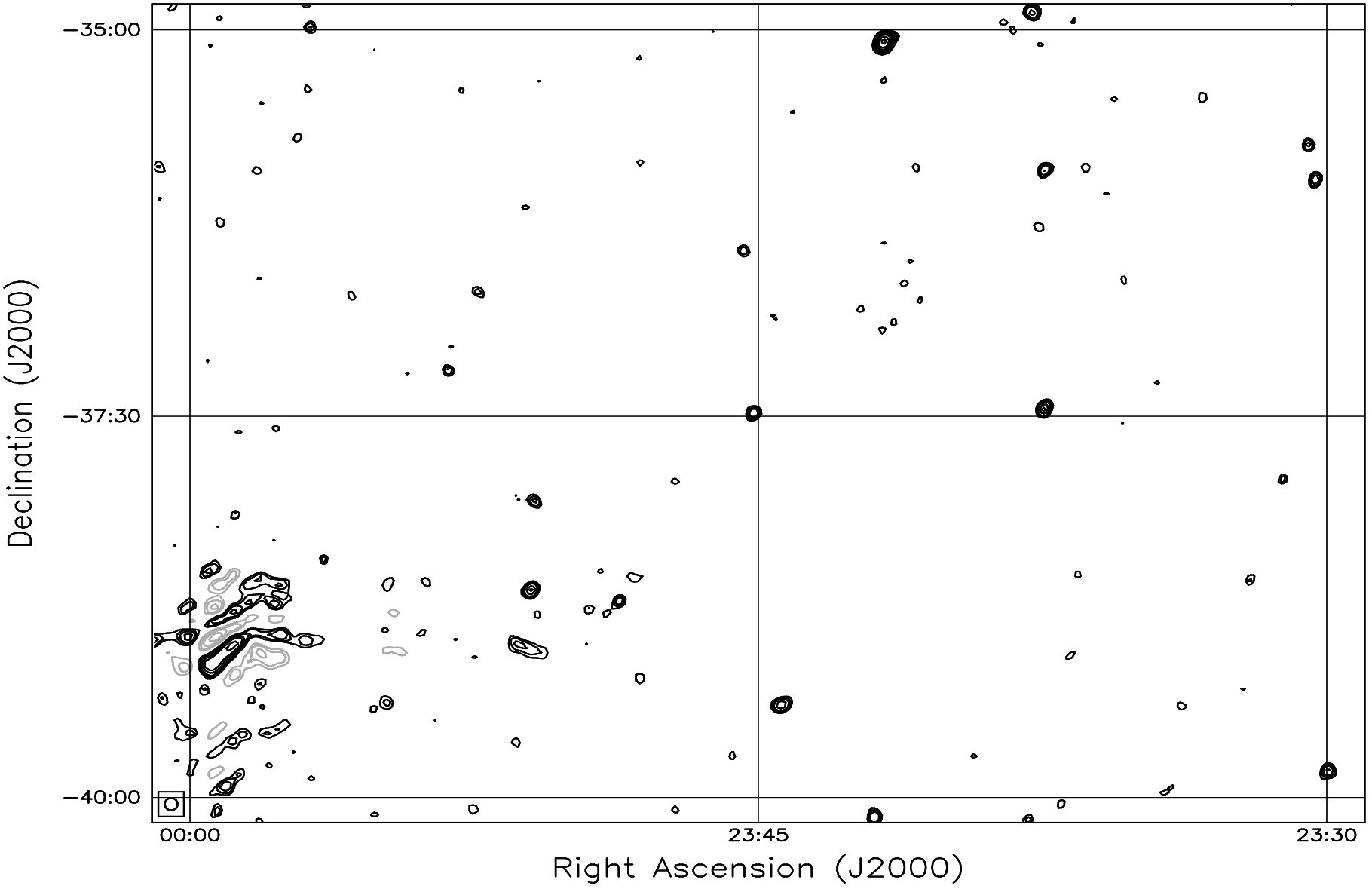

Fig. 7.202: Contour map covering the right ascension range 23h30m to 00h00m and declination range -40° to -35 °. The contour levels are -5, -3.6, -2.5, -1.8, 1, 1.4, 2, 2.8, 3.6, 5, 7, 10, 14, 20, 29, 40, 54, 72, 90, 100, 136, 180, 216, 252, 288 Jy beam^{-1}. The rms noise in the image is ≈300 mJy beam^{-1}.

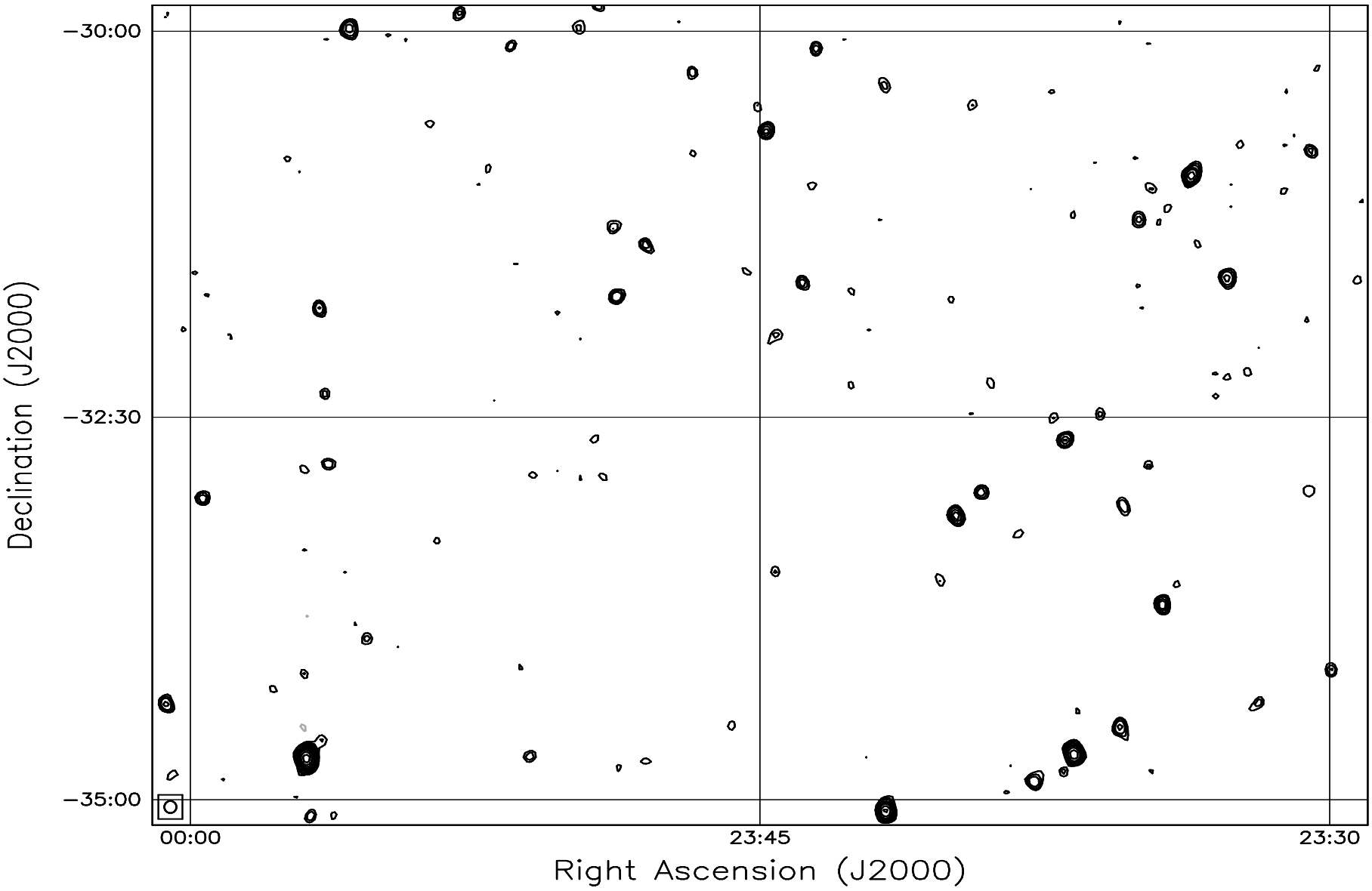

Fig. 7.203: Contour map covering the right ascension range 23h30m to 00h00m and declination range -35° to -30 °. The contour levels are -5, -3.6, -2.5, -1.8, 1, 1.4, 2, 2.8, 3.6, 5, 7, 10, 14, 20, 29, 40, 54, 72, 90, 100, 136, 180, 216, 252, 288 Jy beam^{-1}. The rms noise in the image is ≈310 mJy beam^{-1}.

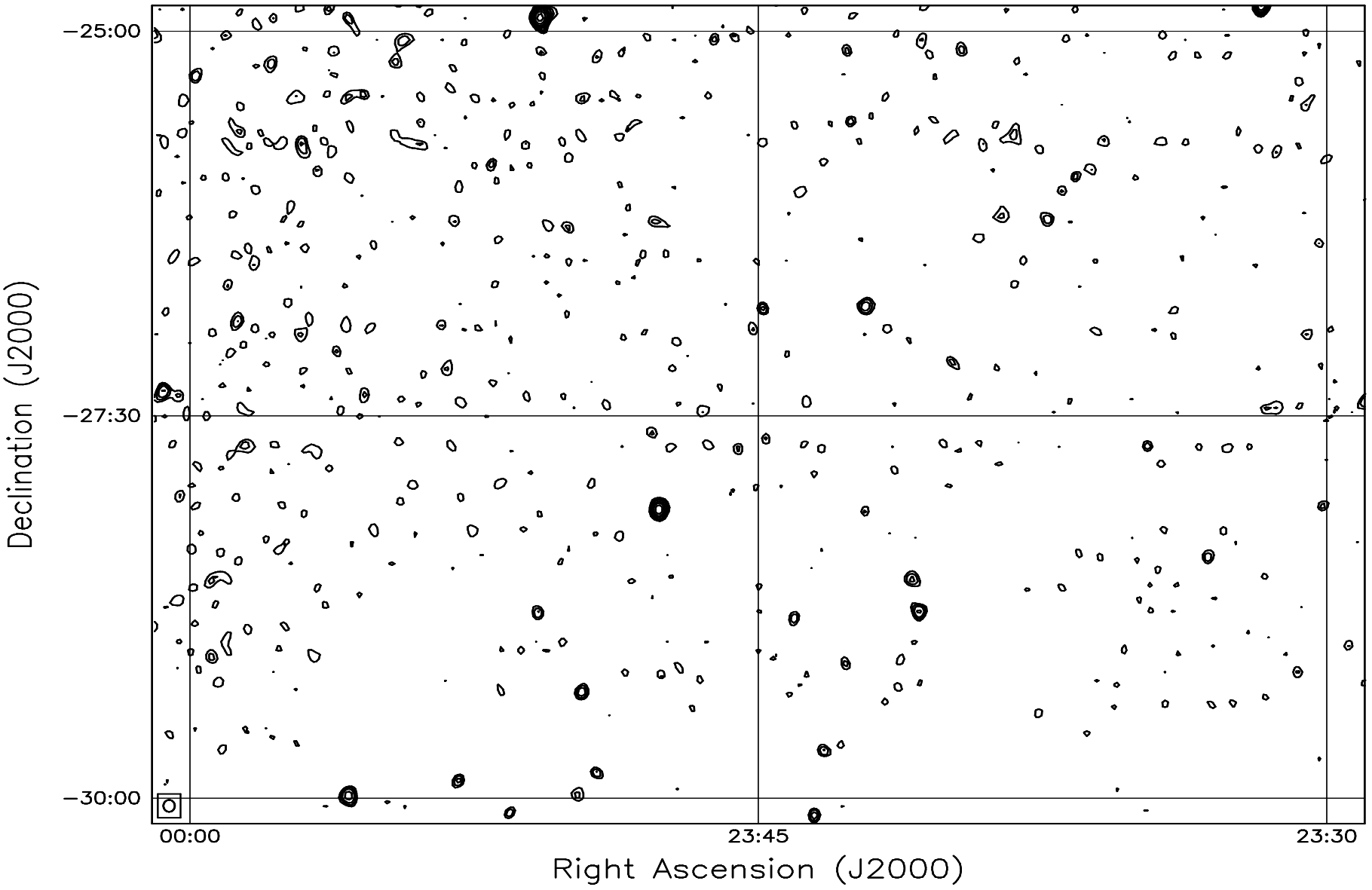

Fig. 7.204: Contour map covering the right ascension range 23h30m to 00h00m and declination range -30° to -25 °. The contour levels are -5, -3.6, -2.5, -1.8, 1, 1.4, 2, 2.8, 3.6, 5, 7, 10, 14, 20, 29, 40, 54, 72, 90, 100, 136, 180, 216, 252, 288 Jy beam^{-1}. The rms noise in the image is ≈330 mJy beam^{-1}.

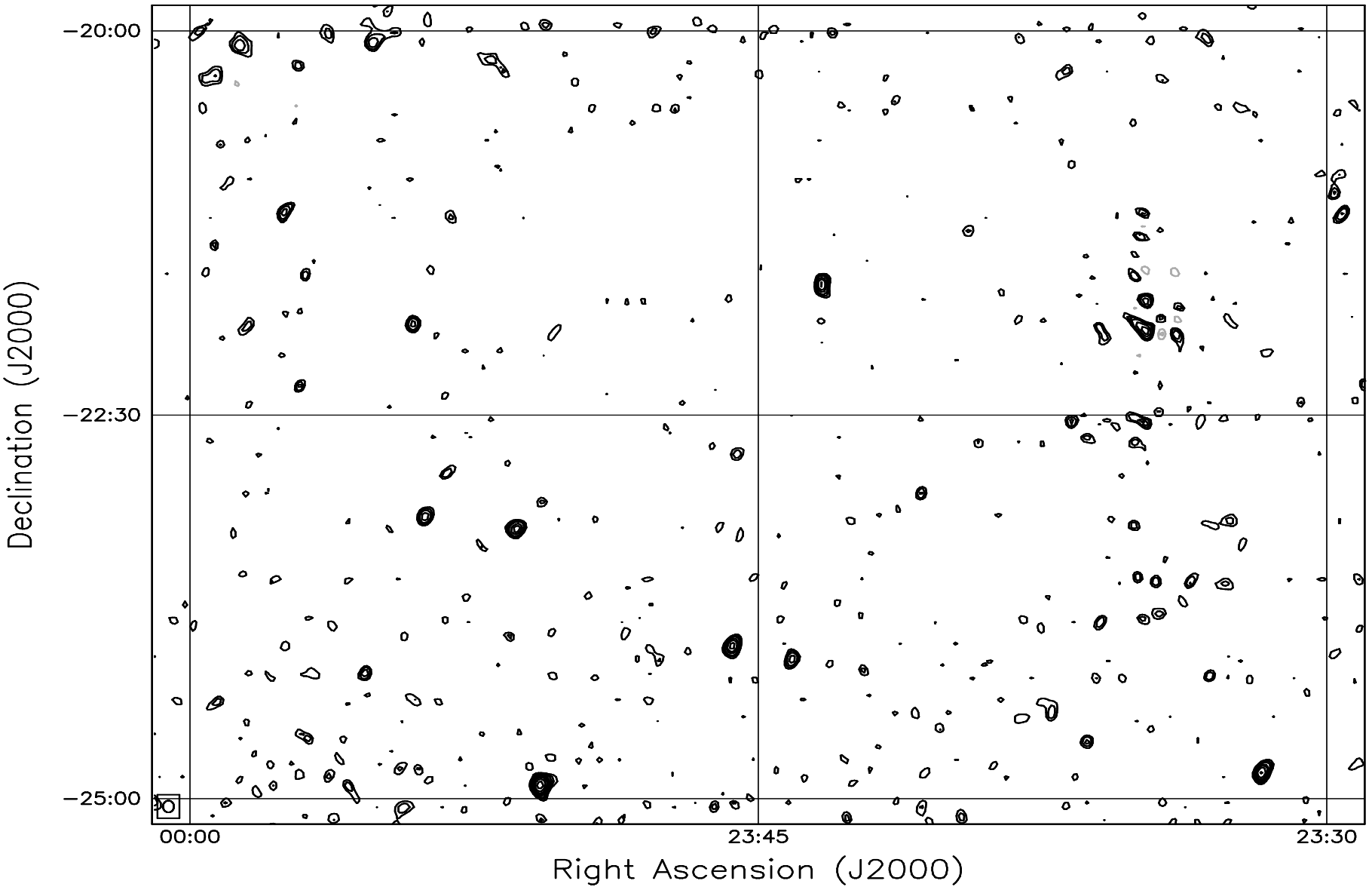

Fig. 7.205: Contour map covering the right ascension range 23h30m to 00h00m and declination range -25° to -20 °. The contour levels are -5, -3.6, -2.5, -1.8, 1, 1.4, 2, 2.8, 3.6, 5, 7, 10, 14, 20, 29, 40, 54, 72, 90, 100, 136, 180, 216, 252, 288 Jy beam^{-1}. The rms noise in the image is ≈365 mJy beam^{-1}.

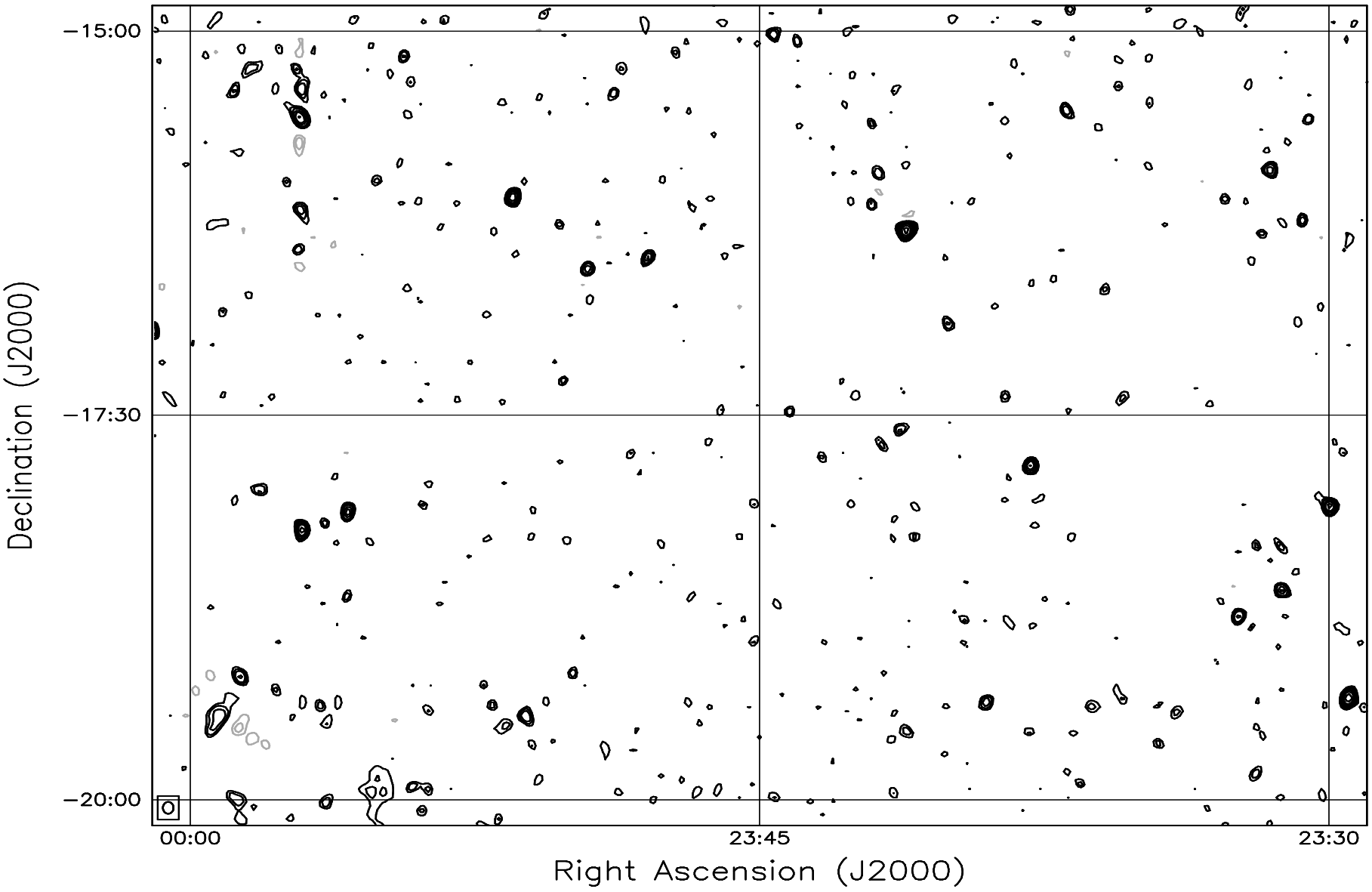

Fig. 7.206: Contour map covering the right ascension range 23h30m to 00h00m and declination range -20° to -15 °. The contour levels are -5, -3.6, -2.5, -1.8, 1, 1.4, 2, 2.8, 3.6, 5, 7, 10, 14, 20, 29, 40, 54, 72, 90, 100, 136, 180, 216, 252, 288 Jy beam^{-1}. The rms noise in the image is ≈420 mJy beam^{-1}.

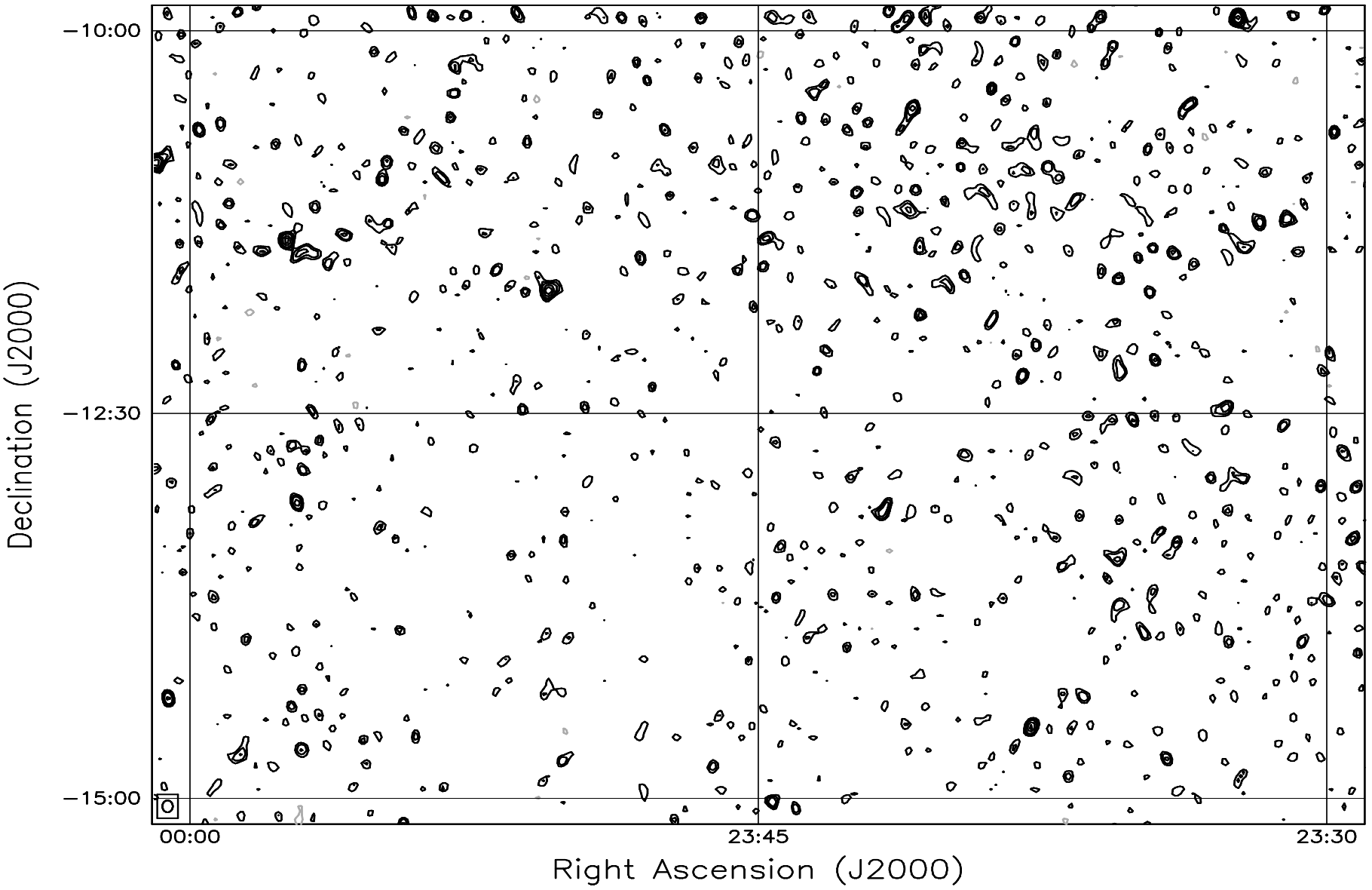

Fig. 7.207: Contour map covering the right ascension range 23h30m to 00h00m and declination range -15° to -10 °. The contour levels are -5, -3.6, -2.5, -1.8, 1, 1.4, 2, 2.8, 3.6, 5, 7, 10, 14, 20, 29, 40, 54, 72, 90, 100, 136, 180, 216, 252, 288 Jy beam^{-1}. The rms noise in the image is ≈510 mJy beam^{-1}.